nature

www.nature.com/nature

Vol 461 | Issue no. 7266 | 15 October 2009

Psychology: a reality check

If clinical psychology in the United States wants to remain viable and relevant in today's health systems, it needs to publicly embrace science.

Anyone reading Sigmund Freud's original works might well be seduced by the beauty of his prose, the elegance of his arguments and the acuity of his intuition. But those with a grounding in science will also be shocked by the abandon with which he elaborated his theories on the basis of essentially no empirical evidence. This is one of the main reasons why Freudian-style psychoanalysis has long since fallen out of fashion: its huge expense — treatment can stretch over years — is not balanced by evidence of efficacy.

Clinical psychology at least has its roots in experimentation, but it is drifting away from science. Concerns about cost–benefit issues are growing, especially in the United States. According to a damning report published last week (T. B. Baker *et al. Psychol. Sci. Public Interest* **9,** 67–103; 2008), an alarmingly high proportion of practitioners consider scientific evidence to be less important than their personal — that is, subjective — clinical experience.

The irony is that, during the past 20 years, science has made great strides in directions that could support clinical psychology — in neuroimaging, for example, as well as molecular and behavioural genetics, and cognitive neuroscience. Numerous psychological interventions have been proved to be both effective and relatively cheap. Yet many psychologists continue to use unproven therapies that have no clear outcome measures — including, in extreme cases, such highly suspect regimens as 'dolphin-assisted therapy'.

The situation has created tensions within the American Psychological Association (APA), the body that accredits the courses leading to qualification for a clinical psychologist to practise in the United States and Canada. The APA requires that such courses have a scientific component, but it does not require that science be as central as some members would like. In frustration, representatives of some two-dozen top research-focused graduate-training programmes grouped together in 1994 to form the Academy of Psychological Clinical Science (APCS), with a mission to promote scientific psychology.

The APCS effort has not been enough to change attitudes among all practitioners. But, in the United States, political pressure for change is building rapidly. The debates swirling around health-care reform have made it clear that key decision-makers expect medical caregivers to justify their therapies in terms of proven cost-effectiveness. If clinical psychologists cannot do this plausibly, they will be marginalized.

> "There is a moral imperative to turn psychology into a robust and valued science."

A quick and effective way to break this impasse would be to create a US version of the system that transformed clinical psychology (and medical practice generally) in England and Wales. There, the National Institute for Health and Clinical Excellence (NICE) evaluates therapies for evidence of efficacy, and approves the ones to be covered by the state health system (see *Nature* **461,** 336–339; 2009). Private health insurers are influenced by NICE's decisions, and any clinical psychologist wishing to offer dolphin-assisted therapy in Britain will be hard-pushed to find patients.

For many opponents of health-care reform in the United States, however, NICE represents the epitome of big-government intrusion into individual freedom of choice; it remains to be seen whether such a body can ever be created in America. Still, as Baker *et al.* point out, interested US psychologists could take matters into their own hands by establishing a new accreditation system for scientifically trained psychologists in parallel with the APA system.

The APCS is well-positioned to take such a step. But whoever takes it should do so soon. Unmet mental-health needs are massive and growing: the number of Americans receiving mental-health care has almost doubled in the past 20 years. There is a moral imperative to turn the craft of psychology — in danger of falling, Freud-like, out of fashion — into a robust and valued science informed by the best available research and economic evidence. ■

Windfall warning

Without forward planning, the billions of dollars in the US stimulus package will go to long-term waste.

In a week that would be capped by winning the Nobel Peace Prize, US President Barack Obama hosted public events celebrating the winners of the National Medal of Science and the National Medal of Technology and Innovation, as well as the White House's first-ever stargazing party. The week before that, Obama visited the campus of the National Institutes of Health (NIH) in Bethesda, Maryland, to announce that the agency had distributed half of the extra US$10.4 billion that Congress awarded it in February in the $787-billion stimulus bill.

Indeed, Obama has made the promotion of science and technology — and evidence-based decision-making — a frequent theme of his young presidency, and most US researchers consider this a refreshing contrast to the previous administration. But they would be wise to remind themselves that Congress, not the president, is in charge of most of the key issues affecting American research. And in particular, the stimulus money that Congress has funnelled into science this year and next has the potential to create a long-term problem.

In the short term, the stimulus bill passed last February has poured billions of dollars into the research agencies (see page 856), with the largest chunk going to the Department of Energy for much-needed programmes in energy efficiency, environmental clean-up and research. At other agencies, such as the NIH and the National Science

Foundation (NSF), stimulus money has allowed managers to fund a backlog of individual grants and accelerate planning for major infrastructure projects such as the NSF's real-time ocean observatory (see go.nature.com/aV6ZIF).

This is all to the good. The problem, however, is that the party will soon be over: the unexpected influx of funds will largely end a year from now. US science as a whole could all too easily hurtle over the same cliff from which the NIH fell in 2003, when a doubling of its budget over five years came to a sudden end and young investigators who had been drawn into the research pipeline during the boom years suddenly found themselves scrambling for grants in hyper-competitive lean years.

The Obama administration is hoping to avoid a repeat of that meltdown by asking Congress to double the budgets of basic-research agencies over ten years — presumably a more sustainable pace of increase. But it's far from clear whether Congress will grant such a request, or even whether such funds are warranted. In fact, one helpful project coming from the stimulus funds is an NSF programme to study the effects of short-term boosts in science and technology funding on society at large — in effect, using stimulus money to study the stimulus itself. Results, however, are not due for at least two years.

In the meantime, institutions and individual researchers need to prepare now for the end of the largesse. Too many institutions have been content just to feed at the stimulus trough, encouraging their researchers to resurrect long-dead grant proposals and resubmit them without questioning the potential pain for students and staff when the monies disappear again. Instead, universities should be thinking strategically about what actions they can take now to alleviate that pain when it comes. Such actions might include finding ways to structure the funding flow by carrying out expensive data-taking tasks now, while providing support for graduate and postdoctoral students that goes beyond the end of the stimulus.

Scientific societies and professional organizations can also help, by sending out fewer congratulatory notes about landing stimulus funding and instead urging their members to think cleverly about what to do in the aftermath. Other innovative ways about how to keep the stimulus from going to waste can be found on page 876, where high-level experts weigh in with their views.

There is no mystery about the pain that will come when funding shrinks back down. The time to start planning is now. ■

Caught on camera

What to do when you are interviewed for an unscientific documentary.

Stephen Schneider, a climatologist at Stanford University in Palo Alto, California, has always had to deal with angry e-mails from people who think that global warming isn't happening, and that Schneider is part of a conspiracy to promote it. He has been vocal about the dangers of climate change for decades.

In the past week, however, Schneider has been deluged by furious messages. They have been provoked by a clip circulating on the Internet from *Not Evil Just Wrong*, a documentary film claiming that global-warming fears are 'hysteria'. The clip explains how Schneider did an interview — and then how the university informed the film-makers that it had rescinded permission for using any of the Stanford footage and that Schneider had withdrawn permission to use his name or interview. Schneider says he backed out when he realized that the film-makers were polemicists who had lied to him about their intentions. Some climate-sceptic commentators are accusing him of censorship.

Schneider is by no means the first scientist to feel hoodwinked by film-makers. British evolutionary biologist Richard Dawkins ended up in *Expelled: No Intelligence Allowed*, a film purporting to show how academics who do not accept evolution are frozen out of academia. Dawkins says that he was conned — that the film-makers had presented the project to him as an even-handed effort entitled *Crossroads: The Intersection of Science and Religion*. Carl Wunsch, an oceanographer at the Massachusetts Institute of Technology in Cambridge, felt he was "swindled" in a like manner by the producers of *The Great Global Warming Swindle*. And Nikos Logothetis of the Max Planck Institute for Biological Cybernetics in Tübingen, Germany, let a seemingly objective film crew into his primate laboratory — only to see the footage used in an animal-rights documentary that slams him as cruel.

For many scientists, the natural response to such stories is to stop talking to the media. But that would be an overreaction. For one thing, such misrepresentations are rare. Schneider estimates that he has given some 3,500 interviews since the 1970s, and only twice has he been "set up". Most journalists and documentarians are honestly trying to report the facts, and scientists have a responsibility to tell the public about their work — especially if it is supported by public money.

Fortunately, scientists can do much to protect themselves. When someone asks for an interview, for example, a scientist should enquire about starting assumptions, the intended audience and the identity of the project's backers. And, if possible, researchers should check the earlier work of the journalists and any companies behind the film for a partisan tone, or unacceptable levels of sensationalism.

But if these efforts fail, and it is discovered too late that the film-makers are bent on using an on-tape interview to promote a view that seems unscientific, the question becomes what steps to take. There is rarely a way to withdraw an interview that was given on the record, for good reason. In any case, making a fuss can be a gift of publicity to film-makers. Schneider admits that he might have spared himself the deluge of e-mails had he just ignored the makers of *Not Evil Just Wrong*.

A better approach might well be to complain to the television channels and broadcasting regulators, many of which have standards for their programming. *The Great Global Warming Swindle* was censured by Ofcom, Britain's broadcasting regulator, for breaking several rules in its broadcasting code. And when the same documentary was aired by the Australian Broadcasting Corporation, it was followed by a point-by-point debate and rebuttal.

In the end, this is perhaps the most effective way to limit the damage. Bad journalism is best met not with red-faced indignation, but with good journalism. The truth is the best revenge. ■

RESEARCH HIGHLIGHTS

Copy bat

M. KNÖRNSCHILD

Biol. Lett. doi:10.1098/rsbl.2009.0685 (2009)
Humans, elephants and seals can do it, but can bats also imitate sounds? It's long been thought that the flying mammals can, and Mirjam Knörnschild at the University of Erlangen-Nuremberg in Germany and her colleagues set out to find the evidence.

They recorded a total of 337 songs from 17 pups of the greater sac-winged bat (*Saccopteryx bilineata*) in Costa Rica and compared them with 57 territorial songs from six adult males belonging to the same harems as the pups. Acoustic analysis showed that as the pups matured, their calls developed into territorial songs that were similar to those of harem males. The team ruled out relatedness, gender and physical maturation as factors. The bats learned through imitation.

The authors suggest that this mammalian model — easier to study than others — could permit further investgation of how vocal imitation evolved.

ATMOSPHERIC SCIENCE

Monsoon madness

J. Geophys. Res. doi:10.1029/2009JD011733 (2009)
The severity of the east Asian summer monsoon, which affects more than 1 billion people, may be better forecast by analysing the North Atlantic Oscillation (NAO). This describes a large-scale system in which atmospheric pressure rises and falls in a see-saw motion from the polar to the subtropical region.

The monsoon's strength has been linked to the El Niño and La Niña cycles, but the NAO connection may further improve predictions, say Zhiwei Wu of the Chinese Academy of Sciences in Beijing and colleagues.

By combining data on global precipitation and atmospheric circulation with other indices of atmospheric activity, the researchers found that changes in the spring NAO can influence how strong or weak the monsoon gets later in the year.

PHYSICS

Holy yocto!

Phys. Rev. Lett. **103,** 152301 (2009)
Scientists want to image atomic processes occurring in real time, which requires extremely short pulses of light. Current state-of-the-art lasers can take attosecond (10^{-18} second) snapshots, but Andreas Ipp, Christoph Keitel and Jörg Evers at the Max Plank Institute for Nuclear Physics in Heidelberg, Germany, think that they can do a million times better using heavy-ion collisions.

When nuclei such as those of lead or gold collide, the quarks inside protons and neutrons briefly become free to move on their own. Over the course of a few yoctoseconds (10^{-24} second) they expand, releasing a super-short pulse of light. Only a few yoctosecond-long photons would be released by even the highest-energy collisions, but on the basis of their calculations, the authors believe that under the right conditions, the pulses could be used for ultrafast imaging.

STRUCTURAL BIOLOGY

DNA first responder

Cell **139,** 87–99; 100–111 (2009)
Work by two independent groups has deduced the structure and role of a key component of a protein complex that repairs dangerous double-stranded breaks in DNA.

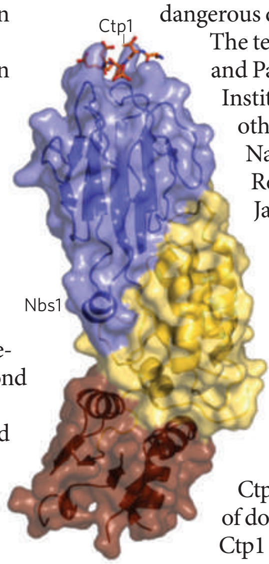

The teams — one led by John Tainer and Paul Russell of the Scripps Research Institute in La Jolla, California, the other by Steve Smerdon of the National Institute for Medical Research in London and Stephen Jackson of the University of Cambridge, UK — crystallized and characterized one of three subunits that make up the MRN protein complex, which responds to DNA damage.

The researchers found that the subunit, Nbs1 (pictured left), extends from the complex like a flexible arm and tethers the protein Ctp1, which is essential for the repair of double-stranded breaks. Nbs1 helps Ctp1 to home in on the site of the break.

ELSEVIER

BIOGEOCHEMISTRY

Preindustrial carbon

Glob. Biogeochem. Cycles doi:10.1029/2009GB003488 (2009)
Even before industrialization, humans were having an effect on atmospheric carbon dioxide levels by transforming natural land for agricultural uses, report researchers from the Max Planck Institute for Meteorology in Hamburg, Germany.

Julia Pongratz and her co-workers combined a reconstruction of historical land cover with a coupled biosphere–atmosphere–ocean general-circulation model going back over more than a millennium. The work suggests that land-use changes resulted in the release of 53 gigatonnes of carbon between AD 800 and 1850. Only 21% of this remained airborne, with the rest being reabsorbed by the oceans and biosphere, but that was enough to bump CO_2 emissions up above background levels by the late medieval period.

The team also looked at the impact of wars and epidemics, and found that the thirteenth-century Mongol invasion of China resulted in carbon sequestration, because the massive death toll led to vegetation regrowth on abandoned farmlands.

VIROLOGY

Infectious fatigue

Science doi:10.1126/science.1179052 (2009)
Researchers have linked chronic fatigue syndrome, a debilitating disease of unknown cause, to an infectious retrovirus that has also been associated with prostate tumours.

Judy Mikovits at the Whittemore Peterson Institute in Reno, Nevada, and her colleagues

found that 67% of 101 patients diagnosed with chronic fatigue syndrome carried the retrovirus XMRV in their blood, whereas fewer than 4% of 218 healthy individuals did.

The virus was able to spread from infected immune cells to cultured prostate cancer cells. The genomes of the XMRV strains associated with prostate cancer are more than 99% identical to those correlated with chronic fatigue syndrome, which is marked by increased cancer susceptibility. The authors say further study is needed to determine whether the virus causes the syndrome and if it is responsible for the elevated cancer risk.

For a longer story on this research, see go.nature.com/X72Lco

GENOMICS

Human genome in 3D

Science **326,** 289–293 (2009)

The three-dimensional structure of the human genome has been mapped. Job Dekker of the University of Massachusetts Medical School in Worcester, Eric Lander of the Broad Institute in Cambridge, Massachusetts, and their co-workers identified segments of the genome that tend to sit close together. They then used next-generation sequencing technology to build up a map showing the proximity of the segments to each other — a novel method they call 'Hi-C'.

The team found that each chromosome weaves between two compartments: one contains active genes; the other, more compact compartment houses inactive stretches of the genome. On a larger scale, the chromosomes are tightly packed into a 'fractal globule' (pictured right) that remains unknotted to allow easy access to genes.

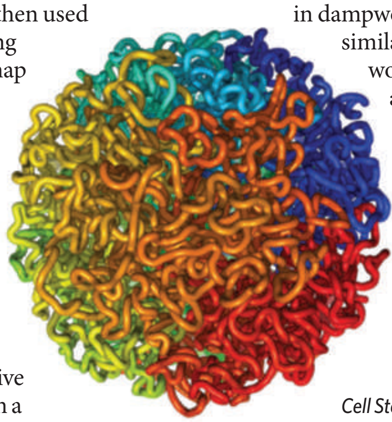

AAAS

ASTROPHYSICS

Merge, no surge

Astrophys. J. **704,** 324–340 (2009)

When galaxies merge, the gravitational jostling of gases can lead to a bump in the galaxies' star formation rate. But this effect is short-lived and does not significantly add to overall star numbers, say Aday Robaina of the Max Planck Institute for Astronomy in Heidelberg, Germany, and his colleagues.

In analysing images of 2,551 galaxies from the Spitzer and Hubble space telescopes, the researchers found that merging and closely interacting galaxies gave birth to stars at rates only 1.8 times higher than non-interacting galaxies — a smaller effect than previously thought. For the portion of the Universe between about 1 billion and 2 billion parsecs away, the researchers estimate that only about 8% of star births are triggered by galaxy mergers.

BIOLOGY

When colonies collide

Proc. Natl Acad. Sci. USA **106,** 17452–17456 (2009)

Many insect species organize themselves into social classes with distinct roles, such as reproductive queens and sterile workers. How this 'eusociality' evolved is an open question.

Barbara Thorne at the University of Maryland, College Park, and her colleagues staged encounters between 25 pairs of colonies of dampwood termites (*Zootermopsis nevadensis*). During encounters, at least one colony in each pair lost its king or queen and the pairs merged.

The team found that worker termites developed into reproductive ones in 17 of the 25 merged colonies and that interbreeding occurred in 14 colonies. This shows that, in dampwood termites, which are similar to ancestral termites, workers can become breeders and inherit a colony and its resources, providing them with an incentive to stay with their colony and cooperate with non-relatives — a key aspect of eusociality.

STEM-CELL BIOLOGY

Chemical reset

Cell Stem Cell doi:10.1016/j.stem.2009.09.012 (2009)

Adult cells can be turned into 'pluripotent' or embryonic-like stem cells with the insertion of four genes — *Sox2*, *Oct4*, *Klf4* and *c-Myc*. However, this method is not clinically useful because *c-Myc* and *Sox2* have been linked to cancer and the viral vectors used to transfer those genes are also cancer-promoting.

Using chemical screening, Lee Rubin and Kevin Eggan at Harvard University in Cambridge, Massachusetts, and their colleagues discovered a small molecule, which they call RepSox, that essentially does the jobs of *c-Myc* and *Sox2*. Mouse cells expressing only *Klf4* and *Oct4* became pluripotent after treatment with RepSox.

This may be a step towards chemical cell reprogramming that avoids gene transfer altogether.

JOURNAL CLUB

Sam Wang
Princeton University, New Jersey

A neuroscientist explores the energy efficiency of the brain.

Considering its substantial processing capacity, the human brain consumes remarkably little power — about as much as an idling laptop computer. So I was interested to learn that action potentials — the electrical 'spikes' that are the fundamental units of neuronal activity — are likewise remarkably energy efficient (H. Alle *et al.* *Science* **325,** 1405–1408; 2009).

During a spike, the voltage across a neuron's membrane is reversed when sodium ions flow into the cell and potassium ions move out. This reversal spreads as a wave down the neuron's axon towards its terminals, where it triggers synaptic transmission to other neurons.

Henrik Alle of the Max Planck Institute for Brain Research in Frankfurt, Germany, and his colleagues recorded charge movements at axon terminals in mammalian hippocampal neurons. They found that sodium and potassium ions flow at largely non-overlapping times, with more than 75% of all charge contributing unopposed to the rise or fall of a spike.

Such efficiency comes as a surprise. These axons outperform the much-studied squid giant axon by a factor of three. If the findings apply to other mammalian neurons, brain tissue may support more firing than suspected. The authors suggest that synaptic transmission may dominate the energy budget of brain tissue.

These results have implications for functional magnetic resonance imaging, which measures increases in blood oxygenation in the brain as an indicator of neural activity. What causes the blood-oxygen boost is unknown: suggested triggers include synaptic transmission and action potentials. This paper is evidence for the former, because energy-intensive events such as synaptic signalling are more likely to be oxygen-hungry and to stimulate blood flow. The idea is supported by other recent evidence — a wonderful convergence.

Discuss this paper at **http://blogs.nature.com/nature/journalclub**

NEWS BRIEFING

P. DASILVA/EPA/CORBIS

MOON SMASH GIVES OFF FLASH

For many eager astronomers (pictured watching outside the Ames Research Center in Moffett Field, California) NASA's frontal assault on the Moon ended in a fizzle on Friday. The Lunar Crater Observation and Sensing Satellite crashed near the lunar south pole as planned, but an expected plume of bright debris was nowhere to be seen, even by powerful telescopes. Mission scientists did, however, spot a thermal flash and a crater, perhaps 20 metres wide, created by the impact. They were most excited about a tiny bump in brightness seen by a mission spectrometer, which could signal the presence of water that some think exists as ice in the bottom of the target crater. See go.nature.com/ZbzDDe for more.

POLICY

Climate advice: Britain requires a major shift in pace if it is to meet its self-imposed targets for cutting greenhouse-gas emissions, according to the Committee on Climate Change. In its first annual report to Parliament on the country's progress, the committee, established last year, says that Britain's current 0.5% annual drop must increase to 2–3% a year if the nation is to cut its emissions to 80% below 1990 levels by 2050. It also recommends more investment in nuclear power, wind farms and carbon capture and storage, and notes that "recession-induced reductions must not be confused with underlying progress".

Energy investment: The European Commission has proposed investing an additional €50 billion (US$74 billion) into research and development for low-carbon energy over the next decade, increasing annual investment from the current €3 billion to €8 billion. The proposal lays out funding goals in seven sectors — wind, solar, nuclear, bioenergy, fuel cells, electricity grids and carbon capture and storage. Janez Potočnik, European Union commissioner for science and research, says that most of the money will need to come from the private sector. Policy-makers, researchers and business representatives will discuss the proposal at the 21–22 October European Energy Technology Summit in Stockholm. See go.nature.com/Shr8W2 for more.

Grant cuts: A new ¥270-billion (US$3-billion) funding programme in Japan may be slashed to ¥100 billion, after the science and education ministry last week announced cuts to the supplementary budget of which the programme forms a part. Before it lost a 30 August election, the Liberal Democratic Party had chosen 30 research groups to receive money from the Funding Program for World-Leading Innovative R&D on Science and Technology. That programme's fate now awaits a decision by the Democratic Party of Japan. For more, see page 854.

Carbon capture: One hundred large-scale carbon capture and storage (CCS) plants will be needed around the world by 2020, and 3,400 by 2050, the International Energy Agency said in a 'CCS roadmap'. Most of the plants would need to be built in industrializing nations such as China and India, and from 2010 to 2020, governments in developed nations should invest US$3.5 billion–4 billion each year for CCS demonstrations. The report's release on 13 October coincided with calls from energy ministers — including US energy secretary Steven Chu — to rapidly advance CCS technology as they gathered at the Carbon Sequestration Leadership Forum in London this week.

NUMBER CRUNCH

1 in 250,000

The probability that asteroid Apophis will hit Earth in 2036, revised from NASA's previous estimate of 1 in 45,000. Phew.

AWARDS

Stars over Washington: A select group of astronomers and schoolchildren flooded the south lawn of the White House on 7 October for the first-ever presidential star party. Before stepping up to telescopes to look at the night sky, US President Barack Obama introduced several young astronomers, including high-school student Lucas Bolyard of West Virginia, who explained to him what a pulsar was. Earlier in the day, Obama had handed out this year's National Medals of Science and National Medals of Technology and Innovation to 14 researchers in a White House ceremony.

Ribosome reward: Three structural biologists who mapped the structure and workings of the ribosome — the cell's machinery for churning out proteins from genetic code — have won the 2009 Nobel Prize in Chemistry. Venkatraman Ramakrishnan, who works at the Medical Research Council's Laboratory of Molecular Biology in Cambridge, UK; Ada Yonath of the Weizmann Institute of Science in Rehovot, Israel, and Thomas Steitz at Yale University in New Haven, Connecticut, share the prize equally. See page 860 for more.

SOUND BITES

"In virtually every aspect of the talks there has been minimal progress of any substance."

Saleemul Huq, a lead scientist on the Intergovernmental Panel on Climate Change, reports back from climate negotiations in Bangkok that were meant to set the stage for the crucial Copenhagen summit in December. See go.nature.com/NEBbNs for more.

RESEARCH

Physicist charged: French police have charged a researcher working at CERN, Europe's particle-physics laboratory near Geneva in Switzerland, with having links to terrorists. Adlène Hicheur, a postdoc at the Swiss Federal Institute of Technology in Lausanne, was arrested on 8 October in Vienne, France. Authorities have accused the 32-year-old of supplying the North African branch of al-Qaeda with possible targets for future attacks in France. Hicheur was working on the beauty experiment, one of four main projects at CERN's Large Hadron Collider, the world's most powerful particle accelerator. See go.nature.com/H5f7deg for more.

Peer-review probe: A dispute is widening between the editorial board of the *Proceedings of the National Academy of Sciences* (*PNAS*) and academy member Lynn Margulis, a cell biologist at the University of Massachusetts, Amherst. Under a *PNAS* submission route to be phased out by July 2010, Margulis had "communicated" a paper by a non-academy member to the journal, which it published online in August. In the wake of rows over Margulis's alleged selective communication of reviews for the work, two additional papers, one co-authored by Margulis and one communicated by her, are now also in limbo. See go.nature.com/7wTuld for more.

Misconduct ban: The DFG, Germany's major national research agency, has disciplined two senior biodiversity researchers at the University of Göttingen by banning them from sitting on DFG committees for three years. The agency says that Teja Tscharntke and Christoph Leuschner misrepresented the publication status of 54 research papers in applications for continued funding of major research grants. Three other scientists in the Collaborative Research Centre and graduate college supported by the DFG were given a formal rebuke. In August, an independent investigation committee found the scientists guilty of "gross negligence" (see *Nature* **460**, 791; 2009).

S. J. FERRELL/CONGRESSIONAL QUARTERLY/GETTY IMAGES

Leader lost: The US National Institutes of Health (NIH) said goodbye last week to institution icon Ruth Kirschstein (pictured), who died on 6 October at the age of 82. In 1974, Kirschstein became the first female director of an NIH institute when she took over the National Institute of General Medical Sciences, which she led until 1993. She also served as acting director for the NIH twice, once in 1993 and again from 2000 to 2002.

BUSINESS

Patents tiff: The US Patents and Trademark Office has changed its mind about proposed rules intended to cut down on the number of times an applicant can add claims to an existing patent. In 2007, the drug company GlaxoSmithKline sued the patent office to try to keep the proposals from going into effect. A district court ruled in the firm's favour, and the proposals have been tied up in court since then; however, the patent office dumped them completely on 8 October.

THE WEEK AHEAD

15 OCTOBER

NASA begins six years of flights over Antarctica, in what will be the largest airborne survey of sea ice, glaciers and ice sheets.

www.espo.nasa.gov/arcticicegap

18–21 OCTOBER

Portland, Oregon, hosts the annual meeting of the Geological Society of America.

www.geosociety.org/meetings/2009

19–22 OCTOBER

Paris hosts the AIDS vaccine conference 2009.

www.hivvaccineenterprise.org

20–24 OCTOBER

The American Society of Human Genetics annual meeting will be held in Honolulu, Hawaii.

www.ashg.org

21 OCTOBER

The World Health Organization releases its *State of the World's Vaccines and Immunization* report.

go.nature.com/dIZEPu

FUNDING WATCH

Developing countries have more than doubled their spending on science over a 5-year period, from US$134 billion in 2002 to $272 billion in 2007, a new report shows. The figures are adjusted to take into account the relative cost of living in different countries. Over this period, the number of researchers jumped by 50% in developing nations, but by just 8.6% in developed countries, according to data released by the UNESCO Institute for Statistics on 6 October. Developing nations also upped their average expenditure on research and development as a percentage of gross domestic product, from 0.8% in 2002 to 1.0% in 2007 — although spending varied greatly between countries. China saw a rise from 1.1% to 1.5%, whereas India nudged up from 0.7% to 0.8%.

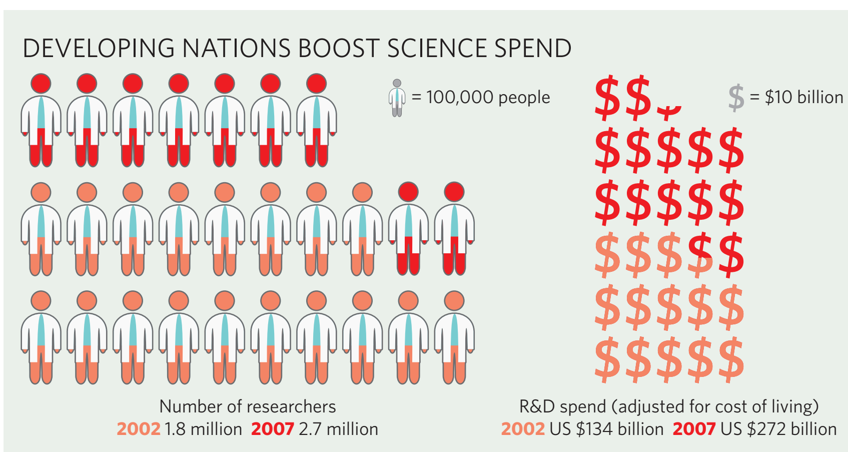

NEWS

Japan to slash huge grant scheme

Upstart government brings fresh priorities to science.

In September, 30 research groups in Japan, led by some of the country's biggest scientific names, were celebrating their selection to a new ¥270-billion (US$3-billion) funding programme. But the programme is now under fire from both politicians and researchers, and its funding may be cut by almost two-thirds.

The projects were selected on 4 September — five days after the ruling Liberal Democratic Party lost an election in a landslide, and 12 days before it had to yield power to the Democratic Party of Japan (DPJ). The DPJ needed money to fund campaign promises, such as stipends for families with children (see *Nature* **460**, 938; 2009), and asked all ministries to cut back by at least ¥3 trillion the ¥14.7 trillion that had been allocated this spring as part of a government supplemental funding package.

On 6 October, the science and education ministry announced that it would cut 21% from its supplementary budget. It has not revealed details of where those cuts would be made, but Japan's deputy prime minister Naoto Kan has reportedly laid out a framework by which the Funding Program for World-Leading Innovative R&D on Science and Technology (FIRST) would be reduced from ¥270 billion to ¥100 billion. According to the plan, which had

Y. TSUNO/AFP/GETTY

Deputy prime minister Naoto Kan has laid out a plan to cut back on Japan's big-science funding.

not been made official as *Nature* went to press, ¥70 billion would be cut altogether and the other ¥100 billion would be used for smaller grants to other groups or transferred to a scheme for sending young scientists abroad.

The 30 groups scheduled to receive FIRST funding span a variety of fields, from mathematics to neurogenetics and nanobiotechnology. The list includes many of Japan's most famous scientists, including Shinya Yamanaka of Kyoto University, who received funding to set up a stem-cell bank for the induced pluripotent stem (iPS) cells he created; Shizuo Akira of Osaka University, for a project on manipulating immune responses; and Nobel laureate Koichi Tanaka of Shimadzu Corporation in Kyoto, for a mass-spectrometry project on drug discovery and diagnosis.

The shortage of new faces, critics say, could stem from a rushed application and selection process. The 3-week application period ended on 24 July; a team of 24 scientists then gunned through the 565 proposals to reduce the field to 60. One team member told *Nature* that the committee often had to abstain or make ill-informed judgements based on skimming materials. "It's incredible to give that kind of money with no long-term feasibility study or in-depth analysis," says the member, who asked to remain anonymous.

Takafumi Matsui, a planetary scientist at the Chiba Institute of Technology who sat on the second-stage committee that chose the final 30 grantees, defends the process. "I normally read

Cancer metastasis scrutinized

BOSTON
Most cancer research has focused on blocking primary-tumour growth, even though cancer cells that cut loose from tumours and invade other tissues account for 90% of cancer-associated deaths.

But at the first conference on Frontiers in Basic Cancer Research, hosted by the American Association for Cancer Research last week in Boston, Massachusetts, cancer biologists reported that this focus is changing. Many experts are turning to study the secondary tumours that form when circulating cancer cells infiltrate and colonize other organs — a process known as metastasis.

"The time is now ripe for scientifically deconstructing the process of metastasis in different types of cancer," says Joan Massagué of the Memorial Sloan-Kettering Cancer Center in New York City.

At the conference, Daniel Haber of the Massachusetts General Hospital in Charlestown described a microfluidic chip that can detect vanishingly rare tumour cells circulating in the bloodstream. This technique, he says, could identify rogue cancer cells long before metastases form.

And using a novel genetically engineered mouse model of lung cancer, Tyler Jacks of the Massachusetts Institute of Technology in Cambridge and his postdoc Monte Winslow found that a transcription factor called Nkx2-1 is a metastatic suppressor, specific to lung cancer, that is active in primary tumours but shut off in secondary cancers. "This is probably the closest thing you have to taking metastasis from a patient," says Winslow.

Whether a metastatic cancer cell triggers a new tumour is "a big if", says Massagué. What's more likely, he says, is that these cells reseed the same tumour from which they originated. Massagué presented data from mice showing that the circulating cells express genes allowing them to infiltrate tissues. But the primary tumours from which the cells came release signals to attract them back, so if they don't land in a new organ they return home and aggravate tumour growth there. "The tumour is selecting for the worst of its children," says Massagué. He is testing whether these tissue-adapted metastatic cells account for the high rates of relapse seen following many cancer therapies.

Robert Weinberg of the Whitehead Institute for Biomedical Research in Cambridge, Massachusetts, linked metastatic cells to cancer stem cells — rare cells thought to fuel primary-tumour growth — through a common molecular transformation called the epithelial-mesenchymal transition. Weinberg says that this transition allows the metastatic cells

THE BUTTERFLY EFFECT GETS ENTANGLED
Cold-atom experiments show chaotic fingerprints in the quantum world.
go.nature.com/qz6yoY

about a lot of fields of science," he says, "so I could quickly judge their merits."

Many critics took exception to the premise of funding such large-scale, focused projects, saying that fundamental research could be losing out. For instance, on 3 October Shinichi Aizawa, president of the Japanese Society of Developmental Biologists, called for policy-makers to better balance applied research with basic science.

Yamanaka told *Nature* that he was reserving comment until the DPJ makes an official statement about the fate of the programme.

Atsushi Sunami, director of the science and technology policy doctoral programme at the National Graduate Institute for Policy Studies in Tokyo, also thinks that the grants are too big. "With this kind of funding, you could do more high-risk, high-return smaller projects," he says. "What will the extra funding achieve for these groups that are already funded? It's not clear. You're pouring water into something that's already full."

But two aspects of the FIRST programme could set a good precedent for Japan, Sunami says. Grantees can take the funding to any institution they please — an attempt to introduce competition and fluidity among research centres. And the grants are given for five-year terms so that grantees don't need to rush to spend, and potentially waste, money at the end of each fiscal year. ■

David Cyranoski

to become both motile and self-renewing. Many aggressive secondary tumours might form from newly converted cancer stem cells, he notes, overturning the standard dogma that stem cells generate non-stem cells.

Meanwhile, Sijin Liu of Tufts University School of Medicine in Boston reported one of the first drug compounds that can directly block metastasis, in a mouse model of breast cancer. Liu showed that inhibiting the ROCK signalling pathway with a small molecule led to around 35% fewer metastases, as well as decreasing the mass of the resulting secondary tumours by nearly 80%.

Until such therapies exist, however, understanding primary tumours remains a major route to indirectly mitigating metastasis, Jacks says. "It could be that we will enter an era of cancer management," he says, "in which our understanding of how tumours advance through these early stages will present us with preventative strategies to block the emergence of later lesions." ■

Elie Dolgin

Fusion delays sow concern

Construction at the site of ITER — the multibillion-euro project to prove controlled nuclear fusion — has been at a standstill since April, *Nature* has learned.

The stoppage comes as European contributors negotiate how to pay for their share of ITER, a collaboration between Europe, Japan, South Korea, Russia, the United States, China and India. The European Union (EU) is by far the largest participant, providing some 45% of construction costs, including the buildings that will eventually house the giant machine in St Paul lez Durance, in the south of France.

Excavations for the buildings, slated to begin this autumn, will not start until spring 2010 — roughly a year after site preparations were completed.

European officials say that the reasons for the delay are technical rather than political, and that they will be able to meet the 2018 deadline for completing construction. "The project is not on standby," says Catherine Ray, a spokeswoman for research for the European Commission in Brussels.

But some researchers are concerned that the political impasse could push back ITER's start date. "I'm worried that whatever we lose now could delay the project's completion," says Günther Hasinger, scientific director of the Max Planck Institute of Plasma Physics in Garching, Germany.

"I'm worried that whatever we lose now could delay the project's completion."

When completed, the machine will heat and compress hydrogen isotopes until they fuse into helium, releasing energy.

In 2006, ITER was slated to cost around €5 billion (US$7.4 billion) to construct and another €5 billion to operate over a 20-year period. But following an extensive design review, the construction costs are now expected to at least double (see *Nature* 459, 488; 2009).

Ray says that the EU had budgeted nearly €10 billion for construction, operation and decommissioning over a 35-year period. But now the 27 EU member states, plus Switzerland, must come up with additional commitments to cover the cost increase. Hasinger says that until they provide a plan for funding, construction is unlikely to begin. "The problem in the European situation is that they need the whole commitment for construction before they can award the contracts," he says.

Sources close to the negotiations say that a number of options are being considered. One would be to secure additional commitments from member states. Another would be a promise from the European Investment Bank, headquartered in Kirchberg, Luxembourg, to provide loans for any additional funds needed.

Such a loan scheme would not be unprecedented: in 2002 CERN, Europe's high-energy physics laboratory near Geneva, Switzerland, took out a €300-million loan to pay for construction costs for the Large Hadron Collider particle accelerator.

Officials say that the situation is under control. Although the budget delays could cause problems down the line, "I am not limited by the amount of money for right now," says Didier Gambier, the director of Fusion for Energy in Barcelona, Spain, which oversees the contracts for ITER's buildings.

Gambier says that the decision to delay contracts was purely technical, and driven in part by the fact that the design of ITER is still being finalized. "We still need to have more information from the other parties," he says. Nevertheless, he says, "we are pushing as hard as we can".

ITER is expected to be completed in 2018 and to conduct its first power-producing experiments in 2026. ■

Geoff Brumfiel

The ITER site: ready for buildings.

ITER

Where the US stimulus money is going

The American Recovery and Reinvestment Act, passed by Congress in February 2009, provides about US$787 billion of stimulus funding to boost the country's economy.

Here, *Nature* looks at where $52.65 billion of the money for science is being directed. For some concerns about how it is being spent, see page 876.

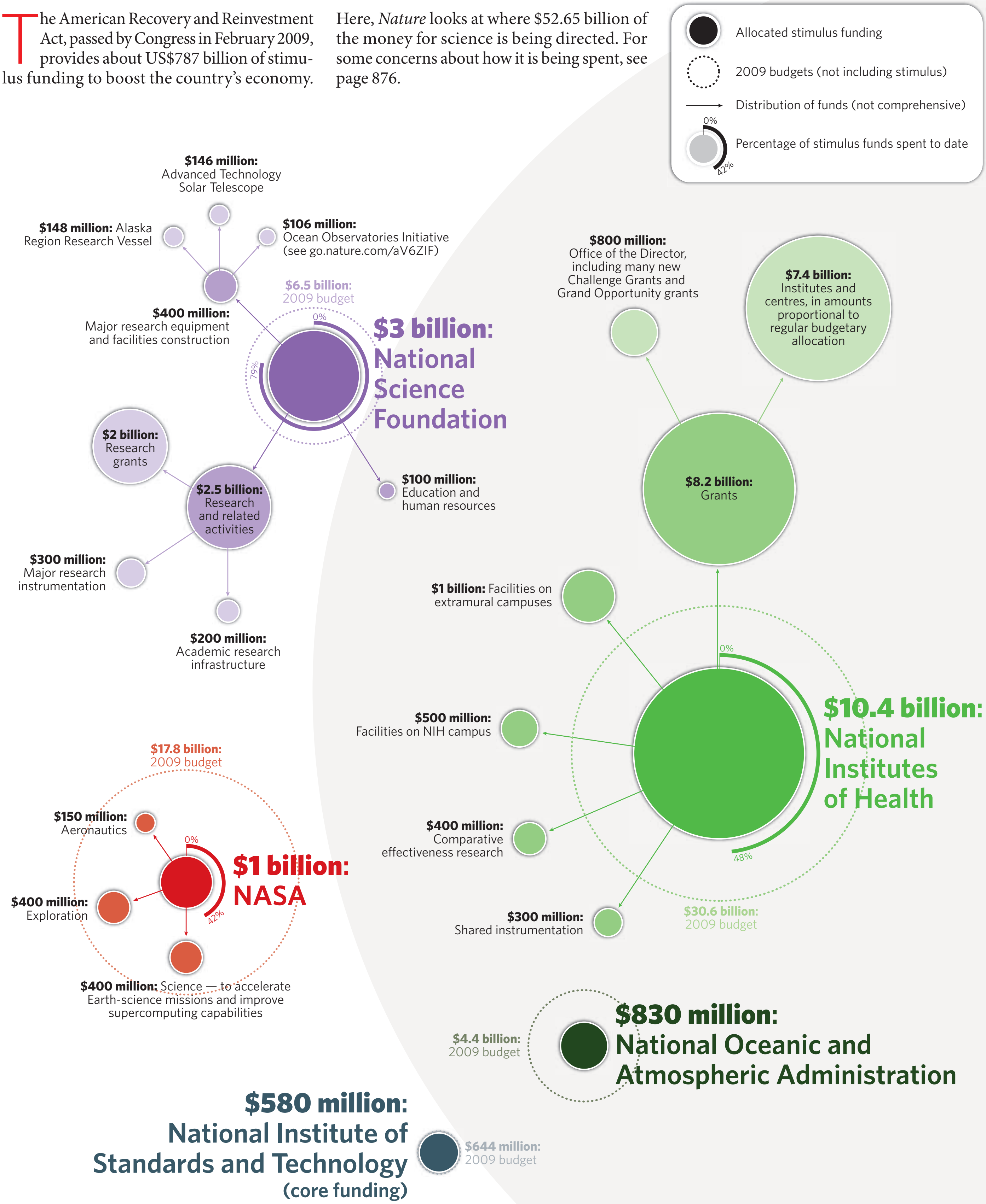

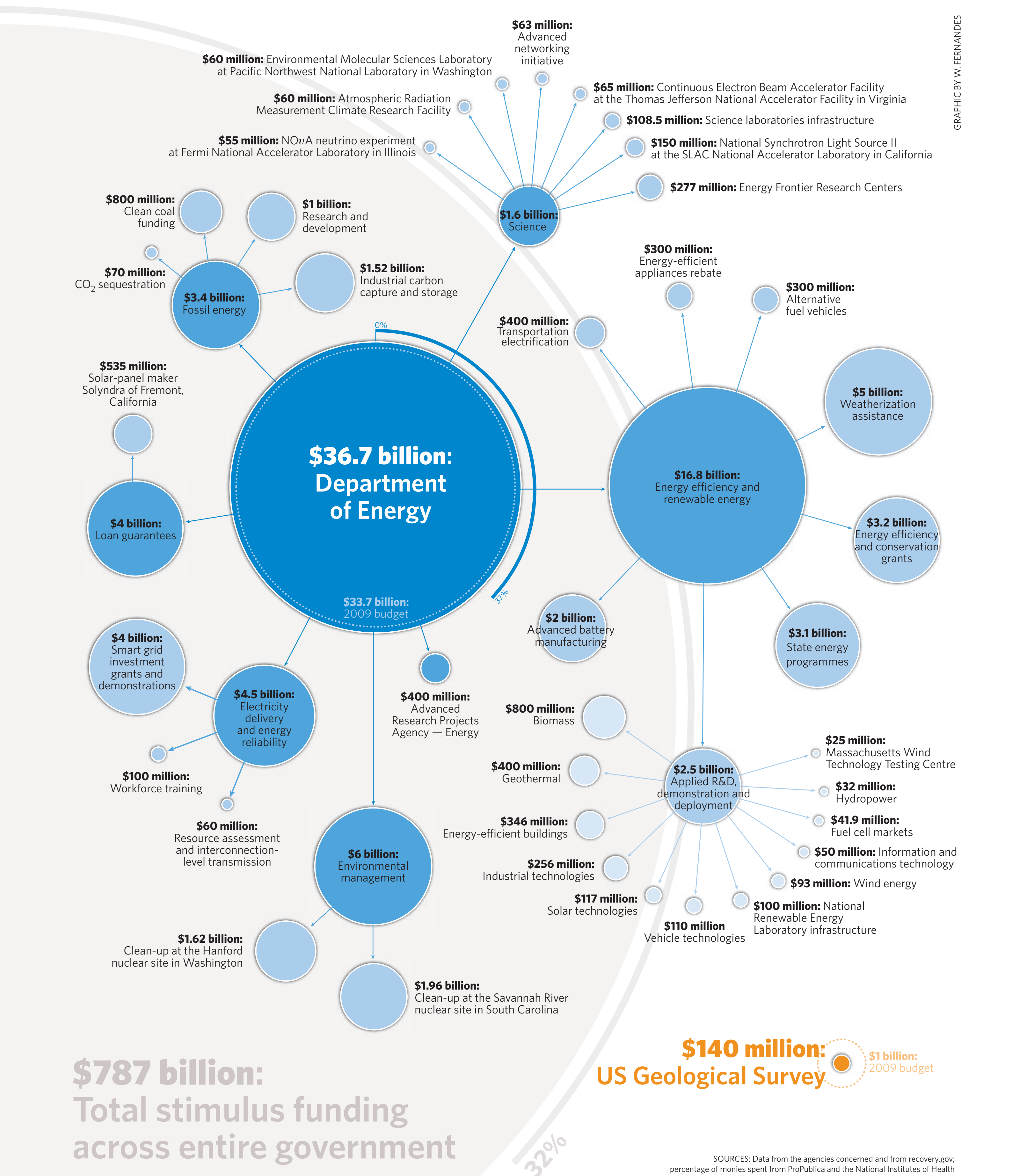

SOURCES: Data from the agencies concerned and from recovery.gov; percentage of monies spent from ProPublica and the National Institutes of Health

Key protein-design papers challenged

Chemists question stability of proteins from 2003 *Nature* study.

Two papers published by protein engineer Homme Hellinga's lab at Duke University Medical Center in Durham, North Carolina, have been challenged.

Last year, Hellinga retracted papers in *Science*[1] and the *Journal of Molecular Biology*[2] after John Richard, a physical chemist at the State University of New York at Buffalo, found that enzymes designed by Hellinga's lab did not work as reported[3]. Now, questions have been raised about a 2003 paper in *Nature*[4] and a 2004 paper in the *Proceedings of the National Academy of Sciences*[5]. In both, Hellinga's group used a computer program called Dezymer to design proteins that could bind new molecules, or ligands.

The work was considered a milestone for showing that it was possible to use computer algorithms to design proteins that bind tightly to small molecules.

Birte Höcker, a former postdoctoral fellow of Hellinga's, and her team at the Max Planck Institute for Developmental Biology in Tübingen, Germany, assembled and analysed five of the designed proteins that seemed to work best[6]. She found that all five were very unstable, and one was too unstable to analyse further. The group then examined the structure of one of the proteins using crystallography and found that its binding pocket was similar to that predicted by Dezymer — but that it did not bind its intended ligand.

And using three methods to detect the changes in stability, heat and shape that normally occur when proteins bind their ligands, the team found no evidence that the designed proteins were binding their intended ligands.

Hellinga says that Höcker used higher concentrations of proteins in her tests than his group did in its original paper, and that this could have affected her results. He wrote in a statement that his lab will study the designs she reanalysed. "If we fail to observe binding in the studies outlined above," he says, "then we will draw the same conclusions" as Höcker.

Höcker speculates that she obtained different results because she used different methods to test binding, including direct measurements. Hellinga used an indirect method: he designed the proteins so that they included a fluorophore that emitted a signal when the proteins changed shape, which his team interpreted as a sign that the proteins had bound their ligands.

Other scientists call the results puzzling. David Baker, of the University of Washington in Seattle, says that Höcker did not test every protein reported in the original papers, so it is possible that some of the proteins do work. But for the proteins Höcker did characterize biochemically, he says, "it's a little hard to see how they could have worked as designed".

"There is a qualitative difference in the results from Hellinga's lab and the German lab," adds Jack Kirsch, a chemist and biologist at the University of California, Berkeley. "Clearly they can't both be right."

"Clearly they can't both be right."

Jeff Smith, who collaborated on the 2003 *Nature* paper while a postdoctoral fellow in Hellinga's lab, says that he performed follow-up studies on three of the proteins after the paper was published. Two of them consistently did not work, but a third — which Höcker did not analyse — did, says Smith, now chief science officer of a biotechnology company in Durham. This, he says, convinced him that the third protein did work: "I would stand by it," he says.

Hellinga says the proteins' instability was mentioned in his papers.

In 2007, Hellinga charged Mary Dwyer, a co-author of the *Nature* paper, with misconduct in connection with the retractions. Dwyer denied the charges. Duke University School of Medicine convened an enquiry and cleared Dwyer in February 2008. Hellinga wrote to *Nature* in July 2008 indicating that Duke had, at his request, opened an enquiry into his own actions involving the retractions[7]. Duke declined to answer questions about the status of the enquiry. ■

Erika Check Hayden

1. Dwyer, M. A., Looger, L. L. & Hellinga, H. W. *Science* **304,** 1967–1971 (2004).
2. Allert, M., Dwyer, M. A. & Hellinga, H. W. *J. Mol. Biol.* **366,** 945–953 (2007).
3. Check Hayden, E. *Nature* **453,** 275–278 (2008).
4. Looger, L. L., Dwyer, M. A., Smith, J. L. & Hellinga, H. W. *Nature* **423,** 185–190 (2003).
5. Allert, M., Rizk, S. S., Looger, L. L. & Hellinga, H. W. *Proc. Natl Acad. Sci. USA* **101,** 7907–7912 (2004).
6. Schreier, B., Stumpp, C., Wiesner, S. & Höcker, B. *Proc. Natl Acad. Sci. USA* doi:10.1073/pnas.0907950106 (2009).
7. Hellinga, H. W. *Nature* **454,** 397 (2008).

For more, see go.nature.com/HFWfmZ

Structural biology bags chemistry prize

Chemistry Nobel for trio who described the ribosome.

Thomas Steitz, Venkatraman Ramakrishnan and Ada Yonath share this year's chemistry Nobel.

LEFT TO RIGHT: L. JACKSON/REUTERS; A. GRANT/AP PHOTO; XINHUA NEWS AGENCY/EYEVINE

Three structural biologists who mapped the structure and inner workings of the ribosome — the cell's machinery for churning out proteins from genetic code — have won this year's Nobel Prize in Chemistry.

Venkatraman Ramakrishnan, who works at the Medical Research Council's Laboratory of Molecular Biology in Cambridge, UK; Ada Yonath of the Weizmann Institute of Science in Rehovot, Israel; and Thomas Steitz at Yale University in New Haven, Connecticut, share the prize equally.

"So many people contributed, and the ribosome is so important, that I am just pleased to be one of the three," says Ramakrishnan.

Explaining the ribosome's structure was a key step towards understanding how it translates DNA into proteins. "Until you see how atoms are arranged, it's hard to integrate biochemical knowledge into that framework," Ramakrishnan says. "High-resolution pictures change the nature of the field, directing biochemical experiments. They have a disproportionate impact."

Ramakrishnan and Steitz's groups used X-ray crystallography to solve increasingly high-resolution structures of different ribosomes, mostly from simple organisms such as bacteria. Yonath paved the way for these studies by creating the first ribosome crystals. From such structures, researchers have worked out how the ribosome grabs messenger RNA — transcribed from DNA — follows its amino-acid recipe, and binds these units together to produce proteins.

"High-resolution pictures change the nature of the field. They have a disproportionate impact."

Even in its smaller bacterial form, the ribosome is a large and complex structure, consisting of two subunits and more than 50 different proteins. In the late 1970s, this was orders of magnitude larger than other biological molecules that had been coaxed into forming crystals, such as haemoglobin and myoglobin. Yonath tried anyway.

"The idea of crystallizing the ribosome was completely outrageous, but Ada had a deep-rooted belief that she knew what she was doing," says Yehiam Prior, head of the Weizmann Institute's chemistry department.

By using resilient organisms with particularly stable ribosomes, including salt-loving creatures from the Dead Sea, Yonath succeeded in creating three-dimensional crystals of the molecule. By hitting these with X-rays, she produced the first blurry images of the ribosome.

At that point, other teams piled in to create structures of high enough resolution to determine atomic structure. Steitz's team focused on the molecule's larger 50S subunit, which joins amino acids together into proteins, and published the first atomic-resolution structure in 2000 (N. Ban *et al. Science* **289,** 905–920; 2000).

"These were very exciting times, with huge competition with other groups in the field. We had hourly discussions every day," recalls Nenad Ban, who worked in Steitz's laboratory as a postdoc and is now at the Swiss Federal Institute of Technology Zurich.

Ramakrishnan's group, meanwhile, attacked the smaller 30S subunit, which latches onto mRNA (B. T. Wimberley *et al. Nature* **407,** 327–339; 2000).

Unravelling the ribosome's structure may produce dividends in terms of the potential to develop novel antibiotics. "The ribosome is already starting to show its medical importance," Ramakrishnan notes. All three researchers have published analyses of how antibiotics attack bacteria by disrupting their ribosomes and so preventing them from creating proteins.

Chloramphenicol, for example, binds to the 50S subunit's active site, preventing it from joining amino acids together, whereas erythromycin 'constipates' the ribosome by blocking the channel through which a completed chain of amino acids is normally released into the cell's cytoplasm to fold up.

As bacteria have evolved resistance to these antibiotics, start-up companies such as Rib-X Pharmaceuticals — based in New Haven, Connecticut, and spun out of Steitz's team — are using knowledge of the ribosome's structure to create new antibiotics, which are currently in clinical trials.

It is the third time in seven years that the chemistry Nobel has been awarded to crystallographers who have determined the structure and function of a complex biological molecule. "It does seem to be a recurring theme," says Thomas Lane, president of the American Chemical Society in Washington DC.

But at its heart, this structural biology is "fundamentally chemistry", adds Jeremy Sanders, head of physical sciences at the University of Cambridge, UK. "Even if many chemists had never heard of any of the winners." ■

Richard Van Noorden

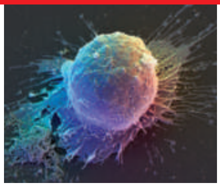

D. SCHARF/SPL

FINDING TRUE STEM-LIKE CELLS
Imaging identifies bona fide reprogrammed cells.
go.nature.com/iuBQeO

Impact theory under fire once more

Independent studies are casting more doubt on a controversial theory that a comet exploded over North America nearly 13,000 years ago, wiping out the Clovis people and many of the continent's large animals.

Archaeologists have examined sediments at seven Clovis-age sites across the United States, and found that the concentration of magnetic debris was insufficient to confirm an extraterrestrial impact at that time, says a report in the *Proceedings of the National Academy of Sciences* (*PNAS*)[1].

In 2007, a team led by Californian researchers proposed that a comet or asteroid had exploded over the North American ice sheet, creating widespread fire and an atmospheric soot burst followed by a cooling period known as the Younger Dryas[2]. Sometime after this, the Clovis people, large-animal hunters known for their spear points, mysteriously disappeared.

Key evidence for the purported impact was magnetic microspherules discovered in sediments at 25 locations. Richard Firestone, of Lawrence Berkeley National Laboratory in California, and his colleagues argued that the microspherules were cosmic debris from an explosion. But in more than 18 months of sedimentary analysis, a team led by Todd Surovell, an archaeologist at the University of Wyoming in Laramie, was unable to detect high levels of microspherules at any of the sites, including two where Firestone's team had reported finding them.

"I didn't find any physical evidence to support their theory."

"I spent hundreds of hours at the microscope examining sediment samples," says Surovell, "and I didn't find any physical evidence to support their theory."

The other team isn't backing down. "Their study doesn't negate our hypothesis," says James Kennett, a palaeoceanographer at the University of California, Santa Barbara, and one of Firestone's co-authors. Another co-author, geophysicist Allen West of Prescott, Arizona, says that Surovell's group didn't use the correct techniques to extract, identify and quantify the microspherules.

In a *PNAS* article[3] published in February, Jennifer Marlon, a doctoral geography student at the University of Oregon in Eugene, and her colleagues found no evidence of systematic burning of biomass — as would have occurred if continent-wide fires had happened — at the time of the Younger Dryas in pollen and charcoal records at 35 sites. ■

Rex Dalton

1. Surovell, T. A. *et al. Proc. Natl Acad. Sci. USA* advance online publication doi:10.1073/pnas.0907857106 (2009).
2. Firestone, R. B. *et al. Proc. Natl Acad. Sci. USA* **104,** 16016–16021 (2007).
3. Marlon, J. R. *et al. Proc. Natl Acad. Sci. USA* **106,** 2519–2524 (2009).

For more, see go.nature.com/kWeeKL

Small, furry … and smart

Researchers have engineered more than 30 strains of 'smart mice', revealing possible ways to boost human brains. But, as **Jonah Lehrer** finds, cognitive enhancement may come at a cost.

P. MURPHY

Ten years ago, Joe Tsien eased a brown mouse, tail first, into a pool of opaque water. The animal squirmed at first; mice don't generally like getting wet. But once released, it paddled in a wide circle, orienting itself by the array of coloured shapes hung above the pool. Within seconds, the mouse headed straight for the safety of a small platform hidden just beneath the water's surface.

Most mice require at least six sessions before they can remember the location of the platform in a Morris water maze. But this animal needed just three.

Tsien, based at Princeton University in New Jersey at the time, named his creation Doogie after the teenage genius in the television programme *Doogie Howser, MD*. The work was one of the earliest examples of neuroscientists using genetic engineering to generate cognitively enhanced animals in a bid to understand memory and learning.

"There's something magical about taking a mind and making it work better," says Alcino Silva, a professor of neuroscience at the University of California, Los Angeles, and one of the pioneers in the field of enhanced cognition.

Researchers have now created or identified at least 33 mutant mouse strains that, like Doogie, have enhanced cognitive abilities. The animals tend to learn faster, remember events longer and solve complex mazes better than ordinary mice. And because the molecular pathways used in the brain to form long-term memories are almost identical in humans and rodents, the hope is that the work will inform research into treatments for a wide variety of learning and memory problems, from dyslexia to dementia.

PRINCETON UNIV.

Much of the work involves making an adult brain behave more like a younger, more flexible version of itself by increasing the organ's plasticity. This, in turn, means that some problems, long believed to have been made permanent during development, might actually be reversed.

Moreover, the mice raise a tantalizing possibility that normally functioning human brains could be improved. Already, drugs designed to help with attention deficit and sleep disorders are infiltrating college campuses and workplaces around the world, where they are being used without prescription to enhance cognition. Within the next decade, it might be possible to take a pill that will not only help alleviate the symptoms of learning disorders but also act as an intellectual steroid, pumping up the brain's potential. What the mice have clearly shown, in ways that pill-popping humans have not, is that enhancement could have unexpected trade-offs.

Improving on evolution

It was while Silva was studying mouse models of neurofibromatosis, a genetic disorder characterized by learning disabilities and benign tumours in nerve tissue, that he inadvertently created his first smart mouse. The disorder is caused by a mutation in a single gene, and Silva thought that models of the disease might allow him to investigate the molecular mechanisms underlying learning and memory.

In one model, Silva and his colleagues found that Ras, a family of growth-promoting signalling proteins, had enhanced activity in a subset of neurons that inhibit the firing rate of connected neurons. Steven Kushner, a postdoc in Silva's lab, engineered a mouse that had a constantly active form of one of the Ras proteins, Hras, but only in excitatory neurons, which increase the firing rate of connected neurons. The team was

T. SILVA

surprised to find that these animals learned and remembered things much faster than normal mice in certain memory tests[1]. After just a single trial, the engineered mice learned to link a minor electrical shock with specific surroundings, causing the animals to freeze in fear when placed back in the cage where it first received the shock. Normal animals don't learn this association with such a mild shock.

The team was able to identify how this enhanced learning came about at the molecular level. Long-term memory is believed to be based on the strength of the link between two nerve cells. What Silva's team saw was an increase in the amount of the neurotransmitter glutamine being released at the synapse — the junction between two neurons — in the Hras mutants, which strengthened the connection at that junction through a process called long-term potentiation (LTP).

"The thrilling part is being able to connect these seemingly slight differences at the molecular level to dramatic differences in observed behaviour," Silva says. "That's a sign that we're really starting to understand the core processes of learning and memory in the brain."

Unlike Silva, Tsien had set out to create a smart mouse when he developed Doogie. He focused on brain-cell receptors for the chemical NMDA (*N*-methyl-D-aspartate). First linked to long-term memory in the late 1980s, the NMDA receptor is often referred to as the brain's 'coincidence detector' as it is activated only when two connected cells fire simultaneously. The receptor enhances LTP, with the end result that the brain can detect the connections between seemingly separate events, such as seeing fire and feeling pain.

Tsien created Doogie by overexpressing a subunit of the NMDA receptor called NR2B. This kept the receptors open for longer, strengthening the synaptic link and making it easier for disparate events to be linked together. "They all thought I was crazy," recalls Tsien. "They said the brain has been optimized by evolution. You won't be able to improve it."

When Tsien published his results[2] in 1999, the media reacted with excitement and hyperbole. *Time* magazine put the research on its cover, asking whether researchers had finally found the "IQ gene".

Doogie and the enhanced mutants that have followed in its wake share more than just the accolade of being smart. "What's most striking about these different animals is the convergence," Silva says. Nearly all of the mouse strains show enhanced LTP. "There are so many different ways to tinker with learning and memory, and yet almost all of these improvements work through the same mechanism," he says. According to Silva and others, this is evidence that LTP is a fundamental feature of learning and memory, and that by increasing plasticity it is possible to increase cognitive capacity.

The damage undone

Being able to genetically engineer an animal with enhanced brain power is exciting, but can a brain that has already developed abnormally be fixed? In some instances, the answer may be yes.

One promising example involves work on a protein called CREB, which is implicated in memory formation. In 1995, Tim Tully, a neuroscientist then at Cold Spring Harbor Laboratory in New York, managed to improve memory and learning in a mutant fruitfly[3] by overexpressing a form of CREB. He and others built on this work in mice to try to tackle a rare genetic condition called Rubinstein–Taybi syndrome.

Characterized in humans by severe learning difficulties, as well as short stature and an increased risk of developing tumours, Rubinstein–Taybi syndrome is caused by mutations in the gene for the CREB-binding protein. Neuroscientists had assumed that the cognitive defects caused by the syndrome were irreversible — especially as the condition can be diagnosed before birth. But in 2003, Tully and several others showed that administering drugs that increase CREB activity in mouse models of the disease dramatically improves the animals' ability to learn[4–6].

UNIV. TEXAS SOUTHWESTERN MED. CENTER

"We get complete recovery in adult mice," says Mark Mayford, a neuroscientist at the Scripps Research Institute in La Jolla, California, who was an author on one of the studies. "I was pretty amazed."

The success stretches beyond Rubinstein–Taybi syndrome — the cognitive defects in other developmental diseases such as neurofibromatosis, Down's syndrome and fragile X, a genetic disorder that causes a wide range of behavioural and intellectual deficits, have all proved to be reversible in mice[7]. Although it remains unclear if the same approach can be applied to humans, Tully and others are bullish. "This work is a shot across the bow of the future," says Tully, now chief science officer at Dart NeuroScience in San Diego, California, which has been investigating compounds that manipulate the CREB pathway. "It shows us just how important increasing plasticity can be, and how we can put plasticity to work."

James Bibb at the University of Texas Southwestern Medical Center in Dallas says that drugs developed as a result of this work could be used to treat conditions such as post-traumatic stress disorder and drug addiction, which require people to unlearn negative associations. "The purpose of the brain is to help us learn useful information," Bibb says. "By increasing plasticity, you can push that process along."

Silva imagines a near future in which people with learning and memory disorders will be slotted into a number of categories, based on the molecular specifics of their disorder. "We could then target the therapy," he says. "We could use what we've learned from these enhanced mice to selectively fix what isn't working."

The concern for some is that otherwise healthy humans would want to take such drugs in a bid to make themselves smarter or stave off age-related cognitive decline. "I think these drugs are going to lead to some real slippery-slope issues," says Martha Farah, who heads

the Center for Neuroscience and Society at the University of Pennsylvania in Philadelphia. "There is no clear or objective line between a normal brain and one that needs treatment. For instance, we can say that we're only going to use these memory drugs for people with demonstrated memory decline. But your memory starts to diminish in your thirties. Does that mean every 40-year-old is going to be taking these pills?"

Farah notes that this is already starting to happen with drugs used to treat attention deficit or sleep disorders, as these act as mental stimulants. For instance, one in five respondents to a web poll run by *Nature* in 2008 admitted to using some of these drugs, such as Ritalin (methylphenidate) or Provigil (modafinil), to enhance their focus and productivity[8]. "You get more and more people taking them for less and less severe conditions," she says.

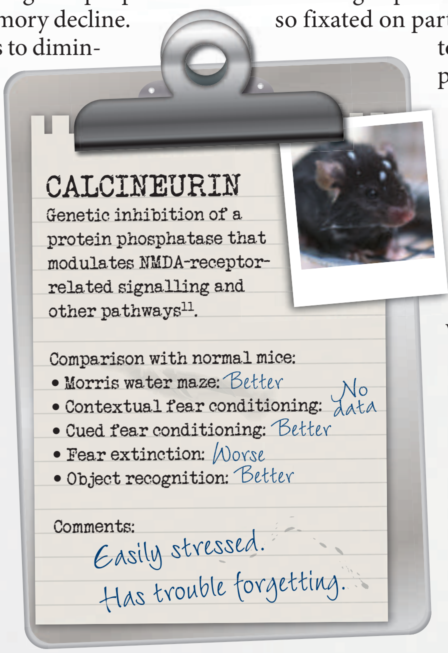

I. MANSUY/UNIV. ZURICH

Risky business

Little is known about the side effects and trade-offs of both the current usage or the drugs in development, but initial clues offered by smart mice raise concerns. The Hras strain developed in Silva's lab might be good at learning, but its fear response for a relatively benign stimulus would be counterproductive for a wild mouse. Its enhanced memory is both a blessing and a burden. Silva cites other strains of smart mice that excel at solving complex exercises, such as the Morris water maze, but that struggle with simpler mazes. "It's as if they remember too much," he says — possibly taking in irrelevant information such as the position of windows or lights but missing the big clues.

Farah sees a parallel between these mice and one of the few case studies of an individual with profoundly enhanced memory. In the early 1920s, the Russian neurologist Alexander Luria began studying the learning skills of a newspaper reporter called Solomon Shereshevsky, who had been referred to the doctor by his editor. Shereshevsky had such a perfect memory that he often struggled to forget irrelevant details. After a single read of Dante's *Divine Comedy*, he was able to recite the complete poem by heart. Although this flawless memory occasionally helped Shereshevsky at work — he never needed to take notes — Luria also documented the profound disadvantages of such a capacious memory. Shereshevsky, for instance, was almost entirely unable to grasp metaphors, as his mind was so fixated on particulars. When he tried to read poetry, for example, "the obstacles to his understanding were overwhelming", Luria wrote in his book *The Mind of a Mnemonist*. "Each expression gave rise to a remembered image; this, in turn, would conflict with another image that had been evoked."

For Luria, Shereshevsky's struggles were a powerful reminder that the ability to forget is as important as the ability to remember. Enhancing human memory in individuals without severe cognitive defects might prove counterproductive.

Many scientists are concerned that the animal models of enhanced cognition might obscure subtle side effects, which can't be studied in rodents or primates. Farah is currently looking at the trade-off between enhanced attention — she gives human subjects a mild amphetamine — and performance on creative tasks. Other researchers have used computer models to show that memory is actually optimized by slight imperfections, as they allow one to see connections between different but related events[9]. "The brain seems to have made a compromise in that having a more accurate memory interferes with the ability to generalize," Farah says. "You need a little noise in order to be able to think abstractly, to get beyond the concrete and literal."

And then there's the problem of non-cognitive side effects. Because many of these learning and memory enhancements involve molecules that regulate a wide variety of fundamental cellular pathways, such as CREB, it might be impossible to restrict their action to the brain. The Doogie mice, for example, seem to have an increased sensitivity to pain. And the *Hras* gene mutated in Silva's mice is commonly mutated in cancer.

"There's no such thing as an enhancement without side effects," says Nobel laureate Eric Kandel, a neuroscientist at Columbia University in New York and co-founder of Memory Pharmaceuticals, a biotechnology company in Montvale, New Jersey, that is trying to turn his research on LTP into novel drug therapies for memory disorders. "It often takes years to fully understand all the side effects. The mice will help us work out some of the bugs, but these will still be very risky treatments."

Although Silva recognizes the risks of enhancement, he remains hopeful that the performance of the normal human brain can be improved by neuroscience. "We're getting to a point where we almost need these enhancements," he says. "We don't have enough attention, we don't have enough memory, we don't have enough awake hours. There's clearly a demand to optimize the human brain given what it needs to do in the information age."

Like Kandel, Tully has spent much of the past decade trying to translate the biochemistry of memory into useful medical therapies. He remains enthusiastic, although he is also aware that the road ahead is littered with false leads, mistaken hypotheses and treatments that work in mice but fail in clinical trials. It's been ten years since Tsien, now at the Medical College of Georgia in Augusta, created Doogie, and although that's a short time in research years, Tully, for one, is getting impatient.

"When I began working on these learning and memory drugs, I had no grey hair and I thought I'd find a drug that might be able to help my parents," Tully says. "Now my hair is mostly white and my parents are dead. I'm just hoping that we can find a drug in time for me." ■

Jonah Lehrer is a freelance writer based in Los Angeles, California.

1. Kushner, S. A. *et al. J. Neurosci.* **25,** 9721–9734 (2005).
2. Tang, Y.-P. *et al. Nature* **401,** 63–69 (1999).
3. Yin, J. C. P., Del Vecchio, M., Zhou, H. & Tully, T. *Cell* **81,** 107–115 (1995).
4. Bourtchouladze, R. *et al. Proc. Natl Acad. Sci. USA* **100,** 10518–10522 (2003).
5. Alarcón, J. M. *et al. Neuron* **42,** 947–959 (2004).
6. Korzus, E., Rosenfeld, M. G. & Mayford, M. *Neuron* **42,** 961–972 (2004).
7. Ehninger, D., Li, W., Fox, K., Stryker, M. P., & Silva, A. J., *Neuron* **60,** 950–960 (2008).
8. Maher, B. *Nature* **452,** 674–675 (2008).
9. McClelland, J. L. in *Memory Distortion: How Minds, Brains, and Societies Reconstruct the Past* (ed. Schacter, D. L.) 69–90 (Harvard Univ. Press, 1995).
10. Hawasli, A. H. *et al. Nature Neurosci.* **10,** 880–886 (2007).
11. Malleret, G. *et al. Cell* **104,** 675–686 (2001).

P. MURPHY

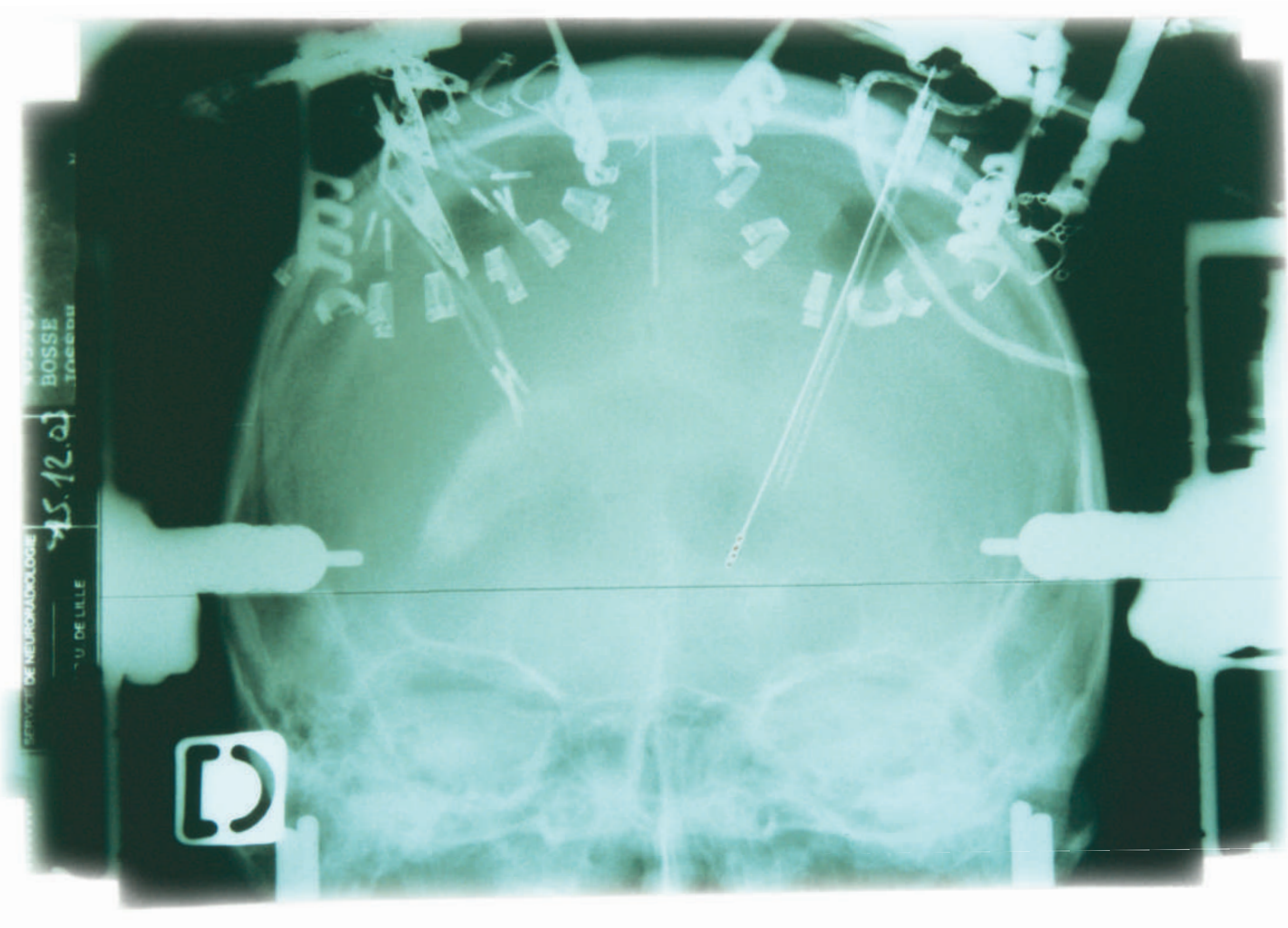

BSIP, A.-C. LILLE/SPL

OPENING UP BRAIN SURGERY

Neurosurgeons have unparalleled access to the human brain. Now they are teaming up with basic researchers to work out what makes it unique, finds **Alison Abbott**.

Two years ago, a top salesman in a major Italian engineering company drove himself to the emergency department of the San Matteo Hospital in Pavia. He was frightened. He could think clearly and he could move his hand normally, but for the past few days he hadn't been able to write. The business e-mails he had confidently typed out on his computer made no sense when he read them back. And he found he was unable to write a simple word by hand.

Tests at the hospital showed him to be apparently fit. He could express himself without problem, read, spell words out orally letter by letter — and he could even draw simple objects. The doctors started to wonder whether they should call in a psychiatrist. But when a brain scan showed what seemed to be a tiny tumour, they called neurosurgeon Lorenzo Magrassi instead. Magrassi immediately prescribed drugs to treat the swelling, which was pressing on surrounding brain areas, and within a couple of days the patient was able to write again.

Magrassi was intrigued. He had not heard of a similar case of agraphia — the inability to write. So when he operated the following week to remove the tumour, he also undertook a little research. The patient, who was in full agreement, was asked to speak while Magrassi stimulated his brain with an electrode. He was also provided with paper and a pen to jot down dictated sentences until the surgeon found just the spot that controlled writing.

Magrassi's techniques were not new: brain surgeons frequently stimulate around a tumour or other diseased tissue that they plan to remove while a patient is awake and able to answer questions. This 'functional brain mapping' allows them to identify the areas involved in speech and other functions that they would prefer not to cut into (see 'Open brain biography', page 868).

What is new is the way that neurosurgeons are using these techniques for bolder exploratory brain mapping, often in collaboration with basic researchers. In short, the surgeons have a unique opportunity to access and stimulate the human brain, and, as technologies improve, more of them are starting to use it. "Neurosurgery can contribute to neuroscience by giving a glimpse into the mind, a rare window into the brain," says surgeon Itzhak Fried from the University of California, Los Angeles. "We can start to look at uniquely human abilities."

> "Neurosurgery can contribute to neuroscience by giving a glimpse into the mind."
> — Itzhak Fried

Some of the collaborations springing up are tackling aspects of humanness — such as consciousness or language — that are of long-standing interest to neuroscientists and of practical relevance to neurosurgeons. Magrassi emphasizes that his probing was not purely experimental, but has application for future surgery. "It is often as clinically important to preserve writing after surgery as it is to preserve speech, and we need to understand which areas to avoid," he says.

Nonetheless, brain science has benefited. Over the next few months, and again with informed consent, Magrassi repeated his map-

ping activity in two other patients with brain tumours even though they had not shown writing difficulties. He found that the area required for writing was always in the same spot in a structure called the superior parietal gyrus on the left side of the cortex. His results — yet to be published — extend theories about the neural circuitry of writing, a quintessentially human activity. Writing seems to co-opt brain structures in areas involved in language, visual processing and facilitating movement, and lesions in some of these areas can drastically interfere with writing ability. Normally these deficits are accompanied by others, such as an inability to speak, read or move normally. Since stimulation of the 'writing spot' did not interfere with these, Magrassi's studies suggest that the linguistic and motor circuits involved in writing are more integrated with each other than previously thought.

Exploratory brain studies are not yet commonplace. It can be difficult to experiment in the operating theatre with the active participation of patients, who are stressed and distracted.

But in some circumstances patients' brains can be available for days after the surgery. When neurosurgeons implant electrodes into the subcortical part of the brain to treat Parkinson's disease with deep-brain stimulation (DBS), they sometimes leave the leads outside the skull for a day or two to make sure that the procedure was successful before connecting them to a stimulator and battery and sewing everything under the skin.

In clinical trials of patients with psychiatric disorders, neurosurgeon Volker Sturm, at the University of Cologne, Germany, leaves the electrode leads hanging out even longer — up to four days — to provide time to experiment. Sturm is extending DBS treatment to disorders such as major depression, obsessive-compulsive disorder and alcoholism. The operation involves placing electrodes in a small area within the nucleus accumbens, a tiny structure that has a fundamental role in reward and is easily hijacked by addictive substances. Many of the tests that Sturm's neuroscience collaborators perform while the electrode leads are exposed have direct clinical relevance. Some, for example, are designed to investigate the effect of stimulation in the nucleus accumbens on neurons' electrophysiological properties and whether these properties can help to predict any psychiatric benefits that might later emerge.

Others look like experiments in basic brain science. In a study published last June[1], Sturm and his collaborators investigated what happens in the brain when patients change strategies to fit new circumstances. A major function of the nucleus accumbens is to assess the value of a reward and adapt behaviour in response. The group analysed data from six patients fresh from surgery. A day after the electrodes were implanted in their left and right nuclei accumbens, the researchers recorded local field potentials around the electrodes. They also used electrodes placed on the scalp to record neurophysiological oscillations in the medial frontal cortex, which has direct connections to the nucleus accumbens.

The patients then did a simple gambling task in which they had to guess which side of



Brain surgery patients increasingly participate in research.

L. MAGRASSI

J. MCNALLY/GETTY

A. ABBOTT

a coin would pay out a cash prize. When the experimenters changed the odds of winning, the patients changed their gambling strategies — and the synchrony of electrical oscillations in the various brain areas also changed. The team concluded that a neural network between the nuclei accumbens and medial frontal cortex activates rapidly when the patients adjusted their behaviour to fit the new facts. "Yes, it is basic science," says Michael Cohen, a member of the collaboration and a psychologist at the University of Amsterdam, "but it may eventually have clinical relevance." For instance, he says, surgery might be avoided if the nucleus accumbens can be modulated indirectly via the medial frontal cortex, which can be stimulated through the skull.

New surgical procedures for epilepsy offer a particularly tantalizing opportunity for neuroscientists, because they allow access to the cortex — the region where thinking goes on — and the opportunity for very precise recording.

Some particularly brutal forms of epilepsy that don't respond to drug treatment originate in the medial temporal cortex and can be cured by surgical removal of the region responsible. Neurosurgeons identify the exact focus by implanting a handful of electrodes around the medial temporal cortex, waiting for the patients to have a spontaneous seizure and then determining the origin of the epileptic activity. They typically use 1-millimetre diameter electrodes that pick up the average signal from some one thousand to one million neurons. But more teams are starting to use 'microelectrodes' too. This technique involves fixing eight very fine recording wires, with diameters of less than 50 micrometres, to the end of the larger electrodes like wiry spiders. Whether the microelectrodes have further clinical benefit remains unknown, but it is not thought to do any harm, and for research it allows many levels of electrical signals to be recorded, from the oscillations in large populations of cells down to firing in single cells.

Fried has been using the electrode systems since the 1970s and is the acknowledged pioneer of this technique in research. In the past half-dozen years, strides in data analysis have allowed faint and infrequent signals from single cells to be extracted from the noise. These are the sort of signals that excite those interested in human consciousness because they reflect rare or subtle events — such as recognizing the face of a celebrity.

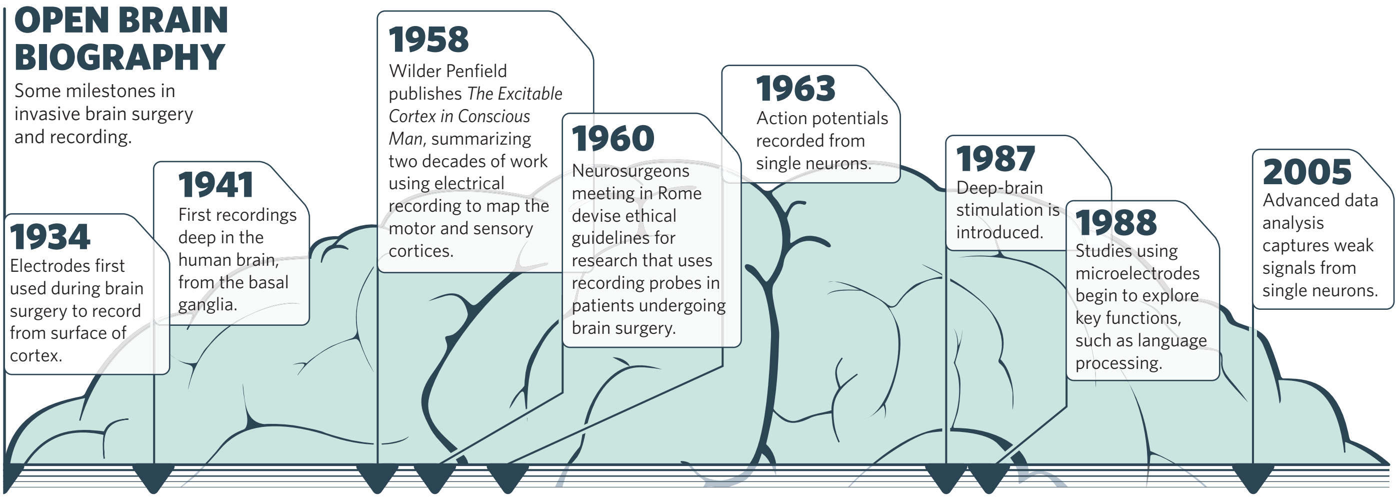

Rodrigo Quian Quiroga, a physicist-turned-neuroscientist and one of Fried's collaborators, hit headlines around the world in 2005 when he and his colleagues unveiled their concept of the 'Jennifer Anniston neuron'[2]. Quian Quiroga came to the California Institute of Technology (Caltech) in Pasadena as a postdoc in 2001 mainly for the opportunity of recording from single neurons in patients with epilepsy who were being operated on by Fried. He was particularly interested in how the human hippocampus, part of the medial temporal lobe, is involved in recognition of people or objects.

Recording from an array of 64 individual electrodes in a brain can generate hundreds of gigabytes of information a day. So Quian Quiroga made it his first task to find a better way to sort through the vast dumps of data. Having a background in physics helped, and by 2003 he had devised a neat algorithm that could sort through the tangled electrical signals and unambiguously identify spikes from single neurons. In one step he raised the entire game.

He tackled the recognition question by following the activity of single neurons while patients looked at hundreds of pictures on his laptop — from the actress Jennifer Aniston to the Sydney Opera House. Each neuron typically fired to one concept, but it did so rather flexibly: the Jennifer Aniston neuron would fire to different pictures of the actress but not to other celebrities. In some patients, Jennifer Aniston neurons would also fire to other actresses in *Friends*, the popular television series in which she starred. But they would never fire to other similar-looking, but otherwise unconnected, actresses. Quian Quiroga, now at the University of Leicester, UK, recalls his amazement when he found a single neuron in a patient firing in reaction to himself, even though they had met just a couple of days before.

He went on to show that these neurons fire only if the patients consciously recognize the pictures[3] and that they would also fire if a person was told the name of a person or object[4].

"These neurons in the hippocampus encode information in a very abstract way, whatever type of sensory information leads to it," says Quian Quiroga. "This makes sense given that long-term memories are stored as abstractions — 'Jennifer Aniston as a concept' — and we tend not to remember details like what her hair looked like."

With these types of revelation emerging, it is perhaps not surprising that other epilepsy neurosurgeons are getting in on the act, starting to use microelectrodes and forge imaginative collaborations with neuroscientists, particularly now that the sophisticated components can be bought commercially.

It is a slow business though. One reason is the scarcity of patients who undergo this sort of neurosurgery. Even Fried's large centre operates on barely a dozen such people per year. Another is that it takes time to develop the expertise and build up a team. Neurologist Mark Richardson from King's College London, acknowledges that two years after implanting microelectrodes into his first patients, he is still very much at the beginning when it comes to research. "It takes a very long time for things to become routine," he says.

Neurosurgeon Adam Mamelak of the Cedars-Sinai Medical Center in Los Angeles, California, has built up collaborations with neuroscientists at Caltech. One such effort explored people's ability to detect 'novelty', something fundamental to many types of learning. The researchers identified some neurons in the hippocampus and amygdala that increase their rate of firing when the brain is confronted with new images, and some that do so when confronted with familiar images[5]. In another Caltech collaboration, he is looking at conscious decision-making in gambling tasks with neuroeconomist Antonio Rangel. "Animals can't perform these sorts of tasks," he says.

A big advantage of animals, though, is that the experimenter can decide where in the brain to place the electrodes. In patients, electrodes must be positioned strictly according to clinical need. "The task of experimenters is to work out what we can do, given a particular distribution," says Quian Quiroga. "Patients always come first and we don't do anything with them if they are tired or have visitors."

"There is absolutely no risk for the patients, and they are just sitting around getting bored."
— Adam Mamelak

All experiments are carefully regulated by ethics boards. Neurosurgeons say that patients nearly always agree to participate — and enjoy it. "There is absolutely no risk for them, and they are just sitting around getting bored," says Mamelak. "They take pride in contributing to the field of brain science," adds Fried.

Fried says that his collaborations with Qian Quiroga and others have allowed him to follow a line of research on memory. "Everything that you will consciously remember will have to be processed in the hippocampus," he says, adding that such studies could eventually help guide epilepsy surgery in the medial temporal lobe, "where memory networks sometimes overlap with epilepsy networks".

Fried says that some neurosurgeons wonder whether it would actually be unethical not to experiment, given how little is known about the brain entrusted to their hands, and given that the opportunity is there. The potential to learn about the neural basis of humanness — so that they can try to preserve it — is an opportunity that few want to pass up. ■

Alison Abbott is *Nature*'s senior European correspondent.

1. Cohen, M. X. *et al. J. Neurosci.* **29,** 7591–7598 (2009).
2. Quian Quiroga, R., Reddy, L., Kreiman, G., Koch, C. & Fried, I. *Nature* **435,** 1102–1107 (2005).
3. Quian Quiroga, R. Mukamel, R., Isham, E. A., Malach, R. & Fried, I. *Proc. Natl Acad. Sci. USA* **105,** 3599–3604 (2008).
4. Quian Quiroga, R., Kraskov, A., Koch, C. & Fried, I. *Curr. Biol.* **19,** 1308–1313 (2009).
5. Rutishauser, U., Mamelak, A. N. & Schuman, E. M. *Neuron* **49,** 805–813 (2006).

CORBIS

Shaking up earthquake theory

Geological faults are not behaving as scientists once expected. **Glennda Chui** reports on efforts to forge a new understanding of quake behaviour.

That low rumbling emanating from California is no earthquake. It is the sound of the state's carefully honed earthquake-forecasting process being shaken hard and put back together.

"We're talking about a radical overhaul," says Ned Field, a seismologist with the US Geological Survey (USGS) in Denver, Colorado, and chairman of the Working Group on California Earthquake Probabilities. The group is charged with forecasting the probability of damaging earthquakes throughout the state over the next 30 years.

The group's report is due out in 2011 and, like its predecessors (see 'Earthquake probabilities in the California area'), it is expected to have enormous influence — not only on research but also on public policy in California, the most populous state in America and home to three-quarters of the nation's seismic risk. California has the most comprehensive earthquake-forecasting effort in the world and some of the best-studied faults, so lessons learned there will have ripple effects on other quake-plagued nations.

From the standpoint of seismology, the report could push aside an influential family of ideas that have long dominated earthquake research and forecasting. One hypothesis views faults as creatures of habit that tend to rupture in large, 'characteristic' earthquakes of about the same magnitude again and again. Another model asserts that big quakes are most likely to strike in 'seismic gaps' that haven't suffered major jolts in a long time. Both attempt to explain quake behaviour in relatively simple physical terms, and make intuitive sense. But recent research has caused confidence in them to waver.

The world of characteristic earthquakes is "a world we all wish we lived in", says Thomas Jordan, director of the Southern California Earthquake Center in Los Angeles. "It hasn't worked out that way because earthquakes don't occur on simple fault structures, but on fault systems that are rather complicated." Jordan contends that earthquakes involve complex interactions among faults, leading to chaotic behaviour that is very difficult to predict. The physics of individual faults and the way in which they influence each other may, in fact, be so complex that no simple deterministic rules can explain their behaviour.

This new understanding challenges not only the idea of characteristic earthquakes but also an older and more fundamental notion that faults obey regular patterns of behaviour. Called the elastic rebound theory, that concept sprang from the earthquake that levelled large parts of San Francisco in 1906 (pictured above). It was developed by geologist Henry Fielding Reid of Johns Hopkins University in Baltimore, Maryland, who led the official investigation into the geology and physics of the disaster.

After studying the rupture along the San Andreas fault and the aftermath of the ground movement, Reid came to view earthquakes as a repeating pattern of pressure accumulation and release. Strain would build up in the ground until it reached a critical level. At that point, the rocks on one side of a fault would jerk forward relative to their neighbours on the other side. The sudden movement would release almost all the pent-up energy in the ground, and it would take some time before enough strain would accrue to make another quake possible.

Reid's was a revolutionary idea, coming as it did half a century before plate tectonics explained where all that stress on the San Andreas fault was coming from. And it was wonderfully appealing, because it implied that the cycles might be regular enough to predict earthquakes. In his 1910 report detailing the results of his investigation[1], Reid proposed a way to foretell when the next earthquake was due: plant a line of piers at a right angle across the fault and measure their relative angles, distances and heights from time to time. When the measurements show that the strain has built to a critical level, he wrote, "we should expect a strong shock".

Stretched too far

For a century, the elastic rebound theory has been a foundation on which later seismic hypotheses were built: after all, the strain that builds up in the ground as Earth's crustal plates jostle past each other must be released, eventually, in the form of earthquakes or through a slow, quiet alternative called aseismic slip. But the idea that quakes come tumbling out as

steadily as stress goes in is increasingly coming under attack as earthquakes prove to be much more complicated — and more staunchly individual — than Reid ever imagined.

That individuality has made itself known in numerous ways. In some cases, quakes have come in clusters, such as the giant magnitude-9.1 shock that hit off the northwest coast of Sumatra in 2004 and was followed by a series of nearby quakes, including one last month. In other instances, they rupture large sections of faults, combining patches that had not been known to move together in previous seismic events. Earthquakes even hop from fault to fault, as seen in the magnitude-7.3 earthquake that struck the town of Landers in California's Mojave Desert and the magnitude-7.9 shock that hit central Alaska in 2002. Both of these quakes also had other claims to fame: they triggered tremors, geyser eruptions and other seismic activity thousands of kilometres away.

EARTHQUAKE PROBABILITIES IN THE CALIFORNIA AREA

A 2009 earthquake forecast for California based on theoretical models of how faults behave.

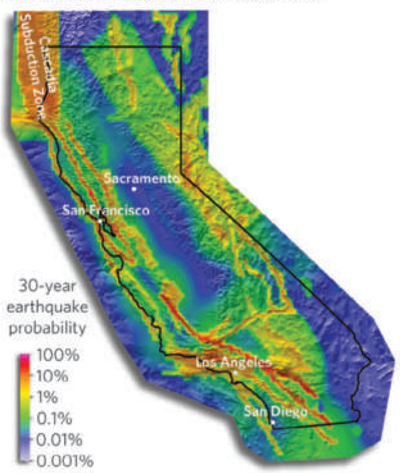

SOUTHERN CALIFORNIA EARTHQUAKE CENTER

The evidence against seismic regularity has emerged even along the San Andreas fault, where earlier research had provided the appearance of a repeating pattern of large earthquakes. That picture had come from research done in the late 1970s and early 1980s on the south-central section of the San Andreas fault, north of Los Angeles. Geologists working there had determined how much streams and other features had been offset by the great Fort Tejon earthquake of 1857, which measured magnitude 7.9. Trenches dug along the fault had revealed a series of earlier, similar quakes spread about 200–400 years apart. In each spot, the fault appeared to have slipped about the same amount during each quake[2].

But recent excavations have dramatically changed that picture. In 2004, Lisa Grant Ludwig of the University of California at Irvine, began digging trenches in a place called the Bidart Fan, where a series of small streams have cut channels across the south-central San Andreas fault through a thick deposit of sediment. Along the trench walls, past earthquakes show up as disruptions in the sedimentary layers, which can be dated using carbon-14 analysis. In January, she and two other geologists published a paper[3] that lowered the recurrence interval for large earthquakes on this part of the fault to 137 years. Since then they have dropped their estimate to less than 100 years, with some large quakes striking as few as 50 years apart — implying that earthquakes are not as regular as the previous studies suggested.

"Elastic rebound, I think, is still kind of like the foundation," Grant Ludwig says, "but maybe the building that's going to be built on that foundation is going to look a little different."

Thomas Fumal, a palaeoseismologist with the USGS in Menlo Park, California, who has been investigating the San Andreas Fault for 25 years, says that the picture along most other parts of the fault also does not conform with past expectations: scientists are finding large quakes striking sections of the fault much more often than previous studies suggested — and with a wide range of magnitudes.

Tardy quake

The idea of characteristic earthquakes suffered another blow in 2004, when the San Andreas fault let loose a magnitude-6 shock near the central Californian town of Parkfield. Researchers had set up a dense network of instruments there in the 1980s, anticipating a moderate quake by 1993 as part of a roughly 22-year cycle that had been witnessed in quakes going back to the 1800s. When it finally arrived more than a decade late, its timing and other idiosyncracies "confounded nearly all simple earthquake models" according to a 2005 report[4].

David Jackson has long expected these kinds of developments because they match what he has been seeing in earthquake patterns around the world. In 1991, Jackson and Yan Kagan, both at the University of California, Los Angeles, analysed a global catalogue of seismic events and concluded that large earthquakes bunch together in space and time[5]. This wasn't supposed to happen. If earthquakes obeyed the elastic rebound theory, large quakes should reset the seismic clock and there should be a gap before another big shock hit the same region.

Kagan and Jackson argued that regions hit by a big quake were more likely, rather than less likely, to be struck by another[6]. Other geophysicists largely dismissed their claims, but then a stunning sequence of earthquakes hit California's Mojave Desert. A magnitude-6.2 earthquake struck Joshua Tree in April 1992, followed two months later by the Landers quake and the magnitude-6.5 Big Bear quake, and then seven years later by the magnitude-7.1

Hector Mine earthquake.

Scientists had known for some time that smaller earthquakes can come in clusters; that's what happens when the ground rattles with aftershocks following a major tremor. But the idea that one large quake could follow on the heels of another was startling. Researchers now routinely talk about large quakes triggering others, both on nearby and distant faults.

In fact, the giant 2004 Sumatran quake was followed by an unusual pattern of small tremors near Parkfield — suggesting that the Indonesian event had weakened the San Andreas fault some 8,000 kilometres away, according to an analysis published this month[7]. In that study, Taka'aki Taira, a seismologist at the University of California, Berkeley, and his colleagues suggest that the Indonesian quake also could have triggered a spate of magnitude-8 shocks around the world.

Trigger happy

Karen Felzer of the USGS in Pasadena, California, says that she has come to believe that many quakes of all sizes are triggered by other shocks, rather than simply responding to local forces. "Personally I agree with Jackson and Kagan that elastic rebound doesn't really happen — that what is controlling the timing of all earthquakes is the triggering process."

The upheaval in the world of seismology will play out most strikingly in the work leading up to the 2011 report on California earthquake probabilities. When Earth scientists drew up the first incarnation of this report in 1988, the picture was much simpler. An expert group of geophysicists and geologists divided the faults of the San Andreas system into well-delineated segments. They assigned probabilities of future seismic shocks to each segment on the basis of how much time had passed since that particular locale had generated a major quake.

But over the years, successive versions of the report have addressed complexities that have emerged from studies of past earthquakes, laboratory experiments and theory. Models were introduced that allowed fault segments to combine in various ways to create bigger quakes. And researchers recognized the hazard of as-yet unknown faults and assigned probabilities to them.

The latest version of the report, published this year[8], identified several issues that needed to be addressed urgently. "Does the interactive complexity of a fault system effectively erase or at least significantly reduce any predictability implied by elastic rebound theory?" asked the report. To this and other troubling questions, the working group acknowledged that the answer may be 'yes'.

S. AKCIZ

Lisa Grant Ludwig (second from top) and team study trenches dug along the San Andreas fault.

Field says that the layers of complexity in the most recent forecasts have accumulated to the point that "in some ways we've built a house of cards. We've identified several things we don't like about the model, things that need to be improved."

"We're in a situation where we can tear down the whole thing and start from scratch."
— Ned Field

But every time scientists tweak one part of the structure, another part starts to wobble. Now, Field says, "we're in a situation where we can tear down the whole thing and start from scratch. I think we'll end up with a much cleaner, simpler model rather than a patchwork of modifications".

The 2011 report, known as Uniform California Earthquake Rupture Forecast 3, will put less emphasis on fault segmentation or maybe even eliminate it, acknowledging that an earthquake may start or end anywhere. And although it won't throw elastic rebound out the window, neither will it assume that this model is the dominant factor in shaping patterns of seismic activity over the relatively short timescales — decades to centuries — that people care about most.

"We want to include elastic rebound, because there's still a lot of the community that thinks it is very important at the larger magnitudes, at least," Field says. However, no one yet knows how the model will be incorporated into a world of constant fault interaction and fewer constraints on fault ruptures, he says.

In fact, some say earthquakes are so complex that it may be impossible — as well as impractical — to pin them down based on an understanding of their physics alone. That has led researchers to propose purely statistical models to forecast upcoming quake behaviour in much the same way that they forecast aftershocks now. "There's a lot of push now toward the statistical side," says Andrew Michael of the USGS.

Geophysicists are putting some of their forecasting theories to the test through an Internet-based project called the Collaboratory for the Study of Earthquake Predictability. "The idea is to provide an environment where people can do scientific earthquake-prediction experiments that will be evaluated objectively," says Jordan, who started the centre three years ago with funding from the W. M. Keck Foundation. The project has testing centres in Southern California, New Zealand, Japan and Switzerland. Thirty-nine forecasting models are being tested at the Southern California Earthquake Center, and more than 40 in other countries. Each will run for five years, with no tweaking allowed along the way.

Information from these simulations, along with new data from the San Andreas fault and elsewhere, will be folded into the deliberations of the working group as it seeks to reconcile the competing views of how earthquakes work. Whether this overhaul of the forecasting method will be as radical as Field anticipates remains to be seen. In the end, the working group will use complex logic trees based on the full range of expert opinion to reach its conclusions. David Schwartz, a geologist with the USGS and one of the founders of the characteristic quake model, says that it would be a mistake to toss out the basic elements of elastic rebound or the idea that earthquakes on at least some fault systems come in regular cycles. He does not mind researchers exploring new models outside of the public-forecasting exercise, which has real consequences for state residents. "That's fine, to see where it leads," he says, "but not to set my earthquake insurance rates." ■

Glenda Chui is a science writer based in California.

1. Reid, H. F. (ed.) *The California earthquake of April 18, 1906, Report of the State Investigation Commission* Vol. 2 (Carnegie Institution of Washington, 1910).
2. Schwartz, D. P. & Coppersmith, K. J. *J. Geophys. Res.* **89,** 5681–5698 (1984).
3. Akçiz, S. O., Grant Ludwig, L. & Arrowsmith, J. R. *J. Geophys. Res.* **1144,** B01313 (2009).
4. Bakun, W. H. *et al. Nature* **437,** 969–974 (2005).
5. Kagan, Y. Y. & Jackson, D. D. *Geophys. J. Intern.* **104,** 117–133 (1991).
6. Kagan, Y. Y. & Jackson, D. D. *J. Geophys. Res.* **96,** 21419–21431 (1991).
7. Taira, T. *et al. Nature* **461,** 636–639 (2009).
8. Field, E. H. *et al. Bull. Seismol. Soc. Am.* **99,** 2053–2107 (2009).

CORRESPONDENCE

Pakistan: basic education essential to underpin reforms

SIR — The overhauling of Pakistan's academic institutions (*Nature* **461,** 11–12 and 38–39; 2009) would have been more effective and sustainable if policy-makers had opted instead for a two-pronged approach, promoting basic education alongside higher education.

Only 56% of children are enrolled in primary schools in Pakistan, compared with 83% in India, 94% in Iran and 98% in South Korea (see go.nature.com/RtyZks). These figures are lower for secondary schools, but Pakistan's are lowest by far. To increase enrolment in higher education, we have to increase the supply of potential candidates by investing more in primary and secondary schooling.

You mention that candidates for Pakistan's domestic PhD programmes are less well qualified than those going abroad. It is difficult to see how this situation will "correct itself", as your Editorial claims, if "too many ill-prepared students [are] gaining doctorates", as Athar Osama and colleagues suggest in their Opinion article. More than twice as many postgraduates are produced at home as abroad, and these are more likely to stay in the country to become future supervisors, so the cycle of poorly trained researchers is set to continue.

Pakistan's Higher Education Commission has not provided figures for the percentage of candidates who return to the country after studying abroad. If a substantial number decide to stay away, the reforms could backfire and boost the brain drain to developed countries.

Muhammad Naim Siddiqi Department of Psychiatry, Aga Khan University, Stadium Road, Karachi 74800, Pakistan
e-mail: naim.siddiqi1@gmail.com
Abdul Wahab Yousafzai Department of Psychiatry, Ayub Medical College, Abbottabad 22010, Pakistan
Raza Ur Rahman Department of Psychiatry, Dow University of Health Sciences, Baba-e-Urdu Road, Karachi 74200, Pakistan

Pakistan: cash infusion of limited use to universities

SIR — Athar Osama and colleagues' Opinion article (*Nature* **461,** 38–39; 2009) aims to provide a factual balance-sheet for Pakistan's higher-education system under General Pervez Musharraf. But several critical omissions leave it less than factual.

For example, the former government wasted enormous sums of money on prestige mega-projects. Nine new universities were abandoned after partial construction because of a lack of trained faculty, and expensive imported scientific equipment remains under-utilized many years later. The claimed 400% increase in publications was a result of salary bonuses awarded to professors who published in international journals, largely irrespective of substance and quality. These payments fostered a plagiarism culture that still goes unpunished.

The authors draw attention to a large increase in "relative impact" in some disciplines, based on citation of papers published in 2003–07. But were self-citations (a common ploy) eliminated from this count? I used an option available from Thomson Scientific and found the opposite result after eliminating self-citations.

The authors also praise the Higher Education Commission for increasing university professors' salaries. But this has created social disparities — a full professor now earns 20–30 times more than a school teacher. Professors, bent on removing barriers to their promotions and incomes, take on very large numbers of PhD students. To ensure that these students get their degrees, many professors seek the elimination of international testing, hitherto used as a metric for gauging student performance.

Pakistan's failed experiment provides a counter-example to the conventional wisdom that money is the most crucial element in the reform process. An enormous cash infusion has failed to improve teaching and research quality. There is much that other developing countries can learn from our experience — sadly, this is not what the authors convey.

Pervez Hoodbhoy Department of Physics, Quaid-e-Azam University, Islamabad 45320, Pakistan
e-mail: hoodbhoy@mit.edu

Pakistan: sense of urgency powered education reforms

SIR — As head of the Higher Education Commission (HEC) in Pakistan in 2003–08, I would like to add some points to those made in the Opinion article by Athar Osama and others on Pakistan's reform experiment in higher education (*Nature* **461,** 38–39; 2009).

We awarded research grants to qualified faculty to develop a high-quality indigenous PhD programme — not to produce "5,000 new PhDs ... over 5 years", as the authors suggest. Measures were introduced to ensure the quality of local PhDs, including mandatory evaluation of theses by at least two professors from technologically advanced countries. Because there were not enough suitable PhD supervisors in the universities, we sent some 3,800 students abroad, mainly to the United States and Europe, to study for a PhD, at a total cost of about US$1 billion.

The work carried out was overseen by an 18-member board that included federal secretaries of science and technology and education, representatives of the four provincial ministries of education, representatives of the senate and eminent private citizens. This board was empowered to change the budgetary allocations as well as the overall directions of the programme.

There followed a huge increase in international scientific research publications, from 600 or so in 2001 to more than 4,200 in 2008. About 50 new universities and degree-awarding institutes were established during this period, and enrolment in higher education almost tripled to about 400,000 by the end of 2008, having been just 135,000 in 2003.

A digital library was established to provide free access to 25,000 international journals and 45,000 textbooks for all public-sector university students. In the 2008 *Times Higher Education* rankings, four Pakistani universities are among the top 600 in the world — an unattainable position before 2003.

Our accounts were audited by government auditors and by an international private auditing company (we were the only government organization to employ one) to ensure transparency in expenditure.

We do not agree with the authors' view that we acted in too much of a hurry. We did implement the programmes with a certain sense of urgency, but that had nothing to do with the transient nature of the Musharraf government. It was due to our eagerness to get on with things and to avoid bureaucratic hurdles. They were a breathless six years, but all rules were strictly observed and no shortcuts were taken in achieving the huge positive changes that took place.

Atta-ur-Rahman COMSTECH Secretariat, 33 Constitution Avenue, G-5/2, Islamabad 44000, Pakistan
e-mail: aurahman786@gmail.com

"Who would have guessed that the working record of a mathematical project would read like a thriller?" Timothy Gowers and Michael Nielsen, page 879

Battlefield: hitting the supporters of biotechnology

SIR — You misidentify the victims in your News Feature on conflicts among scientists over genetically modified (GM) crops (*Nature* **461,** 27–32; 2009). The real victims on this "battlefield" are not the handful of people criticized for their research, but those scientists who want to realize the potential of plant biotechnology and the farmers who apply authorized products.

These people have to endure bomb threats, insulting letters and telephone calls, destruction of their fields (almost no UK field experiment has survived since 2000) and harassment of their children at school. As author of a UK Food Standards Agency report concluding that organic food provides no additional nutritional or health benefit, Alan Dangour was bombarded with hate mail from activists.

The whole biotech debate is an emotionalized mess, fuelled by lobbyists and society's zero-risk mentality. Scientists should not be wary of publishing their results just because they could be deliberately misinterpreted. But they must be vigilant. As Kai Diekmann, chief editor of *Bild*, the largest newspaper in Germany, said in a recent television broadcast, "More than 10 million readers is a huge responsibility. I have to consider every single word before it is printed."

Why are some scientists so sensitive if weak data are published? When I first met Ingo Potrykus, the inventor of the famous transgenic 'golden rice' (so called because of its extra β-carotene content), I was still Germany's top anti-GM campaigner with Friends of the Earth. Some 15 years after our public debate, I now understand his frustration. As a humanitarian and Roman Catholic, he has worked hard to develop rice varieties he believes could improve the lives of millions of poor children likely to become blind. But Greenpeace and other activists are sabotaging his efforts with false claims, initially that children could be poisoned by excess vitamin A (see go.nature.com/DFzvpc) and later that 4 kilograms of rice is the daily requirement for a therapeutic effect (see go.nature.com/GvkID9).

Scientists should think more carefully about the impact their words might have on the future of society, and their responsibility towards it.

Jens A. Katzek An der Elbe 5, 39104 Magdeburg, Germany
e-mail: katzek@biomitteldeutschland.de

A. SOTIRIOU/GETTY

Battlefield: useful debate needs caution and civility

SIR — The rage that is sometimes unleashed by proponents of genetically modified (GM) crops when they encounter evidence for potential risks is well described in your News Feature (*Nature* **461,** 27–32; 2009). Several pointers could help remedy the problem of abuse in this "battlefield".

Reviewers and editors of scientific journals should insist that critiques of GM studies are well-reasoned and constructive, and free of emotionally charged language that might inflame the issues. They should resist the temptation to publish potentially exciting but very preliminary studies that might attract unwarranted media attention (this also applies to findings on the potential benefits of transgenic crops).

Authors of controversial papers must be prepared for their conclusions to be misinterpreted and quoted out of context, even by reputable science writers, as the news flashes around the globe. Oversimplification by the media is prevalent, but careful wording of the paper's findings will encourage more accurate reporting.

Without caution and civility by all participating scientists, effective debate on the benefits and risks of GM crops will continue to be hampered.

Allison A. Snow Department of Evolution, Ecology and Organismal Biology, 318 W. 12th Avenue, The Ohio State University, Columbus, Ohio 43210, USA
e-mail: snow.1@osu.edu

Commercial pressure quelling creation of new microscopes

SIR — Your collection of articles on microscopy (*Nature* **459,** 629–639; 2009) rightly celebrates the success of innovators in the field. Unfortunately, the supply of new technologies is being threatened by commercial concerns.

Microscope manufacturers are obliged by world competition to specialize in a few high-end products only. Even though these products are hugely expensive, their total sales volume is now so small that the profits do not support the research and development of new microscopes. High prices call for purchase by a group, so the specification list expands and the cost spirals up.

Companies are wary of producing a low-cost microscope, such as SPIM (selective plane illumination, ideal for low-bleach imaging of embryos) for fear of losing their high-end sales. Several other new technologies, including CARS (coherent anti-Stokes Raman scattering microscopy, which provides chemical information similar to that given by infrared spectroscopy) and PALM (photoactivated localization microscopy, which brings the resolution down to a few nanometres), are not yet available commercially. Another method of super-resolution is being produced (STED, or stimulated emission depletion microscopy), but is not working as well as it does in the hands of the inventor.

Sadly, there are now several examples of inventions that might have been beneficial to science and medicine being suppressed by companies for marketing reasons — including one of my own design, an attractive and inexpensive confocal system.

Given that the normal route of exploitation is grinding to a halt, perhaps inventors could be funded directly to clone their inventions. There should be a pre-commercial phase of development by the public sector. It would also help to set up, where it does not exist already, an institute with the capability (optics, software, electronics experts and biologists) to develop these elaborate new microscopes. It is too much for any individual university or biomedical lab.

Brad Amos, Cambridge, UK

OPINION

Is the stimulus working for you?

More money for science is always good. Or is it? Six experts tell *Nature* what concerns them most about the US stimulus spending and suggest ways to ensure that it benefits research and society in the long term.

Richard Freeman
Harvard economist

Prospects for young researchers will worsen without additional funds.
In February 2009, President Barack Obama made "the biggest increase in basic research funding in the long history of America's noble endeavour to better understand our world" — a $20.5-billion addition to research and development (R&D) budgets over two years. With rare prescience for economists, in 2008 and 2009 John Van Reenen of the London School of Economics and I published analyses of how bursts in R&D spending affect the market for research. To avoid a post-burst hangover, we argued for smoother changes in spending.

Our analysis was based on what happened when the National Institutes of Health (NIH) spending dropped after the 1998–2003 budget doubling. The large adjustment costs in ramping up research produce less-science-per-dollar than if budgets change smoothly. The inevitable post-boom slowdown disrupts research careers.

The 2009 stimulus adds more to federal R&D per year than the NIH doubling. Even a strong economic recovery will not increase non-federal spending enough to offset the loss of stimulus monies in 2011. Corporate R&D has been fairly steady in the recession and will not rise greatly in recovery. The end of the stimulus thus risks replaying the NIH post-doubling disaster with the NIH forced to reject promising projects, young faculty unable to do their research and the careers of postdocs and graduate students in chaos.

We have two advantages over the past. We know what can happen when R&D spending drops sharply. And we know the stimulus funding ends in 2011. We must seek to prevent a foreseeable crash. John Holdren has proposed increasing normal budgets to reduce the impact of the drop off. Agencies and universities can smooth stimulus expenditures by allowing recipients to spend funds obligated in 2009 or 2010 over a longer period. Universities could earmark stimulus money for overheads to support research after the stimulus. But none of these policies can compensate for the loss of $10 billion or so in stimulus R&D funding in 2011.

G. HERBERT/AP

US President Barack Obama boosted research and development by $20.5 billion.

Congress should consider supplementary R&D 'smoothing' funds to prevent a hard landing. They would begin in 2011 and taper off rapidly. In April, President Obama endorsed devoting 3% of gross domestic product to R&D, compared to 2.7% in the recent past. Setting numerical targets is not the ideal way to determine R&D budgets. If spending promises transformative breakthroughs, spend more. If not, spend less. But assuming the country accepts the 3% goal, short-term soft-landing increments would help move R&D smoothly towards this higher long-term level.

> "Congress should consider supplementary 'smoothing' funds to prevent a hard landing."

Fred Block
Department of Sociology, University of California, Davis

Energy innovation could be wasted if there is no long-term political support.
President Obama's chief of staff, Rahm Emanuel, famously said that "you never want a serious crisis to go to waste". The Department of Energy (DoE), under the leadership of Steven Chu, has taken this wisdom to heart. Using billions of dollars from the 2009 economic stimulus and loan guarantees that Congress approved earlier, the DoE has moved quickly to accelerate innovation in energy technologies across industrial and research sectors.

In June, the agency announced that it was providing US$8 billion in conditional loans to support three firms to build production capacity for electric vehicles — Nissan, Ford and Tesla, a 2003 start-up based in San Carlos, California. In August, they announced $777 million over five years to fund 46 Frontier Energy Research Centers — at universities and federal labs — each of which will tackle a specific energy-related technological challenge. Also in August, the agency announced $2.4 billion in matching funds to support production capacity for advanced batteries and drive systems for electric vehicles. Similar announcements support biofuels, solar power and wind power.

With this approach, the DoE is trying to replicate the Silicon Valley model whereby intense technological competition generates a virtuous cycle of key breakthroughs that drive costs down. Many of these breakthroughs will come from scientists and engineers working in university and federal labs in collaboration with private firms. The DoE doesn't have to get every investment right; once it sparks a technological race, even companies tied to older technologies will have no choice but to join in. Chevron, for example, recently announced that it was partnering with a start-up to use algae to produce biodiesel.

It will take time to find out whether this DoE gamble will succeed. Given the challenge of global climate change, the US economy's dependence on imported oil and the urgency of creating 'green jobs' to put people back to work, the advantages seem clear. Moreover, the DoE is not starting from scratch; most of these alternative technologies have been nurtured by

federal programmes for the past two decades, albeit with more modest financing.

Unfortunately, the stimulus dollars are likely to run out well before the DoE's alternative-energy initiatives become self-sustaining. If the political system can't generate support for continuing funding beyond 2011, the whole effort could die on the launch pad. To prevent this, the DoE and Obama need to educate the public about the strategy they are pursuing and challenge the free-market myth that government lacks the competence to accelerate private-sector innovation.

Daniel Greenberg
Washington DC journalist and author of several books on science policy and politics

A new virtual agency could do better than existing agencies.

The stimulus money will, unfortunately, mainly reinforce the status quo at government research agencies. Political priorities for the stimulus were speed of delivery, job preservation and job creation. Even abiding by those criteria, the windfall still might have done some good, especially at the NIH. Its $10.4 billion could have been used to overcome two chronic failings long lamented by the NIH's own leadership: neglect of the young and aversion to risk.

How? By setting up a virtual alternative to its creaky grant system. Imagine a nimble, online-only proposal, review and award process dedicated to youth and scientific risk. Under the present costly and slow system, thousands of NIH peer reviewers travel each year to meet for face-to-face discussions. The results, by the NIH's own account, favour established researchers and humdrum proposals.

In response, the NIH has devoted tiny slices of its $30-billion-a-year budget to various remedies, including awards for younger researchers. But the efforts are minuscule. The median age for first grants now stands at 41, according to *The New York Times*. The bulk of the NIH's stimulus bonanza is going to a backlog of previously approved proposals that went unfunded for lack of money. Thus, more of the same. The National Science Foundation (NSF), graced with $3 billion in stimulants, is following suit.

Last year, the NIH reported funding more people over the age of 70 than under the age of 30. This was nothing new. Despite repeated demands for concrete actions from NIH leadership, the response, too often, is anguished oratory.

> "Bypass the venerable agencies, set up a new virtual agency and belt out a few billions to bold, young researchers."

The NSF and the NIH can both cite many scientific successes. The dedication, good intentions and skills of their staffs are not in doubt. But the system is geriatric. The gold-plated secret of US science is that it is stuffed with so much money that not even the dysfunctional ways of its chief paymasters can prevent a good deal of excellent research.

Next time politicians wants to add billions for research, they might consider a truly risky approach: bypass the venerable agencies, set up a new virtual agency and belt out a few billions to bold, young researchers. The results could be stimulating.

Michael Levi and **Adam M. Segal**
Council on Foreign Relations

Department of Energy pursuing sound strategy but funding is vulnerable.

The DoE got $36.7 billion in stimulus funds, more than double its annual budget for activities unrelated to nuclear weapons. At least $4 billion of that is devoted to R&D, and a good portion of the rest is for demonstration projects of new technologies to promote innovation. The agency's strategy for investing stimulus money in R&D has been prudent and sound, despite some worries that the department might be administratively overwhelmed by the massive inflow of funds, and some carping about the slower funding of transformational research.

G. J. PUSKAR/AP

The Department of Energy led by Steven Chu (second from right) is trying to accelerate private-sector innovation.

The biggest worry is that Congress may have unrealistic expectations about what energy R&D can achieve in the short term, and might be tempted to cannibalize research to pay for other, more politically attractive, activities. Already, in July, Congress chose to fund an extension of the popular but environmentally and economically dubious 'cash-for-clunkers' car-scrapping programme by raiding the renewable-energy loan guarantee budget at the DoE, thereby hurting long-term progress for short-term gain.

Basic research funding is a small part of the DoE stimulus package — but a large boost in the context of existing efforts. The DoE Office of Science has been given $1.6 billion on top of its annual $4-billion budget. As of early September, 78% of that had already been awarded, compared to 28% across the whole department. Some of this speed results from spending $500 million on construction and equipment procurement that has more in common with traditional stimulus than with research funding.

By directing money towards ongoing projects, the DoE has ensured that it supports areas that have already been vetted and probably have long-term prospects. A short-term funding boost risks creating new institutions with uncertain prospects. The DoE may avoid this pitfall by making longer-term plans: for example, it committed $277 million to 16 of the new Energy Frontier Research Centers to support five years of operation.

What about blue-sky research? The Advanced Research Projects Agency — Energy, the new agency tasked with supporting high-risk energy research, has $388 million to spend. The DoE Office of Energy Efficiency and Renewable Energy has another $2.5 billion for development, demonstration and deployment. Critics say this is not enough to jump-start any transformational research. They cite large amounts going into energy R&D in China by comparison. But it is unclear whether the US monies are insufficient for fundamental research; most of the big energy-innovation spending that is needed won't be for R&D, but for big demonstration projects, such as commercial-scale biofuel facilities. And the DoE's stimulus spending so far has been well structured — its focus on broad categories, not specific bets, is bottom–up and flexible, and yet is steering enough money to each area to have the potential for real impact.

The DoE will need to continue making the case for strong R&D funding — particularly by demonstrating results and linking them to real-world promise — to show that the money is being spent wisely.

Michael Crow
President, Arizona State University

The United States needs to shift to outcome-based research.

The decision of President Obama and Congress to greatly increase R&D funding as part of the 2009 stimulus plan is good news for science. To direct this investment, excellent policy planning is coming from the president's science adviser, John Holdren. But to get to where the White House wants to go will require broader and deeper innovation.

For too long, American science policy at the highest level has been mostly about the amount of funding and not enough about the outcomes of funding. The stimulus funding will not generate the changes that the overall enterprise needs for real economic growth. Billions of dollars of short-term, one-time funding is like that tenth cup of coffee on an all-nighter: it keeps things moving. But then there is the next day.

Now, with the American economy and its scientific dominance in question, is the perfect moment to think about what is being done and why. The Obama administration needs to focus its energies on new institutional designs and new innovation networks to allow universities, government laboratories and corporations to move forward in new alignments.

New forms of innovation are desperately needed to speed science-based technologies into the entrepreneurial market economy. Current networks are overly reliant on government-supported laboratories. What goes into research doesn't come out in economic or social impact. This is unacceptable if America is to improve its global competitiveness.

In terms of regional innovation, the United States has a few winners but many losers when ranked on a global scale. In the losing regions, the translation of scientific knowledge to improving quality of life is stalled at best. The stimulus funding will demonstrate the weaknesses in the American model for innovation, and will do so quickly. The country produces basic science, but it fails to capture the social and economic returns. Many of those who are best-equipped to produce basic science have the least incentive to ensure that those returns are captured. However, the nation can develop solutions to poverty, health inequities and environmental sustainability if it can approach research from an outcomes basis, and if it can orient knowledge towards real-world applications.

"The stimulus funding will demonstrate the weaknesses in the American model for innovation."

One-off stimulus funding will produce new ideas, and some will have impact. In recent months, the American research establishment has advanced thousands of new ideas and some bold technology development efforts. These projects have come from a research enterprise that is capable and hungry for resources. Nonetheless, it remains an enterprise that must mature its overall logic if it is to help the nation meet its national and global goals.

Michael S. Teitelbaum
Alfred P. Sloan Foundation

Incentives for universities do not promote sustainable behaviour.

One major weakness of the world-class US biomedical research system is that its own health depends on substantial continuing funding increases. Indeed, its very stability is undermined if research budget increases fall below 6% annually, and it is deeply vulnerable to funding accelerations and decelerations — the most destabilizing being a rapid cash injection that lasts only a few years.

The results of the 1998–2003 doubling of NIH funding are well known: even though the research budget increased by 100%, the biomedical research system was hit by a 'funding crisis' in 2003. Yet the structural lessons from that experiment seem not to have been learnt, because US researchers and universities continue to face conflicting incentives.

First, faculty members (especially in medical schools) are encouraged to obtain much of their remuneration from NIH research grants. Second, during the 1998–2003 period, many universities responded to the promise of NIH budget growth by expanding their laboratory facilities, often using borrowed funds in expectation that they could be financed by further funding increases. Although most doubted that the period's very rapid budget increases (14–15%) would continue, many behaved as though later budgets would grow at the roughly 8% levels before 1998. For some this proved to be a damaging miscalculation when NIH budget increases essentially ceased in 2003. Third, because the biomedical workforce consists heavily of graduate-student and postdoctoral research assistants, more NIH funding creates short-term demand for these workers, but a later excess of recent PhD recipients seeking faculty positions and funding.

These elements drive the research funding system towards instability. Further hardships have been created by state funding cuts at public universities and sharp declines in endowments at private universities.

It is unclear how US research universities and especially their medical schools will address these enduring structural challenges. The 2009 stimulus act's sudden spike of an additional $10.4 billion to the NIH over two years makes this question even more pressing.

In the short term, the incentives for universities seem clear: obtain as much of these short-term stimulus funds as possible, recognizing that they are intended to be spent quickly and may fill gaps left by reduced revenues from state budgets and private endowments. When the NIH announced that some of its stimulus funds would support 200 new Challenge Grants of up to $1 million each, the agency received an astounding 21,000 grant proposals.

But research universities need to plan for what happens when this funding wanes. If the economy recovers by that time, universities' current financial stringencies could diminish. If not, there is a danger of a repeat of the NIH feast–famine experience. ■

The views expressed are the author's and not necessarily those of the Alfred P. Sloan Foundation.

See Editorial, page 847; News, page 856.
Join the discussion at go.nature.com/wYicmJ.

Has America learnt from previous funding boosts at the National Institutes of Health?

NIH

nature

OPINION

ILLUSTRATIONS BY M. HODSON

Massively collaborative mathematics

The 'Polymath Project' proved that many minds can work together to solve difficult mathematical problems. **Timothy Gowers** and **Michael Nielsen** reflect on the lessons learned for open-source science.

On 27 January 2009, one of us — Gowers — used his blog to announce an unusual experiment. The Polymath Project had a conventional scientific goal: to attack an unsolved problem in mathematics. But it also had the more ambitious goal of doing mathematical research in a new way. Inspired by open-source enterprises such as Linux and Wikipedia, it used blogs and a wiki to mediate a fully open collaboration. Anyone in the world could follow along and, if they wished, make a contribution. The blogs and wiki functioned as a collective short-term working memory, a conversational commons for the rapid-fire exchange and improvement of ideas.

The collaboration achieved far more than Gowers expected, and showcases what we think will be a powerful force in scientific discovery — the collaboration of many minds through the Internet.

The specific aim of the Polymath Project was to find an elementary proof of a special case of the density Hales–Jewett theorem (DHJ), which is a central result of combinatorics, the branch of mathematics that studies discrete structures (see 'Multidimensional noughts and crosses'). This theorem was already known to be true, but for mathematicians, proofs are more than guarantees of truth: they are valued for their explanatory power, and a new proof of a theorem can provide crucial insights. There were two reasons to want a new proof of the DHJ theorem. First, it is one of a cluster of important related results, and although almost all the others have multiple proofs, DHJ had just one — a long and complicated proof that relied on heavy mathematical machinery. An elementary proof — one that starts from first principles instead of relying on advanced techniques — would require many new ideas. Second, DHJ implies another famous theorem, called Szemerédi's theorem, novel proofs of which have led to several breakthroughs over the past decade, so there is reason to expect that the same would happen with a new proof of the DHJ theorem.

The project began with Gowers posting a description of the problem, pointers to background materials and a preliminary list of rules for collaboration (see go.nature.com/DrCmnC). These rules helped to create a polite, respectful atmosphere, and encouraged people to share a single idea in each comment, even if the idea was not fully developed. This lowered the barrier to contribution and kept the conversation informal.

> "Who would have guessed that the working record of a mathematical project would read like a thriller?"

Building momentum

When the collaborative discussion kicked off on 1 February, it started slowly: more than seven hours passed before Jozsef Solymosi, a mathematician at the University of British Columbia in Vancouver made the first comment. Fifteen minutes later a comment came in from Arizona-based high-school teacher Jason Dyer. Three minutes after that Terence Tao (winner of a Fields Medal, the highest honour in mathematics) at the University of California, Los Angeles, made a comment. Over the next 37 days, 27 people contributed approximately 800 substantive comments, containing 170,000 words. No one was specifically invited to participate: anybody, from graduate student to professional mathematician, could provide input on any aspect. Nielsen set up the wiki to distil notable insights from the blog discussions. The project received commentary on at least 16 blogs, reached the front page of the Slashdot technology-news aggregator, and spawned a closely related project on Tao's blog. Things went smoothly: neither Internet 'trolls' — persistent posters of malicious or purposefully distracting comments — nor well-intentioned but unhelpful comments were significant problems, although spam was an occasional issue on the wiki. Gowers acted as a moderator, but this involved little more than correcting a few typos.

Progress came far faster than anyone expected. On 10 March, Gowers announced that he was confident that the Polymath participants had found an elementary proof of the special case of DHJ, but also that, very surprisingly (in the light of experience with similar problems), the argument could be straightforwardly generalized to prove the full theorem. A paper describing this proof is being written up, along with a second paper describing related results. Also during the project, Tim Austin, a graduate student at the University of California, Los Angeles, announced another new (but non-elementary) proof of DHJ that made crucial use of ideas from the Polymath Project.

NATURE|Vol 461|15 October 2009

The working record of the Polymath Project is a remarkable resource for students of mathematics and for historians and philosophers of science. For the first time one can see on full display a complete account of how a serious mathematical result was discovered. It shows vividly how ideas grow, change, improve and are discarded, and how advances in understanding may come not in a single giant leap, but through the aggregation and refinement of many smaller insights. It shows the persistence required to solve a difficult problem, often in the face of considerable uncertainty, and how even the best mathematicians can make basic mistakes and pursue many failed ideas. There are ups, downs and real tension as the participants close in on a solution. Who would have guessed that the working record of a mathematical project would read like a thriller?

Broader implications

The Polymath Project differed from traditional large-team collaborations in other parts of science and industry. In such collaborations, work is usually divided up in a static, hierarchical way. In the Polymath Project, everything was out in the open, so anybody could potentially contribute to any aspect. This allowed ideas to be explored from many different perspectives and allowed unanticipated connections to be made.

The process raises questions about authorship: it is difficult to set a hard-and-fast bar for authorship without causing contention or discouraging participation. What credit should be given to contributors with just a single insightful contribution, or to a contributor who is prolific but not insightful? As a provisional solution, the project is signing papers with a group pseudonym, 'DHJ Polymath', and a link to the full working record. One advantage of Polymath-style collaborations is that because all contributions are out in the open, it is transparent what any given person contributed. If it is necessary to assess the achievements of a Polymath contributor, then this may be done primarily through letters of recommendation, as is done already in particle physics, where papers can have hundreds of authors.

The project also raises questions about preservation. The main working record of the Polymath Project is spread across two blogs and a wiki, leaving it vulnerable should any of those sites disappear. In 2007, the US Library of Congress implemented a programme to preserve blogs by people in the legal profession; a similar but broader programme is needed to preserve research blogs and wikis.

New projects now under way will help to explore how collaborative mathematics works best (see go.nature.com/4ZfIdc). One question of particular interest is whether the process can be scaled up to involve more contributors. Although DHJ Polymath was large compared with most mathematical collaborations, it fell short of being the mass collaboration initially envisaged. Those involved agreed that scaling up much further would require changes to the process. A significant barrier to entry was the linear narrative style of the blog. This made it difficult for late entrants to identify problems to which their talents could be applied. There was also a natural fear that they might have missed an earlier discussion and that any contribution they made would be redundant. In open-source software development, this difficulty is addressed in part by using issue-tracking software to organize development around 'issues' — typically, bug reports or feature requests — giving late entrants a natural starting point, limiting the background material that must be mastered, and breaking the discussion down into modules. Similar ideas may be useful in future Polymath Projects.

Towards open science

The Polymath process could potentially be applied to even the biggest open problems, such as the million-dollar prize problems of the Clay Mathematics Institute in Cambridge, Massachusetts. Although the collaborative model might deter some people who hope to keep all the credit for themselves, others could see it as their best chance of being involved in the solution of a famous problem.

Outside mathematics, open-source approaches have only slowly been adopted by scientists. One area in which they are being used is synthetic biology. DNA for the design of living organisms is specified digitally and uploaded to an online repository such as the Massachusetts Institute of Technology Registry of Standard Biological Parts. Other groups may use those designs in their laboratories and, if they wish, contribute improved designs back to the registry. The registry contains more than 3,200 parts, deposited by more than 100 groups. Discoveries have led to many scientific papers, including a 2008 study showing that most parts are not primitive but rather build on simpler parts (J. Peccoud *et al. PLoS ONE* **3,** e2671; 2008). Open-source biology and open-source mathematics thus both show how science can be done using a gradual aggregation of

Multidimensional noughts and crosses

To understand the density Hales–Jewett theorem (DHJ), imagine a multidimensional noughts-and-crosses (or tic-tac-toe) board, with k squares on a side (instead of the usual three), and in n dimensions rather than two. Any square in this board has n coordinates between 1 and k, so for instance if $k = 3$ and $n = 5$, then a typical point might be (1,3,2,1,2). A line on such a board has coordinates that either stay the same from one point to the next, or go upwards or downwards. For instance, the three points (1,2,3,1,3), (2,2,3,2,2) and (3,2,3,3,1), form a line. DHJ states that, for a very large number of dimensions, filling in even a tiny fraction of the board always forces a line to be filled in somewhere — there is no possible way of avoiding such a line. More than this, there is no way to avoid a 'combinatorial line', in which the coordinates that vary have to vary in the same direction (rather than some going up and some going down), as in the line (1,2,3,1,1), (2,2,3,2,2) and (3,2,3,3,3). The initial aim of the polymath project was to tackle the first truly difficult case of DHJ, which is when $k = 3$.

insights from people with diverse expertise.

Similar open-source techniques could be applied in fields such as theoretical physics and computer science, where the raw materials are informational and can be freely shared online. The application of open-source techniques to experimental work is more constrained, because control of experimental equipment is often difficult to share. But open sharing of experimental data does at least allow open data analysis. The widespread adoption of such open-source techniques will require significant cultural changes in science, as well as the development of new online tools. We believe that this will lead to the widespread use of mass collaboration in many fields of science, and that mass collaboration will extend the limits of human problem-solving ability. ■

Timothy Gowers is in the Department of Pure Mathematics and Mathematical Statistics, University of Cambridge, Wilberforce Road, Cambridge CB3 0WB, UK, and a Royal Society 2010 Anniversary Research Professor. **Michael Nielsen** is a Toronto-based writer and physicist working on a book about the future of science.
e-mails: W.T.Gowers@dpmms.cam.ac.uk; mn@michaelnielsen.org

Stitching science together

Google Wave is the kind of open-source online collaboration tool that should drive scientists to wire their research and publications into an interactive data web, says **Cameron Neylon**.

Science communication today remains firmly wedded to its print origins. We cling to the notion that 'the real version' exists on the page. Beyond ease of delivery, we take very little advantage of the potential of the World Wide Web to transform the way we store and transfer knowledge. We rarely take the opportunity to update material with new data, or to provide a record of how a document or data set has changed. Gene names and protein structures should be routinely linked to database entries through hyperlinks. The outputs of computational processes should be connected to their inputs, so analyses can be redone. If we can make these records accessible to humans and readable by machines, then whole new types of analysis will become possible, indeed standard.

Many of these things are possible today. But they are hard to achieve. Much effort has gone into solving parts of the problem, by big players such as Microsoft and Amazon as well as by smaller organizations. Electronic lab notebooks can help to capture the details of science, and databases can make it available to the user. Reference-management tools such as Delicious, semantic data stores and Wikipedia can help to wire up and monitor knowledge. But the tools are often difficult to use and don't 'talk' to each other. There is no single framework that makes it easy to link all the steps of science. Scientists do their analysis and writing using different software, and prepare graphs and record data using different tools.

Very few companies worldwide have both the expertise and resources to take on the task of stitching this together. So it is with great interest that I have watched Google develop its product, Google Wave. The company describes Google Wave as "what e-mail would look like if it were invented today". It blends elements of e-mail with instant messaging and online collaborative authoring. The big change is that the 'document' or 'wave' is shared between all the participants and updates flow in real time. You no longer need to worry about which version of a document you have e-mailed around. This is helpful for scientists, but not revolutionary. Where Wave offers a big step for science is in two other functionalities.

Two steps forward

First, Wave introduces the idea of robots: automated agents that can be invited into a document. Robots could look through your paper checking for Protein Data Bank codes or gene names, for example, and putting in links to the databases. A robot might represent a lab instrument, adding data automatically to your laboratory record when they become available. You can easily add maps, video or three-dimensional graphics to your work using 'gadgets' or 'applications', familiar from services such as iGoogle and Facebook. Robots can interact with this information, making it possible to have a dashboard in your inbox to monitor and control instruments in the lab.

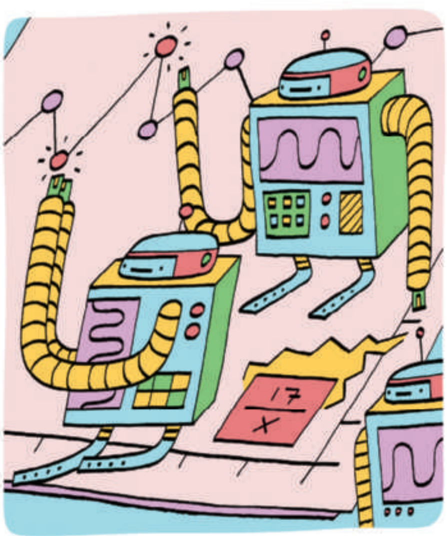

ILLUSTRATION BY M. HODSON

The second step forward is using versions. Each wave maintains a record of every change. It could be possible to check each step from data collection to drawing a graph and its publication. This would allow a reader to step through an analysis to see where conclusions have come from, and would make detecting fraud — or honest mistakes — much easier.

Google has done a good thing in making the protocol and programming tools open source, enabling people to test and build. Perhaps 50 people, myself included, from experimental scientists to journal publishers, have been testing the prototype system for science applications since June, building robots that link chemical information, visualize data and format references. Since 30 September, a much bigger group has been testing. But real benefits will come only if the system is widely adopted. Perhaps a new generation of scientists will be required to exploit the power that working with these dynamic documents and tools offers.

Solving the current problems in science communication requires the intervention of strong companies such as Google. But it will take more than technical advances to provoke scientists into taking full advantage of the web. We need pressure, and perhaps compulsion, from journals and funders to raise publishing standards to the new level made possible by such tools. Google Wave may not be, indeed is probably not, the whole answer. But it points the way to tools that build records and reproducibility into every step. And that has to be good for science. ■

Cameron Neylon is senior scientist in biomolecular sciences at the Science and Technology Facilities Council Rutherford Appleton Laboratory, Didcot OX11 0QX, UK.
e-mail: cameron.neylon@stfc.ac.uk

BOOKS & ARTS

Art history's window onto the mind

Neuroscientists should worry less about testing abstract qualities such as beauty, and work with art historians towards a concrete understanding of types of viewing, argues **Martin Kemp**.

"Art is clearly an expression of our aesthetic response to beauty," wrote neuroscientist Vilayanur Ramachandran in the October 2006 issue of *Scientific American Mind*, before noting that there is no consensus in the worlds of art about the definition of 'art', 'aesthetic' or 'beauty'.

The lack of accepted definitions for such key terms has, however, proved to be no deterrent to their investigation by scientists. It seems that, released into an arena of analysis in which the rules of science are perceived as not operating, these researchers discard the rigour they would normally observe.

Yet our responses to artworks offer much for neuroscience to investigate, without resorting to such generalizations. Art's diversification has been matched by our sophistication in the perception of it. Happily, a few scientists and art historians are beginning to direct their efforts to the more pragmatic questions of how we perceive and attach significance to forms.

Studying the arts is not a science, but the field has standards in the taking and use of evidence. The process of hypothesis formulation and the quest for evidence, evaluation and analysis of sources, matching and reformulation have their own kind of discipline. As an art historian, I dislike one hypothesis sitting on the shoulders of another unproven one as much as any scientist.

Most art historians would not regard 'art', 'aesthetic' and 'beauty' as absolute terms that are the goal of their enquiries or even major guiding principles. Many, like myself, deny their use as absolutes at all. At best they serve as subjects of period study. Instead, in the past 30 years or so, the discipline of art history has increasingly focused on contexts — on the complex conditions under which artefacts were generated and have functioned in particular societies.

However, several prominent neuroscientists continue to address the absolutes, using the formal criteria of outdated Modernist theory to define problems in the study of art with little concern for complex content. It was this striking disjunction that erupted in a wonderfully bloody seminar in 2002 at the Getty Research Institute in Los Angeles, California, at which Ramachandran and fellow neuroaesthetics pioneer Semir Zeki were confronted by the resident and visiting art historians.

> "Art history is about the conscious creation of works by artists for viewers who make selective demands on what they are seeing."

These art historians were mainly 'social deconstructivists' who dissected the social and political factors behind artworks' creation and public reception. They were concerned with the quality of communication and visual potency of the artworks, not with defining their beauty. What resulted was a discourteous dialogue of the deaf — and the two distinguished scientists did not stay to the end. I had a good deal of sympathy with them.

Mark Rothko's abstract art created new neurological responses.

Neuroscience fares a little better with philosophical theory. However, in the tradition of Immanuel Kant, the certainty that art exists in a definable aesthetic realm that serves no purpose beyond itself is no longer sustainable.

Writers on art have accumulated terms to describe the characteristics of things that are considered beautiful or aesthetically pleasing: they may be uplifting, exalting, transcendent, delightful, graceful, poetic, harmonious, expressive and so on. We can describe something as beautiful to someone who shares our cultural instincts, but we cannot define beauty itself.

The 'fuzzy group' concept offers a way out of this dilemma. Things we call beautiful share family traits. Although they have qualities in common, no individual characteristic is absolutely necessary to define their resemblance. The overarching descriptor of 'beauty' has no validity beyond this loose level of family likeness. This explains how we can categorize as 'art' both an installation of felt and fat by Joseph Beuys and an altarpiece of the Madonna and saints by Botticelli.

Neuroscientific data fit better with this interpretation of aesthetics as dealing with associations of overlapping groups than with the quest to define what the brain finds eternally beautiful. Zeki and others' demonstrations that formal arrangements of shapes activate different brain regions from figurative images help explain why, in the early twentieth century, many did not recognize abstract art as 'art'. The sight of a Rothko painting, with its abstract patches of colour, generated an unfamiliar neurological response.

Blurred boundaries

With each move of the avant-garde beyond the established boundaries of art, these groups of related art types are rendered even fuzzier and more ill-defined to the point that the boundaries disappear altogether. Although still referred to as art, there is no reason why the painting of a traditional portrait and the genetic engineering of a fluorescent rabbit, such as by artist Eduardo Kac, should be classified as the same kind of activity. It would be interesting to investigate to what extent comparable brain activity is triggered by such divergent creations; I suspect that there would be striking differences.

If not in the quest for beauty, where might joint research in science and art history flow? The most tractable areas are in viewing and reception, bearing on the messy business of selective looking and slanted cognition, which determine that we notice some things and filter out others. Art history is about the conscious creation of works by artists for viewers who make selective demands on what they are seeing. The investigation of the ways in which we view different artworks may also eventually

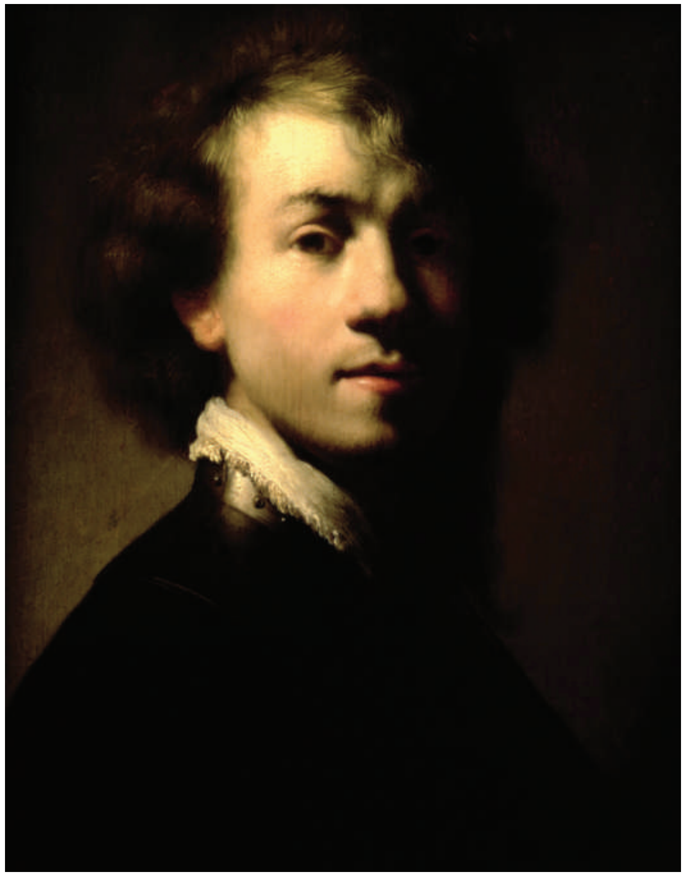

BOTH IMAGES: BRIDGEMAN ART LIBRARY

Viewers respond differently to authentic artworks and copies, such as this pair of portraits of Rembrandt, one painted by the master and the other by a follower[1].

bear on the big questions of 'art' and 'beauty', if only to dissolve them.

Some neuroscientists have begun to look at the psychological complexities of how we view and value artwork. Karl Friston, of the Wellcome Trust Centre for Neuroimaging at University College London, and his colleagues have proposed a method of 'psychophysiological interaction' to assess the effect that psychological factors have on physical processes in the brain through analysis of scans. This procedure has the potential to show how complex and interactive the viewing of artworks is, both between individuals and for an individual under different conditions. Another promising study, addressing how brand awareness affects the value we place on something, was that by psychologist Samuel McClure and his colleagues, then at Baylor College of Medicine in Houston, Texas, who reported on the neurology of preferences for the two main cola drinks (S. McClure *et al.* *Neuron* **44,** 379–387; 2004).

A glimpse of further possibilities is provided by an exploratory study, yet to be published, which was undertaken this year by Mengfei Huang and Andrew Parker at the University of Oxford, UK, with my assistance. The research tested people's responses to authentic Rembrandt portraits and works by other artists that are close in appearance to the master's portraits. It is widely acknowledged in the art world that once a work is revealed as 'not right', it discernibly looks different to a viewer. Features that were previously overlooked suddenly become glaringly obvious. It is as if a former lover is no longer blinded by love.

Rembrandt was chosen because of the large number of portraits he painted, and the even larger number of portraits produced in his style, ranging from works by close followers to downright fakes. In our experiment, viewers were presented with a brief statement explaining Rembrandt's importance, his style development, the large number of imitations and the huge implications, not least financial, of a painting's authenticity.

Protocols were devised so that two sets of viewers were presented with the same group of pictures, a mix of Rembrandts and non-Rembrandts, but with each group labelled differently. The labelling did not correspond to the actual status of each painting and was reversed for each set of participants. The main purpose was to detect differential brain responses to the flagging of authenticity, but we were also able to detect if the portraits that were authentic triggered a different reaction. The results suggest some subtle interactions between neural activity, expectation, memory and value systems.

This kind of investigation is only a beginning. It would be useful to extend the study to bodies of expert viewers. By expert, I do not just mean art historians who know their Rembrandts from their Flincks. Rather, I mean people who have different types of engagement with the faces of the historic people depicted, from psychologists to costume historians, from picture restorers to cartoonists. The problems of method here are legion, but protocols can be devised to overcome them.

Let us look beyond 'art', 'beauty' and 'aesthetics' and engage with concrete problems that tell us about varied modes of viewing. Art historians and scientists need to work together to define new questions that are both tractable and of genuinely shared interest. ■

Martin Kemp is emeritus professor in history of art at the University of Oxford, Oxford, UK.

[1]Rembrandt's self-portrait is on the left.

See online at go.nature.com/phyLwm for more on neuroscience.

In Retrospect: Brodmann's brain map

A classic neurology text written 100 years ago still provides the core principles for linking the anatomy of the cerebral cortex to its functions today, explains **Jacopo Annese**.

Localisation in the Cerebral Cortex
by Korbinian Brodmann
First published 1909 (in German).

The development of advanced magnetic resonance imaging techniques over the past 30 years has heralded today's 'golden age' of human brain mapping. Yet in the quest to chart structural and functional subdivisions in the brain, and in the cerebral cortex in particular, the first quarter of the twentieth century was at least as momentous.

At the forefront of that pioneering effort was a German physician who is still revered by brain scientists today, but whose seminal book on cortical anatomy is read by few. Korbinian Brodmann's *Localisation in the Cerebral Cortex*, published 100 years ago, details his system for subdividing the cortex into 52 areas, each signified by a number, on the basis of their cell type and laminar structure. It is a classic of neurology: Brodmann's numbers are still used to indicate the location and function of cortical areas, and his trademark drawings of the human brain are reprinted wherever neuroscience is taught or practised. Personally, I have re-read the book carefully because my laboratory is engaged in producing a map of the cortical surface based on anatomical criteria, just like Brodmann, but using modern digital technology (see http://thebrainobservatory.ucsd.edu/brodmann.html).

In Brodmann's era, most cortical mapping took place in pathological laboratories that were linked to mental asylums and overseen by government bodies. But his effort started in an independent institute — the Neurobiological Laboratory in Berlin, supported and run by the neurologists Oskar Vogt and Cécile Vogt. The Vogts were mainly concerned with the architecture of myelinated nerve fibres, and how different areas of the cortex were linked to specific physiological functions, which they tested by stimulating the brains of animals. They brought in Brodmann to carry out a topographical analysis of the human cerebral cortex based exclusively on its cellular structure (the cytoarchitecture), using a staining method developed by their contemporary, Franz Nissl.

The task was theoretically straightforward, yet it occupied Brodmann for almost a decade. Using a microscope designed for the purpose, he undertook meticulous examinations of cortical tissue from the brains of humans and many other mammals, the results of which enabled him to construct his map of the human cortex. The map looks simple, yet the book makes it clear it is based on a monumental analytical effort. His exquisite powers of observation and great attention to detail transform for the reader the tedium of scientific annotation into an exercise in anatomical voyeurism.

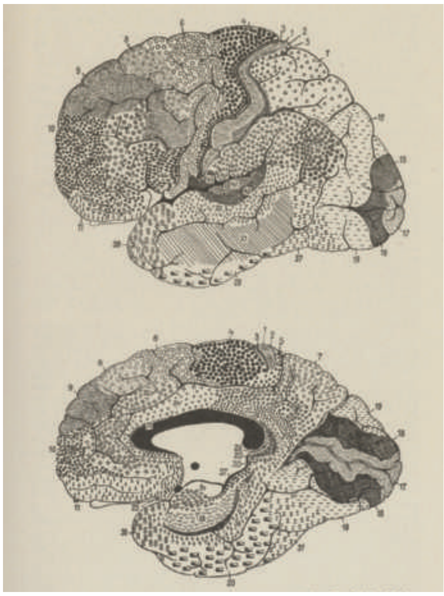

Two of Brodmann's classic drawings from 1909.

The descriptions alone mark out the book as a classic, but it is well worth reading today for several reasons. It touches on issues that are highly relevant to modern neuroscience, starting with the idea that specific physiological functions in the cerebral cortex depend on specific histological structure and connectivity.

Although Brodmann's numbers are widely used to link brain regions with function — area 4 for the primary motor cortex, for example — you get the sense from the book that he did not want to tarnish his mapping effort by making predictions about functional properties that might not stand the test of time. He reminded his readers that his investigation was based "exclusively on anatomical features", rather than on physiological or clinical approaches, although he does discuss these towards the end. Some of his peers were more forthright about labelling cortical regions according to function, notably the Australian-born neurologist A. W. Campbell, who used clinical evidence with results from physiological experiments and anatomical analysis to make his case. Still, Brodmann's objective approach has ensured that his maps have endured, eclipsing others of the time such as Campbell's.

Another of Brodmann's long-lasting achievements documented in the book is his defence of the accepted view that the cerebral cortex is divided into six fundamental layers, a view shared by some — but not all — neurologists of the time. Brodmann's rationale was based on his own interpretation of developmental and anatomical evidence that was potentially disputable, but his strong stance quieted the debate and it has been universally accepted with time. Indeed, the only valid criticism of *Localisation in the Cerebral Cortex* is that Brodmann failed to provide a clear photographic record of the cortical areas he was classifying. This technical drawback has made it hard to challenge or invalidate his conclusions about the way the cortex is subdivided, and has therefore preserved the impact of his map.

Brodmann's enterprise has stood up against what we have learned recently about brain architecture from modern neuroimaging techniques remarkably well. His approach remains convincing because it is based on a small number of unambiguous postulations and a deep personal involvement with the data. The arsenal of chemical and molecular techniques and digital-microscopy tools now at our disposal gives us far greater power to analyse brain structure than Brodmann had. Yet future projects should seek to learn from his impressive methods of synthesis rather than focusing solely on surpassing his methods. Whatever a new microscopic map of the cerebral cortex may look like, it will doubtless be based on the principles that Brodmann defended a century ago. ■

Jacopo Annese is director of The Brain Observatory at the University of California, San Diego, California 92121, USA.
e-mail: jannese@ucsd.edu

See online at go.nature.com/phyLwm for more on neuroscience.

JUPITER 9 PRODUCTIONS

Q&A: The space entrepreneur

After completing simultaneous doctorates in physics and chemistry, **Harry Kloor** became a space-exploration consultant and film-maker. As his three-dimensional animated feature *Quantum Quest* — made with real footage from the Cassini spacecraft — is previewed in New York, Kloor shares his thoughts on manned space flight and the use of prizes to motivate adventurous science.

How did you become interested in science?
Through science fiction and watching the Apollo Moon landings. As a child I had a lot of time to explore the Universe through books because I was born partially crippled with my legs backwards. The doctors said that I would spend my life in braces and would never be able to run. My parents told me not to let those ideas limit me, and by the age of seven I ran for the first time. Overcoming that first hurdle showed me that experts often close their minds to possibilities.

How did the idea for the movie arise?
The genesis was from my science outreach work at Purdue University, where I collaborated with Marvel Entertainment and Paramount Pictures to make posters to promote science education using Spider-Man and *Star Trek*. In 1997, NASA wanted me to make a documentary to promote its Cassini and Huygens missions. But I came back with a different idea: an animated movie in which science concepts come to life.

What does the film teach?
It covers a host of physics concepts and real space discoveries. We travel over three-dimensional recreations of the surfaces of Mercury, Venus, Mars and the moons of Saturn, ending with a grand tour of its largest moon, Titan, based on the Cassini and Huygens radar and visual data. We have characters representing matter and antimatter. Actor Chris Pine is a photon, Amanda Peet is a neutrino, Hayden Christensen and Doug Jones are solar-surfing protons. We also have characters to represent fear and ignorance, things that keep you from learning.

Why did *Quantum Quest* take more than a decade to complete?
I knew from the start that it would be a long haul, because the radar data we needed to create the surface images of Titan would not arrive until 2008. Naively, I had recorded the script in 1997, not realizing that new discoveries would require a complete rewrite. Just like when you launch a spacecraft, there was a long gap of time in which nothing happened on the film. Then in October 2007 the project came out of hibernation. I rewrote the script and recorded it with the voices of a new cast that includes actors Samuel L. Jackson and Mark Hamill, as well as astronaut Neil Armstrong.

JUPITER 9 PRODUCTIONS

Quantum Quest charts the Solar System journey of Dave the photon, helped by The Core of the Sun.

You have been an adviser to NASA and private space firms for 20 years. What do you think of US President Barack Obama's agenda for manned space exploration?
We can't predict what we will find on other planets, so until we have Terminator-like robots who can do everything we could do, a human presence is good for science. I think we should be going to Mars and doing it faster than currently scheduled, using a mix of public and private funding.

You were chief science adviser on the $10-million X PRIZE for suborbital flight. Are there drawbacks to stimulating scientific research with cash prizes?
I don't think prizes work for everything. But where they do work, they can serve as a massive multiplier. The X PRIZE Foundation doesn't put up the research funds for the contests; that comes from private, non-governmental sources. They just put up the prize money and say, 'try to tackle this problem' — whether it's the Archon X PRIZE to sequence 100 human genomes in 10 days for less than $10,000 per genome, or the Progressive Automotive X PRIZE to design a car that achieves 100 miles per gallon or the Google Lunar X PRIZE to land a rover on the Moon. The contests motivate firms to invest hundreds of millions of dollars in private funds, adding a legitimacy and prestige that can spur on innovation.

Should scientists get out of the lab more?
Spending all your time in a lab reduces your health and intellect. By engaging in a variety of activities, you can stimulate your brain. Skydiving and scuba diving have opened up my world. And some things should be done just because they are fun and exciting. ■

Interview by **Jascha Hoffman**, a writer based in San Francisco, California.

See go.nature.com/Jp67ab for Nature Network's blog of the Imagine Science Film Festival.

Quantum Quest: A Cassini Space Odyssey
Imagine Science Film Festival,
CUNY Graduate Center, New York City
Preview on 21 October

NEWS & VIEWS

BEHAVIOURAL NEUROBIOLOGY

Chemical love

Nicolas Gompel and Benjamin Prud'homme

Male and female fruitflies use pheromones to flaunt their species identity and gender as they court amid other fruitfly species. The grammar of this chemical language is surprisingly sophisticated.

Successful mating is all about making the right choices. But, as we all know, this is not an easy undertaking. Before engaging in courtship, a male needs to make sure that a potential mate is actually female, that she is of the same species, and is sexually mature and receptive. Meanwhile, in addition to checking species and gender, a female needs to assess her suitor's qualities before she accepts him as a mate. Therefore, although males often make the first move by deciding whom to court, females have the last word in deciding with whom they will mate. The primary signals that animals use to guide these decisions are sensory inputs, but it is largely unclear how such signals translate into stereotyped behavioural decisions. On page 987 of this issue, Billeter and colleagues[1] shed light on this matter by deciphering the chemical dialogue that takes place between male and female fruitflies as they vie for success in the mating game.

The fruitfly *Drosophila melanogaster* mates at dinner, which typically takes place in a compost heap. The trouble is that this dining area is abuzz with many different fruitfly species, which often look remarkably similar. How can a male distinguish a female of the same species among the crowd? Chemical communication in the form of pheromones seems to constitute the key signal[2,3]. Pheromones are compounds that are exchanged between prospective mates by means of olfaction or gustation before and during mating[4,5]. They have long been known to have a central role in mate choice and the decision to mate in various animals, from insects to mammals. But the precise role of individual pheromones in sexual communication has been difficult to assess because pheromones are usually secreted as blends[6] (about 30 different molecules cover the fly body), and they function in conjunction with other signals.

Billeter *et al.*[1] tackled this problem by assessing the function of individual pheromones one at a time using a simple but powerful approach. First, they engineered *D. melanogaster* flies that are devoid of any pheromone by using genetic tools to deplete the cells that secrete these molecules. Then they perfumed these chemically mute flies with individual pheromones or blends of pheromones, and tested the effects on other flies.

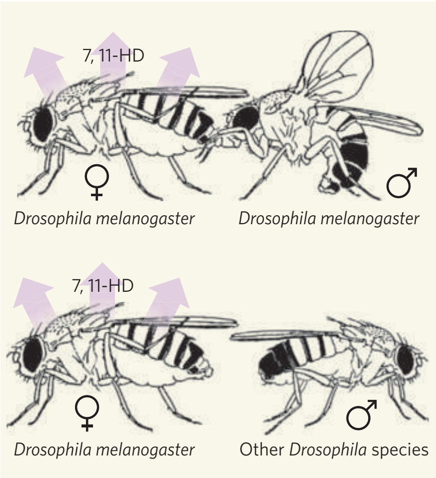

Figure 1 | Pheromones impart species identity in *Drosophila*. Billeter *et al.*[1] report that the pheromone 7,11-HD, produced by *Drosophila melanogaster* females, acts as an aphrodisiac on males of the same species (upper panel) but as a deterrent to males of other species (lower panel). The upper panel shows a *D. melanogaster* male serenading a female by vibrating his wing while he licks her genitalia — a prelude to copulation.

To their surprise, unlike Patrick Süskind's odourless protagonist Jean-Baptiste Grenouille in the novel *Perfume*, the unscented flies, regardless of their gender, are hyperattractive to males. This result contradicts the widespread belief that pheromones are required to initiate courtship[3] and suggests that other sensory inputs such as vision may be a trigger for mating. Moreover, when perfumed with the female *D. melanogaster* pheromone 7,11-HD, long thought to be an aphrodisiac, the scentless flies do not become any more appealing to males — as the authors reveal, the aphrodisiac role of 7,11-HD is more subtle than previously thought.

During copulation, a male-specific chemical compound, cVA, is transferred to the female. This pheromone modifies the female's post-copulatory behaviour — for instance, by inducing egg-laying — and deters other suitors[7]. Billeter *et al.* show that, as expected, the sex appeal of odourless flies perfumed with cVA decreases. Surprisingly, however, they find that the addition of 7,11-HD on top of cVA lowers the deterrent effect of cVA in a dose-dependent manner. Hence, a female compound, 7,11-HD, can counter the chemical chastity belt imposed by cVA and broadcast a female's receptivity. This pheromonal negotiation illustrates the conflicting agendas of sexual partners: it is in the male's interest that his conquest doesn't re-mate with another male, whereas the female seeks to maximize the chances of having her eggs fertilized by mating with several different males.

Now, what happens when a male of species A approaches a female of species B? Odourless flies elicit courtship from males of different species, indicating that pheromones impart species identity. Billeter *et al.*[1] show that, although 7,11-HD attracts *D. melanogaster* males, it deters males of other species whose female members do not secrete 7,11-HD, and is sufficient to discriminate between different species (Fig. 1). Therefore, a single fly pheromone has a central role in mate choice by tagging both female and species identity.

By studying the effect of single pheromones, Billeter and colleagues reveal the unexpectedly subtle and complex nature of the chemical dialogue that takes place between sexual partners, and lay the groundwork to address related questions. Flies, like other animals, receive countless sensory signals that are integrated to generate appropriate behaviours. How this integration is computed in the brain is still a mystery. The neural integration of different pheromones is illustrated by the opposite effects of 7,11-HD and cVA. When exposed to both compounds at the same time, a fly has to decide what to do — whether to exhibit one behaviour (courting) or another (not courting). Where and how does this integration happen in the brain? The receptor for cVA has been identified[8,9], as have aspects of the neuronal pathway that mediates its response[10]. However, for 7,11-HD, neither its receptor nor the neuronal circuitry transducing its effects is known — this information is a prerequisite for understanding the neural basis of pheromone-signal integration.

The authors' work[1] also touches on how

the chemical dialogue of courtship evolves by changes in both signal emission (the pheromones) and signal reception (the neuronal circuit processing the signal). Although it is well documented that the composition of the pheromone bouquet evolves quickly among species[4,5], little is known about the evolution of the perception of these chemical cues. What is the difference between *D. melanogaster* males that are attracted by 7,11-HD and their kin from other species that are deterred by the same compound? Are these distinctions located in sensory neurons — for example, does 7,11-HD bind different receptors in different species, triggering divergent responses? Or are disparities in pheromone perception due to processes lodged more deeply in the brain's circuitry? The difference among fruitfly species parallels that of male and female *D. melanogaster*, which respond differently to cVA. In this case, the sexually dimorphic response is known to lie deeper in the neuronal circuit, in the form of subtle differences in synapse morphology[10].

Billeter *et al.*[1] have taken a crucial step in dissecting pheromonal inputs to courtship initiation in the fruitfly. But how sensory representation leads to decision-making, and the evolution of this representation among species, awaits further study. ■

Nicolas Gompel and Benjamin Prud'homme are at the Institut de Biologie du Développement de Marseille-Luminy, Parc scientifique de Luminy, case 907, 13288 Marseille cedex 9, France.
e-mails: gompel@ibdml.univ-mrs.fr; prudhomme@ibdml.univ-mrs.fr

1. Billeter, J.-C., Atallah, J., Krupp, J. J., Millar, J. G. & Levine, J. D. *Nature* **461,** 987–991 (2009).
2. Wyatt, T. D. *Pheromones and Animal Behaviour: Communication by Smell and Taste* (Cambridge Univ. Press, 2003).
3. Dickson, B. J. *Science* **322,** 904–909 (2008).
4. Jallon, J.-M. *Behav. Genet.* **14,** 441–478 (1984).
5. Shirangi, T. R., Dufour, H. D., Williams, T. M. & Carroll, S. B. *PLoS Biol.* **7,** e1000168 (2009).
6. Yew, J. Y. *et al. Curr. Biol.* **19,** 1245–1254 (2009).
7. Ejima, A. *et al. Curr. Biol.* **17,** 599–605 (2007).
8. Kurtovic, A., Widmer, A. & Dickson, B. J. *Nature* **446,** 542–546 (2007).
9. Ha, T. S. & Smith, D. P. *J. Neurosci.* **26,** 8727–8733 (2006).
10. Datta, S. R. *et al. Nature* **452,** 473–477 (2008).

CONDENSED-MATTER PHYSICS

Wien route to monopoles

Shivaji Sondhi

Determining the magnetic charge of monopoles in a crystalline host seemed a mountain too high for physicists to climb. An experiment based on Wien's theory of electrolytes has now measured its value.

The exotic class of crystalline solids known as 'spin ices' has proved, perhaps surprisingly, to be a repository of some elegant physical phenomena. Spin ices are rare, three-dimensional systems in which the magnetic moments (spins) of the ions remain disordered even at the lowest temperatures available. In these crystalline solids, it has been recognized that a material's collective excitations above the ground state behave as point-like objects that are the condensed-matter versions of magnetic monopoles[1] — particles that, unlike iron magnets, have a single magnetic pole and hence carry an overall magnetic charge.

Initially, it was not evident that their charge could be measured in a straightforward way. After all, magnetic monopoles live in a lattice at a moderate density under normal laboratory conditions — not the sort of setting in which you could carry out a magnetic version of Millikan and Fletcher's oil-drop experiment to determine the electric charge of the electron. Happily, such obstacles have triggered ingenuity, and on page 956 of this issue Bramwell and colleagues[2] report a measurement of the magnetic charge of the monopoles in spin ice that is in surprisingly good agreement with the robust theoretical prediction[1] of the same.

The route that Bramwell *et al.* take begins with the Wien effect. In its normal incarnation, this is the increase in the conductance of an electrolyte at strong electric fields. The theory underlying this phenomenon was first worked out by Lars Onsager[3], and central to it is the association and dissociation of the molecules of the electrolyte under the influence of an applied electric field. Essentially, the electric field rips molecules apart into oppositely charged ions at an enhanced rate while they recombine at a rate that is unchanged — the latter phenomenon was first discovered by Paul Langevin[4] in 1903. The net result is a greater density of ions and hence an enhanced conductance. Specifically, the increase is linear, with a coefficient that readily allows determination of the charge of the ions — a memory of the attraction between the ions, which the electric field overcomes.

In their study, Bramwell and colleagues[2] map the fractionalization of magnetic dipoles in a spin-ice material ($Dy_2Ti_2O_7$) on to the ionization of molecules in Onsager's theory. The dipoles can be viewed as 'molecules' consisting of monopole–anti-monopole pairs. The monopoles and anti-monopoles play the part of ions that can separate and take on a reality through spin-flipping processes. The dissociation of dipoles is stimulated by an externally applied magnetic field, and the energetics of this process involve the magnetic 'Coulomb' interaction — in exactly the same manner as the energetics of molecule dissociation under the action of an electric field involves the true Coulomb interaction.

So far, so good — as far as the application of Onsager's theory to magnetic dipoles goes. All that is left to be done is to measure the magnetic conductance of the spin-ice material. Unfortunately, this is not so easy — our magnetic monopoles live only in spin ice, and the analogue of the external electric circuit in an experiment with an electrolyte is not obvious (although it could conceivably be done with various pieces of spin ice).

To get around this obstacle, Bramwell *et al.* turned to another insight from Onsager's theory — that the enhanced density of ions (or of the magnetic monopoles in the authors' mapping) should bring with it an enhanced relaxation rate for departures of the ionic density (monopole density) from its equilibrium value. As fluctuations of the monopole density produce fluctuations of the magnetic fields inside the material, their task was reduced to measuring the relaxation rate for such fluctuations in an applied magnetic field. For spin ice, they chose to probe the relaxation rate with a technique known as muon spin rotation, which consists of implanting spin-polarized muons in the material and detecting the positrons emitted when they decay. The distribution of the positrons 'remembers' the orientation of the muons, and its time evolution yields information about the time evolution of the magnetic fields in the material. Happily, the authors found a linear enhancement of the relaxation rate with increasing magnetic field, and extracted a magnetic-monopole charge that agrees surprisingly well with the theoretical prediction[1].

I think it is clear that Bramwell and colleagues' result[2] is a triumph of a bold experimental foray down a chain of inference that others may have prudently refrained from following. For that very reason, though, it raises several fascinating questions that will occupy theorists until the 'Wien effect' in spin ice can be declared a closed subject. For one thing, Onsager's theory is for a system out of thermal equilibrium, and the set-up in spin ice is, in theory, an equilibrium set-up. That said, the experiment itself and the determination of the charge of magnetic monopoles are striking, and strongly suggest that we are on our way to developing a consistent picture of the low-temperature behaviour of spin ice — one in which magnetic monopoles become entirely familiar objects. The results of the latest low-temperature neutron-scattering experiments[5,6] also line up very well with the physics of monopoles in these spin-ice materials. No doubt there is still room for more insightful experimental work in this area.

Beyond establishing the basic physics of magnetic monopoles, it would be interesting to see whether monopoles could be manipulated

in a controlled manner. For example, one could aim to build the magnetic counterparts of alternating-current electrical circuits. On the way to turning the study of monopoles into a proper applied science, it will be necessary to ask if the basic ideas of dipole fractionalization that give a spin-ice material its special properties can be realized in other magnetic settings. Spin ice may be the first fractionalized magnet in three dimensions, but surely should not be the only one. ■

Shivaji Sondhi is in the Department of Physics, Princeton University, Princeton, New Jersey 08544, USA.
e-mail: sondhi@princeton.edu

1. Castelnovo, C., Moessner, R. & Sondhi, S. L. *Nature* **451,** 42–45 (2008).
2. Bramwell, S. T. *et al.* **461,** 956–959 (2009).
3. Onsager, L. *J. Chem. Phys.* **2,** 599–615 (1934).
4. Langevin, P. *Ann. Chim. Phys. VII* **28,** 433 (1903).
5. Fennell, T. *et al. Science* doi:10.1126/science.1177582 (2009).
6. Morris, D. J. P. *et al. Science* doi:10.1126/science.1178868 (2009).

NEUROSCIENCE

The inside story on place cells

Douglas Nitz

Neurons known as place cells encode spatial information that is needed to guide an animal's movement. Nearly 40 years after these cells were discovered, neuroscience gets a look at their internal dynamics.

On page 941 of this issue, Harvey *et al.*[1] describe a novel combination of techniques that they have used to address unresolved questions about brain function. The experiments involve mice navigating within a virtual-reality setting while intracellular electrophysiological recordings are made of particular neurons — pyramidal neurons — in the hippocampus. The ability to gather such data adds greatly to the information that can be gleaned from the accompanying extracellular recordings.

The gap in our knowledge between findings obtained from intracellular and extracellular electrophysiology experiments is closing fast, and the timing could hardly be better. Today especially, it is difficult to overstate the importance of understanding how the dynamics of electrical activity within single neurons is related to firing patterns among collections of neurons that accompany the performance of complex tasks. Such information is necessary to fully understand the operational principles of neural networks that have been newly revealed by subtle manipulations of their elements[2]. It is equally relevant to teams of scientists who are struggling to develop large-scale, spiking-neuron models of the brain that apply to the real world[3].

Into this mix comes research from David Tank's group, in the form of the paper by Harvey *et al.*[1], which proves that it is not impossible to examine brain correlates of higher cognitive processes and at the same time identify their underlying causes at the cellular level. The authors' work unveils the membrane-potential dynamics of 'place cells', a subtype of pyramidal neuron, whose spike-firing patterns reflect both the animal's present spatial position in the environment and the specific trajectory taken to reach that position. Beyond this impressive technical achievement is a result that clarifies a basic principle by which temporal coding of neuronal spike firing can be realized.

The 1971 discovery of place cells[4] was a strong early indication of how much would eventually be learned through new methods for extracellular single-neuron recordings in freely behaving animals. After decades of subsequent place-cell recording experiments, there is a growing consensus about the mechanisms by which the hippocampus simultaneously functions to map environmental position and to generate episodic memories. Critical to this understanding was the discovery of 'phase precession'[5], wherein place-specific firing of hippocampal neurons is itself temporally organized against a background rhythm that takes the form of theta-frequency (6–10 Hz) oscillations of the whole hippocampal neuron population. Here, over short intervals of time (about 125 milliseconds), the firing order for a set of hippocampal place cells with partially overlapping place fields is found to match the animal's physical trajectory corresponding to those fields. Phase precession stands as perhaps the most robust example of temporal coding of information in the mammalian brain. The means by which phase precession of place-specific activity occurs is, at present, a matter of intense debate.

Harvey *et al.*[1] provide a powerful example of what will be learned in the decades to come. The broader promise of the technique lies in learning exactly how the myriad incoming synaptic potentials to any given neuron are integrated to yield spike-firing patterns that closely track specific thoughts, perceptions or actions. Aside from the intellectual reward in understanding — at macro- and microscopic levels — how the brain functions, some, including myself, also see this as a prerequisite for the development of brain-based, non-biological devices capable of autonomous function in a constantly changing environment. Neurons condense complex collections of information arriving at their synapses into the more concise messages contained in their action-potential firing patterns. The mathematical rules governing such transformations may well be applied in tomorrow's computers and robots.

The experiments themselves involve a novel integration of existing techniques, each presenting its own complications. Combined intracellular and extracellular recordings are obtained

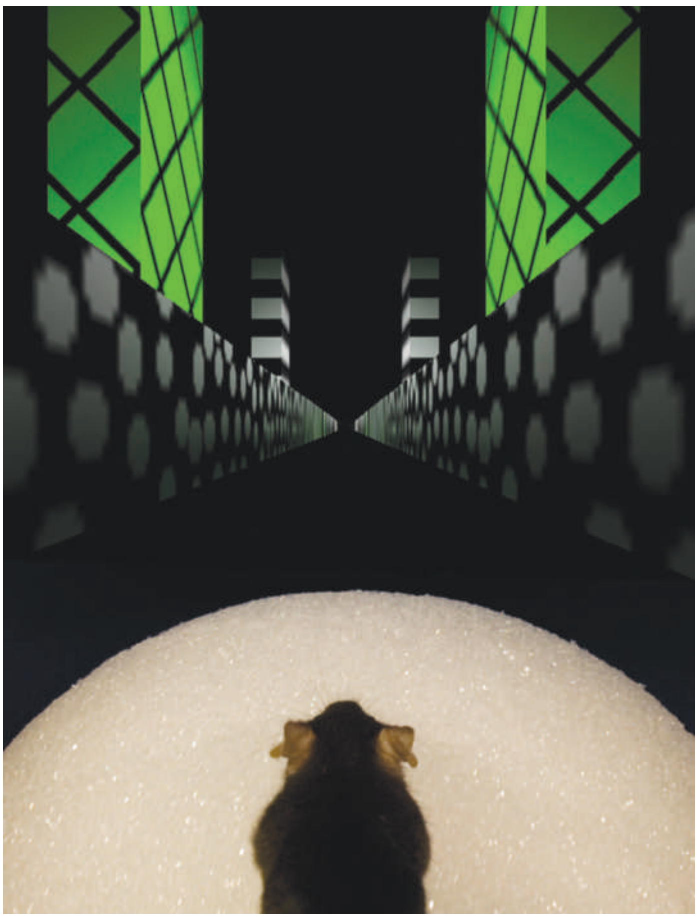

F. COLLMAN

Figure 1 | Mouse navigation in virtual reality. The integration of approaches used by Harvey *et al.*[1] allows extracellular as well as intracellular place-specific activity in the brain to be monitored.

from awake mice whose heads are restrained and whose feet rest on a large spherical treadmill (picture a very large ping-pong ball). The speed and direction of treadmill rotation, induced by the animal's leg movements, is integrated and used to move the mouse through a virtual-reality environment presented on screens shaped to cover much of its visual field (Fig. 1). Effectively, the animal moves through an environment of its own volition, a known requirement for normal place-specific activity[6].

The effort and patience involved in developing such a difficult technique are to be applauded, especially given the risk of failure involved. Lacking the normal vestibular inputs from movements of its head that help an animal monitor its own motion during actual running, it was not at all a given that place-specific activity would be observed. And yet, under these conditions, normal-sized, trajectory-dependent, 'virtual' place fields were indeed apparent. Traversal through such fields was consistently accompanied by phase precession, albeit to a lesser degree than seen in freely moving rodents.

Having shown this, the authors[1] deliver a first payment on the promise of the technique. Virtual movement of the animal through a given neuron's place field is accompanied by a ramp-like depolarization of the cell's membrane potential that spans the length of that field. Moreover, the depolarization envelope carries a theta-frequency rhythm that is much more prominent than when the animal moves outside the place field of the recorded neuron. Considered together, these results are consistent with the predictions of a set of explanations for phase precession[7,8]. A feature of such 'somato-dendritic interference models' is the interaction of theta-rhythmic excitatory and inhibitory oscillations between different compartments of the cell. This is an exciting result in that it may prove generalizable to other brain structures, in particular the cerebral cortex[9].

There are many other similar, as well as qualitatively different, questions that may be addressed using this technique. The technique features a great degree of control over what the animal sees at any given time, and so it will probably permit in-depth studies of how the complex arrangements of visual stimuli that define environmental positions drive hippocampal firing. The observation of robust place-field activity in a virtual-reality environment sets the stage for more direct comparisons between hippocampal function in rodents and primates. Finally, the initial development of the technique in mice suggests that the authors may in the future conduct experiments in genetically modified animals. The impact of excitation or inhibition of specific components of the hippocampus on intracellular dynamics could then be assessed. ■

Douglas Nitz is in the Department of Cognitive Science, University of California at San Diego, La Jolla, California 92093, USA.
e-mail: dnitz@ucsd.edu

1. Harvey, C. D., Collman, F., Dombeck, D. A. & Tank, D. W. *Nature* **461**, 941–946 (2009).
2. Sohal, V. S., Zhang, F., Yizhar, O. & Deisseroth, K. *Nature* **459**, 698–702 (2009).
3. Izhikevich, E. M. & Edelman, G. M. *Proc. Natl Acad. Sci. USA* **105**, 3593–3598 (2008).
4. O'Keefe, J. & Dostrovsky, J. *Brain Res.* **34**, 171–175 (1971).
5. O'Keefe, J. & Recce, M. L. *Hippocampus* **3**, 317–330 (1993).
6. Foster, T. C., Castro, C. A. & McNaughton, B. L. *Science* **244**, 1580–1582 (1989).
7. Magee, J. C. *J. Neurophysiol.* **86**, 528–532 (2001).
8. Harris, K. D. *et al. Nature* **417**, 738–741 (2002).
9. Klausberger, T. & Somogyi, P. *Science* **321**, 53–57 (2009).

ANALYTICAL CHEMISTRY

The matrix neutralized

Ilia Fishbein and Robert J. Levy

Many of the best methods available for monitoring biological binding events can't be used in a diverse range of clinical samples. An ultrasensitive assay based on magnetic signals overcomes this problem.

The Matrix and its two sequel films explore the complex reality of an eponymous cyber-generated world that allows machines to dominate humans. This science-fiction trilogy was famous for its distinctive visual effects, which were generated using innovative combinations of previously existing photographic techniques. In *Nature Medicine*, Gaster *et al.*[1] report how they have used a similar strategy — the combination of established techniques — to devise an ultra-sensitive assay that detects biomarker proteins associated with disease or metabolic states. Their pioneering approach uses magnetic signals to overcome the effects of the biological matrix, the host of compounds found in all biological samples that cause interference in assays. The sensitivity of the authors' technique is 1,000 times better than the current gold-standard method, the enzyme-linked immunosorbent assay (ELISA).

Interference by biological matrices is a real problem in immunoassays, which rely on the binding of an antibody to its target antigen. Such interference has been defined as "the sum of the effects of all of the components [in a sample], qualitative and quantitative, with the exception of the analyte to be measured"[2]. It occurs ubiquitously, both at the stage of specific antigen–antibody binding and during the detection phase, when the amount of antigen–antibody coupling is quantitatively translated into a measurable signal (such as light absorption or fluorescence). The intrinsic, non-zero light absorption and/or fluorescence of biological milieux hinder accurate measurements of analytes (antigens), especially at lower concentrations.

Gaster and colleagues' approach[1] is based on the fundamental observation that even the most complex biological matrices lack a detectable magnetic signal, and would therefore not interfere with a magnetic-field-based detection method. Their assay uses magnetic nanoparticles, bound with high affinity specifically to the biomarkers of interest, as the basis of its detection system. To generate an electronic readout of the assay, they adapted the magnetic-sensing capabilities of giant magnetoresistive (GMR) sensors, devices that were originally developed for use in the read heads of computer hard drives.

So how exactly does Gaster and colleagues' assay work? The authors first attach specific antibodies for a target biomarker to the surface of a GMR sensor, and expose the surface to a fluid sample containing that biomarker, whereupon the target molecules bind to the immobilized antibodies (Fig. 1). The authors then wash the sensor with a second set of antibodies that have been labelled with a compound called biotin; these antibodies also bind

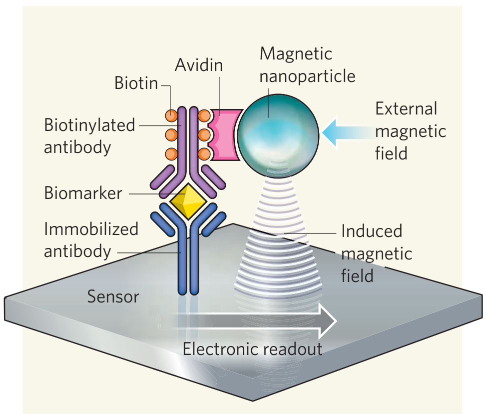

Figure 1 | Mechanism of a magneto-biosensor. Gaster *et al.*[1] describe an ultra-sensitive nanoscale sensor that detects biomarker proteins. Antibodies on the surface of the sensor specifically trap the biomarker of interest from a sample. The sensor is then washed with a solution containing more antibodies, which also bind specifically to the biomarker. These antibodies are tagged with biotin molecules, which bind to the protein avidin. When avidin-coated magnetic nanoparticles are passed over the sensor, they bind to the biotinylated antibody. The sensor is activated by applying an external magnetic field. This induces a magnetic field in the nanoparticles, which causes an electronic response in the sensor that correlates with the number of bound nanoparticles.

specifically to the trapped biomarkers. The next step is to treat the sensor with an aqueous suspension of magnetic nanoparticles — tiny spheres containing iron oxide — to which the protein avidin has been attached. Avidin binds with high affinity to biotin, and so the magnetic nanoparticles become strongly linked to the biomarker–antibody complexes on the surface of the sensor. Finally, the authors activate the sensor by exposing it to a magnetic field. The resulting electronic readout is proportional to the extent of nanoparticle binding, and thus provides a quantitative measure of the amount of biomarker bound to the sensor's surface.

Bioassays that use GMR sensors to detect molecules sandwiched between a pair of antibodies (one immobilized and the other introduced in solution) have been reported previously[3,4]. But there are two factors that distinguish Gaster and colleagues' results[1] from the others. First, they have meticulously characterized their approach for several candidate analytes to prove its generality and its superiority to ELISA. And second, they demonstrate that their nanosensor can be used for multiplexing, so that as many as 64 assays can be performed on the same device. This capability is possible because of the specificity and sensitivity of their design, and because of the lack of biological-matrix interference.

The authors showed that their nanosensor assay system works in all biological fluids studied, including blood, urine, saliva and cell lysates — although the signal strength in saliva is less than that in other media, perhaps because the viscosity of saliva affects the binding kinetics of the assay. The authors also demonstrated that real-time readouts of binding are possible with their system, and that it can be used *in vivo* to follow the earliest stages of tumour progression by monitoring appropriate biomarkers. Turbidity and sample pH do not significantly affect the assay, but Gaster *et al*. found that the output signal is affected by temperature, so that hot or cold samples create undesirable spikes in the baseline of the electronic readout before they equilibrate to room temperature. The authors were able to correct for this, however, by processing the data using a mathematical algorithm. No other assay system, including ELISA, has such a combination of broad applicability, high sensitivity and low background 'noise' caused by biological-matrix interference.

It should be noted that Gaster and colleagues' approach does not actually prevent the biological matrix from physically interfering with antigen–antibody interactions. Nevertheless, such interference can be minimized by carefully screening antibodies to find those that don't interact with components of the biological matrix[2]. The assay could also be adversely affected by inadvertent exposure to strong magnetic fields, such as those present in nuclear magnetic resonance imaging scanners, but this can be prevented by appropriate shielding.

Gaster *et al*. speculate that their assay will be useful for several applications, such as studying protein–protein interactions and screening compounds for biological activity in drug-discovery programmes. Furthermore, the sensitivity and rapid responsiveness of the system permit biomarker monitoring with both high spatial and temporal resolution. This might open up exciting medical applications — for example, by tracking appropriate biomarkers, tumour responses to therapy could be anticipated before any effect becomes apparent. That could reduce the risk of untoward drug effects, and allow adjustments to be made to medication in a more timely way than is currently possible. ■

Ilia Fishbein and Robert J. Levy are in the Division of Cardiology, The Children's Hospital of Philadelphia, Philadelphia, Pennsylvania 19104-4318, USA.
e-mail: levyr@email.chop.edu

1. Gaster, R. S. *et al. Nature Med.* doi:10.1038/nm2032 (2009).
2. Selby, C. *Ann. Clin. Biochem.* **36,** 704–721 (1999).
3. Dittmer, W. U. *et al. J. Immunol. Meth.* **338,** 40–46 (2008).
4. Osterfeld, S. J. *et al. Proc. Natl Acad. Sci. USA* **105,** 20637–20640 (2008).

STEM CELLS

A fateful age gap

Tim Stearns

When a stem cell divides, one sister cell differentiates and the other retains its stem-cell identity. Differences in the age of an organelle — the centriole — inherited at cell division may determine these differing fates.

One of the enduring mysteries of biology is how two genetically identical sister cells become different from each other after cell division. Stem cells are particularly interesting in this respect because they can divide so that one of the two resulting cells remains an undifferentiated stem cell while the other becomes a differentiated cell type. It has long been thought that such asymmetric cell division may reflect an underlying asymmetry in the segregation of a cellular component at division; the asymmetrically inherited component would have properties that allow it to control the fate of its recipient cell. In this issue (page 947), Wang *et al.*[1] present evidence that the centrosome, a multifunctional organelle that is common to all animal cells, might be such a determinant.

The centrosome is an ancient organelle[2] and is one of the cell structures that distinguishes eukaryotic cells (animal and plant cells) from prokaryotes (bacteria and archaea). It helps to form the microtubule cytoskeleton, a network of protein filaments that serve as tracks for moving cellular cargo. It also organizes the primary cilium, a whip-like structure that extends from the surface of cells. In most cells the primary cilium is non-motile, in contrast to the beating cilium of sperm cells, but it is responsive to chemical and mechanical signals outside the cell. For more than a century, the main function of the centrosome was thought to be organization of the mitotic spindle — the filamentous network that carries out the segregation of chromosomes at cell division. But it is now clear that the spindle can form without the centrosome, and that formation of a cilium is actually the centrosome's essential function[3]. This revelation is particularly exciting because it has coincided with the recognition that the primary cilium is a key signalling centre in vertebrate organisms, thereby placing it, and the centrosome, in the thick of important regulatory processes[4].

Each centrosome consists of a pair of cylindrical centrioles and associated microtubule-organizing material. The two centrioles in a pair usually lie in close association at right angles to each other. One centriole, the mother, has structural appendages that confer the ability to anchor microtubules and to organize a cilium; the other centriole, the daughter, lacks these appendages.

The centrosome duplicates once during the cell cycle, and it derives an intrinsic asymmetry from its mechanism of duplication. Centriole duplication is initiated by disengagement of the centriole pair at the end of mitosis, followed in S phase (the phase of DNA synthesis) by assembly of two new daughter centrioles, each adjacent to one of the existing centrioles. This pattern of duplication and segregation results in an age difference in the two centrosomes that are segregated to sister cells at division. One sister cell receives a centrosome containing a newly minted mother centriole (one that was a daughter centriole before duplication and cell division), and the other sister cell receives a centrosome containing the older mother centriole.

Might there be a correlation between the asymmetric fates of dividing stem cells and differences in the age of the centrioles inherited at cell division? Wang *et al*.[1] addressed this question by studying the asymmetric divisions of radial glial cells, a type of neural stem cell that is important for the development of the mammalian cerebral cortex. These cells are highly polarized, stretching between the epithelial surface of the cerebral ventricles

and the adjoining layer of cells. The nucleus in these elongated radial glial cells moves up and down during the cell-division cycle, with mitosis occurring at the apical end, adjacent to the ventricle. After division, one cell remains a radial glial cell while the other differentiates into a neuron or a neuronal precursor that migrates away from the ventricular zone.

When Wang *et al*. labelled the centrioles in developing mouse brain with fluorescently tagged proteins, they found that the older mother centriole was preferentially inherited by the cell that retained the stem-cell fate. To test whether this pattern is important for stem-cell function, they used RNA interference to remove the protein ninein, a component of the centriolar appendages required for mother-centriole functions. Strikingly, when ninein was removed, centriole asymmetry was lost, and the pool of stem cells became depleted, suggesting that inheritance of the older mother centriole is crucial for maintaining stem-cell fate in radial glial cells.

How does the older mother centriole specify stem-cell fate after cell division? On the basis of the properties of centrioles, I consider three possibilities. First, the mother centriole initiates the formation of a primary cilium at the beginning of the cell cycle in most cells. A recent report[5] indicates that the cell that inherits the older mother centriole usually projects a cilium before its sister, and that the sister cell thus differs in its response to signals mediated by the cilium. Such a temporal difference in receptiveness to external differentiation signals might result in a cell-fate difference in recently divided cells.

A second possibility is that the older and newer mother centrioles differ in their complement of anchored microtubules during the cell cycle before division. As anchored microtubules can serve as tracks on which to move components towards the centrosome, the older mother centriole might accumulate proteins[6] or RNA[7] that influence cell fate after division.

Last, it has been proposed that stem cells are maintained by asymmetric segregation of a set of 'stem' chromosomes, all of a similar replicative age[8]. Such asymmetric chromosome segregation is at odds with the known mechanisms of mitosis, but has been observed in some types of mammalian stem-cell division[9]. Perhaps the older mother centriole maintains a connection to the chromosomes (the nuclear envelope notwithstanding) from one mitosis, through interphase to the next mitosis, allowing all similarly aged sister chromatids (the copies of a replicated chromosome) to segregate together.

Possibly the most exciting result from Wang and colleagues' work[1] is that their findings are remarkably similar to those of studies[10] of male germline stem cells in the fruitfly *Drosophila melanogaster*. In that system, the older centrosome also stays in the stem cell, and this asymmetric segregation is part of a stereotyped division choreographed by signals from the stem-cell niche. We can hope that a unifying mechanistic principle of differentiation will be revealed by future experiments investigating this remarkable organelle and its behaviour during division. ■

Tim Stearns is in the Department of Biology, Stanford University, and the Department of Genetics, Stanford School of Medicine, Stanford University, California 94305, USA.
e-mail: stearns@stanford.edu

1. Wang, X. *et al. Nature* **461,** 947–955 (2009).
2. Marshall, W. F. *Curr. Opin. Cell Biol.* **21,** 14–19 (2009).
3. Basto, R. *et al. Cell* **125,** 1375–1386 (2006).
4. Berbari, N. F., O'Connor, A. K., Haycraft, C. J. & Yoder, B. K. *Curr. Biol.* **19,** R526–R535 (2009).
5. Anderson, C. T. & Stearns, T. *Curr. Biol.* **19,** 1498–1502 (2009).
6. Fuentealba, L. C., Eivers, E., Geissert, D., Taelman, V. & De Robertis, E. M. *Proc. Natl Acad. Sci. USA* **105,** 7732–7737 (2008).
7. Lambert, J. D. & Nagy, L. M. *Nature* **420,** 682–686 (2002).
8. Cairns, J. *Genetics* **174,** 1069–1072 (2006).
9. Rando, T. A. *Cell* **129,** 1239–1243 (2007).
10. Cheng, J. *et al. Nature* **456,** 599–604 (2008).

50 & 100 YEARS AGO

50 YEARS AGO

In his presidential address to the British Association at York on September 2, Sir James Gray pleaded strongly for a wider outlook in the teaching of science and stressed the need for a considered judgment as to the proportion of our total educational effort which should be devoted to the training of scientists and technicians — upon whom we depend for maintaining or extending our standard of living — and the proportion which should be expended on raising the intellectual standards whereby the bulk of the population forms its judgments on matters which are susceptible to personal prejudice or political propaganda. Sir James recognized the implications of Dr. Trenaman's inquiry into the impact of the mass media and maintained that the key to the problem lies in the schools. The responsibility resting on secondary school teachers is not easily exaggerated, and Sir James pointed out that really inspired teachers, working with adequate but simple equipment, would achieve far more for general education than specialists in highly equipped laboratories.

From *Nature* 17 October 1959.

100 YEARS AGO

The British School of Archaeology at Athens has made further important discoveries on the site of the city of Sparta. The great temple of Artemis Orthia has been now completely cleared. The site known as the Menelaion, at Therapne, about two miles south-east of Sparta, has been partially examined. The sanctuary of Menelaus and Helen, mentioned by Herodotus, Livy, Pausanias, and Polybius, was a favourite resort of the Spartan ladies, where the goddess was believed to confer the gift of beauty on her worshippers. The discovery of Mycenaean remains on this site suggests that this was the famous palace of Menelaus.

From *Nature* 14 October 1909.

MATERIALS SCIENCE

Quasicrystals from nanocrystals

Alfons van Blaaderen

Quasicrystals have a host of unusual physical properties. These intermediates between amorphous solids and regular crystalline materials can now be made to self-assemble from nanoparticles.

The discovery of quasicrystals about 25 years ago[1,2] brought about a paradigm shift in solid-state physics. The observation that the arrangement of atoms in these solids exhibited long-range order yet lacked the three-dimensional periodicity and translational symmetry that characterizes conventional crystals puzzled physicists[3–5] — not least because certain 'forbidden' rotational symmetries occur in these materials. Initially discovered in certain exotic metal alloys, quasicrystals were later found in more common mixtures of elements and even in soft matter[3]: liquid crystals, surfactants and polymers. Adding to this growing list, Talapin *et al.*[6] (page 964 of this issue) now report that binary colloidal nanoparticle

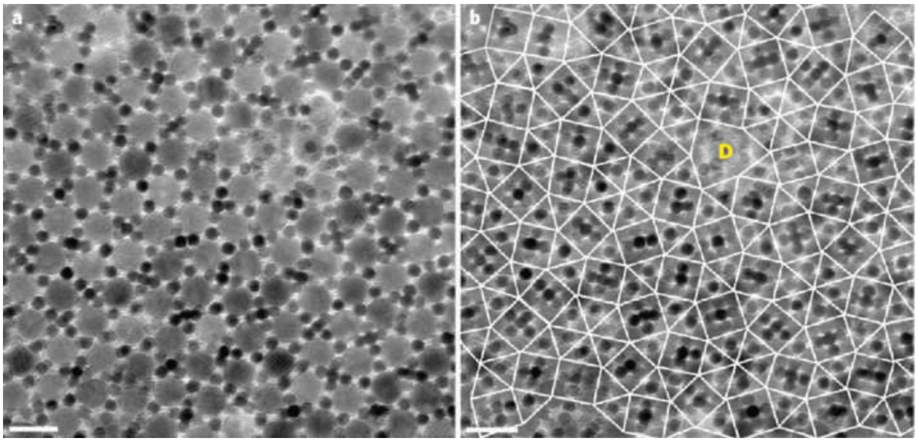

Figure 1 | Binary colloidal quasicrystal. Talapin and colleagues[6] demonstrate self-assembly of a binary quasicrystal that involves a mixture of two types of nanoparticle: 13.4-nm Fe_2O_3 and 5-nm gold colloidal spheres. **a**, Transmission electron microscopy (TEM) image of the quasicrystal. **b**, Square–triangular tiling overlaid onto the TEM image. A structural defect ('D') is visible. (Scale bars, 20 nm.)

systems, involving mixtures of two kinds of nanocrystal, self-assemble with quasicrystalline order.

Talapin and colleagues' colloidal quasicrystal self-assemblies are dodecagonal — that is, they display a 12-fold 'forbidden' rotational symmetry (a rotation about a particular axis by an angle 360°/12 does not change the material's scattering pattern). The assemblies are aperiodic in a certain plane but periodic in the direction perpendicular to this plane. Larger, micrometre-sized colloidal particles had already been reported to arrange in a decagonal (ten-fold) quasicrystalline pattern, but this was achieved by using laser beams and forcing them to form an interference pattern that conferred the desired symmetry on the system[7].

Many of the unique properties of quasicrystals — hardness, low thermal conductivity, low friction and remarkable electronic properties (such as strong anisotropy in electronic transport) — have to do with the interplay between short-range and long-range order in these materials. The short-range order mainly refers to recurrent structural building units, and the long-range order to how these units are arranged in patterns that never repeat themselves. This interplay makes it hard for conventional methods to reconstruct the three-dimensional structure of quasicrystals from their diffraction patterns, although the quality of some of the quasicrystalline diffraction data is as good as the best obtained for periodic crystals. The interplay is also responsible for the lack of positional atomic data of high quality. Finally, it is at the root of the debate about the mechanisms that underlie the growth and stabilization of quasicrystals. All this despite the fact that the number of research papers on quasicrystals is running towards 10,000.

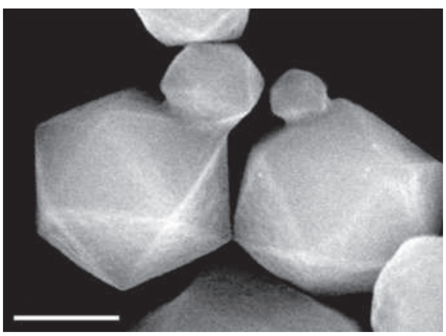

ACS

Figure 2 | Icosahedral quasicrystals. Scanning electron microscopy image[10] of quasicrystal isocahedra (20-faced regular polyhedra displaying five-fold rotational symmetry) formed from composite silica spheres (not shown) about 30 nm across. (Scale bar, 2 μm.)

In their experiment, Talapin and colleagues[6] used nanoparticles that are large enough to show up clearly in transmission electron micrographs (Fig. 1) but sufficiently small to be considered 'designer atoms', or 'quantum dots'. In binary arrangements of quantum dots, the collective quantum behaviour of the interacting particles can give rise to novel 'metamaterial' properties. For example, a regular arrangement of two sets of different-sized semiconducting nanoparticles has been shown to create a new kind of semiconductor[8]. Combining the properties of such binary metamaterials with those of quasicrystals would no doubt lead to new opportunities in materials design.

Talapin *et al.* resorted to projection transmission electron microscopy, which led, for instance, to the clear identification of a structural defect (Fig. 1). However, the use of transmission electron microscopy tomography on several periodic binary-crystal structures made of similar nanoparticles has previously succeeded in determining the three-dimensional particle locations[9]. Application of this technique to the dodecagonal quasicrystal structures studied by Talapin and colleagues would allow a full, three-dimensional characterization of the materials, and could provide insight into how these quasicrystals grow.

The authors[6] observed that several different binary mixtures of nanoparticles (involving metals, magnetic materials and semiconductors), whose only common trait is a particle-size ratio of 0.43, self-assembled into the same type of quasicrystal. This observation is important both for unravelling some of the many mysteries associated with this type of aperiodic crystal and for our ability to design and fabricate novel materials. Most likely, it means that there is no strict requirement for a specific inter-particle interaction, allowing quasicrystal self-assemblies of many combinations of materials and, possibly, of (much) larger colloidal particles.

In fact, the formation of icosahedral quasicrystals (Fig. 2) made up of silica-coated surfactant spheres about 30 nanometres across, twice the size of Talapin and colleagues' largest nanoparticles, has already been reported[10] — although the authors do not actually identify them as quasicrystals. The central part of the underlying formation mechanism, if correct, is that the surfactant/silica composite spheres form before the quasicrystal self-assembles. The size of the beautiful quasicrystal icosahedra formed, roughly 2 micrometres across, is within the colloidal length-scale regime, leading one to daydream that these icosahedra themselves might be made to self-assemble on yet another level of order. The sequence of structural order at which matter could be arranged would then range from an amorphous glass to an aperiodic quasicrystalline solid made of nanoparticles, to finally a periodic structure made of micrometre-sized particles.

Lastly, quasicrystals could provide the means to the development of photonic quasicrystals by self-assembly. These materials differ from photonic crystals — materials specially engineered to trap and guide light — in the quasiperiodicity and forbidden symmetries of their crystal structures. These differences could make photonic quasicrystals outperform their conventional analogues. A photonic band gap — the forbidden energy range of photon propagation that characterizes photonic crystals — in the microwave regime has already been demonstrated for quasicrystalline structures made by lithography[11]. The development of photonic quasicrystals by self-assembly may well be within reach. ■

Alfons van Blaaderen is in the Debye Institute for Nanomaterials Science, Utrecht University, 3582 CC Utrecht, the Netherlands.
e-mail: a.vanblaaderen@uu.nl

1. Shechtman, D., Blech, I., Gratias, D. & Cahn, J. W. *Phys. Rev. Lett.* **53,** 1951–1953 (1984).
2. Levine, D. & Steinhardt, P. J. *Phys. Rev. Lett.* **53,** 2477–2480 (1984).
3. Steurer, W. *Z. Kristallogr.* **219,** 391–446 (2004).
4. Dubois, J.-M. *Useful Quasicrystals* (World Scientific, 2005).
5. Zeng, X. *Curr. Opin. Colloid Interface Sci.* **9,** 384–389 (2005).
6. Talapin, D. V. *et al. Nature* **461,** 964–967 (2009).
7. Mikhael, J., Roth, J., Helden, L. & Bechinger, C. *Nature* **454,** 501–504 (2008).
8. Urban, J. J., Talapin, D. V., Shevchenko, E. V., Kagan, C. R. & Murray, C. B. *Nature Mater.* **6,** 115–121 (2007).
9. Friedrich, H. *et al. Nano Lett.* **9,** 2719–2724 (2009).
10. Tang, J. *et al. J. Am. Chem. Soc.* **129,** 9044–9048 (2007).
11. Man, W., Megens, M., Steinhardt, P. J. & Chaikin, P. M. *Nature* **436,** 993–996 (2005).

NATURE|Vol 461|15 October 2009

OBITUARY

Norman E. Borlaug (1914–2009)

Plant scientist who transformed global food production.

"More than any other single person of this age, he has helped provide bread for a hungry world. We have made this choice in the hope that providing bread will also give the world peace." These were the words of the Nobel committee when presenting the 1970 Peace Prize to Norman Borlaug. Borlaug died on 12 September. His brilliance as a plant breeder, and life-long dedication to taking scientific innovations to farmers without delay, were driving forces behind what came to be known as the Green Revolution.

He was born on 25 March 1914, and his upbringing on an Iowa farm and experience of hardship during the early 1930s gave him a first-hand view of the ills of low farm productivity, poverty and hunger. After completing his PhD degree in plant pathology at the University of Minnesota in 1942, he joined the Rockefeller Foundation's agricultural programme in Mexico, which led to the birth of the International Maize and Wheat Improvement Center (CIMMYT). There he began his work with wheat, with special emphasis on controlling the fungal diseases called rusts. He introduced a multi-pronged approach, including the development of composite varieties of wheat characterized by phenotypic identity but genotypic diversity in resisting different species of the pathogen.

Drawing on the availability of the Norin 10 dwarfing gene from Japan, in 1953 Borlaug launched a programme to breed semi-dwarf, high-yielding varieties of wheat that responded well to irrigation and fertilizer application. Traditional wheat varieties are tall, and tend to topple over if grown in highly fertile soil. Conditions for good crop growth are also conducive to the spread of pathogens, however, so he intensified his research on combining high yield potential with disease resistance.

Borlaug decided to adopt a 'shuttle' programme that involved growing different generations (F_2, F_3 and so on) under two diverse conditions — a summer crop in the cooler highlands near Mexico City and a winter crop in the warmer conditions of Sonora in northwest Mexico. This procedure led to the breeding of semi-dwarf, disease-resistant wheat strains with broad adaptation, such as Sonora 63, Sonora 64, Lerma Rojo 64 and Mayo 64. These were varieties with a yield potential of 5–6 tonnes per hectare that in the 1960s transformed wheat productivity in Mexico, then in India and Pakistan.

In 1966, in a strategy supported by Borlaug, India imported 18,000 tonnes of seeds of Lerma Rojo 64-A and a few other varieties from Mexico. The result was a

AP PHOTO

jump in wheat production from 12 million tonnes in 1965 to 17 million tonnes in 1968. Similar results were obtained in rice, as a result of the introduction of the Dee-gee-woo-gen dwarfing gene from China into tall varieties of *indica* rice at the International Rice Research Institute in the Philippines. This Green Revolution, a term coined in 1968 by William Gaud, remains an astonishing phenomenon that not only boosts productivity but also saves land resources. For example, in 2009 India produced 80 million tonnes of wheat from 26 million hectares of land. At pre-Green Revolution yield levels, 80 million hectares would have been needed.

Africa, however, did not witness the same success. Beginning in 1986, Borlaug organized a programme known as Sasakawa-Global 2000, in which numerous small-scale farmers were helped to double and triple their yield of maize (corn), rice, sorghum, millet, wheat, cassava and grain legumes. Unfortunately, the spectacular results in demonstration plots were not reflected at the national level owing to the lack of effective systems of irrigation, roads, seed production, remunerative marketing and other elements of infrastructure.

In 1984, Borlaug accepted a part-time professorship at Texas A&M University, where for more than 15 years he taught a graduate course in international agriculture. Aware of the lack of recognition for scientists working in food and agriculture, he had the World Food Prize established in 1986, which he hoped would come to be regarded as the Nobel prize for these subjects. Throughout his career, he devoted time to training young scholars and researchers. This led him to promote the World Food Prize Youth Institute programme, which helps high-school students to work in other countries, a life-changing experience for them.

Borlaug's seminal research involved traditional breeding methods, but he was a great supporter of biotechnology research, including the use of recombinant DNA technology. He believed firmly in exploiting the new opportunities for creating novel genetic combinations to meet the challenges arising from climate change. He was also an advocate of 'public good' research, and argued for the free exchange of genetic material and the continuous development of germ plasm by approaches such as hybridization between winter and spring wheats. In 2006, the Norman Borlaug Institute for International Agriculture was set up at Texas A&M to promote science-based solutions for the challenges facing global agriculture.

Norman Borlaug was a remarkable man who was supported by a remarkable woman, his wife Margaret, who died in 2007. To my mind she is the unsung heroine of the Green Revolution: without her unwavering support, Borlaug might not have accomplished nearly so much in his long and demanding career. He is survived by a daughter and a son.

Towards the end of his life, he received two especially notable honours. In 2004, to mark his youthful prowess as a wrestler, he was inducted into the Iowa Wrestling Hall of Fame. And in 2007 he was awarded the Congressional Gold Medal. On that occasion he pointed out that between the years 1960 and 2000 the proportion of "the world's people who felt hunger during some portion of the year" had fallen from perhaps 60% to about 14%. The latter figure, he went on, still "translates to 850 million men, women and children who lack sufficient calories and protein to grow strong and healthy bodies", and that "the battle to ensure food security for hundreds of millions of miserably poor people is far from won". This is the unfinished task that Norman Borlaug leaves to scientists and political leaders worldwide.

M. S. Swaminathan

M. S. Swaminathan is at the M. S. Swaminathan Research Foundation, Third Cross Street, Taramani Institutional Area, Chennai 600 113, India. He was director-general of the International Rice Research Institute, Manila, between 1982 and 1988.
e-mail: chairman@mssrf.res.in

Q&A

NEUROSCIENCE

Alzheimer's disease

Lennart Mucke

The neurodegenerative disorder Alzheimer's disease is becoming more prevalent in ageing populations worldwide. The identification of effective treatments will require a better understanding of the physiological mechanisms involved, and innovative approaches to drug development and evaluation.

Lots of people are forgetful. Are there any particular warning signs of Alzheimer's disease?

Most people's memory declines a little with age, so the line between normal age-related forgetfulness and the earliest signs of Alzheimer's disease (AD) can be fine — so fine that a category of 'mild cognitive impairment', or MCI, has been created, in part to avoid diagnosing AD in people with more benign memory impairments. However, many people with MCI progress to AD. Typically, AD shows itself as a gradual loss of episodic memory (for instance, forgetting that a conversation took place the day before). This is often more apparent to others than to the patient. But AD can also present as word-finding difficulties, getting lost in familiar neighbourhoods, or more complex behavioural changes, sometimes brought on suddenly by a change in environment (such as hospitalization).

How is AD diagnosed?

Diagnosing AD with 100% certainty requires a detailed post-mortem microscopic examination of the brain. But nowadays, AD can be diagnosed with more than 95% accuracy in living patients by using a combination of tools. These include taking a careful history from patients and their families, and assessing cognitive function by neuropsychological tests. Other causes of dementia must be ruled out, such as low thyroid function, vitamin deficiencies, infections, cancer and depression. It's also crucial to differentiate AD from other neurodegenerative dementias, including frontotemporal dementia, Lewy-body dementia and Creutzfeldt–Jakob disease. Brain imaging and tests of cerebrospinal fluid (CSF) can help to distinguish AD from these conditions. Patients with AD typically show shrinkage of brain regions involved in learning and memory on magnetic resonance images, as well as decreased glucose metabolism and increased uptake of radioligands that detect abnormal protein deposits (amyloid) on positron emission tomography scans. CSF abnormalities include low levels of amyloid-β (Aβ) peptides and increased levels of the protein tau.

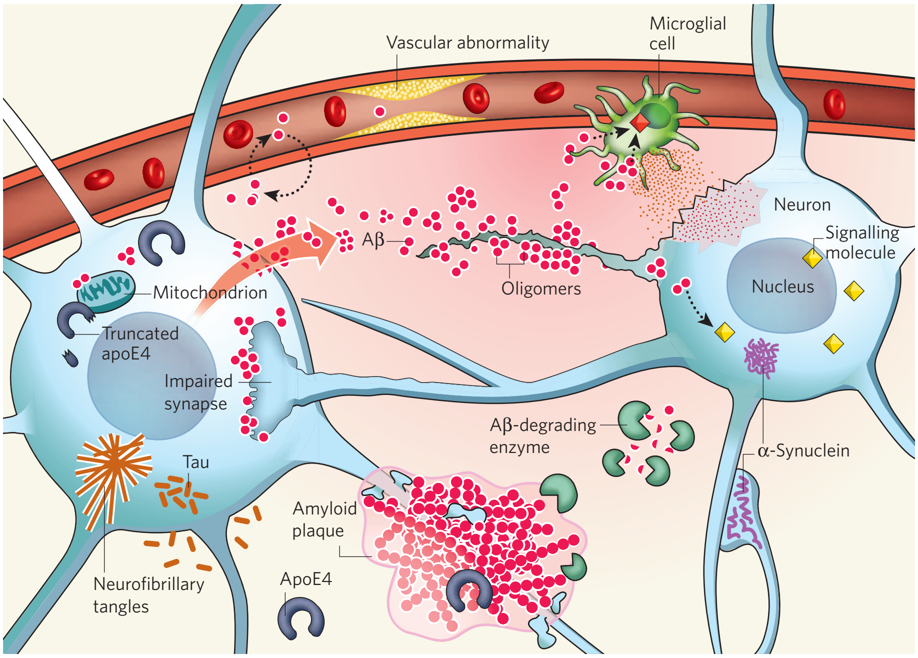

Figure 1 | Some key players in the pathogenesis of AD. Aggregation and accumulation of amyloid-β (Aβ) in the brain may result from increased neuronal production of Aβ, decreased activity of Aβ-degrading enzymes, or alterations in transport processes that shuttle Aβ across the blood–brain barrier. Aβ oligomers impair synaptic functions, whereas fibrillar amyloid plaques displace and distort neuronal processes. Aβ oligomers interact with cell-surface membranes and receptors, altering signal-transduction cascades, changing neuronal activities and triggering the release of neurotoxic mediators by microglia (resident immune cells). Vascular abnormalities impair the supply of nutrients and removal of metabolic by-products, cause microinfarcts and promote the activation of astrocytes (not shown) and microglia. The lipid-carrier protein apoE4 increases Aβ production and impairs Aβ clearance. When produced within stressed neurons, apoE4 is cleaved into neurotoxic fragments that destabilize the cytoskeleton and, like intracellular Aβ, impair mitochondrial functions. The proteins tau and α-synuclein can also self-assemble into pathogenic oligomers and can form larger intra-neuronal aggregates, displacing vital intracellular organelles. (Modified from E. D. Roberson and L. Mucke *Science* 314, 781–784; 2006.)

How big a problem is the disease?

Very big — in large part because people are living longer, and ageing is a major risk factor. The Alzheimer's Association estimates that, without better ways to prevent the disease, the number of people with AD could rise from around 5 million in the United States today to between 11 million and 16 million, and from about 26 million to more than 100 million worldwide, by 2050. This could severely strain health-care systems because the disease is so persistent, disabling and costly.

What are the causes of AD?

There are many. A lot of evidence suggests that neurodegenerative diseases, including AD, stem from the abnormal accumulation of harmful proteins in the nervous system (Fig. 1). In AD, these include Aβ peptides, the lipid-carrier protein apolipoprotein E (apoE), the microtubule-associated protein tau, and the presynaptic protein α-synuclein, which is also involved in

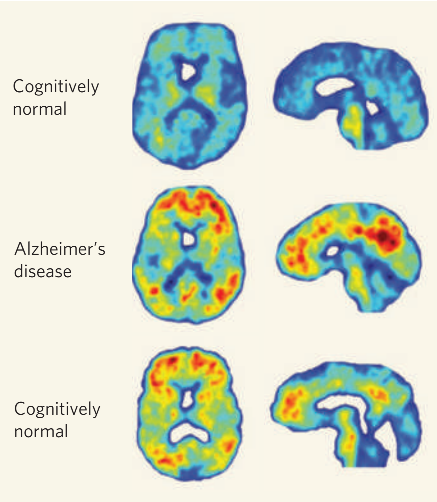

Figure 2 | The challenge of finding AD biomarkers. Two normal controls (top and bottom rows) and an age-matched AD patient (middle row) were given an intravenous injection of the radioligand PIB, which binds to fibrillar Aβ deposits. PIB retention in the brain is detected by positron emission tomography. Low levels of PIB binding (cooler colours) are seen in most cognitively normal people (top) and high levels of PIB binding (warmer colours) in people with AD (middle). But some cognitively normal people also have high levels of PIB binding (bottom), suggesting that the presence of amyloid plaques is not sufficient to cause cognitive deficits. Whether cognitively normal people with high levels of PIB binding will develop AD later on is unknown. Images courtesy of Gil Rabinovici (University of California, San Francisco) and William Jagust (Lawrence Berkeley National Laboratory).

Parkinson's disease. All of us make Aβ peptide in the brain and other organs — it's released from the amyloid precursor protein (APP) after cleavage by β-secretase and γ-secretase enzymes. But Aβ is usually quickly removed from our brains by clearance mechanisms. When its concentration is increased by overproduction or defective clearance, Aβ self-aggregates into assemblies ranging from oligomers to protofibrils, fibrils and amyloid plaques. Tau and α-synuclein can also self-aggregate into oligomers and into larger inclusions in neurons, known as neurofibrillary tangles and Lewy bodies, respectively. By definition, all patients with AD have many plaques and tangles; most patients also have Lewy bodies.

How do these changes cause cognitive decline?

This is a hotly debated issue. Most probably, Aβ and tau cause faulty neural-network activity and impair synapses between neurons that form and maintain microcircuits supporting learning, memory and other cognitive functions. Ultimately, vulnerable groups of neurons atrophy and die in a process that may involve excitotoxicity (overstimulation of neurotransmitter receptors on neuronal surface membranes), collapse of calcium homeostasis, inflammation, and depletion of energy and growth factors. A form of apolipoprotein E, apoE4, contributes to the abnormal accumulation of Aβ and tau, but probably also damages mitochondria and the cellular cytoskeleton. Aβ, tau, apoE and α-synuclein interact with many other molecules and modulate diverse signalling cascades that regulate neuronal activity and survival. Genetically modified rodents and other experimental models are being used to tease out this complexity and to determine which biochemical cascades have the greatest impact on the initiation and progression of the disease.

Can AD be inherited?

Yes. A small number of patients (probably fewer than 1%) have early-onset AD because they have inherited autosomal dominant mutations in genes whose protein products — APP, presenilin 1 (PS1) or PS2 — are involved in the production of Aβ peptides. Presenilin is the enzymatic centre of the γ-secretase complex. The most powerful genetic risk factor for the more common forms of AD is the *APOE* ε4 gene, which encodes the apoE4 lipid carrier. The more common apoE3 and the rare apoE2 forms of apoE are relatively protective against AD. More than 60% of Caucasian patients with AD carry at least one *APOE* ε4 gene. Certain variants of genes encoding another lipid carrier, clusterin (apoJ), the intracellular trafficking protein PICALM, or complement component (3b/4b) receptor 1 also modulate AD risk, possibly by affecting Aβ levels, synaptic functions or inflammation.

What about non-genetic causes?

The risk of AD may be increased by a low level of education, severe head injury, cerebrovascular disease, diabetes and obesity. But it remains uncertain whether avoiding these risk factors can significantly lower one's chances of getting the disease, especially in people with genetic risks for AD. It is likely that AD-predisposing genes interact with other disease genes and environmental factors. An otherwise healthy person may get AD early in life simply because they've inherited an aggressive *PS1* mutation. Another may get AD because they've inherited two *APOE* ε4 genes, and yet another because they've inherited one or more minor risk genes, but are also overweight and diabetic.

What has ageing got to do with it?

Ageing is the most important risk factor for AD. Even aggressive autosomal dominant AD mutations typically don't lead to obvious deficits until the fourth or fifth decade of life. Several mechanisms may protect the young brain against AD, including higher levels of growth factors, better energy metabolism and more efficient mechanisms for clearing misfolded proteins and repairing cells. Failure of these protective mechanisms may contribute to the development of AD. Ageing also increases the prevalence of obesity, diabetes and atherosclerosis, which may promote AD through metabolic or vascular mechanisms. Inflammation could be the common denominator here, as the inflammatory activity of immune cells, particularly macrophages and microglia, and of astrocytes, increases with ageing. Some of these activities are probably beneficial, whereas others may promote or allow the development of ageing-related disorders such as AD.

Are there any available treatments?

Medicines currently prescribed for AD fall into three groups: inhibitors of acetylcholinesterase; an antagonist of a receptor for the neurotransmitter glutamate; and drugs from the psychiatric toolbox to control depression and behavioural abnormalities. The neurotransmitter acetylcholine is depleted in AD brains, and inhibition of acetylcholinesterase, its degrading enzyme, aims to improve cholinergic neurotransmission. Excitotoxicity resulting from overstimulation of NMDA-type glutamate receptors may contribute to AD, providing a rationale for blocking these receptors. Several clinical trials have shown beneficial effects for inhibitors of acetylcholinesterase or NMDA receptors, although the benefits were typically small, and these drugs don't seem to arrest or reverse AD.

How about diet and lifestyle changes?

It's often suggested that adopting a healthy diet and lifestyle to avoid high cholesterol and high blood pressure may help because of the potential contribution of vascular disease to AD. Regular physical exercise also increases growth factors in memory centres of the brain. Social engagement and mental activity have also been linked to lower AD risk in epidemiological studies. In mouse models, increased activity and environmental enrichment prevent or delay the development of AD-like signs. But the control groups in many of these mouse studies were kept in rather impoverished conditions, which may have exaggerated the benefits of the 'enriched' conditions.

Are there any other treatment options?

In my opinion, one of the most productive things to do is for patients and their relatives to enrol in carefully controlled prospective clinical trials. There is an urgent need to increase the proportion of patients with AD and of healthy elderly people who participate in these trials. By contrast, dietary fads and unproven over-the-counter drugs and herbs should be discouraged. The claims to fame for these compounds are notoriously transient. They've also added a troublesome burden of confounding variables ('noise') among trial subjects and complicate the task of designing informative clinical trials.

Why have so many drug trials failed?

For several reasons. In some cases, the trial may reveal that the drug target does not have a crucial pathogenic role. In other cases, the drug may block a truly pathogenic pathway, but the overall impact may be negligible because other

branches of the multifactorial pathogenic cascade are untouched. For example, in a recent trial of an anti-Aβ agent, *APOE* ε4 gene carriers had more side effects and may have benefited less than non-carriers. Assessing whether the drug affects the most relevant target can also be challenging. Considerable evidence suggests that small Aβ oligomers cause more damage to synaptic and cognitive functions than larger amyloid plaques. Plaque loads can be estimated by radiological imaging, but brain levels of Aβ oligomers can't be reliably measured in living patients, making it unclear whether anti-Aβ treatments in clinical trials actually lower levels of the harmful Aβ oligomers. Treatment failure may also be the result of 'too little, too late'. AD probably develops insidiously over many years, if not decades. Some of my colleagues believe that even so-called early clinical stages of AD reflect advanced-stage brain failure that may be impossible to reverse.

Is there any chance of disease reversal?

This depends, in part, on the 'plasticity' of the brain, which is much greater than that of other organs, although AD-associated factors such as Aβ and apoE4 may impair these adaptive mechanisms, adding insult to injury. The flip side of this coin is that removing these factors might unleash powerful repair mechanisms that could fix or help circumvent broken neural circuits so that functional recovery may be possible. Many people have shown an impressive recovery of neurological functions after extensive loss of nerve cells from other causes. The test will be to see if the AD-damaged brain is capable of similar feats when all inhibitors of effective regeneration have been eliminated.

Is stem-cell therapy an option?

The idea behind using stem cells is that these cells might be used to replace destroyed neurons. But AD poses particular challenges in this regard, as it affects diverse types of neuron in different brain regions. For now, it's unclear if stem cells can be induced to differentiate into all these cell types and if the resulting neurons would effectively integrate into broken circuits, particularly in a hostile environment full of harmful proteins and inflammatory mediators. Again, regeneration and repair might be assisted by removing these hostile factors. Where stem cells could yield more immediate rewards is as models for studying the heterogeneity of AD. It is now possible to establish pluripotent stem-cell lines from skin cells of individual patients and to differentiate them into neurons or other brain cells. Comparing these cellular models might lead to the identification of patient-specific pathogenic pathways and modifier genes.

And prevention — is this feasible?

Preventative treatments would probably have to be started years, if not decades, before the first symptoms of AD appear. Treating people for such long periods would require drugs with minimal side effects and the ability to identify people with significant risk factors early on. We still do not have reliable early biomarkers for AD, although progress has been made (Fig. 2). An Alzheimer's Disease Neuroimaging Initiative is under way to determine if measuring changes in brain volume over time, glucose metabolism and amyloid deposition in the brain, and levels of Aβ and tau in the CSF, can identify people at high risk of developing the disease. Proteomics profiling of blood plasma has yielded protein 'fingerprints' that might be diagnostic and possibly even predictive of AD. Although whole-genome sequencing as a routine screening method is still quite a way off, it is relatively straightforward to screen for the known autosomal dominant AD mutations in the *APP*, *PS1* and *PS2* genes, and for the *APOE* ε4 gene.

TABLE 1 | ONGOING CLINICAL TRIALS FOR TREATING ALZHEIMER'S DISEASE

Approach or drug	Proposed mechanism of action	Phase
β-Secretase inhibition	Decreases formation of Aβ from amyloid precursor protein	II
γ-Secretase inhibition	Decreases formation of Aβ from amyloid precursor protein	II/III
Active immunization with Aβ peptides	Generates anti-Aβ antibodies that interact with Aβ and remove it from the brain by uncertain downstream mechanisms	II
Passive immunization with anti-Aβ antibodies	The antibodies interact with Aβ and remove it from the brain by uncertain downstream mechanisms	III
Intravenous pooled immunoglobulins	May enhance clearance of Aβ and other harmful proteins from the brain; may decrease harmful inflammatory processes	III
Scyllo-inositol	Decreases formation and stability of pathogenic Aβ assemblies	II
Latrepirdine	Prevents mitochondrial dysfunction	III
Inhibition of receptor for advanced glycation end products (RAGE)	Blocks stimulation of the cell-surface receptor RAGE, which binds Aβ, decreasing Aβ levels in the brain and preventing Aβ from activating pathogenic pathways	II
Stimulation of insulin signalling	Prevents hyperglycaemia; may overcome insulin resistance in the brain	II
Selective oestrogen-receptor modulator	Promotes neuroprotective effects of oestrogen without eliciting its harmful effects	II
Neurotrophic and neuroprotective agents	Stimulate neurotrophic and antioxidant pathways or pathways that protect against excitotoxicity	II

The above selection focuses on potentially disease-modifying strategies and is based on a review of websites, oral reports at scientific meetings, and discussions with Paul Aisen (University of California, San Diego) and Laurie Ryan (National Institute on Aging).

Phase II and phase III trials assess the safety and efficacy of new treatments; phase III trials involve many more subjects, are conducted in multiple centres, and are required for drug approval by regulatory agencies.

So should everyone get genetic testing?

This depends on many factors, including one's family history, outlook on life and the desire to secure certain types of insurance. If early-onset AD runs in the family and one is contemplating having children, genetic testing for autosomal dominant AD mutations may be appropriate. In general, genetic testing for AD should be undertaken only with the advice of a physician and a genetic counsellor who are experienced in helping people weigh up all the risks and benefits. Many clinicians advise against genotyping for *APOE* ε4 and other susceptibility genes because these genes are primarily risk factors, and some carriers never develop AD. The lack of established preventative treatments also diminishes the value of knowing one's risks, although greater public awareness of AD risks might help to intensify the fight against this devastating condition.

Is there reason for hope?

Indeed there is. As we gain a greater understanding of the mechanisms of AD, drugs can be aimed at its root causes (not just at its symptoms). Several drugs with disease-modifying potential are already in advanced clinical trials (Table 1), and more are in the pipeline. Large-scale risk-factor profiling using genomic and proteomic screens may make it possible to identify subgroups of patients who stand to benefit from particular drugs or drug combinations. Zeroing in on the most responsive patient populations could make clinical trials more effective and guide long-term prevention strategies. ■

Lennart Mucke is at the Gladstone Institute of Neurological Disease and the Department of Neurology, University of California, San Francisco, California 94158, USA.
e-mail: lmucke@gladstone.ucsf.edu

FURTHER READING
Alzheimer's Association *2009 Alzheimer's Disease Facts and Figures* (2009).
Chin, J., Roberson, E. D. & Mucke, L. in *Learning and Memory: A Comprehensive Reference* Vol. 4 (ed. Byrne, J. H.) Ch. 15 (Academic, 2008).
Mahley, R. W., Weisgraber, K. H. & Huang, Y. Apolipoprotein E4: A causative factor and therapeutic target in neuropathology, including Alzheimer's disease. *Proc. Natl Acad. Sci. USA* **103,** 5644–5651 (2006).
Roberson, E. D. & Mucke, L. 100 years and counting: Prospects for defeating Alzheimer's disease. *Science* **314,** 781–784 (2006).
www.alzforum.org
www.clinicaltrials.gov

The author declares competing financial interests. See online article for details.

See online at go.nature.com/phyLwm for more on neuroscience.

NEUROTECHNIQUES

Cover illustration
(Artwork by N. Spencer)

I t is an exciting time to be a neuroscientist. The experimental landscape has changed markedly over the past few years, given the technological advances in molecular genetics, optogenetics and functional imaging. The focus is now shifting towards the application of these techniques in a variety of experimental systems so that their promise can be fulfilled.

Neuroscience research was once dominated by anatomical techniques. But, with the advent of electrophysiology, and subsequently molecular biology, anatomical labelling techniques were eclipsed as the pre-eminent experimental strategy. Now, anatomical methodology is experiencing a renaissance, thanks to the ability to deliver molecules genetically in a cell-type-specific manner and as a result of advances in imaging methods. This powerful combination, together with electrophysiological techniques, now makes it feasible to study the relationships between specific neural circuits and particular behaviours in rodents, previously the domain of invertebrate model systems. However, despite the rise of new techniques, electrophysiology is unlikely to suffer the earlier fate of neuroanatomy and will remain an integral part of neuroscience experimentation.

Neuroscientists are also poised to benefit from systems-based approaches to data collection and analysis but lag behind other researchers, such as tumour biologists, in implementing these strategies. Using the results from such approaches to direct hypothesis-driven work and improve the design of these experiments could be a crucial development in psychiatric-disease genetics, focusing efforts on key candidate genes in the genetic network associated with disease. Systems biology could also aid in attempts to identify specific markers of neurodegenerative diseases.

We thank the authors and reviewers of these Reviews for their contributions to this Insight, which offers visions for tackling the next set of challenging neurobiological questions.

Noah Gray, Chief Commissioning Editor
Tanguy Chouard, Contributing Editor

REVIEWS

nature insight

NATURE|Vol 461|15 October 2009|doi:10.1038/nature08536

Molecular genetics and imaging technologies for circuit-based neuroanatomy

Benjamin R. Arenkiel[1] & Michael D. Ehlers[1,2]

Brain function emerges from the morphologies, spatial organization and patterns of connectivity established between diverse sets of neurons. Historically, the notion that neuronal structure predicts function stemmed from classic histological staining and neuronal tracing methods. Recent advances in molecular genetics and imaging technologies have begun to reveal previously unattainable details about patterns of functional circuit connectivity and the subcellular organization of synapses in the living brain. This sophisticated molecular and genetic 'toolbox', coupled with new methods in optical and electron microscopy, provides an expanding array of techniques for probing neural anatomy and function.

Individual neurons are the elemental building blocks of the brain. However, understanding how neurons are 'wired' through synapses, understanding the microcircuits they form and understanding how those microcircuits participate in neural networks to drive perception and behaviour remain some of biology's major challenges. To unravel complex neural computations and representations fully, we must consider both the structure of the connections formed between intermingled cell types and how electrical activity propagates through the network to allow its dynamic function. Our understanding of how neuronal circuits produce sensory perception, memory and behaviour remains nascent. In most cases, it is far from clear how brain functions emerge from existing circuit diagrams. Bridging this conceptual divide requires knowledge across several scales, ranging from cell-type-specific genetic identity and population-level network connectivity to the function and dynamics of individual synapses and circuit output.

The study of neuroanatomy in the twenty-first century is being rekindled by the merger of molecular and genetic manipulations aimed at probing circuit function using gene expression profiling, high-resolution imaging and electrophysiology. In addition, endeavours are underway to build high-resolution maps of all the neurons and their full complement of synapses in multiple model organisms (ref. 1 and the Connectome Project (http://iic.harvard.edu/research/connectome)). These new techniques for monitoring and manipulating circuits, neurons and synapses are increasing our capabilities to a degree that heralds a new era of functional neuroanatomy. Here we briefly trace the evolution of the array of technology currently available for probing neuron and circuit architecture. In addition, we provide a critique of current experimental limitations and propose future convergent methodologies to advance a deeper understanding of neuroanatomy.

Resolving neuronal architecture

With the advent of biological electron microscopy, it became possible to study new subcellular details of neuronal organelles and structures, including the organization of synaptic contacts[2]. Early electron microscopy circuit maps included single cells, intact invertebrate nervous systems[3,4], retinal assemblages and dendritic synapse maps for single cortical neurons in mammals[5–7]. Recently, the power and utility of electron microscopy have expanded with the evolution of new methods for collecting and reconstructing large sets of volume electron microscopy data[8], which can reveal the fine detail of neuronal morphology and subcellular structure and provide near-molecular resolution in a native three-dimensional environment (Box 1).

Complementing electron microscopy volume reconstruction, array tomography coupled with fluorescence imaging allows submicrometre investigation of individual cells or subcellular structures labelled using fluorescent probes[9]. In this technique, nanometre-scale resolution of molecule location in the perpendicular (z axis, or axial) direction is achieved by collecting ultrathin sections (50–100 nm) and then performing molecular localization using antibodies or fluorescent proteins. Array tomography is a relatively simple platform that combines light microscopy and electron microscopy to reveal both molecular and ultrastructural details of intact nervous tissue.

The development of new methods of serial sectioning, alignment and computational analysis is continually increasing the speed and utility of electron microscopic reconstruction for investigating the ultrastructural features of nervous tissue[10]. However, a major challenge of using electron and light microscopy to map brain connectivity is the current lack of the high-throughput data-mining and image-reconstruction approaches required to move beyond small-scale experimentation. With further development of technology to collect, curate and analyse high-resolution imaging data more rapidly[8,10,11], ultrastructural analysis will become easier. However, this type of data does not provide dynamic information in real time or within living tissue. For that, optical imaging and genetic strategies must be used.

The expanding field of molecular genetics now offers numerous avenues for the investigation of neuroanatomy. Advances in the creation of conditional knockout mice, inducible gene expression systems and genetic control of neuronal activity provide means to probe circuit biology with unprecedented precision[12]. The seminal discovery of genes encoding fluorescent proteins in marine invertebrates has allowed the expression of fluorescent proteins and fluorescent-protein-tagged biomolecules in living neurons of the mammalian brain[13,14], providing a widening array of sophisticated imaging and genetic profiling techniques[15–18].

The molecular genetics revolution

Neuronal populations have genetically specified identities. Classical definitions of neuronal cell types based on morphology or electrical

[1]Department of Neurobiology, [2]Howard Hughes Medical Institute, Duke University Medical Center, Box 3209, Durham, North Carolina 27710, USA.

Box 1 | Volume electron microscopy

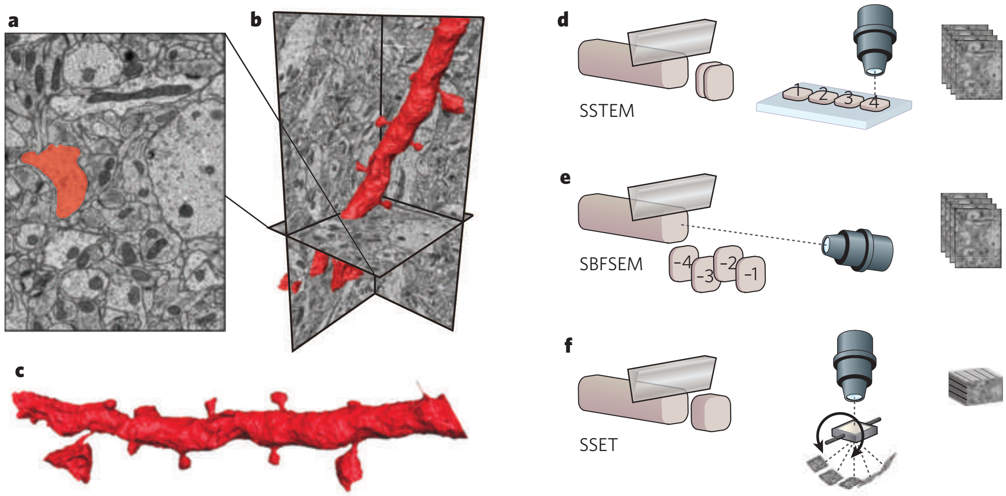

Current methods for volume electron microscopy rely on three-dimensional (3D) image reconstruction from ultrathin serial sections made through intact nervous tissue. Individual section planes (box figure, panel **a**) are reconstructed in the *z* axis to build a block of image planes that can be digitally navigated in all axes using image analysis software (box figure, panel **b**). 3D image reconstruction further allows the volumetric isolation of complete neuronal architecture, ranging from subcellular organelles to cell morphology[10,82] (box figure, panel **c**). Serial-section transmission electron microscopy (SSTEM) was the first volumetric electron microscopy technique to allow the assembly of high-resolution circuit data and has remained the primary method of resolving 3D neuronal ultrastructure[3,4,10,82]. This approach relies on the manual collection of ultrathin tissue sections onto grids that are imaged and reconstructed in series (box figure, panel **d**). Although SSTEM is often the method of choice, it is labour intensive and has limited ability to routinely reconstruct high-quality data sets of sections less than ~50 nm in thickness.

Instead of cutting ultrathin sections that require manual collection and subsequent imaging, serial-block-face scanning electron microscopy (SBFSEM) relies on generating images from electrons that are scattered from the face of an embedded tissue block that undergoes repeated rounds of surface sectioning to reveal deeper structures[83] (box figure, panel **e**; progressively deeper sections are indicated using negative numbers). Because the images are captured from the face of the block before each cut, there is no need to collect tissue, which reduces section thickness variability and allows the process to be automated. Ion-beam milling of the block face for serial imaging provides an alternative to mechanical cutting[11]. Although SBFSEM holds promise for streamlining volume electron microscopy, technical limitations have so far prevented its widespread use; sample quality and image resolution are still inferior to those possible using SSTEM[8].

A permutation of SSTEM that provides higher *z*-section resolution than microtome sectioning is that of serial-section electron tomography[84] (SSET; box figure, panel **f**). In this method, subcellular structures are reconstructed by assembling multiple images captured from an angular two-dimensional-projection tilt series to generate a 3D tomogram. The primary benefit of this technique is that the number of sections required to build a high-resolution image volume is lower than that needed in SSTEM or SBFSEM.

A major challenge to all of these techniques is the need for accurate image alignment, contour recognition, automated segmentation and error checking in order to assemble detailed volume sets. All current accurate methods require this to be done (or at least curated) manually[8,10,85,86]. It remains to be determined to what extent computational methods will replace manual tracing. (K. M. Harris (Univ. Texas, Austin) provided the raw electron microscopy data series used to generate the images used in panels **a**–**c**. The 3D data set was prepared for graphic representation using AMIRA software, Visage Imaging.)

properties can now be linked to, and perhaps ultimately replaced by, discrete patterns of gene expression. With the advancement of molecular genetics has come the ability to query the genetic make-up of individual cells or entire brain regions. In the near future, such methods will help determine, for instance, whether neurons of a given genotype form stereotyped patterns of connections in the mammalian brain, or whether such connections result in predictable patterns of circuit function or behavioural output. Genetically marking and manipulating cells in the brain now allows such issues to be addressed. Major advances in manipulating genetic programs in mice permit the generation of loss-of-function, gain-of-function and conditional mutations at will[19]. Conditional genetic strategies are already proving crucial in understanding neuronal circuits. Implementation of phage-derived recombination systems such as Cre/*loxP* technology provides intersectional approaches to genetic manipulation in neurons, ranging from the single-cell level[20,21] to controlling gene activity in selected brain structures[22,23]. However, harnessing cell-type-specific promoter activity to manipulate neuronal subsets precisely in the mammalian brain remains a challenge. Often genes that are transcribed in target neuron populations show overlapping patterns of expression in other brain areas, or exhibit dynamic regulation during development that can confound their use in the mature brain.

Alongside the ability to investigate single cells by targeted expression of molecular markers, large-scale efforts to map patterns of endogenous gene expression in the rodent brain have provided a wealth of data to the neuroscience community (for example the Gene Expression Nervous System Atlas (http://www.gensat.org) and the Allen Brain Atlas[24] (http://www.brain-map.org)). These open resources now make it unnecessary for individual labs to conduct exhaustive gene expression experiments, as the relevant data for nearly any neuron type or brain structure can be accessed through the Allen Brain Atlas (see also page 908). However, most expression data are still limited to healthy adult animals. More complete data sets that are currently being assembled by the Allen Institute for Brain Science include those for gene expression in the developing mouse brain, the mouse spinal cord and the human cortex. A future can be imagined in which the spatial and temporal patterns of all genes are available across the lifespans of diverse species, and in the context of specific mutations or disease states.

Dissection of genetic circuits

A basic principle of neuroscience is that information is stored and encoded by the properties of neurons and the connections they make with one another. Thus, identifying patterns of neuronal connectivity is required for understanding brain function. To piece together these

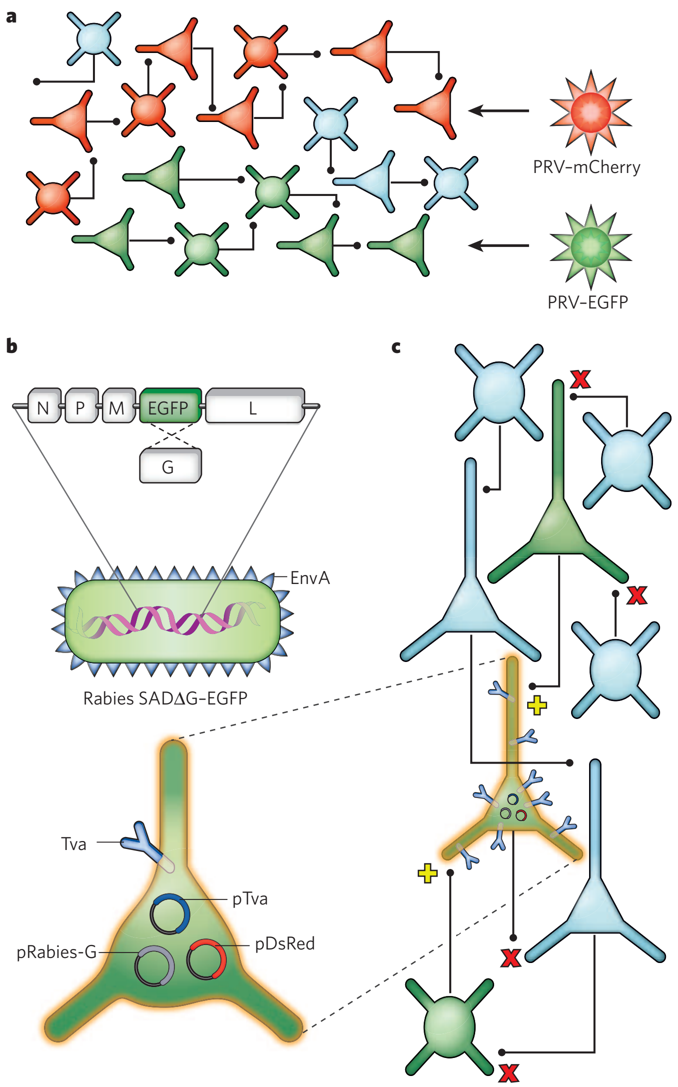

Figure 1 | Viral vectors for trans-synaptic labelling. Several viruses show trans-synaptic spread, including pseudorabies virus (PRV) and rabies virus[25–27,33]. **a**, PRV can be used to trace intact brain circuits differentially through the expression of fluorescent proteins of different colours, such as enhanced green fluorescent protein (EGFP) and mCherry. A drawback of replicating viral vectors such as PRV is that they continue to propagate from cell to cell, making it difficult to discern monosynaptic patterns of connectivity from polysynaptic. Synaptically connected neurons show viral spread. Red-labelled neurons represent the synaptic network associated with a single cell infected with PRV–mCherry, green-labelled neurons represent the synaptic network of a PRV–EGFP-infected cell, and blue neurons represent uninfected cells not associated with either network. **b**, An alternative method relies on the generation of recombinant rabies virus deficient in the gene encoding the G-protein coat particle, which is replaced by an EGFP reporter[26]. To target desired neuronal subsets with EGFP-expressing rabies virus, rabies virus particles can be pseudotyped with the avian leukosis virus EnvA coat protein, which specifically binds to avian-specific Tva-class receptors. By targeting neurons for heterologous Tva-receptor expression, rabies virus infection can be limited to those neurons that express Tva. SADΔG–EGFP is the strain of rabies virus used for monosynaptic tracing. This viral strain has been genetically engineered to have the G protein deleted and replaced with an EGFP reporter. N, P, M and L respectively represent the viral genomic sequences encoding the wild-type nucleoprotein, phosphoprotein, matrix protein and polymerase required for rabies virus expression. **c**, A twist on this approach includes the introduction of plasmids that encode the Tva receptor (pTva) and the wild-type rabies virus G protein (pRabies-G), allowing a non-infective EGFP-expressing virus to specifically enter Tva-expressing cells by interaction with the EnvA coat protein. Once inside, the G-deleted virus is repackaged with G coat protein expressed from the pRabies-G plasmid, allowing subsequent trans-synaptic spread to presynaptic partners of Tva-targeted neurons[27]. Because only the initially infected neuron contains the wild-type rabies virus G protein, viral spread is halted after one round of monosynaptic jumping. Adding a plasmid encoding a red fluorescent protein (for instance pDsRed) allows the cell originally targeted for infection to be identified within the monosynaptic network of GFP-labelled cells. Yellow plus signs represent sites of monosynaptic viral transfer; red crosses represent polysynaptic sites that lack viral transfer owing to the absence of wild-type G protein.

patterns, information describing both circuit anatomy and the flow of neuronal activity is essential. Several technologies have recently emerged that allow both trans-synaptic circuit analysis and precise control of neuronal firing[12], including the use of retrogradely transported viral vectors[25–27], optogenetic tools such as light-activated ion channels[28–30] and heterologous receptor activation[28,31,32].

Advances in the engineering of viral vectors have included the development of neurotropic viral particles as tools to study synaptic connectivity[33] (Fig. 1). For example, engineered pseudorabies vectors can be modified to express fluorescent proteins and thus label interconnected neurons by retrograde trans-synaptic transfer of viral particles to presynaptic cells[25]. One limitation to using pseudorabies virus is its polysynaptic spread. Owing to the high degree of neuronal interconnectivity in intact circuits, polysynaptic spread makes it difficult to assign synaptically coupled partners unambiguously. Circumventing this problem, a novel coat-protein complementation strategy has been devised that allows monosynaptic tracing of neural connections by using rabies virus particles engineered to express green fluorescent protein[27] (GFP; Fig. 1).

Beyond making possible a more-detailed analysis of anatomy and synaptic connectivity, genetic methods are now being harnessed to facilitate selective control of activity among populations of interconnected neurons in the mammalian brain. Alongside the new subdiscipline called optogenetics (see page 923), efforts to develop heterologous receptor expression systems now provide alternative and potentially non-invasive means to modulate neuronal activity using chemical genetic approaches. Heterologous expression of modified opiate receptors provided an initial demonstration that neuronal subsets in the brains of mice could be genetically targeted for activation by synthetic, exogenous ligands[34]. As another example, mice engineered to harbour high-affinity nicotinic acetylcholine receptors in dopaminergic neurons show hyperdopaminergic behaviour on low-dose administration of nicotine[35]. Furthermore, conditional expression and activation of the rat capsaicin receptor TRPV1 in genetically targeted subsets of neurons in the mouse brain has made it possible to stimulate desired neuronal populations in a conditional Cre-dependent manner by application of TRPV1 agonist[28]. Complementing these strategies has been the engineering of different families of G-protein-coupled receptors to respond to synthetic compounds[36].

In many applications, inhibition rather than excitation of genetically defined neuronal populations is desired. To this end, a number of methods have been developed for *in vivo* experimentation. One such model takes advantage of the sensitivity of the wild-type GABA (γ-aminobutyric acid) receptor $GABA_A$ to the allosteric modulator zolpidem, which normally enhances receptor function. In this design, a knock-in mouse was generated that harbours both a point mutation in the $GABA_A$ receptor γ2 subunit, making it insensitive to zolpidem, and flanking *loxP* sites, to facilitate the conditional replacement of the mutant gene. On Cre-mediated recombination, wild-type receptor activity is reinstated in genetically targeted neuronal subsets, rendering those cells sensitive to pharmacological inhibition by zolpidem[37]. Orthogonal models have been used to drive neuronal hyperpolarization and inhibit action-potential generation by heterologous expression of the *Caenorhabditis elegans* ivermectin-gated chloride channel[31] or the *Drosophila* allostatin receptor, which inactivates neurons by opening G-protein-coupled inward-rectifying K^+ channels[32]. An alternative

Box 2 | Super-resolution imaging techniques

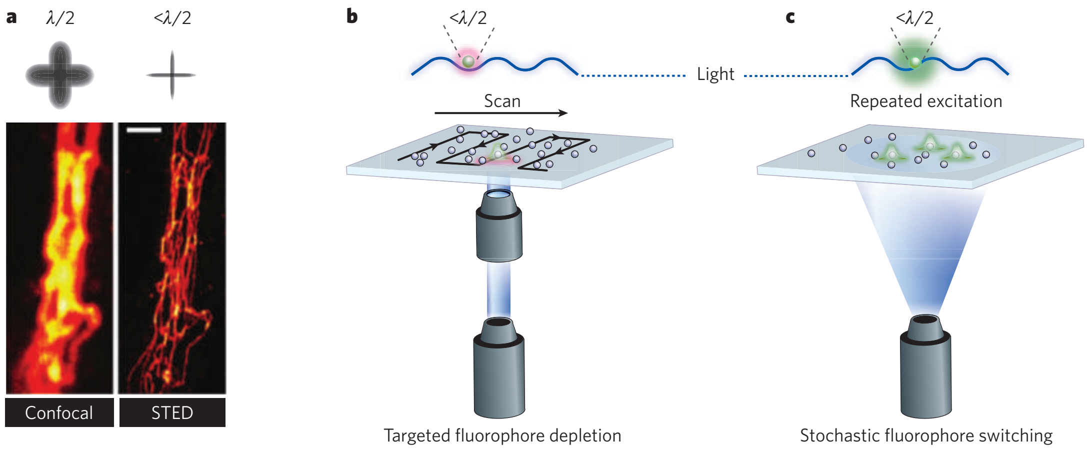

Super-resolution imaging techniques now enable light microscopy to obtain information below the diffraction limit of light. Unlike standard confocal imaging, which is constrained in resolution by the wavelength of light (λ) as defined by the Abbe limit ($<\lambda/(2n\sin\alpha)$, where n is the smallest refractive index in the optical path and α is one-half the angular aperture of a cone of light entering the lens; box figure, left-hand part of panel **a**), super-resolution imaging is capable of nanoscale resolution (box figure, right-hand part of panel **a**; scale bar, 1 μm). Here we discuss two such techniques.

(1) Nanoscale imaging by targeted fluorophore depletion. In STED microscopy, two lasers are used to generate a reduced focal volume. The excitation laser is used to excite a fluorescent molecule into the high-energy excited state, and an additional offset laser is used to deplete the excited state without the production of fluorescence. The optical configuration generates an area in which molecules may be excited but do not fluoresce (box figure, panel **b**). This is the fundamental principle that allows techniques such as STED microscopy[69], ground-state depletion microscopy[87], saturated pattern excitation and saturated structured-illumination microscopy[88] and reversible saturable optically linear fluorescence transition microscopy to image and localize molecules at the nanoscale. Although this technology is rapidly evolving, its common application is still constrained by some practical limitations. For many of these methods, the optics are relatively sophisticated to assemble or expensive to purchase, and the number of currently available fluorophores that can be readily used is limited and awaits development of new variants with different spectral properties, biophysical characteristics and compatibility as protein fusions.

(2) Nanoscale imaging by stochastic fluorophore switching. By broadly illuminating a sample while simultaneously imaging with a high-speed digital camera, individual fluorophore molecules that are sparsely and stochastically photoactivated can be imaged sequentially. Photons emitted from these molecules can be differentiated in space by recording individual on–off states and using centroid analysis[89]. This approach makes it possible to record the position of many different molecules from distinct coordinates, because each photoactivated molecule renders distinct, resolvable spots at the camera (box figure, panel **c**). This is the principle behind the techniques of photoactivated localization microscopy[70], fluorescence photoactivation localization microscopy[71], stochastic optical reconstruction microscopy[71], ground-state depletion microscopy with individual-molecule return[90] and point accumulation for imaging in nanoscale topography[91]. 3D stochastic optical reconstruction microscopy now allows resolution approaching ten times the diffraction-limited value (20–30 nm)[92,93], whereas further resolution (below 20 nm) has been gained with interferometric photoactivation localization microscopy[94]. A clear advantage of super-resolution imaging by stochastic fluorophore switching is its relative simplicity and the fact that each molecule is not forced to undergo many photoswitching cycles, as it is using reversible saturable optically linear fluorescence transition microscopy, where photobleaching is a significant issue. A main disadvantage is the long acquisition time required to capture the stochastic events of single-molecule photon emission. However, together these new super-resolution imaging techniques allow visualization of cells with a detail not previously possible. (Fluorescence images in panel **a** reproduced, with permission, from ref. 18.)

strategy has been to block synaptic transmission rather than induce hyperpolarization. Genetic expression of small molecules for inactivation of synaptic transmission, or expression of *Clostridium* toxins, has allowed selective inactivation of targeted synapses[38–40].

Each of these approaches has unique limitations. For example, controlled inhibition by ivermectin-gated chloride channels relies on the availability of multiple subunits whose functionality requires the appropriate stoichiometry. By contrast, small-molecule-mediated inhibition of synapses[39], which induces dimerization of genetically modified forms of presynaptic proteins, shows toxicity after prolonged exposure to dimerizer at high concentrations. Furthermore, the use of ligands to induce neuronal activation requires transport across the blood–brain barrier and is concentration dependent. Interestingly, the mouse model system for genetic control of neuronal activity by conditional TRPV1 expression may obviate some of these limitations. Multiple TRPV1 agonists and antagonists with an array of different binding affinities, solubilities and blood–brain barrier permeabilities offer the potential for pharmacogenetic manipulations of deep and dispersed neuronal populations in a potentially non-invasive manner. A similar advantage in blood–brain barrier permeability exists for compounds that activate engineered G-protein-coupled receptors[36].

The dynamic synapse

The fundamental element that couples cells of the brain into a functional network is the synapse. The basic input–output relationship of the synapse depends on a finite number of molecular elements, most notably the features of neurotransmitter release from presynaptic terminals and the number and properties of postsynaptic receptors. Synapses act cooperatively as 'computational engines' to sum, transform and relay input from discrete dendritic regions to specific neuronal outputs[41]. Thus, the ability to visualize synapses, as well as discern and manipulate their properties, is paramount for understanding circuit function.

An important and realistic goal for the foreseeable future is to move beyond the categorization of synapses by simply characterizing neurotransmitter phenotype, and instead to define and visualize their functional states. Achieving this goal could help address fundamental issues concerning the properties of synaptic networks, such as determining how strong neighbouring synapses are relative to each other or how synapses function together within a given region of dendrite. Other parameters of categorization could include whether a synapse has a high or a low release probability, whether it is relatively active or mostly quiet, whether it is new or old and whether it has recently been potentiated or

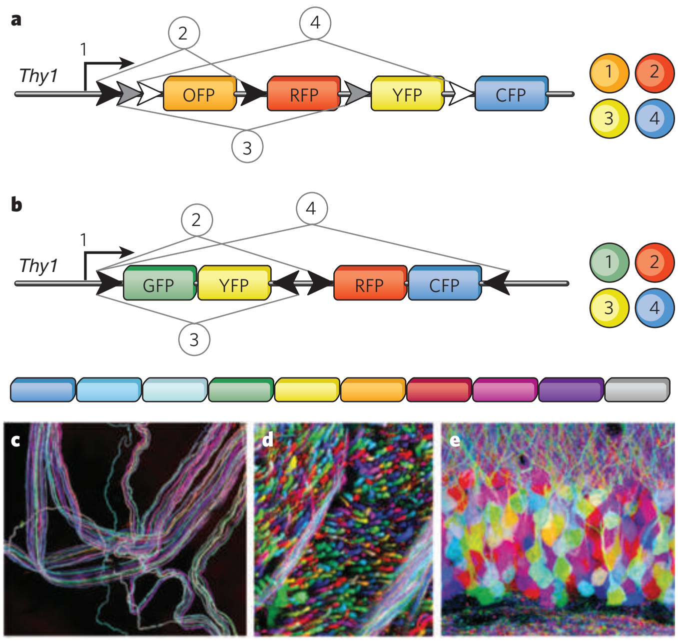

Figure 2 | Conditional anatomy using the Brainbow system. Brainbow mice can be used to identify neuronal subsets by conditional activation of fluorescent reporters[76]. Cre-mediated recombination between *loxP* sequences is orientation dependent. If *loxP* sites are in the same 5′–3′ direction, recombination results in excision of the flanked DNA sequence. When *loxP* sites are in the opposite orientation, recombination drives inversion of the flanked DNA. **a**, A Cre-mediated excision strategy based on a transgenic allele containing pairs of mutated *loxP* sites and multiple fluorescent proteins (orange, OFP; red, RFP; yellow, YFP; cyan, CFP) to generate cells of different colours. Black, grey and white arrowheads represent different *loxP* sequence mutations. Recombination occurs only between mutant pairs, resulting in cells with different colour codes depending on the random recombination events between like pairs. The events labelled 1–4 correspond to patterns of fluorescent-protein expression shown on the right. **b**, A Cre-mediated inversion strategy based on an allele that harbours multiple *loxP* sites of the same type with both orientations. Stochastic recombination events between inversion pairs results in different colour possibilities (1–4; resulting colour code shown on the right). The spectrum of colours that cells can express with different Brainbow alleles and recombination events is shown underneath. **c**–**e**, Images of Brainbow tissue after Cre-mediated recombination to stochastically label different types of neuron (reproduced, with permission, from ref. 81): fibres from a motor nerve innervating the ear (**c**); axon tracts coursing through the brainstem (**d**); cells of the hippocampal dentate gyrus (**e**).

depressed. Visualizing such parameters of synapse status will ultimately require predictable molecular signatures for specific functional states.

Drawing on techniques ranging from fluorescence time-lapse imaging and photoswitching to single-particle tracking (SPT), it is now possible to visualize single synapses directly and monitor movements of individual molecules within them[42,43]. A number of methods have been developed to follow proteins at synapses using targeted expression of molecules tagged with fluorescent proteins. Such methods allow direct visualization of neurotransmitter release[44–46] and dynamic movements of neurotransmitter receptors and postsynaptic scaffold proteins[43].

Expression of fluorescent-protein fusions can be used to measure fluorescence recovery after photobleaching or fluorescence decay in the complementary technique of fluorescence loss after photoactivation of a given cellular domain. These approaches have been widely applied to measure apparent diffusion rates and protein exchange within synaptic microdomains[47,48]. Superecliptic pHluorin, which fluoresces at neutral pH but is quenched at the acidic pH of intracellular compartments, allows direct imaging of surface lateral diffusion, exocytosis and endocytosis of synaptic receptors and neurotransmitter release *in vitro* and *in vivo*[44–46,49–51]. GFP reconstitution across synaptic partners builds on fluorescent-protein reporter technology by revealing information about specific synaptic pairs[52]. By tethering individual GFP fragments to separate presynaptic and postsynaptic proteins, reconstitution of GFP fluorescence is observed when genetically targeted cells form synaptic pairs. One possible limitation of this approach is the potential to induce phenotypes on overexpression of synaptic-protein fusions, which may themselves induce new synapses or alter synapse function. Gene-targeted alleles that facilitate reporter expression from endogenous loci may mitigate such concerns. The range of fluorescent-protein reporters that can be used to visualize synapse function continues to grow, and recent studies using reporters of Förster resonance energy transfer have begun to reveal dynamic protein-activation events and protein–protein interactions accompanying synapse plasticity[53,54].

Complementing genetic expression methods to label and track populations of synaptic molecules, SPT can reveal the dynamics of individual synaptic molecules in real time. SPT affords both high spatial and high temporal resolution for single-molecule tracking by allowing the calculation of diffusion, exchange and dwell times for individual molecules. An important development in SPT has been the use of extremely bright semiconductor quantum dots, which assists the precise spatial tracking of receptors in dendritic microdomains and permits long-term tracking of receptors across dendritic segments[55]. SPT has been used to follow individual α-amino-3-hydroxy-5-methyl-4-isoxazole propionic acid (AMPA) receptors at nanometre resolution within discrete domains of the postsynaptic density[38] and, more recently, to monitor individual synaptic-vesicle fusion events during neurotransmission[56,57]. Quantum dot technology continues to improve with the creation of smaller dots, monovalent labelling and improved targetability[58].

At the tissue level, multiphoton imaging in living brain allows direct visualization of synaptic-protein dynamics[59] and spine morphological and synaptic plasticity within intact circuits[16,17,60,61]. Although *in vivo* imaging has provided a wealth of information on neuronal dynamics in the living brain, the approach is still constrained by the depth of target cells and is most useful for investigating superficial brain areas. The convergence of multiple techniques to mark single neurons, identify specific synapses on them and monitor the dynamics of individual proteins has rapidly expanded our understanding of synaptic organization and function. Ultimately, by using this group of novel methods to investigate the dynamic synapse *in vivo*, we will begin to understand how circuit elements behave in the native environment of the intact brain and in response to sensory experience.

Nanoscopic interrogation

Electron microscopy provides very high spatial resolution of neuronal features but does not allow dynamic imaging of cells in living tissue. Confocal and two-photon light microscopy provide dynamic information at the expense of reduced spatial resolution. The emergence of super-resolution imaging using fluorescent microscopy makes it possible to combine the best aspects of these techniques[62]. These new methods of nanoscale imaging in living cells circumvent classic optical limitations by altering the point spread function of collected light. These optical tricks allow super-resolution imaging of dendrites and spines that approaches the resolution offered by serial electron microscopy[18,63,64].

The first major steps towards enhancing the resolution of light microscopy came in the 1990s when efforts were placed on increasing axial resolution. Methods such as 4Pi and I^{5}M microscopy[65,66] are grounded in perfecting the focus of light along the *z* axis, although they are still constrained by the diffraction barrier. By spatially mixing the frequency patterns of specimen illumination, structured-illumination microscopy increased resolution by a factor of two[67,68]. Stimulated-emission depletion (STED) microscopy, one of the first methods to achieve super-resolution, is based on the ability to shape the point spread function through the nonlinear de-excitation of fluorescent molecules in a ring surrounding a non-depleted region of interest[69] (Box 2). Initially, STED imaging was used with synthetic small-molecule dyes and thus has had limited application in the study of intact nervous tissue or genetically encoded reporters. However, recent improvements have allowed STED

Box 3 | Combinatorial circuit genetics to study the nervous system

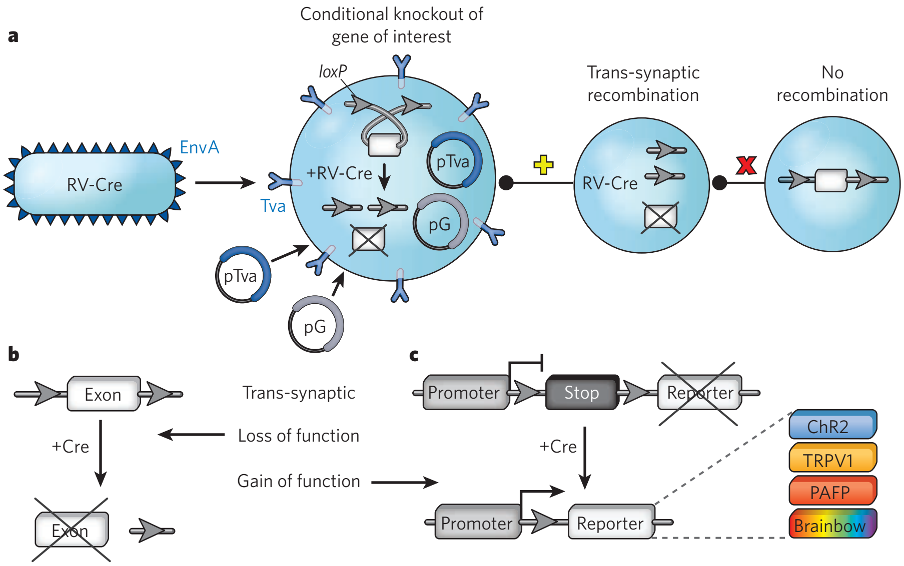

Trans-synaptic tracing of neural circuits using viral technology could allow genomic modifications of connected cells. Advances in viral engineering now allow genetic targeting of precise subsets of neurons with viral expression vectors; a strategy similar to that described in ref. 27 could be used to modify the genomes of interconnected neurons. Panel **a** of the box figure illustrates the genetic targeting of specified neurons in mice, harbouring conditional alleles for trans-synaptic mutagenesis, with Cre-expressing rabies virus vectors (RV-Cre). Cells targeted for primary rabies virus infection by directed expression of the Tva receptor (pTva) will be recombined, as will those that are presynaptic to the initially infected neuron, owing to the presence of a plasmid (pG) expressing the wild-type G coat protein. All other neurons within the circuit will remain unaltered. The white boxes represent a conditional gene of interest that is flanked on either side by a *loxP* site (arrowhead). As in Fig. 1, the yellow plus sign represents monosynaptic viral transfer; the red cross represents a polysynaptic site that lacks viral transfer owing to the absence of wild-type G protein. With such a system, any cell that receives RV-Cre will show monosynaptic conditional mutagenesis, whereas polysynaptic neurons will remain unrecombined and thus wild type. Panels **b** and **c** of the box figure show how trans-synaptic mutagenesis could potentially be used with conditional alleles of all sorts. These may include Cre-dependent conditional loss-of-function reporters (**b**) or gain-of-function reporters (**c**). ChR2, channelrhodopsin-2; PAFP, photoactivatable fluorescent protein.

imaging of fluorescent-protein-expressing hippocampal neurons in organotypic slices, providing substantial technical improvement in the ability to image spine neck width and spine head curvature[64].

Further expanding the super-resolution light microscopy repertoire, several new forms of single-molecule imaging have been developed. The position of a single fluorescent object can be determined with nanometre accuracy by fitting the fluorescence signals from many emitted photons to a two-dimensional Gaussian distribution. Expression of photoconvertible proteins permits the detection of single fluorescent molecules in the presence of a dense total population, because the number of photoactivated molecules can be controlled by the intensity and duration of the activation illumination. In such approaches, variously termed photoactivated localization microscopy[70], fluorescence photoactivation localization microscopy[71] and stochastic optical reconstruction microscopy[72], the centroid of each molecule is calculated in successive rounds of stochastic activation and excitation. Ultimately, super-resolution is achieved by building spatial maps of sequentially activated molecules (Box 2). Together, these methods make it experimentally possible to define cellular structures down to the nanoscale using light microscopy.

The ability to image molecular anatomy at the nanoscale level will be very valuable in neuroscience. Many key neuronal and circuit properties are defined by synapse composition and function that can now be probed at the nanoscale. Of course, single-molecule analysis is not new to neuroscience; the wealth of biophysical information gained from single-channel recordings profoundly influenced neuroscience and the study of excitable tissue[73]. Nanoscopic imaging may have a comparable effect, by advancing standard measurements of synapse and circuit function from macroscopic population measurements to stochastic probabilistic measurements at precise positions on single neurons. Being able to image individual molecules present at synapses might allow us to begin assigning discrete identities or 'states' to different types of neuronal connections, and, thus, more precisely ascertain their contribution to circuit function. For example, tagging and following the movements of molecular identifiers such as channels, receptor subtypes, scaffolding elements or signal transduction machinery to a given synapse may ultimately help in predicting the functional nature of the connections that define neural circuits. At the moment, molecular tags for synapse state remain largely speculative, but emerging technologies are laying the groundwork for future tools to define and probe synaptic circuits.

The future of functional circuit analysis

A 'connectome' is defined as a detailed map of the full set of neurons and synaptic connections within the nervous system of an organism[1]. Important current issues concern which connectomes will be generated and what kind of data will be made available[74,75]. A significant challenge will be incorporating long-range connectivity with more experimentally tractable dissection of local connectivity. Notable progress, ranging from the complete[4] to the ongoing (ref. 1 and the Connectome Project), has been made towards assembling anatomical circuit maps in model systems. Ideally, connectome data will provide not just a useful resource for individual laboratories but also a more comprehensive view of complex circuits from which previously elusive properties emerge.

A missing link to realizing the full potential of any given circuit diagram is information regarding functional connectivity. Existing data sets reveal neither functional signalling properties of the circuit nor dynamic processes such as synapse plasticity. Perhaps most importantly, connectivity data will serve only as snapshots and we will need to remain cognizant of the changing nature of neural circuits, particularly in more complex and malleable nervous systems.

Scepticism has always surrounded similar large-scale informatics-type projects, including the sequencing of the human genome, high-throughput crystallography and the mapping of protein interactions using searchable protein 'interactomes'. Such large-scale approaches, which are often criticized as being unimaginative, have so far had varying success: whereas structural genomics and interactomes are in more nascent states, large-scale genome sequencing stands out as a clear achievement[74].

Alternative approaches to building models of functional brain circuits are being pursued in the absence of model organisms. For example, one of the goals of the Blue Brain Project (http://bluebrain.epfl.ch/page17871.html) is to understand brain function by reconstructing anatomical and signalling properties of circuits through the assembly of known cellular, molecular and computational information, generating detailed brain models *in silico*. It is possible that some animal experiments will eventually be supplanted by computational and computer-assisted modelling, but it is not clear how such models would be validated or which neural circuits should be fully elucidated. Although insufficient in isolation to understand the functionality of neural circuits, complete neuronal wiring diagrams are certain to provide a crucial frame of reference.

Future approaches to neuroanatomical experimentation and functional circuit analysis will rely on a combination of genetics, high-resolution imaging, circuit tracing and electrophysiology. These techniques will increasingly intersect in single experiments to assemble both anatomical and functional circuit information. For example, Brainbow technology allows multichannel stochastic colouring schemes for labelling neurons in the brain using the Cre/*loxP* recombination system[76] (Fig. 2). A shortcoming of this approach is that it does not reveal functional synaptic contacts between neurons of different colours. One way in which this might be achieved is by combining different synapse labelling methods within conditional Brainbow-like engineered tissue. Instead of using standard cytosolic fluorescent proteins for stochastic conditional expression, alternative reporters might include synaptically targeted fluorescent proteins with different spectral properties, to be used in combination with super-resolution imaging.

Ultimately, it would be particularly valuable to be able to visualize functional connections. By combining conditional genetics in the mouse with recently described trans-synaptic viral labelling approaches, circuit-specific genetic dissection may be possible. This might include trans-synaptic mobilization of fluorescent-protein spectral variants, optogenetic reporters, genetically encoded Ca^{2+} sensors and even Cre recombinase across the synaptic cleft. By mobilizing Cre through a circuit in a trans-synaptic manner, conditional mutagenesis could be achieved across synaptic partners based on anatomy rather than gene expression. Technology of this type would allow cellular and circuit-dependent knockouts, activation of floxed genetically encoded neuronal activators and the triggering of floxed fluorescent reporters such as those used in the Brainbow system (Box 3).

Perspectives

Not all of the emerging technologies for probing cells and circuits will necessarily aid us in our understanding of overall brain function. It is conceivable that these new techniques will simply continue to generate piecemeal data that has to be incorporated into a much larger framework to provide significant conceptual advances. It is not yet clear what this larger framework should be. The challenge for the future will be to move from descriptive observations to explanatory theories that provide predictive models of complex brain functions. It seems reasonable to believe that such predictive models will emerge from the mesoscale of microcircuits. Full knowledge of the molecular and structural components of local microcircuits will be insufficient, and long-range interactions and inputs must also be included. Brain processing relies on connections on both scales, although limitations in current technology have perforce focused attention on spatially proximate connectivity. However, with advances in technologies such as optogenetics, progress towards clarifying such long-range functional interactions is under way[77–80]. Perhaps the future will merge cellular and circuit mapping with larger-scale imaging techniques such as functional magnetic resonance imaging to combine knowledge of microarchitecture with macro-circuit function. Ultimately, a combination of these approaches will be needed to advance our knowledge of the brain. The promise of finalizing any accurate blueprint for the mammalian brain remains an ambitious goal, but a range of emerging genetic and imaging technologies provide a basis on which to both formulate predictive models and validate existing theories to begin such a task. Although the challenge ahead is great, the pace of progress in decoding brain circuitry is brisk and quickening. ■

1. Helmstaedter, M., Briggman, K. L. & Denk, W. 3D structural imaging of the brain with photons and electrons. *Curr. Opin. Neurobiol.* **18,** 633–641 (2008).
2. Palay, S. L. & Palade, G. E. The fine structure of neurons. *J. Biophys. Biochem. Cytol.* **1,** 69–88 (1955).
3. Macagno, E. R., Levinthal, C. & Sobel, I. Three-dimensional computer reconstruction of neurons and neuronal assemblies. *Annu. Rev. Biophys. Bioeng.* **8,** 323–351 (1979).
4. White, J. G., Southgate, E., Thomson, J. N. & Brenner, S. The structure of the nervous system of the nematode *Caenorhabditis elegans*. *Phil. Trans. R. Soc. Lond. B* **314,** 1–340 (1986).
5. Ahmed, B., Anderson, J. C., Martin, K. A. & Nelson, J. C. Map of the synapses onto layer 4 basket cells of the primary visual cortex of the cat. *J. Comp. Neurol.* **380,** 230–242 (1997).
6. Anderson, J. C., Douglas, R. J., Martin, K. A. & Nelson, J. C. Map of the synapses formed with the dendrites of spiny stellate neurons of cat visual cortex. *J. Comp. Neurol.* **341,** 25–38 (1994).
7. Stevens, J. K., McGuire, B. A. & Sterling, P. Toward a functional architecture of the retina: serial reconstruction of adjacent ganglion cells. *Science* **207,** 317–319 (1980).
8. Briggman, K. L. & Denk, W. Towards neural circuit reconstruction with volume electron microscopy techniques. *Curr. Opin. Neurobiol.* **16,** 562–570 (2006).
9. Micheva, K. D. & Smith, S. J. Array tomography: a new tool for imaging the molecular architecture and ultrastructure of neural circuits. *Neuron* **55,** 25–36 (2007).
10. Harris, K. M. *et al.* Uniform serial sectioning for transmission electron microscopy. *J. Neurosci.* **26,** 12101–12103 (2006).
11. Knott, G., Marchman, H., Wall, D. & Lich, B. Serial section scanning electron microscopy of adult brain tissue using focused ion beam milling. *J. Neurosci.* **28,** 2959–2964 (2008).
12. Luo, L., Callaway, E. M. & Svoboda, K. Genetic dissection of neural circuits. *Neuron* **57,** 634–660 (2008).
13. Giepmans, B. N., Adams, S. R., Ellisman, M. H. & Tsien, R. Y. The fluorescent toolbox for assessing protein location and function. *Science* **312,** 217–224 (2006).
14. Feng, G. *et al.* Imaging neuronal subsets in transgenic mice expressing multiple spectral variants of GFP. *Neuron* **28,** 41–51 (2000).
15. Heiman, M. *et al.* A translational profiling approach for the molecular characterization of CNS cell types. *Cell* **135,** 738–748 (2008).
16. Kerr, J. N. & Denk, W. Imaging *in vivo*: watching the brain in action. *Nature Rev. Neurosci.* **9,** 195–205 (2008).
17. Svoboda, K. & Yasuda, R. Principles of two-photon excitation microscopy and its applications to neuroscience. *Neuron* **50,** 823–839 (2006).
18. Hell, S. W. Microscopy and its focal switch. *Nature Methods* **6,** 24–32 (2009).
19. Capecchi, M. R. Altering the genome by homologous recombination. *Science* **244,** 1288–1292 (1989).
20. Young, P. *et al.* Single-neuron labeling with inducible Cre-mediated knockout in transgenic mice. *Nature Neurosci.* **11,** 721–728 (2008).
21. Zong, H., Espinosa, J. S., Su, H. H., Muzumdar, M. D. & Luo, L. Mosaic analysis with double markers in mice. *Cell* **121,** 479–492 (2005).
22. Branda, C. S. & Dymecki, S. M. Talking about a revolution: the impact of site-specific recombinases on genetic analyses in mice. *Dev. Cell* **6,** 7–28 (2004).
23. Tsien, J. Z. *et al.* Subregion- and cell type-restricted gene knockout in mouse brain. *Cell* **87,** 1317–1326 (1996).
This was the first primary research paper describing the use of the Cre/*loxP* recombination system for conditional mutagenesis in the mouse nervous system.
24. Lein, E. S. *et al.* Genome-wide atlas of gene expression in the adult mouse brain. *Nature* **445,** 168–176 (2007).
This paper describes the development and function of the publicly accessible digital atlas of *in situ* gene expression patterns created by the Allen Institute for Brain Science for all annotated genes in the rodent brain.
25. Boldogkoi, Z. *et al.* Genetically timed, activity-sensor and rainbow transsynaptic viral tools. *Nature Methods* **6,** 127–130 (2009).
26. Wickersham, I. R., Finke, S., Conzelmann, K. K. & Callaway, E. M. Retrograde neuronal tracing with a deletion-mutant rabies virus. *Nature Methods* **4,** 47–49 (2007).
27. Wickersham, I. R. *et al.* Monosynaptic restriction of transsynaptic tracing from single, genetically targeted neurons. *Neuron* **53,** 639–647 (2007).
This paper describes a creative approach to genetically targeting neuronal subsets for rabies virus infection and circuit tracing while also restricting viral propagation to single presynaptic targets by viral capsid complementation.
28. Arenkiel, B. R., Klein, M. E., Davison, I. G., Katz, L. C. & Ehlers, M. D. Genetic control of neuronal activity in mice conditionally expressing TRPV1. *Nature Methods* **5,** 299–302 (2008).
29. Boyden, E. S., Zhang, F., Bamberg, E., Nagel, G. & Deisseroth, K. Millisecond-timescale, genetically targeted optical control of neural activity. *Nature Neurosci.* **8,** 1263–1268 (2005).
30. Zhang, F. *et al.* Multimodal fast optical interrogation of neural circuitry. *Nature* **446,** 633–639 (2007).
31. Lerchner, W. *et al.* Reversible silencing of neuronal excitability in behaving mice by a genetically targeted, ivermectin-gated Cl^- channel. *Neuron* **54,** 35–49 (2007).
32. Tan, E. M. *et al.* Selective and quickly reversible inactivation of mammalian neurons *in vivo* using the *Drosophila* allatostatin receptor. *Neuron* **51,** 157–170 (2006).

33. Callaway, E. M. Transneuronal circuit tracing with neurotropic viruses. *Curr. Opin. Neurobiol.* **18,** 617–623 (2008).
34. Zhao, G. Q. *et al.* The receptors for mammalian sweet and umami taste. *Cell* **115,** 255–266 (2003).
35. Drenan, R. M. *et al.* *In vivo* activation of midbrain dopamine neurons via sensitized, high-affinity α6* nicotinic acetylcholine receptors. *Neuron* **60,** 123–136 (2008).
36. Conklin, B. R. *et al.* Engineering GPCR signaling pathways with RASSLs. *Nature Methods* **5,** 673–678 (2008).
37. Wulff, P. *et al.* From synapse to behavior: rapid modulation of defined neuronal types with engineered $GABA_A$ receptors. *Nature Neurosci.* **10,** 923–929 (2007).
38. Ehlers, M. D., Heine, M., Groc, L., Lee, M. C. & Choquet, D. Diffusional trapping of GluR1 AMPA receptors by input-specific synaptic activity. *Neuron* **54,** 447–460 (2007).
39. Karpova, A. Y., Tervo, D. G., Gray, N. W. & Svoboda, K. Rapid and reversible chemical inactivation of synaptic transmission in genetically targeted neurons. *Neuron* **48,** 727–735 (2005).
40. Nakashiba, T., Young, J. Z., McHugh, T. J., Buhl, D. L. & Tonegawa, S. Transgenic inhibition of synaptic transmission reveals role of CA3 output in hippocampal learning. *Science* **319,** 1260–1264 (2008).
41. Sjostrom, P. J., Rancz, E. A., Roth, A. & Hausser, M. Dendritic excitability and synaptic plasticity. *Physiol. Rev.* **88,** 769–840 (2008).
42. Groc, L. *et al.* Surface trafficking of neurotransmitter receptor: comparison between single-molecule/quantum dot strategies. *J. Neurosci.* **27,** 12433–12437 (2007).
43. Newpher, T. M. & Ehlers, M. D. Glutamate receptor dynamics in dendritic microdomains. *Neuron* **58,** 472–497 (2008).
44. Fernandez-Alfonso, T., Kwan, R. & Ryan, T. A. Synaptic vesicles interchange their membrane proteins with a large surface reservoir during recycling. *Neuron* **51,** 179–186 (2006).
45. Miesenbock, G., De Angelis, D. A. & Rothman, J. E. Visualizing secretion and synaptic transmission with pH-sensitive green fluorescent proteins. *Nature* **394,** 192–195 (1998).
46. Zhu, Y., Xu, J. & Heinemann, S. F. Two pathways of synaptic vesicle retrieval revealed by single-vesicle imaging. *Neuron* **61,** 397–411 (2009).
47. Ashby, M. C., Maier, S. R., Nishimune, A. & Henley, J. M. Lateral diffusion drives constitutive exchange of AMPA receptors at dendritic spines and is regulated by spine morphology. *J. Neurosci.* **26,** 7046–7055 (2006).
48. Blanpied, T. A., Kerr, J. M. & Ehlers, M. D. Structural plasticity with preserved topology in the postsynaptic protein network. *Proc. Natl Acad. Sci. USA* **105,** 12587–12592 (2008).
49. Bozza, T., McGann, J. P., Mombaerts, P. & Wachowiak, M. *In vivo* imaging of neuronal activity by targeted expression of a genetically encoded probe in the mouse. *Neuron* **42,** 9–21 (2004).
50. Park, M. *et al.* Plasticity-induced growth of dendritic spines by exocytic trafficking from recycling endosomes. *Neuron* **52,** 817–830 (2006).
51. Yudowski, G. A. *et al.* Real-time imaging of discrete exocytic events mediating surface delivery of AMPA receptors. *J. Neurosci.* **27,** 11112–11121 (2007).
52. Feinberg, E. H. *et al.* GFP reconstitution across synaptic partners (GRASP) defines cell contacts and synapses in living nervous systems. *Neuron* **57,** 353–363 (2008).
53. Harvey, C. D., Yasuda, R., Zhong, H. & Svoboda, K. The spread of Ras activity triggered by activation of a single dendritic spine. *Science* **321,** 136–140 (2008).
54. Lee, S. J., Escobedo-Lozoya, Y., Szatmari, E. M. & Yasuda, R. Activation of CaMKII in single dendritic spines during long-term potentiation. *Nature* **458,** 299–304 (2009).
55. Triller, A. & Choquet, D. New concepts in synaptic biology derived from single-molecule imaging. *Neuron* **59,** 359–374 (2008).
56. Zhang, Q., Cao, Y. Q. & Tsien, R. W. Quantum dots provide an optical signal specific to full collapse fusion of synaptic vesicles. *Proc. Natl Acad. Sci. USA* **104,** 17843–17848 (2007).
57. Zhang, Q., Li, Y. & Tsien, R. W. The dynamic control of kiss-and-run and vesicular reuse probed with single nanoparticles. *Science* **323,** 1448–1453 (2009).
58. Howarth, M. *et al.* Monovalent, reduced-size quantum dots for imaging receptors on living cells. *Nature Methods* **5,** 397–399 (2008).
59. Gray, N. W., Weimer, R. M., Bureau, I. & Svoboda, K. Rapid redistribution of synaptic PSD-95 in the neocortex *in vivo*. *PLoS Biol.* **4,** e370 (2006).
60. Mizrahi, A. Dendritic development and plasticity of adult-born neurons in the mouse olfactory bulb. *Nature Neurosci.* **10,** 444–452 (2007).
61. Nagerl, U. V., Kostinger, G., Anderson, J. C., Martin, K. A. & Bonhoeffer, T. Protracted synaptogenesis after activity-dependent spinogenesis in hippocampal neurons. *J. Neurosci.* **27,** 8149–8156 (2007).
62. Huang, B., Bates, M. & Zhuang, X. Super-resolution fluorescence microscopy. *Annu. Rev. Biochem.* **78,** 993–1016 (2009).
63. Lippincott-Schwartz, J. & Manley, S. Putting super-resolution fluorescence microscopy to work. *Nature Methods* **6,** 21–23 (2009).
64. Nagerl, U. V., Willig, K. I., Hein, B., Hell, S. W. & Bonhoeffer, T. Live-cell imaging of dendritic spines by STED microscopy. *Proc. Natl Acad. Sci. USA* **105,** 18982–18987 (2008).
This paper describes the first study implementing stimulated-emission depletion techniques to image morphological plasticity of dendritic spines non-invasively at subdiffraction resolution.
65. Gustafsson, M. G., Agard, D. A. & Sedat, J. W. I^5M: 3D widefield light microscopy with better than 100 nm axial resolution. *J. Microsc.* **195,** 10–16 (1999).
66. Hell, S. W. & Stelzer, E. H. K. Fundamental improvement of resolution with a 4Pi-confocal fluorescence microscope using two-photon excitation. *Opt. Commun.* **93,** 277–282 (1992).
This paper reports the first significant increase in axial resolution of fluorescent confocal imaging by coherent use of opposing lenses.
67. Bailey, B., Farkas, D. L., Taylor, D. L. & Lanni, F. Enhancement of axial resolution in fluorescence microscopy by standing-wave excitation. *Nature* **366,** 44–48 (1993).
68. Kner, P., Chhun, B. B., Griffis, E. R., Winoto, L. & Gustafsson, M. G. Super-resolution video microscopy of live cells by structured illumination. *Nature Methods* **6,** 339–342 (2009).
69. Klar, T. A., Jakobs, S., Dyba, M., Egner, A. & Hell, S. W. Fluorescence microscopy with diffraction resolution barrier broken by stimulated emission. *Proc. Natl Acad. Sci. USA* **97,** 8206–8210 (2000).
This paper reports the first study describing the bettering of diffraction-limited resolution by stimulated-emission depletion, a technique that relies on quenching excited organic molecules at the edge of focal spot being stimulated.
70. Betzig, E. *et al.* Imaging intracellular fluorescent proteins at nanometer resolution. *Science* **313,** 1642–1645 (2006).
This paper describes the first use of super-resolution imaging in photoactivated localization microscopy of fixed cells, a technique that allows super-resolution by stochastic fluorophore switching and counter-bleaching to detect the positions of individual fluorescent molecules.
71. Hess, S. T., Girirajan, T. P. & Mason, M. D. Ultra-high resolution imaging by fluorescence photoactivation localization microscopy. *Biophys. J.* **91,** 4258–4272 (2006).
72. Rust, M. J., Bates, M. & Zhuang, X. Sub-diffraction-limit imaging by stochastic optical reconstruction microscopy (STORM). *Nature Methods* **3,** 793–795 (2006).
This paper describes stochastic optical resolution microscopy, a super-resolution imaging technique that allows the localization of individual fluorescent molecules at nanometre resolution by switching the fluorescent tags on and off using light of different colours and variable energies.
73. Sakmann, B. & Neher, E. Patch clamp techniques for studying ionic channels in excitable membranes. *Annu. Rev. Physiol.* **46,** 455–472 (1984).
74. Lichtman, J. W. & Sanes, J. R. Ome sweet ome: what can the genome tell us about the connectome? *Curr. Opin. Neurobiol.* **18,** 346–353 (2008).
75. Seung, H. S. Reading the book of memory: sparse sampling versus dense mapping of connectomes. *Neuron* **62,** 17–29 (2009).
76. Livet, J. *et al.* Transgenic strategies for combinatorial expression of fluorescent proteins in the nervous system. *Nature* **450,** 56–62 (2007).
This paper describes a creative genetic approach to stochastically label neuronal subsets in the living mouse brain with different colours using Cre-mediated recombination to drive fluorescent-reporter expression.
77. Arenkiel, B. R. *et al.* *In vivo* light-induced activation of neural circuitry in transgenic mice expressing channelrhodopsin-2. *Neuron* **54,** 205–218 (2007).
78. Gradinaru, V., Mogri, M., Thompson, K. R., Henderson, J. M. & Deisseroth, K. Optical deconstruction of Parkinsonian neural circuitry. *Science* **324,** 354–359 (2009).
79. Petreanu, L., Huber, D., Sobczyk, A. & Svoboda, K. Channelrhodopsin-2-assisted circuit mapping of long-range callosal projections. *Nature Neurosci.* **10,** 663–668 (2007).
80. Petreanu, L., Mao, T., Sternson, S. M. & Svoboda, K. The subcellular organization of neocortical excitatory connections. *Nature* **457,** 1142–1145 (2009).
81. Lichtman, J. W., Livet, J. & Sanes, J. R. A technicolour approach to the connectome. *Nature Rev. Neurosci.* **9,** 417–422 (2008).
82. Bourne, J. N. & Harris, K. M. Balancing structure and function at hippocampal dendritic spines. *Annu. Rev. Neurosci.* **31,** 47–67 (2008).
83. Denk, W. & Horstmann, H. Serial block-face scanning electron microscopy to reconstruct three-dimensional tissue nanostructure. *PLoS Biol.* **2,** e329 (2004).
84. Soto, G. E. *et al.* Serial section electron tomography: a method for three-dimensional reconstruction of large structures. *Neuroimage* **1,** 230–243 (1994).
85. Harlow, M. L., Ress, D., Stoschek, A., Marshall, R. M. & McMahan, U. J. The architecture of active zone material at the frog's neuromuscular junction. *Nature* **409,** 479–484 (2001).
86. Macke, J. H. *et al.* Contour-propagation algorithms for semi-automated reconstruction of neural processes. *J. Neurosci. Methods* **167,** 349–357 (2008).
87. Hell, S. W. & Kroug, M. Ground-state-depletion fluorescence microscopy: a concept for breaking the diffraction resolution limit. *Appl. Phys. B* **60,** 495–497 (1995).
88. Gustafsson, M. G. Nonlinear structured-illumination microscopy: wide-field fluorescence imaging with theoretically unlimited resolution. *Proc. Natl Acad. Sci. USA* **102,** 13081–13086 (2005).
89. Thompson, R. E., Larson, D. R. & Webb, W. W. Precise nanometer localization analysis for individual fluorescent probes. *Biophys. J.* **82,** 2775–2783 (2002).
90. Folling, J. *et al.* Fluorescence nanoscopy by ground-state depletion and single-molecule return. *Nature Methods* **5,** 943–945 (2008).
91. Sharonov, A. & Hochstrasser, R. M. Wide-field subdiffraction imaging by accumulated binding of diffusing probes. *Proc. Natl Acad. Sci. USA* **103,** 18911–18916 (2006).
92. Huang, B., Wang, W., Bates, M. & Zhuang, X. Three-dimensional super-resolution imaging by stochastic optical reconstruction microscopy. *Science* **319,** 810–813 (2008).
93. Huang, B., Jones, S. A., Brandenburg, B. & Zhuang, X. Whole-cell 3D STORM reveals interactions between cellular structures with nanometer-scale resolution. *Nature Methods* **5,** 1047–1052 (2008).
94. Shtengel, G. *et al.* Interferometric fluorescent super-resolution microscopy resolves 3D cellular ultrastructure. *Proc. Natl Acad. Sci. USA* **106,** 3125–3130 (2009).

Acknowledgements We thank I. Davison, D. Fitzpatrick, M. Fernandez Suarez, K. Harris, J. Hernandez, M. Kennedy, A. Mabb, R. Mooney, T. Newpher, T. Roberts, C. Robinson, J. Schwartz, R. Weinberg, X. Zhuang and J. Yi for helpful input and comments on the manuscript. We apologize to those whose work we could not cite owing to space limitations. B.R.A. is supported by a K99 award from the US National Institutes of Health (NIH). Work in the lab of M.D.E. is supported by grants from the National Institute of Neurological Disorders and Stroke, the National Institute of Mental Health and the National Institute on Aging of the NIH. M.D.E. is an Investigator of the Howard Hughes Medical Institute.

Author Information Reprints and permissions information is available at www.nature.com/reprints. The authors declare no competing financial interests.
Correspondence should be addressed to M.D.E. (ehlers@neuro.duke.edu).

NATURE|Vol 461|15 October 2009|doi:10.1038/nature08537

Neuroscience in the era of functional genomics and systems biology

Daniel H. Geschwind[1,2] & Genevieve Konopka[1]

Advances in genetics and genomics have fuelled a revolution in discovery-based, or hypothesis-generating, research that provides a powerful complement to the more directly hypothesis-driven molecular, cellular and systems neuroscience. Genetic and functional genomic studies have already yielded important insights into neuronal diversity and function, as well as disease. One of the most exciting and challenging frontiers in neuroscience involves harnessing the power of large-scale genetic, genomic and phenotypic data sets, and the development of tools for data integration and mining. Methods for network analysis and systems biology offer the promise of integrating these multiple levels of data, connecting molecular pathways to nervous system function.

The molecular biology revolution allowed neuroscientists to move from the study of circuits and systems to the detailed study of individual molecules of interest. However, moving from genes to an understanding of interacting signalling or metabolic pathways within cells, let alone combining these data to achieve a systems-level understanding of brain circuit function in health and disease, poses enormous challenges. The integration of data across a wide range of observations is especially important in neurobiology. In contrast to the physical sciences, the biological sciences have few guiding theories or laws (with the exception of evolution) with which to direct and prioritize investigations. At the same time, we are in the midst of a genomic and informatics revolution that permits us to view specific gene products in the context of all others. The adoption of functional genomic or molecular-systems methods that permit dynamic measurement of gene products in a highly parallel manner, coupled with an underlying systems-level knowledge of the organization of these gene products, has the potential to provide a more integrative understanding of nervous system function.

The field of neuroscience has been slow to adopt functional genomic and genetic methods and the large-scale databases and resources that ideally result from their use. For example, neuroscience has consistently lagged behind cancer biology in the adoption of new molecular and genetic methods, starting with molecular cloning and continuing to functional genomics and genetics today. There are legitimate reasons for this, including the extreme cellular heterogeneity and complexity of neural circuits relative to most non-neural tissues, and the reliance on post-mortem materials for most human studies[1–4]. Another obstacle is the generation of enormous amounts of data. Similarly to what occurred in the field of genetics, clusters of computationally oriented researchers have to form within or around the laboratories more concentrated on the '-ology' fields ('ologies'). This integration of computational biology or bioinformatics in modern neuroscience laboratories or groupings will become even more critical as more powerful technologies that generate many orders of magnitude more data, such as next-generation sequencing techniques, replace microarrays. An additional, sometimes unspoken, impediment to the more widespread adoption of '-omics' fields ('omics') in neuroscience research is an underlying tension between the hypothesis-testing approach applied in the typical neurobiology laboratory and the discovery-based disciplines of genetics, genomics and proteomics (Box 1).

The revolutionary nature of these genomic advances and the rapidly evolving technologies that continue to further the high-throughput omics agenda clearly distinguish this form of research from the more hypothesis-driven work performed in most neurobiology laboratories. Omics research requires not only large-scale instrumentation and multidisciplinary teams of biologists, computer scientists, mathematicians and statisticians, but also a fundamental change in perspective[5]. The omics view is that an understanding of the organization and structure of the genome and the high-throughput measurements of the relationships of its elements, or gene products, provides a systematic basis on which to understand biological processes. Furthermore, significant value is placed on resource building and data sharing. Omics is not exclusive of more standard methods, and in fact is ultimately at its most powerful when combined with careful experimental validation. From this vantage point, the potential for discovery through large-scale screening and analysis provided by omics contrasts with the ability to incrementally advance science through individual hypothesis testing, one gene at a time.

The power of functional genomics in neuroscience is highlighted by several successful demonstrations of the strength of such methods to identify the molecular basis of neuronal diversity[6–10], synaptogenesis[11], disease biomarkers[12,13], disease mechanisms and pathways[13–16] and the development of user-friendly genome-scale resources[17,18]. These projects, along with other early proofs of principle[19,20], have clearly weakened the notion of the superiority of research based on single-hypothesis testing over hypothesis generation and prioritization using omics-based or discovery-based methods as a starting point. These approaches, which provide a new framework for the rapidly growing fields of neurogenetics, neurogenomics and systems biology, and the challenges that accompany them, are the subject of this Review. We discuss the value of data sharing and provide some key examples of neuroinformatics-based or omics-based resources, highlighting areas in which genetic and functional genomic approaches have brought new biological insight to different areas of neuroscience. We conclude with a discussion of the new frontiers in biological networks and systems biology.

Public data sharing and resource generation

Omics data provide a platform for small-scale and large-scale *in silico* discovery and hypothesis generation that often goes beyond the scope

[1]Program in Neurogenetics and Neurobehavioural Genetics, Department of Neurology and Semel Institute, [2]Department of Human Genetics, David Geffen School of Medicine, Los Angeles, California 90095, USA.

of the original experiment. This notion supports the proposition that data from microarray studies have most value in the public domain, where they can be mined or combined with other studies[21]. However, proteomic and transcriptomic data are inherently less generic than sequence data, so obstacles such as variable sample preparation, experimental annotation and platform differences prevent a single fully unified data resource. The development of a framework, MIAME (minimal information about a microarray experiment), allowed the creation of centralized repositories for these data created on multiple platforms in laboratories around the world (Box 2). A growing number of studies that have capitalized on such databases, including those cited above and others[22–27], have demonstrated that the widespread availability of these proteomic and transcriptomic data are of great benefit. One caveat with any resource based on compilation from multiple sources is that the data are only as good as the experimental and sample phenotype annotation. As microarray-based hybridization platforms for expression analysis give way to sequencing-based approaches, these data will become more generic, diminishing, but not eliminating, cross-platform compatibility issues.

In parallel with the growth of generic data repositories, standardized resources built by coupling high-throughput analyses with bioinformatics tools provide a clear demonstration of the value of large-scale omics data. The development of such resources requires significant foresight, planning and investment, but their worth is unquestionable if they are properly managed. Additionally, just as for DNA sequences and the genome databases, errors exist. Quality control must be balanced with throughput. Ideally, such resources would provide access for users to post corrective data or suggest annotations that would enhance the accuracy of the resource in real time.

Use of these resources to reanalyse public data is often a necessary feature of the well-rounded systems biology approach, raising the issue of the primacy of data analysis versus data generation. There is a clear tension between biological advances obtained in this way and the generation of new data, the latter usually carrying more weight in terms of novelty and degree of difficulty. Often, data analysis is not considered to be as much of an advance as the generation of new data, no matter how narrow the new data may be. However, a new perspective must be adopted to take into account studies that analyse data generated by others or in the public domain, to lead to new levels of understanding, or provide database tools around these data, even if no 'new biology' is done. The notion of what constitutes an experiment must expand to include analysis only, in addition to standard bench work. Similarly, we need to ensure that the next generation of neuroscientists has the quantitative skills to allow them to take full advantage of these opportunities. Here we highlight a few examples of advances based either on the generation of new omics data resources or on the analysis of data from such resources to provide fresh biological insights.

Box 1 | In search of hypotheses

The reluctance of neurobiologists to adopt omics approaches has many roots, including the often-stated aversion to 'fishing expeditions' without clearly defined hypotheses. Yet omics, or discovery-based, approaches do not eschew hypotheses; rather, they seek to elevate hypothesis testing to a new level, by allowing high-throughput hypothesis generation and prioritization. It is also notable that although functional genomics has led to a revolution in the field of cancer research, it has taken much longer to appeal to neuroscientists. Discovery-based research appears to be of more interest in disease-based fields, because the focus is on generating novel hypotheses and discovering new therapeutic and diagnostic approaches. It is only over the past two decades that disease-focused research has gradually evolved to become a considerable force in neuroscience. A corollary of this comparison is that, in general, the field of modern cancer research has been much more successful in developing new therapeutic techniques that have subsequently been translated into clinical practice[71]. There are many reasons for this, including access to tissue. However, advances in cancer research have also been catalysed by the core omics methods, which have not yet been as widely applied in disease-related neuroscience. The prediction is that a wider application of omics methods to neurological and psychiatric diseases[14,16] in both model systems and patients will significantly accelerate advances in therapeutic development in neuroscience. One area in which this appears promising is in the detection of disease biomarkers (see page 916) based on transcriptional profiles[12,13,72,73]. Because brain tissue at the appropriate developmental or disease stages in humans is rarely available, molecular biomarkers do pose a particular challenge. The use of peripheral tissues, such as blood, lymphoblasts or fibroblast-derived induced pluripotent stem cells, by omics methods provides a potential solution. Published data suggest that peripheral gene expression profiles might reflect aetiological subtypes of disease on which to stratify patients for genetic studies of complex neurologic or psychiatric disorders[69–71], in a loose parallel with the tissue-biopsy approach central to the cancer field.

Surveying the nervous system transcriptome

Knowledge of the spatial and temporal expression of every gene in the nervous system is a natural, neuroscience-specific extension of the human genome project. Thus, a number of different approaches have been undertaken to identify neuroanatomical patterns of expression on a global scale. The most complete gene expression resource for neuroscientists is the Allen Brain Atlas (ABA; http://www.brain-map.org), which is a neuroanatomical repository of gene expression information in both mouse and human brain. Using high-throughput, standardized *in situ* hybridization to display messenger RNA expression in a given section of brain tissue, the Allen Institute for Brain Science has generated an interactive guide into the entire known brain transcriptome. Users can query the maps by gene or brain structure and generate three-dimensional overlays of any permutation of gene and structure. Such a tool can be useful in determining the developmental and regional specificity of a particular gene, as well as the combinatorial expression of groups of genes. GenePaint (http://www.genepaint.org) and the Brain Gene Expression Map (BGEM; http://www.stjudebgem.org) are two other databases of mouse gene expression based on *in situ* hybridization at various developmental stages. Both contain more embryonic data than the ABA, but they are more limited in scope and do not reference a three-dimensional atlas.

The first project involving the Allen Institute focused on adult mouse brain in one strain (C57BL/6J)[18], but since then its research has expanded to encompass a variety of adult and developing mouse data sets and will soon also contain a first-generation data set from adult human brain. Additional data-mining tools that take advantage of the digital nature of the data include the Anatomic Gene Expression Atlas, which integrates all of the data from the ABA and the Allen Reference Atlas to build three-dimensional maps of correlated gene expression patterns. For example, this level of analysis permits the querying of different cortical layers and laminar gene expression to find clusters of co-expressed genes.

These tools have been used[28] to study hippocampal molecular anatomy, further subdividing the CA3 region of the hippocampus into nine distinct regions, each with its own genomic signature presumably underlying different functionalities. Using both computational and manual methods of analysis, the hippocampus was recurrently subdivided into smaller subsections based on overlapping patterns of gene expression. This subdivision allowed the generation of novel three-dimensional modelling of the hippocampus, as well as functional analysis of gene expression within a given subsection. The validity of the approach was confirmed using a combination of retrograde labelling and *in situ* hybridization. Thus, using the publicly available ABA, this study verified that hippocampal circuitry is driven, at least in part, by regional gene expression. These findings are critical for future experiments examining hippocampal function in targeted transgenic model systems.

The Gene Expression Nervous System Atlas (GENSAT; http://www.gensat.org) is a multifaceted resource that includes a public database of gene expression in the central nervous system of both the developing mouse and the adult mouse, based on bacterial artificial chromosome (BAC)-transgenic reporter mice[29]. These mice, which are

Box 2 | Major public databases

The Gene Expression Omnibus (GEO; http://www.ncbi.nlm.nih.gov/geo), supported by the US National Institutes of Health, is the most widely used open-access repository for storing and uploading unfiltered, unmanipulated microarray and sequencing data. ArrayExpress (http://www.ebi.ac.uk/microarray-as/ae), housed at the European Bioinformatics Institute, is the other major public repository of microarray data. A large non-public repository of microarray data is the Stanford Microarray Database (http://smd.stanford.edu). Investigators can easily access archived data and implement their analyses on these data sets, allowing continued analysis of any deposited data set using future methodologies. The ability to query several parameters from a vast number of deposited samples across many species and tissues should allow for the development of interconnected data sets at multiple expression levels to build a wider view of expression in a given species and between species. The Celsius database (http://celsius.genomics.ctrl.ucla.edu) is one such attempt, and combines nearly 100,000 publicly available Affymetrix microarray data sets for global analysis of particular gene co-expression patterns[74]. ArrayExpress provides a portal through which to query highly annotated meta-summary data from approximately 1,000 microarray experiments and nearly 30,000 microarrays. Similarly valuable proteomic and protein-interaction databases exist[75–78], including lab-based systems such as the Organelle Map Database[79] (http://141.61.102.16/ormd/), which organizes 1,405 proteins into ten specific organelles on the basis of correlation profiling. Considerable work is going into centralizing and curating proteomics data; databases include PeptideAtlas (http://www.peptideatlas.org) and The Human Proteinpedia[80] (http://www.humanproteinpedia.org), which involves the efforts of over 70 laboratories and provides the most integrated, searchable portal to many data types from diverse platforms, ranging from cytochemistry to mass spectrometry.

publicly available, provide unique, high-spatial-resolution information on the morphological pattern of expression of specific genes *in vivo*. The genetic labelling of individual and specific neuronal populations has implications for a wide range of investigations in fields from physiology[30] to functional genomics[9]. For example, such techniques can be used to purify neurons, in combination with other approaches such as retrograde injections, fluorescence-activated cell sorting, manual dissections or immunopanning, to uncover cell-class-specific neuronal gene expression profiles[6,7,9,10].

On a related theme, the recently developed 'bacTRAP' technology uses BAC-transgenic mice with green fluorescent protein fused to a ribosomal protein under the direction of a specific cell-type promoter to permit translating-ribosome affinity purification (TRAP)[8]. All mRNAs in the process of translation, which are thus attached to ribosomes, can be isolated from a specific cell type by using an antibody against green fluorescent protein. This approach avoids the potential for stress-induced or injury-induced changes in gene expression and is amenable to high-throughput analysis, once the mice are grown. An impressive 24 lines of bacTRAP mice generated deep expression profiles[31], providing thousands of new markers and cell-specific targets for further investigation. Future studies will be needed to validate this approach and determine its improvement over the other well-studied methods mentioned above. All of these investigations of purified neuronal or glial populations demonstrate how the generation of large-scale microarray data from a single study facilitates further studies into the identification of neuronal classes.

Resources such as the ABA and GENSAT, which are based on anatomical expression patterns, provide high spatial resolution but are inherently qualitative, so atlases of gene expression based on quantitative expression profiling are important adjuncts. However, most current quantitative atlases, such as BioGPS (http://biogps.gnf.org), and those curated at centralized browsers such as the GEO or GeneCards (http://www.genecards.org), have very low spatial resolution, limiting their use to the most basic analyses. A notable exception is the Cerebellar Development Transcriptome Database (http://www.cdtdb.brain.riken.jp), which approaches a systems level of analysis by integrating not only high-resolution spatial imaging but also temporal and tissue-specific patterns of expression, connecting genes with overlapping gene ontologies, and linking to other databases such as the ABA, GenePaint and the BGEM. Finally, quantitative areal maps of the adult mouse brain using microarray profiling of dissected brain regions have yielded important data and emphasized the enormous differences in gene expression and regulation between different inbred mouse strains[20,32,33], which is an important consideration for those using mice as a model system.

Recent work[34] moves towards the idea of combining genome-wide expression data with higher-resolution neuroanatomical correlates, by creating a first-generation map of gene expression in the fetal human brain. Thirteen brain regions from both hemispheres in four fetal brains were assessed on Affymetrix exon arrays. Extensive experimental validation, bioinformatic analysis and data mining were performed, confirming regional patterns of expression, identifying previously unknown splice isoforms and gene groupings related to regional specificity, and showing an association of regionally enriched patterns with highly evolving regulatory elements. Network analysis of gene co-expression relationships was also used to organize these data. Notably, several of the genes that co-expression network analysis related to specific cortical areas were not detected by standard analysis of differential expression. These data and the accompanying database provide an early quantitative foundation for the field of developmental neurobiology that will serve as a reference for comparisons between model systems and the human brain.

Exploring the synaptic proteome

Synaptic transmission is a fundamental component of nervous system function, and its dysfunction is implicated in virtually every neurological or psychiatric disease. Thus, identification and functional annotation of its molecular components provide a foundational resource for neuroscience that is as important as more ubiquitous cellular organelle-related proteomes or transcriptomes are for biology in general[35,36]. Proteomics is probably the method of choice for identification of specific synaptic components, because unless more complex experimental designs that include network analysis[25,37] are used, transcriptional profiling cannot usually provide organelle-specific data. This work requires a long-term approach[38], as it typically involves laborious purification of different synaptic components by means of immunoprecipitation, subcellular fractionation or other methods, followed by mass spectrometry analysis[37,39–41]. So far, more than 1,000 synapse-related proteins have been identified, a level of complexity that was initially unexpected[42].

One exemplary study[11] of the synaptic proteome represents the vanguard of genetics, genomics and systems biology applied to neuroscience. In it, genome databases were mined to compare the postsynaptic proteome across 19 species, and the expansion of the synaptic proteome was found to correspond to known evolutionary hierarchies; the largest expansion in the number of synaptic proteins was observed during the transition between the invertebrate and vertebrate lineages. It was concluded that the regionalization of the cortex at both the anatomical and the functional levels is associated with evolution in synaptic diversity at the proteomic level. By combining gene expression and immunochemical data from their own laboratory and from multiple public-domain data sources including the BGEM[43] and an adult-mouse microarray expression atlas[44], the authors determined that genes of more recent origin show the greatest regional variation in expression in mammalian brain. These results are of particular interest, as the newer genes are involved in complex processes such as extracellular signalling and scaffolding at the synapse. Whether the anatomical differences are due to changes in DNA *cis*-regulatory sequence or instead are a consequence of antecedent differences in anatomy and physiology remains to be determined. Nevertheless, this tour-de-force study, essentially driven by the mining of previously existing data sets from multiple publicly available data sources, complemented by wet-bench experimentation, provides a new list of molecular tools for exploring synaptic structure–function relationships, their correspondence with specific brain circuits and the emergence of higher cognition.

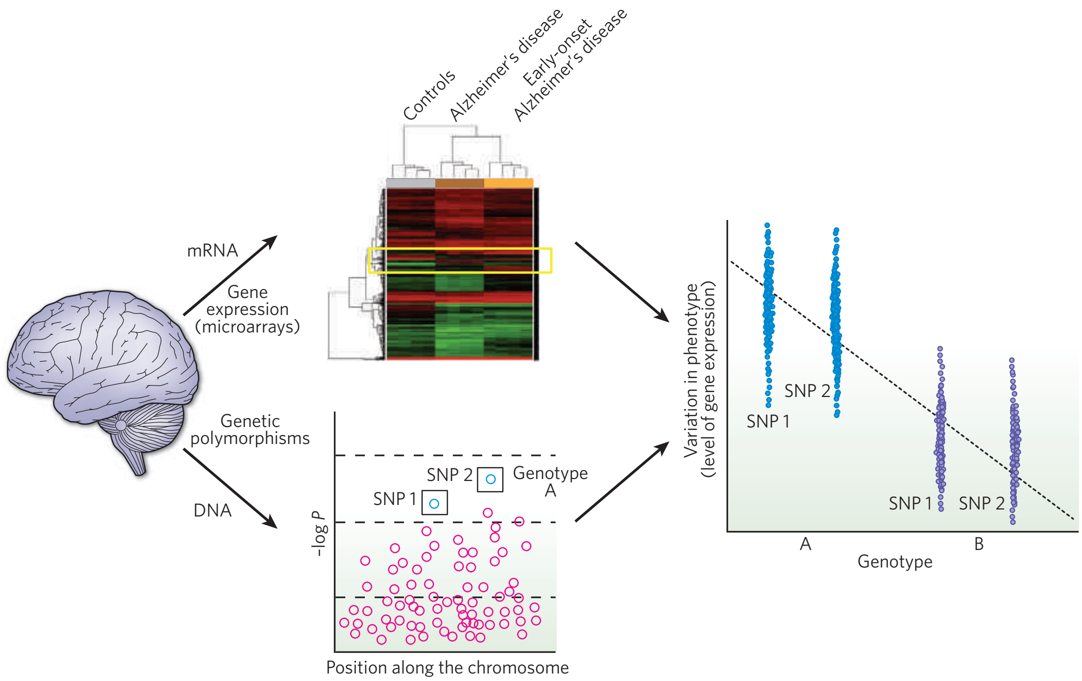

Figure 1 | Correlating genetic polymorphism and gene expression data. Investigation of whole-genome single-nucleotide polymorphism (SNP) data from different phenotypic subgroups is typically used to perform genetic association based on diagnostic categories such as dementia. By treating gene expression data as a quantitative phenotype for genetic association, these two data sets can be combined to identify genetic loci that control quantitative variation in gene expression (which are known as eQTLs). Here, an analysis of mRNA and DNA from three types of brain sample (healthy individuals, patients with Alzheimer's disease and those with early-onset Alzheimer's disease) is depicted. The heat map (centre top) depicts the expression levels of all genes as determined by microarray analysis. The yellow box highlights genes with expression variations across the patient groups. The plot beneath shows DNA data from the same patients assessed for genetic polymorphisms (negative logarithm of the *P* value versus position on a chromosome); two SNPs (1 and 2) are found to correlate with a subset of patients (genotype A). Combining these data (right), the different genotypes are found to correlate with differences in gene expression.

From a systems perspective, a daunting combination of additional levels of electrophysiological and anatomical phenotypes will be required to relate molecular pathways operating at the synapse to cellular function and, subsequently, to complex circuits. As a step in this direction, multi-electrode recording has been combined with microarrays to correlate genome-wide mRNA expression with synaptogenesis and synaptic activity in dissociated hippocampal neurons cultured on multi-electrode grids[45]. By conducting a time-course analysis of these parameters together with morphological measurements, the authors found that gene expression changes occurred first, followed by concurrent changes in electrical activity and synaptic maturation. These data suggest that the program of gene expression initiating synaptogenesis is independent of neuronal network activity, a hypothesis that they test *in vitro* by blocking neuronal activity and assessing key gene expression changes. This work stops short of a functional assessment of any of the novel genes identified. However, by coupling multiplexed physiological measurements and global expression profiling by microarrays it prefigures future studies, in which data from both neural and gene expression networks must be integrated to bridge systems and molecular neuroscience.

Integrating genetic and phenotypic data

Another approach to adding systems-level structure to transcriptome data is the analysis of these data in concert with genetic and phenotypic data to integrate across all three levels of observation. Thus, the advent of expression quantitative trait locus (eQTL) analysis is a major advance in integrating large-scale genomic or genetic data sets to understand a model system or cohort of patients at a systems level. In eQTL mapping, gene expression data are used as a phenotype on which to base quantitative genetic association mapping (Fig. 1), the rationale being that gene expression is a more proximal, intermediate quantitative phenotype to the underlying genetic risk than heterogeneous behavioural or anatomical phenotypes. Because large samples are necessary to provide statistical power for whole genome-wide association, peripheral tissues such as blood cells were used in the initial pioneering studies in humans[46]. Recent studies in animal models demonstrate its utility in brain samples[47,48]. A very promising avenue is the combination of gene network analyses of expression for eQTL analysis as first demonstrated in ref. 49 and, more recently, ref. 50, both of which studied phenotypes related to metabolism. Another intriguing recent paper merges a different form of gene network analysis with structural chromosomal variation identified in patients with autism, suggesting a role for genes related to glycobiology in this disorder[51].

One comprehensive, user-friendly interface for eQTL analysis in mouse is the database and toolkit provided by WebQTL[17] (http://www.genenetwork.org). WebQTL allows integration of genetic polymorphism data from several strains of mice and rats, gene expression data from microarrays, and neurobiological traits based on neuroanatomy, pharmacology and behaviour. These tools have been implemented to provide proof-of-principle evidence of the utility of this approach; behavioural, microarray and genotyping data from a recombinant inbred mouse strain have been recombined[47] to uncover significant QTLs correlating with gene expression and neuronal phenotypes, including, most interestingly, synapse function. Numerous QTLs were mapped to the majority of specific transcripts, which included a number of loci that appear to be 'master' transcriptome regulators, because they account for the expression of hundreds of genes. This study also uncovered QTLs that have polymorphisms associated with phenotypes of a specific behaviour. These links indicate that QTL-related transcript regulation can have wide-ranging effects on numerous functions, from the synapse to behaviour. Most of the transcriptional data in WebQTL is from whole brain, and the resource would benefit greatly from transcriptome analysis at higher spatial resolution, because significant variation occurs regionally[48]. However, this work connects genetic polymorphisms to RNA levels and to variation in both anatomy and behaviour, demonstrating the power of systems-level approaches to uncover complex neurobiological interactions.

Box 3 | The challenges of next-generation sequencing

Next-generation sequencing will be revolutionary in the amount and content of data generated, but there are many obstacles to surmount. Extensive comparisons of sequencing data have not been published demonstrating whether there are batch effects in data due to sample preparation, library generation, flow cell preparation or machine run. Few studies have compared the commercial platforms for either gene expression or gene regulation[81,82]. Data storage and analysis are currently a much larger challenge than data generation. Many researchers have devised their own algorithms for analysing either the raw or the filtered data. But this will change as an official consensus is reached on what constitutes acceptable data in terms of basic features such as quality scores and alignment algorithms. Also, better genome annotations and increased read lengths will aid in improving data interpretation. Ultimately, the advances of sequencing will permit the testing of what is actually expressed without preconception, taking the microarray-based approach many steps farther.

QTL analysis has been extensively employed in rodents, but so far only two studies have combined gene expression data from human brain with genetic polymorphism data[52,53]. In the first study, nearly 200 pathologically proven normal cerebral cortical samples were merged with genome-wide SNP data[53]. Although this is a small number from the standpoint of genetic association in complex disease, the difficulty and cost associated with profiling human tissue makes this an important demonstration of the approach. Furthermore, this study identified a large number of potential *cis*-QTLs that, once replicated, can serve as a basis for understanding the direct functional consequences of human genetic variation on brain gene expression in disease. Supporting this notion, these data were used in a recent comparison with eQTLs identified in a parallel study of the brains of sufferers of Alzheimer's disease, identifying several novel and known candidates for this complex brain disease[52]. The next step for these, and similar, studies is replication of the disease-association or eQTL-association findings in an independent cohort.

Accelerating discovery through next-generation sequencing

The advent of next-generation sequencing has raised multiple possibilities for the study of all layers of regulation leading to gene expression, changing the way we think about designing functional genomic experiments. Early studies clearly indicated that sequence data surpasses microarrays for studying gene expression, in terms of both depth of coverage and analysis of splicing, among other factors[54,55]. This technology can be used to quantitatively query not only mRNA expression but also RNA splicing, microRNA expression, epigenetic modifications, DNA binding, copy number variations and genetic deletions, insertions and mutations. Bridging these different outputs to generate a complete picture, from DNA to modified and bound DNA to precursor mRNA to mature mRNA, challenges even the most seasoned systems biologist. In addition, combining these data with proteomic data sets will completely revolutionize our understanding of the central dogma of molecular biology in action in any given cell. Another feature of next-generation sequencing that surpasses microarrays is the ability to assay species for which arrays do not exist, and eliminate the bias inherent in cross-species comparisons on microarrays[56]. The major challenges in the use of next-generation sequencing revolve around data storage and handling, but they are not unlike those encountered in the early years of microarray technology (Box 3), despite the amount of data involved being several orders of magnitude greater than that gained from microarrays. The relative platform independence of next-generation sequencing, leading to its more generic nature, will lower barriers for data sharing, meta-analysis and integration.

Moving from lists to networks

Even the most elegant of the multilevel functional genomic approaches essentially involve the analysis of overlapping lists of microarray or other data. In most transcriptomic or proteomic studies, data are organized in order from most differentially expressed to least. This is useful because these very large data sets need to be put into a form that allows them to be analysed and understood. However, such simple levels of data organization cannot and do not represent even a small fraction of the potential information inherent in the data. Furthermore, the use of standard pathway tools limits the analysis to known relationships. Fortunately, we are just beginning to appreciate that the data itself has an underlying structure, and acknowledgement of this network structure as a general biological principle is opening new avenues of complementary investigation[57,58].

The demonstration that transcriptome data can be organized into networks based on expression correlation, the application of graph theory, and robust statistical methods to develop weighted gene co-expression network analysis (WGCNA; http://www.genetics.ucla.edu/labs/horvath/CoexpressionNetwork) raised expression profiling to the level of systems biology by elucidating the relationships among all of the elements being studied[27,59] (Fig. 2). Several studies have now demonstrated that such networks derived from human or animal brain represent a reproducible and robust structure (for example refs 22–24), and that network position has significant functional implications. Similarly to earlier work in simpler organisms, this work has shown that proteomic and transcriptomic data derived from complex tissue such as brain show a high level of correspondence[24,25]. Such structure can be used to inform a new level of neuroscientific investigation that is not possible using standard analysis of differential expression[22–25].

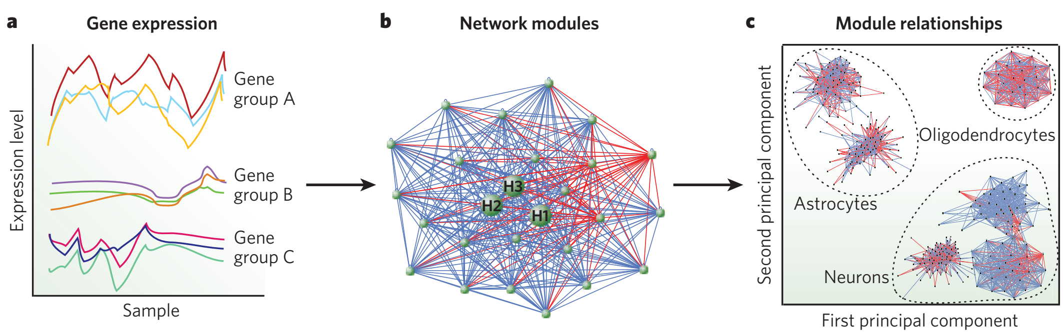

Figure 2 | WGCNA schematic. The underlying structure of a molecular network can be identified from high-dimensionality data sets such as those obtained from proteomic techniques or microarrays. This network structure can be used to guide research. **a**, Co-expression of groups of molecules across samples is measured to build networks, which comprise highly related clusters, or modules (for instance gene groups A, B and C here). **b**, A network module displaying the interconnection of genes. A gene's position within the network has significant functional implications. Hub genes are the most connected, or central, genes within each module (depicted here as H1, H2 and H3). Each gene is depicted as a green node; blue lines indicate positive correlations; and red lines indicate negative correlations. **c**, The multidimensional scaling plot of the first and second principal components of all of the modules in a network demonstrates the meta-module structure, which clusters into functional groups such as, in this example, different central-nervous-system cell subtypes.

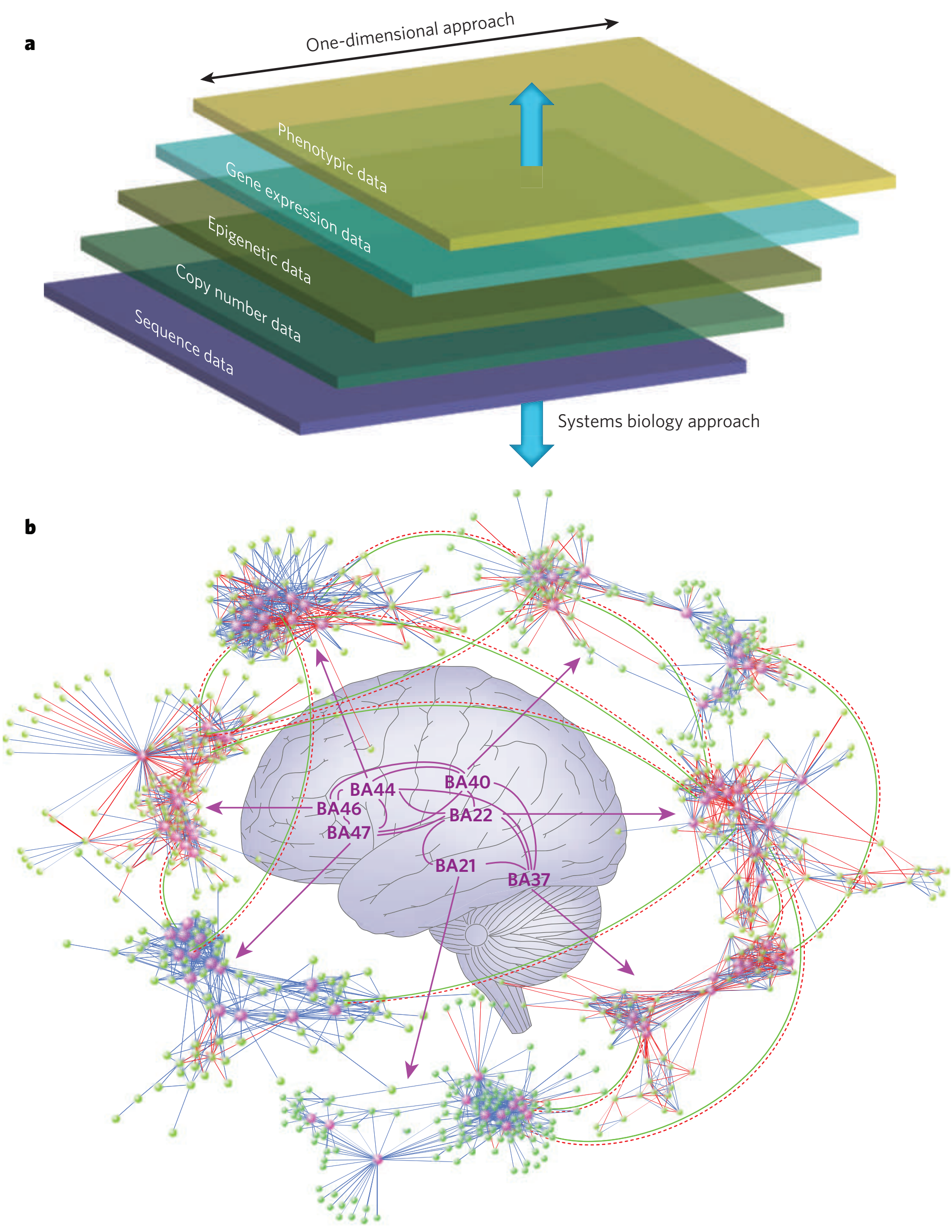

Figure 3 | The systems biology approach to high-dimensional data sets allows integration of multiple layers of data. a, The traditional experimental approach to the complexity of neuronal systems and diseases usually stretches across one or two layers of information. Typically, efforts are directed towards genetic data (such as sequence variants and epigenetic modifications), genomic data (such as gene expression) or phenotypic data (such as electrophysiological and clinical data). The systems biology approach seeks to consider all of these aspects at the same time, through the creation of comprehensive relational databases. The identification of a higher structure in high-dimensional data sets (for example by using network methods) facilitates the connection between different types of information (for example between genetic data and genomic data). **b**, Illustration of a potential systems-level integration of regional brain gene expression, coupled with network-based analysis methods and imaging data, to provide insights into brain connectivity. This is a stylized visualization of the combination of diffusion tensor imaging data for language areas[70] with gene expression and WGCNA analysis to reveal integration of gene co-expression across brain areas (BA, Brodmann area), as well as novel brain-region wiring. The green lines and dashed red lines indicate information flow in both directions and can be extrapolated to suggest excitatory and inhibitory interconnections. The integration of network analysis, gene expression data and imaging analysis will elucidate the relationships among key genetic drivers in distinct regions and their relationship to brain regional connectivity in normal conditions and in disease. Each gene is depicted as a node (green or pink), with hub genes represented by pink nodes. Blue lines indicate positive correlations, and red lines indicate negative correlations. Lines between Brodmann areas indicate real and potential interactions through white-matter tracts.

For example, one of the first such studies[23] showed that gene networks could be used to provide a unifying method of identifying transcriptional targets of human brain evolution in the context of the neutral model of evolution for the transcriptome[60]. More recently, it has been demonstrated that the human cerebral cortex transcriptome is organized into a robust network and shown how its modular nature could be used to drive functional understanding and discovery in many directions, including the identification of markers for human adult neural stem cells[24]. One of the more remarkable observations here, especially with relevance to the discussion of neuronal heterogeneity and the need for individual cell study, is that from whole tissue WGCNA can recover modules that represent the transcriptional programs of the major cell classes in human brain, an example of *in silico* tissue dissection[24]. Importantly, these analyses relied on several public data sources, including the ABA and a resource provided by the transcriptional analysis of purified neurons, astrocytes and oligodendrocytes[7].

These same network methods have recently been applied to provide a platform-independent comparison of pathways altered in normal ageing and dementia[22]. Data from two different microarray studies were combined and reanalysed to identify overlapping network modules corresponding to the synapse and mitochondria, illustrating common mechanisms shared by normal ageing and Alzheimer's disease. Similarly, reanalysis[25] of single-cell expression data[10] has confirmed the initial findings and led to new biological insights, including a major transcriptional distinction between two classes of mitochondria: those located in the synapse and neuronal processes, and those located in the cell body. Both of these studies show how network methods can elucidate organelle-specific or cellular-component-specific expression profiles without the need for their purification (another form of *in silico* dissection), and further demonstrate the value of data placed in the public domain for subsequent reanalysis or use by others.

Proteomic networks can be constructed either through the investigation of actual protein–protein interactions or by the correlation of protein levels across samples or observations. The coupling[15] of a high-throughput proteomic screen for protein interactions with bioinformatic analyses has been used to uncover an interaction network specific to ataxia. A screen for protein partners of ataxia-associated proteins was performed using the yeast two-hybrid system and a human-brain complementary DNA library, ultimately validating interactions *in silico* and *in vivo*. These interactions were expanded by culling known protein–protein interactions from public databases and the literature to create a final interaction network containing nearly 7,000 protein–protein pairs among almost 4,000 proteins. This network is an important resource for researchers studying neurodegeneration; it has already

either provided confirmation of specific interactions or the impetus for their study[61,62].

A more recent example of the combination of network methods and proteomic analysis identified a large number of postsynaptic protein complexes that show significant overlap with putative schizophrenia-susceptibility genes[37]. Five interconnected protein clusters were found by combining *in vivo* tandem affinity purification of PSD-95 (also known as DLG4) and mass spectrometry with network analysis. Almost half of the proteins in the clusters were related to at least one neurological disease, and, remarkably, 70% of the constituents of one of the clusters were specifically linked to schizophrenia. These and other early protein network analyses in brain should fuel future investigations and database development to catalogue and organize the entire neuronal proteome.

Conclusions and future directions

Many of the systems-level approaches that have been described here involve omics-level analysis of large data sets that span one or two dimensions of biological experimentation (Fig. 3). The most ambitious systems approach would see the integration of enormous data sources across multiple levels of genotypic, genomic, proteomic, epigenetic and phenotypic data (Fig. 3). Great efforts and powerful tools will be needed to achieve this in neuroscience, including the standardization of complex measurements of animal and human nervous system phenotypes and the development of accompanying ontologies[63]. Most forms of molecular data can be made into relatively generic forms, but translating complex phenotypes, from neuronal morphologies to the cognitive and behavioural profiles of neuropsychiatric disease entities, will require far more groundwork. Furthermore, although there is a compelling rationale to study nervous system phenotypes as they evolve over time, in many cases current funding and review processes are barriers to the collection of longitudinal data.

However, even one data dimension, such as knowledge of transcriptome organization by means of network analysis, can promote large conceptual leaps by providing a new view of gene function, independent of the proteome or genome. For example, we have observed groups of genes annotated by gene ontology as mitochondrial, ribosomal and proteasomal within single co-expression modules in several data sets. From a proteomics standpoint these organelles are distinct, but the high co-expression of genes within them suggests that they are part of a highly coordinated and interconnected system that spans cellular compartments as they are typically defined. Here transcriptional network analysis provides a new, systems-level view of gene function within cellular pathways that was not readily apparent from proteomic or genomic data alone.

Another frontier in systems-level analysis in neuroscience is highlighted by the necessary scale and complexity of endeavours analysing human phenotype data from a genetic perspective. Recent work combines text mining[64,65] with genetic analysis and modelling to integrate across disease phenotypes[66,67]. In a remarkable study[67], the co-morbidity among 161 different medical conditions abstracted from 1.5 million medical records was analysed in the context of a basic probabilistic model of inheritance. This work not only detected known genetic relationships between diseases, but also showcased the power of such methods to detect unexpected genetic relationships between human disorders considered to be distinct. For example, it predicted significant causal overlap between disorders such as bipolar disorder, autism and schizophrenia, as well as a shared genetic connection among autism and autoimmune and infectious disorders. In the future, such work should be greatly facilitated by detailed and standardized clinical phenotype ontologies, as well as integration with other levels of quantifiable phenotypic data, from molecular biomarkers such as gene expression and epigenetic profiles to neuroimaging data.

The application of systems-level analyses to neuroimaging data alone, based on a theoretical framework similar to WGCNA, has also begun to reveal remarkable insights into human brain networks[68]. This work shows a robust relationship between specific aspects of brain functional networks and structural connectivity[69]. Analogously to gene-based networks, particular functional modules and key hub regions can be identified on the basis of maps of functional or structural connectivity. At this point, the possibility of connecting such networks to the panoply of potential genetic, genomic or environmental factors that regulate them may seem distant. However, there is likely to be a reasonable systems biology solution. Standardized network analyses based on graph theory, such as WGCNA, could be used to integrate anatomically based brain networks with gene expression or proteomic networks from profiling of the same brain regions from post-mortem samples (Fig. 3b). This type of analysis would reach a level of integration of 'neuro-omic' and neuroimaging data that goes far beyond the current state of genotype–phenotype correlations. Such studies would be greatly accelerated by the requirement that data from all published neuroimaging studies be made publicly available in a usable, normalizable form, similar to omics data.

In many ways, the omics revolution provides an example of the enormous value of public data sharing in making efficient use of our relatively limited resources to fuel scientific and biomedical advances. The value of these data highlights the urgent need for common language and measurements in addition to incentives and portals for data sharing from even the smallest-scale studies. In parallel, it also speaks to the need for large-scale collaborative endeavours that collect data in a way that facilitates such sharing and permits integration across multiple disciplines. This is not to suggest that omics should or could necessarily replace ology in any way. However, omics approaches offer the possibility of a new foundation for ologies to build on, by allowing for the testing of many hypotheses in parallel and providing a systems-level context for data interpretation that is necessary to further our understanding of brain function. ■

1. Coppola, G. & Geschwind, D. H. Microarrays and the microscope: balancing throughput with resolution. *J. Physiol. (Lond.)* **575,** 353–359 (2006).
2. Nelson, S. B., Hempel, C. & Sugino, K. Probing the transcriptome of neuronal cell types. *Curr. Opin. Neurobiol.* **16,** 571–576 (2006).
3. Mirnics, K. & Pevsner, J. Progress in the use of microarray technology to study the neurobiology of disease. *Nature Neurosci.* **7,** 434–439 (2004).
4. Geschwind, D. H. Mice, microarrays, and the genetic diversity of the brain. *Proc. Natl Acad. Sci. USA* **97,** 10676–10678 (2000).
5. Hood, L., Heath, J. R., Phelps, M. E. & Lin, B. Systems biology and new technologies enable predictive and preventative medicine. *Science* **306,** 640–643 (2004).
6. Arlotta, P. *et al.* Neuronal subtype-specific genes that control corticospinal motor neuron development *in vivo*. *Neuron* **45,** 207–221 (2005).
7. Cahoy, J. D. *et al.* A transcriptome database for astrocytes, neurons, and oligodendrocytes: a new resource for understanding brain development and function. *J. Neurosci.* **28,** 264–278 (2008).
8. Heiman, M. *et al.* A translational profiling approach for the molecular characterization of CNS cell types. *Cell* **135,** 738–748 (2008).
9. Lobo, M. K., Karsten, S. L., Gray, M., Geschwind, D. H. & Yang, X. W. FACS-array profiling of striatal projection neuron subtypes in juvenile and adult mouse brains. *Nature Neurosci.* **9,** 443–452 (2006).
10. Sugino, K. *et al.* Molecular taxonomy of major neuronal classes in the adult mouse forebrain. *Nature Neurosci.* **9,** 99–107 (2006).
11. Emes, R. D. *et al.* Evolutionary expansion and anatomical specialization of synapse proteome complexity. *Nature Neurosci.* **11,** 799–806 (2008).
In this paper, a combination of genomics and proteomics is used to identify synaptic proteins that have changed with evolution and study how they might relate to brain anatomy and function.
12. Nagasaka, Y. *et al.* A unique gene expression signature discriminates familial Alzheimer's disease mutation carriers from their wild-type siblings. *Proc. Natl Acad. Sci. USA* **102,** 14854–14859 (2005).
13. Nishimura, Y. *et al.* Genome-wide expression profiling of lymphoblastoid cell lines distinguishes different forms of autism and reveals shared pathways. *Hum. Mol. Genet.* **16,** 1682–1698 (2007).
14. Karsten, S. L. *et al.* A genomic screen for modifiers of tauopathy identifies puromycin-sensitive aminopeptidase as an inhibitor of tau-induced neurodegeneration. *Neuron* **51,** 549–560 (2006).
15. Lim, J. *et al.* A protein–protein interaction network for human inherited ataxias and disorders of Purkinje cell degeneration. *Cell* **125,** 801–814 (2006).
16. Mirnics, K., Middleton, F. A., Marquez, A., Lewis, D. A. & Levitt, P. Molecular characterization of schizophrenia viewed by microarray analysis of gene expression in prefrontal cortex. *Neuron* **28,** 53–67 (2000).
This paper was the first to demonstrate the utility of microarray analysis to uncover new genes and properties associated with neuropsychiatric disease.
17. Wang, J., Williams, R. W. & Manly, K. F. WebQTL: web-based complex trait analysis. *Neuroinformatics* **1,** 299–308 (2003).
18. Lein, E. S. *et al.* Genome-wide atlas of gene expression in the adult mouse brain. *Nature* **445,** 168–176 (2007).
19. Cirelli, C., Gutierrez, C. M. & Tononi, G. Extensive and divergent effects of sleep and wakefulness on brain gene expression. *Neuron* **41,** 35–43 (2004).
20. Sandberg, R. *et al.* Regional and strain-specific gene expression mapping in the adult mouse brain. *Proc. Natl Acad. Sci. USA* **97,** 11038–11043 (2000).
21. Geschwind, D. H. Sharing gene expression data: an array of options. *Nature Rev. Neurosci.* **2,** 435–438 (2001).
22. Miller, J. A., Oldham, M. C. & Geschwind, D. H. A systems level analysis of transcriptional

changes in Alzheimer's disease and normal aging. *J. Neurosci.* **28,** 1410–1420 (2008).
23. Oldham, M. C., Horvath, S. & Geschwind, D. H. Conservation and evolution of gene coexpression networks in human and chimpanzee brains. *Proc. Natl Acad. Sci. USA* **103,** 17973–17978 (2006).
24. Oldham, M. C. *et al.* Functional organization of the transcriptome in human brain. *Nature Neurosci.* **11,** 1271–1282 (2008).
This paper demonstrates that the brain transcriptome in its normal state has a reproducible structure that can be used to guide discovery.
25. Winden, K. *et al.* The organization of the transcriptional network in specific neuronal classes. *Mol. Syst. Biol.* **5,** 291 (2009).
26. Stuart, J. M., Segal, E., Koller, D. & Kim, S. K. A gene-coexpression network for global discovery of conserved genetic modules. *Science* **302,** 249–255 (2003).
27. Lee, H. K., Hsu, A. K., Sajdak, J., Qin, J. & Pavlidis, P. Coexpression analysis of human genes across many microarray data sets. *Genome Res.* **14,** 1085–1094 (2004).
28. Thompson, C. L. *et al.* Genomic anatomy of the hippocampus. *Neuron* **60,** 1010–1021 (2008).
This paper is an example of the power of using tools such as the ABA as a reference together with other wet-lab tools to uncover new neuroanatomical connections, in this case new hippocampal subdivisions.
29. Gong, S. *et al.* A gene expression atlas of the central nervous system based on bacterial artificial chromosomes. *Nature* **425,** 917–925 (2003).
30. Okaty, B. W., Miller, M. N., Sugino, K., Hempel, C. M. & Nelson, S. B. Transcriptional and electrophysiological maturation of neocortical fast-spiking GABAergic interneurons. *J. Neurosci.* **29,** 7040–7052 (2009).
31. Doyle, J. P. *et al.* Application of a translational profiling approach for the comparative analysis of CNS cell types. *Cell* **135,** 749–762 (2008).
32. Cowley, M. J. *et al.* Intra- and inter-individual genetic differences in gene expression. *Mamm. Genome* **20,** 281–295 (2009).
33. Nadler, J. J. *et al.* Large-scale gene expression differences across brain regions and inbred strains correlate with a behavioral phenotype. *Genetics* **174,** 1229–1236 (2006).
34. Johnson, M. B. *et al.* Functional and evolutionary insights into human brain development through global transcriptome analysis. *Neuron* **62,** 494–509 (2009).
35. Kislinger, T. *et al.* Global survey of organ and organelle protein expression in mouse: combined proteomic and transcriptomic profiling. *Cell* **125,** 173–186 (2006).
36. Brunner, E. *et al.* A high-quality catalog of the *Drosophila melanogaster* proteome. *Nature Biotechnol.* **25,** 576–583 (2007).
37. Fernandez, E. *et al.* Targeted tandem affinity purification of PSD-95 recovers core postsynaptic complexes and schizophrenia susceptibility proteins. *Mol. Syst. Biol.* **5,** 269 (2009).
38. Anderson, C. N. & Grant, S. G. High throughput protein expression screening in the nervous system — needs and limitations. *J. Physiol.* (*Lond.*) **575,** 367–372 (2006).
39. Husi, H., Ward, M. A., Choudhary, J. S., Blackstock, W. P. & Grant, S. G. Proteomic analysis of NMDA receptor–adhesion protein signaling complexes. *Nature Neurosci.* **3,** 661–669 (2000).
40. Takamori, S. *et al.* Molecular anatomy of a trafficking organelle. *Cell* **127,** 831–846 (2006).
41. Trinidad, J. C. *et al.* Quantitative analysis of synaptic phosphorylation and protein expression. *Mol. Cell. Proteomics* **7,** 684–696 (2008).
42. Croning, M. D., Marshall, M. C., McLaren, P., Armstrong, J. D. & Grant, S. G. G2Cdb: the Genes to Cognition database. *Nucleic Acids Res.* **37,** D846–D851 (2009).
43. Magdaleno, S. *et al.* BGEM: an *in situ* hybridization database of gene expression in the embryonic and adult mouse nervous system. *PLoS Biol.* **4,** e86 (2006).
44. Zapala, M. A. *et al.* Adult mouse brain gene expression patterns bear an embryologic imprint. *Proc. Natl Acad. Sci. USA* **102,** 10357–10362 (2005).
45. Valor, L. M., Charlesworth, P., Humphreys, L., Anderson, C. N. & Grant, S. G. Network activity-independent coordinated gene expression program for synapse assembly. *Proc. Natl Acad. Sci. USA* **104,** 4658–4663 (2007).
This paper exemplifies the combination of multiple layers of functional data — in this case neuronal activity recordings and morphological measurements — with gene expression data to directly uncover how changes in function and gene expression relate to each other over time.
46. Cheung, V. G. *et al.* Mapping determinants of human gene expression by regional and genome-wide association. *Nature* **437,** 1365–1369 (2005).
47. Chesler, E. J. *et al.* Complex trait analysis of gene expression uncovers polygenic and pleiotropic networks that modulate nervous system function. *Nature Genet.* **37,** 233–242 (2005).
This paper provides an early example of combining data across multiple levels of function, factoring genotypes, phenotypes and gene expression in mouse to identify systems-level interactions.
48. Hovatta, I. *et al.* DNA variation and brain region-specific expression profiles exhibit different relationships between inbred mouse strains: implications for eQTL mapping studies. *Genome Biol.* **8,** R25 (2007).
49. Ghazalpour, A. *et al.* Integrating genetic and network analysis to characterize genes related to mouse weight. *PLoS Genet.* **2,** e130 (2006).
50. Chen, Y. *et al.* Variations in DNA elucidate molecular networks that cause disease. *Nature* **452,** 429–435 (2008).
51. van der Zwaag, B. *et al.* Gene-network analysis identifies susceptibility genes related to glycobiology in autism. *PLoS ONE* **4,** e5324 (2009).
52. Webster, J. A. *et al.* Genetic control of human brain transcript expression in Alzheimer disease. *Am. J. Hum. Genet.* **84,** 445–458 (2009).
53. Myers, A. J. *et al.* A survey of genetic human cortical gene expression. *Nature Genet.* **39,** 1494–1499 (2007).
54. Marioni, J. C., Mason, C. E., Mane, S. M., Stephens, M. & Gilad, Y. RNA-seq: an assessment of technical reproducibility and comparison with gene expression arrays. *Genome Res.* **18,** 1509–1517 (2008).
55. Liu, F. *et al.* Comparison of hybridization-based and sequencing-based gene expression technologies on biological replicates. *BMC Genomics* **8,** 153 (2007).
56. Preuss, T. M., Caceres, M., Oldham, M. C. & Geschwind, D. H. Human brain evolution: insights from microarrays. *Nature Rev. Genet.* **5,** 850–860 (2004).
57. Barabási, A. L. & Oltvai, Z. N. Network biology: understanding the cell's functional organization. *Nature Rev. Genet.* **5,** 101–113 (2004).
58. Jeong, H., Tombor, B., Albert, R., Oltvai, Z. N. & Barabási, A.-L. The large-scale organization of metabolic networks. *Nature* **407,** 651–654 (2000).
This paper is a seminal demonstration of the higher-order organization of metabolism across phylogeny.
59. Zhang, B. & Horvath, S. A general framework for weighted gene co-expression network analysis. *Stat. Appl. Genet. Mol. Biol.* **4,** 17 (2005).
60. Khaitovich, P. *et al.* A neutral model of transcriptome evolution. *PLoS Biol.* **2,** e132 (2004).
61. Lam, Y. C. *et al.* ATAXIN-1 interacts with the repressor Capicua in its native complex to cause SCA1 neuropathology. *Cell* **127,** 1335–1347 (2006).
62. Canterini, S., Bosco, A., De Matteis, V., Mangia, F. & Fiorenza, M. T. THG-1pit moves to nucleus at the onset of cerebellar granule neurons apoptosis. *Mol. Cell. Neurosci.* **40,** 249–257 (2009).
63. Bilder, R. M. *et al.* Phenomics: the systematic study of phenotypes on a genome-wide scale. *Neuroscience* doi:10.1016/j.neuroscience.2009.01.027 (20 January 2009).
64. Rzhetsky, A. *et al.* GeneWays: a system for extracting, analyzing, visualizing, and integrating molecular pathway data. *J. Biomed. Inform.* **37,** 43–53 (2004).
65. Rodriguez-Esteban, R., Iossifov, I. & Rzhetsky, A. Imitating manual curation of text-mined facts in biomedicine. *PLoS Comput. Biol.* **2,** e118 (2006).
66. Iossifov, I., Zheng, T., Baron, M., Gilliam, T. C. & Rzhetsky, A. Genetic-linkage mapping of complex hereditary disorders to a whole-genome molecular-interaction network. *Genome Res.* **18,** 1150–1162 (2008).
67. Rzhetsky, A., Wajngurt, D., Park, N. & Zheng, T. Probing genetic overlap among complex human phenotypes. *Proc. Natl Acad. Sci. USA* **104,** 11694–11699 (2007).
This paper demonstrates that with enough phenotypic information it is possible to build modelling networks that predict the underlying genetic overlap among neuropsychiatric diseases with previously distinct aetiologies.
68. Bullmore, E. & Sporns, O. Complex brain networks: graph theoretical analysis of structural and functional systems. *Nature Rev. Neurosci.* **10,** 186–198 (2009).
69. Honey, C. J., Kotter, R., Breakspear, M. & Sporns, O. Network structure of cerebral cortex shapes functional connectivity on multiple time scales. *Proc. Natl Acad. Sci. USA* **104,** 10240–10245 (2007).
70. Rilling, J. K. *et al.* The evolution of the arcuate fasciculus revealed with comparative DTI. *Nature Neurosci.* **11,** 426–428 (2008).
71. Mischel, P. S., Cloughesy, T. F. & Nelson, S. F. DNA-microarray analysis of brain cancer: molecular classification for therapy. *Nature Rev. Neurosci.* **5,** 782–792 (2004).
72. Tang, Y., Lu, A., Aronow, B. J. & Sharp, F. R. Blood genomic responses differ after stroke, seizures, hypoglycemia, and hypoxia: blood genomic fingerprints of disease. *Ann. Neurol.* **50,** 699–707 (2001).
73. Thomas, E. A. *et al.* The HDAC inhibitor 4b ameliorates the disease phenotype and transcriptional abnormalities in Huntington's disease transgenic mice. *Proc. Natl Acad. Sci. USA* **105,** 15564–15569 (2008).
74. Day, A., Carlson, M. R., Dong, J., O'Connor, B. D. & Nelson, S. F. Celsius: a community resource for Affymetrix microarray data. *Genome Biol.* **8,** R112 (2007).
75. McDowall, M. D., Scott, M. S. & Barton, G. J. PIPs: human protein–protein interaction prediction database. *Nucleic Acids Res.* **37,** D651–D656 (2009).
76. Kamburov, A., Wierling, C., Lehrach, H. & Herwig, R. ConsensusPathDB — a database for integrating human functional interaction networks. *Nucleic Acids Res.* **37,** D623–D628 (2009).
77. Chatr-Aryamontri, A., Zanzoni, A., Ceol, A. & Cesareni, G. Searching the protein interaction space through the MINT database. *Methods Mol. Biol.* **484,** 305–317 (2008).
78. Mathivanan, S. *et al.* An evaluation of human protein-protein interaction data in the public domain. *BMC Bioinformatics* **7** (suppl. 5), S19 (2006).
79. Foster, L. J. *et al.* A mammalian organelle map by protein correlation profiling. *Cell* **125,** 187–199 (2006).
80. Mathivanan, S. *et al.* Human Proteinpedia enables sharing of human protein data. *Nature Biotechnol.* **26,** 164–167 (2008).
81. Linsen, S. E. *et al.* Limitations and possibilities of small RNA digital gene expression profiling. *Nature Methods* **6,** 474–476 (2009).
82. Passalacqua, K. D. *et al.* Structure and complexity of a bacterial transcriptome. *J. Bacteriol.* **191,** 3203–3211 (2009).

Acknowledgements This Review would not have been possible without help from members of the Geschwind laboratory, especially G. Coppola, who helped with several figures and provided critical comments on the manuscript; M. Oldham, for his pioneering use of WGCNA in the brain; and D. Crandall of the Mental Retardation Research Centre media core at the University of California, Los Angeles, for assistance with Fig. 3. We are also grateful to our collaborators S. Horvath, S. Nelson and P. Mischel, for their generosity of time and expertise. We apologize to the authors of the many outstanding studies we were not able to cite owing to space limitations. We acknowledge support from the US National Institutes of Health (grants NIMH R37 MH60233-06A1 and NINDS U24 NS52108), the US National Institute on Aging, and the Dr Miriam & Sheldon G. Adelson Medical Research Foundation programme on neural repair and rehabilitation for our work in functional genomics (D.H.G.); and the A. P. Giannini Foundation Medical Research Foundation and NARSAD (G.K.).

Author Information Reprints and permissions information is available at www.nature.com/reprints. The authors declare competing financial interests: details accompany the full-text HTML version of the paper at www.nature.com/nature. Correspondence should be addressed to D.H.G. (dhg@ucla.edu).

NATURE|Vol 461|15 October 2009|doi:10.1038/nature08538

Multimodal techniques for diagnosis and prognosis of Alzheimer's disease

Richard J. Perrin[1,3,4], Anne M. Fagan[2,3,4] & David M. Holtzman[2,3,4]

Alzheimer's disease affects millions of people around the world. Currently, there are no treatments that prevent or slow the disease. Like other neurodegenerative diseases, Alzheimer's disease is characterized by protein misfolding in the brain. This process and the associated brain damage begin years before the substantial neurodegeneration that accompanies dementia. Studies using new neuroimaging techniques and fluid biomarkers suggest that Alzheimer's disease pathology can be detected preclinically. These advances should allow the design of new clinical trials and early mechanism-based therapeutic intervention.

With the emergence of disease-modifying strategies for the treatment of Alzheimer's disease, impetus to diagnose the condition in its early 'preclinical' stages — before significant brain damage has occurred — has intensified. Fortunately, advances in technology and in our perspective on what defines Alzheimer's disease may soon make such antecedent diagnosis possible.

Since their first description, in 1907 (ref. 1), 'senile' plaques and neurofibrillary tangles (NFTs) have been the hallmark histopathological features of Alzheimer's disease and are employed by three sets of diagnostic histological criteria[2–4]. Historically, they have also been associated with the dementia caused by the disease. It is clear, however, that these lesions begin to accrue in significant amounts in many 'cognitively normal' elderly individuals[5] and, probably together with other damage, need to reach a threshold before the clinical manifestations we know as dementia are observed. A growing body of evidence now supports the idea that amyloid plaques and NFTs actually define (but do not fully represent) the disease process, which also involves inflammation as well as neuronal, axonal and synaptic loss and dysfunction. All of these changes appear to begin before significant cognitive decline occurs. Consistent with this, neuropathological studies involving large numbers of non-demented subjects have identified significant Alzheimer's disease pathology in the brains of older individuals[6,7]. Neocortical cerebral amyloid deposits have been identified in approximately 50% of brains from individuals more than 75 years old[7]. In contrast, the prevalence of Alzheimer's disease dementia does not reach 50% until age 85 or more[8]. The onset of very mild dementia is correlated best not with plaque or NFT burden but with significant synaptic and neuronal loss[9,10]. Together, these data support the concept of preclinical Alzheimer's disease, a phase during which plaques and, subsequently, NFTs accumulate for ~10–15 years before the synaptic and neuronal loss they accompany manifest as cognitive decline[9] (Fig. 1). This concept fits with genetic, biochemical and animal model data which demonstrate that the aggregation of the amyloid-β peptide plays a necessary part[11], especially in the preclinical phase of the disease, and that aggregation of microtubule-associated protein tau, which occurs in bulk later, drives neurodegeneration during and just before the clinical phase.

Nevertheless, the pathological process of Alzheimer's disease currently is noticeable during life only when it manifests clinically. The early clinical signs that are believed to result from Alzheimer's disease (decline in memory and executive functions) are referred to in different ways by clinicians. Some report this syndrome as very mild dementia of the Alzheimer type[12]. Others prefer the term mild cognitive impairment[13]. Because many of the biomarkers that provide insight into the underlying pathology of Alzheimer's disease are not yet used in day-to-day patient care, these diagnoses reflect attempts to describe clinical syndromes in the absence of definitive proof of the underlying pathology. However, in combination with clinical methods and cognitive tests, biomarkers will soon contribute to a more accurate assessment of cognitive impairment and its cause (Box 1). Perhaps more importantly, biomarkers are expected to enable clinicians to identify and monitor the pathology caused by Alzheimer's disease before the onset of cognitive dysfunction, and suggest prognosis.

The purpose of this Review is to discuss the most promising targets, techniques and implications of Alzheimer's disease biomarker research so far. Advances in neuroimaging now allow accurate measurements of atrophy, metabolism, inflammation, plaque and NFT abundance, and 'default network' activity in the brain. Furthermore, fluid biomarker research has employed powerful 'unbiased' screening approaches, increasingly sensitive proteomics techniques and novel applications of mass spectrometry to identify new fluid biomarkers and even monitor fluid biomarker metabolism in living subjects. The use of genetics in combination with biomarkers will probably provide more diagnostic and prognostic information than the use of biomarkers alone. However, a detailed discussion of the genetics of Alzheimer's disease is beyond the scope of this Review. The most up-to-date information on the genetics of the disease can be found at the Alzheimer Research Forum (http://www.alzgene.org).

Imaging atrophy and aggregates of amyloid-β and tau

Although cellular resolution has not yet been achieved, recent advances in functional and molecular neuroimaging have provided insights into brain structure and physiology, allowing the study of specific proteins and protein aggregates in ways that are difficult or impossible to achieve through autopsy. Moreover, neuroimaging biomarker studies can immediately correlate data with structure and (dys)function.

The characteristic patterns of cortical and hippocampal volume loss in advanced Alzheimer's disease are well known but difficult to quantify with precision during post-mortem examination. Atrophy is particularly difficult to measure in the early stages of the disease, when it superficially resembles the inconspicuous volume loss commonly observed among elderly individuals without neurodegeneration ('healthy' ageing).

[1]Department of Pathology and Immunology, [2]Department of Neurology, [3]Hope Center for Neurological Disorders, [4]Alzheimer's Disease Research Center, Washington University School of Medicine, 660 South Euclid Avenue, Box 8111, St Louis, Missouri 63110, USA.

Distinguishing such subtle differences is not difficult using high-resolution quantitative magnetic resonance imaging. Applied longitudinally, this technique can distinguish between the global atrophy rate of healthy ageing and that of the disease[14] and predict progression from normal cognition to mild cognitive impairment[15] and from the latter to Alzheimer's disease on the basis of regional volume losses and ventricular expansion over time[16] (Fig. 2b, c). However, atrophy and cognitive decline occur in most neurodegenerative disorders, and although volume changes in certain brain regions may be suggestive of, or consistent with, Alzheimer's disease, they do not reveal the underlying pathology.

Patterns of plaque and NFT formation in Alzheimer's disease have been thoroughly studied. Until recently, however, ante-mortem examination of these pathological changes has been nearly impossible. Within the past decade, a number of radiological-contrast compounds have been developed that specifically bind to and highlight pathological structures in the central nervous system, including amyloid plaques, neurofibrillary tangles, activated microglia and reactive astrocytes.

So far, five compounds ([^{18}F]FDDNP, ^{18}F-BAY94-9172, ^{11}C-SB-13, ^{11}C-BF-227 and ^{11}C-PIB) have been reported as probes for imaging amyloid plaques in humans. One of these, [^{18}F]FDDNP, may be retained by NFTs[17], but no agent that selectively binds to aggregates of tau has yet been described. Such a discovery would be a major advance for molecular imaging.

Of the amyloid-binding compounds, ^{11}C-PIB (PIB, Pittsburgh compound B), has been the most extensively studied and applied in research into Alzheimer's disease. Uptake of PIB can be measured by positron-emission tomography (PET). In individuals with the disease, increased retention of PIB shows a very specific pattern that is restricted to brain regions typically associated with amyloid deposition[18] (Fig. 2b, c). Notably, an appreciable number of cognitively normal individuals over the age of 60 show a PIB signal pattern indistinguishable from that of individuals with Alzheimer's disease, suggesting that measurement of PIB using PET can detect a preclinical stage of the disease[19]. When PIB PET was performed and concentrations of Aβ_{42} peptide (the 42-residue-long isoform of amyloid-β) in the cerebrospinal fluid were measured at the same time in individuals ranging from the cognitively normal to those with Alzheimer's disease, two discrete groups were distinguished: 'PIB-negative' individuals and 'PIB-positive' ones. Without exception, the PIB-positive group had low Aβ_{42} levels in the cerebrospinal fluid[20] (Fig. 2a). This finding is consistent with the idea that soluble Aβ_{42} is retained in the brain once plaques are formed. Larger longitudinal studies of cognitively normal subjects, comparing those with amyloid to those without amyloid, will be required to evaluate whether the presence of amyloid confers a greater risk of 'conversion' to dementia. An initial study suggests that this is the case[21].

Complementing these radiological studies of amyloid deposition, other PET labelling agents have been developed to image inflammation as reflected by activated microglia and reactive astrocytes that surround plaques. Among the changes that microglia undergo on activation, increased expression of the peripheral benzodiazepine receptor has been exploited as a target for the radiological compounds [^{11}C]DAA1106 (ref. 22), [^{11}C]vinpocetine (ref. 23) and [^{11}C](*R*)-PK11195. Only the third of these has been reported in studies of Alzheimer's disease in humans, in conjunction with PIB. In these studies of individuals with mild cognitive impairment or Alzheimer's disease, PK11195 and PIB signals showed similar anatomical patterns, but their intensities did not show regional correlation[24]; among subjects with Alzheimer's disease, there was an inverse correlation between PK11195 signal and cognitive performance. These findings suggest that microgliosis occurs concomitantly with amyloid deposition and may have a direct role in cognitive dysfunction. However, better imaging agents are needed to visualize microglial activation in Alzheimer's disease. Like microglia, astrocytes show changes on association with plaques, including elevation of monoamine oxidase B activity[25], but studies that use inhibitors of monoamine oxidase B as radiotracers in Alzheimer's disease are only now appearing[26]. Larger studies will be needed to understand whether imaging inflammation may inform subject selection for clinical trials, contribute to predictions of prognosis and allow monitoring of response to therapy.

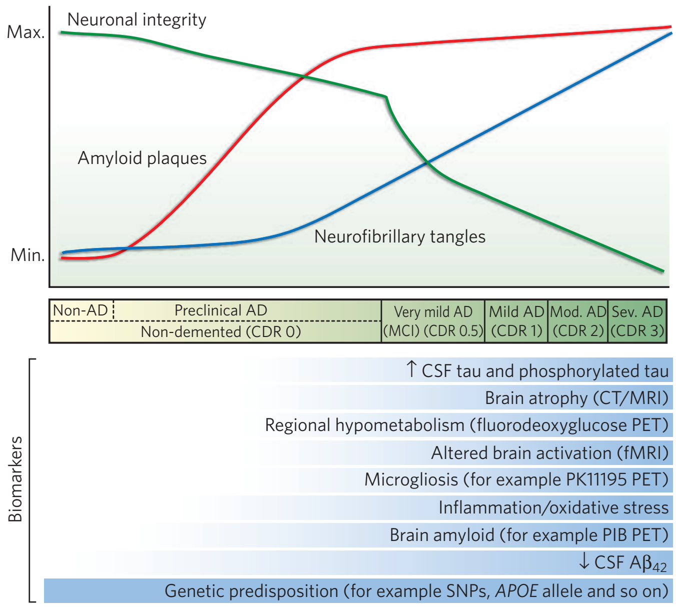

Figure 1 | Biomarkers and Alzheimer's disease: proposed changes in biomarkers in relation to the time course of pathological and clinical stages. The clinical stages of Alzheimer's disease (AD), marked by progressive dementia described as 'very mild/mild cognitive impairment' (MCI), 'mild', 'moderate' and 'severe', correspond to clinical dementia rating (CDR) scores of 0.5, 1, 2 and 3, respectively (see bar below plot). These stages are associated with abundant amyloid plaques (red line), the gradual accumulation of NFTs (blue line) and synaptic and neuronal loss in certain brain regions (green line). In the preclinical stage of Alzheimer's disease, Aβ_{42} peptide forms amyloid plaques in the brains of non-demented individuals (CDR 0) for approximately 10–15 years, and damages neuronal processes and synapses. Eventually, drastic neuronal losses occur in association with the onset of dementia. Alzheimer's disease biomarker research seeks to measure changes in the structure and function of the brain (for example atrophy, regional activity changes and hypometabolism, amyloid-plaque and NFT formation, microgliosis, inflammation and oxidative stress) that might be useful for diagnosis and prognosis during this preclinical phase of the disease, before irreversible neuronal loss occurs. These changes can be measured by radiological imaging modalities (for example computed tomography (CT), magnetic resonance imaging (MRI), functional magnetic resonance imaging (fMRI), and positron-emission tomography (PET) with various imaging contrast agents) and/or by biochemical examination of cerebrospinal fluid (CSF). The most promising biomarker candidates at present are listed (in chronological order from bottom to top) according to the earliest stage of the pathological process at which they seem to show utility. A reduced concentration of Aβ_{42} in cerebrospinal fluid may provide the earliest definitive evidence of Alzheimer's pathology in the brain. Genetic variations (for example single-nucleotide polymorphisms (SNPs)) may also be considered biomarkers that allow the earliest possible estimation of risk. PIB, Pittsburgh compound B. (Modified, with permission, from ref. 77).

Watching the mind at work

Neurons of the medial temporal lobe and hippocampus are particularly susceptible to loss in Alzheimer's disease, and their loss seems to coincide with the onset of clinically significant cognitive impairment. Functional magnetic resonance imaging is believed to provide a measure of synaptic activity, and this technique seems to show hypoactivation of the medial temporal lobe memory system in the clinical stages of the disease. However, hyperactivation of the same structures seems to occur in mild cognitive impairment, when memory is only mildly impaired and neuronal loss is less severe; this increased activity may represent an attempt to compensate for functional inefficiencies[27].

Although the medial temporal lobe memory system seems to be selectively vulnerable in Alzheimer's disease, other regions of the cortex (for example the posterior cingulate cortex, the precuneus, the temporoparietal region and the medial frontal cortex) also experience amyloid deposition, gliosis and atrophy during the long preclinical phase[28] (Fig. 2).

Box 1 | Assessment of cognitive impairment and dementia

Dementia is an acquired syndrome in which there is a decline in memory and thinking that is sufficient to interfere with everyday performance. Some individuals demonstrate deficits either in memory alone or in memory and other cognitive domains that are indicative of an abnormality but are not yet severe enough to be termed dementia. Most people who go on to develop dementia go through a transitional stage that some term very mild dementia and others term mild cognitive impairment or 'cognitively impaired no dementia'. Many different things can lead to cognitive impairment and dementia, including a variety of neurodegenerative disorders, vascular damage, infections, tumours and other causes. Alzheimer's disease is the most common cause of cognitive impairment and dementia in people over the age of 65. Determination that acquired cognitive impairment or dementia is present, and diagnosis of its probable cause, is based on clinical history (especially from a reliable informant), neurological and psychiatric examinations, and certain laboratory tests. The assembled information allows assessment of whether an individual's faculties have decreased relative to their past abilities (intra-individual change) and can be used for determining the level of dementia (very mild, mild, moderate or severe) as well as the most likely diagnosis.

Formal cognitive testing can aid these determinations and is particularly useful in clinical situations in which cognitive symptoms and signs are subtle or are confounded by other medical factors such as depression. A variety of neuropsychological tests can be used to accurately assess the different cognitive domains, including orientation, intellect, language, memory, attention, concentration, executive function, visual/perceptual abilities, sensorimotor function, mood and personality[79]. Serial neuropsychological evaluations are also very useful for tracking the progress of an individual over time relative to an established baseline. At present, the diagnosis of dementia due to Alzheimer's disease can only be confirmed with certainty at autopsy. However, many of the biomarkers reviewed here, when used together with clinical evaluation and cognitive testing, can assist with differential diagnosis and prognosis. To determine the presence of diseases such as Alzheimer's disease before the emergence of cognitive impairment or dementia as detected through neuropsychological testing or by clinicians, antecedent biomarkers will be required.

Accordingly, abnormalities of these cortical regions in individuals with mild cognitive impairment and mild Alzheimer's disease can be seen by using functional magnetic resonance imaging[27] and single-photon-emission computed tomography (which measures regional blood flow), and can be used to predict progression from mild cognitive impairment to Alzheimer's disease[29].

As might be expected for brain regions that display atrophy, neuronal loss and reduced perfusion, these cortical regions also show evidence of decreased glucose metabolism in subjects with the disease, as measured by fluorodeoxyglucose PET[28] (Fig. 2b, c). Additionally, although its accuracy has not been thoroughly compared with that of other biomarkers assessed in the same subjects, fluorodeoxyglucose PET has been reported to predict conversion from cognitive normalcy to mild cognitive impairment[30] and thence to Alzheimer's disease[31]. Furthermore, fluorodeoxyglucose PET has been used to demonstrate the effects of pharmacological agents, correlated with level of cognitive impairment[32]. Therefore, these imaging measures of synaptic activity (functional magnetic resonance imaging), perfusion (single-photon-emission computed tomography) and glucose metabolism (fluorodeoxyglucose PET) may serve as biomarkers to guide diagnosis and to predict and monitor progression, and might be used in the future to evaluate responses to therapy.

The default network

Although imaging studies have contributed tremendously to our understanding of Alzheimer's disease by allowing us to compare afflicted subjects with age-matched controls, valuable insights into the pathophysiology of the disease have also been gained through the study of young, healthy volunteers. In 2001, the hypothesis of a 'default' mode of human brain activity[33] that is engaged during internally focused tasks such as remembering past events, imagining the future and considering the perspectives of others (comprehensively reviewed in ref. 34) was put forward on the basis of numerous functional imaging studies done over the past four decades. In 2005, a remarkable correlation was demonstrated between the neuroanatomical substrates of the default network (the medial temporal lobe and hippocampus, the medial prefrontal association cortex, the posterior cingulate cortex, the retrosplenial cortex, the inferior parietal cortex and the lateral temporal lobe) and the anatomical distributions of amyloid deposition, atrophy, glucose metabolism and blood flow in Alzheimer's disease[28] (Fig. 2c). It was suggested that young-adult activity and metabolism patterns might be conducive to amyloid deposition in Alzheimer's disease. Indeed, amyloid-β production is dependent on synaptic activity[35,36], and those regions of the default network that show high resting metabolism are also those that are most affected in subjects with the disease. It seems clear that any substantive insight into the aetiological connection between default-network metabolism and the pathology of Alzheimer's disease will contribute seminally to our understanding of the illness.

Amyloid-β and tau as Alzheimer's disease biomarkers

Without going so far as to perform brain biopsy or place a microdialysis catheter directly into the brain[37], the sampling of cerebrospinal fluid and plasma represents the most direct and convenient means to study the biochemical changes occurring in the central nervous system. Therefore, these fluids are the most attractive resources for ongoing research into Alzheimer's disease biomarkers. Implicated by biochemical and immunohistological studies of Alzheimer's brain tissue, the major protein constituents of the pathology of the disease ($A\beta_{40}$, $A\beta_{42}$, tau and phosphorylated forms of tau) have emerged as the current leading diagnostic and prognostic fluid biomarkers.

Amyloid-β is a secreted peptide of unknown physiological function that is cleaved from amyloid precursor protein by the sequential activities of β-secretase and γ-secretase enzymes. The majority of amyloid-β is produced in the brain, but it effluxes into the cerebrospinal fluid and plasma, appearing in relatively high and low concentrations, respectively. Amyloid-β occurs in multiple forms ranging from 38 to 43 amino acids in length. Among these, $A\beta_{40}$ is the most abundant species, but $A\beta_{42}$ seems to be essential for initiating amyloid-β aggregation, and is considered central to the amyloid cascade hypothesis of Alzheimer's disease[11]. Of these two species, $A\beta_{42}$ has emerged as a more useful biomarker for Alzheimer's disease than its shorter counterpart, $A\beta_{40}$, most probably in reflection of their roles in the pathogenesis of the disease.

Although the finding is initially counter-intuitive, the mean concentration of $A\beta_{42}$ in the cerebrospinal fluid is significantly reduced in subjects with Alzheimer's disease relative to age-matched controls[38] (Fig. 3b); this phenomenon is thought to result from deposition of the peptide in plaques, preventing its transit from the brain into the cerebrospinal fluid (the 'amyloid sink' hypothesis). In support of this hypothesis, when ante-mortem cerebrospinal-fluid $A\beta_{42}$ concentrations are compared with PET PIB scan results or with post-mortem measurements of brain amyloid-β load, virtually all individuals with fibrillar amyloid-β deposits show low concentrations of $A\beta_{42}$ in the cerebrospinal fluid, independent of cognitive status[20,39,40] (Fig. 2a). Thus, cerebrospinal-fluid $A\beta_{42}$ may serve as both a diagnostic biomarker for Alzheimer's disease and a surrogate biomarker for amyloid deposition.

The utility of cerebrospinal-fluid $A\beta_{42}$ may not end with diagnosis and surrogacy, however. In several longitudinal studies, especially when combined with information about the levels of tau or phosphorylated tau in the cerebrospinal fluid, cerebrospinal-fluid $A\beta_{42}$ has shown a capacity to predict progression from cognitive normalcy to mild cognitive impairment or dementia of the Alzheimer's type, and from mild cognitive impairment to dementia of the Alzheimer's type[41–43] (Fig. 3c). Low concentrations of cerebrospinal-fluid $A\beta_{42}$ may also be a harbinger of amyloid deposition; recently, we identified a class of individuals who have low concentrations of cerebrospinal-fluid $A\beta_{42}$ but show no evidence of amyloid on PET PIB scans[39] (Fig. 2a). The autopsy of one of these individuals showed widespread diffuse — but minimal fibrillar — amyloid-plaque deposits[44]. Thus,

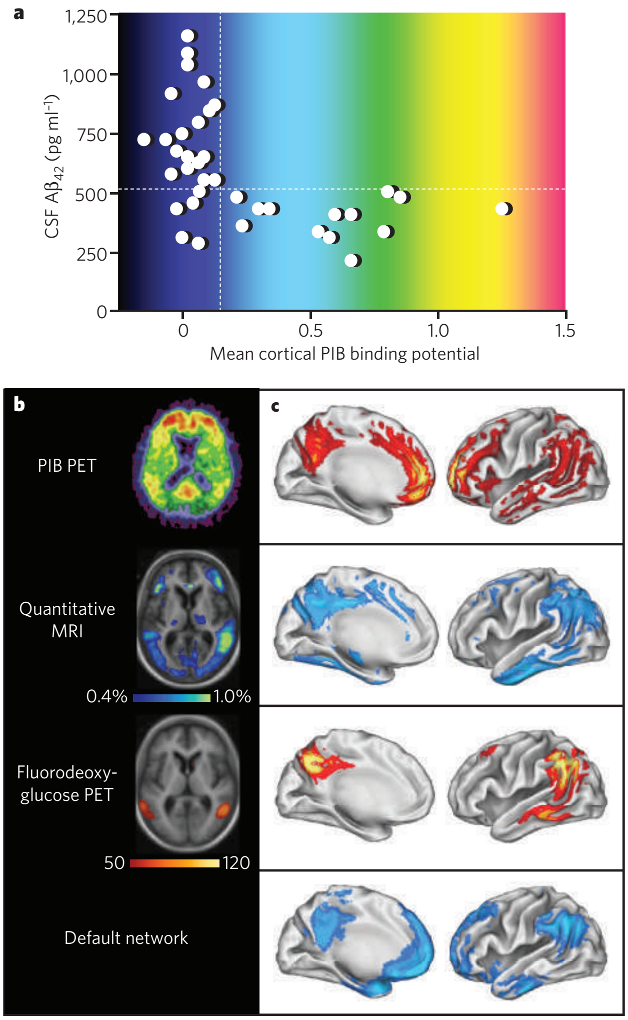

Figure 2 | Imaging biomarkers. **a**, Relationship of PIB PET to cerebrospinal-fluid $A\beta_{42}$ concentration in cognitively normal individuals. Subjects with mean cortical PIB binding potentials >0.16 (calculated from an average of PIB retention in the prefrontal cortex, the lateral temporal cortex, the precuneus and the gyrus rectus, divided by PIB retention in the cerebellar cortex) are considered PIB-positive and uniformly have low CSF $A\beta_{42}$ concentrations (<500 pg ml^{-1}); PIB-negative subjects with low $A\beta_{42}$ concentrations may have non-fibrillar (diffuse) $A\beta_{42}$ deposits that do not retain PIB. Whether non-demented individuals with high PIB and/or low cerebrospinal-fluid $A\beta_{42}$ are more likely to develop dementia than those with low PIB and/or high cerebrospinal-fluid $A\beta_{42}$ has not yet been reported on for large numbers of people, but an initial study supports this idea[21]. **b**, Axial (horizontal) view of Alzheimer's brain, imaged to quantify amyloid (PIB PET), annual rates of regional atrophy (quantitative MRI) and hypometabolism in relation to dementia severity (fluorodeoxyglucose PET). The intensity of the PIB binding potential is depicted using a colour scale (approximated by the colours in **a**) in which red reflects greatest PIB retention, and black and dark blue reflect least PIB retention. The regional extent of atrophy is depicted colorimetrically, with rates ranging from 0.4% per year (dark blue) to 1% per year (yellow/green). Regional hypometabolism is also depicted colorimetrically, with red and yellow representing greater and lesser hypometabolism, respectively. The units of this scale reflect the slope of the regression between hypometabolism and dementia severity as measured by mini-mental status examination; high slope suggests a steeper decline in metabolism in relation to decreasing cognitive ability. **c**, Illustrations of left hemi-brain surfaces (medial, left; lateral, right), allowing comparison of averaged anatomical signal maps for amyloid (top), atrophy (second from top), hypometabolism (third from top) and default-network activity (bottom). Regional amyloid load (PIB binding potential) is depicted as percentage increase of PIB binding potential over that of the brainstem, ranging from 5% (red) to 40% (yellow/white). Colorimetric scales for atrophy and hypometabolism are as in **b**. The colour scale for regional default-network activity shows the degree of association, ranging from greatest association with default-network activity (light blue) to least statistically significant association (darker blue). (Panels **a** and **b** (top view) modified, with permission, from ref. 20; panels **b** (remaining views) and **c** modified, with permission, from ref. 28.)

cerebrospinal-fluid $A\beta_{42}$ may have utility as a biomarker for diagnosis, plaque burden and prognosis, and may provide the earliest clue to the identification of preclinical Alzheimer's disease (as defined by the emergence of amyloid-β deposition).

The utility of plasma $A\beta_{42}$ as a biomarker for Alzheimer's disease is less compelling. Concentrations of $A\beta_{42}$ in cerebrospinal fluid and plasma show no apparent correlation[39,45,46]. Some studies suggest that the $A\beta_{40}/A\beta_{42}$ ratio in plasma may be predictive of conversion from cognitive normalcy to mild cognitive impairment and Alzheimer's disease[47,48], but the plasma amyloid-β markers do not seem to approach the predictive value of cerebrospinal-fluid $A\beta_{42}$.

Tau is a cytosolic protein predominantly expressed in neurons, wherein its primary function seems to be regulation of microtubule stability within the axon. This function is regulated by several different post-translational modifications, principally phosphorylation of numerous serine and threonine residues. In Alzheimer's disease, hyperphosphorylated tau often fills the dystrophic neurites of neuritic plaques and is the principal component of the paired helical filaments that constitute NFTs (Fig. 3a). The precise forms of tau that appear in the cerebrospinal fluid, and the mechanism or mechanisms by which they get there, are not entirely understood, but recent studies[49] demonstrate that virtually all domains of the protein are represented, and it is widely assumed (but not proven) that the major sources of tau and phosphorylated tau in the cerebrospinal fluid of sufferers of Alzheimer's disease are neuronal injury or death and possibly neurofibrillary tangles.

Like $A\beta_{42}$, tau and phosphorylated tau have emerged as important cerebrospinal-fluid biomarkers for Alzheimer's disease. Mean concentrations of tau and phosphorylated tau are higher in the cerebrospinal fluid of subjects with Alzheimer's disease than in that of age-matched controls[50] (Fig. 3b). These increases appear in the setting of formed fibrillar amyloid deposits[40] (consistent with the amyloid cascade hypothesis), and correlate with both neuritic-plaque density and Braak NFT stage[40]. In conjunction with $A\beta_{42}$, tau and phosphorylated tau seem to be useful as prognostic biomarkers for conversion to dementia from cognitive normalcy or mild cognitive impairment[41–43] (Fig. 3c).

Together, these results suggest that longitudinal measurements of cerebrospinal-fluid $A\beta_{42}$ and tau may allow clinicians to monitor and even predict the progress of Alzheimer's disease pathology throughout its entire course. Of course, the pathophysiology of the disease involves many more processes than amyloid-β deposition and NFT formation. Amyloid precursor protein is cleaved by β-secretase and γ-secretase complexes. Once released as monomers, amyloid-β may form oligomers that are cytotoxic and/or neuromodulatory. To form plaques, amyloid-β must accumulate. Once amyloid-β has formed oligomers and amyloid deposits, microglial cells become activated and migrate towards plaques as they form[51]. Astrocytes become reactive, and numerous inflammatory mediators, signalling molecules, oxidative processes, complement cascades and modulators of protease activities and protein-folding activities are released. Dendrites and axons in the vicinity of plaques become dystrophic as transport processes malfunction. The metabolism of the brain changes[28]. Amyloid-β is deposited in vessel walls. In addition to forming NFTs, neurons show many other changes. Synapses exhibit dysfunction and are lost. Neurons die. Each of these changes — and others not mentioned and not yet recognized — may represent a therapeutic target and may also cause changes in the composition of the cerebrospinal fluid and plasma. Recognizing this potential, many research groups continue to search for other fluid biomarkers that may complement or improve the well-established utility of cerebrospinal-fluid $A\beta_{42}$ and tau.

Oxidative stress and inflammation

Increasing evidence implicates oxidative damage as a mediator of toxicity in Alzheimer's disease. By-products of lipid peroxidation (isoprostanes) and RNA oxidation (8-hydroxyguanine) have shown the most promise as biomarkers. Produced by free-radical-mediated peroxidation of polyunsaturated fatty acids, isoprostanes in cerebrospinal fluid are increased in Alzheimer's disease[52,53] and may predict the development of mild cognitive impairment and Alzheimer's disease[54]. The utility of plasma isoprostanes as biomarkers for the disease is less promising; some[55], but not all[56], studies have found elevated concentrations in subjects with Alzheimer's disease relative to controls. The other oxidative marker, 8-hydroxyguanine, representing oxidized RNA, has been reported to be elevated in the cerebrospinal fluid of subjects with Alzheimer's disease in one small study[57] and is worthy of further research.

Inflammation, represented by plaque-associated microglia and astrocytes, is also implicated in Alzheimer's disease pathology. In addition to any immediate role these inflammatory cells may have, their secreted products — including acute-phase proteins such as α_1-antichymotrypsin (ACT, also known as SERPINA3 protein)[58] and α_2-macroglobulin (α2M)[59], activated factors of the classical pathway of complement[60], and cytokines such as interleukin-1β (IL-1β) and tumour-necrosis factor-α (TNF-α, also known as TNF) — persist within plaques. Although the contribution of these deposited inflammatory mediators to the pathophysiology of Alzheimer's disease is not entirely clear, there is evidence to suggest that they have an important role.

Appearing in cerebrospinal fluid in proportion to cognitive impairment, ACT has emerged as a potential biomarker for Alzheimer's disease[61], although its utility in plasma — and that of α2M — remains unclear[61–64]. By comparison, fluid biomarker studies of complement factors (C3a anaphylatoxin chemotactic receptor and C1q) have been inconclusive[65,66], as have more traditional fluid biomarker studies of cytokines[67].

In contrast, supporting a role for cytokines in Alzheimer's disease, several groups have measured their spontaneous production by mononuclear cells obtained from the peripheral blood (PBMCs). This approach is relevant to Alzheimer's disease because perivascular macrophages and microglia derived from circulating monocytes may participate in intraparenchymal inflammation in the brain[68]. In one report, PBMCs from sufferers of the disease produced larger amounts of cytokines than PBMCs from controls[69]; in another study of over 600 participants, increased PBMC production of either IL-1β or TNF-α was associated with increased hazard ratios for developing the disease[67].

Other recent work, measuring 120 signalling proteins in plasma, suggested that sporadic Alzheimer's disease may be accompanied — and diagnosed in its very early stages — by a systemic inflammatory state characterized by a panel of 18 signalling molecules[70]. If confirmed, this biomarker discovery[70] demonstrates the potential power of multiple biomarkers incorporated into a panel to diagnose Alzheimer's disease accurately, and also illustrates the value of a less-targeted, 'unbiased', high-throughput approach to biomarker discovery.

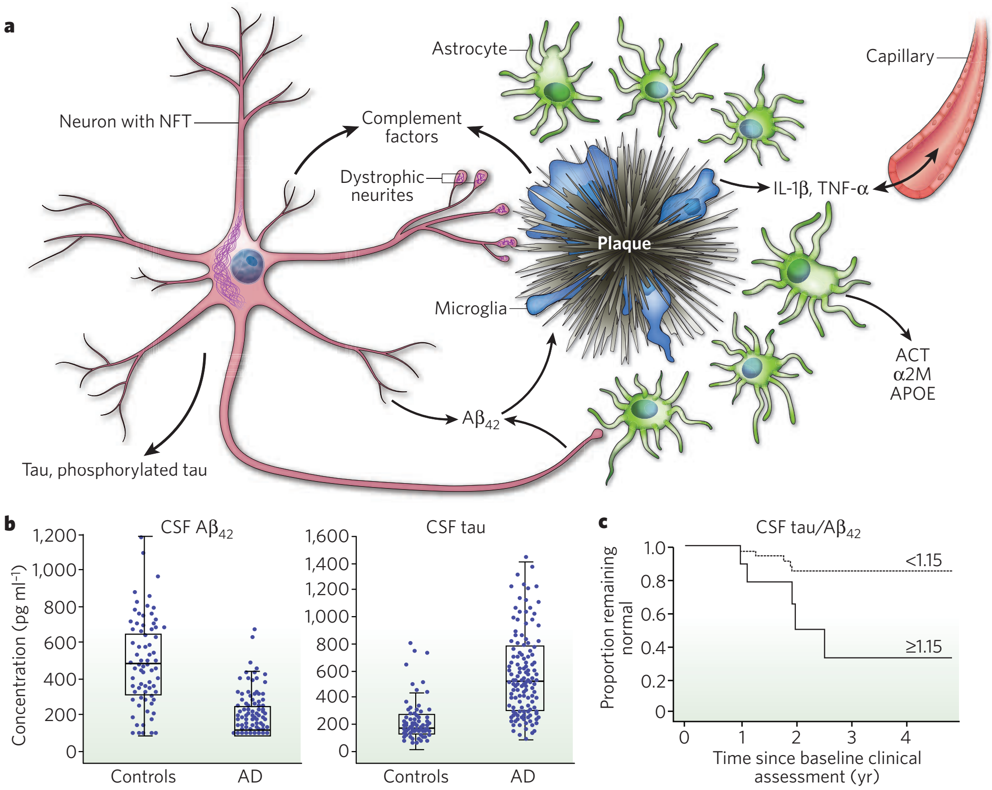

Figure 3 | Fluid biomarkers. a, Schematic histological representation of fluid biomarkers in relation to Alzheimer's disease pathology. Produced by neurons, $A\beta_{42}$ becomes deposited in plaques, which activate microglia. Microglia release cytokines (for example IL-1β and TNF-α) that can cross the blood–brain barrier and activate astrocytes, inducing production of α_1-antichymotrypsin (ACT) and α_2-macroglobulin (α2M). Microglia and neurons also produce complement factors that can be activated by amyloid-β aggregates, and cause synapse loss. Tau becomes hyperphosphorylated and aggregates into NFTs in neurons and dystrophic neurites around plaques; its mechanism of release from neurons is uncertain. Lipid peroxidation in neurons leads to isoprostane formation (not shown). Most factors entering the extracellular space migrate into the cerebrospinal fluid (CSF); $A\beta_{42}$ preferentially partitions into plaques. **b,** Representative data demonstrating utility of CSF concentrations of $A\beta_{42}$ (left) and tau (right) in distinguishing groups of subjects with Alzheimer's disease and age-matched controls. Boxes represent the 25th, 50th and 75th centiles of the data; box length is interquartile range; lower and upper whiskers represent the 25th and, respectively, 75th centiles plus/minus 1.5 times the interquartile range. (Reproduced, with permission, from ref. 78.) **c,** Ratio of CSF concentrations of tau and $A\beta_{42}$ as predictors of conversion from cognitive normalcy to mild cognitive impairment or dementia, using Kaplan–Meier estimates of rates of conversion with a cut-off value of 1.15 (representing the top 15% of distribution values). More than 80% of subjects with low tau and high $A\beta_{42}$ (tau/$A\beta_{42}$ < 1.15; dashed line) remain cognitively normal four years after baseline assessment; among those with high tau and low $A\beta_{42}$ (tau/$A\beta_{42}$ ≥1.15; solid line), approximately 30% remain cognitively normal. (Reproduced, with permission, from ref. 41.)

Proteomics

Ongoing advances in mass spectrometry and protein-handling technology continue to broaden the methodological diversity and increase the sensitivity of proteomic analyses; as many as several thousand proteins can now be measured in a sample of human cerebrospinal fluid. Complementing the 'directed' fluid biomarker investigations discussed above, several groups have pursued 'unbiased' proteomics to discover novel Alzheimer's disease biomarkers empirically in cerebrospinal fluid[63,71–73]. Using different techniques, these studies have generated multiple lists of candidate biomarker proteins that show individual and collective abilities to 'recognize' and classify samples appropriately. A comprehensive discussion of these proteomic studies is beyond the scope of this Review; however, the following observations are worthy of note.

First, many of the proteins that distinguish the Alzheimer's disease cerebrospinal-fluid proteome reflect the pathological changes already known to occur in the Alzheimer's brain. Therefore, new candidate biomarkers without known relevance to the disease may provide clues into pathophysiological processes that are underappreciated or are not yet recognized. Second, in our experience, post-translational modification — limited proteolysis *in vivo* in particular— seems to be common among cerebrospinal-fluid proteins showing differential abundance in Alzheimer's disease. Yet when proteins are identified by mass spectrometric evaluation of trypsinized fragments, such modifications may be overlooked. This issue has received relatively little attention, despite its critical importance to the design of assays that might be used in validation experiments for these biomarkers. Third, and finally, most proteomics studies reported so far have compared subjects who have Alzheimer's disease with age-matched non-demented controls (or with controls who have a dementia other than Alzheimer's disease) and are therefore designed to identify diagnostic biomarkers. To advance the discovery of predictive or surrogate biomarkers using unbiased proteomics, more studies should compare groups of subjects with Alzheimer's disease that differ in terms of rate of progression, presence of amyloid and tau deposits, or other relevant characteristics.

Monitoring biomarker metabolism and treatment effects

As treatments that target the production or clearance of specific molecules involved in the pathophysiology of Alzheimer's disease come to clinical trial, the capacity to monitor the metabolism of relevant fluid biomarkers before, during and after drug administration would be very helpful in verifying treatment effect and optimizing dosage. To this end, a new *in vivo* technique has been developed to measure the production and clearance rates of cerebrospinal-fluid proteins in human subjects. In this technique, a stable (non-radioactive) isotope-labelled amino acid (for example $^{13}C_6$-leucine) is administered intravenously and becomes incorporated into newly synthesized proteins. Cerebrospinal fluid and plasma are sampled using intrathecal and intravenous catheters. Using liquid chromatography and tandem mass spectroscopy (LC–MS/MS) to compare labelled and unlabelled proteins over time and/or at different doses of a candidate therapeutic agent, very precise synthesis, clearance and dose–response curves can be developed. This technique was first applied to determine the synthesis and clearance rates of amyloid-β in the central nervous system[74] and was used more recently in a randomized, double-blind, placebo-controlled study to demonstrate the pharmacokinetic/pharmacodynamic relationship between an inhibitor of amyloid-β synthesis and the absolute rate of amyloid-β synthesis in the central nervous system[75]. The potential of this technique is that it automatically labels all newly synthesized proteins when using the appropriate precursor; as such, it should allow evaluation of the metabolism of other proteins relevant to Alzheimer's disease (and other neurodegenerative diseases) and the metabolism of multiple biomarkers simultaneously.

Future directions

Advances in technology, knowledge and perspective now promise the tools to diagnose, monitor and predict the course of sporadic Alzheimer's disease, even before clinical symptoms begin. Of equal importance is that parallel advances promise treatments for Alzheimer's disease that will make such information far more valuable. Nevertheless, achieving these goals will require a great deal more work. More-effective radiographic biomarkers are needed to monitor central nervous system inflammation and tau pathology, as well as other neurodegenerative features. Likewise, fluid biomarkers are needed that can distinguish Alzheimer's disease from other types of dementia and provide even better prognostic information. Once identified, biomarker assays must be standardized in forms that are amenable for use in existing clinical laboratories and that can be evaluated in suitably large sample sets. To facilitate such biomarker validation studies and provide sufficient statistical power, longitudinally followed cohorts of study participants (including individuals with a dementia other than Alzheimer's disease), complete with uniformly collected and stored specimens, must continue to grow in size and number; a successful example of this is the Alzheimer's Disease Neuroimaging Initiative (http://www.adni-info.org). Finally, once this work has identified a satisfactory panel of antecedent Alzheimer's disease biomarkers, and one or more effective treatments for the disease have been approved, appropriate clinical guidelines must be developed to support and encourage widespread clinical testing.

In the more distant future, we may be able to evaluate risk for Alzheimer's disease even earlier in life. Just as biomarker data from well-characterized, longitudinally followed cohorts of study participants may be interpreted to guide diagnosis, estimate prognosis and monitor response to treatments, they will also be used to identify genetic markers that are associated with particular biomarker values. In comparison with genetic studies of Alzheimer's disease that rely on less precise diagnoses that are clinically based, genetic studies based on quantitative endophenotype data can provide greater statistical power[76]. Indeed, quantitative biomarker data have already been used with success in genetic studies of Alzheimer's disease. Elevated concentrations of cerebrospinal-fluid tau and phosphorylated tau have been found to associate with single-nucleotide polymorphisms in the *MAPT* gene (from which tau protein is produced). Likewise, concentrations of amyloid-β in cerebrospinal fluid have been found to associate with polymorphisms in several genes[76]. In this way, by 'converting' endophenotype data derived from fluid and imaging biomarkers to novel genetic biomarkers, it may be possible to identify individuals at greater risk of developing Alzheimer's disease and, in the near future, provide treatment options before even a single plaque has formed. ■

1. Alzheimer, A. About a peculiar disease of the cerebral cortex [translation]. *Alzheimer Dis. Assoc. Disord.* **1,** 7–8 (1987).
2. Khachaturian, Z. S. Diagnosis of Alzheimer's disease. *Arch. Neurol.* **42,** 1097–1105 (1985).
3. Mirra, S. S. *et al.* The consortium to establish a registry for Alzheimer's disease (CERAD). Part II. Standardization of the neuropathologic assessment of Alzheimer's disease. *Neurology* **41,** 479–486 (1991).
4. Hyman, B. T. & Trojanowski, J. Q. Consensus recommendations for the postmortem diagnosis of Alzheimer disease from the National Institute on Aging and the Reagan Institute Working Group on diagnostic criteria for the neuropathological assessment of Alzheimer disease. *J. Neuropathol. Exp. Neurol.* **56,** 1095–1097 (1997).
5. Crystal, H. *et al.* Clinico-pathologic studies in dementia: nondemented subjects with pathologically confirmed Alzheimer's disease. *Neurology* **38,** 1682–1687 (1988).
6. Price, J. L. *et al.* Neuropathology of nondemented aging: presumptive evidence for preclinical Alzheimer disease. *Neurobiol. Aging* **30,** 1026–1036 (2009).
7. Braak, H. & Braak, E. Frequency of stages of Alzheimer-related lesions in different age categories. *Neurobiol. Aging* **18,** 351–357 (1997).
8. Evans, D. A. *et al.* Prevalence of Alzheimer's disease in a community population of older persons. Higher than previously reported. *J. Am. Med. Assoc.* **262,** 2551–2556 (1989).
9. Morris, J. C. & Price, J. L. Pathologic correlates of nondemented aging, mild cognitive impairment, and early stage Alzheimer's disease. *J. Mol. Neurosci.* **17,** 101–118 (2001).
10. Gomez-Isla, T. *et al.* Profound loss of layer II entorhinal cortex neurons occurs in very mild Alzheimer's disease. *J. Neurosci.* **16,** 4491–4500 (1996).
11. Hardy, J. The amyloid hypothesis of Alzheimer's disease: progress and problems on the road to therapeutics. *Science* **297,** 353–356 (2002).
12. Morris, J. C. The clinical dementia rating (CDR). Current version and scoring rules. *Neurology* **43,** 2412–2414 (1993).
13. Petersen, R. C. *et al.* Mild cognitive impairment: clinical characterization and outcome. *Arch. Neurol.* **56,** 303–308 (1999).
14. Fox, N., Warrington, E. & Rossor, M. Serial magnetic resonance imaging of cerebral atrophy in preclinical Alzheimer's disease. *Lancet* **353,** 2125 (1999).
This paper reports how 5 of 28 cognitively normal individuals at risk of autosomal-dominant early-onset Alzheimer's disease developed "probable Alzheimer's disease" and could be distinguished by a mean rate of global cerebral atrophy of 1.5% per year from clinically stable subjects with a rate of 0.1% to 0.2% per year.
15. Carlson, N. E. *et al.* Trajectories of brain loss in aging and the development of cognitive impairment. *Neurology* **70,** 828–833 (2008).
16. Devanand, D. P. *et al.* Hippocampal and entorhinal atrophy in mild cognitive impairment: prediction of Alzheimer disease. *Neurology* **68,** 828–836 (2007).
17. Small, G. W. *et al.* PET of brain amyloid and tau in mild cognitive impairment. *N. Engl. J. Med.* **355,** 2652–2663 (2006).

18. Klunk, W. E. *et al.* Imaging brain amyloid in Alzheimer's disease with Pittsburgh compound-B. *Ann. Neurol.* **55,** 306–319 (2004).
This first study of the tracer compound PIB in humans describes both the retention of PIB in areas of Alzheimer's-disease-affected brains known to contain amyloid and an inverse relationship between the PIB PET signal and cerebral glucose metabolism, measured by fluorodeoxyglucose PET.
19. Mintun, M. A. *et al.* [^{11}C]PIB in a nondemented population: potential antecedent marker of Alzheimer disease. *Neurology* **67,** 446–452 (2006).
20. Fagan, A. M. *et al.* Inverse relation between *in vivo* amyloid imaging load and CSF $A\beta_{42}$ in humans. *Ann. Neurol.* **59,** 512–519 (2006).
This study illustrates an inverse relationship between mean cortical retention of PIB and cerebrospinal-fluid $A\beta_{42}$ concentrations among both demented and non-demented subjects, suggesting that brain amyloid deposition results in low cerebrospinal-fluid $A\beta_{42}$ and that amyloid imaging and cerebrospinal-fluid $A\beta_{42}$ might serve as antecedent biomarkers of preclinical Alzheimer's disease.
21. Morris J. C. *et al.* PIB imaging predicts progression to symptomatic Alzheimer's disease. *Arch. Neurol.* (in the press).
22. Zhang, M. R. *et al.* Development of a new radioligand, *N*-(5-fluoro-2-phenoxyphenyl)-*N*-(2-[^{18}F]fluoroethyl-5-methoxybenzyl)acetamide, for PET imaging of peripheral benzodiazepine receptor in primate brain. *J. Med. Chem.* **47,** 2228–2235 (2004).
23. Vas, A. *et al.* Functional neuroimaging in multiple sclerosis with radiolabelled glia markers: preliminary comparative PET studies with [^{11}C]vinpocetine and [^{11}C]PK11195 in patients. *J. Neurol. Sci.* **264,** 9–17 (2008).
24. Edison, P. *et al.* Microglia, amyloid, and cognition in Alzheimer's disease: an [^{11}C](*R*)PK11195-PET and [^{11}C]PIB-PET study. *Neurobiol. Dis.* **32,** 412–419 (2008).
25. Nakamura, S. *et al.* Expression of monoamine oxidase B activity in astrocytes of senile plaques. *Acta Neuropathol.* **80,** 419–425 (1990).
26. Hirvonen, J. *et al.* Assessment of MAO-B occupancy in the brain with PET and [^{11}C]-L-deprenyl-D2: a dose-finding study with a novel MAO-B inhibitor, EVT 301. *Clin. Pharmacol. Ther.* **85,** 506–512 (2009).
27. Dickerson, B. C. & Sperling, R. A. Functional abnormalities of the medial temporal lobe memory system in mild cognitive impairment and Alzheimer's disease: insights from functional MRI studies. *Neuropsychologia* **46,** 1624–1635 (2008).
28. Buckner, R. L. *et al.* Molecular, structural, and functional characterization of Alzheimer's disease: Evidence for a relationship between default activity, amyloid, and memory. *J. Neurosci.* **25,** 7709–7717 (2005).
In this paper, five *in vivo* neuroimaging methods are used to illustrate the similarities among the anatomical distributions of atrophy, reduced glucose metabolism and amyloid deposits seen in Alzheimer's disease, and of the default network, suggesting that young-adult brain activity and metabolism patterns may be conducive to cortical amyloid deposition.
29. Hirao, K. *et al.* The prediction of rapid conversion to Alzheimer's disease in mild cognitive impairment using regional cerebral blood flow SPECT. *Neuroimage* **28,** 1014–1021 (2005).
30. de Leon, M. J. *et al.* Prediction of cognitive decline in normal elderly subjects with 2-[^{18}F]fluoro-2-deoxy-D-glucose/positron-emission tomography (FDG/PET). *Proc. Natl Acad. Sci. USA* **98,** 10966–10971 (2001).
31. Chetelat, G. *et al.* Mild cognitive impairment — can FDG-PET predict who is to rapidly convert to Alzheimer's disease? *Neurology* **60,** 1374–1377 (2003).
32. Kadir, A. *et al.* Effect of phenserine treatment on brain functional activity and amyloid in Alzheimer's disease. *Ann. Neurol.* **63,** 621–631 (2008).
33. Gusnard, D. A. & Raichle, M. E. Searching for a baseline: functional imaging and the resting human brain. *Nature Rev. Neurosci.* **2,** 685–694 (2001).
34. Buckner, R. L., Andrews-Hanna, J. R. & Schacter, D. L. The brain's default network: anatomy, function, and relevance to disease. *Ann. NY Acad. Sci.* **1124,** 1–38 (2008).
35. Kamenetz, F. *et al.* APP processing and synaptic function. *Neuron* **37,** 925–937 (2003).
36. Cirrito, J. R. *et al.* Synaptic activity regulates interstitial fluid amyloid-beta levels *in vivo. Neuron* **48,** 913–922 (2005).
37. Brody, D. L. *et al.* Amyloid-beta dynamics correlate with neurological status in the injured human brain. *Science* **321,** 1221–1224 (2008).
38. Motter, R. *et al.* Reduction of β-amyloid peptide$_{42}$ in the cerebrospinal fluid of patients with Alzheimer's disease. *Ann. Neurol.* **38,** 643–648 (1995).
39. Fagan, A. M. *et al.* Decreased cerebrospinal fluid $A\beta_{42}$ correlates with brain atrophy in cognitively normal elderly. *Ann. Neurol.* **65,** 176–183 (2009).
40. Tapiola, T. *et al.* Cerebrospinal fluid β-amyloid 42 and tau proteins as biomarkers of Alzheimer-type pathologic changes in the brain. *Arch. Neurol.* **66,** 382–389 (2009).
41. Fagan, A. M. *et al.* Cerebrospinal fluid tau/β-amyloid$_{42}$ ratio as a prediction of cognitive decline in nondemented older adults. *Arch. Neurol.* **64,** 343–349 (2007).
42. Hansson, O. *et al.* Association between CSF biomarkers and incipient Alzheimer's disease in patients with mild cognitive impairment: a follow-up study. *Lancet Neurol.* **5,** 228–234 (2006).
This report illustrates the utility of cerebrospinal-fluid biomarkers $A\beta_{42}$, tau and phosphorylated tau in predicting the progression of patients from mild cognitive impairment to dementia attributed clinically to Alzheimer's disease.
43. Li, G. *et al.* CSF tau/$A\beta_{42}$ ratio for increased risk of mild cognitive impairment: a follow-up study. *Neurology* **69,** 631–639 (2007).
44. Cairns, N. J. *et al.* PiB-PET detection of cerebral Aβ may lag clinical, cognitive, and CSF markers of Alzheimer's disease: a case report. *Arch. Neurol.* (in the press).
45. Mehta, P. D., Pirttila, T., Patrick, B., Barshatzky, M. & Mehta, S. Amyloid β protein 1–40 and 1–42 levels in matched cerebrospinal fluid and plasma from patients with Alzheimer disease. *Neurosci. Lett.* **304,** 102–106 (2001).
46. Vanderstichele, H. *et al.* Standardization of measurement of β-amyloid$_{(1-42)}$ in cerebrospinal fluid and plasma. *Amyloid* **7,** 245–258 (2000).
47. Graff-Radford, N. R. *et al.* Association of low plasma Aβ42/Aβ40 ratios with increased imminent risk for mild cognitive impairment and Alzheimer disease. *Arch. Neurol.* **64,** 354–362 (2007).
48. Mayeux, R. *et al.* Plasma amyloid β-peptide 1–42 and incipient Alzheimer's disease. *Ann. Neurol.* **46,** 412–416 (1999).
49. Portelius, E. *et al.* Characterization of tau in cerebrospinal fluid using mass spectrometry. *J. Proteome Res.* **7,** 2114–2120 (2008).
50. Vandermeeren, M. *et al.* Detection of tau proteins in normal and Alzheimer's disease cerebrospinal fluid with a sensitive sandwich enzyme-linked immunosorbant assay. *J. Neurochem.* **61,** 1828–1834 (1993).
51. Meyer-Luehmann, M. *et al.* Rapid appearance and local toxicity of amyloid-β plaques in a mouse model of Alzheimer's disease. *Nature* **451,** 720–724 (2008).
52. Montine, T. J. *et al.* The magnitude of brain lipid peroxidation correlates with the extent of degeneration but not with density of neuritic plaques or neurofibrillary tangles or with *APOE* genotype in Alzheimer's disease patients. *Am. J. Pathol.* **155,** 863–868 (1999).
53. Praticò, D., Lee, M.-Y.V., Trojanowski, J. Q., Rokach, J. & Fitzgerald, G. A. Increased F2-isoprostanes in Alzheimer's disease: evidence for enhanced lipid peroxidation *in vivo. FASEB J.* **12,** 1777–1783 (1998).
54. de Leon, M. J. *et al.* Longitudinal CSF isoprostane and MRI atrophy in the progression to Alzheimer's disease. *J. Neurol.* **254,** 1666–1675 (2007).
55. Pratico, D. *et al.* Increased 8,12-*iso*-iPF$_{2\alpha}$-VI in Alzheimer's disease: correlation of a noninvasive index of lipid peroxidation with disease severity. *Ann. Neurol.* **48,** 809–812 (2000).
56. Montine, T. J. *et al.* No difference in plasma or urinary F2-isoprostanes among patients with Huntington's disease or Alzheimer's disease and controls. *Ann. Neurol.* **48,** 950 (2000).
57. Abe, T., Tohgi, H., Isobe, C., Murata, T. & Sato, C. Remarkable increase in the concentration of 8-hydroxyguanosine in cerebrospinal fluid from patients with Alzheimer's disease. *J. Neurosci. Res.* **70,** 447–450 (2002).
58. Abraham, C. R., Selkoe, D. J. & Potter, H. Immunochemical identification of the serine protease inhibitor α_1-antichymotrypsin in the brain amyloid deposits of Alzheimer's disease. *Cell* **52,** 487–501 (1988).
59. Thal, D. R., Schober, R. & Birkenmeier, G. The subunits of α_2-macroglobulin receptor/low density lipoprotein receptor-related protein, native and transformed α_2-macroglobulin and interleukin 6 in Alzheimer's disease. *Brain Res.* **777,** 223–227 (1997).
60. Zanjani, H. *et al.* Complement activation in very early Alzheimer disease. *Alzheimer Dis. Assoc. Disord.* **19,** 55–66 (2005).
61. DeKosky, S. T. *et al.* Plasma and cerebrospinal fluid α_1-antichymotrypsin levels in Alzheimer's disease: correlation with cognitive impairment. *Ann. Neurol.* **53,** 81–90 (2003).
62. Hye, A. *et al.* Proteome-based plasma biomarkers for Alzheimer's disease. *Brain* **129,** 3042–3050 (2006).
63. Hu, Y. *et al.* Identification and validation of novel CSF biomarkers for early stages of Alzheimer's disease. *Proteomics Clin. Appl.* **1,** 1373–1384 (2007).
64. Thambisetty, M. *et al.* Proteome-based identification of plasma proteins associated with hippocampal metabolism in early Alzheimer's disease. *J. Neurol.* **255,** 1712–1720 (2008).
65. Smyth, M. D. *et al.* Decreased levels of C1q in cerebrospinal fluid of living Alzheimer patients correlate with disease state. *Neurobiol. Aging* **15,** 609–614 (1994).
66. Loeffler, D. A. *et al.* Cerebrospinal fluid C3a increases with age, but does not increase further in Alzheimer's disease. *Neurobiol. Aging* **18,** 555–557 (1997).
67. Tan, Z. S. *et al.* Inflammatory markers and the risk of Alzheimer disease: the Framingham study. *Neurology* **68,** 1902–1908 (2007).
68. Simard, A. R., Soulet, D., Gowing, G., Julien, J. P. & Rivest, S. Bone marrow-derived microglia play a critical role in restricting senile plaque formation in Alzheimer's disease. *Neuron* **49,** 489–502 (2006).
69. Guerreiro, R. J. *et al.* Peripheral inflammatory cytokines as biomarkers in Alzheimer's disease and mild cognitive impairment. *Neurodegener. Dis.* **4,** 406–412 (2007).
70. Ray, S. *et al.* Classification and prediction of clinical Alzheimer's diagnosis based on plasma signaling proteins. *Nature Med.* **13,** 1359–1362 (2007).
This paper identified a panel of 18 signalling proteins in blood plasma that might be used to predict and diagnose early Alzheimer's disease. This work illustrates the potential of 'unbiased' screening of multiple analytes in biological fluids to identify early diagnostic and prognostic biomarkers for Alzheimer's disease.
71. Davidsson, P. *et al.* Proteome analysis of cerebrospinal fluid proteins in Alzheimer patients. *Neuroreport* **13,** 611–615 (2002).
72. Zhang, J. *et al.* Quantitative proteomics of cerebrospinal fluid from patients with Alzheimer disease. *J. Alzheimer's Dis.* **7,** 125–133; discussion 173–180 (2005).
73. Finehout, E. J., Franck, Z., Choe, L. H., Relkin, N. & Lee, K. H. Cerebrospinal fluid proteomic biomarkers for Alzheimer's disease. *Ann. Neurol.* **61,** 120–129 (2007).
74. Bateman, R. J. *et al.* Human amyloid-β synthesis and clearance rates as measured in cerebrospinal fluid *in vivo. Nature Med.* **12,** 856–861 (2006).
This report uses amyloid-β peptide species as an example to describe a novel technique that will facilitate the evaluation of disease-modifying treatments for Alzheimer's disease by measuring the production and clearance rates of proteins in the human central nervous system, following administration of a non-radioactive isotopically labelled amino acid (in this case leucine).
75. Bateman, R. J. *et al.* A γ-secretase inhibitor decreases amyloid-β production in the central nervous system. *Ann. Neurol.* **66,** 48–54 (2009).
76. Kauwe, J. S. *et al.* Alzheimer's disease risk variants show association with cerebrospinal fluid amyloid beta. *Neurogenetics* **10,** 13–17 (2009).
77. Craig-Schapiro, R., Fagan, A. M. & Holtzman, D. M. Biomarkers of Alzheimer's disease. *Neurobiol. Dis.* **35,** 128–140 (2009).
78. Sunderland, T. *et al.* Decreased β-amyloid$_{1-42}$ and increased tau levels in cerebrospinal fluid of patients with Alzheimer disease. *J. Am. Med. Assoc.* **289,** 2094–2103 (2003).
79. Welsh-Bohmer, K. A. & Johnson, S. in *Handbook of Dementing Illnesses* 2nd edn (eds Morris, J. C., Galvin, J. E. & Holtzman, D. M.) 59–87 (Taylor & Francis, 2006).

Acknowledgements We thank J. Cirrito and MedPIC, the art and design centre at Washington University School of Medicine, for assistance with graphic design. Work in the authors' laboratories was supported by US National Institutes of Health grants P01-AG026276, PO1-AG03991, P50AG00568125 and T32NS007205.

Author Information Reprints and permissions information is available at www.nature.com/reprints. The authors declare competing financial interests: details accompany the full-text HTML version of the paper at www.nature.com/nature. Correspondence should be addressed to D.M.H. (holtzman@neuro.wustl.edu).

Reverse engineering the mouse brain

Daniel H. O'Connor[1], Daniel Huber[1] & Karel Svoboda[1]

Behaviour is governed by activity in highly structured neural circuits. Genetically targeted sensors and switches facilitate measurement and manipulation of activity *in vivo*, linking activity in defined nodes of neural circuits to behaviour. Because of access to specific cell types, these molecular tools will have the largest impact in genetic model systems such as the mouse. Emerging assays of mouse behaviour are beginning to rival those of behaving monkeys in terms of stimulus and behavioural control. We predict that the confluence of new behavioural and molecular tools in the mouse will reveal the logic of complex mammalian circuits.

A central goal of modern neuroscience is to link the dynamics of neural circuits to behaviour. The operational principles of a neural circuit must be deduced through analysis of its structure and function, a process generically referred to as reverse engineering. Here we advocate a programme of reverse engineering with the aim of linking patterns of action potentials in distinct nodes of neural circuits to animal behaviour.

The circuit diagram, depicting the connections between defined groups of neurons, is necessary to decipher the function of neural circuits. The first step in reverse engineering is the enumeration of the elemental components of the circuit, the cell types[1], typically on the basis of dendritic and axonal structure. Cell types often express distinct patterns of genes, which potentially provide access to these cell types by transgenesis[2,3] (Fig. 1). In some regions of the brain, such as the retina and the cerebellum, the major cell types are known. In other regions, such as the cerebral cortex, discovery of cell types is ongoing. Each cortical layer corresponds neatly to distinct sets of neurons[4] (Fig. 1). However, each layer harbours multiple intermingled cell types; the total number of neocortical cell types and their relative proportions remain to be determined.

The second step in reverse engineering requires mapping the connections between cell types. In some structures, such as the cerebellum, the connectivity at the level of cell types is well understood. Neuroanatomists and electrophysiologists have measured the connections between the major types of neuron in the neocortex on the basis of position[5–7]. For example, in brain slices of the mouse barrel cortex, the functional connections between excitatory neurons in different layers have been mapped[5] (Fig. 1a). Although this circuit diagram is only a rough draft (see refs 8, 9 for evidence of fine-scale specificity beyond cell types), it reveals that neocortical cell types are connected into orderly circuits.

Because neural circuits have evolved to support specific types of behaviour, the functional logic of neural circuits can probably only be determined in the context of behavioural experiments that engage the circuits of interest. The third step in reverse engineering therefore requires recording the activity of specific cell types in behaving animals. Measurements of spiking activity in behaving subjects are typically made with extracellular recordings of single units[10–12]. In these measurements, the cell type and the unit's relationship with the underlying neural circuit are poorly defined. Responses from all types of neuron are mixed together (however, see refs 10, 13). In addition, neurons are detected on the basis of brisk responses to selected stimuli. These and other factors cause strong sampling biases, a problem that was recognized by early investigators in the field[12,14] but is often underappreciated. Perhaps as a consequence, current network models of cortical activity can afford to ignore information about cortical cell types and connectivity and represent all cortical neurons by a few simple cell types, connected in generic ways[15,16]. Assigning patterns of activity to defined nodes in the circuit diagram requires cell-type-specific methods for neurophysiology.

Measurements of neural activity naturally lead to models of the computations performed by neural circuits[15–17]. However, inferring design principles from measurements of neural activity alone is treacherous[18]. Hypotheses ultimately need to be tested by manipulating neural activity during behaviour. The fourth step in reverse engineering therefore requires inactivation and activation of specific cell types. Classical experiments involving lesions (reversible and permanent) and electrical microstimulation have led to major discoveries in neuroscience, for example about the neural basis of movement[19] and perception[20]. However, these methods lack cell-type specificity and reveal relatively little about circuit-level mechanisms, except in unusual circumstances[21,22]. Routine manipulation of defined nodes of the circuit diagram will require cell-type-specific methods for controlling neural activity.

Molecular tools to interrogate and manipulate defined cell types in intact circuits, which have long been advocated[23], are now becoming a reality[3]. These tools will allow reverse engineering of neural circuits with the precise goal of linking patterns of activity in specific cell types, within well-defined neural circuits, to animal behaviour. Because of the power of genetic methods, these tools are most amenable to use in genetically tractable organisms. Among mammals, the mouse holds a special place as the only established genetic model system.

Here we review recent progress in the deployment of these molecular tools in behaving mice. We discuss advances in mouse behavioural experiments with excellent stimulus control, quantitative behavioural measurements and repeatability. We argue that the confluence of molecular methods for circuit analysis, genetic targeting in mice and quantitative mouse behaviour will help to establish causal relationships between patterns of action potentials in specific neuronal populations and behaviour. Beyond the analysis of cell types, it may be possible to directly explore the function of heterogeneous response types within a single class of neuron. The examples we consider focus on neocortical mechanisms of perceptual behaviour in mice, reflecting space limitations and our research interests, but the concepts and techniques we discuss are applicable to other problems in genetic or, with limitations, non-genetic model organisms.

Molecules for cell-type-specific physiology

Protein sensors and switches are beginning to revolutionize neuroanatomy and neurophysiology in genetic model organisms (see ref. 3 for a discussion of the complex technical issues involved in the use of

[1]Janelia Farm Research Campus, Howard Hughes Medical Institute, 19700 Helix Drive, Ashburn, Virginia 20147, USA.

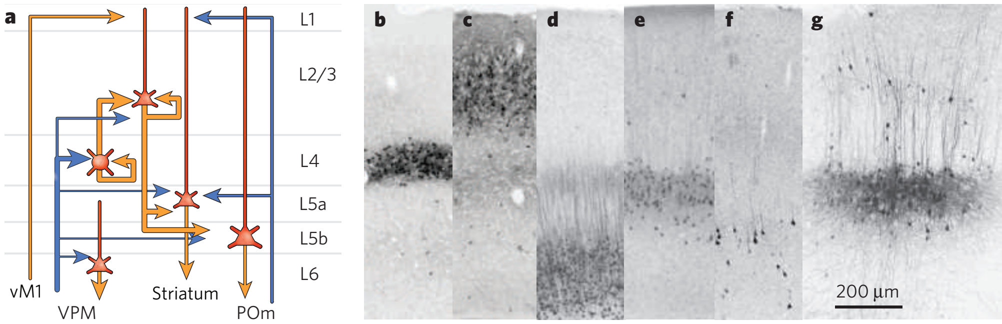

Figure 1 | Major excitatory pathways in the mouse somatosensory cortex and genetic access to the cell types. a, Circuit diagram[5,55]. Blue, ascending thalamocortical input from the ventral posterior medial nucleus (VPM) and the medial subdivision of the posterior nucleus (POm); orange, intracortical (including from whisker-related motor cortex (vM1)) and descending projections; red, dendritic arborizations. **b–g**, Sections through the somatosensory cortex of bacterial artificial chromosome (BAC)-transgenic mice: Scnn1a-Tg3-Cre driver line crossed with reporter mice, labelling L4 stellate cells (**b**); Wfs1-Tg2-Cre driver line crossed with reporter mice, labelling L2/3 pyramidal neurons (**c**); Ntsr1-Cre line[2] crossed with reporter mice, labelling corticothalamic L6 neurons (**d**); Etv1-Cre line[2] crossed with reporter mice, labelling mainly L5a corticostriatal neurons (**e**); Glt25d2 line expressing green fluorescent protein, labelling mainly L5b neurons (**f**); spatially restricted Cre-dependent expression of fluorescent protein in L5a after injection of reporter virus[36] into Etv1-Cre mice (**g**). (Images courtesy of H. Zeng (Allen Institute for Brain Science, Seattle, Washington) (**b**, **c**), N. Heintz and E. Schmidt (GENSAT Project, Rockefeller University, New York) (**d**–**f**) and T. Mao (Janelia Farm Research Campus, Ashburn, Virginia) (**g**).

these methods). Protein sensors convert changes in neural state (for example membrane potential, Ca^{2+} concentration ($[Ca^{2+}]$), exocytosis, protein–protein interaction) to changes in fluorescence signals. Genetically encoded calcium indicators are particularly promising for neurophysiology because they efficiently monitor cytoplasmic $[Ca^{2+}]$ changes induced by trains of action potentials[3], but genetically encoded voltage sensors are catching up[24]. Imaging populations of neurons expressing protein indicators may allow measurement of activity in multiple — perhaps all — neurons of a particular type over time[25] (Fig. 2).

The development of genetically targeted molecular switches has made possible the manipulation of activity in defined cell types in intact mice with relatively high temporal and spatial precision[3]. Protein switches couple light, or the application of small-molecule drugs, to hyperpolarization or depolarization of the neuronal membrane or to changes in synaptic transmission. Inducible silencing, for example using small-molecule or light-gated channels, can be used to determine whether activity in specific cell types is necessary for behaviour. Inducible activation can be used to test whether activity in specific cell types is sufficient to drive behaviour. The light-sensitive channel channelrhodopsin-2 (ChR2) from *Chlamydomonas reinhardtii* has proven to be especially useful and versatile[26]: ChR2-expressing neurons can be entrained by light to fire precisely timed trains of action potentials[27,28]. ChR2 can thus establish causality between precise patterns of activity in a specific set of neurons and behaviour[29–31]. ChR2 can also be used to map the postsynaptic partners of ChR2-expressing neurons[32] and to identify specific types of neuron, tagged by ChR2 expression, in blind extracellular recordings[33].

Protein sensors and switches can be targeted to specific cell types using a variety of genetic methods[3]. Genetic targeting is not limited to genetic model systems. For example, in some cases cell-type-specific expression can be achieved by including *cis*-regulatory elements in viral promoters[34,35]. However, by far the most versatile methods rely on transgenic mice expressing 'drivers' (typically Cre recombinase) in specific cell types[3] (Fig. 1). The driver mice can be mated with mice containing 'floxed-stop' reporter alleles to achieve expression of sensors or switches in the cell types of interest. Alternatively, the reporter can be carried in a Cre-dependent viral vector[36]. Cre mice are currently being produced in large-scale projects (for example the Gene Expression Nervous System Atlas (http://www.gensat.org) and the Allen Institute for Brain Science transgenic mouse study (http://transgenicmouse.alleninstitute.org)), informed by comprehensive gene expression databases (such as the Allen Mouse Brain Atlas (http://mouse.brain-map.org)).

Protein switches have already been used to analyse the contributions of specific cell types to behaviour. Early *in vivo* studies using molecular silencers were mainly designed to demonstrate the methods[3]. However, molecular silencers have begun to reveal the functions of specific cell types in the context of innate behaviour. For example, silencing somatostatin-positive neurons in the pre-Bötzinger complex causes rapid respiratory failure, linking activity in these neurons to the control of breathing[35].

Photostimulation of ChR2-positive neurons *in vivo* has established causal links between electrical activity in specific types of neuron and behaviour. For example, dopaminergic neurons in the ventral tegmental area are thought to encode reward-prediction errors, but it is unclear whether changes in activity in these neurons are sufficient to signal reward or aversive stimuli. Expression of ChR2 in dopaminergic neurons in the ventral tegmental area allows control of the activity of these neurons in behaving mice[31]. Pairing short epochs of high-frequency photostimulation with mouse exploration of one of two chambers produced a place preference for that chamber, demonstrating that phasic firing in dopaminergic neurons by itself can cause behavioural conditioning.

So far, protein switches have been applied to manipulate relatively slow processes, in which behavioural changes are observed seconds or more after stimulation, driven by peptidergic[30] or neuromodulatory[31] systems. Typical reaction times for complex sensory-guided behaviours are on the order of 200 ms (ref. 37). The neural activity underlying these behaviours crosses multiple synapses. The core neural circuits implementing behaviour are likely to be driven largely by glutamatergic and GABAergic (γ-aminobutyric-acid-producing) neurons with fast dynamics in the 1–10-ms range. To reverse engineer these fast processes, it is therefore necessary to monitor behavioural parameters while measuring and controlling neural activity, ideally in a rapid closed loop, all on a millisecond-by-millisecond basis.

Mouse behaviour

New molecular tools for cell-type-specific neurophysiology and manipulation facilitate genetic dissection of neural circuits in the mouse, but the limited demonstrated behavioural potential of the mouse is often perceived as a major obstacle. New mouse lines are routinely subjected to a battery of tests for the basic characterization of sensory, cognitive, motor and temperamental traits[38] (see also the Mouse Phenome Database from The Jackson Laboratory (http://www.jax.org/phenome)). These assays are used to describe differences across groups of animals. Although the standardization achieved using these tests is unmatched in the field of animal behaviour, the levels of behavioural control are often inadequate to determine the relationships between sensory stimuli, behaviour and neural activity.

Tasks based on mazes or arenas, such as the Morris water maze[39], in which a mouse must remember and swim to the location of a hidden

platform, have shed light on the neural and molecular basis of spatial learning and memory[40]. Maze tasks have been adapted to assay sensory discrimination[41] and working memory[42]. However, maze tasks yield few trials (typically tens of trials) and stimulus control is relatively poor because the animal is free to move with respect to the stimuli.

The head-fixed, behaving monkey preparation has been the 'gold standard' in the exploration of the dynamics of the mammalian brain, and of the cerebral cortex in particular. Monkeys are typically trained on tasks designed to isolate the core sensory[12,20], cognitive[11] or motor functions[10] of interest. Head fixation and body restraint provide a high degree of stimulus control (for example visual scene) and behavioural read-out (for example eye or arm position)[10,12]. Monkeys perform many hundreds of trials per day for a juice reward. The combination of precise stimulus control, monitoring of motor output and single-unit recordings over large numbers of trials is the foundation on which many conceptually rich and quantitative studies of the neural basis of sensation, cognition and movement have been built. Monkey experiments have also led the way in separating causation from correlation in neurophysiological experiments[19,20], but cell-type-specific measurements and manipulation will probably remain exceptional in monkeys[10]. In contrast, in the mouse brain, cell-type-specific neurobiology is becoming routine.

Inspired by the experiments on behaving monkeys, procedures for quantitative head-fixed behaviours are being developed for mice. Motor learning in the vestibulo-ocular reflex, long studied in monkeys, has been adapted to the mouse[43]. Head fixation is central to this scheme, because precise control of head motion with respect to visual stimuli is essential, as is precise measurement of eye position. Head-fixed mice can also run freely on spherical treadmills[44]. In this experimental situation, complex terrains could be simulated in closed-loop virtual-reality environments, making possible the study of navigation with precise experimental control.

Beyond reflexive behaviour, mice have also been trained in choice-based, learned tasks. Studies in olfaction have come close to matching the standard of monkey experiments for experimental control and trial repeatability. In olfactory discrimination tasks, mice sample odours and learn to choose a correct response on the basis of the identities of two odours, often with performance levels approaching 100% for simple discriminations[45,46]. In these types of experiment, mice are motivated by thirst — as in most monkey studies but in contrast to most other rodent work — and routinely perform hundreds of trials.

In the remainder of this Review, we draw examples from the somatosensory system of mice. Rodents use their whiskers to detect and locate objects when moving through an environment[47]. The measurement of the locations of object features is also an important aspect of object identification. Inspired by previous work in freely moving rats[48,49], we have trained head-fixed mice to locate an object (a vertical pole) near their heads with their whiskers (Fig. 3). In each trial, mice report with go/no-go lick responses whether the pole has been presented in a target location or in a distractor location. Mice perform at high levels (>90% correct for simple discriminations) for hundreds of trials (Fig. 3c). High-speed imaging of whisker position reveals the whisker motor programs underlying somatosensory discrimination. Changes in whisker shape, caused by contact between whisker and object, report the mechanical inputs to the somatosensory system[50] (Fig. 3a). The object-localization task is ideally suited to probing the cortical basis of tactile spatial perception and sensorimotor integration in the context of active sensation.

Repeatability over hundreds of trials, a major strength of monkey studies that is now achievable with mice, allows powerful statistical analyses but also merits a caveat. In these tasks, animals become expert performers in a specific task. The neural activity, and even the basic circuits, underlying a specific behaviour can change profoundly with expertise[51], and may differ from those underlying natural behaviours. Massively parallel recordings of single neurons may eventually obviate the statistical need to accumulate data over many repeated trials[52].

Behaving mice are emerging as an important model in systems neurobiology. Because of genetic access to cell types, the use of mice will allow more precise and reductionist neuron-level experiments than will the use of head-fixed monkeys. Next, we illustrate this point by outlining possible experiments in mice performing the somatosensory discrimination task.

Reverse engineering neocortical circuits

Rodents move their whiskers in the horizontal plane to localize objects along the anterior–posterior axis (Fig. 3a). It is not clear what neural mechanisms underlie the encoding of horizontal object location. Object location is computed, at least in part, in the barrel cortex. Information about contact between whisker and object appears in the barrel cortex as a brief burst of action potentials coincident with mechanical forces on the whiskers[53] (Fig. 3b, c). As a whisker protracts, objects that are more distant are contacted later in a whisk cycle. The timing of these action potentials within the whisk cycle could therefore encode horizontal location[47].

Information about whisker–object contact is conveyed by the ventral posterior medial nucleus of the thalamus to stellate cells in L4 barrels[54,55] (Fig. 1a; L, cortical layer). The only other major excitatory input received by stellate cells comes from other stellate cells in the same barrel, which are presumably excited by deflection of the same whisker[5]. The L4 barrel relays peripheral contact signals to cortical targets, mainly in L3. L3 neurons project to L5 neurons, which include the major output neurons of the cortex.

To determine whether a short burst of activity (Fig. 3b, c) in L4 neurons is necessary and sufficient to perceive object location, molecular switches can be targeted to L4 neurons by using mouse lines expressing Cre in L4 (for example the Six3Cre transgenic mouse line 69 (ref. 56) or the Scnn1a-Tg3-Cre line from the Allen Institute for Brain Science; Fig. 1b). Stereotactic injection of adeno-associated virus, expressing switches in a

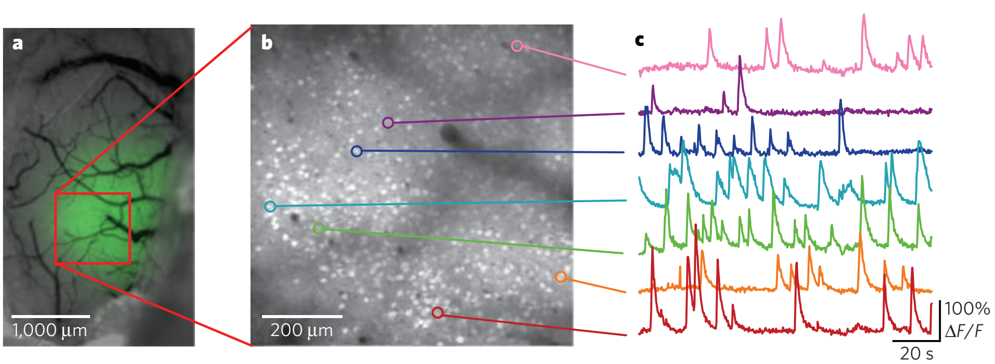

Figure 2 | Monitoring the activity of large neuronal populations with a genetically encoded calcium indicator. a, Overlay of bright-field (grey) and wide-field fluorescence (green, virally expressed indicator) images of mouse neocortex. **b,** Two-photon image showing approximately 500 L2/3 neurons expressing the calcium indicator. **c,** Example traces showing neural-activity-induced calcium transients in multiple individual neurons. Images are from awake, head-fixed mice (see also Fig. 3). $\Delta F/F$, change in fluorescence divided by baseline fluorescence.

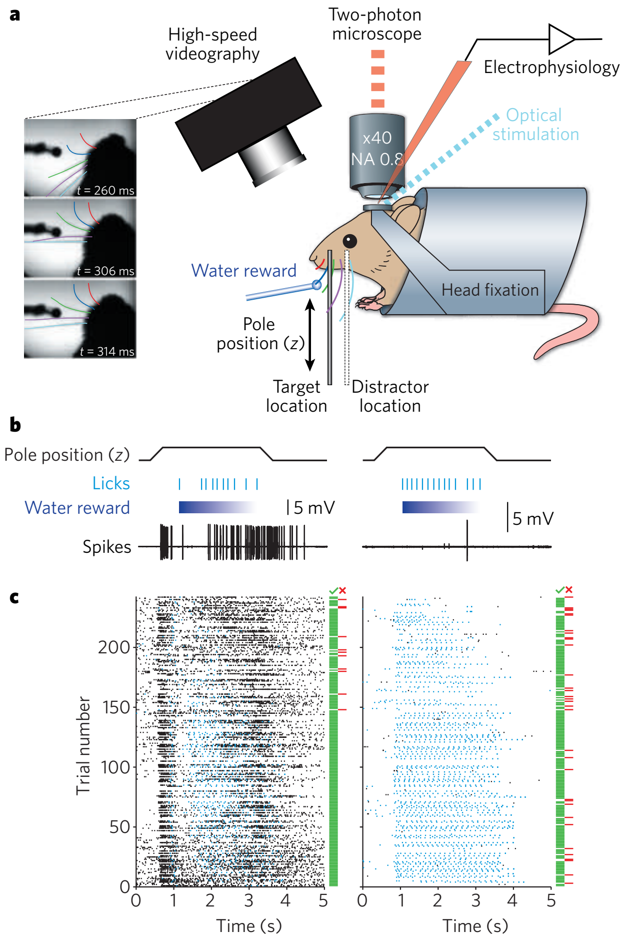

Figure 3 | Tactile object localization in the head-fixed mouse. a, Schematic of apparatus for behaviour, high-speed videography, neurophysiological recording, neuron-level imaging and optical stimulation. A head-fixed mouse moves its whiskers to determine the location of a small pole presented on one side of its head. In each trial, the pole is moved vertically to within reach of the whiskers, in either a target or a distractor location. Behavioural choice is reported with go/no-go licking. High-speed video measures the positions and shapes of whiskers as they search for and contact the pole (left-hand image panels). Neural activity can be monitored using electrophysiology and two-photon microscopy, or manipulated with optical stimulation. NA, numerical aperture. **b,** Example trials showing behaviour and action potentials for two neurons (left and right). **c,** Rasters of 242 trials for two neurons: black tick-marks represent action-potential times; blue tick-marks represent licks. Horizontal green and red bars to the right of each raster indicate trials that were correct and incorrect, respectively. Although recorded in the barrel cortex of the same mouse, the two cells show different patterns of activity.

Cre-dependent manner, causes expression in L4 neurons in these mice[55]. Somatotopic specificity can be achieved by injecting the virus into the barrel column corresponding to a specific whisker (Fig. 1g), aided by intrinsic signal imaging[5].

Expression of small-molecule-activated K^+ channels[57] could be used to silence L4 neurons reversibly on a timescale of one hour, corresponding to a typical behavioural session. The behavioural performance in sessions before, during and after silencing would indicate whether activity in L4 neurons is necessary for object localization. However, prolonged silencing over many trials might confuse or discourage the animal because of loss of reward. This confound can probably be solved with rapid light-activated silencing methods, such as using the light-sensitive chloride pump *Natronomonas pharaonis* halorhodopsin[58,59], which can provide silencing at the level of single trials.

The timing of a brief burst of activity beginning in L4 neurons may be sufficient to determine horizontal object location. Precisely timed ChR2 photostimulation of L4 neurons, with the goal of producing fictive objects, could be used to test this hypothesis. The speed of active sensation presents challenges: whiskers move millimetres in milliseconds. The photostimuli therefore need to be triggered with millisecond accuracy by whisker position. This type of closed-loop experiment is allowed by the precise behavioural control made possible by head fixation. If the mouse responds to photostimulation of L4 neurons (the fictive object) as if true contact had been made (based on the trained stimulus–response associations), it can be inferred that a timed burst of activity in L4 neurons is sufficient to lead to the percept of object contact at a particular location. Similar approaches could be used to impose more subtle perturbations of activity, such as changing the temporal correlations in spike trains.

Testing the necessity and sufficiency of different patterns of neural activity during tactile object localization can be extended to other genetically accessible cell types within the circuit (Fig. 1). For example, action-potential timing as a code for object distance can only be interpreted in the context of a signal encoding the position of the whisker over time[47]. Some barrel cortex neurons show activity that is modulated by whisking. A subset of neurons show brief responses modulated by the whisking cycle, suggesting that they could encode object location within whisker phase[53]. Cortical (whisker-related primary motor cortex) and thalamic (medial subdivision of the posterior nucleus) regions have been proposed as the source of the whisker-position reference signal[47] (Fig. 1a). Molecular switches, in the context of quantitative behaviour, are well suited to revealing the identity and properties of this reference signal.

Synthetic brain science

In the previous section, we considered the manipulation of cell types to study the role of these neurons in normal sensation. However, stimulation of subsets of neurons can also be used as a 'synthetic stimulus' to probe fundamental properties of neural circuits.

For instance, the observation that some types of neuron show extremely sparse activity *in vivo*[60] raises the possibility that sparse activity patterns can be sufficient to drive behaviour. To test this possibility, ChR2 photostimulation has been used to mimic the sparse activity patterns observed in L2/3 pyramidal neurons[61] in awake, behaving mice[29]. Mice were trained to report photostimulation of ChR2-positive neurons by selecting one of two ports for a water reward. The number of activated neurons was quantified using histological and electrophysiological methods. After a learning period of a few weeks, mice were able to reliably report the activation of a small subset (≤1%) of L2/3 neurons; only 300 photostimulated action potentials were required to drive reliable behaviour[29]. This corresponds to a tiny fraction of the ongoing activity in the barrel cortex. Other experiments suggest that the stimulation even of individual neurons can have measurable effects on network activity[62] and behaviour[22]. These findings show that mechanisms exist to read out ultra-sparse activity from cortical networks.

Similar experiments could help unravel the circuit mechanisms underlying detection of ultra-sparse activity. One possibility is that the ChR2-positive neurons form part of a special cortical network defined by learning-induced plasticity at their output synapses. Alternatively, mice may generally learn to discern small increases in activity across the L2/3 population. These possibilities could be distinguished by training on photostimulation detection using one set of ChR2-positive neurons and testing with detection using another set of neurons. If, during learning, the ChR2-positive neurons do not form an ad hoc circuit, then mice should generalize to stimulation of a different set of intermingled neurons, with no change in threshold. The results of these experiments would profoundly affect our understanding of perceptual learning.

One striking observation in photostimulation-driven behaviour is that the number of stimulated neurons can be traded off against the number of action potentials per neuron[29]. In other words, trains of N action potentials (spread out over 250 ms) in n neurons are as efficacious in driving behaviour as one action potential in Nn neurons. This suggests that the networks reading out activity from L2/3 neurons integrate activity over times of at least 250 ms, the longest trains probed.

Future work may address the temporal limits, as well as the locus and mechanism, of this integration.

Detection of photostimulation could be used to study the essential neural components of decision making. The advantage over sensory-driven detection tasks is that the stimulus driving the decision, for example the ensemble of photostimulated L2/3 neurons, is under precise control. Even photostimulation close to the detection threshold is repeatable and not subject to the variability associated with sensory stimuli. Under these conditions of precise activation, it might be possible to track the evolution of network activity leading from deterministic stimuli to stochastic choice behaviour[63].

Beyond cell types

So far we have labelled neurons as members of a cell type; but cell type is only a first approximation of the functional description of any one neuron. Although the activity patterns of neurons belonging to a particular cell type are distinct on average, neural responses are often extremely heterogeneous even for a cell type and brain region. For example, neighbouring L2/3 neurons in the rodent visual cortex can have sharp but divergent orientation tuning[64]. Similarly, neurons in the barrel cortex have diverse response types, including excitation by contact with an object, or tonic excitation coupled to whisking, as well as inhibition[53,65] (Fig. 3c). Neurons differ not only in their selectivity for particular stimuli (their 'tuning'), but also in the amount of information they carry. The activity of some neurons bears no obvious relation to the task, whereas other neurons discriminate stimuli as well as the animal does[66,67] (Fig. 3c). Furthermore, the relationship between individual neurons and behaviour is flexible: experiments involving biofeedback have shown that the activity of individual motor cortex neurons is under volitional control and can be tuned to maximize reward[68]. Without manipulating the activity of neurons showing specific response types, however, there can be no definitive answer to the question of whether some neurons are more relevant to behaviour than others.

Although studies that directly target neuronal response types for manipulation have not yet been done, the technical challenges facing such experiments are rapidly being overcome. Functional imaging may allow the mapping of response types of tens of thousands of neurons in volumes on the order of a cubic millimetre[64] (Fig. 2). Neurons could then be selected for manipulation on the basis of their response type (Fig. 4). For example, if the neurons express ChR2, targeted groups of neurons could be photostimulated by two-photon excitation of ChR2 (Fig. 4b). However, a conventional focused laser excites only a tiny patch of neuronal membrane, containing a small amount of low-conductance ChR2, which produces insufficient depolarization to drive action potentials in most neurons[69]. Achieving routine two-photon stimulation of single neurons may require new types of ChR2 with longer open times[70] or greater conductances, combined with beam shaping to allow larger membrane areas to be excited[69,71]. In behaving animals it would then be possible to study how activity in subsets of neurons, selected on the basis of response type, contributes to behaviour.

A different strategy for targeting neurons on the basis of response type might rely on transcription activated by light[72] (Fig. 4c, f), or the conjunction of neural activity and an exogenous trigger (using small molecules or light) (Fig. 4d, f). In fact, existing transgenic mice couple neural activity to expression of protein markers[73]; molecular switches could be expressed instead, to manipulate the activity of neurons that were active in an earlier time window.

It may be possible to trigger expression of protein activators and silencers in arbitrary groups of neurons *in vivo*, using illumination of multiple individual neurons. The targeted neurons could be those exhibiting particular response types identified in prior imaging experiments. Single-cell resolution could be achieved by two-photon excitation (Fig. 4c, f). Subsequently, neurons expressing the switch could be activated or silenced using small molecules or diffuse light (Fig. 4e). This strategy, based on two-photon excitation of transcription followed by one-photon photostimulation of ChR2, might be less demanding of photophysics than direct two-photon photostimulation of ChR2.

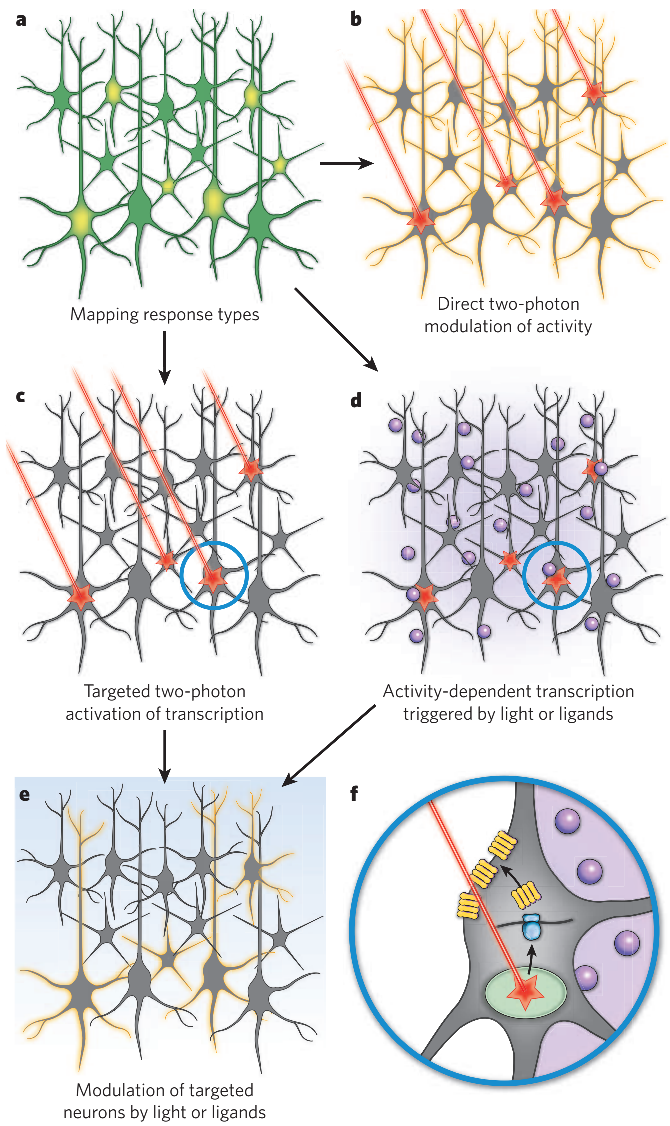

Figure 4 | Manipulating groups of neurons on the basis of their response type. a, Mapping response types using optical indicators or electrodes. **b,** Modulation of activity by two-photon excitation of photoswitches (yellow) in neurons showing particular response types. **c, d, f,** Expression of genetically encoded switches by hypothetical transcription systems triggered directly by light (**c**; **f**, left) or by a combination of neuronal activity and small molecules (purple circles) or light (purple glow) (**d**; **f**, right). The cellular production and transport of protein switches (yellow) is indicated schematically (blue, ribosome). **e,** Manipulating neurons previously targeted for expression of a molecular switch (yellow). Activation (or inhibition) could be achieved using diffuse light or a small-molecule ligand (blue glow).

In general, the relationship between cell type and response type is not understood. Whereas cell type is a category defined largely by development, a neuron's response type is most probably malleable, possibly even changing with behavioural context[68]. The anatomical underpinnings of the diverse neuronal response types are not known. The axons of excitatory neurons connect to only a small fraction of available target neurons of any given type. This sparse connectivity is known not to be random; rather, relatively strongly connected and interdigitated subnetworks are embedded within the cortical circuit defined by cell types[8,9]. It is likely that this anatomical fine-scale specificity in some way underlies different response types.

However, the question of which circuits determine any particular response type remains unanswered, even in the well-studied example

of orientation selectivity in the visual cortex[17,64]. A minimal explanation will require characterization of the inputs that drive a particular response type. One approach might involve measurement of population responses using $[Ca^{2+}]$ imaging and post hoc large-volume ultrastructural analysis to recover the detailed connectivity between characterized neurons[74]. Another approach could be based on labelling the target neuron and all of its inputs with a trans-synaptic virus[75], for subsequent physiological analysis.

In this Review, we have advocated a programme of reverse engineering with the goal of linking patterns of activity in specific cell types to behaviour. This experimental programme would be most effective if it were tightly integrated with theory. Useful theoretical models could take many shapes. For example, semi-realistic compartmental models of single neurons, combined with information on the distributions of specific types of input within their dendritic arborizations, might reveal the mechanisms of how synaptic input interacts with postsynaptic membrane properties to drive particular response types. Other types of model might focus on the dynamics of the neural network or on information transmission within the network. The vast amounts of data collected in behavioural and physiological experiments can only be exploited with new approaches for data reduction and mining. Ultimately, progress in systems neuroscience will require the development of new theoretical tools in conjunction with cell-type-specific recordings and manipulations in behaving animals. ■

1. Masland, R. H. Neuronal cell types. *Curr. Biol.* **14,** R497–R500 (2004).
2. Gong, S. *et al.* Targeting Cre recombinase to specific neuron populations with bacterial artificial chromosome constructs. *J. Neurosci.* **27,** 9817–9823 (2007).
3. Luo, L., Callaway, E. M. & Svoboda, K. Genetic dissection of neural circuits. *Neuron* **57,** 634–660 (2008).
4. Thomson, A. M. & Lamy, C. Functional maps of neocortical local circuitry. *Front. Neurosci.* **1,** 19–42 (2007).
5. Lefort, S., Tomm, C., Floyd Sarria, J. C. & Petersen, C. C. The excitatory neuronal network of the C2 barrel column in mouse primary somatosensory cortex. *Neuron* **61,** 301–316 (2009).
6. Binzegger, T., Douglas, R. J. & Martin, K. A. A quantitative map of the circuit of cat primary visual cortex. *J. Neurosci.* **24,** 8441–8453 (2004).
7. Weiler, N., Wood, L., Yu, J., Solla, S. A. & Shepherd, G. M. Top-down laminar organization of the excitatory network in motor cortex. *Nature Neurosci.* **11,** 360–366 (2008).
8. Song, S., Sjostrom, P. J., Reigl, M., Nelson, S. & Chklovskii, D. B. Highly nonrandom features of synaptic connectivity in local cortical circuits. *PLoS Biol.* **3,** e68 (2005).
9. Yoshimura, Y., Dantzker, J. L. & Callaway, E. M. Excitatory cortical neurons form fine-scale functional networks. *Nature* **433,** 868–873 (2005).
10. Evarts, E. V. Relation of pyramidal tract activity to force exerted during voluntary movement. *J. Neurophysiol.* **31,** 14–27 (1968).
This study pioneered the head-fixed, awake, behaving monkey preparation and cell-type-specific recording methods with the goal of relating the activity of pyramidal tract neurons to movement.
11. Moran, J. & Desimone, R. Selective attention gates visual processing in the extrastriate cortex. *Science* **229,** 782–784 (1985).
12. Wurtz, R. H. Visual cortex neurons: response to stimuli during rapid eye movements. *Science* **162,** 1148–1150 (1968).
This paper reports the training of monkeys to fixate a spot of light, introducing a powerful method of controlling sensory and motor variables in combination with electrophysiological recordings.
13. Fujisawa, S., Amarasingham, A., Harrison, M. T. & Buzsaki, G. Behavior-dependent short-term assembly dynamics in the medial prefrontal cortex. *Nature Neurosci.* **11,** 823–833 (2008).
14. Mountcastle, V. B. The parietal system and some higher brain functions. *Cereb. Cortex* **5,** 377–390 (1995).
15. Murphy, B. K. & Miller, K. D. Balanced amplification: a new mechanism of selective amplification of neural activity patterns. *Neuron* **61,** 635–648 (2009).
16. Wang, X. J. Decision making in recurrent neuronal circuits. *Neuron* **60,** 215–234 (2008).
17. Hubel, D. H. & Wiesel, T. N. Receptive fields, binocular interaction and functional architecture in the cat's visual cortex. *J. Physiol. (Lond.)* **160,** 106–154 (1962).
18. Marom, S. *et al.* On the precarious path of reverse neuro-engineering. *Front. Comput. Neurosci.* **3,** 5 (2009).
19. Hikosaka, O. & Wurtz, R. H. Modification of saccadic eye movements by GABA-related substances. I. Effect of muscimol and bicuculline in monkey superior colliculus. *J. Neurophysiol.* **53,** 266–291 (1985).
20. Salzman, C. D., Britten, K. H. & Newsome, W. T. Cortical microstimulation influences perceptual judgements of motion direction. *Nature* **346,** 174–177 (1990).
This landmark study established causality between activity of directionally selective neurons in visual cortex and perceptual judgments of motion direction.
21. Gray, P. A., Janczewski, W. A., Mellen, N., McCrimmon, D. R. & Feldman, J. L. Normal breathing requires preBötzinger complex neurokinin-1 receptor-expressing neurons. *Nature Neurosci.* **4,** 927–930 (2001).
22. Houweling, A. R. & Brecht, M. Behavioural report of single neuron stimulation in somatosensory cortex. *Nature* **451,** 65–68 (2008).
23. Siegel, R. M. & Callaway, E. M. Francis Crick's legacy for neuroscience: between the α and the Ω. *PLoS Biol.* **2,** e419 (2004).
24. Tsutsui, H., Karasawa, S., Okamura, Y. & Miyawaki, A. Improving membrane voltage measurements using FRET with new fluorescent proteins. *Nature Methods* **5,** 683–685 (2008).
25. Mank, M. *et al.* A genetically encoded calcium indicator for chronic *in vivo* two-photon imaging. *Nature Methods* **5,** 805–811 (2008).
26. Nagel, G. *et al.* Channelrhodopsin-2, a directly light-gated cation-selective membrane channel. *Proc. Natl Acad. Sci. USA* **100,** 13940–13945 (2003).
27. Boyden, E. S., Zhang, F., Bamberg, E., Nagel, G. & Deisseroth, K. Millisecond-timescale, genetically targeted optical control of neural activity. *Nature Neurosci.* **8,** 1263–1268 (2005).
28. Li, X. *et al.* Fast noninvasive activation and inhibition of neural and network activity by vertebrate rhodopsin and green algae channelrhodopsin. *Proc. Natl Acad. Sci. USA* **102,** 17816–17821 (2005).
Reference 26 showed that ChR2 is a directly light-gated cation channel that can be used to depolarize mammalian cells. References 27 and 28 demonstrated that light can be used to impose precise patterns of action-potential trains on ChR2-expressing neurons.
29. Huber, D. *et al.* Sparse optical microstimulation in barrel cortex drives learned behaviour in freely moving mice. *Nature* **451,** 61–64 (2008).
This study used excitation of L2/3 pyramidal neurons by ChR2 to show that sparse activity in the neocortex could drive behaviour.
30. Adamantidis, A. R., Zhang, F., Aravanis, A. M., Deisseroth, K. & de Lecea, L. Neural substrates of awakening probed with optogenetic control of hypocretin neurons. *Nature* **450,** 420–424 (2007).
31. Tsai, H. C. *et al.* Phasic firing in dopaminergic neurons is sufficient for behavioral conditioning. *Science* **324,** 1080–1084 (2009).
32. Petreanu, L., Huber, D., Sobczyk, A. & Svoboda, K. Channelrhodopsin-2-assisted circuit mapping of long-range callosal projections. *Nature Neurosci.* **10,** 663–668 (2007).
33. Lima, S. Q., Hromadka, T., Znamenskiy, P. & Zador, A. M. PINP: a new method of tagging neuronal populations for identification during *in vivo* electrophysiological recording. *PLoS ONE* **4,** e6099 (2009).
34. Han, X. *et al.* Millisecond-timescale optical control of neural dynamics in the nonhuman primate brain. *Neuron* **62,** 191–198 (2009).
35. Tan, W. *et al.* Silencing preBötzinger Complex somatostatin-expressing neurons induces persistent apnea in awake rat. *Nature Neurosci.* **11,** 538–540 (2008).
36. Atasoy, D., Aponte, Y., Su, H. H. & Sternson, S. M. A FLEX switch targets channelrhodopsin-2 to multiple cell types for imaging and long-range circuit mapping. *J. Neurosci.* **28,** 7025–7030 (2008).
37. Uchida, N., Kepecs, A. & Mainen, Z. F. Seeing at a glance, smelling in a whiff: rapid forms of perceptual decision making. *Nature Rev. Neurosci.* **7,** 485–491 (2006).
38. Bucan, M. & Abel, T. The mouse: genetics meets behaviour. *Nature Rev. Genet.* **3,** 114–123 (2002).
39. Morris, R. Developments of a water-maze procedure for studying spatial learning in the rat. *J. Neurosci. Methods* **11,** 47–60 (1984).
40. Nakazawa, K. *et al.* Requirement for hippocampal CA3 NMDA receptors in associative memory recall. *Science* **297,** 211–218 (2002).
41. Prusky, G. T., West, P. W. & Douglas, R. M. Behavioral assessment of visual acuity in mice and rats. *Vision Res.* **40,** 2201–2209 (2000).
42. Zeng, H. *et al.* Forebrain-specific calcineurin knockout selectively impairs bidirectional synaptic plasticity and working/episodic-like memory. *Cell* **107,** 617–629 (2001).
43. Boyden, E. S. & Raymond, J. L. Active reversal of motor memories reveals rules governing memory encoding. *Neuron* **39,** 1031–1042 (2003).
44. Dombeck, D. A., Khabbaz, A. N., Collman, F., Adelman, T. L. & Tank, D. W. Imaging large-scale neural activity with cellular resolution in awake, mobile mice. *Neuron* **56,** 43–57 (2007).
References 43 and 44 showed that head-fixed mice perform relatively normal reflexive behaviours.
45. Bodyak, N. & Slotnick, B. Performance of mice in an automated olfactometer: odor detection, discrimination and odor memory. *Chem. Senses* **24,** 637–645 (1999).
46. Rinberg, D., Koulakov, A. & Gelperin, A. Speed-accuracy tradeoff in olfaction. *Neuron* **51,** 351–358 (2006).
47. Diamond, M. E., von Heimendahl, M., Knutsen, P. M., Kleinfeld, D. & Ahissar, E. 'Where' and 'what' in the whisker sensorimotor system. *Nature Rev. Neurosci.* **9,** 601–612 (2008).
48. Knutsen, P. M., Pietr, M. & Ahissar, E. Haptic object localization in the vibrissal system: behavior and performance. *J. Neurosci.* **26,** 8451–8464 (2006).
49. Mehta, S. B., Whitmer, D., Figueroa, R., Williams, B. A. & Kleinfeld, D. Active spatial perception in the vibrissa scanning sensorimotor system. *PLoS Biol.* **5,** e15 (2007).
50. Birdwell, J. A. *et al.* Biomechanical models for radial distance determination by the rat vibrissal system. *J. Neurophysiol.* **98,** 2439–2455 (2007).
51. Balleine, B. W., Liljeholm, M. & Ostlund, S. B. The integrative function of the basal ganglia in instrumental conditioning. *Behav. Brain Res.* **199,** 43–52 (2009).
52. Churchland, M. M., Yu, B. M., Sahani, M. & Shenoy, K. V. Techniques for extracting single-trial activity patterns from large-scale neural recordings. *Curr. Opin. Neurobiol.* **17,** 609–618 (2007).
53. Curtis, J. C. & Kleinfeld, D. Phase-to-rate transformations encode touch in cortical neurons of a scanning sensorimotor system. *Nature Neurosci.* **12,** 492–501 (2009).
54. White, E. L. Identified neurons in mouse SmI cortex which are postsynaptic to thalamocortical axon terminals: a combined Golgi-electron microscopic and degeneration study. *J. Comp. Neurol.* **181,** 627–661 (1978).
55. Petreanu, L., Mao, T., Sternson, S. M. & Svoboda, K. The subcellular organization of neocortical excitatory connections. *Nature* **457,** 1142–1145 (2009).
56. Liao, G. Y. & Xu, B. Cre recombinase-mediated gene deletion in layer 4 of murine sensory cortical areas. *Genesis* **46,** 289–293 (2008).
57. Armbruster, B. N., Li, X., Pausch, M. H., Herlitze, S. & Roth, B. L. Evolving the lock to fit the key to create a family of G protein-coupled receptors potently activated by an inert ligand. *Proc. Natl Acad. Sci. USA* **104,** 5163–5168 (2007).
58. Zhang, F. *et al.* Multimodal fast optical interrogation of neural circuitry. *Nature* **446,** 633–639 (2007).
59. Han, X. & Boyden, E. S. Multiple-color optical activation, silencing, and desynchronization of neural activity, with single-spike temporal resolution. *PLoS ONE* **2,** e299 (2007).

60. Hahnloser, R. H., Kozhevnikov, A. A. & Fee, M. S. An ultra-sparse code underlies the generation of neural sequences in a songbird. *Nature* **419,** 65–70 (2002).
61. de Kock, C. P., Bruno, R. M., Spors, H. & Sakmann, B. Layer- and cell-type-specific suprathreshold stimulus representation in rat primary somatosensory cortex. *J. Physiol. (Lond.)* **581,** 139–154 (2007).
62. Li, C. Y., Poo, M. M. & Dan, Y. Burst spiking of a single cortical neuron modifies global brain state. *Science* **324,** 643–646 (2009).
63. de Lafuente, V. & Romo, R. Neural correlate of subjective sensory experience gradually builds up across cortical areas. *Proc. Natl Acad. Sci. USA* **103,** 14266–14271 (2006).
64. Ohki, K., Chung, S., Ch'ng, Y. H., Kara, P. & Reid, R. C. Functional imaging with cellular resolution reveals precise micro-architecture in visual cortex. *Nature* **433,** 597–603 (2005).
This two-photon-calcium-imaging study in the rodent primary visual cortex showed that even neighbouring neurons can have highly different response types.
65. Jadhav, S. P., Wolfe, J. & Feldman, D. E. Sparse temporal coding of elementary tactile features during active whisker sensation. *Nature Neurosci.* **12,** 792–800 (2009).
66. Newsome, W. T., Britten, K. H. & Movshon, J. A. Neuronal correlates of a perceptual decision. *Nature* **341,** 52–54 (1989).
67. de Lafuente, V. & Romo, R. Neuronal correlates of subjective sensory experience. *Nature Neurosci.* **8,** 1698–1703 (2005).
68. Fetz, E. E. Operant conditioning of cortical unit activity. *Science* **163,** 955–958 (1969).
69. Rickgauer, J. P. & Tank, D. W. Infrared two-photon excitation of channelrhodopsin-2 at saturation. *Proc. Natl Acad. Sci. USA* **106,** 15025–15030 (2009).
70. Berndt, A., Yizhar, O., Gunaydin, L. A., Hegemann, P. & Deisseroth, K. Bi-stable neural state switches. *Nature Neurosci.* **12,** 229–234 (2009).
71. Papagiakoumou, E., de Sars, V., Oron, D. & Emiliani, V. Patterned two-photon illumination by spatiotemporal shaping of ultrashort pulses. *Opt. Express* **16,** 22039–22047 (2008).
72. He, Q. *et al.* White collar-1, a DNA binding transcription factor and a light sensor. *Science* **297,** 840–843 (2002).
73. Reijmers, L. G., Perkins, B. L., Matsuo, N. & Mayford, M. Localization of a stable neural correlate of associative memory. *Science* **317,** 1230–1233 (2007).
74. Helmstaedter, M., Briggman, K. L. & Denk, W. 3D structural imaging of the brain with photons and electrons. *Curr. Opin. Neurobiol.* **18,** 633–641 (2008).
75. Wickersham, I. R. *et al.* Monosynaptic restriction of transsynaptic tracing from single, genetically targeted neurons. *Neuron* **53,** 639–647 (2007).

Acknowledgements We thank E. Boyden, G. Buzsaki, A. Hires, Z. Mainen, S. Peron, L. Petreanu, D. Rinberg and T. Sato for comments on the manuscript, and L. Tian and L. Looger for the genetically encoded calcium indicator (GCaMP3) used in Fig. 2.

Author Information Reprints and permissions information is available at www.nature.com/reprints. The authors declare no competing financial interests. Correspondence should be addressed to K.S. (svobodak@janelia.hhmi.org).

NATURE|Vol 461|15 October|doi:10.1038/nature08540

Electrophysiology in the age of light

Massimo Scanziani[1] & Michael Häusser[2]

Electrophysiology, the 'gold standard' for investigating neuronal signalling, is being challenged by a new generation of optical probes. Together with new forms of microscopy, these probes allow us to measure and control neuronal signals with spatial resolution and genetic specificity that already greatly surpass those of electrophysiology. We predict that the photon will progressively replace the electron for probing neuronal function, particularly for targeted stimulation and silencing of neuronal populations. Although electrophysiological characterization of channels, cells and neural circuits will remain necessary, new combinations of electrophysiology and imaging should lead to transformational discoveries in neuroscience.

More than 200 years ago, Galvani discovered that the function of the nervous system is intrinsically linked to electrical activity[1] (Fig. 1). Since then, generations of investigators have invested immense effort into building instruments capable of measuring and controlling this electrical activity. The unprecedented sensitivity and temporal resolution of modern electrophysiological tools allow us to study the properties of single ion channels and more complex phenomena extending to the activity of hundreds of cells within networks of neurons (Fig. 2). Thus, electrophysiology embraces all levels of our understanding of nervous system function, from the molecular to the behavioural.

By using metal, glass or silicon electrodes to record electrical signals associated with ion fluxes across neuronal membranes, electrophysiology allows us to listen directly to the 'language' of neurons at an extremely high signal-to-noise ratio. This is the main strength of the method, because electrical activity is recorded directly, without the need for a 'translator', that is, a probe that transforms electrical activity into a different signal. However, this is also the main weakness of electrophysiology, because electrical access to the nervous system necessitates physical contact with the tissue under investigation.

The use of light to probe neuronal function avoids the need for direct physical contact with the tissue, because light can travel through biological membranes. Furthermore — with a few exceptions such as the retina, where specific wavelengths need to be used — light does not interfere with neuronal function. Importantly, light offers numerous additional crucial advantages (Fig. 2): outstanding spatial resolution, allowing signals in even the smallest neuronal structures to be resolved[2,3]; the possibility for simultaneous measurement from a wide range of spatial locations[2,4]; and — with the use of genetically encoded and targetable probes — the critical advantage of being able to access specific cellular subtypes and subcellular domains[5].

To investigate neuronal function using light, however, a reporter is required. This typically takes the form of a molecule that converts membrane potential (or its consequences) into an optical signal. Thus, optical measurements are necessarily indirect. This means that careful calibration is required for quantitative measurements, and the properties of the molecular reporters and optical detection systems can limit the temporal resolution of functional measurements. However, owing in part to advances in our understanding of the biophysical, molecular and genetic mechanisms of excitability and synaptic transmission, the development and refinement of optical reporters is occurring at a very high pace. By harnessing these mechanisms, it is possible to develop optical reporters to monitor previously inaccessible variables with unprecedented spatial resolution and limited invasiveness (Table 1). In combination with new forms of microscopy, these reporters have been used to make a wide range of discoveries about nervous system function, including the quantitative link between presynaptic calcium and neurotransmitter release; the degree of chemical and electrical compartmentalization of dendritic spines[6]; the spatial extent and plasticity of dendritic spikes[7]; the spatial organization of cortical maps on the level of individual neighbouring neurons[8]; and functional map topography in the visual system[9]. Together, these discoveries herald a revolution in the way we investigate the function of the nervous system.

Does this revolution spell the end of electrophysiology? In this Review, we debate the respective strengths and weaknesses of electrophysiological and imaging approaches in neuroscience, and identify those applications in which optical approaches surpass, or will probably soon surpass, electrophysiology for both the monitoring and the manipulation of neuronal function. We also describe applications in which electrophysiology will remain necessary, and point towards important future developments. Finally, we highlight how, by being used in concert, these two techniques will lead to transformational discoveries in neuroscience.

The fundamentals

A fundamental consideration when comparing electrophysiological and optical approaches is the signal-to-noise ratio that can be achieved for a particular measurement. In electrophysiology, the noise sources are primarily instrumental, and the signal-to-noise ratio has been maximized by developing low-noise headstages and amplifiers, as well as by the gigaohm seal of the patch-clamp technique[10], which provides sufficient signal-to-noise ratio to allow resolution of the opening of single ion channels. In imaging, the measured signal — photon flux — results from conversion of the electrical (or chemical) signal into photons by means of a reporter, and is normally observed as a change in fluorescence (although some indicators use a change in reflectance, absorbance or even the ratio of two different fluorescence processes). By contrast to electrophysiology, in which electrons associated with the signal are typically plentiful, only a small number of photons are usually detected in optical measurements from small structures. If this number becomes sufficiently low, fluctuations around the mean become relatively large, a phenomenon called shot noise, and the signal-to-noise ratio of the measurement drops. To illustrate the contribution of shot noise, we will use the most common case, namely a change in fluorescence, which is

[1]Howard Hughes Medical Institute and Department of Biology, University of California, San Diego, 9500 Gilman Drive, La Jolla, California 92093-0634, USA. [2]Wolfson Institute for Biomedical Research and Department of Neuroscience, Physiology and Pharmacology, University College London, Gower Street, London WC1E 6BT, UK.

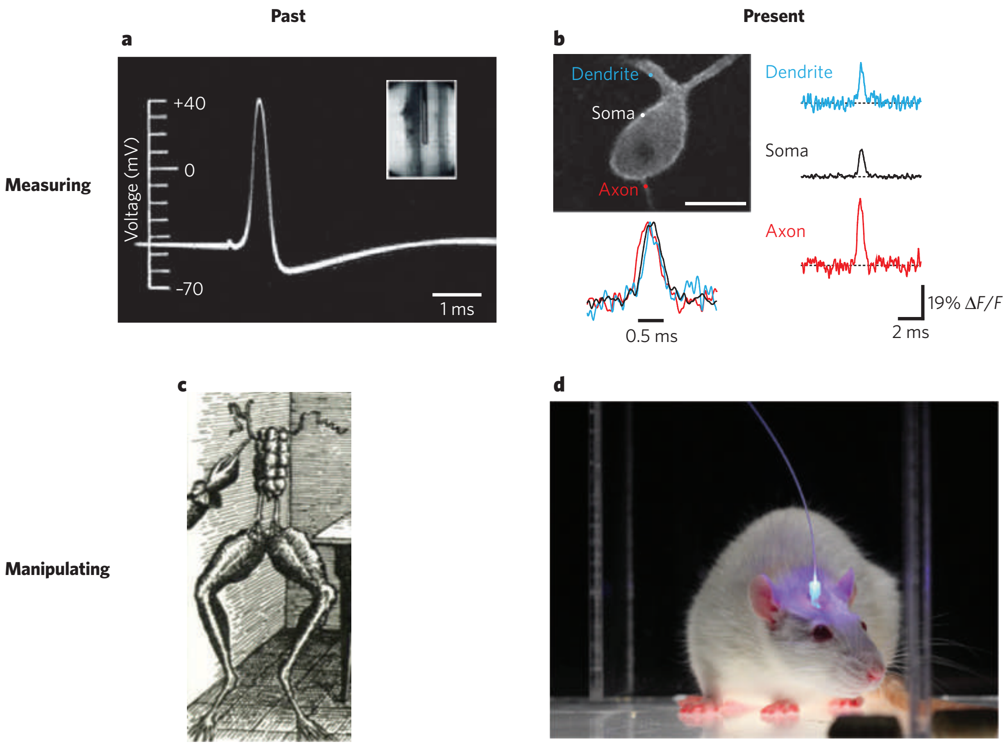

Figure 1 | Recording and stimulation: past and present. a, The first action potential recorded intracellularly from a neuron, by Hodgkin and Huxley[91]; inset, the electrode inserted into a giant squid axon. **b,** The multisite optical recording of action potentials in a cerebellar Purkinje neuron by using voltage-sensitive dyes[22]. **c,** The electrical stimulation of a frog nerve as illustrated by Galvani[1]. **d,** Optical deep-brain stimulation of neurons expressing microbial opsin genes. (Courtesy of V. Gradinaru, M. Mogri, J. Carnett and K. Deisseroth, Stanford University, California.)

measured as $\Delta F = F_{peak} - F_0$, where F_0 is the baseline fluorescence and F_{peak} is the above-baseline peak of the fluorescence transient associated with the electrical (or chemical) transient. The signal-to-noise ratio (SNR) of the measurement is thus proportional to the ratio of the signal change, ΔF, and the baseline shot noise ($F_0/\sqrt{N}$, where N is the number of photons detected): SNR $\propto (\Delta F/F_0)\sqrt{N}$.

Therefore, to optimize the signal-to-noise ratio, it is crucial to maximize both the change in fluorescence relative to the baseline and the total number of photons generated by the conversion of the electrical or chemical signal and detected by the instrumentation. Increasing the number of emitted photons can be achieved simply by increasing the number of reporter molecules (that is, the effective concentration of the reporter; however, at high concentrations there is a risk of perturbing the biological system studied and reducing $\Delta F/F_0$) and by improving reporter efficiency. Furthermore, improvements in excitation and detection efficiency — particularly with the use of two-photon microscopy[11], in which excitation is highly restricted in space and thus can be targeted to the source of the signal, and in which all collected photons can be used to form an image[12] — can also significantly improve the signal-to-noise ratio. Because the signal-to-noise ratio is linearly dependent on $\Delta F/F_0$, and only on the square root of N, optimizing reporter properties to maximize $\Delta F/F_0$ is in general a better strategy than simply increasing photon counts. In practice, additional considerations are important when choosing a reporter, such as photobleaching (which effectively reduces reporter concentration) and photodamage (which can affect physiological processes and cell health, and constrains the amount of excitation light that can be used and, thus, photon counts). Finally, electrical signals in neurons can be very rapid (<1 ms), which places further severe constraints on the kinetics of the reporter, and also on the detection system, with rapid scanning technology (together with improved collection optics and highly efficient detectors, such as those using photon counting) being required to faithfully record signals across single neurons or across networks[4]. Next we discuss how these principles and limitations apply when optical methods are used to record different kinds of electrical signal.

Measuring voltage

The primary language of neurons is electrical and involves changes in membrane voltage. The relevant fluctuations of membrane voltage associated with different electrical signals span three orders of magnitude, from ~100 μV (for quantal synaptic potentials) to ~100 mV (for action potentials), and the underlying currents can exhibit time courses of microsecond duration (Fig. 2). Being able to record these signals accurately is fundamental for our understanding of the computations performed by neurons. Developing optical approaches with the requisite sensitivity, dynamic range and speed would represent a tremendous advance over electrophysiology and would allow measurement of the spatiotemporal dynamics of membrane potential over the entire cell or across a population of neurons, information that is difficult or impossible to obtain using electrodes. Early attempts to use imaging to record activity focused on detecting changes in intrinsic optical properties of neurons, such as changes in light scattering correlated with membrane potential[13]. Although it was ultimately successful for low-resolution (~100 μm) imaging of brain function[14], this approach suffers from an inadequate signal-to-noise ratio for cellular imaging. More recently, there has been an intensive effort to develop optical reporters for recording membrane voltage, in conjunction with new developments in laser-scanning microscopy[4,15].

Let us be clear about the ultimate goal: to be able to compete with electrode-based techniques, a voltage-imaging method must be able to record subthreshold and suprathreshold events, without averaging, deep in intact tissue with submicrometre and submillisecond resolution, ideally from identified neurons. Currently, we are still far from this goal. The first milestone towards it would be to achieve reliable optical detection of single action potentials without averaging. So far, the most successful reporters have been the classic fast voltage-sensitive dyes (VSDs), such as the merocyanine dyes, which partition into one leaflet of the plasma membrane and generate fluorescence that depends on the electric field across the membrane[16]. By injecting these dyes into single neurons, it has been possible to record single-trial action potentials in small neuronal compartments such as distal dendrites[17], and such reporters have been used extensively to examine single-trial population activity *in vivo*[18,19]. Averaging of multiple trials has recently allowed the measurement of postsynaptic potentials and action potentials in dendritic spines in cortical slices[20,21], which represents a fundamental breakthrough as spines are currently inaccessible to patch-clamp recording electrodes. However, achieving single-trial resolution of subthreshold events has so far proved elusive. Averaging is an important limitation, as it prevents the measurement of spontaneous, non-stimulus-triggered subthreshold activity and response variability.

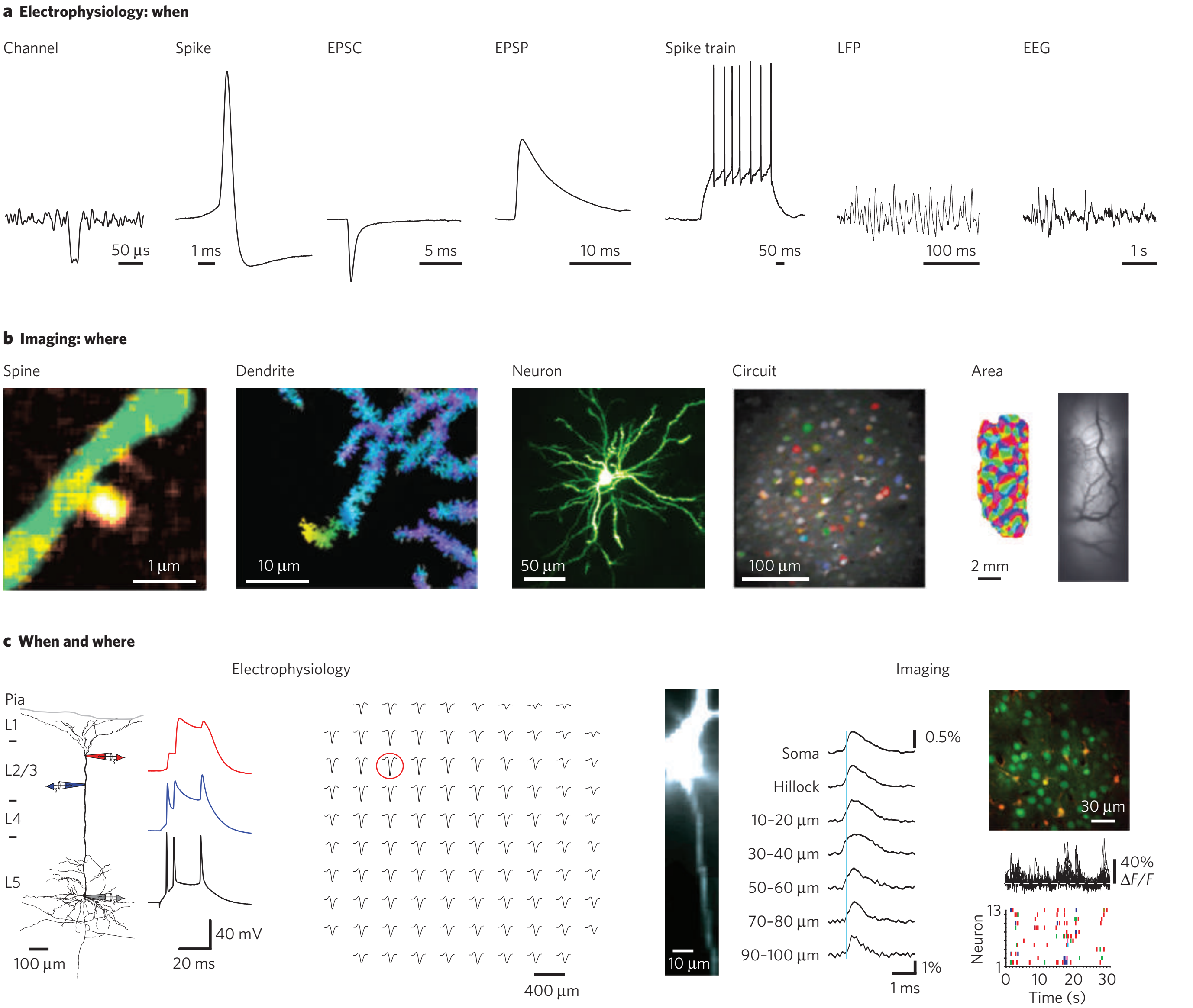

Figure 2 | Measuring the 'when' and 'where' of neuronal signals using electrophysiological and optical approaches. a, The primary strength of electrophysiology is its combination of time resolution and sensitivity, allowing the precise determination of the temporal pattern of neuronal signals over many orders of magnitude, with high signal-to-noise ratio. Representative examples shown are of a single nicotinic acetylcholine channel opening (courtesy of S. Hallerman, D. Ljaschenko and M. Heckmann, University of Würzburg, Germany); an action potential in a cerebellar interneuron *in vivo* (courtesy of P. Chadderton, University College London, UK); an excitatory postsynaptic current (EPSC), an excitatory postsynaptic potential (EPSP; courtesy of I. Duguid, University College London) and a spike train (P. Chadderton) from cerebellar granule cells *in vivo*; gamma oscillations (local field potential, LFP) recorded in the hippocampus of an anaesthetized rat (courtesy of B. Atallah, University of California, San Diego); and an electroencephalogram from an anaesthetized mouse during visual stimulation (B. Atallah). **b**, The primary strength of imaging approaches is their spatial resolution, allowing physiological events to be localized with high spatial precision over a wide range of scales. Representative examples shown are of calcium compartmentalization in a single hippocampal spine measured using a genetically encoded calcium sensor and two-photon microscopy (courtesy of Y.-P. Zhang and T. Oertner, Friedrich Miescher Institute, Basel, Switzerland); local calcium transient triggered by parallel-fibre synaptic input to a fine spiny branchlet in the dendritic tree of a cerebellar Purkinje cell (courtesy of A. Konnerth, Technical University Munich, Germany); a layer-2/3 pyramidal neuron filled with a calcium dye and visualized in mouse visual cortex *in vivo* using two-photon microscopy (courtesy of S. L. Smith, University College London); an orientation map in rat visual cortex measured using two-photon microscopy[8]; and optical imaging of voltage-sensitive-dye fluorescence to record receptive-field properties across cat visual cortex (courtesy of A. Benucci and M. Carandini, University College London). **c**, In some cases, both spatial and temporal information can be obtained using electrophysiological or imaging approaches on their own. Examples include measuring the interaction of backward-propagating action potentials with dendritic calcium spikes recorded in layer-5 (L5) cortical pyramidal neurons using three simultaneous patch-clamp recordings (courtesy of M. Larkum, University of Bern, Switzerland); recording the origin of the LFP signal in cat visual cortex using a 96-electrode array with a spatial resolution of 400 µm (reference spike from the electrode indicated in red; courtesy of I. Nauhaus and M. Carandini, University College London); optical mapping of the initiation site of the action potential in layer-5 pyramidal neurons using voltage-sensitive dyes (courtesy of L. Palmer and G. Stuart, Australian National University, Canberra, Australia); and optical monitoring of activity patterns in rat visual cortex loaded with a calcium dye (green), counterstained with an astrocyte-specific marker (sulforhodamine 101, orange) and imaged using two-photon microscopy, with traces showing calcium transients and detected spiking activity (raster; for ≥2 detected spikes; 2 spikes red, 3 green, 4 dark blue, 5 light blue, 6 pink and 7 brown) simultaneously recorded from 13 neurons in the awake animal (courtesy of D. Greenberg, A. Houweling and J. Kerr, Max Planck Institute for Biological Cybernetics, Tübingen, Germany).

A number of factors contribute to the relatively low effective signal-to-noise ratio of this approach. First, despite decades of screening experiments, for many of the commonly used dyes the fluorescence change per unit change in membrane potential is relatively small, although there are some exceptions (see, for example, ref. 22). Second, VSDs indiscriminately label internal and plasma membranes; dye that labels internal compartments does not contribute to the signal but does contribute to the resting fluorescence, which decreases the $\Delta F/F_0$ value per unit change in membrane potential and, thus, the signal-to-noise ratio. Finally, VSDs suffer from the dual problems of phototoxicity and bleaching, which limit the available excitation intensity and the duration of the experiments. The use of second-harmonic-generation microscopy can help eliminate the problem of intracellular background fluorescence, as in this approach only dye molecules in the plasma membrane contribute to the signal[21,23]. However, the effective signal-to-noise ratio of second-harmonic-generation microscopy remains limited, owing in part to photodamage associated with the need for high laser intensities; furthermore, given that second-harmonic generation normally relies on the detection of transmitted light, it is unlikely to be suitable for most mammalian *in vivo* preparations.

An approach that shows tremendous promise is the design of genetically encoded voltage sensors. Such sensors have an important advantage over conventional VSDs: their expression can be genetically targeted, both to subpopulations of neurons, making them particularly useful for targeted imaging of population activity, and subcellularly, to the plasma membrane and away from intracellular organelles. The design of such sensors has broadly followed one of two strategies. First, fusions between green fluorescent protein (GFP) and a voltage-gated channel, such as the Shaker potassium channel[24], allow voltage-dependent conformational changes in the channel to be translated into GFP fluorescence changes. An alternative strategy is the use of hybrid GFP systems, in which fluorescence resonant energy transfer is used to report the interaction between GFP, anchored to the cytoplasmic face of the membrane, and a dye that undergoes voltage-dependent redistribution between the inner and outer membrane leaflets.

Both strategies have yielded sensors with good voltage sensitivity. The hybrid voltage sensors have $\Delta F/F$ values of up to 34% per 100 mV (ref. 25), and further improvements are expected, particularly for sensors based on GFP–channel fusions, which can exploit the cooperativity of channel gating. However, the favourable voltage sensitivity of these sensors is undermined by their slow kinetics, with on-rates typically of the order of tens of milliseconds (although hybrid voltage sensors have more rapid kinetics), making detection of single action potentials difficult. Other problems include poor targeting to the plasma membrane, increasing the background signal; low brightness, resulting in low photon counts; and the fact that the inclusion into the membrane of mobile molecules (that is, compounds or proteins that translocate from one leaflet of the membrane to the other when the voltage across the membrane changes) leads to the increase of membrane capacitance (so-called capacitive loading). In some cases, this is so severe that it can block action-potential generation[15]. As a consequence of these limitations, the technical milestone of reliably recording single action potentials using a genetically encoded voltage reporter has not yet been achieved in any neuron. Furthermore, as with any genetically encoded probe, possible unanticipated physiological effects resulting from exogenous expression of proteins need to be assessed, in part by using electrophysiological approaches. Nevertheless, there is great optimism in the field that rational probe design, coupled with high-throughput screening methods, will soon allow us to achieve this milestone.

Table 1 | Classes of optical probes and reporters

Type of molecule	Illustration	Examples
Measuring		
Voltage sensors	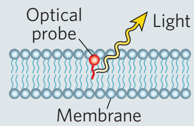	JPW3028* (refs 17, 20) hVOS† (ref. 25) VSFP† (ref. 96)
Calcium sensors	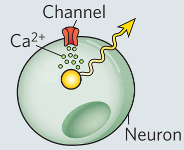	OGB-1* (refs 8, 30) Fluo-4* (ref. 97) D3cpv† (ref. 38) TN-XXL† (ref. 39) GCaMP3† (ref. 98)
Receptor/channel reporters	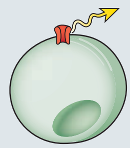	Fluorescence-labelled Shaker† (ref. 69)
Synaptic release reporters	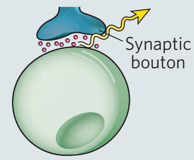	FM 1-43* (ref. 63) SynaptopHluorin† (ref. 65) FLIPE† (ref. 66) SuperGluSnFR† (ref. 64)
Manipulating		
Optogenetic activators	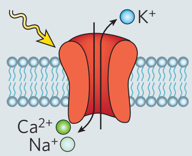	ChR2† (refs 40, 47, 48, 54) LiGluR† (ref. 49)
Optogenetic inhibitors	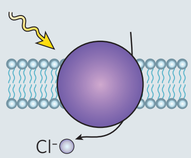	Halorhodopsin (NpHR)† (refs 50, 51)

Classes of optical probes used for measuring and manipulating neuronal activity. Representative examples of probes in current use are provided, along with relevant citations. The illustrations show in schematic form the operation of the respective probes. ChR2, channelrhodopsin-2; FLIPE, fluorescent indicator protein for glutamate; hVOS, hybrid voltage sensor; LiGluR, light-gated ionotropic glutamate receptor; NpHR, *Natronomonas pharaonis* halorhodopsin; VSFP, voltage-sensitive fluorescent protein. *Organic probe. †Genetically encodable probe.

Calcium as a reporter of activity

Calcium is a major signalling molecule in neurons, and synaptic input and membrane voltage fluctuations often trigger changes in intracellular calcium concentration. Hence, calcium indicators have long been successfully used to infer both subthreshold and suprathreshold activity in neurons. Organic calcium-sensitive dyes, which take advantage of the pronounced calcium concentration gradient across the plasma membrane, represent one of the great success stories of synthetic chemistry[26]. Such dyes are sensitive enough to allow the opening of a single calcium-permeable channel in a spine to be detected using two-photon microscopy[27]. These dyes can therefore be used to monitor the occurrence of both action potentials and synaptic input to spines, allowing even single-vesicle events to be detected reliably, which in turn permits optical quantal analysis[28] and the demonstration that spines can act as individual functional compartments in terms of calcium signalling[6]. Although light scattering, movement problems and the unknown dendritic distribution of active synaptic input have so far prevented the direct detection of synaptic input patterns *in vivo* (with rare exceptions; see ref. 29), membrane-permeant calcium dyes have been used very successfully to monitor network activity in neurons and glia in the intact brain, under both anaesthetized and awake conditions[8,30–32]. However, even with these outstanding indicators, the slow time course of the intracellular calcium signal triggered by action potentials, coupled with the limitations of *in vivo* imaging, have made it challenging to reliably detect single action potentials and reconstruct the action-potential firing pattern[31,33].

The design of genetically encoded calcium indicators has also attracted intense interest in recent years. These indicators are typically based on a calcium-sensitive molecule, such as calmodulin[34] or troponin[35], fused to GFP or other fluorescent proteins, with calcium binding reported by fluorescence changes due to alterations in the efficiency of fluorescence resonance energy transfer or changes to the chromophore environment. Although several generations of sensor development have yielded vastly improved properties, the current range of indicators remain inferior to synthetic indicators in terms of brightness, speed and signal-to-noise ratio when making direct comparisons under identical conditions[36,37]. Furthermore, in practice their use in transgenic animals has often been associated with sensor inactivation, reduced dynamic range or poor protein stability. Thus, despite tantalizing recent advances[38,39], as with genetically encoded voltage reporters, no genetically encoded calcium sensor has yet been shown to reliably report single action potentials in neurons *in vivo*, although the genetically encoded calcium indicators are closer to doing so. Again, rational optimization of sensor properties, aided by structure–function analysis, should soon allow this goal to be achieved.

Replacing the stimulation electrode with a beam of light

Since a method for the direct stimulation of nerves was first reported, over 200 years ago[1], the basic approach, which is based on the use of metal electrodes, has changed surprisingly little; that is, until the advent of optical methods (Fig. 1c, d).

The two main ways to trigger activity in the nervous system are sensory and electrical stimulation. The former is the method preferred by sensory physiologists, because by engaging the nervous system in an ethologically relevant manner it allows the study of the representation of the various features of the physical world through neuronal activity. By contrast, electrical stimulation is used to study mechanisms, such as synaptic transmission, because by bypassing sensory interfaces it can be applied to isolated preparations; furthermore, the activity generated by electrical stimuli is temporally precise and reproducible. Electrical stimulation involves the use of metal or glass electrodes to trigger action potentials in individual neurons or groups of neurons. This approach has three key limitations: it lacks specificity (except when stimulating single neurons or single synapses); inhibiting neurons is difficult; and it is invasive, causing damage at high stimulation intensities. These problems can be overcome by using two complementary optical approaches. The first is the use of caged compounds, which involves a pharmacologically active substance that excites or inhibits neurons, delivered in an inert ('caged') form and activated ('uncaged') by breaking a photolabile bond, generally with ultraviolet radiation. The second is the use of optogenetic tools, a new class of light-sensitive proteins that, when expressed in neurons, allow their activity to be modulated by light. These proteins are either intrinsically coupled to ionic conductances or pumps, or affect neuronal excitability through second-messenger pathways[40–43].

In the brain, neurons of various types and genetic compositions (for example excitatory, inhibitory, projection and local neurons) spatially intermingle with fibres of passage. Consequently, stimulation electrodes are unselective with respect to the structures and cell types that they activate. By contrast, caged compounds and optogenetic tools allow groups of neurons, individual neurons and specific subcellular compartments to be stimulated with extraordinary spatial and genetic specificity. Simply uncaging glutamate (the main excitatory transmitter in the brain) predominantly activates somatodendritic compartments of neurons rather than intermingled axons, consistent with the distribution of glutamate receptors. This approach allows the rapid generation of connectivity maps between cortical layers in cortical slices[44]. With two-photon activation, glutamate uncaging can be used to activate individual synapses along a dendrite[45]. Genetic specificity can be obtained by expressing receptors that are not naturally present in the system. Expression of purinoceptors in genetically defined fly neuronal populations, for example, allows activation of these neurons through ATP uncaging, and the study of the ensuing behavioural outputs[46].

Optogenetic tools represent another valid alternative to the stimulation electrode, and greatly surpass it in specificity and versatility[40–43]. Targeted expression of light-activated molecules such as channelrhodopsin[47,48], light-gated ionotropic glutamate receptor[49] or halorhodopsin[50,51] allows neurons or their subcellular compartments to be stimulated with extraordinary spatial, temporal and genetic specificity. These new optical tools can perform tasks well beyond the capabilities of conventional stimulation electrodes, such as independent stimulation of multiple intermingled populations[52], bistable activation of neurons[53] and stimulation of defined second-messenger pathways (for example to mimic modulatory neurotransmitter pathways[41,43]). These approaches can be harnessed to map functional connectivity[54], to influence the dynamics of neuronal circuits[47,48,50,55] and, ultimately, to control behaviour[49,56,57]. In the long term, complete cellular-level and subcellular-level structural, molecular and genetic maps of the nervous system — the connectome[58] — will be required to target probes to select cell types or subcellular locations to further enhance the precision of these optical probes.

Finally, the inducible expression of optogenetic tools will make it possible to bridge the current gap between sensory and electrical stimulation. One important drawback of electrical stimulation is the uncertainty over whether the ensemble of stimulated inputs actually corresponds to a physiologically relevant pattern, that is, whether a sensory stimulus would ever activate that particular combination of stimulated afferents. The activity-dependent expression of optogenetic tools such that only neurons recruited by a specific sensory stimulus or by a particular task express the protein[59] will represent a first step in solving this problem. Such activity-driven expression will allow the study of the behavioural output generated by the selective activation or inhibition of functionally defined neuronal subpopulations. Similarly, activity-driven expression of optogenetic tools will make it possible to determine connectivity patterns and circuit dynamics of functionally related neuronal ensembles. These recent developments thus afford more specific and much more controlled manipulation of the nervous system, allowing sophisticated tests of causality (see page 923). We can now imagine a time in the near future when activation of neuronal circuits will no longer rely on the centuries-old metal stimulation electrode.

Voltage clamp

A difficult technique to perform using optical tools is voltage clamp, a method that allows the measurement of currents passing through membranes. Electrophysiologists achieve voltage clamp using feedback amplifiers that hold the potential across the membrane at a defined voltage by injecting into the neuron currents equal in amplitude and opposite in sign to those that flow through the membrane. These injected currents provide a measure of the ionic and capacitive currents naturally flowing in and out of neurons. Voltage clamp has led to fundamental discoveries, such as the biophysical mechanisms underlying action potentials[60], the characteristics of synaptic conductances[61] and the functional properties of single ion channels[62]. Let us consider how voltage clamp might be achieved by optical means.

An 'optical voltage clamp' could be realized by expressing two light-gated ion channels, one selective for Na^+, the other for K^+, and each activated by different wavelengths, thus providing the basis for selective light activation of an inward and an outward current. Given sufficient expression of these channels, it should be possible to achieve any arbitrary membrane potential between the reversal potentials of the two channels. The membrane potential would be simultaneously monitored using a voltage probe and coupled to the source of excitation light with a feedback mechanism, with the clamp speed depending on the kinetics of the channels and their density relative to the membrane capacitance. Although this system would permit voltage clamp, quantifying the light-activated currents would be difficult, requiring knowledge of factors including the membrane area, the intensity of the light hitting the membrane, the density of the light-activated channels and the relationship between the light intensity and the single-channel photocurrent. A potential benefit of this optical voltage clamp would be improved 'space clamp', that is, voltage control of all neuronal compartments, which is normally impossible to

achieve with a single electrode. This would allow proper measurement of current sources from all over the dendritic tree.

Given that implementing such a system will be very challenging, it is worth asking whether voltage clamp itself can be replaced. Indeed, our knowledge of the molecular mechanisms of excitability and synaptic transmission may allow us to investigate channel and synaptic function without current measurements, thus making voltage-clamp recordings unnecessary. For example, synaptic function can be assessed by probing the status of the underlying components, such as by monitoring neurotransmitter release[63–66] or the activation of transmitter-gated channels[6,28]. In turn, activation of distinct subtypes of voltage-gated channel can be probed by directly monitoring conformational changes rather than conductance, for example by using subunit-specific resonance energy transfer as a spectroscopic molecular ruler[67,68]. Preliminary work has shown that even single-channel resolution can be achieved using such an all-optical approach[69], revealing information about channel conformations not obtainable through electrophysiological recordings. However, such a targeted approach can only be used to identify known, and well-characterized, channels; and biophysical characterization of channels demands voltage control. Thus, voltage clamp is likely to remain an indispensable tool for neuroscientists in the future.

Promises and challenges

To replace or complement electrophysiological approaches, optical probes must be implemented *in vivo,* ideally in a behaving organism. This will provide a range of unprecedented opportunities, but it also highlights several hurdles that must be overcome.

Recording from populations

One of the key arenas in which imaging can already surpass the use of electrodes is simultaneous recording from many neurons. Sensory stimuli and motor output are represented by the activity of ensembles of neurons. Within these ensembles, each neuron may respond to a particular feature, or a specific combination of features, of the stimulus, such as position in space, frequency or intensity. The same is true for motor output, where a particular movement in space is specified by the activity of select ensembles within a population of neurons in the motor cortex. Thus, the experimental ideal would be to record every spike from every neuron in response to a sensory input and during the ensuing behavioural output, and use this information as a first step in working out the neural processes underlying this transformation. This is an enormous challenge, because computations in the mammalian nervous system engage thousands to millions of neurons. Electrophysiologists have increased the sampling density in their experiments by using microarrays featuring multiple electrodes[70], but such approaches are limited by the electrodes' invasiveness and finite spacing, and by the difficulty of identifying the origin of blindly recorded neuronal signals.

Optical probes may ultimately make this dream experiment possible. Early steps have involved using multicellular loading of membrane-permeant calcium dyes[8,30–32], as indicators of spiking activity in networks (Fig. 2). In combination with transgenic mouse lines expressing genetically encoded fluorescent markers in specific neuronal subtypes, this approach allows identification of the imaged cells[71]. Unfortunately, as discussed above, the imaging of calcium transients does not offer the same signal-to-noise ratio as electrophysiological recordings, and the slow kinetics of the recorded signal often prevent resolution of individual spikes in a train, unless sophisticated analysis techniques are used[31,33]. These problems, coupled with limitations in scanning speed, make it difficult to define the temporal relationship of spiking between different neurons. Finally, calcium transients are best correlated with suprathreshold neuronal activity, and provide little information about subthreshold membrane-potential fluctuations. Despite all of these drawbacks, however, no electrophysiological approach allows the activity and spatial location of so many active neurons to be monitored simultaneously[8].

Recording the activity of a population of neurons using voltage-sensitive dyes[14] is a complementary approach to calcium imaging: although single-cell resolution is usually not achieved, the kinetics of the signal can follow fast, subthreshold fluctuations in membrane potential[72]. This approach has been used to discover important functional organizing principles in the brain, such as how ongoing activity interacts with visually driven activity[19], and the existence of spontaneously emerging maps of activity[18]. Thus, VSD imaging offers not only the advantages of electrophysiological local field potential recordings, but also the ability to monitor large brain areas simultaneously.

Recording at depth

Light scatters and is attenuated as it passes through tissue. This is detrimental to the high spatial resolution possible with optical approaches — a major advantage over electrophysiology — and to the intensity of the signal that can be delivered to and collected from deeper brain areas. Given the unalterable physical properties of brain tissue, this represents an absolute technical barrier that is difficult to overcome. As a consequence, high-resolution one-photon imaging has been limited to thin preparations or only the most superficial regions (depths <50 μm) of intact tissue. Nonlinear microscopy, including two-photon and second-harmonic-generation microscopy, has been shown to increase penetration depth substantially, but these approaches are currently still limited to the superficial regions of the brain (depths of ~1,000 μm; ref. 73). One way to overcome the fundamental limitations imposed by scattering is simply to remove the overlying tissue to image deeper regions[74]. A less damaging alternative is to insert a probe, such as an optical fibre or a gradient-index lens, into the brain region of interest. Such microendoscopy probes can be used for both one-photon and two-photon imaging in deep regions[4]. The localization of the probes themselves limits the spatial extent of the optical sampling possible. Furthermore, their size, which is typically considerably greater than that of a recording electrode, also means that optical probes may be more invasive than using classical electrophysiological approaches.

Independent control of multiple cells

Understanding how the dynamics of neural networks underpin behaviour requires not only the faithful recording of activity across populations in large, three-dimensional volumes *in vivo*, but also the ability to manipulate the activity of the active neurons (see page 923). Because the spatiotemporal dynamics of activity typically are asynchronous, with millisecond timing differences among different cells, this requires an approach that allows targeted manipulation of individual neurons with millisecond precision. When systematic timing differences exist between different genetically defined populations of neurons, such as interneurons and principal cells[75,76], optogenetic tools with different wavelength spectra could be used to regulate the activity of different populations individually[52]. However, ultimately it is necessary to achieve single-cell resolution across the population, which requires spatial restriction of activation to single neurons. This can in principle be achieved using two-photon excitation, which has recently been demonstrated for channelrhodopsin[77]. Protein engineering is likely to yield a new generation of optogenetic probes with large two-photon cross-sections and a wide range of wavelength selectivities. This must be paired with further development of rapid three-dimensional scanning approaches to targeting two-photon excitation at the appropriate cells with millisecond precision[78,79].

Recording activity during natural behaviours

Great progress has recently been made in adapting behavioural assays to head-fixed rodents, thereby allowing high-resolution imaging of the nervous system to be performed during behaviour[32] (see also page 923). However, natural expression of many behaviours requires animals to move freely in their environment. There exists a long tradition of using implanted multi-unit electrodes in freely moving animals to correlate neural activity with behaviour[70,80], and this was recently complemented with whole-cell patch-clamp recording[81] (Fig. 3a), providing a temporal resolution that has not yet been matched by optical approaches. The recent development of head-mounted miniaturized two-photon microscopes[82], together with fibre-optic two-photon microendoscopy for imaging deep

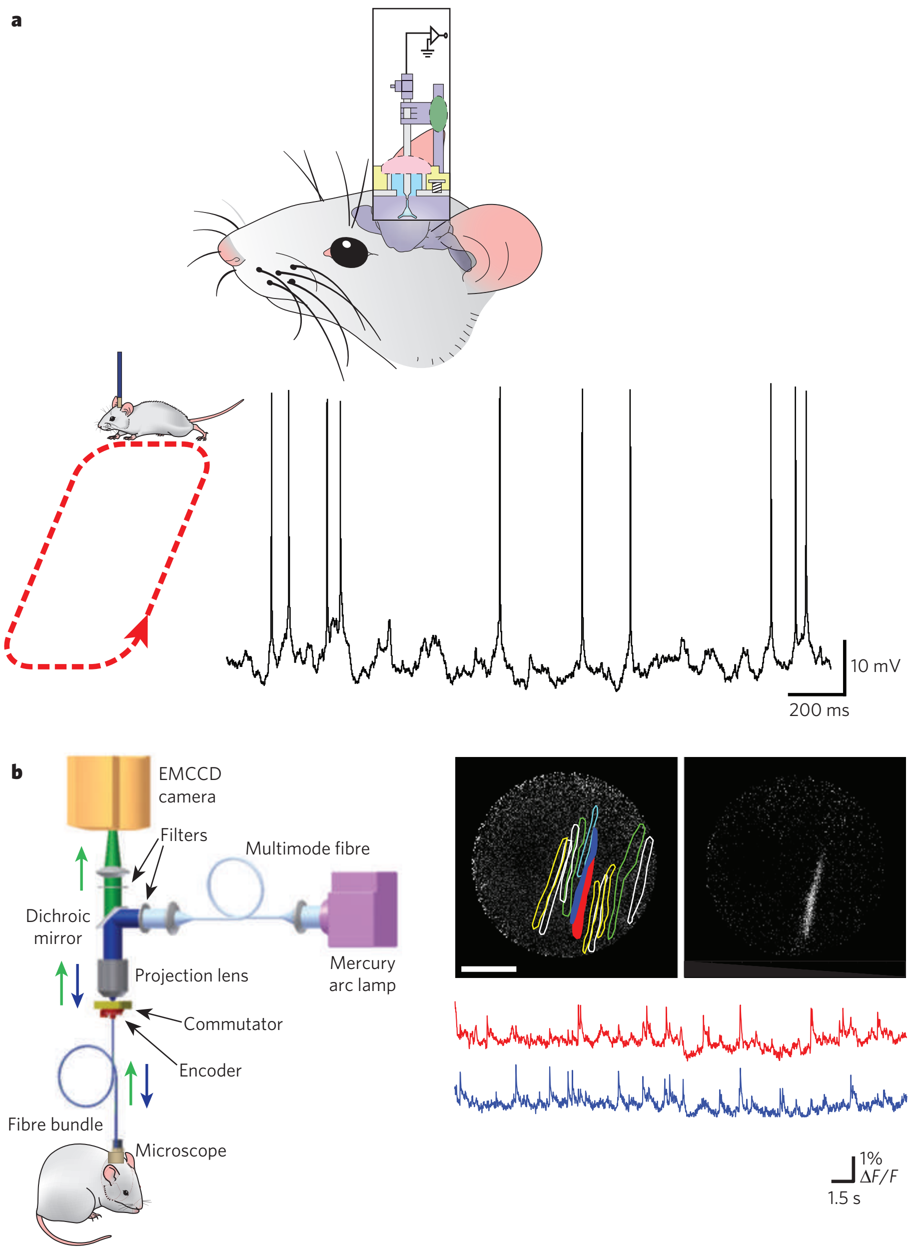

Figure 3 | Recording and imaging on the move. a, Whole-cell patch-clamp recording of a hippocampal neuron in a rat freely moving on a linear track. Top, illustration of the assembly for maintaining patch-clamp recordings in freely moving rats[81]: an electrode holder is mounted on the rat cranium and holds an electrode that is cemented in place at two anchoring sites (shown in green and pink) once a recording is made. Bottom, representative trace of membrane potential recorded from a hippocampal pyramidal neuron during free movement of the rat around a rectangular track (courtesy of J. Tukker and M. Brecht, Humboldt University, Berlin, Germany). **b,** Imaging population activity with single-cell resolution in freely moving animals. Left, illustration of the set-up. Excitation light (blue) propagates in one direction through an optical-fibre bundle. Emitted fluorescence (green) returns along the same path, passes through the dichroic mirror and is imaged using an electron-multiplying charge-coupled-device (EMCCD) camera. Right, viewed from the brain surface, the dendritic arborizations of 12 cerebellar Purkinje cells labelled with calcium-sensitive fluorescent dye are identified as parallel stripes in an unrestrained awake mouse sitting quietly (scale bar, 100 μm); a calcium signal in the red cell is shown in the right-hand image. The traces in the lower panel show the time course of Ca^{2+} signals from the red and blue cells. (Panel **b**, modified, with permission, from ref. 84.)

networks[4] and fibre arrays for one-photon imaging of population activity[83,84] (Fig. 3b), should soon enable us to exploit the many advantages of the optical approach. These imaging strategies, in combination with the development of new generations of genetically encodable optical probes with high signal-to-noise ratios, should allow long-term experiments in freely moving animals in which spatiotemporal patterns of activity in genetically defined networks can be correlated with natural behaviours.

Improving electrophysiology

The optical approaches we have described above are developing very rapidly, but electrophysiology is by no means a static discipline. Even a well-established technique such as patch-clamp recording is still being refined and used in new applications, such as its recent implementation in making whole-cell recordings from single neurons in freely moving animals[81] (Fig. 3a). However, a series of developments are under way that aim to overcome some of the key traditional limitations of electrophysiology. First, there is a widespread effort to produce ever-smaller electrodes — with the target being tip sizes of much less than 1 μm — using nanofabrication techniques such as focused-ion-beam microscopy[85] or by assembling carbon nanotubes[86,87]. Such electrodes could not only be used to record from extremely fine structures such as boutons and spines, but may also improve the signal-to-noise ratio for isolating individual units in extracellular recordings. In addition, owing to their fine calibre, they help to minimize tissue distortion as they are inserted into the brain. Second, to improve spatial sampling in recordings of population activity, multi-electrode arrays are being assembled that contain larger numbers of electrodes with ever-finer spacing[80,88]. These arrays will allow population activity to be sampled, and afferent inputs to be stimulated, with a much higher spatial precision than before. Finally, research into the physical basis for the long-term interactions between silicon-based electrodes and neural tissue[89] should eventually allow invasive brain–machine interfaces to target populations of neurons more precisely, more reliably and over longer timescales.

Perspective

Throughout their history, imaging and electrophysiology have always been closely linked (an example of early work is that in which an optical approach was used to report electrical activity in the electric fish[90]). However, in the context of electrophysiology, imaging was (until recently) primarily used for visualization during electrophysiological recordings. For example, the pioneering experiments of Hodgkin and Huxley[91] relied critically on their visualizing the squid axon at high

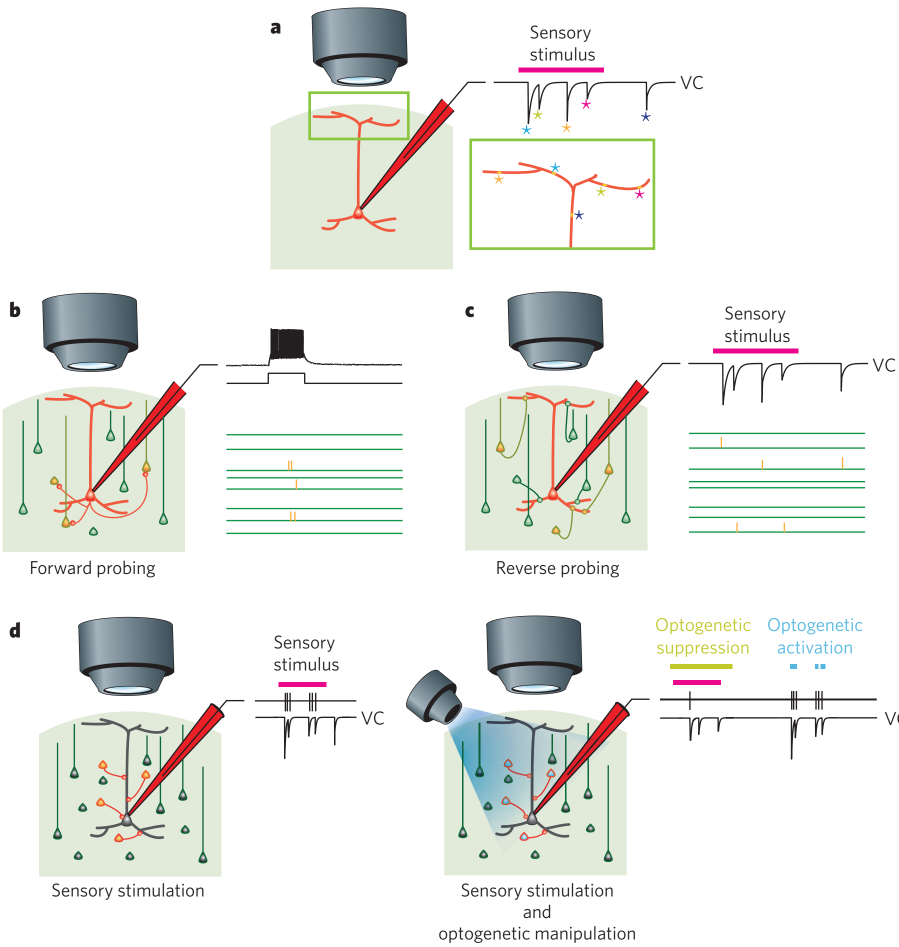

Figure 4 | Synergistic combinations of electrophysiology and imaging. **a**, The superior temporal resolution of electrophysiology can be combined with the spatial resolution offered by imaging to define the spatiotemporal distribution of synaptic inputs to the dendritic tree (red). Patch-clamp recording from the soma of a pyramidal cell *in vivo* is used to measure sensory-evoked synaptic input in voltage clamp (VC), which is then correlated with the location of the input (asterisks) in the dendritic tree by measuring synaptically activated calcium signals using two-photon imaging. **b**, Forward probing of connectivity in networks (see ref. 99). Targeted whole-cell patch-clamp recording from a single principal neuron is accompanied by simultaneous imaging of activity in the local network using a calcium sensor. Triggering of spikes in the principal neuron using an injected current pulse (top traces) allows postsynaptic neurons in the network activated by the recorded neuron (green, silent neurons; yellow, neurons exhibiting spikes) to be identified using two-photon population calcium imaging[8,31,32] with genetically encoded or bulk-loaded[30] calcium indicators. **c**, Reverse probing of presynaptic connectivity in networks (see ref. 100). Recording of sensory-evoked synaptic currents in a postsynaptic neuron using voltage clamp is accompanied by simultaneous imaging of activity in potential presynaptic partners in the local network using two-photon population calcium imaging[8,31,32]. Reverse correlation between presynaptic spikes and synaptic currents can be used to identify functional presynaptic partners activated by sensory stimulation. **d**, Combining targeted patch-clamp recording of receptive-field responses with optogenetic manipulation of defined networks. Sensory responses are recorded from a visually targeted neuron as spiking responses, or the underlying synaptic currents are recorded in voltage clamp (VC). To determine the causal contribution of particular presynaptic cell types to the sensory-evoked response, optogenetic probes (for example channelrhodopsin[47,48] and/or halorhodopsin[50,51]) are expressed in genetically defined cell types (red neurons) in the same network. These probes can then be activated with the appropriate wavelengths of light, either removing the contribution of these neurons to sensory-evoked activity (in the case of halorhodopsin) or activating them (in the case of channelrhodopsin, shown here), to modulate the sensory response or, in the absence of sensory stimulus, to mimic sensory input patterns.

enough resolution to enable them to precisely position the microelectrode inside it (Fig. 1); more recently, two-photon imaging has been used to target patch-clamp recordings to visually or genetically identified cell types *in vivo*[92–94], in turn allowing essential calibrations for a new generation of genetically encoded sensors[38,39].

Optical approaches can now be used to collect functional data and manipulate the nervous system. This provides remarkable opportunities for combining the complementary strengths of electrophysiology and imaging. In particular, the synergism of the exceptional time resolution, signal-to-noise ratio and ability to voltage clamp provided by electrophysiology with the superior spatial sampling and resolution of imaging and optical probing will enable us to link the function of the nervous system to its underlying cellular and molecular structures with unprecedented precision.

Compelling examples of such synergisms between electrophysiology and imaging in linking function to structure include the localization of the functional inputs onto a dendritic tree to constrain the rules for dendritic computations (Fig. 4a); the combination of optical imaging and single-unit[18,19] or multi-unit[95] recording to reveal the role of single neurons in network dynamics; and the combination of patch-clamp recording and two-photon population imaging to map functional connectivity in networks *in vivo* (Fig. 4b, c), which can ultimately reveal the composition of functional ensembles of neurons during behaviour. In addition, combining electrophysiology with optogenetic tools offers the possibility of directly testing causality between structure and function: by selectively and rapidly activating or silencing specific structures, such as neuronal compartments, neuronal types and entire circuits, we will be able to assess their impact on the function of a neuron, on the

dynamics of a circuit and on the behaviour of an organism. For example, such optogenetic tools will be instrumental in establishing the roles of specific dendritic compartments, specific inhibitory neurons or specific layers of neurons in determining the receptive-field properties of cortical sensory responses (Fig. 4d).

This synergism should significantly quicken the pace of discovery as we move towards one of the major goals in neuroscience, namely to link the structure of the brain to its function, and will allow both imaging and electrophysiology to flourish in harmony long into the future. ■

1. Galvani, L. De viribus electricitatis in motu musculari, commentarius. *Bonon. Sci. Art. Inst. Acad.* **7,** 364–415 (1791).
2. Ji, N., Shroff, H., Zhong, H. & Betzig, E. Advances in the speed and resolution of light microscopy. *Curr. Opin. Neurobiol.* **18,** 605–616 (2008).
3. Hell, S. W. Far-field optical nanoscopy. *Science* **316,** 1153–1158 (2007).
4. Wilt, B. A. *et al.* Advances in light microscopy for neuroscience. *Annu. Rev. Neurosci.* **32,** 435–506 (2009).
5. Luo, L., Callaway, E. M. & Svoboda, K. Genetic dissection of neural circuits. *Neuron* **57,** 634–660 (2008).
6. Nimchinsky, E. A., Sabatini, B. L. & Svoboda, K. Structure and function of dendritic spines. *Annu. Rev. Physiol.* **64,** 313–353 (2002).
7. Losonczy, A., Makara, J. K. & Magee, J. C. Compartmentalized dendritic plasticity and input feature storage in neurons. *Nature* **452,** 436–441 (2008).
By using two-photon glutamate uncaging on individual dendritic branches, this study shows that propagation of dendritic spikes to the soma can be persistently strengthened in a branch-specific manner, and may thus represent a mechanism to store branch-specific synaptic input patterns.
8. Ohki, K., Chung, S., Ch'ng, Y. H., Kara, P. & Reid, R. C. Functional imaging with cellular resolution reveals precise micro-architecture in visual cortex. *Nature* **433,** 597–603 (2005).
This paper uses *in vivo* two-photon calcium imaging of large neuronal populations in the visual cortex with single-cell resolution to reveal the fine-scale architecture of orientation maps in rats and cats, and demonstrates an unexpectedly sharp border between populations of neurons tuned to distinct orientations in cats (but not rats).
9. Bonhoeffer, T. & Grinvald, A. Iso-orientation domains in cat visual cortex are arranged in pinwheel-like patterns. *Nature* **353,** 429–431 (1991).
In vivo optical imaging of intrinsic signals in cat visual cortex reveals that the two-dimensional structure of orientation maps is organized around orientation centres in a pinwheel manner.
10. Hamill, O. P., Marty, A., Neher, E., Sakmann, B. & Sigworth, F. J. Improved patch-clamp techniques for high-resolution current recording from cells and cell-free membrane patches. *Pflügers Arch.* **391,** 85–100 (1981).
11. Denk, W., Strickler, J. H. & Webb, W. W. Two-photon laser scanning fluorescence microscopy. *Science* **248,** 73–76 (1990).
12. Denk, W. & Svoboda, K. Photon upmanship: why multiphoton imaging is more than a gimmick. *Neuron* **18,** 351–357 (1997).
13. Stepnoski, R. A. *et al.* Noninvasive detection of changes in membrane potential in cultured neurons by light scattering. *Proc. Natl Acad. Sci. USA* **88,** 9382–9386 (1991).
14. Grinvald, A. & Hildesheim, R. VSDI: a new era in functional imaging of cortical dynamics. *Nature Rev. Neurosci.* **5,** 874–885 (2004).
15. Sjulson, L. & Miesenböck, G. Optical recording of action potentials and other discrete physiological events: a perspective from signal detection theory. *Physiology* **22,** 47–55 (2007).
16. Salzberg, B. M., Obaid, A. L., Senseman, D. M. & Gainer, H. Optical recording of action potentials from vertebrate nerve terminals using potentiometric probes provides evidence for sodium and calcium components. *Nature* **306,** 36–40 (1983).
17. Djurisic, M., Antic, S., Chen, W. R. & Zecevic, D. Voltage imaging from dendrites of mitral cells: EPSP attenuation and spike trigger zones. *J. Neurosci.* **24,** 6703–6714 (2004).
18. Tsodyks, M., Kenet, T., Grinvald, A. & Arieli, A. Linking spontaneous activity of single cortical neurons and the underlying functional architecture. *Science* **286,** 1943–1946 (1999).
19. Arieli, A., Sterkin, A., Grinvald, A. & Aertsen, A. Dynamics of ongoing activity: explanation of the large variability in evoked cortical responses. *Science* **273,** 1868–1871 (1996).
20. Palmer, L. M. & Stuart, G. J. Membrane potential changes in dendritic spines during action potentials and synaptic input. *J. Neurosci.* **29,** 6897–6903 (2009).
21. Nuriya, M., Jiang, J., Nemet, B., Eisenthal, K. B. & Yuste, R. Imaging membrane potential in dendritic spines. *Proc. Natl Acad. Sci. USA* **103,** 786–790 (2006).
22. Bradley, J., Luo, R., Otis, T. S. & DiGregorio, D. A. Submillisecond optical reporting of membrane potential *in situ* using a neuronal tracer dye. *J. Neurosci.* **29,** 9197–9209 (2009).
23. Dombeck, D. A., Blanchard-Desce, M. & Webb, W. W. Optical recording of action potentials with second-harmonic generation microscopy. *J. Neurosci.* **24,** 999–1003 (2004).
24. Siegel, M. S. & Isacoff, E. Y. A genetically encoded optical probe of membrane voltage. *Neuron* **19,** 735–741 (1997).
25. Chanda, B. *et al.* A hybrid approach to measuring electrical activity in genetically specified neurons. *Nature Neurosci.* **8,** 1619–1626 (2005).
This breakthrough paper in voltage-sensitive dye imaging reports a new strategy in which large voltage-dependent optical signals are obtained by fluorescence resonance energy transfer between dipicrylamine, a voltage-sensing molecule intercalated into the membrane, and a membrane-anchored form of GFP.
26. Grynkiewicz, G., Poenie, M. & Tsien, R. Y. A new generation of Ca^{2+} indicators with greatly improved fluorescence properties. *J. Biol. Chem.* **260,** 3440–3450 (1985).
27. Sabatini, B. L. & Svoboda, K. Analysis of calcium channels in single spines using optical fluctuation analysis. *Nature* **408,** 589–593 (2000).
By combining two-photon calcium imaging from individual dendritic spines with fluctuation analysis of the recorded calcium signals, this study estimates the number of voltage-gated calcium channels in individual spines.
28. Yuste, R., Majewska, A., Cash, S. S. & Denk, W. Mechanisms of calcium influx into hippocampal spines: heterogeneity among spines, coincidence detection by NMDA receptors, and optical quantal analysis. *J. Neurosci.* **19,** 1976–1987 (1999).
29. Bollmann, J. H. & Engert, F. Subcellular topography of visually driven dendritic activity in the vertebrate visual system. *Neuron* **61,** 895–905 (2009).
30. Stosiek, C., Garaschuk, O., Holthoff, K. & Konnerth, A. *In vivo* two-photon calcium imaging of neuronal networks. *Proc. Natl Acad. Sci. USA* **100,** 7319–7324 (2003).
31. Greenberg, D. S., Houweling, A. R. & Kerr, J. N. Population imaging of ongoing neuronal activity in the visual cortex of awake rats. *Nature Neurosci.* **11,** 749–751 (2008).
32. Dombeck, D. A., Khabbaz, A. N., Collman, F., Adelman, T. L. & Tank, D. W. Imaging large-scale neural activity with cellular resolution in awake, mobile mice. *Neuron* **56,** 43–57 (2007).
This paper reports how placing awake, head-fixed mice on a spherical treadmill allows two-photon imaging of large neuronal populations with single-cell resolution in behaving animals.
33. Vogelstein, J. T. *et al.* Spike inference from calcium imaging using sequential Monte Carlo methods. *Biophys. J.* **97,** 636–655 (2009).
34. Miyawaki, A. *et al.* Fluorescent indicators for Ca^{2+} based on green fluorescent proteins and calmodulin. *Nature* **388,** 882–887 (1997).
35. Heim, N. & Griesbeck, O. Genetically encoded indicators of cellular calcium dynamics based on troponin C and green fluorescent protein. *J. Biol. Chem.* **279,** 14280–14286 (2004).
36. Mao, T., O'Connor, D. H., Scheuss, V., Nakai, J. & Svoboda, K. Characterization and subcellular targeting of GCaMP-type genetically-encoded calcium indicators. *PloS ONE* **3,** e1796 (2008).
37. Mank, M. & Griesbeck, O. Genetically encoded calcium indicators. *Chem. Rev.* **108,** 1550–1564 (2008).
38. Wallace, D. J. *et al.* Single-spike detection *in vitro* and *in vivo* with a genetic Ca^{2+} sensor. *Nature Methods* **5,** 797–804 (2008).
39. Mank, M. *et al.* A genetically encoded calcium indicator for chronic *in vivo* two-photon imaging. *Nature Methods* **5,** 805–811 (2008).
40. Nagel, G. *et al.* Channelrhodopsin-2, a directly light-gated cation-selective membrane channel. *Proc. Natl Acad. Sci. USA* **100,** 13940–13945 (2003).
This paper reports the first functional characterization of channelrhodopsin-2, a microbial light-gated cation channel, demonstrating that the protein can be used to depolarize the membrane potential of mammalian cells "simply by illumination", and opening the way to the temporally precise manipulation of neuronal activity with light.
41. Kim, J. M. *et al.* Light-driven activation of β_2-adrenergic receptor signaling by a chimeric rhodopsin containing the β_2-adrenergic receptor cytoplasmic loops. *Biochemistry* **44,** 2284–2292 (2005).
This study reports the creation of the first functional chimaera between rhodopsin and a G-protein-coupled receptor that allows G-protein signalling pathways to be controlled using light.
42. Zhang, F., Aravanis, A. M., Adamantidis, A., de Lecea, L. & Deisseroth, K. Circuit-breakers: optical technologies for probing neural signals and systems. *Nature Rev. Neurosci.* **8,** 577–581 (2007).
43. Airan, R. D., Thompson, K. R., Fenno, L. E., Bernstein, H. & Deisseroth, K. Temporally precise *in vivo* control of intracellular signalling. *Nature* **458,** 1025–1029 (2009).
44. Yoshimura, Y., Dantzker, J. L. & Callaway, E. M. Excitatory cortical neurons form fine-scale functional networks. *Nature* **433,** 868–873 (2005).
45. Matsuzaki, M. *et al.* Dendritic spine geometry is critical for AMPA receptor expression in hippocampal CA1 pyramidal neurons. *Nature Neurosci.* **4,** 1086–1092 (2001).
46. Lima, S. Q. & Miesenböck, G. Remote control of behavior through genetically targeted photostimulation of neurons. *Cell* **121,** 141–152 (2005).
47. Boyden, E. S., Zhang, F., Bamberg, E., Nagel, G. & Deisseroth, K. Millisecond-timescale, genetically targeted optical control of neural activity. *Nature Neurosci.* **8,** 1263–1268 (2005).
48. Li, X. *et al.* Fast noninvasive activation and inhibition of neural and network activity by vertebrate rhodopsin and green algae channelrhodopsin. *Proc. Natl Acad. Sci. USA* **102,** 17816–17821 (2005).
References 47 and 48 show that light pulses can trigger action potentials with millisecond precision in mammalian neurons expressing channelrhodopsin-2, demonstrating that light can be used to stimulate the nervous system efficiently and with high temporal precision.
49. Szobota, S. *et al.* Remote control of neuronal activity with a light-gated glutamate receptor. *Neuron* **54,** 535–545 (2007).
50. Zhang, F. *et al.* Multimodal fast optical interrogation of neural circuitry. *Nature* **446,** 633–639 (2007).
51. Han, X. & Boyden, E.S. Multiple-color optical activation, silencing, and desynchronization of neural activity, with single-spike temporal resolution. *PloS ONE* **2,** e299 (2007).
References 50 and 51 show that the combined expression of channelrhodopsin-2 and halorhodopsin, a light-activated chloride pump from archaea, allows excitation or inhibition of neurons using two different wavelengths.
52. Zhang, F. *et al.* Red-shifted optogenetic excitation: a tool for fast neural control derived from *Volvox carteri*. *Nature Neurosci.* **11,** 631–633 (2008).
53. Berndt, A., Yizhar, O., Gunaydin, L. A., Hegemann, P. & Deisseroth, K. Bi-stable neural state switches. *Nature Neurosci.* **12,** 229–234 (2009).
54. Petreanu, L., Mao, T., Sternson, S. M. & Svoboda, K. The subcellular organization of neocortical excitatory connections. *Nature* **457,** 1142–1145 (2009).
55. Cardin, J. A. *et al.* Driving fast-spiking cells induces gamma rhythm and controls sensory responses. *Nature* **459,** 663–667 (2009).
56. Huber, D. *et al.* Sparse optical microstimulation in barrel cortex drives learned behaviour in freely moving mice. *Nature* **451,** 61–64 (2008).
57. Tsai, H. C. *et al.* Phasic firing in dopaminergic neurons is sufficient for behavioral conditioning. *Science* **324,** 1080–1084 (2009).
58. Helmstaedter, M., Briggman, K. L. & Denk, W. 3D structural imaging of the brain with photons and electrons. *Curr. Opin. Neurobiol.* **18,** 633–641 (2008).

59. Reijmers, L. G., Perkins, B. L., Matsuo, N. & Mayford, M. Localization of a stable neural correlate of associative memory. *Science* **317,** 1230–1233 (2007).
By using an activity-dependent promoter, this study opens the way to the genetic tagging of neurons activated by a specific sensory experience, thereby allowing the identification — and potentially the manipulation — of select neuronal circuits in complex networks.
60. Hodgkin, A. L. & Huxley, A. F. A quantitative description of membrane current and its application to conduction and excitation in nerve. *J. Physiol. (Lond.)* **117,** 500–544 (1952).
61. Anderson, C. R. & Stevens, C. F. Voltage clamp analysis of acetylcholine produced end-plate current fluctuations at frog neuromuscular junction. *J. Physiol. (Lond.)* **235,** 655–691 (1973).
62. Neher, E. & Sakmann, B. Single-channel currents recorded from membrane of denervated frog muscle fibres. *Nature* **260,** 799–802 (1976).
63. Betz, W. J., Mao, F. & Smith, C. B. Imaging exocytosis and endocytosis. *Curr. Opin. Neurobiol.* **6,** 365–371 (1996).
64. Hires, S. A., Zhu, Y. & Tsien, R. Y. Optical measurement of synaptic glutamate spillover and reuptake by linker optimized glutamate-sensitive fluorescent reporters. *Proc. Natl Acad. Sci. USA* **105,** 4411–4416 (2008).
65. Miesenböck, G., De Angelis, D. A. & Rothman, J. E. Visualizing secretion and synaptic transmission with pH-sensitive green fluorescent proteins. *Nature* **394,** 192–195 (1998).
66. Okumoto, S. *et al.* Detection of glutamate release from neurons by genetically encoded surface-displayed FRET nanosensors. *Proc. Natl Acad. Sci. USA* **102,** 8740–8745 (2005).
67. Cha, A., Snyder, G. E., Selvin, P. R. & Bezanilla, F. Atomic scale movement of the voltage-sensing region in a potassium channel measured via spectroscopy. *Nature* **402,** 809–813 (1999).
68. Glauner, K. S., Mannuzzu, L. M., Gandhi, C. S. & Isacoff, E. Y. Spectroscopic mapping of voltage sensor movement in the Shaker potassium channel. *Nature* **402,** 813–817 (1999).
69. Sonnleitner, A., Mannuzzu, L. M., Terakawa, S. & Isacoff, E. Y. Structural rearrangements in single ion channels detected optically in living cells. *Proc. Natl Acad. Sci. USA* **99,** 12759–12764 (2002).
70. Churchland, M. M., Yu, B. M., Sahani, M. & Shenoy, K. V. Techniques for extracting single-trial activity patterns from large-scale neural recordings. *Curr. Opin. Neurobiol.* **17,** 609–618 (2007).
71. Sohya, K., Kameyama, K., Yanagawa, Y., Obata, K. & Tsumoto, T. GABAergic neurons are less selective to stimulus orientation than excitatory neurons in layer II/III of visual cortex, as revealed by *in vivo* functional Ca^{2+} imaging in transgenic mice. *J. Neurosci.* **27,** 2145–2149 (2007).
This paper reports *in vivo* two-photon calcium imaging in the visual cortex of transgenic mice expressing GFP in specific neuronal populations, showing that tuning characteristics differ in distinct neuron types.
72. Berger, T. *et al.* Combined voltage and calcium epifluorescence imaging *in vitro* and *in vivo* reveals subthreshold and suprathreshold dynamics of mouse barrel cortex. *J. Neurophysiol.* **97,** 3751–3762 (2007).
73. Theer, P., Hasan, M. T. & Denk, W. Two-photon imaging to a depth of 1000 μm in living brains by use of a $Ti:Al_2O_3$ regenerative amplifier. *Opt. Lett.* **28,** 1022–1024 (2003).
74. Mizrahi, A., Crowley, J. C., Shtoyerman, E. & Katz, L. C. High-resolution *in vivo* imaging of hippocampal dendrites and spines. *J. Neurosci.* **24,** 3147–3151 (2004).
75. Klausberger, T. *et al.* Brain-state- and cell-type-specific firing of hippocampal interneurons *in vivo*. *Nature* **421,** 844–848 (2003).
76. Pouille, F. & Scanziani, M. Routing of spike series by dynamic circuits in the hippocampus. *Nature* **429,** 717–723 (2004).
77. Rickgauer, J.P. & Tank, D.W. Optimizing two-photon activation of channelrhodopsin-2 for stimulation at cellular resolution. *Soc. Neurosci. Abstr.* 496.12 (2008).
78. Duemani Reddy, G., Kelleher, K., Fink, R. & Saggau, P. Three-dimensional random access multiphoton microscopy for functional imaging of neuronal activity. *Nature Neurosci.* **11,** 713–720 (2008).
79. Göbel, W., Kampa, B. M. & Helmchen, F. Imaging cellular network dynamics in three dimensions using fast 3D laser scanning. *Nature Methods* **4,** 73–79 (2007).
80. Miller, E. K. & Wilson, M. A. All my circuits: using multiple electrodes to understand functioning neural networks. *Neuron* **60,** 483–488 (2008).
81. Lee, A. K., Manns, I. D., Sakmann, B. & Brecht, M. Whole-cell recordings in freely moving rats. *Neuron* **51,** 399–407 (2006).
82. Helmchen, F., Fee, M. S., Tank, D. W. & Denk, W. A miniature head-mounted two-photon microscope: high-resolution brain imaging in freely moving animals. *Neuron* **31,** 903–912 (2001).
83. Ferezou, I., Bolea, S. & Petersen, C. C. Visualizing the cortical representation of whisker touch: voltage-sensitive dye imaging in freely moving mice. *Neuron* **50,** 617–629 (2006).
84. Flusberg, B. A. *et al.* High-speed, miniaturized fluorescence microscopy in freely moving mice. *Nature Methods* **5,** 935–938 (2008).
85. Qiao, Y. *et al.* Fabrication of nanoelectrodes for neurophysiology: cathodic electrophoretic paint insulation and focused ion beam milling. *Nanotechnology* **16,** 1598–1602 (2005).
86. Krapf, D. *et al.* Fabrication and characterization of nanopore-based electrodes with radii down to 2 nm. *Nano Lett.* **6,** 105–109 (2006).
87. Heller, I. *et al.* Individual single-walled carbon nanotubes as nanoelectrodes for electrochemistry. *Nano Lett.* **5,** 137–142 (2005).
88. Smith, S. L., Judy, J. W. & Otis, T. S. An ultra small array of electrodes for stimulating multiple inputs into a single neuron. *J. Neurosci. Methods* **133,** 109–114 (2004).
89. Fromherz, P. Three levels of neuroelectronic interfacing: silicon chips with ion channels, nerve cells, and brain tissue. *Ann. NY Acad. Sci.* 1**093,** 143–160 (2006).
90. Piccolino, M. & Bresadola, M. Drawing a spark from darkness: John Walsh and electric fish. *Trends Neurosci.* **25,** 51–57 (2002).
91. Hodgkin, A. L. & Huxley, A. F. Action potentials recorded from inside a nerve fibre. *Nature* **144,** 710–711 (1939).
92. Margrie, T. W. *et al.* Targeted whole-cell recordings in the mammalian brain *in vivo*. *Neuron* **39,** 911–918 (2003).
93. Kitamura, K., Judkewitz, B., Kano, M., Denk, W. & Häusser, M. Targeted patch-clamp recordings and single-cell electroporation of unlabeled neurons *in vivo*. *Nature Methods* **5,** 61–67 (2008).
94. Liu, B. H. *et al.* Visual receptive field structure of cortical inhibitory neurons revealed by two-photon imaging guided recording. *J. Neurosci.* **29,** 10520–10532 (2009).
95. Katzner, S. *et al.* Local origin of field potentials in visual cortex. *Neuron* **61,** 35–41 (2009).
96. Akemann, W., Lundby, A., Mutoh, H. & Knöpfel, T. Effect of voltage sensitive fluorescent proteins on neuronal excitability. *Biophys. J.* **96,** 3959–3976 (2009).
97. Sabatini, B. L., Oertner, T. G. & Svoboda, K. The life cycle of Ca^{2+} ions in dendritic spines. *Neuron* **33,** 439–452 (2002).
98. Tian, L. *et al.* Imaging neural activity in worms, flies and mice with improved GCaMP calcium indicators. *Nature Methods* (in the press).
99. Peterlin, Z. A., Kozloski, J., Mao, B. Q., Tsiola, A. & Yuste, R. Optical probing of neuronal circuits with calcium indicators. *Proc. Natl Acad. Sci. USA* **97,** 3619–3624 (2000).
100. Aaron, G. & Yuste, R. Reverse optical probing (ROPING) of neocortical circuits. *Synapse* **60,** 437–440 (2006).

Acknowledgements We are grateful to T. Branco, S. J. Caddick, M. Carandini, B. Clark, W. Denk, D. Kleinfeld, J. Isaacson, B. Judkewitz, R. Malinow, R. Morris, A. Roth, S. J. Smith, S. L. Smith, K. Svoboda and C. Wilms for helpful discussions and/or comments on the manuscript. We apologize to our colleagues whose work could not be cited owing to space constraints. Work in our laboratories is supported by grants from the Howard Hughes Medical Institute and the US National Institutes of Health (M.S.); and the Wellcome Trust, the European Union and the Gatsby Charitable Foundation (M.H.).

Author Information Reprints and permissions information is available at www.nature.com/reprints. The authors declare no competing financial interests.
Correspondence should be addressed to M.S. (massimo@ucsd.edu) or M.H. (m.hausser@ucl.ac.uk).

ARTICLES

Intracellular dynamics of hippocampal place cells during virtual navigation

Christopher D. Harvey[1,2,3], Forrest Collman[1,2,3], Daniel A. Dombeck[1,2,3] & David W. Tank[1,2,3]

Hippocampal place cells encode spatial information in rate and temporal codes. To examine the mechanisms underlying hippocampal coding, here we measured the intracellular dynamics of place cells by combining *in vivo* whole-cell recordings with a virtual-reality system. Head-restrained mice, running on a spherical treadmill, interacted with a computer-generated visual environment to perform spatial behaviours. Robust place-cell activity was present during movement along a virtual linear track. From whole-cell recordings, we identified three subthreshold signatures of place fields: an asymmetric ramp-like depolarization of the baseline membrane potential, an increase in the amplitude of intracellular theta oscillations, and a phase precession of the intracellular theta oscillation relative to the extracellularly recorded theta rhythm. These intracellular dynamics underlie the primary features of place-cell rate and temporal codes. The virtual-reality system developed here will enable new experimental approaches to study the neural circuits underlying navigation.

Hippocampal place cells encode spatial information during navigation using rate and temporal codes[1,2]. The rate code refers to a selective increase in firing rate at a specific location in a local environment[3], and the temporal code includes the precise timing of spikes relative to the hippocampal theta rhythm (phase precession)[4–6]. To explain the origins of these codes, theoretical network and cellular models have been proposed[4,7–16]. These models make differing predictions about the subthreshold membrane potential dynamics of place cells (Fig. 1a–e, g–i), reflecting differences in the proposed mechanisms underlying hippocampal coding. The predicted intracellular dynamics include steady oscillations at theta frequencies that reflect a global hippocampal theta rhythm[7–9,12] (Fig. 1e), modulation of the amplitude and frequency of membrane potential theta oscillations[4,10,11,13–15] (Fig. 1b–d), and ramps of depolarization of the baseline membrane potential[7–10,12,13] (Fig. 1d–e). To account for phase precession, these models also make differing predictions about the relationship between intracellular theta oscillations and the local field potential (LFP) theta rhythm. Models predict either that intracellular theta is phase-locked to the LFP theta rhythm with phase precession resulting from a ramp of depolarization[7–9,12], or that intracellular theta in the place field is at a higher frequency than the LFP rhythm[4,10,11,13–15] (Fig. 1g–i).

Because the models of hippocampal coding make differing predictions of subthreshold membrane potential dynamics, it is possible to distinguish between these models by intracellular measurements from place cells during spatial behaviours. However, intracellular recording methods require a level of mechanical stability that is difficult to obtain in freely moving animals[17,18]. Previously, head restraint on a spherical treadmill has been used to facilitate optical imaging at cellular resolution in awake, mobile mice[19]. Furthermore, a previous study has provided evidence that body-tethered rats can navigate through virtual environments[20]. We reasoned that these could be combined to facilitate whole-cell recordings to show the intracellular dynamics of place cells, and thus distinguish between models of hippocampal coding.

Spatial behaviour in a virtual environment

The visual virtual-reality system for head-restrained mice we developed is shown in Fig. 2a. A mouse runs on top of an air-supported spherical treadmill with its head held fixed in space using a head plate. The mouse is surrounded by a toroidal screen that covers a wide area to accommodate a rodent's large field of view[20]. An image is projected onto the screen from a digital light processing projector by an angular amplification mirror[21] (Fig. 2a, Supplementary Fig. 1 and Methods). To control the virtual-reality system, we developed custom software using the open source Quake2 video game engine. The visual display was updated on the basis of the movements of the animal, measured as rotations of the spherical treadmill using an optical computer mouse (Methods).

We addressed whether head-restrained mice can perform visually guided spatial behaviours in a virtual environment. We trained water-scheduled mice using operant conditioning to run along a virtual linear track (180 cm long) that had proximal and distal walls with varying patterns for location cues (Fig. 2b). Mice were able to turn around at any position along the track's length. Small water rewards were given for running between reward zones located at opposite ends of the track; consecutive rewards were not available at a single reward site. After several training sessions, mice ran large total distances with high peak running speeds (session 4: total distance $= 217 \pm 97$ m per 40 min, peak speed $= 41 \pm 17\ \mathrm{cm\,s^{-1}}$ over a 2 s period, mean $\pm$ s.d.). Individual mice received rewards at increasing rates over time (Fig. 2c, d). Also, the average distance travelled between rewards decreased across sessions (Fig. 2e), consistent with learning of the task. After ten training sessions, mice ran 281 ± 53 cm between rewards, on average, approaching an ideal performance of 180 cm per reward (that is, the distance between reward zones). These data indicate that head-restrained mice can perform visually guided spatial behaviours in a virtual-reality environment.

Place cells in a virtual environment

Although our behavioural results indicate that mice have a spatial understanding of the virtual environment, the activation of navigation circuits during these behaviours would provide further evidence. To assess the function of the hippocampal place-cell circuitry, we performed acute extracellular recordings in the dorsal hippocampus from CA1 pyramidal neurons (Fig. 3a). We recorded during behaviour along the virtual linear track from mice that had been trained

[1]Princeton Neuroscience Institute, [2]Lewis-Sigler Institute for Integrative Genomics, [3]Department of Molecular Biology, Princeton University, Princeton, New Jersey 08544, USA.

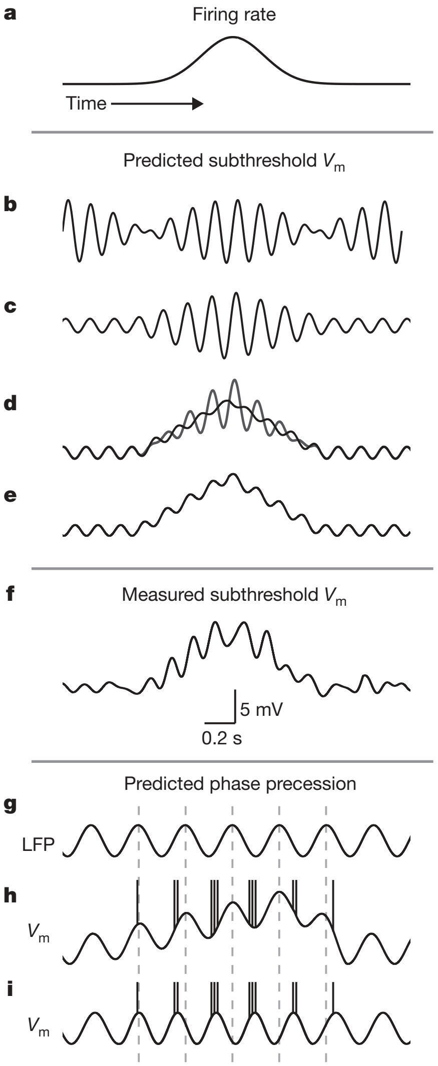

Figure 1 | Predicted and measured subthreshold membrane potential dynamics during a run through a cell's place field. **a**, Schematic of a place-cell's firing rate. **b–e**, Schematics of predicted subthreshold membrane potentials (aligned to **a**) from a dual oscillator interference model[2,4] (**b**), a modified dual oscillator model[14] (**c**), a soma-dendritic interference model[10,11,13,15] (**d**), and network[7–9] and experience-dependent[12] models (**e**). In **b**, two sets of theta-modulated inputs at different frequencies interfere to create a beat-like pattern of membrane potential fluctuations. In **c**, two oscillations are phase-locked outside the place field. In the place field, the frequency of one oscillation increases, resulting in a modulation of the summed oscillation. In **d**, the cell receives theta-modulated inhibitory and excitatory inputs. In the place field, the excitatory drive increases, resulting in a ramp-like depolarization and an increase in the amplitude of excitatory theta oscillations. Depending on the conductances used, the summed oscillation can have either increased (grey)[15] or decreased (black)[11] amplitude. In **e**, a ramp of excitatory drive interacts with theta-modulated inhibitory inputs. Asymmetric ramps have also been proposed[12]. Schematics in **b–e** only illustrate depolarizations and changes in theta amplitude. **f**, Example of a subthreshold membrane potential (filtered from DC-10 Hz) recorded intracellularly from a place cell. Note the simultaneous ramp of depolarization and increase in theta oscillation amplitude. Scale bars refer to the experimentally measured trace only. **g**, Schematic of the LFP theta rhythm. Dashed lines denote peaks. **h–i**, Schematics of predicted relationships between intracellular and LFP theta to account for phase precession. In **h**, intracellular and LFP theta are the same frequency. Phase precession of spikes occurs relative to both intracellular and LFP theta owing to a ramp of depolarization[7–9,12]. An asymmetric ramp is shown. In **i**, intracellular theta in the place field is a higher frequency than LFP theta. Spikes precess relative to LFP theta but not intracellular theta[2,4,10,11,13–15]. Schematics in **h** and **i** only illustrate the relationships between spike times, intracellular theta and LFP theta.

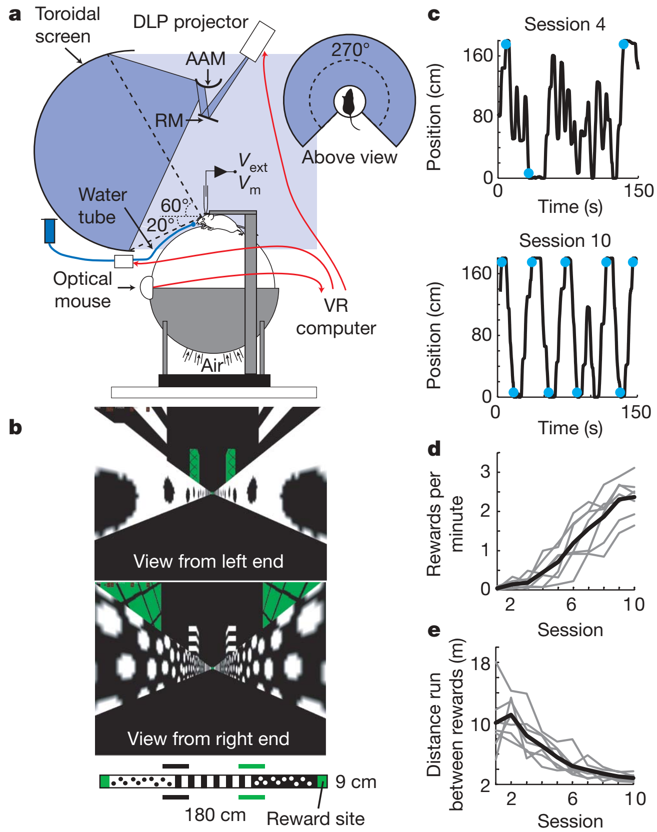

Figure 2 | Spatial behaviours in a virtual-reality environment. **a**, Schematic of the experimental set-up. A head-restrained mouse runs on an air-supported spherical treadmill. An image from a digital light processing projector is displayed on a toroidal screen (−20–60° vertically, 270° horizontally) by a reflecting mirror (RM) and an angular amplification mirror (AAM). Movements of the treadmill are measured using an optical computer mouse. Water rewards are delivered through a lick tube by a computer-controlled solenoid valve. See Methods and Supplementary Fig. 1 for details. **b**, The virtual linear track. Screenshots (without the fisheye perspective, see Methods) from the right and left ends of the track are shown. The track (180 × 9 cm) was divided into three regions with different textures on the proximal walls (black dots, vertical stripes, white dots). Distal walls (horizontal stripes, green with black crosses) were present at the boundaries between regions. Water rewards were given at the ends of the track, with available rewards alternating between reward sites. **c**, Example trajectories for an individual mouse on training sessions 4 and 10. Position is the animal's location along the track's long axis. Blue dots indicate rewards. **d**, Rate of rewards for individual mice. **e**, Average distance travelled by the mouse between consecutive rewards. In **d** and **e**, grey lines indicate individual mice, and the black line is the mean; $n = 7$ mice.

for at least 5 days. Recorded cells had spiking patterns characteristic of hippocampal pyramidal neurons. Cells fired bursts of action potentials at high frequencies (>50 Hz) with decreasing spike amplitudes[22–24]; bursts occurred at intervals of ~130 ms corresponding to theta frequencies of ~6–10 Hz (Fig. 3a, b). In all mice tested, we identified units with place-cell characteristics (23 cells from 8 mice; Methods). Place cells had low overall firing rates with spatially modulated firing patterns (overall firing rate = 1.0 ± 0.3 Hz; in-field firing rate = 4.7 ± 2.6 Hz; out-of-field firing rate = 0.6 ± 0.2 Hz; Fig. 3c). Place field size was, on average, 41 ± 14 cm. Place-cell activity in some cases had directionality, with different place fields and firing rates depending on the direction of running[25] (directionality index = 0.6 ± 0.2; Methods and Fig. 3c). We also measured phase precession of spike times relative to LFP theta oscillations during runs through the place field[4,5]. Spike times shifted to earlier phases during movement through the place field, and the phase and position of spikes were negatively correlated (Δphase = −72.6 ± 47.7°

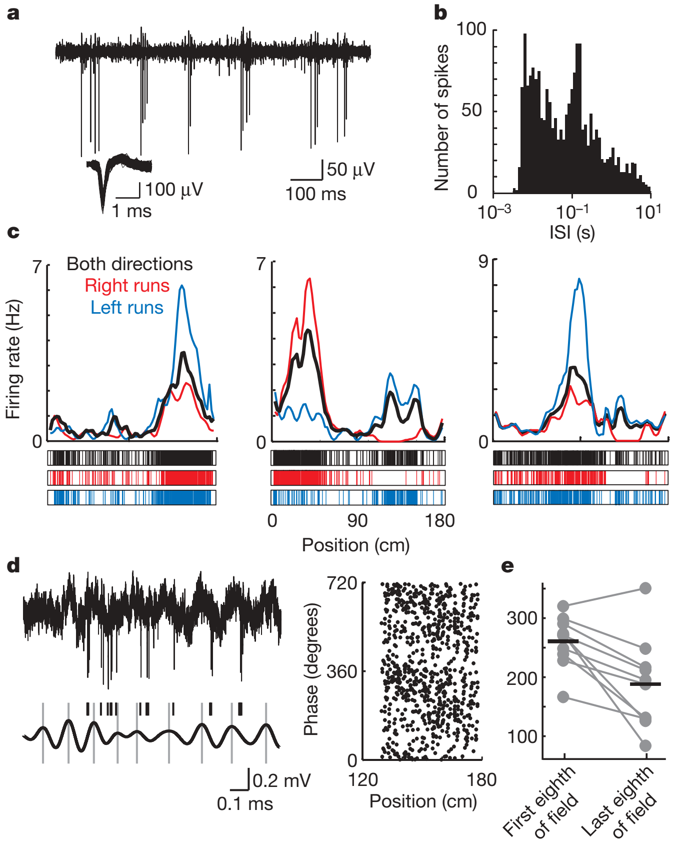

Figure 3 | Extracellular recordings of CA1 place cells along the virtual linear track. a, An example extracellular recording filtered between 500 Hz and 7.5 kHz. The inset shows overlaid spike waveforms from the recording. **b,** ISI distribution for the full duration of the recording shown in **a.** The time axis is plotted on a log scale. **c,** Example firing rate maps for 3 place cells from 3 different mice. Top, firing rates at positions along the track are shown for rightward runs (red), leftward runs (blue) and runs in either direction (black). Bottom, the position on the track of each spike in the recording is shown as a vertical line. A total of 23 place cells from 8 mice were recorded. **d,** Phase precession of spike times relative to LFP theta. Top left, an example extracellular recording, filtered between 2 Hz and 10 kHz, during a run through the place field. Spikes and the LFP were recorded on the same electrode. Bottom left, the extracellular recording band-pass filtered between 6 and 10 Hz. Grey lines denote peaks (0°) in the filtered trace, black lines denote the times of spikes. Right, an example plot of phase (two cycles) versus position on the virtual track for all spikes during complete runs through the place field for a single cell. **e,** Phase values for spikes in the first and last eighth of the place field. Connected points represent a single place field. Horizontal lines indicate the means. $n = 10$ place fields from 8 cells and 3 mice (multiple place fields are owing to the directionality of firing rates).

between the first and last eighth of the field, $P < 0.01$; correlation coefficient $(C) = -0.17 \pm 0.09$ between phase and position, $P < 0.01$; $n = 10$ place fields, 8 cells, 3 mice; Fig. 3d, e). These firing rate and phase precession characteristics along the virtual linear track are highly similar to those measured in freely moving mice in real environments[26–29]. These data therefore demonstrate that hippocampal place-cell circuitry is operational in head-restrained mice during visually guided spatial behaviours in the virtual-reality system.

Intracellular dynamics of place cells

We next developed methods to measure the intracellular activity of hippocampal neurons during behaviour along the virtual linear track. Because the mouse's head is stationary in the virtual-reality set-up, we were able to perform whole-cell patch-clamp recordings using a patch electrode with a long taper mounted on a standard micromanipulator positioned outside the mouse's field of view (see Methods). We obtained recordings in awake mice[17,18,30,31] as they ran on the spherical treadmill. Recordings lasted many minutes on average (7.7 ± 3.8 min, maximum 20.4 min; $n = 46$ cells from 15 mice), during which time mice ran long distances at high speeds in the virtual environment (27 ± 5 m per min; total distance range 125–458 m). We did not detect any major motion-induced artefacts in the electrophysiology recordings. Recordings could be performed from the same animal across several days (≥6 days per mouse; ≥3 days per hemisphere).

A subset of our whole-cell recordings was made from place cells (overall firing rate = 2.2 ± 0.4 Hz; in-field firing rate = 7.3 ± 1.4 Hz; out-of-field firing rate = 1.5 ± 0.4 Hz; field size = 43 ± 13 cm; $n = 8$ cells from 8 mice; Fig. 4a, b and Supplementary Figs 2a and 3). Approximately 36% of the spontaneously active putative pyramidal neurons had a place field along the virtual track, which is consistent with estimates from extracellular recordings and immediate early

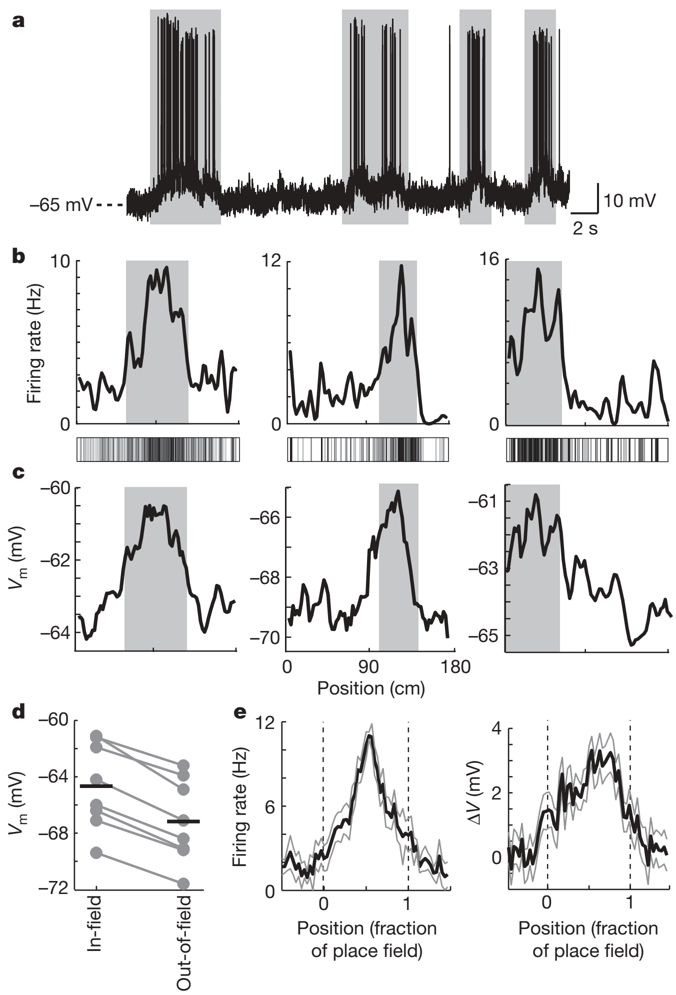

Figure 4 | Ramp-like membrane potential depolarization inside place fields. a, Example whole-cell recording during runs through the cell's place field. Grey boxes indicate the place field (middle example from **b**). **b,** Firing rates along the virtual linear track for 3 place cells recorded intracellularly from 3 different animals. The grey boxes indicate the primary place field determined by firing rates (Methods). Bottom, vertical lines mark the location along the track of every action potential in the recording. **c,** Average baseline membrane potential, excluding action potentials, sorted by position along the track for the 3 place cells from **b. d,** Average membrane potential inside and outside the place field. Each pair of connected points is from a single cell. Horizontal lines indicate the means. $n = 8$ cells from 8 mice. **e,** Average firing rates and changes in baseline membrane potential during complete runs through the place field. To combine data from several cells, position values in the place field were normalized. Black lines indicate the mean. Grey lines indicate the mean ± s.e.m. Data are averaged over 84 complete runs through the place field (8 cells).

gene studies in rats exploring real environments[32,33] (see Methods). Place cells recorded intracellularly fired in theta bursts (high frequency bursts at >50 Hz occurring at theta frequencies of ~6–10 Hz), resulting in interspike interval (ISI) distributions with peaks at <10 ms and ~130 ms, consistent with our extracellular measurements (compare Supplementary Fig. 4 and Fig. 3b). The individual action potentials during a theta burst often occurred during the ascending phase of an underlying theta oscillation (Fig. 5a, d). Spike amplitudes decreased within a burst without a change in the peak potential of the spike, suggesting that depolarizing intracellular oscillations contribute to intra-burst decreases in spike amplitude[34]. Whole-cell recordings from place cells can therefore be obtained in head-restrained mice behaving in virtual environments.

From our whole-cell recordings of place-cell activity, we examined two types of membrane potential dynamics proposed by the theoretical models of place-cell function: ramps of depolarization, and modulation of theta oscillations (Fig. 1b–e, h–i). We first analysed changes in the average baseline membrane potential during behavioural epochs inside and outside the place field. As a mouse approached the recorded cell's place field, the average membrane potential, excluding action potentials, increased in a ramp-like manner and remained increased until the place field was passed (Fig. 4a). The ramp of depolarization often began before action potential firing in the place field started, and in some cases reached a steady depolarization as large as ~10 mV (peak depolarization = 5.7 ± 2.9 mV; Fig. 4a and Supplementary Figs 5 and 6). These depolarization events occurred preferentially in place fields; the average membrane potential excluding action potentials was higher in place fields than outside of place fields ($V_{\text{in-field}} - V_{\text{out-of-field}} = 2.5 \pm 0.5$ mV, $P < 0.0001$; Fig. 4c, d and Supplementary Fig. 2b). Consistently, the baseline membrane potential and firing rate were strongly correlated ($C = 0.55 \pm 0.10$, $P < 0.001$). On complete runs through the place field, ramps of depolarization were asymmetric, with the peak depolarization shifted towards the end of the field (position of the peak depolarization = 72 ± 24% of the distance through the field, $P < 0.05$ versus 50%; slope before peak = 3.0 mV per place field length, slope after peak = 5.4 mV per field length, $P < 0.001$; Fig. 4e). In contrast, firing rates were symmetric within the place field (position of the peak firing rate = 52 ± 17% of the distance through the field, $P > 0.6$ versus 50%; slope before peak = 13.3 Hz per place field length, slope after peak = 13.6 Hz per field length, $P > 0.4$; Fig. 4e), perhaps because firing rates were highest on the ascending part of a ramp depolarization[13] (Supplementary Fig. 7a). An asymmetric ramp-like depolarization of the baseline membrane potential is therefore a subthreshold signature of place fields.

We next examined the modulation of the amplitude and phase of membrane potential oscillations occurring at theta frequencies during runs along the virtual track. We measured intracellular theta oscillations by band-pass filtering our membrane potential recordings from 6–10 Hz, after action potentials were removed (Fig. 5a and Methods). When the mouse entered the recorded cell's place field, the amplitude

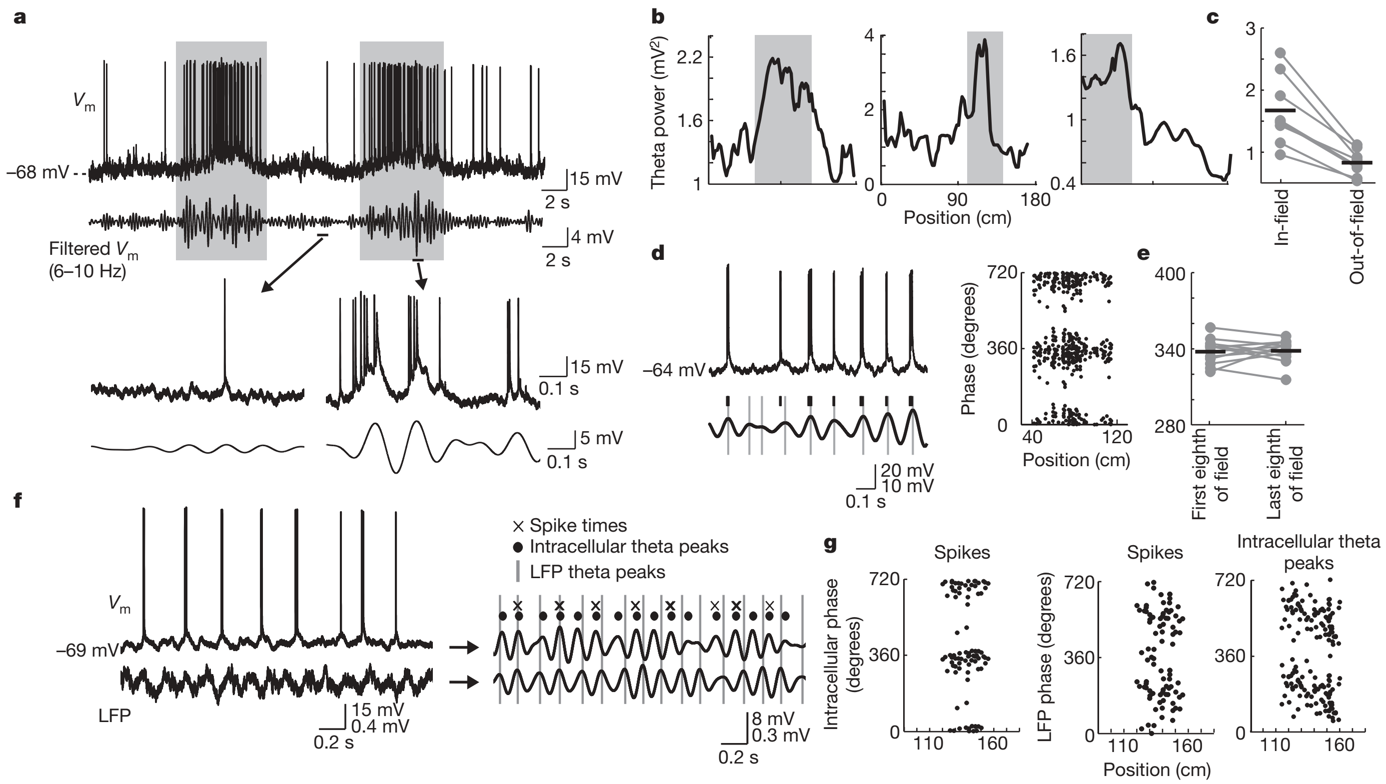

Figure 5 | Membrane potential theta oscillations in place cells. a, Top, example raw and filtered (6–10 Hz after spikes were removed) membrane potential traces during runs through the cell's place field (grey boxes). Bottom, expanded portions of the raw and filtered traces. **b**, Power in the theta-frequency band sorted by position along the track for the cells from Fig. 4. Power was measured as the squared amplitude of the filtered trace. Grey boxes denote the primary place fields. **c**, Theta power inside and outside the place field for individual cells. Horizontal bars are means. $n = 8$ cells from 8 mice. **d**, Spike times relative to intracellular theta. Left, example raw and filtered (6–10 Hz) membrane potential traces in the place field. Grey lines indicate peaks of theta oscillations (0°), black lines are times of spikes. Right, example phase (two cycles) versus position plot during place field traversals for a single cell. **e**, Intracellular phase values for spikes in the first and last eighth of the place field for individual place fields. Horizontal lines are the means. $n = 12$ place fields and 8 cells from 8 mice. **f**, Raw (left) and filtered (6–10 Hz, right) membrane potential and LFP traces in the place field from a simultaneous LFP and whole-cell recording. The times of LFP theta peaks (grey lines), intracellular theta peaks (circles) and spikes (crosses) are shown to illustrate the phase precession of spikes and intracellular theta relative to LFP theta oscillations, and the absence of phase precession of spikes relative to intracellular theta oscillations. **g**, Phase precession of spike times relative to intracellular theta (left), relative to LFP theta (middle) and phase precession of intracellular theta peak times relative to LFP theta (right) from a simultaneous LFP and whole-cell recording. In **d** and **f**, the top and bottom scale bar labels denote the top and bottom traces, respectively.

of intracellular theta oscillations increased (Fig. 5a). Theta-band power in the membrane potential trace was higher in place fields than outside of place fields ($\mathrm{power}_{\text{in-field}} = 1.7 \pm 0.4\,\mathrm{mV}^2$, $\mathrm{power}_{\text{out-of-field}} = 0.8 \pm 0.2\,\mathrm{mV}^2$, $P < 0.01$; Fig. 5b, c and Supplementary Figs 2c and 8). Consistently, theta oscillation amplitude and firing rate were highly correlated ($C = 0.61 \pm 0.09$, $P < 0.001$). In contrast, the amplitude of membrane potential theta oscillations was similar at all spatial locations for putative CA1 pyramidal neurons that did not have a place field (Supplementary Fig. 9) and for the LFP theta rhythm (Supplementary Fig. 10).

To examine the modulation of the phase of intracellular theta, we compared intracellular theta fluctuations with LFP theta oscillations. We began by looking for phase precession of spike times relative to membrane potential theta oscillations. The intracellular phases of spike times did not change during runs through the place field, and the phase and position of spikes were not correlated ($\Delta\mathrm{phase} = 0.6 \pm 10.4^\circ$ between the first and last eighth of the field, $P > 0.9$; $C = -0.01 \pm 0.08$ between phase and position, $P > 0.6$; Fig. 5d–g). Because spike times advanced relative to LFP theta oscillations but not intracellular theta (compare Figs 3d, e and 5d, e), it is predicted that a phase shift between LFP and intracellular theta occurs during place field traversals. We therefore performed simultaneous whole-cell and LFP recordings to compare directly the phases of intracellular and extracellularly recorded theta. During runs through the place field, the phase difference between intracellular and LFP theta shifted such that the intracellular theta oscillation phase precessed relative to the LFP theta rhythm ($C = -0.26 \pm 0.12$ between LFP phase and position for the times of intracellular theta peaks; $n = 2$ cells from 2 mice; Fig. 5f, g and Supplementary Fig. 11a). Consistently, the frequency of intracellular theta oscillations in the place field was higher than the frequency of LFP theta fluctuations (measured as a ratio of periods of intracellular theta to periods of LFP theta; $\mathrm{ratio}_{\text{in-field}} = 0.97 \pm 0.21$, $P < 0.01$ versus 1; $\Delta\mathrm{frequency} = 0.22\,\mathrm{Hz}$ given a mean LFP frequency of 7.4 Hz; see Methods and Supplementary Fig. 11b). In contrast, the frequencies of intracellular theta and LFP theta during epochs outside the place field were similar ($\mathrm{ratio}_{\text{out-of-field}} = 1.01 \pm 0.22$, $P > 0.2$ versus 1; Supplementary Fig. 11b). Intracellular theta oscillations in place cells were therefore not constant in amplitude or phase (relative to LFP theta) throughout runs on the linear track; rather, membrane potential theta oscillations were dynamically modulated across positions in virtual space.

Ramp-like depolarizations of the membrane potential and increases in intracellular theta oscillation amplitude were present simultaneously, which can be demonstrated directly by filtering the membrane potential trace from DC-10 Hz (Fig. 1f). Consistently, intracellular theta power and the baseline membrane potential were highly correlated ($C = 0.52 \pm 0.07$, $P < 0.001$; Figs 4c and 5b and Supplementary Fig. 2b, c). To determine whether ramps of depolarization trigger increases in theta amplitude, we injected ramps of current at the soma while the animal was running along the virtual track, and measured changes in theta power. Theta power increased weakly with higher levels of depolarization; however, the increase in power was smaller than during runs through the place field ($P < 0.01$ at similar ΔV values; compare Figs 4c, 5b and Supplementary Fig. 7b). Ramp-like depolarizations of the membrane potential therefore were not sufficient to cause the increases in theta oscillation amplitude observed in place fields.

Our whole-cell recordings revealed two further subthreshold phenomena. First, in a fraction of our recordings we observed spikelets, brief small amplitude deflections of the membrane potential (2 out of 8 place cells; amplitude $= 7.4 \pm 1.3\,\mathrm{mV}$, full-width at half-maximum $= 1.6 \pm 0.4\,\mathrm{ms}$; 0.06 ± 0.05 spikelets per second; Supplementary Fig. 12a)[35]. Second, bursts of action potentials were occasionally followed by large (~10–25 mV) depolarizations lasting up to 50–100 ms[23] (Supplementary Fig. 12b). These events sometimes contained broadened spikes of reduced amplitude, consistent with Ca^{2+} spikes recorded in slices[36]. Further analysis is required to assess the prevalence, significance and mechanisms of these events.

Discussion

Here we have developed a visual virtual-reality system in which head-restrained mice performed spatial behaviours along a virtual linear track. Hippocampal place-cell activities were triggered during runs along the track, with similar properties to those recorded in real environments. Because the mouse was head-restrained, we were able to obtain whole-cell recordings lasting many minutes in awake mice using standard patch-clamp techniques. Furthermore, this set-up can probably be combined with two-photon laser scanning microscopy, which has previously been performed in mice running on the spherical treadmill[19]. Virtual reality also offers the ability to design highly custom environments, and to manipulate these environments rapidly through software. We therefore anticipate that our virtual-reality system will make new types of experiments exploring spatial information encoding possible.

We identified three subthreshold signatures of place fields: an asymmetric ramp-like depolarization of the baseline membrane potential, an increase in the amplitude of membrane potential theta oscillations, and a phase precession of intracellular theta relative to LFP theta, such that spike times advanced relative to LFP theta but not intracellular theta (Figs 1f, 4 and 5). These findings seem inconsistent with the mechanisms underlying dual oscillator models[2,4,14], network models[7–9] and an experience-dependent model[12] of hippocampal rate and temporal coding because each model predicts membrane potential dynamics that differ significantly from our observed subthreshold signatures (Figs 1b, c, e–h). Our data are most consistent with a soma-dendritic interference model that proposes interactions between a spatially independent inhibitory oscillatory input near the soma, and a spatially dependent (increasing in the place field) and temporally patterned (at theta) dendritic excitatory input[10,11,13,15]. With an appropriate choice of conductances[15], the soma-dendritic interference model predicts, in the place field, ramp-like depolarizations (Figs 1d and 4), an increase in theta amplitude (Figs 1d and 5a–c), and precession of intracellular theta relative to extracellular theta (Figs 1i and 5f, g). We note, however, that we observed an asymmetric ramp-like depolarization (Fig. 4e), which may be important for phase precession across the entire place field[12], compared with a symmetric ramp proposed in this model. We do not exclude the possibility that revised forms of other models could potentially explain the intracellular dynamics we observed. Other experiments will be necessary to define and quantify the cellular and synaptic mechanisms underlying the intracellular dynamics we measured, including in the context of the entorhinal cortex[2,16,37], and to establish their causal relationship to rate and temporal codes in the hippocampus. The virtual-reality system developed here, combined with electro- and opto-physiological methods, will probably facilitate this analysis.

METHODS SUMMARY

A virtual-reality system was designed using an air-supported spherical treadmill for head-restrained mice[19], in combination with a projection-based visual display system[20], in which a toroidal screen presented an image from a projector by an angular amplification mirror[21]. Custom software to control the virtual-reality system was developed on the basis of the Quake2 game engine. Rotations of the spherical treadmill, measured by an optical computer mouse, were used to update the visual display. Water-scheduled C57BL/6J mice (8–12 weeks old) were trained using operant conditioning to run from end-to-end of a virtual linear track (180 cm long) to obtain water rewards. For electrophysiology measurements, a small craniotomy (~0.5 mm diameter) was made centred over dorsal hippocampus (2.2 mm caudal, 1.7 mm lateral to bregma). The craniotomy was sealed with silicone grease and then covered with silicone elastomer to allow recordings across several days. Extracellular recordings were made using a glass electrode (filled with 0.5 M NaCl, ~2.5 MΩ pipette resistance) mounted on a micromanipulator positioned behind the mouse. Whole-cell recordings were obtained using standard blind patch methods. Patch pipettes were pulled with a long taper (~100 μm

diameter at 1 mm from the tip) to minimize damage to the overlying cortical tissue, and were mounted on a micromanipulator positioned outside the field of view. Firing rate maps were calculated for 80 spatial bins along the virtual track as the number of spikes in a bin divided by the time spent in that bin. Changes in baseline membrane potential in the place field were measured from membrane potential traces excluding spikes. Theta oscillations were analysed after band-pass filtering (6–10 Hz) of the membrane potential recording using a linear phase finite impulse response filter.

Full Methods and any associated references are available in the online version of the paper at www.nature.com/nature.

Received 8 July; accepted 15 September 2009.

1. Moser, E. I., Kropff, E. & Moser, M. B. Place cells, grid cells, and the brain's spatial representation system. *Annu. Rev. Neurosci.* **31,** 69–89 (2008).
2. O'Keefe, J. & Burgess, N. Dual phase and rate coding in hippocampal place cells: theoretical significance and relationship to entorhinal grid cells. *Hippocampus* **15,** 853–866 (2005).
3. O'Keefe, J. & Dostrovsky, J. The hippocampus as a spatial map. Preliminary evidence from unit activity in the freely-moving rat. *Brain Res.* **34,** 171–175 (1971).
4. O'Keefe, J. & Recce, M. L. Phase relationship between hippocampal place units and the EEG theta rhythm. *Hippocampus* **3,** 317–330 (1993).
5. Skaggs, W. E., McNaughton, B. L., Wilson, M. A. & Barnes, C. A. Theta phase precession in hippocampal neuronal populations and the compression of temporal sequences. *Hippocampus* **6,** 149–172 (1996).
6. Buzsáki, G. Theta oscillations in the hippocampus. *Neuron* **33,** 325–340 (2002).
7. Tsodyks, M. V., Skaggs, W. E., Sejnowski, T. J. & McNaughton, B. L. Population dynamics and theta rhythm phase precession of hippocampal place cell firing: a spiking neuron model. *Hippocampus* **6,** 271–280 (1996).
8. Jensen, O. & Lisman, J. E. Hippocampal CA3 region predicts memory sequences: accounting for the phase precession of place cells. *Learn. Mem.* **3,** 279–287 (1996).
9. Wallenstein, G. V. & Hasselmo, M. E. GABAergic modulation of hippocampal population activity: sequence learning, place field development, and the phase precession effect. *J. Neurophysiol.* **78,** 393–408 (1997).
10. Kamondi, A., Acsady, L., Wang, X. J. & Buzsaki, G. Theta oscillations in somata and dendrites of hippocampal pyramidal cells *in vivo*: activity-dependent phase-precession of action potentials. *Hippocampus* **8,** 244–261 (1998).
11. Magee, J. C. Dendritic mechanisms of phase precession in hippocampal CA1 pyramidal neurons. *J. Neurophysiol.* **86,** 528–532 (2001).
12. Mehta, M. R., Lee, A. K. & Wilson, M. A. Role of experience and oscillations in transforming a rate code into a temporal code. *Nature* **417,** 741–746 (2002).
13. Harris, K. D. *et al.* Spike train dynamics predicts theta-related phase precession in hippocampal pyramidal cells. *Nature* **417,** 738–741 (2002).
14. Lengyel, M., Szatmary, Z. & Erdi, P. Dynamically detuned oscillations account for the coupled rate and temporal code of place cell firing. *Hippocampus* **13,** 700–714 (2003).
15. Gasparini, S. & Magee, J. C. State-dependent dendritic computation in hippocampal CA1 pyramidal neurons. *J. Neurosci.* **26,** 2088–2100 (2006).
16. Maurer, A. P. & McNaughton, B. L. Network and intrinsic cellular mechanisms underlying theta phase precession of hippocampal neurons. *Trends Neurosci.* **30,** 325–333 (2007).
17. Lee, A. K., Manns, I. D., Sakmann, B. & Brecht, M. Whole-cell recordings in freely moving rats. *Neuron* **51,** 399–407 (2006).
18. Lee, A. K., Epsztein, J. & Brecht, M. Head-anchored whole-cell recordings in freely moving rats. *Nature Protocols* **4,** 385–392 (2009).
19. Dombeck, D. A., Khabbaz, A. N., Collman, F., Adelman, T. L. & Tank, D. W. Imaging large-scale neural activity with cellular resolution in awake, mobile mice. *Neuron* **56,** 43–57 (2007).
20. Hölscher, C., Schnee, A., Dahmen, H., Setia, L. & Mallot, H. A. Rats are able to navigate in virtual environments. *J. Exp. Biol.* **208,** 561–569 (2005).
21. Chahl, J. S. & Srinivasan, M. V. Reflective surfaces for panoramic imaging. *Appl. Opt.* **36,** 8275–8285 (1997).
22. Ranck, J. B. Jr. Studies on single neurons in dorsal hippocampal formation and septum in unrestrained rats. I. Behavioral correlates and firing repertoires. *Exp. Neurol.* **41,** 461–531 (1973).
23. Kandel, E. R. & Spencer, W. A. Electrophysiology of hippocampal neurons. II. After-potentials and repetitive firing. *J. Neurophysiol.* **24,** 243–259 (1961).
24. Quirk, M. C. & Wilson, M. A. Interaction between spike waveform classification and temporal sequence detection. *J. Neurosci. Methods* **94,** 41–52 (1999).
25. McNaughton, B. L., Barnes, C. A. & O'Keefe, J. The contributions of position, direction, and velocity to single unit activity in the hippocampus of freely-moving rats. *Exp. Brain Res.* **52,** 41–49 (1983).
26. Nakazawa, K. *et al.* Hippocampal CA3 NMDA receptors are crucial for memory acquisition of one-time experience. *Neuron* **38,** 305–315 (2003).
27. Kentros, C. G., Agnihotri, N. T., Streater, S., Hawkins, R. D. & Kandel, E. R. Increased attention to spatial context increases both place field stability and spatial memory. *Neuron* **42,** 283–295 (2004).
28. Cacucci, F., Wills, T. J., Lever, C., Giese, K. P. & O'Keefe, J. Experience-dependent increase in CA1 place cell spatial information, but not spatial reproducibility, is dependent on the autophosphorylation of the alpha-isoform of the calcium/calmodulin-dependent protein kinase II. *J. Neurosci.* **27,** 7854–7859 (2007).
29. Sun, L. D. & Wilson, M. A. *Impaired and Enhanced Spatial Representations of the PSD-95 Knockout Mouse.* PhD thesis, Massachusetts Institute of Technology (2003).
30. Margrie, T. W., Brecht, M. & Sakmann, B. *In vivo*, low-resistance, whole-cell recordings from neurons in the anaesthetized and awake mammalian brain. *Pflugers Arch.* **444,** 491–498 (2002).
31. Crochet, S. & Petersen, C. C. Correlating whisker behavior with membrane potential in barrel cortex of awake mice. *Nature Neurosci.* **9,** 608–610 (2006).
32. Wilson, M. A. & McNaughton, B. L. Dynamics of the hippocampal ensemble code for space. *Science* **261,** 1055–1058 (1993).
33. Guzowski, J. F., McNaughton, B. L., Barnes, C. A. & Worley, P. F. Environment-specific expression of the immediate-early gene Arc in hippocampal neuronal ensembles. *Nature Neurosci.* **2,** 1120–1124 (1999).
34. Henze, D. A. *et al.* Intracellular features predicted by extracellular recordings in the hippocampus *in vivo. J. Neurophysiol.* **84,** 390–400 (2000).
35. Kandel, E. R. & Spencer, W. A. Electrophysiology of hippocampal neurons. IV. Fast prepotentials. *J. Neurophysiol.* **24,** 272–285 (1961).
36. Wong, R. K. & Prince, D. A. Participation of calcium spikes during intrinsic burst firing in hippocampal neurons. *Brain Res.* **159,** 385–390 (1978).
37. Hafting, T., Fyhn, M., Bonnevie, T., Moser, M. B. & Moser, E. I. Hippocampus-independent phase precession in entorhinal grid cells. *Nature* **453,** 1248–1252 (2008).

Supplementary Information is linked to the online version of the paper at www.nature.com/nature.

Acknowledgements We thank E. Chaffin for help with mouse behaviour, J. Carmack and id Software for providing the Quake2 code, A. Shishlov for programming advice, G. Buzsaki, J. Magee, H. Dahmen and D. Markowitz for discussions, and C. Brody, M. Berry and E. Civillico for comments on the manuscript. This work was supported by the NIH (1R01MH083686-01, 5R01MH060651-09), a Helen Hay Whitney Fellowship (to C.D.H.), and a Patterson Trust Fellowship (to D.A.D.).

Author Contributions C.D.H. performed behaviour and intracellular recording experiments with technical assistance from D.A.D. C.D.H. and D.A.D. performed extracellular recording experiments. F.C., D.A.D. and D.W.T. designed, and C.D.H., F.C. and D.W.T. implemented, the virtual-reality instrumentation. F.C. performed virtual-reality software development. C.D.H. analysed all data with strategy and methods contributions from all authors. C.D.H. and D.W.T. wrote the paper.

Author Information Reprints and permissions information is available at www.nature.com/reprints. Correspondence and requests for materials should be addressed to D.W.T. (dwtank@princeton.edu).

METHODS

Virtual-reality set-up. The virtual-reality system (Fig. 2a and Supplementary Fig. 1) was designed around an air-supported spherical treadmill (8-inch diameter Styrofoam ball) for head-restrained mice that was previously used for *in vivo* optical imaging at cellular resolution[19]. A projection-based visual display, similar to the system used in a body-tethered rat virtual-reality system[20], presented a computer rendered scene with a 270° horizontal field of view and a vertical field from +60° to −20° relative to the mouse's head. The toroidal screen displayed the two-dimensional image from a Mitsubishi HC3000 digital light processing projector reflected off of a 15 cm diameter round mirror and a 15 cm diameter angular amplification mirror (AAM)[21] with an angular amplification factor of 12. The AAM was machined out of aluminium using a CNC machine and then polished by hand. The screen was ~46 cm tall and ~80 cm in outer diameter, and was constructed out of a semi-reflective nylon material (Rose Brand fabrics) supported by a frame of stainless steel rods. Water rewards were delivered by a solenoid valve (NResearch) attached to a water-feeding tube (Popper and Sons) positioned directly in front of the animal's mouth such that the mouse could lick the meniscus. Rotations of the Styrofoam ball were measured by an optical computer mouse (Logitech MX1000) that was positioned below the field of view in front of the animal at the point where the ball's equator intersected the animal's rostral-caudal body axis. A computer running Labview used USB-communicated signals from the optical mouse to compute low-pass filtered ball rotational velocity around both the horizontal axis (perpendicular to the body axis) and vertical axis. These velocities were then output as analogue control voltages using a D/A converter (National Instruments) and used as input control signals to a separate computer running the virtual-reality software.

The virtual-reality software we developed was on the basis of the open source Quake2 game engine (id software), using code ported to Visual Studio 2008 (Microsoft). The rendering engine was modified, using cube map texturing in OpenGL graphics[38], to display a 'fisheye' transform of the perspective of the virtual player, such that the image reflected off the AAM and displayed on the screen had the geometrically correct perspective for the mouse on the ball. Software to control the water reward system, input information on ball rotation velocity, and output voltages proportional to position and view angle within the environment was also developed by adding A/D and D/A control to the game engine, using National Instruments multifunction cards. Ball velocity around the vertical axis was used as a control signal for changing view angle in the virtual environment, whereas velocity around the horizontal axis was used as a control signal for forward and backward movement. Other open source gaming software (Quark, http://quark.planetquake.gamespy.com/) was used to build the virtual linear track. To synchronize behaviour data with electrophysiology recordings, an independent computer with a Digidata 1440A interface running Clampex software (Molecular Devices) digitized and stored real time information about the mouse's location in the virtual environment together with solenoid (water reward) control signals, ball rotational velocities, and electrophysiological data.

Behavioural training. Eight-to–twelve-week-old male C57BL/6J mice (Jackson Labs) were used for all experiments. C57BL/6J mice were selected because they have good vision compared to other inbred strains[39] and are a common background strain for transgenic mice. All experimental procedures were performed in compliance with the Guide for the Care and Use of Laboratory Animals (http://www.nap.edu/readingroom/books/labrats/) and were approved by Princeton University's Institutional Animal Care and Use Committee. Before behavioural training, titanium head plates with a large central opening (2.5 cm wide × 0.9 cm long × 0.08 cm thick; central opening: 0.89 cm wide × 0.61 cm long) were implanted on mice and affixed to the skull using dental cement (Metabond, Parkell). Sites for future craniotomies over the left and right dorsal hippocampi were marked using stereotactic coordinates (2.2 mm caudal, 1.7 mm lateral to bregma). After head plate implantation, mice were placed on a water schedule in which they received 1 ml of water per day. Body weights were checked to ensure mice were ~80% of their pre-water-restriction weight[40,41].

After at least 5 days of water scheduling, behaviour training began. In each training session, mice were placed on the experimental apparatus with their head fixed in place. The head was centred over the middle of the Styrofoam ball with the headplate ~2.6 cm from the top of the ball. A lick tube to deliver water rewards was positioned in front of the mouse's mouth. The water rewards earned during behaviour were included in the mouse's daily water allotment such that a mouse received exactly 1 ml of water per day. Each training session (one per day) lasted 45 min with the virtual-reality system turned on for all sessions. The first several sessions mostly involved acclimation to the apparatus and learning to run on the spherical treadmill.

Mice were trained to perform behaviours along a virtual linear track. The virtual track was 180 cm long and 9 cm wide, measured as the number of rotations of the Styrofoam ball to move from one end of the track to the other times the circumference of the ball. The effective width of the track (that is, the distance the mouse could actually move) was ~1 cm, rather than 9 cm, because in Quake2 the player is surrounded by a bounding box that gives him a fixed width. The track had short proximal walls with different textures for each third of the track (0–60 cm: white with black dots, 61–120 cm: vertical white and black stripes, 121–180 cm: black with white dots). The proximal walls at the ends of the track were green with black dots to mark the reward zones. Tall distal walls were positioned at 60 cm (horizontal black and white stripes) and 120 cm (green with black crosses). The floor and ceiling were black throughout the track. Green was selected as the only non-black or white colour because electrophysiological and behavioural data indicate that mice can detect wavelengths of ~500 nm[42]. Mice received small water rewards (4 μl) for running between reward zones positioned at opposite ends of the track (zone 1 postion: 0–9 cm; zone 2 position: 171–180 cm). After receiving a reward at one reward zone, the mouse then had to run to the other reward zone to receive the next reward; two consecutive rewards could not be obtained from a single reward site. Linear track behavioural data (Fig. 2c–e) were from mice trained only on the linear track. Some animals used for electrophysiology recordings were trained in other virtual environments before training in the linear track. During electrophysiology experiments, behavioural performance was in some cases degraded due to satiation from water rewards and because the visual display was turned off while patch pipettes were changed.

Electrophysiology. After at least five training sessions on the virtual linear track, a small craniotomy (~0.5 mm diameter) was made over the left hippocampus (2.2 mm caudal, −1.7 mm lateral to bregma). The dura was left intact for both extracellular and intracellular recordings. Because behavioural performance was degraded on the day of surgery and anaesthesia, electrophysiology recordings were performed starting the next day. To preserve the craniotomy across days, it was covered with silicone grease (Dow Corning) and then with a layer of silicone elastomer (Kwik-Sil, World Precision Instruments) until the time of recording. Extracellular recordings (Fig. 3 and Supplementary Fig. 10) were made using a single glass electrode filled with 0.5 M NaCl (~2.5 MΩ pipette resistance). The electrode was mounted vertically (perpendicular to the surface of the brain) on a micromanipulator (Sutter MP285) that was positioned behind the mouse and thus outside the mouse's field of view. The reference electrode was positioned outside the craniotomy in extracellular saline containing (in mM): 150 NaCl, 2.5 KCl, 10 HEPES, pH 7.4. Signals were electronically filtered between 500 Hz and 7.5 kHz and digitized at 20 kHz. For measurements of the LFP and phase precession, signals were electronically filtered between 2 Hz and 10 kHz; spikes and the LFP were recorded on the same electrode. The position of the top of the brain was noted as a large resistance increase when the electrode made contact with the dura. As the electrode was advanced through cortex, spikes were present in each layer. Upon entering the external capsule, a change in the recording was noted, especially from changes in sound quality using an audio monitor. The CA1 cell body layer was ~200 μm beneath the external capsule and was characterized by strongly theta-modulated spiking. Putative pyramidal neurons were found as units firing complex bursts separated at theta frequencies[22]. In all animals CA1 recordings were made at a depth of ~1.1 mm; cells were found reproducibly at this depth across several electrodes and days. To confirm that this recording position was in the CA1 cell body layer, in a separate experiment we electroporated Alexa 488 dextran (5% (w/v) in extracellular saline, 4 μA pulses, 25 ms pulse duration, 600 pulses at 2 Hz) using a recording pipette and found bright labelling of CA1 cell bodies in histology sections. At this depth, we searched for well-isolated units of large amplitude and recorded their activity for ~15–30 min, which was enough time for the mouse to sample thoroughly the virtual linear track. Spikes were sorted offline using a threshold analysis. At most one unit was isolated from a single recording. To check the quality of unit isolation, we overlaid all spike waveforms to make sure that they matched by visual inspection (Fig. 3a), and we plotted ISI distributions to make sure no spikes fell within the refractory period (<1–2 ms; Fig. 3b). Extracellular recordings were made from a total of 8 mice. In some cases a second craniotomy was made over the right hemisphere to extend the number of recording sessions from a single animal. Recordings were made for up to 4 days from the same craniotomy. Place cells were found in every mouse tested.

Whole-cell recordings were made using the same experimental set-up as for extracellular recordings. Pipettes (~5–7 MΩ) were filled with internal solution containing (in mM): 135 K-gluconate, 10 HEPES, 10 Na_2-phosphocreatine, 4 KCl, 4 MgATP, 0.3 Na_3GTP (pH 7.25 with KOH, 285 mOsm). We pulled pipettes with a long taper (~100 μm diameter at 1 mm from the tip) to minimize damage to the overlying cortical tissue and to reduce compression of the tissue while advancing the pipette. The pipette was mounted vertically on a standard micromanipulator (Sutter MP285) positioned outside the mouse's field of view; special methods to anchor the pipette[17,18] were not necessary. We used standard blind patch methods to obtain whole-cell recordings[30]. In brief, we applied ~250 mbar of positive pressure

while moving the pipette through the cortex and reduced the pressure to ~15 mbar while searching for cells in the hippocampus. The CA1 cell body layer was located using a depth coordinate obtained from extracellular recordings in the same animal. We attempted to form a seal when we observed large (~50%), reproducible increases in pipette resistance. Recordings were made in current clamp mode with no holding current. Membrane potential values were corrected for liquid junction potentials. We obtained recordings lasting longer than 3 min from 46 cells from 15 mice, with a peak success rate of approximately one such recording in every five attempts. Recordings were abandoned when we observed large increases in resting potential or large decreases in spike amplitude. We obtained whole-cell recordings for up to 3 days from the same craniotomy. Whole-cell recordings from place cells lasted on average 7.1 ± 2.8 min and had series resistances of 48 ± 16 MΩ, input resistances of 98 ± 23 MΩ, and resting membrane potentials of −67 ± 4 mV. Firing rates from place cells recorded intracellularly tended to be higher than those recorded extracellularly, both inside and outside the place field, potentially because a fraction of spikes measured extracellularly were lost during spike sorting. All other place-cell parameters (for example, field size, ISI distribution) were similar between cells recorded extracellularly and intracellularly. Although we cannot exclude possible effects of dialysis of the cell during whole-cell measurements, such effects are probably small owing to short recording durations and relatively high series resistances. In experiments to assess the connection between ramps of depolarization and changes in theta oscillation amplitude (Supplementary Fig. 7), ramps of current (4 s duration, 1–1.5 nA at the peak) were injected at the soma after 11 s without current injection. Only trials in which the animal was running at greater than 10 cm s^{-1} were analysed.

To perform whole-cell and extracellular recordings simultaneously (Fig. 5f, g and Supplementary Fig. 11), we mounted two glass electrodes on separate micromanipulators, which were both positioned behind the mouse, and advanced the electrodes independently through separate craniotomies on the same hemisphere. Whole-cell recordings were made at the standard coordinates as described earlier. The extracellular recording electrode (filled with 0.5 M NaCl) was mounted at a 40° angle relative to the midline and a 45° angle with respect to the vertical. The craniotomy for the extracellular electrode was positioned caudal and either lateral for the left hemisphere or medial for the right hemisphere relative to the craniotomy for intracellular recordings. The tip of the extracellular electrode was positioned at a depth of ~1.2 mm and ~250 μm caudal to the centre of the craniotomy for whole-cell recordings. The extracellular recordings were filtered between 1 Hz and 10 kHz.

From our 46 hippocampal whole-cell recordings, 41 cells were spontaneously active (overall firing rate >0.05 Hz). We classified 7 of the spontaneously active cells as interneurons on the basis of high overall firing rates (>5 Hz) and the absence of complex spike bursts. The remaining 34 spontaneously active cells were categorized as pyramidal neurons. To estimate the fraction of spontaneously active pyramidal neurons that had a place field along the virtual linear track, we considered only those recordings during which the animal visited each of the 80 spatial segments at least 3 times, with visits separated by at least 2 s in time. We estimate that 36% of spontaneously active pyramidal neurons had place fields in the virtual environment (8 out of 22 cells). During whole-cell place-cell recordings, the place field was visited 20 ± 8 times on average, with visits separated by at least 2 s in time.

Data analysis. To create firing rate maps (Figs 3c, 4b and Supplementary Fig. 2a), we divided the virtual linear track into 80 bins (2.25 cm each) and calculated the firing rate as the total number of spikes in a bin divided by the total amount of time spent in a bin. The maps were smoothed using a five point Gaussian window with a standard deviation of one. Periods in which the mouse ran slower than 5 cm s^{-1}, averaged over a 2-s window, were removed from the analysis. To identify place fields, we found groups of adjacent bins with firing rates greater than 0.25 times the rate in the peak bin. We selected only those fields that were larger than 8 bins (18 cm) in length, had mean in-field firing rates of greater than 1.5 Hz, and had mean in-field firing rates more than 3 times larger than the mean out-of-field firing rate. To verify that place fields were a statistically significant increase in firing rate, we performed a bootstrap shuffle test. We shuffled the times of spikes in 10 s segments, calculated new firing rate maps using the unshuffled bin dwell times, and then checked for a place field using the above-stated criteria. This procedure was repeated 1,000 times per place-cell recording. We called a cell a place cell only if a place field was found in the unshuffled data and in fewer than 2% of the shuffled tests ($P < 0.02$). Across the place cells we recorded, we found place fields at all positions along the linear track. Spikes were separated into leftward and rightward runs based on the head direction of the animal with regard to the virtual track (measured as the player's view angle in Quake2). A directionality index for firing based on firing rates in leftward and rightward directions (FR_{left}, FR_{right}) was defined as $|FR_{left} - FR_{right}|/(FR_{left} + FR_{right})$. A directionality index of 0 indicates identical firing in both directions, whereas an index of 1 indicates firing in one direction only.

To quantify the average baseline membrane potential as a function of position along the virtual track (Fig. 4c and Supplementary Fig. 2b), we first removed the contribution of action potentials by discarding all time points between 4 ms before and 7 ms after an action potential's peak. We then created a map of membrane potential values by grouping the membrane potentials into 80 spatial bins along the track and calculating an average membrane potential for each bin. The membrane potential map was smoothed using a five point Gaussian window with a standard deviation of one. Large, long-lasting depolarizations of the baseline membrane potential occurred infrequently outside the place field (2.3 ± 1.3 events per recording for depolarizations of greater than 2 mV lasting longer than 0.5 s).

To analyse ramps of depolarization during complete runs through the place field (that is, the mouse did not turn around inside the place field), we calculated changes in membrane potential (ΔV) after action potentials were removed (Fig. 4e and Supplementary Figs 5 and 6b). We defined the baseline membrane potential as the mean membrane potential from 500 ms to 1 s before the mouse entered the place field and subtracted this baseline from all membrane potential values during the run to get ΔV values. The peak ΔV during a run through the place field (Supplementary Fig. 6b) was calculated after smoothing the ΔV values over a sliding window of length 50 ms such that the peak value was representative of the ramp-like depolarization rather than brief, high frequency depolarizations. To analyse the symmetry of firing rates and ramps of depolarization in place fields (Fig. 4e), we considered runs starting half the place field's width before the place field and ending half the place field's width beyond the place field (total length was twice the length of the place field). Because place fields varied in size between cells and runs through the field differed in duration, we divided each run into 60 equally sized spatial bins and calculated the mean firing rates and ΔV for each 1/60th of the run (that is, 15 spatial bins before the place field, 30 bins in the field, and 15 bins after the field). All runs through the field were plotted with increasing track position values so that runs in opposite directions could be combined.

To analyse subthreshold theta oscillations (Fig. 5 and Supplementary Figs 2c, 7 and 9), spikes were removed over a window of 3 ms preceding and 5 ms after the peak and were replaced using linear interpolation. The resulting trace was then band-pass filtered between 6–10 Hz (a peak in the ISI distribution) using a linear phase finite impulse response (FIR) filter with a Hamming window of width 1 s (Matlab function fir1). To create a map of theta power along the virtual track, power was calculated as the mean of the squared amplitude for a sliding window of length 1 s for the entire recording, with the centre of the window providing the position along the track. The power values were grouped into 80 spatial bins along the track and smoothed using a five point Gaussian window with a standard deviation of one. Power spectra for epochs in and out of the place field were obtained using multi-taper spectral analysis methods (Chronux toolbox, http://chronux.org; Supplementary Fig. 8). Running speed, which can influence theta oscillations[43], was similar inside and outside the place field (in-field speed = 49 ± 6 cm s^{-1}, out-of-field speed = 47 ± 4 cm s^{-1}, $P > 0.7$). LFP theta oscillations were present when the animal was running (Fig. 3d and Supplementary Fig. 10) and absent when the animal was resting.

To analyse phase precession (Figs 3d, e and 5d–g), we considered complete runs through the place field (that is, the animal did not turn around in the field) that had at least 5 spikes and in which the animal ran faster than 10 cm s^{-1}. Only cells with more than 40 total spikes in the place field were included. Extracellular or intracellular (after removing spikes) voltage traces were band-pass filtered between 6–10 Hz using an FIR filter. To assign a phase to a spike occurring at time t, we identified, in the filtered trace, the times of the peaks immediately preceding and following the spike (t_1 and t_2, respectively) and calculated the phase as $360(t - t_1)/(t_2 - t_1)$. We circularly shifted the phase of the spikes in 1° steps from 0° to 360°, continuing across the 360° border, and fit a linear regression line to the phase versus position plot at each rotation[4,37]. We found the rotation with the best fit, such that the sum of squared errors between the fit line and data was minimized, and used the correlation coefficient between phase and position at this rotation as a measure of phase precession. All phase values are from the raw data in relation to theta phase, with 0° indicating the peak. To measure the precession of intracellular theta relative to extracellular theta (Fig. 5g), we first identified the times of the peaks of the filtered (6–10 Hz) membrane potential trace during runs through the place field. For each peak of intracellular theta, we found the corresponding phase of the simultaneously recorded extracellular theta and the position of the mouse along the virtual track and followed the same procedures that were used for the analysis of the phase precession of spike times. To quantify the change in times between intracellular theta peaks and LFP theta peaks during place field traversals (Supplementary Fig. 11a), we found the time difference between the first LFP theta peak and the first intracellular theta peak in the place field, the time difference between the second LFP theta peak and the second intracellular theta peak, and so on. To quantify frequency differences between intracellular and LFP theta (Supplementary Fig. 11b), we calculated the ratio of the period of the first intracellular oscillation to the period of the first LFP oscillation, the ratio of the period of

the second intracellular oscillation to the period the second LFP oscillation, and so on using peaks from the filtered (6–10 Hz) traces. We determined these ratios for complete runs through the place field and 3 s long epochs outside the place field.

Data are presented as mean ± s.d. unless noted otherwise. *P* values are from two-tailed *t*-tests unless stated otherwise. Correlation coefficients (*C*) are from Pearson's correlations.

38. Greene, N. Environment mapping and other applications of world projections. *IEEE Comput. Graph. Appl.* **6**, 21–29 (1986).
39. Wong, A. A. & Brown, R. E. Visual detection, pattern discrimination and visual acuity in 14 strains of mice. *Genes Brain Behav.* **5**, 389–403 (2006).
40. Rinberg, D., Koulakov, A. & Gelperin, A. Sparse odor coding in awake behaving mice. *J. Neurosci.* **26**, 8857–8865 (2006).
41. Huber, D. *et al.* Sparse optical microstimulation in barrel cortex drives learned behaviour in freely moving mice. *Nature* **451**, 61–64 (2008).
42. Jacobs, G. H., Neitz, J. & Deegan, J. F. II. Retinal receptors in rodents maximally sensitive to ultraviolet light. *Nature* **353**, 655–656 (1991).
43. Buzsáki, G., Leung, L. W. & Vanderwolf, C. H. Cellular bases of hippocampal EEG in the behaving rat. *Brain Res.* **287**, 139–171 (1983).

ARTICLES

Asymmetric centrosome inheritance maintains neural progenitors in the neocortex

Xiaoqun Wang[1], Jin-Wu Tsai[2], Janice H. Imai[1,3], Wei-Nan Lian[2], Richard B. Vallee[2] & Song-Hai Shi[1,3]

Asymmetric divisions of radial glia progenitors produce self-renewing radial glia and differentiating cells simultaneously in the ventricular zone (VZ) of the developing neocortex. Whereas differentiating cells leave the VZ to constitute the future neocortex, renewing radial glia progenitors stay in the VZ for subsequent divisions. The differential behaviour of progenitors and their differentiating progeny is essential for neocortical development; however, the mechanisms that ensure these behavioural differences are unclear. Here we show that asymmetric centrosome inheritance regulates the differential behaviour of renewing progenitors and their differentiating progeny in the embryonic mouse neocortex. Centrosome duplication in dividing radial glia progenitors generates a pair of centrosomes with differently aged mother centrioles. During peak phases of neurogenesis, the centrosome retaining the old mother centriole stays in the VZ and is preferentially inherited by radial glia progenitors, whereas the centrosome containing the new mother centriole mostly leaves the VZ and is largely associated with differentiating cells. Removal of ninein, a mature centriole-specific protein, disrupts the asymmetric segregation and inheritance of the centrosome and causes premature depletion of progenitors from the VZ. These results indicate that preferential inheritance of the centrosome with the mature older mother centriole is required for maintaining radial glia progenitors in the developing mammalian neocortex.

Radial glia cells constitute a major population of neural progenitor cells that occupy the proliferative VZ in the developing mammalian neocortex[1–3]. In addition to their well-characterized function as a scaffold in supporting neuronal migration[4], radial glia cells display interkinetic nuclear oscillation and proliferate extensively at the luminal surface of the VZ (that is, the VZ surface). During the peak phase of neurogenesis (around embryonic day 13–18 (E13–E18) in mice) they predominantly undergo asymmetric division to self-renew while simultaneously giving rise either directly to a neuron, or to an intermediate progenitor cell which subsequently divides symmetrically to produce neurons[5–8]. Whereas differentiating progeny progressively migrate away from the VZ to form the cortical plate (CP)—the future neocortex—renewing radial glia progenitors remain in the VZ for subsequent divisions. The distinct migratory behaviour of radial glia progenitors and their differentiating progeny is fundamental to the proper development of the mammalian neocortex; however, little is known about the basis of these behavioural differences.

Centrosomes, the main microtubule-organizing centres in animal cells[9], have an important role in many cell processes, particularly during cell division[10] and cell migration[11–13]. All normal animal cells initially inherit one centrosome, consisting of a pair of centrioles surrounded by an amorphous pericentriolar material. The two centrioles differ in their structure and function[9,14,15]. The older 'mother' centriole, which is formed at least one-and-a-half generations earlier, possesses appendages/satellites that bear specific proteins, such as cenexin (also known as Odf2)[16,17] and ninein[18–20], and anchor microtubules and support ciliogenesis[9,21]. In contrast, the younger 'daughter' centriole, which is formed during the preceding S phase, lacks these structures. Full acquisition of appendages/satellites by the daughter centriole is not achieved until at least one-and-a-half cell cycles later[22,23]. During each cell cycle, the centrosome replicates once in a semi-conservative manner[24], resulting in the formation of two centrosomes: one of which retains the original old mother centriole (that is, the mother centrosome) while the other receives the new mother centriole (that is, the daughter centrosome)[14,15]. This intrinsic asymmetry in the centrosome has recently been demonstrated to be important for proper spindle orientation during the division of male germline stem cells[25,26] and neuroblasts[27,28] in *Drosophila*, although female germline stem cells appear to divide normally in the absence of centrioles/centrosomes[29]. These studies indicate a critical role for the differential behaviour of centrosomes with differently aged mother centrioles in asymmetric division of the progenitor/stem cells[30–33], although it remains unclear whether proper behaviour and development of the progenitor/stem cells and their differentiating daughter cells depend on centrosome asymmetry. Asymmetric division of radial glia progenitors accounts for nearly all neurogenesis in the developing mammalian neocortex[5–8]. Three out of four autosomal recessive primary microcephaly (MCPH) genes identified so far encode centrosomal components[34], suggesting that proper neocortical neurogenesis and development entail a tight regulation of the centrosome[35], which is so far poorly understood. To address these issues, we investigated centrosome regulation during the peak phase of mammalian neocortical neurogenesis (Supplementary Fig. 1).

Centriole and centrosome asymmetry

To examine centrosome behaviour, we introduced a plasmid encoding centrin 1, a central component of the centriole, fused with enhanced green fluorescent protein (EGFP–CETN1) into the developing

[1]Developmental Biology Program, Memorial Sloan Kettering Cancer Centre, 1275 York Avenue, New York, New York 10065, USA. [2]Departments of Pathology and Cell Biology, Columbia University, 630 W. 168th Street, New York, New York 10032, USA. [3]BCMB Allied Program, Weill Cornell Medical College, 1300 York Avenue, New York, New York 10065, USA.

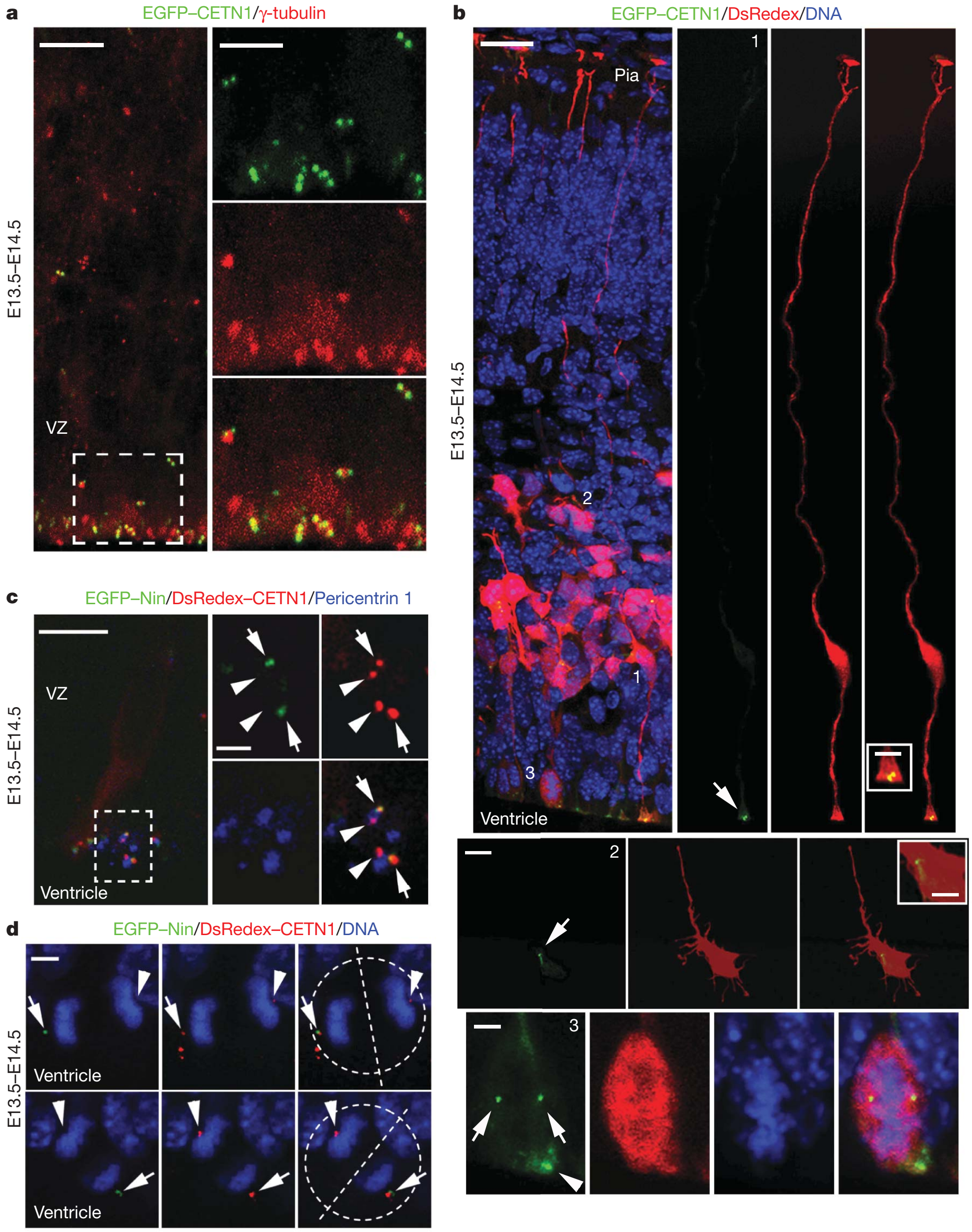

Figure 1 | Centriole and centrosome asymmetry in the developing neocortex. **a**, Images of E14.5 cortices electroporated with EGFP–CETN1 (green) at E13.5 (E13.5–E14.5) and immunostained for γ-tubulin (red). **b**, Images of cortices electroporated with EGFP–CETN1 (green) and DsRedexpress (DsRedex, red) and counterstained with DAPI (blue). Arrows and the arrowhead indicate the centrosomes. Pia represents the pial surface of the neocortex. **c**, Images of cortices electroporated with EGFP–Nin (green, arrows) and DsRedex–CETN1 (red, arrows and arrowheads) and immunostained for pericentrin 1 (blue). **d**, Images of dividing radial glia cells in late mitosis (broken circles) with condensed chromosomes (DAPI, blue) expressing EGFP–Nin (green, arrows) and DsRedex–CETN1 (red, arrows and arrowheads). Broken lines indicate the cleavage plane. Scale bars: **a**, 10 μm and 5 μm; **b**, 25 μm, 2.5 μm, 10 μm, 5 μm and 5 μm (from top to bottom); **c**, 20 μm and 2 μm; **d**, 5 μm.

neocortex of E13.5 mouse embryos by *in utero* electroporation (Supplementary Fig. 2a). As expected, EGFP–CETN1 formed pairs of dots that co-localized with γ-tubulin, a centrosomal marker (Fig. 1a), suggesting that transient expression of EGFP–CETN1 reliably labels the two centrioles of individual centrosomes in the developing neocortex *in vivo*. Moreover, we observed that at the onset of peak neurogenesis (E13–E14), EGFP–CETN1-labelled centrosomes were predominantly located at the VZ surface with a small subset located in the subventricular zone (SVZ) and the intermediate zone (IZ) (Fig. 1a and Supplementary Fig. 2b).

To identify the cell types harbouring EGFP–CETN1-labelled centrosomes, we co-electroporated a plasmid encoding DsRedexpress (DsRedex), a red fluorescent protein that diffuses throughout cells and thereby reveals their morphology (Fig. 1b). We found that in bipolar radial glia progenitors in the VZ the centrosome was located in their ventricular endfeet at the VZ surface (Fig. 1b, cell 1) as previously suggested[36,37], whereas in multipolar cells in the IZ and the SVZ the centrosome was harboured in their cell bodies (Fig. 1b, cell 2). Moreover, we observed dividing radial glia progenitors that possess a pair of centrosomes together with condensed chromosomes at the VZ surface (Fig. 1b, cell 3). Consistent with this differential centrosome localization between radial glia progenitors and their differentiating daughter cells, we observed a progressive increase in the appearance of EGFP–CETN1-labelled centrosomes in the IZ and

the CP as development proceeded, in addition to some that remained at the VZ surface (Supplementary Fig. 2b, c). This gradual increase in centrosome localization in the IZ and the CP coincided with the production and migration of differentiating cells such as neurons to these regions during this period.

The distinct positioning of the centrosome in radial glia progenitors versus their differentiating progeny prompted us to ask whether the centrosomes in these two cell populations/types are different. To explore this, we electroporated a plasmid encoding ninein, a mature centriole-specific protein that localizes to appendages/satellites[18,19], fused with EGFP (EGFP–Nin) together with a plasmid encoding CETN1 fused to DsRedex (DsRedex–CETN1) into the developing mouse neocortex at E13.5. As expected, both EGFP–Nin and DsRedex–CETN1 formed dot-like structures and co-localized to the centrosomes, especially those at the VZ surface, as identified by an antibody to the integral centrosomal protein pericentrin 1 (Fig. 1c). Notably, EGFP–Nin was preferentially concentrated at one of the two centrioles marked by DsRedex–CETN1 in individual centrosomes (Fig. 1c), suggesting that the two centrioles in interphase radial glia progenitors are not identical. Given that Nin specifically associates with mature centrioles[18–20], these results indicate that the centriole with abundant EGFP–Nin is the more mature mother centriole, whereas the one with little EGFP–Nin is the less mature daughter centriole. A similar inequity in the recruitment of EGFP–Nin by the duplicated centrosomes was also observed in dividing radial glia progenitors at the VZ surface (Fig. 1d), indicating that the duplicated centrosomes are not identical during late mitosis. The centrosome with abundant EGFP–Nin is probably the centrosome that retains the mature old mother centriole and the centrosome with little EGFP–Nin is probably the centrosome that bears the relatively immature new mother centriole.

Having found that the centrosomes in dividing radial glia progenitors exhibit asymmetry in their maturity, we next asked whether this centrosome asymmetry is related to the distinct behaviour of radial glia progenitors and their differentiating progeny in the developing neocortex during neurogenesis. To address this, we compared the relative distribution of centrosomes labelled by DsRedex–CETN1 versus those labelled by EGFP–Nin in the developing neocortex as development proceeded (Supplementary Fig. 3). Interestingly, whereas DsRedex–CETN1-labelled centrosomes progressively occupied the IZ and the CP, where differentiating cells are situated, EGFP–Nin-labelled centrosomes were mostly found in the VZ, where radial glia progenitors are located. Given that DsRedex–CETN1 labels all centrosomes whereas EGFP–Nin selectively labels mature centrosomes, these results point to an intriguing possibility that the duplicated centrosomes in dividing radial glia cells are differentially inherited depending on their age and maturity during neocortical neurogenesis. It is known that during each cell division one centrosome retains the old mature mother centriole and the other bears the new less mature mother centriole[14,15,22,38]. Thus, these results suggest that centrosomes with differently aged mother centrioles are differentially inherited by the two daughter cells of asymmetrically dividing radial glia progenitors.

In vivo pulse–chase labelling of centrosomes

To test this, we first developed an assay to distinguish explicitly between the centrosome containing the old mother centriole and the centrosome containing the new mother centriole in the developing neocortex *in vivo* (Fig. 2a, b). The assay takes advantage of the photoconvertible fluorescent protein Kaede[39], which changes from green to red fluorescence on exposure to violet light. Centrioles in the developing neocortex were labelled by transient expression of CETN1 fused with Kaede (Kaede–CETN1). Photoconversion was then performed to switch labelled centrioles from green to red fluorescence. This green-to-red fluorescence conversion of Kaede proteins is irreversible and the red protein is very stable[39], thus allowing long-term tracking of the existing photoconverted proteins and the structures with which they are associated. Moreover, all newly synthesized Kaede proteins are green fluorescent. It is known that centriole duplication requires new protein synthesis of centrin[40]. As a result, newly duplicated centrioles that contain newly synthesized Kaede–CETN1 are green fluorescent, whereas previously existing centrioles are red fluorescent. Hence, in the first cell cycle after photoconversion, both centrosomes contain a red fluorescent mother centriole and a green fluorescent daughter centriole. However, in the second and subsequent cell cycles, centrosomes with the new mother centriole contain only green fluorescent centrioles, whereas centrosomes retaining the original old mother centriole harbour both red and green fluorescent centrioles, thus distinguishing between centrosomes with differently aged mother centrioles (Fig. 2a).

To carry out this assay in the developing neocortex *in vivo*, we developed an *in utero* photoconversion procedure and combined it with *in utero* electroporation (Fig. 2b). Kaede–CETN1, which localized specifically to the centrosomes (Supplementary Fig. 4), was introduced into the developing mouse neocortex at E13.5. One day later, that is, E14.5, the forebrain of electroporated embryos was treated with a short exposure of violet light while still in the uterus, which effectively converted nearly all Kaede–CETN1 proteins and their labelled centrosomes from green to red fluorescence (E13.5–E14.5(PC), Supplementary Fig. 5a, b). The uterus was replaced and the embryos continued to develop *in vivo*. The localization and inheritance of centrosomes were analysed at different developmental stages thereafter.

We found that one day after photoconversion (E13.5–E14.5(PC)–E15.5), around 95% of centrosomes contained both red and green fluorescent centrioles (indicated by yellow colour in the merged image) (Supplementary Fig. 5c, d), consistent with the notion that the labelled cells have undergone one round of division and have duplicated their centrioles during the 24-h period after photoconversion. This was shown directly by imaging centrosomes at high magnification (Supplementary Fig. 6), revealing that each centriole was mostly only red or green fluorescent. This also demonstrates that there is little diffusion of centrin proteins between duplicated centrioles, or between the centrioles and a cytoplasmic pool which was confirmed by fluorescence recovery after photobleaching (FRAP) experiments (Supplementary Fig. 7). Moreover, we found that more than 30% of centrosomes possessed only green fluorescent centrioles 2 days after photoconversion (E13.5–E14.5(PC)–E16.5) (Fig. 2c, d). The appearance of the solely green fluorescent centrosomes 48 h after photoconversion indicates that the initially labelled radial glia progenitors have undergone two rounds of division during this period; this is consistent with the previous observation that the duration of the neocortical progenitor cell cycle is about 12 to 20 h around this developmental stage[41]. The ongoing division of labelled radial glia cells at a normal rate suggests that expression of Kaede–CETN1 and the photoconversion procedure had no effect on their cell cycle. In addition, no obvious DNA damage or cell death was induced by the photoconversion treatment (Supplementary Fig. 8). Besides the green and yellow fluorescent centrosomes, we observed about 4% of solely red fluorescent centrosomes (Fig. 2d), indicating that a few labelled cells do not undergo cell division during this period.

Asymmetric segregation and inheritance of centrosomes

Having successfully distinguished the centrosomes with differently aged mother centrioles in the developing neocortex *in vivo*, we next examined their distribution to determine whether they are asymmetrically segregated. Remarkably, we found that more than 76% of centrosomes with the new mother centriole (that is, only green fluorescent) were located in the IZ and the CP, whereas around 78% of centrosomes with the old mother centriole (that is, both green and red fluorescent) were located in the VZ in addition to the SVZ (Fig. 2c, e, f). These results demonstrate that the centrosomes with differently aged mother centrioles are asymmetrically segregated in the developing neocortex during the peak phase of neurogenesis. It is worth noting that a small fraction of both green and red (that is, yellow) fluorescent centrosomes was found in the IZ and the CP

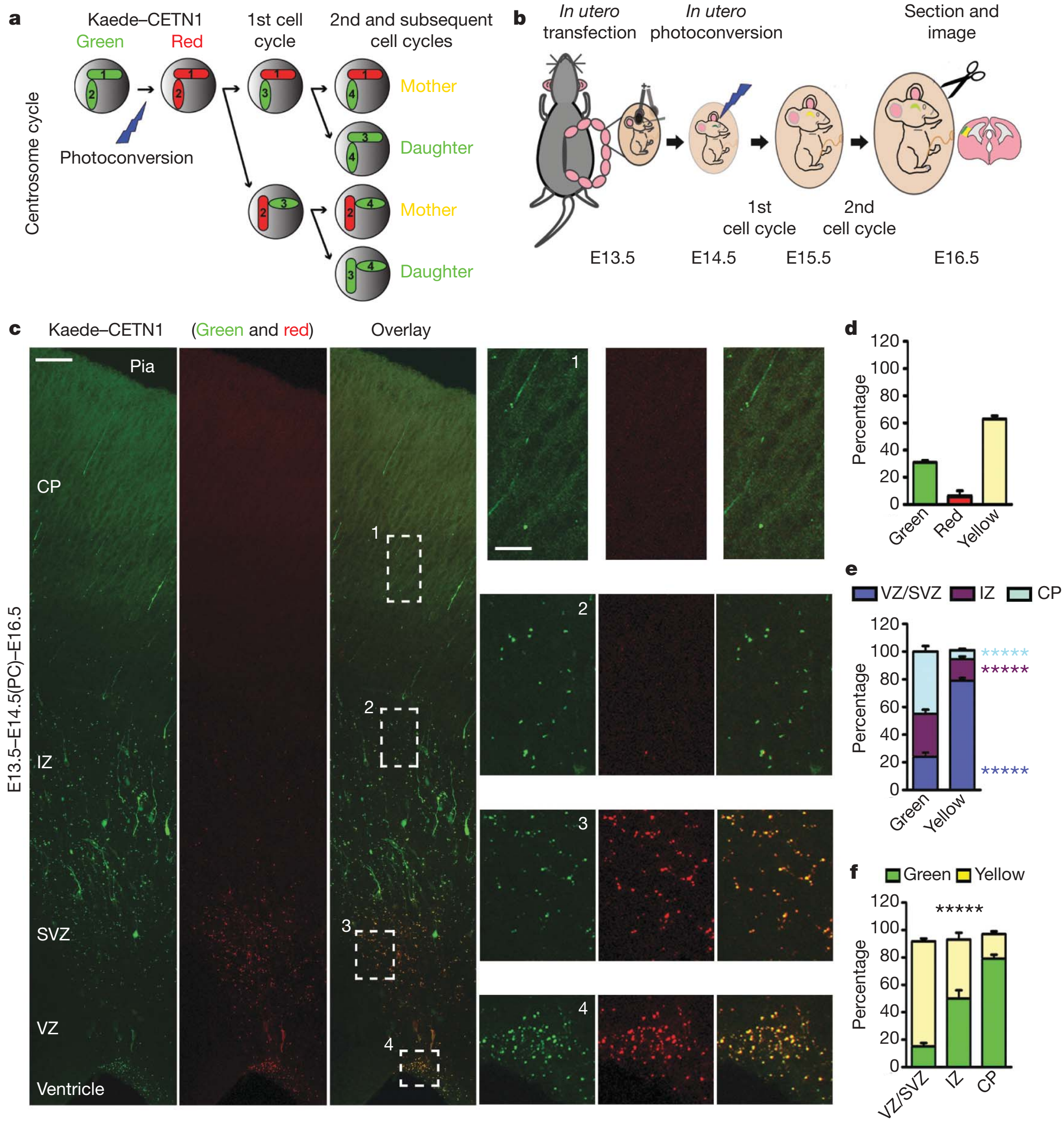

Figure 2 | Asymmetric segregation of centrosomes with differently aged mother centrioles. a, b, Strategy and experimental procedure for using Kaede–CETN1 to distinguish between centrosomes with differently aged mother centrioles. **c,** Images of E16.5 cortices electroporated with Kaede–CETN1 at E13.5 and photoconverted (PC) at E14.5 (E13.5–E14.5(PC)–E16.5). Scale bars: 50 μm and 15 μm. **d–f,** Quantifications of the percentage of labelled centrosomes that are green, red or yellow fluorescent (**d**), the percentage of green or yellow fluorescent centrosomes that are located in different regions of the developing neocortex (**e**), and the percentage of labelled centrosomes located in different regions of the developing neocortex that are green or yellow fluorescent (**f**) (total 4,314 centrosomes from seven individual animals). Data are shown as mean ± s.e.m.; *****, $P < 5 \times 10^{-5}$.

(Fig. 2e, f) and that these centrosomes probably originated from the first cell cycle after photoconversion (Supplementary Fig. 5c, d).

The asymmetric segregation of centrosomes suggests differential regulation of the duplicated centrosomes in dividing radial glia progenitors. To gather further evidence for this, we carried out time-lapse imaging experiments to monitor the behaviour of centrosomes with differently aged mother centrioles in dividing radial glia progenitors at the VZ surface *in situ* (Fig. 3a). Kaede–CETN1 was introduced into radial glia cells together with mPlum, a far-red fluorescent protein, to label cell morphology. Around 24 h later, cortical slices were prepared. Photoconversion of the existing Kaede–CETN1 proteins was then performed in individual slices, which were then cultured for another 24 h before being subjected to time-lapse imaging. Labelled dividing radial glia cells with enlarged and rounded cell bodies possessing a pair of centrosomes at the VZ surface (Fig. 3b) were monitored at 10-min intervals over a period of 5 to 8 h (Fig. 3c, d, Supplementary Video 1 and Supplementary Fig. 9). In six out of seven dividing radial glia cells that proceeded through mitosis at the VZ surface and reached the two-cell stage, the centrosome retaining the old mother centriole in both red and green fluorescence stayed at the VZ surface, whereas the centrosome containing the new mother centriole in solely green fluorescence migrated away from the VZ surface (Fig. 3c, d, Supplementary Video 1 and Supplementary Fig. 9). These results demonstrate that the centrosomes with differently aged mother centrioles in dividing radial glia progenitors exhibit distinct behaviour during the peak phase of neurogenesis.

The distinct behaviour of the centrosomes suggests that they are differentially inherited by the two daughter cells embarking on different routes of fate specification and development. On the basis of their behaviour, we postulated that the centrosome with the new mother centriole is largely inherited by differentiating cells, such as neurons, whereas the centrosome with the old mother centriole that remains located at the VZ is mostly inherited by radial glia progenitors. Indeed, we found that 2 days after photoconversion (E13.5–E14.5(PC)–E16.5) the centrosomes with the new mother centriole, marked by green

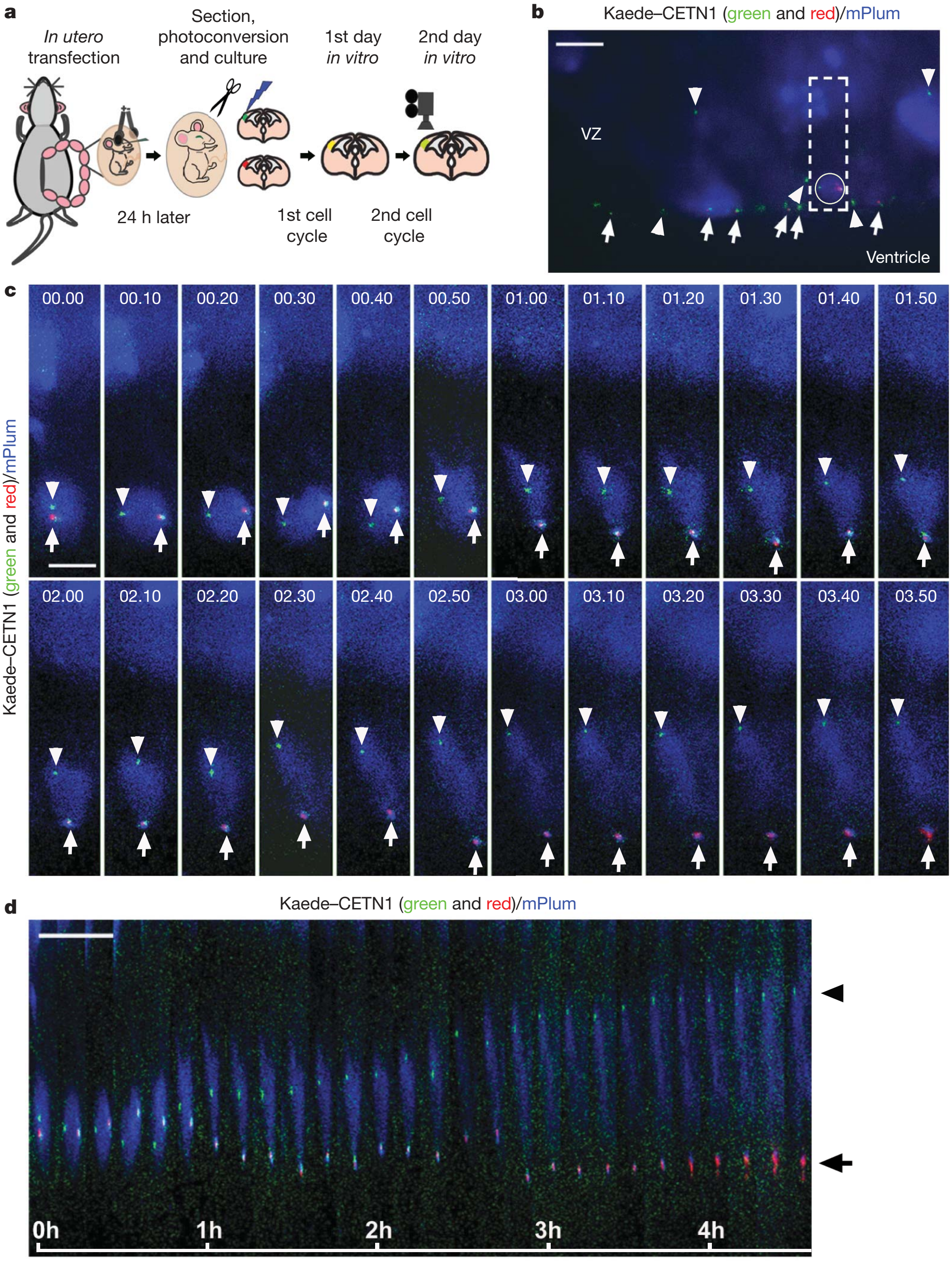

Figure 3 | Distinct behaviour of centrosomes with differently aged mother centrioles. **a**, Experimental procedure for time-lapse imaging analysis of centrosome behaviour. **b**, Image of a cortical slice in culture expressing Kaede–CETN1 (green and red) and mPlum (blue) before time-lapse imaging. Arrows indicate the centrosomes with the old mother centriole (both green and red fluorescent) and arrowheads indicate the centrosomes with the new mother centriole (green fluorescent only). The outlined region contains a dividing radial glia cell possessing a pair of centrosomes with differently aged mother centrioles (circled). **c**, **d**, Time-lapse (**c**) and kymograph (**d**) images of the outlined region in **b**. The time is indicated at the top (**c**) or the bottom (**d**) of images (in hours and minutes). Arrows indicate centrosomes possessing the old mother centriole and arrowheads indicate centrosomes possessing the new mother centriole. Scale bars: **b**, 15 μm; **c**, **d**, 10 μm.

fluorescence alone, were mostly associated with cells expressing TUJ1, a differentiating neuronal marker, in the CP and the IZ (Fig. 4a). In contrast, the centrosomes that retained the old mother centriole in yellow (that is, both green and red) fluorescence at the VZ were largely associated with cells expressing Pax6, a radial glia progenitor marker (Fig. 4b). These results show that the centrosomes with differently aged mother centrioles in dividing radial glia cells are asymmetrically inherited by the two daughter cells: whereas the renewing radial glia progenitor inherits the centrosome with the old mother centriole, the differentiating daughter cell inherits the centrosome with the new mother centriole.

Asymmetric centrosome inheritance maintains progenitors

Our data thus far show that centrosomes with differently aged mother centrioles are differentially inherited by the two daughter cells of asymmetrically dividing radial glia progenitors in the developing neocortex. We next tested whether the selective inheritance of the centrosome with the old mature mother centriole by radial glia progenitors is necessary for their maintenance at the VZ. Should this be the case, given that Nin is an essential component of the appendage/satellite structures specific to the mature centriole, we predicted that removal of Nin, which prevents centriole maturation[19,42], would disrupt asymmetric segregation of centrosomes with differently aged

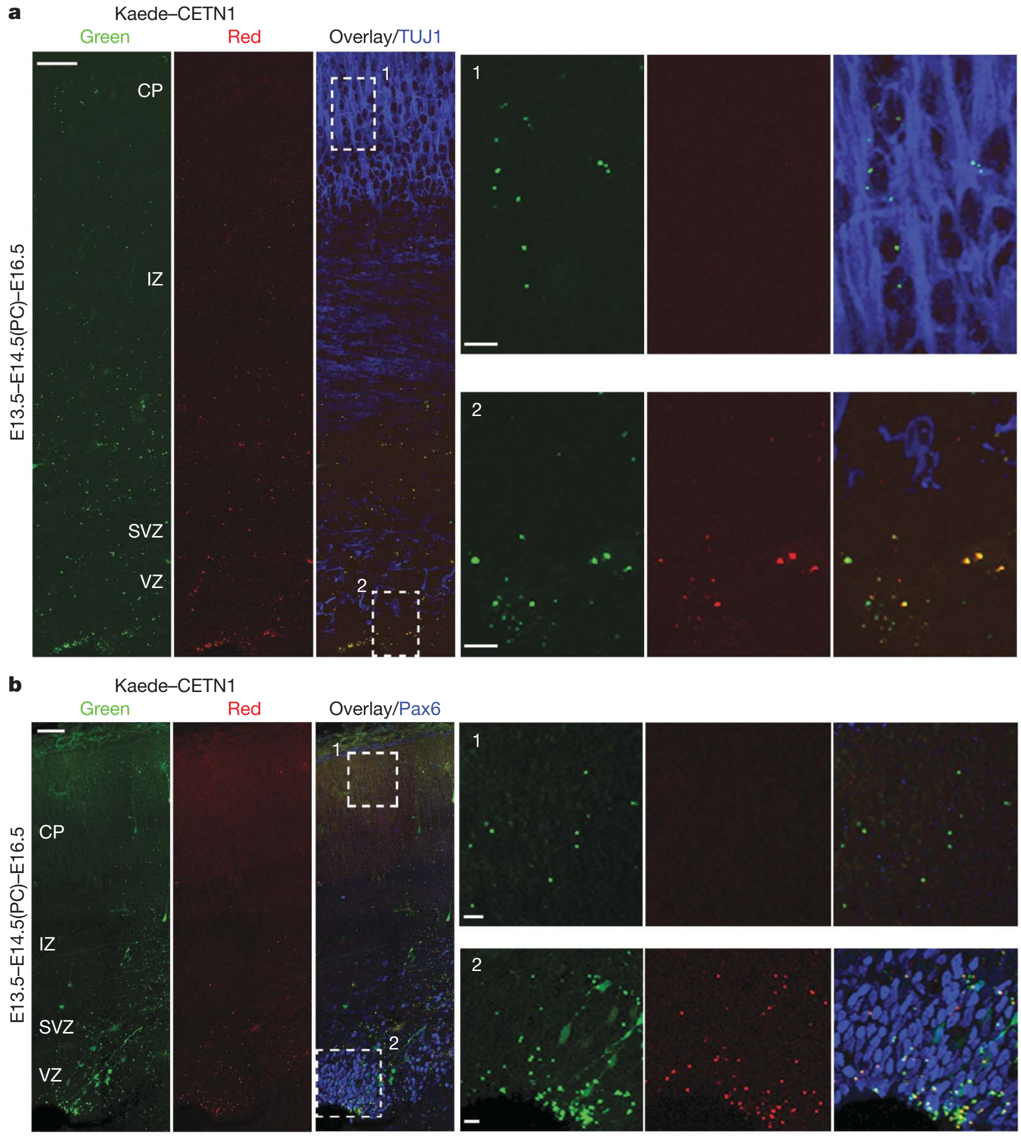

Figure 4 | Asymmetric inheritance of centrosomes with differently aged mother centrioles. Images of cortices electroporated with Kaede–CETN1, photoconverted and immunostained for TUJ1 (**a**) or for Pax6 (**b**) (blue). High magnification images of the outlined regions are shown to the right. Scale bars: 50 μm, 10 μm and 10 μm.

mother centrioles and impair the maintenance of radial glia progenitors in the developing neocortex.

To test this, we developed short hairpin RNA (shRNA) sequences against *Nin* that effectively suppressed its expression (*Nin* shRNAs, Supplementary Fig. 10a). Consistent with our prediction, expression of *Nin* shRNA, but not control shRNA, disrupted asymmetric segregation of centrosomes with differently aged mother centrioles labelled with Kaede–CETN1 in the developing neocortex (Supplementary Fig. 11), suggesting that Nin is necessary for centriole maturation, thereby generating asymmetry between duplicated centrosomes. The presence of solely green fluorescent centrosomes in *Nin* shRNA-expressing cortices indicates that centrosome duplication and segregation and cell division are not severely affected by removal of Nin, as suggested previously[19,42]. More importantly, we found that removal of Nin caused a premature depletion of cells from the VZ, where radial glia progenitors reside (Fig. 5a, b). This effect of *Nin* shRNAs correlated with their efficacy in suppressing Nin protein expression (Supplementary Fig. 10a, b) and was rescued by a shRNA-insensitive Nin plasmid (Supplementary Fig. 10c), suggesting that the effect of the *Nin* shRNA is due to a specific depletion of the endogenous Nin protein. A similar reduction in cells in the VZ was observed when Nin expression was suppressed using small interfering RNA (siRNA) (Supplementary Fig. 10d, e).

To characterize further the extent to which removal of Nin leads to a depletion of radial glia progenitors, we next examined the fate specification of cells expressing either control or *Nin* shRNA (Fig. 5c–f). When compared with the control, expression of *Nin* shRNA led to a marked reduction in the percentage of cells positive for Pax6 and glutamate transporter (GLAST) (Fig. 5c, d and Supplementary Fig. 12), two radial glia progenitor markers, and a significant increase in the percentage of cells positive for TUJ1 (Fig. 5e, f), a differentiating neuronal marker. These results suggest that removal of Nin leads to a depletion of radial glia progenitors and a concomitant increase in differentiating neurons. Consistent with this, we observed a significant reduction in phospho-histone 3 (P-H3)-labelled mitotic cells at the VZ surface (Supplementary Fig. 13) and a marked increase in cell cycle exit (Supplementary Fig. 14). No obvious change in the cleavage plane orientation of late stage mitotic cells at the VZ surface was observed (Supplementary Fig. 15).

Previous studies showed that the carboxy-terminus of Nin is responsible for its localization to the centriole and expression of this region displaces endogenous protein at the centriole[43]. Interestingly, we found that, similar to removal of Nin, expression of the carboxy-terminus of

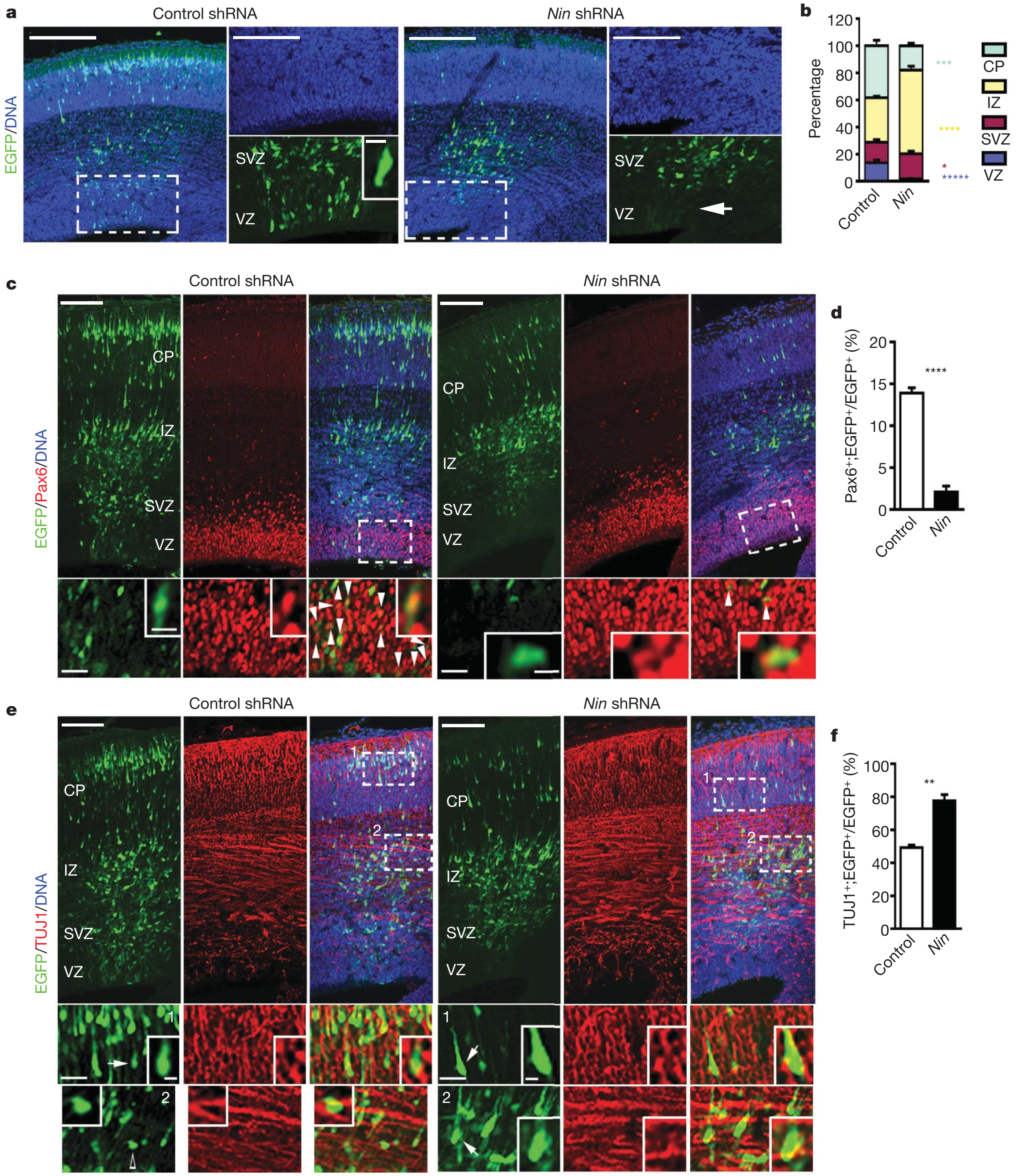

Figure 5 | Preferential inheritance of the centrosome with the mature mother centriole maintains radial glia progenitors. **a**, Images of E16.5 cortices electroporated with either EGFP/control (left, green) or EGFP/*Nin* shRNA (right, green) at E13.5 and counterstained with DAPI (blue). **b**, Quantification of the percentage of EGFP-expressing cells in different regions of the developing neocortex (control shRNA, total 1,873 cells from five individual animals; *Nin* shRNA, total 958 cells from five individual animals). **c**, **e**, Images of E16.5 cortices electroporated with EGFP/control (left, green) or EGFP/*Nin* shRNA (right, green) at E13.5 and immunostained for Pax6 (**c**) or TUJ1 (**e**) (red). Arrowheads indicate EGFP-expressing cells positive for Pax6 (**c**). Arrows indicate EGFP-expressing cells that are positive for TUJ1 and the open arrowhead indicates an EGFP-expressing cell that is not positive for TUJ1 (**e**). **d**, **f**, Quantification of the percentage of EGFP-expressing cells positive for Pax6 (**d**; control shRNA, total 1,752 cells from five individual animals; *Nin* shRNA, total 1,230 cells from five animals) or for TUJ1 (**f**; control shRNA, total 1,383 cells from five individual animals; *Nin* shRNA, total 1,247 cells from five individual animals). Data are shown as mean ± s.e.m.; *, $P < 0.05$; **, $P < 0.005$; ***, $P < 0.001$; ****, $P < 0.0005$; *****, $P < 5 \times 10^{-5}$. Scale bars: **a**, 100 μm, 50 μm and 10 μm; **c**, 100 μm, 5 μm and 25 μm; **e**, 100 μm, 25 μm and 5 μm.

Nin (Nin-Cter) led to a premature depletion of radial glia progenitor cells from the VZ (Supplementary Fig. 16), suggesting that centriolar Nin is critical for maintaining radial glia progenitor cells in the VZ. Taken together, these results indicate that preferential inheritance of a centrosome containing the mature mother centriole is required for the maintenance of radial glia progenitors in the proliferative VZ of the developing neocortex.

The results presented here suggest that the centrosomes with differently aged centrioles in asymmetrically dividing radial glia progenitors exhibit different behaviour and are differentially inherited by the

two daughter cells during the peak phase of mammalian neocortical neurogenesis (Supplementary Fig. 1). Whereas the centrosome with the less mature new mother centriole migrates away from the VZ surface and is largely inherited by differentiating cells, the centrosome with the more mature old mother centriole stays at the VZ surface and is predominantly inherited by renewing radial glia progenitors. Recently, asymmetric behaviour of centrosomes has been observed during asymmetric division of *Drosophila* male germline stem cells and neuroblasts[25–28]. Our findings suggest that this type of asymmetric centrosome regulation may be a general feature of asymmetric cell division across species[30–33]. Furthermore, our findings provide new insight into centrosome regulation in the developing mammalian neocortex, which has been linked to the pathogenesis of human microcephaly[34,44].

Centrosomes with differently aged mother centrioles differ in their protein composition and thereby in their biophysical properties, such as microtubule anchorage activity[9,15] and the capability to mediate ciliogenesis[21,23,45]. In this study, we found that Nin, an appendage/satellite-specific protein required for centriole maturation, localized differently to the duplicated centrosomes in radial glia progenitors in late mitosis. Notably, another appendage/satellite-specific protein cenexin was recently found to be asymmetrically localized to centrosomes in sister cells after mitosis; moreover, the cell receiving the more mature old mother centriole usually grew a primary cilium first[21]. The asymmetric inheritance of centrosomes with distinct biophysical properties may thereby differentially regulate the behaviour and development of the daughter cells that receive them. For example, given that primary cilia have essential roles in a number of signal transduction pathways, including Sonic hedgehog (Shh) and platelet-derived growth factor (PDGF) signalling, the asynchrony in cilium formation could differentially influence the ability of the two daughter cells to respond to environmental signals and thereby their behaviour and fate specification. Furthermore, the strong microtubule anchorage activity associated with the centrosome retaining the older mother centriole would facilitate its anchorage to a specific site (for example, the VZ surface), thereby tethering the cell that inherits it. Indeed, we found that disruption of centriole maturation by removing Nin not only impairs asymmetric segregation of centrosomes, but also depletes radial glia progenitors from the VZ, a proliferative niche in the developing mammalian neocortex. Aside from their participation in microtubule organization and ciliogenesis, centrosomes associate with messenger RNAs (mRNAs)[46] and membrane-bound organelles such as the Golgi and recycling endosomes and regulate protein degradation[47,48], thereby raising the possibility that asymmetric centrosome inheritance might contribute to proper segregation of cell fate determinants to the two daughter cells of asymmetrically dividing progenitor/stem cells.

METHODS SUMMARY

***In utero* electroporation and photoconversion.** *In utero* electroporation of the plasmids (for example, EGFP–CETN1) was performed as previously described[49,50]. For *in utero* photoconversion, a similar surgical procedure was carried out as for *in utero* electroporation. The forebrain of the embryos that received electroporation was exposed to a brief (about three to five minutes) exposure of light at 350–400 nm while in the uterus. All procedures for animal handling and usage were approved by our institutional research animal resource centre (RARC).

Brain section, immunohistochemistry and imaging. Brains were fixed at the desired developmental stages and coronal sections were prepared using a vibratome (Leica Microsystems). Immunohistochemistry were performed as previously described[50]. Images were acquired using a confocal laser scanning microscope (FV1000, Olympus) and analysed using FluoView (Olympus), Volocity (Improvision) and Photoshop (Adobe Systems). Data were presented as mean and s.e.m. and statistical differences were determined using nonparametric tests (Mann–Whitney–Wilcoxon test for two groups of data and Kruskal–Wallis test for three or more groups of data).

Cortical slice culture and time-lapse imaging. Cortical slice cultures were prepared and time-lapse imaging was acquired as previously described[12]. Images were analysed using MetaMorph (Molecular Devices) and Photoshop (Adobe Systems).

Full Methods and any associated references are available in the online version of the paper at www.nature.com/nature.

Received 30 June; accepted 18 August 2009.

1. Miyata, T., Kawaguchi, A., Okano, H. & Ogawa, M. Asymmetric inheritance of radial glial fibers by cortical neurons. *Neuron* **31**, 727–741 (2001).
2. Noctor, S. C., Flint, A. C., Weissman, T. A., Dammerman, R. S. & Kriegstein, A. R. Neurons derived from radial glial cells establish radial units in neocortex. *Nature* **409**, 714–720 (2001).
3. Malatesta, P., Hartfuss, E. & Gotz, M. Isolation of radial glial cells by fluorescent-activated cell sorting reveals a neuronal lineage. *Development* **127**, 5253–5263 (2000).
4. Rakic, P. Elusive radial glial cells: historical and evolutionary perspective. *Glia* **43**, 19–32 (2003).
5. Miyata, T. *et al.* Asymmetric production of surface-dividing and non-surface-dividing cortical progenitor cells. *Development* **131**, 3133–3145 (2004).
6. Noctor, S. C., Martinez-Cerdeno, V., Ivic, L. & Kriegstein, A. R. Cortical neurons arise in symmetric and asymmetric division zones and migrate through specific phases. *Nature Neurosci.* **7**, 136–144 (2004).
7. Chenn, A. & McConnell, S. K. Cleavage orientation and the asymmetric inheritance of Notch1 immunoreactivity in mammalian neurogenesis. *Cell* **82**, 631–641 (1995).
8. Noctor, S. C., Martinez-Cerdeno, V. & Kriegstein, A. R. Distinct behaviors of neural stem and progenitor cells underlie cortical neurogenesis. *J. Comp. Neurol.* **508**, 28–44 (2008).
9. Bornens, M. Centrosome composition and microtubule anchoring mechanisms. *Curr. Opin. Cell Biol.* **14**, 25–34 (2002).
10. Doxsey, S., McCollum, D. & Theurkauf, W. Centrosomes in cellular regulation. *Annu. Rev. Cell Dev. Biol.* **21**, 411–434 (2005).
11. Xie, Z. *et al.* Cep120 and TACCs control interkinetic nuclear migration and the neural progenitor pool. *Neuron* **56**, 79–93 (2007).
12. Tsai, J. W., Bremner, K. H. & Vallee, R. B. Dual subcellular roles for LIS1 and dynein in radial neuronal migration in live brain tissue. *Nature Neurosci.* **10**, 970–979 (2007).
13. Solecki, D. J., Model, L., Gaetz, J., Kapoor, T. M. & Hatten, M. E. Par6α signaling controls glial-guided neuronal migration. *Nature Neurosci.* **7**, 1195–1203 (2004).
14. Meraldi, P. & Nigg, E. A. The centrosome cycle. *FEBS Lett.* **521**, 9–13 (2002).
15. Delattre, M. & Gonczy, P. The arithmetic of centrosome biogenesis. *J. Cell Sci.* **117**, 1619–1630 (2004).
16. Lange, B. M. & Gull, K. A molecular marker for centriole maturation in the mammalian cell cycle. *J. Cell Biol.* **130**, 919–927 (1995).
17. Nakagawa, Y., Yamane, Y., Okanoue, T., Tsukita, S. & Tsukita, S. Outer dense fiber 2 is a widespread centrosome scaffold component preferentially associated with mother centrioles: its identification from isolated centrosomes. *Mol. Biol. Cell* **12**, 1687–1697 (2001).
18. Bouckson-Castaing, V. *et al.* Molecular characterisation of ninein, a new coiled-coil protein of the centrosome. *J. Cell Sci.* **109**, 179–190 (1996).
19. Ou, Y. Y., Mack, G. J., Zhang, M. & Rattner, J. B. CEP110 and ninein are located in a specific domain of the centrosome associated with centrosome maturation. *J. Cell Sci.* **115**, 1825–1835 (2002).
20. Piel, M., Meyer, P., Khodjakov, A., Rieder, C. L. & Bornens, M. The respective contributions of the mother and daughter centrioles to centrosome activity and behavior in vertebrate cells. *J. Cell Biol.* **149**, 317–330 (2000).
21. Anderson, C. T. & Stearns, T. Centriole age underlies asynchronous primary cilium growth in mammalian cells. *Curr. Biol*. doi:10.1016/j.cub.2009.07.034 (12 August 2009).
22. Chretien, D., Buendia, B., Fuller, S. D. & Karsenti, E. Reconstruction of the centrosome cycle from cryoelectron micrographs. *J. Struct. Biol.* **120**, 117–133 (1997).
23. Vorobjev, I. A. & Chentsov Yu. S. Centrioles in the cell cycle. I. Epithelial cells. *J. Cell Biol.* **93**, 938–949 (1982).
24. Tsou, M. F. & Stearns, T. Mechanism limiting centrosome duplication to once per cell cycle. *Nature* **442**, 947–951 (2006).
25. Cheng, J. *et al.* Centrosome misorientation reduces stem cell division during ageing. *Nature* **456**, 599–604 (2008).
26. Yamashita, Y. M., Mahowald, A. P., Perlin, J. R. & Fuller, M. T. Asymmetric inheritance of mother versus daughter centrosome in stem cell division. *Science* **315**, 518–521 (2007).
27. Rebollo, E. *et al.* Functionally unequal centrosomes drive spindle orientation in asymmetrically dividing *Drosophila* neural stem cells. *Dev. Cell* **12**, 467–474 (2007).
28. Rusan, N. M. & Peifer, M. A role for a novel centrosome cycle in asymmetric cell division. *J. Cell Biol.* **177**, 13–20 (2007).
29. Stevens, N. R., Raposo, A. A., Basto, R., St Johnston, D. & Raff, J. W. From stem cell to embryo without centrioles. *Curr. Biol.* **17**, 1498–1503 (2007).
30. Cabernard, C. & Doe, C. Q. Stem cell self-renewal: centrosomes on the move. *Curr. Biol.* **17**, R465–R467 (2007).
31. Spradling, A. C. & Zheng, Y. Developmental biology. The mother of all stem cells? *Science* **315**, 469–470 (2007).
32. Yamashita, Y. M. & Fuller, M. T. Asymmetric centrosome behavior and the mechanisms of stem cell division. *J. Cell Biol.* **180**, 261–266 (2008).
33. Gonzalez, C. Spindle orientation, asymmetric division and tumour suppression in *Drosophila* stem cells. *Nature Rev. Genet.* **8**, 462–472 (2007).

34. Cox, J., Jackson, A. P., Bond, J. & Woods, C. G. What primary microcephaly can tell us about brain growth. *Trends Mol. Med.* **12,** 358–366 (2006).
35. Higginbotham, H. R. & Gleeson, J. G. The centrosome in neuronal development. *Trends Neurosci.* **30,** 276–283 (2007).
36. Hinds, J. W. & Ruffett, T. L. Cell proliferation in the neural tube: an electron microscopic and golgi analysis in the mouse cerebral vesicle. *Z. Zellforsch. Mikrosk. Anat.* **115,** 226–264 (1971).
37. Chenn, A., Zhang, Y. A., Chang, B. T. & McConnell, S. K. Intrinsic polarity of mammalian neuroepithelial cells. *Mol. Cell. Neurosci.* **11,** 183–193 (1998).
38. Bornens, M. & Piel, M. Centrosome inheritance: birthright or the privilege of maturity? *Curr. Biol.* **12,** R71–R73 (2002).
39. Ando, R., Hama, H., Yamamoto-Hino, M., Mizuno, H. & Miyawaki, A. An optical marker based on the UV-induced green-to-red photoconversion of a fluorescent protein. *Proc. Natl Acad. Sci. USA* **99,** 12651–12656 (2002).
40. Salisbury, J. L., Suino, K. M., Busby, R. & Springett, M. Centrin-2 is required for centriole duplication in mammalian cells. *Curr. Biol.* **12,** 1287–1292 (2002).
41. Cai, L., Hayes, N. L. & Nowakowski, R. S. Local homogeneity of cell cycle length in developing mouse cortex. *J. Neurosci.* **17,** 2079–2087 (1997).
42. Mogensen, M. M., Malik, A., Piel, M., Bouckson-Castaing, V. & Bornens, M. Microtubule minus-end anchorage at centrosomal and non-centrosomal sites: the role of ninein. *J. Cell Sci.* **113,** 3013–3023 (2000).
43. Delgehyr, N., Sillibourne, J. & Bornens, M. Microtubule nucleation and anchoring at the centrosome are independent processes linked by ninein function. *J. Cell Sci.* **118,** 1565–1575 (2005).
44. Bond, J. *et al.* A centrosomal mechanism involving CDK5RAP2 and CENPJ controls brain size. *Nature Genet.* **37,** 353–355 (2005).
45. Preble, A. M., Giddings, T. M. Jr & Dutcher, S. K. Basal bodies and centrioles: their function and structure. *Curr. Top. Dev. Biol.* **49,** 207–233 (2000).
46. Lambert, J. D. & Nagy, L. M. Asymmetric inheritance of centrosomally localized mRNAs during embryonic cleavages. *Nature* **420,** 682–686 (2002).
47. Wigley, W. C. *et al.* Dynamic association of proteasomal machinery with the centrosome. *J. Cell Biol.* **145,** 481–490 (1999).
48. Fuentealba, L. C., Eivers, E., Geissert, D., Taelman, V. & De Robertis, E. M. Asymmetric mitosis: unequal segregation of proteins destined for degradation. *Proc. Natl Acad. Sci. USA* **105,** 7732–7737 (2008).
49. Tabata, H. & Nakajima, K. Efficient *in utero* gene transfer system to the developing mouse brain using electroporation: visualization of neuronal migration in the developing cortex. *Neuroscience* **103,** 865–872 (2001).
50. Bultje, R. S. *et al.* Mammalian Par3 regulates progenitor cell asymmetric division via notch signaling in the developing neocortex. *Neuron* **63,** 189–202 (2009).

Supplementary Information is linked to the online version of the paper at www.nature.com/nature.

Acknowledgements We thank A. Hall, A. L. Joyner, K. V. Anderson, J. Kaltschmidt, B. M. Tsou, Y. Chin and L. A. McDowell for comments on the manuscript; members of the Shi laboratory for discussions; A. K. Hadjantonakis for human centrin 1 cDNA; M. Bornens for EGFP–Nin (mouse) and Nin truncation mutant plasmids; Y.-R. Hong for EGFP–Nin (human) plasmid; A. Miyawaki for pCS2+–Kaede plasmid; and H. Zhong, K. Svoboda and R. Tsien for DsRedexpress and mPlum cDNA constructs. We thank C. T. Anderson and T. Stearns for sharing unpublished data. This work is supported by grants from March of Dimes Birth Defects Foundation, Whitehall Foundation, Dana Foundation, Autism Speaks Foundation, Klingenstein Foundation, NARSAD (to S.-H.S.) and NIH (to S.-H.S. and R.B.V.).

Author Contributions X.W. and S.-H.S. conceived the project. X.W. performed most of the experiments. J.-W.T., W.-N.L. and R.B.V. contributed to the time-lapse imaging experiment and J.H.I. contributed to the characterization of Kaede–CETN1 co-localization and *in utero* photoconversion procedure. X.W. and S.-H.S. analysed data, interpreted results and wrote the manuscript. All authors edited the manuscript.

Author Information Reprints and permissions information is available at www.nature.com/reprints. Correspondence and requests for materials should be addressed to S.-H.S. (shis@mskcc.org).

METHODS

Plasmids and *in utero* electroporation and photoconversion. Human centrin 1 cDNA was obtained by polymerase chain reaction (PCR) and cloned into the KpnI and BamHI sites of pEGFP-C1 (Clontech) to generate the EGFP–CETN1 plasmid. Kaede and DsRedexpress (DsRedex) cDNAs were obtained by PCR and cloned into pEGFP–CETN1-C1 to replace EGFP in generating the Kaede–CETN1 and DsRedex–CETN1 plasmids. The mouse ninein (GenBank/EMBL/DDBJ accession number AY515727) plasmid was provided by M. Bornens. Human ninein cDNA (IMAGE ID 3090109, Open Biosystems) was cloned into the EcoRI and NotI sites of pCDNA3.1. Three shRNA sequences against mouse *Nin* were designed as follows: shRNA-a (5′-GCAGAAGGCCAGCTGAGGT-3′), shRNA-b (5′-GGCCGAGATCCGGCACTTG-3′), shRNA-c (5′-GCTTCAATT CAGACAATGG-3′). All sense and antisense oligonucleotides were purchased from Sigma. Annealed oligonucleotides were cloned into the HpaI and XhoI sites of the lentiviral vector pLL3.7, which contains a separate CMV promoter that drives expression of EGFP[50]. In this study, mouse *Nin* shRNA-c was primarily used after extensive characterization to demonstrate that it specifically suppressed Nin protein expression and function. For siRNA experiments, synthetic oligonucleotides against *Nin* and control were purchased from Santa Cruz Biotechnology (sc-61196). Human *NIN* cDNA, which differs from mouse *Nin* cDNA in the shRNA-c targeting region and is thereby insensitive to *Nin* shRNA-c expression, was used for the rescue experiment. The N terminus (nucleotides 1–1120) and C-terminus (nucleotides 5623–6339) of mouse Nin were amplified by PCR and cloned into the EcoRI and NotI sites of pCAG-IRES-EGFP. All plasmids were confirmed by sequencing.

In utero electroporation was performed as previously described[49,50]. In brief, a timed pregnant CD-1 mouse at 13.5 days of gestation (E13.5) or a rat at E16.5 was anaesthetized, the uterine horns were exposed, and $\sim$1 μl of plasmid DNA (1–3 μg μl^{-1}) mixed with Fast Green (Sigma) was manually microinjected through the uterus into the lateral ventricle, using a bevelled and calibrated glass micropipette (Drummond Scientific). For electroporation, five 50-ms pulses of 40–50 mV with a 950-ms interval were delivered across the uterus with two 9-mm electrode paddles positioned on either side of the head (BTX, ECM830). For *in utero* photoconversion, a similar surgical procedure was carried out as for *in utero* electroporation. The forebrain of the embryos that received electroporation was exposed to a brief (about 3 to 5 min) exposure of light at 350–400 nm while in the uterus. Throughout these surgical procedures, the uterus was constantly bathed with warm PBS (pH 7.4). After the procedure, the uterus was placed back in the abdominal cavity and the wound was surgically sutured. The animal was then placed in a 28 °C recovery incubator under close monitoring until it recovered and resumed normal activity. All procedures for animal handling and usage were approved by our institutional research animal resource centre (RARC).

Brain sectioning and confocal imaging and analysis. Embryos were removed and transcardially perfused with ice-cold PBS (pH 7.4) followed by 4% paraformaldehyde in PBS (pH 7.4). For cell cycle exit analysis, electroporated embryos were exposed to bromodeoxyuridine (BrdU, $\sim$50–100 mg kg^{-1} body weight) for 24 h before being killed. Brains were dissected out and coronal sections were prepared using a vibratome (Leica Microsystems). For immunohistochemistry, sections were incubated for 1 h at room temperature in a blocking solution (10% normal goat or donkey serum as appropriate, 0.1% Triton X-100, and 0.2% gelatin in PBS), followed by incubation with the primary antibodies overnight at 4 °C. Sections were then washed in 0.1% Triton X-100 in PBS and incubated with the appropriate secondary antibody for 1–2 h at room temperature.

The primary antibodies used were: rabbit polyclonal anti-γ-tubulin (Sigma, 1:500), mouse monoclonal anti-pericentrin 1 (BD Biosciences, 1:1,000), mouse monoclonal anti-β-III tubulin (clone TUJ1) (Covance, 1:500), rabbit polyclonal anti-Pax6 (Covance, 1:500), rabbit polyclonal anti-Tbr2 (Millipore/Chemicon, 1:500), rat monoclonal anti-BrdU (Abcam, 1:400), mouse polyclonal anti-Ki67 (Novus Biological, 1:200), rabbit polyclonal anti-GLAST (Invitrogen, 1:400), rabbit polyclonal anti-phospho-histone 3 (Millipore/Upstate, 1:1,000), mouse monoclonal anti-phospho-H2AX (Millipore/Upstate, 1:250) and rabbit polyclonal anti-cleaved caspase 3 (Cell Signaling Technology, 1:250). Secondary antibodies used were: goat or donkey anti-mouse or anti-rabbit Alexa-546 and Alexa-647 conjugated antibodies (Invitrogen/Molecular Probes, 1:500). DNA was stained with 4′,6-diamidino-2-phenylindole (DAPI) (Invitrogen/Molecular Probes). Images were acquired with an Olympus FV1000 confocal microscope, and analysed with FluoView (Olympus), Volocity (Improvision) and Photoshop (Adobe Systems).

Data are presented as mean $\pm$ s.e.m. and nonparametric tests (Mann–Whitney–Wilcoxon test for two groups of data and Kruskal–Wallis test for three or more groups of data) were used for statistical significance estimation.

Cortical slice culture and time-lapse imaging. Cortical slice cultures were prepared and time-lapse imaging was acquired as previously described[12]. About 12 h after *in utero* electroporation, embryos were removed and the brain was extracted into ice-cold artificial cerebro-spinal fluid (ACSF) containing (in mM): 125 NaCl, 5 KCl, 1.25 NaH_2PO_4, 1 $MgSO_4$, 2 $CaCl_2$, 25 $NaHCO_3$ and 20 glucose; pH 7.4, 310 mOsm l^{-1}. Brains were embedded in 4% low-melting agarose in ACSF and sectioned at 400 μm using a vibratome (Leica microsystems). Brain slices that contained Kaede–CETN1- and mPlum-expressing cells were transferred on to a slice culture insert (Millicell) in a glass-bottom Petri dish (MatTek Corporation) with culture medium containing (by volume): 66% BME, 25% Hanks, 5% FBS, 1% N-2, 1% penicillin/streptomycin/glutamine (Invitrogen/GIBCO) and 0.66% D-(+)-glucose (Sigma). Cultures were maintained in a humidified incubator at 37 °C with constant 5% CO_2 supply. Twenty-four hours later, Petri dishes with slice cultures were transferred to an inverted microscope DMIRB (Leica) with a $\times$10 objective and the slices were exposed to brief ($\sim$12 s) epifluorescent illumination using a DAPI filter. The slices were returned to the incubator and cultured for another 24 h. Time-lapse images of dividing radial glia cells expressing Kaede–CETN1 and mPlum were acquired using a $\times$40 objective lens and a CoolSnap HQ camera (Roper Scientific) every 10 min for about 5 to 8 h. Images were analysed using MetaMorph (Molecular Devices) and Photoshop (Adobe Systems).

LETTERS

Measurement of the charge and current of magnetic monopoles in spin ice

S. T. Bramwell[1]*, S. R. Giblin[2]*, S. Calder[1], R. Aldus[1], D. Prabhakaran[3] & T. Fennell[4]

The transport of electrically charged quasiparticles (based on electrons or ions) plays a pivotal role in modern technology as well as in determining the essential functions of biological organisms. In contrast, the transport of magnetic charges has barely been explored experimentally, mainly because magnetic charges, in contrast to electric ones, are generally considered at best to be convenient macroscopic parameters[1,2], rather than well-defined quasiparticles. However, it was recently proposed that magnetic charges can exist in certain materials in the form of emergent excitations that manifest like point charges, or magnetic monopoles[3]. Here we address the question of whether such magnetic charges and their associated currents—'magnetricity'—can be measured directly in experiment, without recourse to any material-specific theory. By mapping the problem onto Onsager's theory of electrolytes[4], we show that this is indeed possible, and devise an appropriate method for the measurement of magnetic charges and their dynamics. Using muon spin rotation as a suitable local probe, we apply the method to a real material, the 'spin ice' $Dy_2Ti_2O_7$ (refs 5–8). Our experimental measurements prove that magnetic charges exist in this material, interact via a Coulomb potential, and have measurable currents. We further characterize deviations from Ohm's law, and determine the elementary unit of magnetic charge to be $5\,\mu_B\,\text{Å}^{-1}$, which is equal to that recently predicted using the microscopic theory of spin ice[3]. Our measurement of magnetic charge and magnetic current establishes an instance of a perfect symmetry between electricity and magnetism.

Spin ices are frustrated magnets, a class of magnetic material well known for supporting exotic excitations, both in experiment[9,10] and in theory[11–13]. The spin ice family[5–8] is predicted to support sharply defined magnetic monopole excitations and offers the possibility of exploring the general properties of magnetic charge transport in an ideal model system[3]. There is significant experimental evidence to support the existence of spin ice magnetic monopoles[3,14] (including some reported very recently[15–17]), but this evidence does not include the direct observation of charge or current and relies strongly on interpretation via the microscopic theory of spin ice. In the analogous electrical case, charge and current may be directly measured, with only the basic knowledge that the sample is, say, a semiconductor or a metal. It therefore seems realistic to seek a method of measuring magnetic charge and current that is similarly direct and robust.

The second Wien effect describes the nonlinear increase in dissociation constant K (or equivalently the conductance) of a weak electrolyte (solid or liquid) in an applied electric field E (refs 4, 18). In a seminal work of 1934, Onsager[4] derived a general equation for the Wien effect that provides an excellent description of experimental conductivity measurements on many kinds of electrolytes, including both liquid and lattice systems. Also, remarkably for a thermodynamic relation, it enables the experimental determination of the elementary charge e.

Onsager's theory should apply to any three-dimensional Coulombic fluid governed by two successive thermal equilibria:

$$\text{quasiparticle vacuum} = \text{bound pair of charges} = \text{free charges} \quad (1)$$

an example being the autoionization of water or water ice:

$$2H_2O = [H_3O^+ OH^-] = H_3O^+ + OH^- \quad (2)$$

Here the quasiparticle vacuum is simply the uncharged solvent ($2H_2O$), the square brackets indicate a closely associated ion pair and the absence of square brackets implies dissociated ions. A physical picture of the Wien effect is that an applied field accelerates the free ions and, opposed by Brownian motion, in favourable cases does enough work to overcome the Coulomb potential barrier that binds the ions together. The result is an increase, with field, of the rate of dissociation and hence of the corresponding equilibrium constant K. The field acts only on the forward reaction of the second (dissociation) equilibrium via the electrical force $F = \pm eE$. Onsager's theory[4] is valid under the condition that the concentration of unbound defects is sufficiently small for the Debye screening length to be much greater than the association distance[4,19].

Assuming the equivalence of electricity and magnetism proposed in ref. 3, we apply Onsager's theory to magnetic charges by replacing electrical quantities with the appropriate magnetic ones. Specifically, $e \to Q$, $E \to B$, $\varepsilon_0 \to \mu_0^{-1}$. Here Q is the magnitude of the emergent magnetic charge, B is the magnetic flux density, and ε_0 and μ_0 are the permittivity and permeability of the vacuum, respectively (note that the relative permeability can be set to unity in our case: see Methods). Onsager's main result may be approximated by the following form in the weak field limit[4,20]:

$$K(B) = K(0)\left(1 + b + \frac{b^2}{3}\ldots\right) \quad (3)$$

which is valid for $b < 3$, where b is the dimensionless group

$$b = \frac{\mu_0 Q^3 B}{8\pi k^2 T^2} \quad (4)$$

and k and T denote Boltzmann's constant and the temperature, respectively. The quantity $-kT\sqrt{8b}$ may be interpreted as the Coulombic barrier to ion pair dissociation, at which the field energy $-QBr_z$ balances the Coulomb potential $-\mu_0 Q^2/4\pi r$ (ref. 19; here r is the distance, z is the field direction, and the zero of potential energy is measured at infinite separation). A pictorial representation of the physical content of the theory is shown in Fig. 1.

We define n_b and n_u as the number of bound and unbound pairs, respectively, $n_0 = n_b + n_u$ as the total pair concentration and $\alpha = n_u/n_0$ as the degree of dissociation. The dissociation constant is given by:

[1]London Centre for Nanotechnology and Department of Physics and Astronomy, University College London, 17–19 Gordon Street, London WC1H 0AH, UK. [2]ISIS Facility, Rutherford Appleton Laboratory, Chilton, Oxfordshire OX11 0QX, UK. [3]Department of Physics, Clarendon Laboratory, University of Oxford, Parks Road, Oxford OX1 3PU, UK. [4]Institut Laue-Langevin, 6 rue Jules Horowitz, 38042 Grenoble, France.
*These authors contributed equally to this work.

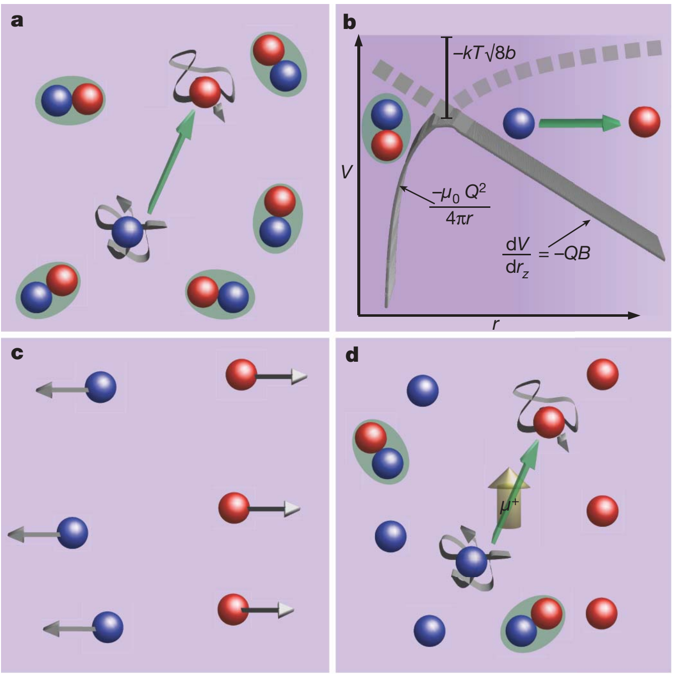

Figure 1 | Magnetic Wien effect, and the detection of magnetic charge by implanted muons. **a**, In zero field, magnetic charges occur as bound pairs, but some dissociate to give a fluctuating magnetic moment (green arrow). **b**, The field energy $-QBr_z$ competes with the Coulomb potential $-\mu_0 Q^2/4\pi r$ to lower the activation barrier to dissociation. **c**, The application of a transverse field causes dissociation as charges are accelerated by the field. **d**, In the applied field, these charges remain dissociated while more bound pairs form to restore equilibrium. Magnetic moment fluctuations due to free charges produce local fields that are detected by implanted muons (μ^+).

$$K = n_0 \frac{\alpha^2}{1-\alpha} \tag{5}$$

If it is assumed that the reaction rates of the left-hand equilibrium in equation (1) are much faster than those of the right hand (dissociation) equilibrium, then all molecules may be considered as bound pairs[4]. Recalling that $\alpha \ll 1$, then to a good approximation $n_0 \approx n_b \approx N$, so the total number of defects is approximately constant at a given temperature. Following a disturbance, the relaxation of $\Delta\alpha$ back to its equilibrium value is determined by charge recombination. Onsager showed that the decay is exponential with time constant $\nu_\alpha = 2\mu_0\kappa$, where κ is the conductivity, which is proportional to the equilibrium value of α: so $\nu_\alpha \propto \kappa \propto \alpha$ (ref. 4). It follows that the fractional increases in these quantities are equal and related by the equation[4]:

$$\frac{\nu_\alpha(B)}{\nu_\alpha(0)} = \frac{\kappa(B)}{\kappa(0)} = \frac{\alpha(B)}{\alpha(0)} = \sqrt{\frac{K(B)}{K(0)}} = 1 + \frac{b}{2} + \frac{b^2}{24} + \ldots \tag{6}$$

The conductivity is seen to increase with field, so is non-Ohmic.

We now deduce a pertinent consequence of Onsager's theory by relating ν_α to the relaxation rate of the magnetic moment ν_μ. Thus, the increase in the equilibrium constant K with increasing magnetic field (the Wien effect) defines a corresponding change in magnetic moment ($\delta\mu$) per unit forward reaction ($\delta\alpha$):

$$\left(\frac{\partial \ln K}{\partial B}\right)_{T,N} = \left(-\frac{\partial \Delta G^0/kT}{\partial B}\right)_{T,N} = \frac{\delta\mu/\delta\alpha}{kT} \tag{7}$$

where ΔG^0 is the change in Gibbs energy per atom. Using equation (3) we find, for the weak field limit,

$$\frac{\delta\mu}{\delta\alpha} = \frac{kTb}{B} \tag{8}$$

which is field independent. This equation may be integrated to find a proportionality between finite changes: $\Delta\mu \propto \Delta\alpha$. If an applied field is suddenly changed to a new value, then the slow relaxation of the moment occurs at the same rate as that of the monopole density: $\nu_\mu \propto \nu_\alpha$.

Combining this result with Onsager's equation (6), we find that measurement of the magnetic moment fluctuation rate as a function of field is equivalent to the observation of the magnetic conductivity, and gives direct access to the magnetic Wien effect:

$$\frac{\nu_\mu(B)}{\nu_\mu(0)} = \frac{\kappa(B)}{\kappa(0)} = 1 + \frac{b}{2} \tag{9}$$

which is an asymptotic expression for $b \to 0$, where b is linear in the applied field (equation (4)). This equation should be valid, provided that both α and its change in field $\Delta\alpha$ are sufficiently small. Corrections to the linear behaviour may be estimated as of the order of $b^2/24$ from equation (6).

The magnetic conductivity is therefore proportional to the fluctuation rate ν_μ of the magnetic moment, and, putting in the numbers, the 'elementary' magnetic charge Q may be derived from the initial slope and intercept of the field dependence of $\nu_\mu(B)$ via the equation:

$$\tilde{Q} = 2.1223\ m^{1/3} T^{2/3} \tag{10}$$

Here m = slope/intercept is the field gradient of the relative magnetic conductivity, and the tilde means that Q is measured in units of $\mu_B\,\text{Å}^{-1}$ (SI units are used elsewhere). This equation predicts a specific data collapse of $\nu_\mu(B,T)$ that is characteristic of the Coulombic interaction of charges and their acceleration by a field. As the charge depends only on the ratio $\nu_\mu(B)/\nu_\mu(0)$, we simply require an experimental quantity that is proportional to $\nu_\mu(B)$ in the weak field limit over a finite range of temperature. This use of relative quantities obviates the need for absolute measurements, which makes the method particularly robust and flexible. We have used this technique to test the theory and to determine the elementary magnetic charge in the spin ice $Dy_2Ti_2O_7$ (refs 6, 8).

We discovered that transverse field muon spin rotation[21] (μSR) affords the most convenient probe of the relative changes in the magnetic fluctuation rate of $Dy_2Ti_2O_7$. In μSR, muons implanted into a sample precess around the sum of the local and applied fields, and their decay characteristics give information on the time dependence of these fields. In an applied transverse field the muon relaxation function has an oscillatory form, resulting from the uniform muon spin precession about the applied field (Fig. 2). However this uniform precession can be dephased by fluctuating local fields that arise from the sample magnetization $\mathbf{M}(r, t)$. In the low temperature limit of

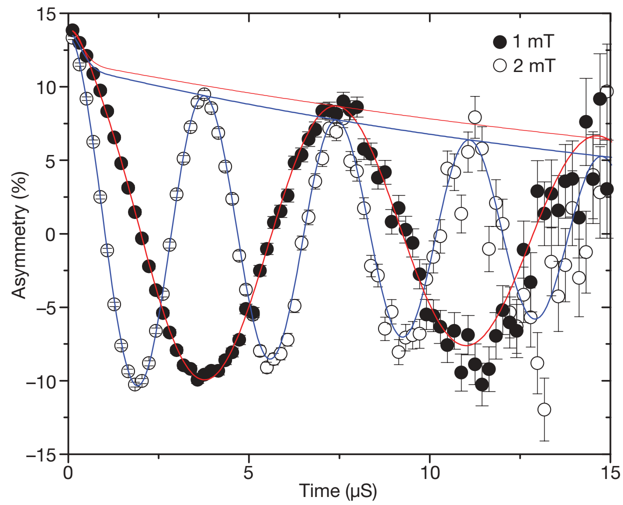

Figure 2 | Exponential decay of muon spin precession in $Dy_2Ti_2O_7$. The experimental data, with estimated standard deviation (e.s.d.) error bars, are at 100 mK in an applied transverse field of 1 mT (filled circles) and 2 mT (open circles). Lines represent the fits to the data (see Methods) and the exponential decay envelopes, clearly revealing a difference in relaxation at long time.

slowly fluctuating magnetization, the dephasing may lead to an exponential decay envelope of the muon relaxation function in which the decay rate λ is proportional to the characteristic rate ν_μ of the magnetic fluctuations[21]. The key property $\nu_\mu(B)/\nu_\mu(0) = \lambda(B)/\lambda(0)$ can therefore be directly measured (see equation (9)). In the opposite (high temperature) limit of fast fluctuations, λ also depends on the width of the field distribution σ and the muon gyromagnetic ratio γ. Here, one expects $\lambda \propto (\sigma\gamma)^2/\nu_\mu$ (ref. 21), with σ independent of temperature, so λ is proportional to the relaxation timescale $\tau = \nu_\mu^{-1}$.

The relaxation rate $\lambda(B)$ of muons implanted into $Dy_2Ti_2O_7$ was measured as a function of field and temperature after zero field cooling the sample to 60 mK (see Methods). Selected experimental results through the region of interest are shown in Figs 2, 3. To compare with theory, it is useful to define an effective magnetic charge by $\tilde{Q}_{\mathrm{eff}} \equiv 2.1223\ m_{\mathrm{experimental}}^{1/3} T^{2/3}$ (see equation (10)), demonstrating that only relative changes in λ are required to obtain $\tilde{Q}_{\mathrm{eff}}$ in absolute units of $\mu_{\mathrm{B}}\,\mathrm{\AA}^{-1}$. We would expect $\tilde{Q}_{\mathrm{eff}}$ to approximate the true $\tilde{Q}$ only in a finite range of temperature. At too low temperature (say $b = 2mB \gg 3$), the theory (equation (9)) breaks down because $\Delta\alpha$ becomes large, while at too high temperature, it breaks down because α becomes large. These limits on the range of validity can be estimated experimentally.

We first consider the temperature dependence of $\lambda(B = 2\,\mathrm{mT})$, as shown in Fig. 4. The high temperature behaviour mirrors the known behaviour of the magnetic relaxation time, decreasing with temperature as $e^{\mathrm{constant}/T}$ (refs 14, 22). At low temperature λ increases with temperature, consistent with the expected $\lambda \propto \nu_{\mu,\alpha} \propto \alpha$. From the graph, we can determine that the crossover from the presumed unscreened regime to the screened regime with rapidly increasing α is at $T_{\mathrm{upper}} \approx 0.3$ K. The inset of Fig. 4 shows the temperature dependence of $\lambda(B = 2\,\mathrm{mT}, 1\,\mathrm{mT})$: note the surprising non-monotonic temperature variation of $\lambda(B)$ at low temperature. By measuring b with equation (9), we estimate that the theory starts to break down below $T_{\mathrm{lower}} = 0.07$ K, the onset of the quadratic regime in equation (6). Thus $0.3 < T < 0.07$ K is the range where the theory (equation (9)) should be valid. It should be emphasized that this represents a relatively large range in the more physically relevant parameter $1/T$.

By fitting the experimental $\lambda(B)$ to extract slope and intercept, we estimate the effective charge $\tilde{Q}_{\mathrm{eff}}(T)$, as described above. In the regime of validity, the value of $\tilde{Q}_{\mathrm{eff}}$ saturates at $\sim 5\,\mu_{\mathrm{B}}\,\mathrm{\AA}^{-1}$, even though both slopes and intercepts depend quite strongly on temperature (Fig. 3). The (inverse) temperature dependence of $\tilde{Q}_{\mathrm{eff}}$ is

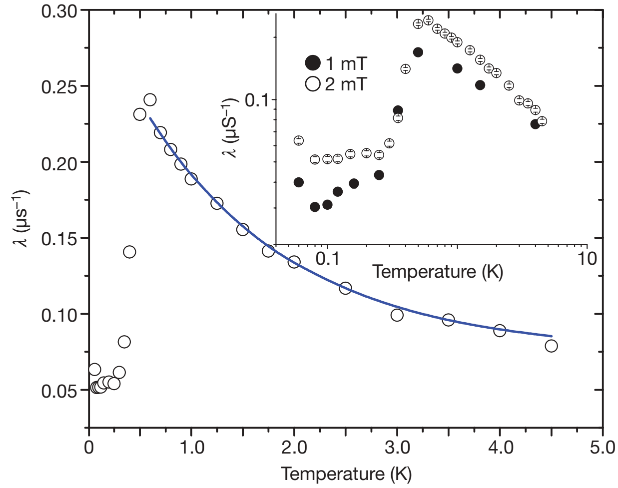

Figure 4 | Temperature dependence of the muon relaxation rate λ in $Dy_2Ti_2O_7$. Main panel, data measured at an applied magnetic field of 2 mT (with e.s.d. error bars). The high temperature regime follows the expected activated behaviour as described in the text (fit is shown as a solid line). At low temperature, λ is proportional to the monopole concentration. Its rapid increase above $T_{\mathrm{upper}} = 0.3$ K marks a crossover from the regime of weak screening to strong screening of the charges. Inset, data on a logarithmic scale along with data taken in 1 mT. The non-monotonic temperature dependence at low temperature is encompassed by Onsager's theory.

illustrated in Fig. 5, where the effective charge is seen to increase rapidly above $T_{\mathrm{upper}} = 0.3$ K, and to decrease slightly below $T_{\mathrm{lower}} = 0.07$ K. There are two strong indications of a Wien effect in these data. First, $Q_{\mathrm{eff}}(T)$ is approximately temperature independent in the regime of validity (Fig. 5), and second, we find a monotonic temperature variation of the intercept $\lambda(0)$, which is transformed by the constant Q_{eff} into the non-monotonic variation in $\lambda(B)$ noted above (see equation (10) and Fig. 4 inset).

We now compare these results with the properties, known and predicted, of $Dy_2Ti_2O_7$. In this material, Ising-like Dy^{3+} magnetic moments or 'spins' adopt a disordered and highly degenerate low temperature state in which each spin configuration corresponds to a hydrogen configuration in the low temperature state of (cubic) water ice[6,7,23,24]. A thermally generated spin flip out of this state corresponds to a bound pair of ice's ionic defects[24,25]. It has been predicted that this excitation should fractionalize, and that the dissociated defects

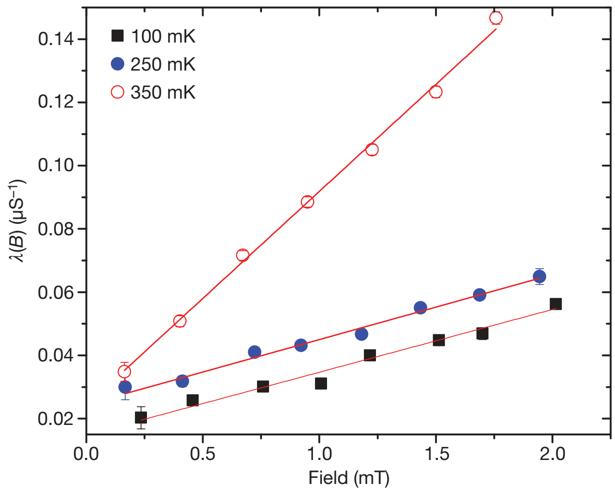

Figure 3 | A quantity that is proportional to magnetic charge conductivity in $Dy_2Ti_2O_7$, illustrating a non-Ohmic increase in conductivity with field. The measured muon relaxation rate $\lambda(B)$ is plotted as a function of field at selected temperatures (e.s.d. error bars). The lines are fits to the data, from which the intercept, slope and consequently the effective charge $\tilde{Q}_{\mathrm{eff}}(T)$ have been obtained.

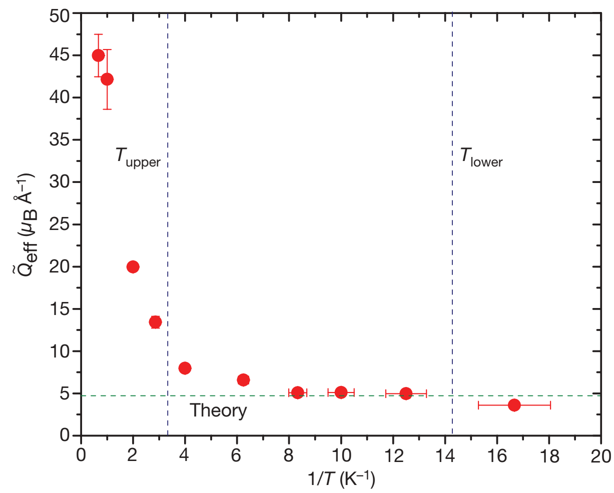

Figure 5 | Experimentally measured 'elementary' magnetic charge $\tilde{Q}_{\mathrm{eff}}$ in $Dy_2Ti_2O_7$. Onsager's theory is valid in the regime $T_{\mathrm{lower}} < T < T_{\mathrm{upper}}$ where the magnetic charges are unscreened. Experimental error bars are e.s.d. The horizontal green line marks the theoretical prediction of ref. 3. Note that $1\,\mu_{\mathrm{B}}\,\mathrm{\AA}^{-1} = 9.274 \times 10^{-14}\,\mathrm{J\,T^{-1}\,m^{-1}}$.

should behave as monopoles in the magnetic *H*-field[3]. The unbound defects are therefore equivalent to dissociated ionic defects in water ice, and the analogy with equation (2) is complete: like water ice[26], spin ice should show the Wien effect.

Specifying $\mu \approx 10\,\mu_B$ as the rare earth moment and $a_d = 4.3356$ Å as the relevant (diamond) lattice constant[3], the magnetic monopoles of $Dy_2Ti_2O_7$ are predicted to behave like Coulombic charges of magnitude $Q_{\mathrm{theoretical}} = \mu/(a_d/2) = 4.6\,\mu_B\,\text{Å}^{-1}$ (ref. 3). Figure 5 illustrates how the experimentally measured charge very closely approaches this value in the temperature range $T_{\mathrm{lower}} < T < T_{\mathrm{upper}}$. The actual value of T_{upper} may be rationalized on the basis of our expectations for spin ice. Thus the monopole concentration per lattice site should increase as $ce^{-2.2/T}$ (ref. 7), with $c \ll 1$ meaning that in the above temperature range it should vary between, at most, 10^{-14} and 10^{-4}. This is indeed a typical degree of dissociation for a weak electrolyte that obeys Onsager's theory (that is, screening is negligible), as has been shown in detail[19].

The success of the method is impressive. For example, regarding Fig. 3, these data may be collapsed (that is, represented as a function of the dimensionless *b*) over a significant range of temperature and field using a single parameter that is in excellent agreement with that calculated by a microscopic theory. However, even more remarkably, the method produces precisely the same data collapse over a range of experimental data on a broad variety of liquid and solid electrolytes[4]. Thus using Onsager's theory, we have demonstrated a perfect equivalence of electricity and magnetism. It is further a testament to Onsager that his theory is not only correct and universal, but also robust, in that it may be applied to straightforward experimental measurements of only modest precision[4]. This quality stems from the use of relative quantities, meaning in our case, that the μSR measurements are not subject to interpretation: many different analysis protocols would yield essentially the same result.

We have thus proved that magnetic charges exist in a spin ice material, that they interact by Coulomb's law and that they are accelerated by an applied field. Our experimental results are consistent with those discussed in refs 3, 14–17, but more directly probe the quantities of interest in the regime of temperature and field where a dilute gas of magnetic monopoles can be interrogated. We have also measured relative changes in the magnetic conductivity (Fig. 3), and proved that monopole currents exist. This demonstration raises an interesting question. As discussed elsewhere[14], the motion of spin ice monopoles is in principle constrained by the Dirac string network and this almost certainly precludes a direct current. However, our result implies that the network is irrelevant to monopole diffusion in the very dilute regime, which in turn suggests that macroscopic alternating currents may also be achievable in spin ice.

Our results have considerable ramifications for our detailed understanding of $Dy_2Ti_2O_7$. In particular, an old paradox—that the spin ice state appears completely static to some probes and completely dynamic to others—is finally resolved. Below $T = 0.7$ K, the zero field cooled state does not relax to the field cooled state when a field is applied[8] (see Methods), but nevertheless appears to be dynamic to μSR[27] and to the nuclear spin specific heat[28]. We ascribe this to magnetic monopoles being sufficiently numerous to equilibrate the zero field cooled state but too few to access, on realistic timescales, the field cooled states that are remote in configuration space.

In the broader context, our results have theoretical, practical and conceptual significance. At a theoretical level, they confirm the first instance of three-dimensional fractionalization[3], provide a comparison with cosmic magnetic monopoles[29], and recommend a close examination of the applicability of Onsager's theory to general Coulombic fluids. In practical terms, they pave the way for research dedicated to the control of magnetic charge currents—for example, in micromagnetic arrays that mimic spin ice[30]. Conceptually, they call for a reappraisal of the role of magnetic charge in physical systems[2].

METHODS SUMMARY

Our experiment was performed on the MuSR spectrometer at the ISIS facility. Single crystals of cubic $Dy_2Ti_2O_7$ were aligned with [110] parallel to the muon spin direction and [100] parallel to the applied transverse field. The sample was zero field cooled and measured on warming. Time spectra were fitted to an exponentially damped cosine function in addition to an expected constant quick relaxation[27].

Full Methods and any associated references are available in the online version of the paper at www.nature.com/nature.

Received 18 June; accepted 14 September 2009.

1. Morrish, A. H. *The Physical Principles of Magnetism* (Wiley and Sons, 1965).
2. Jackson, J. D. *Classical Electrodynamics* (Wiley and Sons, 1998).
3. Castelnovo, C., Moessner, R. & Sondhi, S. L. Magnetic monopoles in spin ice. *Nature* **451**, 42–45 (2007).
4. Onsager, L. Deviations from Ohm's law in weak electrolytes. *J. Chem. Phys.* **2**, 599–615 (1934).
5. Harris, M. J., Bramwell, S. T., McMorrow, D. F., Zeiske, T. & Godfrey, K. W. Geometrical frustration in the ferromagnetic pyrochlore $Ho_2Ti_2O_7$. *Phys. Rev. Lett.* **79**, 2554–2557 (1997).
6. Ramirez, A. P., Hayashi, A., Cava, R. J., Siddharthan, R. B. & Shastry, S. Zero-point entropy in spin ice. *Nature* **399**, 333–336 (1999).
7. Bramwell, S. T. & Gingras, M. J. P. Spin ice state in frustrated magnetic pyrochlore materials. *Science* **294**, 1495–1501 (2001).
8. Snyder, J. *et al.* Low-temperature spin freezing in the $Dy_2Ti_2O_7$ spin ice. *Phys. Rev. B* **69**, 064414 (2004).
9. Lee, S.-H. *et al.* Emergent excitations in a geometrically frustrated magnet. *Nature* **418**, 856–858 (2002).
10. Keren, A. *et al.* Dynamic properties of a diluted pyrochlore cooperative paramagnet $(Tb_pY_{1-p})_2Ti_2O_7$. *Phys. Rev. Lett.* **92**, 107204 (2004).
11. Moessner, R. & Chalker, J. T. Properties of a classical spin liquid: the Heisenberg pyrochlore antiferromagnet. *Phys. Rev. Lett.* **80**, 2929–2932 (1998).
12. Hermele, M., Fisher, M. P. A. & Balents, L. Pyrochlore photons: the U(1) spin liquid in a S=1/2 three-dimensional frustrated magnet. *Phys. Rev. B* **69**, 064404 (2004).
13. Burnell, F. J., Chakravarty, S. & Sondhi, S. L. Monopole flux state on the pyrochlore lattice. *Phys. Rev. B* **79**, 144432 (2009).
14. Jaubert, L. D. C. & Holdsworth, P. C. W. Signature of magnetic monopole and Dirac string dynamics in spin ice. *Nature Phys.* **5**, 258–261 (2009).
15. Fennell, T. *et al.* Magnetic coulomb phase in the spin ice $Ho_2Ti_2O_7$. *Science* doi:10.1126/science.1177582 (26 August 2009).
16. Morris, D. J. P. *et al.* Dirac strings and magnetic monopoles in spin ice $Dy_2Ti_2O_7$. *Science* doi:10.1126/science.1178868 (26 August 2009).
17. Kadowaki, H. *et al.* Observation of magnetic monopoles in spin ice. Preprint at ⟨http://arXiv.org/abs/0908.3568v2⟩ (2009).
18. Moore, W. J. *Physical Chemistry* (Longman, 1978).
19. Bass, L. Wien dissociation as a rate process. *Trans. Faraday Soc.* **64**, 2153–2159 (1968).
20. Mason, D. P. & McIlroy, D. K. A perturbation solution to the problem of Wien dissociation in weak electrolytes. *Proc. R. Soc. Lond. A* **359**, 303–317 (1978).
21. Uemura, Y. J. in *Muon Science: Muons in Physics, Chemistry and Materials* (eds Lee, S., Kilcoyne, S. & Cywinski, R.) 85–113 (SUSSP and Institute of Physics, 1998).
22. Orendáč, M., Hanko, Č. E. & Orendáčová, A. Magnetocaloric study of spin relaxation in dipolar spin ice $Dy_2Ti_2O_7$. *Phys. Rev. B* **75**, 104425 (2007).
23. den Hertog, B. C. & Gingras, M. J. P. Dipolar interactions and origin of spin ice in Ising pyrochlore magnets. *Phys. Rev. Lett.* **84**, 3430–3433 (2000).
24. Bramwell, S. T. & Harris, M. J. Frustration in Ising-type spin models on the pyrochlore lattice. *J. Phys. Condens. Matter* **10**, L215–L220 (1998).
25. Ryzhkin, I. A. Magnetic relaxation in rare-earth oxide pyrochlores. *J. Exp. Theor. Phys.* **101**, 481–486 (2005).
26. Eigen, M. & de Maeyer, L. Self-dissociation and protonic charge transport in water and ice. *Proc. R. Soc. Lond. A* **247**, 505–533 (1958).
27. Lago, J., Blundell, S. J. & Baines, C. μSR investigation of spin dynamics in the spin-ice material $Dy_2Ti_2O_7$. *J. Phys. Condens. Matter* **19**, 326210 (2007).
28. Bertin, E. *et al.* Effective hyperfine temperature in frustrated $Gd_2Sn_2O_7$: two level model and ^{155}Gd Mössbauer measurements. *Eur. Phys. J. B* **27**, 347–354 (2002).
29. Preskill, J. Magnetic monopoles. *Annu. Rev. Nucl. Part. Sci.* **34**, 461–530 (1984).
30. Wang, R. F. *et al.* Artificial 'spin ice' in a geometrically frustrated lattice of nanoscale ferromagnetic islands. *Nature* **439**, 303–306 (2006).

Acknowledgements We thank C. Castelnovo, M. J. P. Gingras, P. C. W. Holdsworth, L. Jaubert, D. F. McMorrow, R. Moessner and I. Terry for discussions.

Author Contributions S.T.B., S.R.G. and T.F. conceived the method; S.T.B. derived the theory; all authors planned the experiment; D.P. prepared the samples; S.R.G., S.T.B., R.A. and S.C. performed the experiment and analysed the data; S.T.B. and S.R.G. wrote the paper; and all authors contributed to the manuscript.

Author Information Reprints and permissions information is available at www.nature.com/reprints. Correspondence and requests for materials should be addressed to S.T.B. (s.t.bramwell@ucl.ac.uk).

METHODS

High quality single crystals of $Dy_2Ti_2O_7$ were grown using the floating zone method, and aligned using an X-ray Laue camera. In the experiment, the crystals were aligned with the initial spin polarization of the muons along the [110] axis, with the magnetic field applied at right angles to this axis, along [100]. In μSR experiments, one measures the asymmetry of the muon beta decay as a function of time $A(t)$, which is proportional to the time evolution of the muon spin polarization. $A(t)$ depends on the distribution of internal magnetic fields and their temporal fluctuations.

Our experiment was performed on the MuSR spectrometer at the ISIS facility in the UK. All data were taken upon warming after zero field cooling (<10 μT) from 4 K to 60 mK, the temperature dependence being repeated twice as a control. Transverse field spectra were fitted out to long times using $A(t) = A\exp(-[\lambda t])\cos(2\pi \upsilon t)$. The frequency of oscillations (υ) can be expressed by $\upsilon = \gamma_\mu |B|/2\pi$, where B is the average magnitude of the local field at the muon site and γ_μ is the muon gyromagnetic ratio. A constant, quick relaxation ($\lambda_0 = 3\,\mu S^{-1}$) was required for all the data, as expected for spin ice materials[27], along with a non-relaxing background term. The fitting procedure allowed the relaxation rate $\lambda(B)$ to vary. The field was allowed to vary but the change from the nominal value was negligible. Figure 2 shows the time evolution of data taken at 100 mK in fields of both 1 and 2 mT, along with the fits to the data: the envelope of the relaxation is also shown. Background measurements were performed on a silver plate to test for the field inhomogeneity in the coils: here the observed relaxation was at least an order of magnitude slower than in the $Dy_2Ti_2O_7$ sample.

When zero field cooled below 0.7 K, the susceptibility of $Dy_2Ti_2O_7$ is sufficiently small to approximate $\mu_r = 1$ and to ignore demagnetizing effects. We have independently verified, using ultralow field magnetization measurements, that in our sample a spin ice freezing occurs at $T = 0.7$ K, below which temperature the zero field cooled magnetization falls to small values.

Data were transformed to $\tilde{Q}_{\rm eff}$ as described in the text. The vertical error bars in Fig. 5 were propagated from the estimated errors in the variables T and m in equation (10); the errors in m were determined from the least squares fits to the muon spectra. The error bars on some points in Fig. 5 are too small to represent on the plot. For example, at 100 mK, $\tilde{Q}_{\rm eff} = 5.1 \pm 0.4\ \mu_B Å^{-1}$ (e.s.d. error).

LETTERS

Cooper pair splitter realized in a two-quantum-dot Y-junction

L. Hofstetter[1]*, S. Csonka[1,2]*, J. Nygård[3] & C. Schönenberger[1]

Non-locality is a fundamental property of quantum mechanics that manifests itself as correlations between spatially separated parts of a quantum system. A fundamental route for the exploration of such phenomena is the generation of Einstein–Podolsky–Rosen (EPR) pairs[1] of quantum-entangled objects for the test of so-called Bell inequalities[2]. Whereas such experimental tests of non-locality have been successfully conducted with pairwise entangled photons, it has not yet been possible to realize an electronic analogue of it in the solid state, where spin-1/2 mobile electrons are the natural quantum objects[3]. The difficulty stems from the fact that electrons are immersed in a macroscopic ground state—the Fermi sea—which prevents the straightforward generation and splitting of entangled pairs of electrons on demand. A superconductor, however, could act as a source of EPR pairs of electrons, because its ground-state is composed of Cooper pairs in a spin-singlet state[4]. These Cooper pairs can be extracted from a superconductor by tunnelling, but, to obtain an efficient EPR source of entangled electrons, the splitting of the Cooper pairs into separate electrons has to be enforced. This can be achieved by having the electrons 'repel' each other by Coulomb interaction[5]. Controlled Cooper pair splitting can thereby be realized by coupling of the superconductor to two normal metal drain contacts by means of individually tunable quantum dots. Here we demonstrate the first experimental realization of such a tunable Cooper pair splitter, which shows a surprisingly high efficiency. Our findings open a route towards a first test of the EPR paradox and Bell inequalities in the solid state.

An 'entangler' that generates correlated EPR pairs of electrons in the solid state has to be based on two-particle interactions, such as exchange interaction and Cooper pairing in superconductors. The former is mediated by electron–photon (Coulomb) interaction and the latter by electron–phonon interaction. Proposal for electron entanglers that make use of Coulomb interaction in quantum dots[6,7] and superconducting devices[8–10] have been put forward. Even more advanced, and in practice also more versatile and efficient, are device proposals that exploit both phenomena[5,11–14].

An electron entangler is a device that converts a charge current on the input to a stream of spin-entangled electron pairs. Each pair is split into its individual electrons, which emerge at two different arms of an electronic fork or Y-junction device (Fig. 1a)[15]. However, if Cooper pairs are injected into the fork, the pairs do not necessarily split as required: they may also be transmitted together into either arm. The ratio between pair splitting and direct pair transmission depends on details of the scattering matrix[15–20]. Such a device does not provide control over the two processes, which is a problem also encountered in experiments on metallic nanostructures, in which the first observations for Cooper pair splitting were made[21,22]. The desired Cooper pair splitting can be enforced if the fork is made up of two quantum dots (QDs) as shown in Fig. 1b (refs 5, 14). Crucial for the separation is the individual tunability of the eigenstates (levels) in each QD. This allows the resonance condition for Cooper pair splitting to be achieved[5]. If the charging energy on the QDs is large, double occupancy on each dot is prohibited. The two electrons of the Cooper pair are then forced either to split into separate arms or to tunnel sequentially through the same dot (Fig. 1c). However, the latter process can be suppressed if relatively opaque tunnelling barriers are chosen[5,14].

We have realized such a tunable Cooper pair splitter (Fig. 2a and Supplementary Information) by defining two QDs (dashed circles) with individual top-gates (yellow stripes) on an InAs semiconducting nanowire[23–25]. A common central superconducting source contact made from aluminium (blue stripe) and two metallic drain contacts

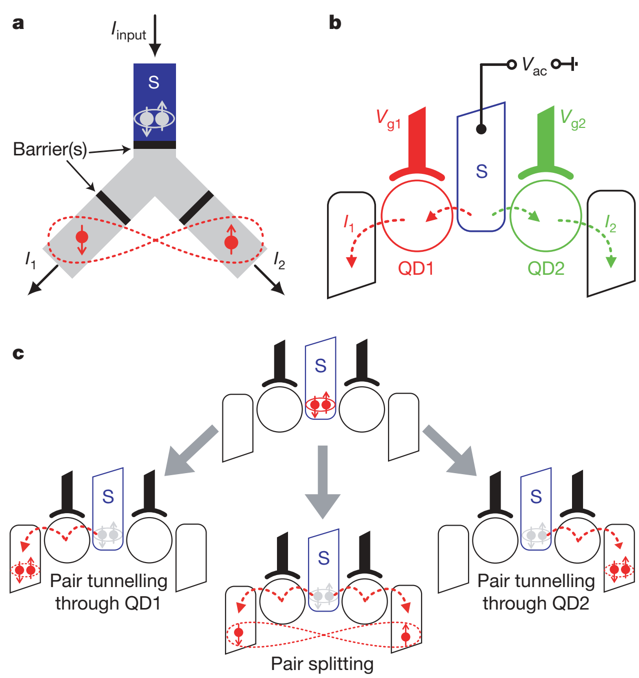

Figure 1 | Cooper pair splitter. a, The basic idea. A Cooper pair arrives from a superconductor (blue), and the two electrons split up and leave the Y-junction in different arms. Because a Cooper pair is a naturally entangled object, the splitting could provide spatially separated spin-entangled electrons. **b,** An efficient Cooper pair splitter can be realized if two tunable quantum dots (QD1 and QD2) are inserted, one into each arm. **c,** Basic transport processes in a Cooper pair splitter: the electrons of a Cooper pair either leave the superconductor into the same arm (pair tunnelling) or split up into different arms (pair splitting).

[1]Department of Physics, University of Basel, Klingelbergstrasse 82, CH-4056 Basel, Switzerland. [2]Department of Physics, Budapest University of Technology and Economics, Budafoki u. 6, 1111 Budapest, Hungary. [3]Nano-Science Center, Niels Bohr Institute, University of Copenhagen, Universitetsparken 5, DK-2100 Copenhagen, Denmark.
*These authors contributed equally to this work.

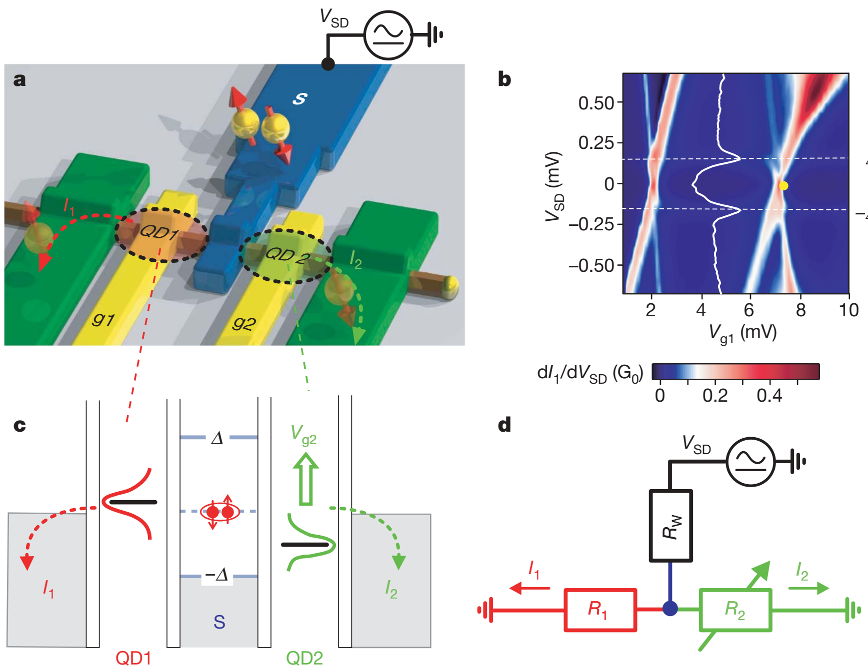

Figure 2 | Device and measurement principle. a, Schematic diagram of the lithographically defined structure of the Cooper pair splitter device. An InAs nanowire is contacted by a central superconducting lead (blue) and two metallic leads (green). Two quantum dots (QD1 and QD2) form between these contacts (dotted circles). They are independently tunable by two top-gates, g1 and g2. The widths of the superconducting lead, metallic contacts and top-gates and the distance between the middle contact and side ones are ~150, ~300, ~100 and ~350 nm, respectively. The conductances G_1 and G_2 of the QDs are determined by applying a small a.c. voltage V_{ac} of 5–10 μV to the superconducting lead and measuring the currents I_1 and I_2 through the two arms. **b**, Colour plot of the nonlinear differential conductance dI_1/dV_{SD} as a function of a d.c. source drain voltage V_{SD} and gate voltage V_{g1} of QD1, showing the features expected for a QD in the Coulomb blockade regime. The dashed lines are guides to the eye for the gap energy $\Delta \approx 150$ μeV of the superconductor. The suppressed electron density-of-state due to the superconductor is clearly visible in the cross-section (white curve) taken in the middle of the Coulomb blockade region. **c**, In the non-local measurement V_{g1} is first set, positioning the eigenstate in QD1 at a fixed value. Then the change ΔG_1 of the linear conductance through QD1 is measured while the position of the eigenstate is varied in the other quantum dot, QD2, through V_{g2}. **d**, Resistor model. R_1 and R_2 are the resistances of QD1 and QD2, and R_W is the total resistance of the measurement line between the voltage source and the superconducting lead. Because of the finite value of R_W, I_1 changes if R_2 is varied, resulting in a negative contribution to the non-local signal. This contribution is small because $R_W \ll R_{1,2}$. This classical resistive cross-talk is plotted with grey lines in Figs 3 and 4.

(green stripes) are attached to the QDs by means of tunnelling barriers. The presence of the superconducting source is clearly visible at a gap energy $\Delta \approx 150$ μeV in the differential conductance dI/dV_{SD} of the individual QDs measured as a function of the source-drain voltage V_{SD} (Fig. 2b). As a function of the top-gate voltage V_g, the conductance of each QD displays Coulomb blockade with a charging energy $E_C \approx 2$–4 meV, which is significantly larger than Δ. Two beam-splitter devices have been investigated. In the first the QDs are relatively strongly coupled to the contacts, yielding QD levels with a broadening of $\Gamma \approx 0.5$ meV (data presented in Figs 2–4a). In the second device the coupling is weaker, with $\Gamma \approx 100$ μeV (data in Fig. 4b).

The independent tunability of the two QDs permits correlations in the linear conductances G_1 and G_2 between the two QDs to be explored. Specifically, we study how G_1 of QD1 responds when the level position of the other quantum dot, QD2, is varied by the gate voltage V_{g2}. In an ideal device these non-local correlations $G_1(V_{g2})$ are caused by Cooper pair splitting.

An ideal device is one in which the source contact is voltage-biased. In the normal state, the source acts as a reservoir that injects electrons to both sides independently. Consequently, there are no correlations. In the superconducting state, in contrast, correlations can appear as a result of the large coherence length ξ of Cooper pairs, which can exceed the width of the superconducting source contact. With reference to Fig. 2c, let us assume that the eigenstate in QD1 is near resonance and that the eigenstate in QD2 is off resonance. If the state in QD2 is moved with the gate voltage V_{g2} upwards closer to resonance, not only will pair tunnelling through QD2 increase, but so also will the probability of Cooper pair splitting. The latter induces an increase in G_1. We define the sign of this non-local correlation as positive if G_1 shows a conductance increase δG_1 in response to a conductance increase δG_2 in QD2; that is, if $\delta G_1/\delta G_2 > 0$.

Classically, the two arms of the beam splitter can be described by two resistors R_1 and R_2 (Fig. 2d). In the ideal device there is no non-local response. In reality, the two arms are not perfectly voltage-biased, because of a wiring resistance R_W of 200 Ω. This leads to a residual negative non-local signal.

Non-local measurements are presented in Fig. 3. QD1 is adjusted with V_{g1} to a position off resonance (yellow dot in Fig. 2b). QD2 is then tuned with V_{g2} through six subsequent charge states, showing Coulomb blockade peaks when a dot level is in resonance (green curves). Simultaneously, the non-local conductance $G_1(V_{g2})$ through QD1 is measured. To see the change in G_1 better, we subtract a mean value $\langle G_1 \rangle$ (see Supplementary Information) and display $\Delta G_1 = G_1 - \langle G_1 \rangle$ (red dots).

When the superconducting contact is driven into the normal state with a magnetic field larger than the critical field (Fig. 3a), a small non-local signal is present. This signal is negative and in full agreement with the resistive cross-talk of the circuit (grey curve). In contrast, in the superconducting state (Fig. 3b) the non-local signal is larger by an order of magnitude and it is positive, as expected for Cooper pair splitting. It leads to a ΔG_1 swing of $9 \times 10^{-3} G_0$ (where G_0 is the quantum conductance, $2e^2/h$), which corresponds to 6.5% relative to the mean G_1 value.

The separate tunability of the two QDs allows us to study Cooper pair splitting for different settings of QD1 (Fig. 4a). As in the experiments before, we first position the level of QD1. We use level positions that are strongly off resonance, intermediate and on resonance.

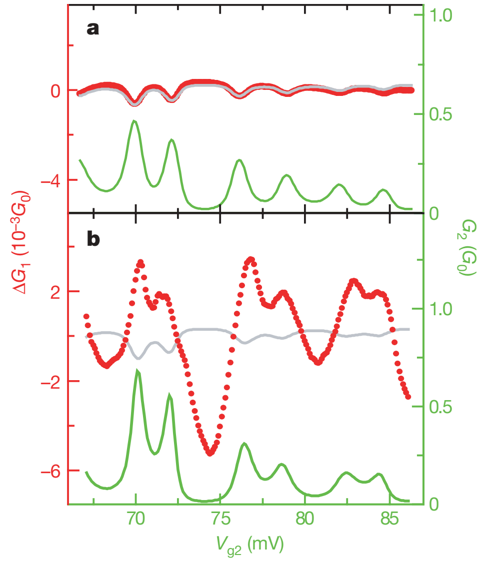

Figure 3 | Non-local signal of Cooper pair splitting. Simultaneous measurements of the linear local conductance G_2 of QD2 (green curves) and the linear non-local conductance change ΔG_1 of QD1 (red dots) as a function of the gate voltage V_{g2} of QD2 (all conductances are in units of G_0). In the non-local conductance change $\Delta G_1(V_{g2})$, the average conductance of QD1 was subtracted and the signal had to be corrected for capacitive cross-talk (see Supplementary Information). The measurements were performed at a base temperature T of 20 mK. **a,** In the normal state with a magnetic field B of 120 mT applied, a small negative non-local signal is seen as QD2 is driven through six Coulomb peaks. This signal is in complete agreement with the expected resistive cross-talk of the measurement configuration (grey line). **b,** In the superconducting state with $B = 0$ mT, an order of magnitude higher non-local signal $\Delta G_1(V_{g2})$ is observed. This correlation between the conductances through the two quantum dots is induced by the superconductor and is due to Cooper pair splitting.

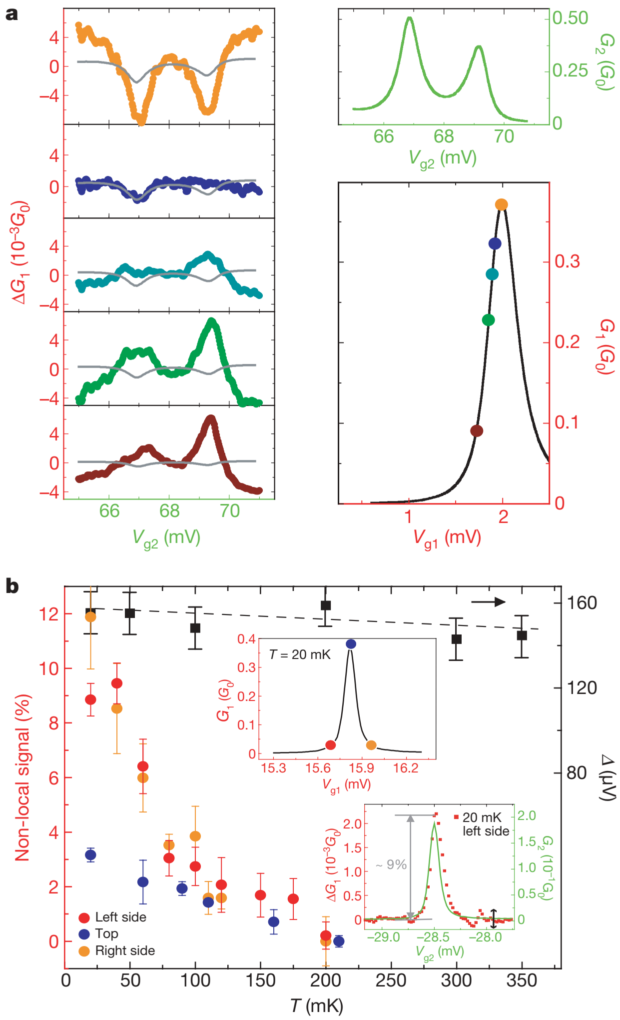

Figure 4 | Level position and temperature dependence. a, The non-local signal $\Delta G_1(V_{g2})$ depends strongly on the level position of QD1. Different non-local signals (left panels) and the corresponding positions of QD1 (bottom right panel) are shown with the same colour. A transition from a positive to a negative signal is found when QD1 is moved closer to resonance. The grey curves always indicate the expected classical resistive cross-talk. The top right panel shows the two Coulomb peaks through which QD2 was swept while measuring the conductance of QD1. **b,** Temperature dependence of the non-local signal for three different settings of QD1 (indicated in the top inset). Independently of the setting of QD1, the non-local signal vanishes at about 200 mK, which is well below the superconducting transition temperature $T_c \approx 850$ mK. The evolution of the superconducting gap Δ is shown (black squares) in addition in the main panel (right axis). It is determined from the nonlinear differential conductance similar to Fig. 2b. The bottom inset shows determination of the non-local signal. As QD2 is driven through a Coulomb peak (green curve), the height of the peak in ΔG_1 (red squares) is measured (see grey arrow) and normalized by the average value of G_1. The error bars estimate the read-off error due to fluctuations around the baseline (black arrow).

These positions are highlighted by differently coloured dots in the bottom right panel. To obtain the non-local signal, QD2 is swept through two Coulomb resonances (top right panel), while measuring the change ΔG_1. The non-local signal $\Delta G_1(V_{g2})$ depends strongly on the level position of QD1. Away from the resonance condition at the side of a Coulomb resonance, the non-local signal obtained is positive (brown and green curves), in agreement with the measurement in Fig. 3. However, if the level of QD1 is tuned towards a resonance condition, the size of the non-local signal first decreases and then changes sign, becoming maximally negative when QD1 is set exactly to the Coulomb resonance peak (orange curve). The same result is obtained for different charge states of QD1 and QD2 in two different samples.

Figure 4b shows the non-local signal as a function of temperature. Here, QD2 is swept through one Coulomb resonance (bottom inset, green curve) and the non-local conductance $\Delta G_1(V_{g2})$ is determined (red squares). The maximal change in $\Delta G_1(V_{g2})$ is normalized to the mean of G_1, which gives ~9% at 20 mK (grey bar). The temperature dependence of the normalized non-local signal is plotted for QD1 tuned to the left, top and right sides of a Coulomb peak (see Fig. 4b, top inset). The non-local signal can be as large as 12% relative to the mean G_1 value, or 2% relative to the total current at the lowest temperature. With increasing temperature the signal decreases, and it disappears at ~200 mK independently of the tuning of QD1. This temperature scale is smaller than the critical temperature of the superconductor $T_c \approx 850$ mK. We have deduced that the superconducting gap $\Delta(T)$ remains roughly constant within this temperature window (Fig. 4b, black squares). The markedly different temperature dependences show that the non-local signal is not controlled by the bulk Δ alone.

To describe the main observations qualitatively, we assume a non-interacting picture and describe the transmission probabilities through QD1 and QD2 by T_1 and T_2 (for further details see Supplementary Information). If both T_1 and T_2 are small, direct Cooper pair tunnelling through QD1 is given by T_1^2. In contrast, the probability of Cooper pair splitting is expected to be proportional to $p(\delta r)T_1T_2$, where $p(\delta r)$ is the probability of finding the two electrons of the Cooper pair at the opposite edges of the superconducting contact[5]. Thus, the total conductance G_1 through QD1 is then proportional to $\alpha T_1^2 + p(\delta r)T_1T_2$. This equation predicts a positive non-local signal that is caused solely by Cooper pair splitting. Its amplitude is determined by the factor $p(\delta r)$. In the experiment the non-local signal is always positive if QD1 is set to low transmission probabilities, in agreement with this simple model. However, the

maximum measured amplitude is much larger than expected. According to a previous study[5], the probability $p(\delta r)$ depends on the separation δr, on the coherence length ξ and on the Fermi wavevector k_F. In our device the mean free path l is smaller than ξ, and therefore $p(\delta r)$ is modified from the clean superconductor value to the one that is valid in diffusive superconductors[26], which is proportional to $|\sin(k_F\delta r)^2/(lk_F)(k_F\delta r)|\exp(-2\delta r/\pi\xi)$. The term $p(\delta r)$ is very small, because the factor $(lk_F)^{-1}(k_F\delta r)^{-1}$ is estimated to be $\sim 5\times 10^{-6}$, taking the Fermi wavelength λ_F as 3.6 Å, the mean free path l as 5 nm, and δr as 150 nm, corresponding to the width of the superconducting contact. To reconcile the very small predicted Cooper pair splitting with our experimental observation, we propose that tunnelling into the two QDs does not occur at the periphery of the superconducting contact. Instead, the Cooper pairs tunnel into the segment of the semiconducting nanowire underneath the superconducting contact. Because of the low carrier density and correspondingly low k_F, the term $p(\delta r)$ can become much larger and might also be enhanced by the confined geometry[12,26]. The contribution of split Cooper pairs found in our samples is very remarkable considering the macroscopic width of the superconducting contact.

According to a previous study[5], the quantum dots of the Cooper pair splitter should be operated out of resonance. On resonance the number of electrons on the dot is not well defined, and this can spoil the generation of EPR pairs by Cooper pair splitting. In view of this, the reversed sign of the non-local signal when the QDs are set close to resonance is not a surprise. The sign change emerges from a competition of pair tunnelling and pair splitting in a regime that is beyond existing theories. The measurements close to resonance are in strong contrast with those off resonance, where the measured non-local signal has the expected positive sign, in agreement with Cooper pair splitting.

As has been detailed in previous theoretical proposals[5,14], two main conditions are required for a Cooper pair splitter to be efficient, namely $U \gg \Gamma$ and $\Delta \gg \Gamma$. In our devices the first condition is fulfilled. However, Γ is on the order of Δ, which enhances direct Cooper pair tunnelling. This shows that there is potential for improving the efficiency of such a device by using more opaque tunnelling barriers. Although the measured splitting efficiency of 2% in our devices may seem small, it is already many orders of magnitude higher than has been achieved in the most efficient production of entangled photon pairs by paramagnetic downconversion (PDC), where an efficiency of $\sim 10^{-12}$ was reached[27]. In addition, the present Cooper pair splitter device outperforms PDC in the total current of pairs almost 100-fold, even for the relatively low Δ value of aluminium. This demonstrates that a source of EPR pairs based on a Cooper pair splitter is a promising alternative for quantum computational schemes.

We have demonstrated a tunable Cooper pair splitter device that opens the way to studies of the entanglement of spatially separated mobile electrons. Because of its remarkable splitting efficiency, such a device could provide a first test of the EPR paradox in the solid state if it were implemented with ferromagnetic drain contacts and noise measurements were performed on it[8,10,28–30].

During the preparation of the manuscript we became aware of similar work on a carbon-nanotube-based Cooper pair splitter device[31].

Received 20 April; accepted 18 August 2009.

1. Einstein, A., Podolsky, B. & Rosen, N. Can quantum-mechanical description of physical reality be considered complete? *Phys. Rev.* **47**, 777–780 (1935).
2. Aspect, A., Grangier, P. & Roger, G. Experimental realization of Einstein-Podolsky-Rosen-Bohm *gedankenexperiment*—a new violation of Bell inequalities. *Phys. Rev. Lett.* **49**, 91–94 (1982).
3. Loss, D. & DiVincenzo, D. P. Quantum computation with quantum dots. *Phys. Rev. A* **57**, 120–126 (1998).
4. Bardeen, J., Cooper, L. N. & Schrieffer, J. R. Theory of superconductivity. *Phys. Rev.* **108**, 1175–1204 (1957).
5. Recher, P., Sukhorukov, E. V. & Loss, D. Andreev tunneling, Coulomb blockade, and resonant transport of non-local spin-entangled electrons. *Phys. Rev. B* **63**, 165314 (2001).
6. Loss, D. & Sukhorukov, E. V. Probing entanglement and nonlocality of electrons in a doubledot via transport and noise. *Phys. Rev. Lett.* **84**, 1035–1038 (2000).
7. Crepieux, A., Guyon, R., Devillard, P. & Martin, T. Electron injection in a nanotube: noise correlations and entanglement. *Phys. Rev. B* **67**, 205408 (2003).
8. Lesovik, G. B., Martin, T. & Blatter, G. Electronic entanglement in the vicinity of a superconductor. *Eur. Phys. J. B* **24**, 287–290 (2001).
9. Samuelsson, P., Sukhorukov, E. V. & Büttiker, M. Orbital entanglement and violation of Bell inequalities in mesoscopic conductors. *Phys. Rev. Lett.* **91**, 157002 (2003).
10. Bouchiat, V. *et al.* Single-walled carbon nanotube-superconductor entangler: noise correlations and Einstein–Podolsky–Rosen states. *Nanotechnology* **14**, 77–85 (2003).
11. Choi, M.-S., Bruder, C. & Loss, D. Spin-dependent Josephson current through double quantum dots and measurement of entangled electron states. *Phys. Rev. B* **62**, 13569–13572 (2000).
12. Recher, P. & Loss, D. Superconductor coupled to two Luttinger liquids as an entangler for electron spins. *Phys. Rev. B* **65**, 165327 (2002).
13. Bena, C., Vishveshwara, S., Balents, L. & Fisher, M. P. A. Quantum entanglement in carbon nanotubes. *Phys. Rev. Lett.* **89**, 037901 (2002).
14. Sauret, O., Feinberg, D. & Martin, T. Quantum master equations for the superconductor-quantum dot entangler. *Phys. Rev. B* **70**, 245313 (2004).
15. Torres, J. & Martin, T. Positive and negative Hanbury-Brown and Twiss correlations in normal metal-superconducting devices. *Eur. Phys. J. B* **12**, 319–322 (1999).
16. Falci, G., Feinberg, D. & Hekking, F. W. J. Correlated tunneling into a superconductor in a multiprobe hybrid structure. *Europhys. Lett.* **54**, 255–261 (2001).
17. Samuelsson, P. & Büttiker, M. Chaotic dot-superconductor analog of the Hanbury Brown–Twiss effect. *Phys. Rev. Lett.* **89**, 046601 (2002).
18. Deutscher, G. Crossed Andreev reflections. *J. Supercond.* **15**, 43–47 (2002).
19. Morten, J. P., Brataas, A. & Belzig, W. Circuit theory of crossed Andreev reflection. *Phys. Rev. B* **74**, 214510 (2006).
20. Golubev, D. S. & Zaikin, A. D. Non-local Andreev reflection in superconducting quantum dots. *Phys. Rev. B* **76**, 184510 (2007).
21. Beckmann, D., Weber, H. B. & v Löhneysen, H. Evidence for crossed Andreev reflection in superconductor-ferromagnet hybrid structures. *Phys. Rev. Lett.* **93**, 197003 (2004).
22. Russo, S., Kruog, M., Klapwijk, T. M. & Morpurgo, A. F. Experimental observation of bias-dependent nonlocal Andreev reflection. *Phys. Rev. Lett.* **95**, 027002 (2005).
23. Bjork, M. T. *et al.* Few-electron quantum dots in nanowires. *Nano Lett.* **4**, 1621–1625 (2004).
24. Fasth, C., Fuhrer, A., Bjork, M. T. & Samuelson, L. Tunable double quantum dots in InAs nanowires defined by local gate electrodes. *Nano Lett.* **5**, 1487–1490 (2005).
25. Csonka, S. *et al.* Giant fluctuations and gate control of the *g*-factor in InAs nanowire quantum dots. *Nano Lett.* **8**, 3932–3935 (2008).
26. Feinberg, D. Andreev scattering and cotunneling between two superconductor-normal metal interfaces: the dirty limit. *Eur. Phys. J. B* **36**, 419–422 (2003).
27. Kurtsiefer, C., Oberparleiter, M. & Weinfurter, H. High-efficiency entangled photon pair collection in type-II parametric fluorescence. *Phys. Rev. A* **64**, 023802 (2001).
28. Burkard, G., Loss, D. & Sukhorukov, E. V. Noise of entangled electrons: bunching and antibunching. *Phys. Rev. B* **61**, R163003 (2000).
29. Chtchelkatchev, N. M., Blatter, G., Lesovik, G. B. & Martin, T. Bell inequalities and entanglement in solid-state devices. *Phys. Rev. B* **66**, 161320 (2002).
30. Samuelsson, P., Sukhorukov, E. V. & Büttiker, M. Electric current noise of a beamsplitter as a test of spin entanglement. *Phys. Rev. B* **70**, 115330 (2004).
31. Herrmann, L. G. *et al.* Carbon nanotubes as Cooper pair beam splitters. Preprint at ⟨http://arxiv.org/abs/0909.3243v1⟩ (2009).

Supplementary Information is linked to the online version of the paper at www.nature.com/nature.

Acknowledgements We thank G. Zaránd, P. Moca and C. W. J. Beenakker for discussions, and C. B. Srensen and M. Aagesen for Molecular Beam Epitaxy growth. This work was supported by the Swiss National Science Foundation, the Swiss National Center of Competence in Research on Nanoscale Science, the Danish Natural Science Research Council, Hungarian Scientific Research Fund (OTKA) project NNF 78842 and Marie Curie project 41139 of the European Union. S.C. is a grantee of the Bolyai János Scholarship.

Author Contributions L.H. and S.C. fabricated the samples and performed the measurements. The idea was born of discussions between C.S., S.C. and L.H. InAs nanowires were grown in the laboratory of J.N. All authors were involved in interpretation, discussion and paper writing.

Author Information Reprints and permissions information is available at www.nature.com/reprints. Correspondence and requests for materials should be addressed to C.S. (christian.schoenenberger@unibas.ch) or S.C. (csonka@dept.phy.bme.hu).

Vol 461|15 October 2009|doi:10.1038/nature08439

LETTERS

Quasicrystalline order in self-assembled binary nanoparticle superlattices

Dmitri V. Talapin[1,2]*, Elena V. Shevchenko[2]*, Maryna I. Bodnarchuk[1], Xingchen Ye[3], Jun Chen[4] & Christopher B. Murray[3,4]

The discovery of quasicrystals in 1984 changed our view of ordered solids as periodic structures[1,2] and introduced new long-range-ordered phases lacking any translational symmetry[3–5]. Quasicrystals permit symmetry operations forbidden in classical crystallography, for example five-, eight-, ten- and 12-fold rotations, yet have sharp diffraction peaks. Intermetallic compounds have been observed to form both metastable and energetically stabilized quasicrystals[1,3,5]; quasicrystalline order has also been reported for the tantalum telluride phase with an approximate $Ta_{1.6}Te$ composition[6]. Later, quasicrystals were discovered in soft matter, namely supramolecular structures of organic dendrimers[7] and tri-block copolymers[8], and micrometre-sized colloidal spheres have been arranged into quasicrystalline arrays by using intense laser beams that create quasi-periodic optical standing-wave patterns[9]. Here we show that colloidal inorganic nanoparticles can self-assemble into binary aperiodic superlattices. We observe formation of assemblies with dodecagonal quasicrystalline order in different binary nanoparticle systems: 13.4-nm Fe_2O_3 and 5-nm Au nanocrystals, 12.6-nm Fe_3O_4 and 4.7-nm Au nanocrystals, and 9-nm PbS and 3-nm Pd nanocrystals. Such compositional flexibility indicates that the formation of quasicrystalline nanoparticle assemblies does not require a unique combination of interparticle interactions, but is a general sphere-packing phenomenon governed by the entropy and simple interparticle potentials. We also find that dodecagonal quasicrystalline superlattices can form low-defect interfaces with ordinary crystalline binary superlattices, using fragments of ($3^3.4^2$) Archimedean tiling as the 'wetting layer' between the periodic and aperiodic phases.

Nanoparticles of different metals, semiconductors and magnetic materials can self-assemble from colloidal solutions into long-range-ordered periodic structures (superlattices)[10]. Combining two types of nanoparticle yields binary nanoparticle superlattices (BNSLs) exhibiting very rich phase diagrams with multiple close-packed and non-close-packed phases[11]. The observed structural diversity is believed to be a result of the interplay of entropy-driven crystallization[12] with isotropic and anisotropic interparticle interactions, such as van der Waals, Coulombic and dipolar forces[13–15]. In this Letter, we report self-assembly of long-range-ordered nanoparticle superstructures whose complexity goes beyond the crystalline packing.

Figure 1a and Fig. 1b show transmission electron microscopy (TEM) images of BNSLs isostructural with AlB_2 and CaB_6 phases, respectively. Both structures self-assembled from 13.4-nm Fe_2O_3 and 5.0-nm Au nanocrystals during slow evaporation of a colloidal solution containing monodisperse Fe_2O_3 and Au nanocrystals in tetrachloroethylene. The Fe_2O_3 and Au nanocrystals were capped with oleic acid and dodecanethiol molecules, respectively (Methods Summary). These surfactant molecules, which have long hydrocarbon chains, introduced short-range steric repulsion counterbalancing the van der Waals forces and preventing uncontrollable aggregation of nanocrystals in the colloidal solution. AlB_2- and CaB_6-type BNSLs could form under the same experimental conditions, with the structure-directing factor being the relative concentration of Fe_2O_3 and Au nanocrystals in the colloidal solution. A large (~10-fold) excess of Au nanoparticles favoured the CaB_6 structure, whereas an AlB_2-type BNSL formed when the Fe_2O_3-to-Au nanoparticle ratio was close to 1:2. When we explored mixtures with intermediate Fe_2O_3-to-Au nanoparticle concentration ratios, highly complex binary structures were observed. Figure 1c shows an assembly in which Fe_2O_3 nanocrystals are separated by individual Au nanocrystals and $(Au)_6$ octahedral clusters. Appearing irregular at first glance, this structure shows sharp small-angle electron diffraction spots outlining four-fold rotational symmetry (Fig. 1d and Supplementary Fig. 1).

A closer look reveals the packing principle: each Fe_2O_3 nanocrystal is surrounded by five equidistant Fe_2O_3 nanocrystals. Moreover, identical arrangements of Au nanocrystals surround each Fe_2O_3 nanocrystal: the clockwise sequence is always $(Au)_6$, Au, $(Au)_6$, Au, Au (Fig. 1c). To visualize this structure, we connected the centres of neighbouring Fe_2O_3 nanocrystals with straight lines, forming the two-dimensional pattern of squares and triangles depicted in Fig. 1c and Supplementary Fig. 1. Such an arrangement of equilateral squares and triangles is known in topology as the ($3^2.4.3.4$) Archimedean tiling (Fig. 1e). Archimedean tilings, first introduced by Kepler in 1619[16], are defined as regular patterns of polygonal tessellation of a plane by regular polygons where only one type of vertex is permitted in each tiling. They are typically described by listing in order the polygons that meet at each vertex using the set of integers, written ($n_1.n_2.n_3\ldots$), corresponding to the numbers of sides of the polygons[17]. Only 11 types of Archimedean tiling can fill the whole plane without gaps; four of them are composed of equilateral squares and triangles (Fig. 1e).

By the above definition, two-dimensional [001] projections of AlB_2- and CaB_6-type structures can be described as (3^6), that is, (3.3.3.3.3.3), and (4^4) Archimedean tiling patterns, respectively. We also observed relatively small fragments of ($3^3.4^2$) Archimedean tiling coexisting with other structures (Fig. 1f). In ($3^2.4.3.4$) and ($3^3.4^2$) patterns, the number ratio of triangles and squares, N_3/N_4, equals two, corresponding to the AB_4 stoichiometry of the superlattice. In crystallography, Archimedean tilings have been used to describe a family of complex alloys with tetrahedral close-packed structures, known as the Frank–Kasper phases[18]. For example, ($3^2.4.3.4$) tiling was observed in Fe–Cr systems and is known as the σ phase in the Frank–Kasper alloy family[19].

[1]Department of Chemistry, The University of Chicago, Chicago, Illinois 60637, USA. [2]Center for Nanoscale Materials, Argonne National Laboratory, Argonne, Illinois 60439, USA. [3]Department of Chemistry, [4]Department of Materials Science and Engineering, University of Pennsylvania, Philadelphia, Pennsylvania 19104, USA.
*These authors contributed equally to this work.

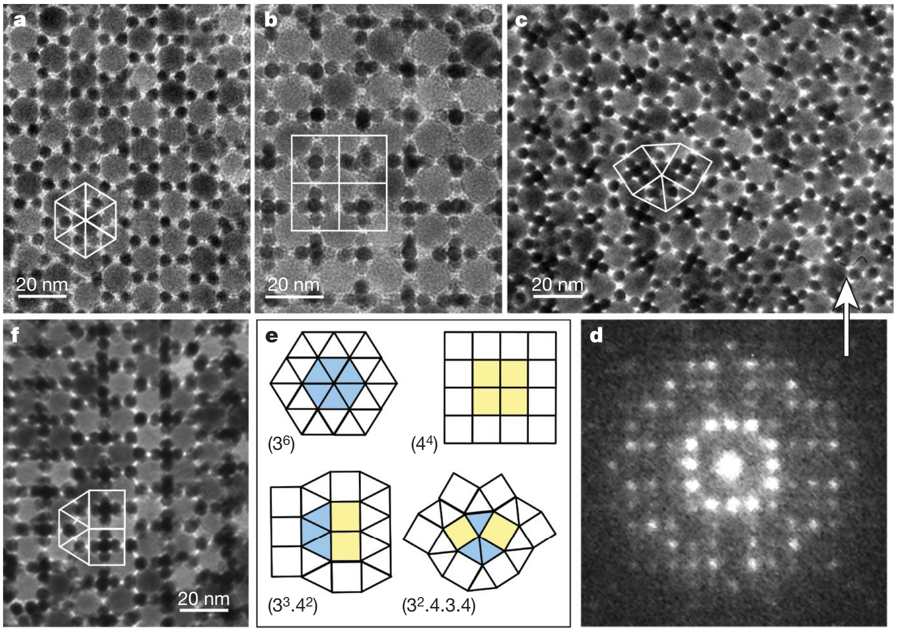

Figure 1 | Periodic binary superlattices self-assembled from 13.4-nm Fe_2O_3 and 5-nm Au nanocrystals. **a**, AlB_2-type superlattice; **b**, CaB_6-type superlattice; **c**, superlattice with AB_4 stoichiometry and the structural motif of the (3^2.4.3.4) Archimedean tiling. **d**, Electron diffraction pattern measured from a ~6-μm^2 domain of the AB_4 superlattice shown in **c**. **e**, Archimedean tilings used to describe the structure of the nanoparticle superlattices. **f**, A fragment of a superlattice corresponding to the ($3^3.4^2$) Archimedean tiling.

In exploring the binary phase diagram of 13.4-nm Fe_2O_3 and 5-nm Au nanoparticles in proximity to the (3^2.4.3.4) phase, we observed reproducible formation of a type of binary superstructure that did not possess any translational symmetry (Fig. 2). The structure also exhibited sharp electron diffraction patterns corresponding to dodecagonal (that is, 12-fold) rotational symmetry (Fig. 2a, inset), which is forbidden in periodic structures. Different superstructure domains showed strikingly similar electron diffraction patterns (Supplementary Fig. 2), ruling out the possibility of diffraction artefacts caused by twin planes or other crystal defects. Straight lines connecting centres of Fe_2O_3 nanocrystals generated patterns of squares and triangles without self-repeating domains (Supplementary Fig. 3). Observed electron diffraction patterns, along with previous theoretical analyses of square–triangle lattices[20–22], allowed us to identify these self-assembled nanoparticle superstructures as aperiodic but long-range-ordered structures known as quasicrystals. Despite the absence of translational symmetry, rotational symmetry originates from the directionality of 'bonds' between adjacent Fe_2O_3 nanocrystals at angles that are multiples of $360°/12 = 30°$.

Formation of the dodecagonal quasicrystal (DDQC) in a square–triangle lattice requires that the total tiling area occupied by squares be equal to that occupied by triangles, that is, $N_3/N_4 = 4/\sqrt{3} \approx 2.31$ (ref. 20). Following the experimentally observed packing rule whereby each triangle has an Au nanoparticle in its centre and each square contains one $(Au)_6$ cluster (Fig. 2a, b), the overall stoichiometry of the DDQC nanoparticle superlattice is derived to be $A_{2+\sqrt{3}}B_{4+6\sqrt{3}}$, or approximately $AB_{3.86}$. We calculated the N_3/N_4 ratio and stoichiometry from several independently formed domains and found that $N_3/N_4 = 2.30 \pm 0.2$, corresponding to stoichiometry $AB_{3.84 \pm 0.09}$, in agreement with the expected values. In three dimensions, the DDQC can be described as a periodic stack of quasi-periodic layers, that is, the planar realization of a quasi-periodic order[5]. Because of the layered structure, the three-dimensional DDQC can be imaged in real space along the 12-fold symmetry axis[5] (Fig. 2). In thick domains, the nanocrystals and $(Au)_6$ clusters followed the one-on-one packing indicated in Fig. 2a, b and Supplementary Fig. 4 by the contrast differences and rotational moiré fringes

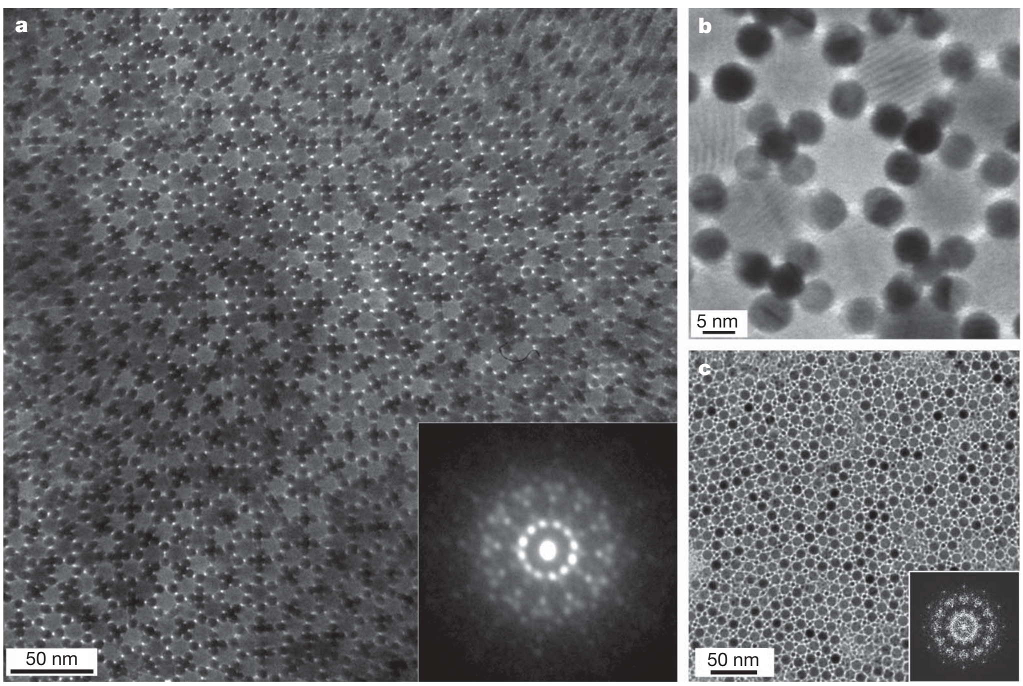

Figure 2 | Dodecagonal quasicrystals self-assembled from spherical nanoparticles. **a**, TEM image of a quasicrystalline superlattice self-assembled from 13.4-nm Fe_2O_3 and 5-nm Au nanocrystals. Inset, selected-area electron diffraction pattern with non-crystallographic 12-fold rotational symmetry measured from a ~6-μm^2 domain. **b**, Magnified view of a dodecagonal nanoparticle quasicrystal. **c**, Dodecagonal quasicrystalline superlattice self-assembled from 9-nm PbS and 3-nm Pd nanocrystals. Inset, fast-Fourier-transform pattern of the quasicrystalline superlattice.

(parallel stripes with spacing much larger than the atomic lattice constant). Fourier analysis of TEM projections of DDQC nanoparticle assemblies imaged normal to the 12-fold axis showed the coexistence of periodic and aperiodic crystallographic directions orthogonal to each other (Supplementary Figs 5 and 6).

The DDQC phase is rare in atomic solids—known examples include small Ni–Cr particles[23] and $Ta_{\sim1.6}Te$ solids[6]—and is the only quasicrystal phase observed in soft matter, namely organic dendrimers and star-shaped tri-block copolymers[7,8]. To evaluate the generality of the DDQC packing motif in nanocrystal assemblies, we investigated a range of binary nanoparticle systems. We observed the self-assembly of a DDQC phase from colloidal solutions containing 12.6-nm Fe_3O_4 and 4.7-nm Au nanocrystals (Supplementary Fig. 7) and from solutions containing 9-nm PbS and 3-nm Pd nanocrystals (Fig. 2c). The iron oxide/gold and PbS–Pd systems formed DDQC phases at very similar size ratios of small and large particles ($\gamma = d_{NC\,small}/d_{NC\,large} \approx 0.43 \pm 0.01$). This parameter was calculated using actual nanocrystal size estimated as $d_{NC} = d_{core} + 2d_{shell}$, where d_{core} is the nanocrystal diameter and d_{shell} is the effective thickness of ligand shells measured for different nanocrystal–ligand pairs in ref. 13.

The size of single-domain DDQC superstructures ranged from hundreds of nanometres to several micrometres (Supplementary Fig. 8), covering large areas of the TEM grids; very similar compositions and electron diffraction patterns were observed in numerous samples. We also observed larger domains, but they usually were too thick to be imaged using TEM and we could not determine whether they consisted of a single DDQC domain or contained several long-range-ordered domains. Within individual domains, we occasionally observed local defects, such as one shown in Supplementary Fig. 3b, c; such defects did not disturb the global order of the quasicrystals, however, and could be considered analogous to the point defects in an ordinary crystalline lattice.

Our DDQC superlattices formed during slow evaporation of tetrachloroethylene solutions at 50 °C. Under these conditions, we routinely observed self-assembly of nearly perfect long-range-ordered periodic BNSLs[11,13] from iron oxide/gold and PbS–Pd nanoparticle pairs when γ was above or below 0.43 or when relative nanoparticle concentrations were inappropriate for formation of the DDQC phase. A defect-free BNSL can form only if assembly occurs not too far from equilibrium conditions through reversible addition and removal of the nanoparticles. Formation of a highly metastable DDQC phase through a far-from-equilibrium quenching process is very unlikely under such conditions. However, we should not exclude the role of kinetic factors in the assembly process. For example, $(Au)_6$ clusters could form in solution before their integration in a DDQC lattice. It is extremely difficult to judge whether a quasicrystal is stable or metastable[3,4]. Even if the quasicrystal would preferentially transform into an approximant (for example the Archimedean tiling), the transformation, which occurs by a process known as zipper motion[21], is slow and will not be observed experimentally. This means that the DDQC might be stable for practical purposes even if it is not a thermodynamically stable phase.

At the periphery of large quasicrystal domains, we often observed coexistence of DDQCs with AlB_2-type BNSLs with sharp interfaces (Fig. 3a). The abrupt change of composition from $AB_{\sim3.86}$ to AB_2 provides additional evidence that the DDQC is a stable phase corresponding to a free-energy minimum. Figure 3b provides a view of the interface between quasicrystalline (DDQC) and crystalline (CaB_6) phases with a resolution hardly achievable in atomic systems. A smooth transition between two topologically different phases was possible owing to a thin 'wetting layer' of ($3^3.4^2$) Archimedean tiling that matched both phases with a low concentration of interfacial defects. This tiling was recently proposed to be an intermediate between a hexagonal crystal and a decagonal quasicrystal[9]. According to our observations, the same ($3^3.4^2$) Archimedean tiling bridges a cubic CaB_6 lattice and a DDQC, demonstrating its unique position as a pseudomorphic phase with both crystalline and quasicrystalline structural properties[9,24].

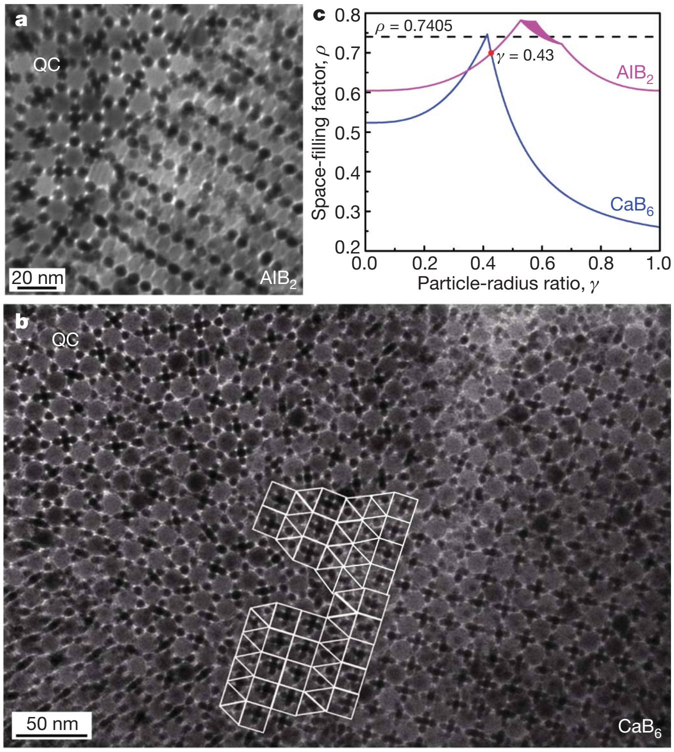

Figure 3 | Structure of the interface between quasicrystalline and crystalline phases. **a**, Interface between the DDQC phase and the AlB_2-type binary superlattice self-assembled from 13.4-nm Fe_2O_3 and 5-nm Au nanocrystals. QC, quasicrystal. **b**, Transition from the DDQC phase to the CaB_6-type binary superlattice of 12.6-nm Fe_3O_4 and 4.7-nm Au nanocrystals is facilitated by the presence of a 'wetting layer' of ($3^3.4^2$) Archimedean tiling. **c**, Space-filling factors calculated for the AlB_2 and CaB_6 structures. The dotted line corresponds to the single-component close-packed structure with the space-filling factor $\rho = 0.7405$. The filled-in section in the AlB_2 line corresponds to different arrangements of densely packed spheres.

Formation of DDQC phases from different nanoparticle combinations (iron oxide/gold and PbS–Pd) suggests that no particular combination of interparticle interactions is necessary to form a DDQC phase. However, the striking coincidence of γ ratios suggests that particle size has an important role. Measurements of electrophoretic mobility for colloids of Au and Fe_2O_3 nanocrystals revealed the domination of electrically neutral nanoparticles in solution (Supplementary Fig. 9). In the absence of strong Coulombic interactions, the space-filling factor, ρ, has a significant effect on the relative stabilities of binary nanoparticle phases[25]. In hard-sphere systems, ρ can often be used as a structure-determining factor as it directly relates to the gain in translational entropy during the crystallization process. Because DDQC and ($3^2.4.3.4$) structures combine the elements of AlB_2 and CaB_6 packings, we compared the ρ values for AlB_2 and CaB_6 lattices at different values of γ (Fig. 3c). For $0.34 < \gamma < 0.43$, the density of the CaB_6 phase exceeds that of the AlB_2 phase, whereas for $\gamma < 0.34$ and $\gamma > 0.43$, the AlB_2 phase is more dense than the CaB_6 phase. In our experiments, the DDQC phase and Archimedean tilings were observed for $\gamma \approx 0.43$, that is, where the $\rho(\gamma)$ curves for the AlB_2 and CaB_6 phases crossed, at $\rho \approx 0.70$. At the crossing point, the translational entropies of the AlB_2, CaB_6 and DDQC phases and Archimedean tilings were very similar. Here some other factors are involved in determining relative phase stabilities.

The quasi-periodicity could be a result of maximizing the entropy of arrangement of square and triangular 'tiles'[5,20,21]—many degenerate ways of packing contribute to the configurational entropy and cause the quasicrystalline state to be more stable than crystalline BNSL states[3]. The entropy of square–triangle tiling is maximized for patterns with N_3/N_4 values of around $4/\sqrt{3}$ (ref. 20). Moreover, the discontinuity in the

entropy density corresponding to the DDQC state[20] can provide a mechanism for locking the quasicrystalline state over a range of nanocrystal concentration ratios. It has been predicted that the unique equilibrium maximum-entropy DDQC state can be approached during growth by sufficiently randomized addition and removal of square and triangular tiles at the surface of pre-nucleated quasicrystal clusters[26].

There are several ways to build square and triangular tiles from spherical particles. As far as we know, the structure shown in Fig. 2 has been neither observed experimentally nor anticipated in quasicrystal models and simulations. The formation of a DDQC in which 'squares' were made from four large particles surrounding one small particle and 'triangles' were formed by three touching large particles has been studied theoretically[22]. In three dimensions, the local ρ value of such triangular tiles will correspond to that of a simple hexagonal lattice, and square tiles can be modelled as a CsCl lattice. The same packing-density conditions for simple hexagonal and CsCl packings occur for $\gamma \approx 0.54$ and $\rho \approx 0.60$. Owing to low packing density, the formation of such structures would require significant cohesive forces and is less likely than formation of the significantly denser structure shown in Fig. 2. As we observed the same packing motif in different nanoparticle systems, the structure in Fig. 2 could correspond to the most stable, highest entropy quasicrystal phase of weakly attractive spherical particles.

Spherical nanoparticles can be used to model both geometrical and electronic properties of individual atoms[10] and can easily be imaged in real space. Studies of the self-assembly of quasicrystal nanoparticle superstructures will provide insight into the formation of the quasicrystal phase in atomic systems. The assembly of the DDQC phase from different nanoparticle combinations shows that quasicrystal ordering could be a relatively common phenomenon in nanocrystal solids. Nanoparticle quasicrystals can be used as a convenient platform for detailed investigation of quasicrystal properties, for example the nearly isotropic Brillouin zone and complete photonic band gap in DDQCs[27]. We expect that stable quasicrystal phases will soon be discovered in other man-made materials, for example metal–organic frameworks.

METHODS SUMMARY

Nanoparticle synthesis. Au and Pd nanoparticles capped with 1-dodecanethiol were prepared as described in ref. 13. Fe_2O_3 nanoparticles (γ phase, maghemite) were synthesized by methods adapted from ref. 28 Details of the synthesis of PbS nanocrystals capped with the oleic acid can be found in ref. 29. Fe_3O_4 nanoparticles (magnetite phase) were synthesized using the method of ref. 30. Additional experimental details are provided in the Supplementary Information.

Preparation of binary superlattices. As-synthesized nanoparticles were carefully washed from reaction by-products and dissolved in tetrachloroethylene. A substrate (a carbon-coated TEM grid or a silicon nitride membrane) was placed in a glass vial containing the colloidal solution of nanoparticles. The vial was tilted by 60° or 70° inside a low-pressure chamber. The quasicrystalline nanoparticle assemblies were obtained by evaporating relatively concentrated colloidal solutions at 50 °C under reduced pressure (~3.2 kPa).

Structural analysis. JEOL JEM-1400 and FEI Tecnai F30 transmission electron microscopes operating at 120 kV and 300 kV, respectively, were used to image the structures of nanoparticle assemblies. The electron diffraction patterns were measured from a 6-μm^2 area of the sample. The TEM images were compared with the structure projections simulated using the Accelrys MS MODELLING 3.1 and CRYSTALMAKER software packages. We also performed a comparison of experimental small-angle electron diffraction patterns, the two-dimensional Fourier-transformation power spectra of real-space TEM images and the fast-Fourier-transformation power spectra of the simulated projections to ensure consistency.

Received 6 April; accepted 13 August 2009.

1. Shechtman, D., Blech, I., Gratias, D. & Cahn, J. W. Metallic phase with long-range orientational order and no translational symmetry. *Phys. Rev. Lett.* **53,** 1951–1953 (1984).
2. Levine, D. & Steinhardt, P. J. Quasicrystals: a new class of ordered structures. *Phys. Rev. Lett.* **53,** 2477–2480 (1984).
3. DiVincenzo, D. P&. Steinhardt, P. J. (eds). *Quasicrystals: The State of the Art* 2nd edn (World Scientific, 1999).
4. Keys, A. S. & Glotzer, S. C. How do quasicrystals grow? *Phys. Rev. Lett.* **99,** 235503 (2007).
5. Abe, E., Yan, Y. & Pennycook, S. J. Quasicrystals as cluster aggregates. *Nature Mater.* **3,** 759–767 (2004).
6. Conrad, M., Krumeich, F. & Harbrecht, B. A dodecagonal quasicrystalline chalcogenide. *Angew. Chem. Int. Ed.* **37,** 1383–1386 (1998).
7. Zeng, X. *et al.* Supramolecular dendritic liquid quasicrystals. *Nature* **428,** 157–160 (2004).
8. Hayashida, K., Dotera, T., Takano, A. & Matsushita, Y. Polymeric quasicrystal: mesoscopic quasicrystalline tiling in ABC star polymers. *Phys. Rev. Lett.* **98,** 195502 (2007).
9. Mikhael, J., Roth, J., Helden, L. & Bechinger, C. Archimedean-like tiling on decagonal quasicrystalline surfaces. *Nature* **454,** 501–504 (2008).
10. Murray, C. B., Kagan, C. R. & Bawendi, M. G. Synthesis and characterization of monodisperse nanocrystals and close-packed nanocrystal assemblies. *Annu. Rev. Mater. Sci.* **30,** 545–610 (2000).
11. Shevchenko, E. V., Talapin, D. V., Kotov, N. A., O'Brien, S. & Murray, C. B. Structural diversity in binary nanoparticle superlattices. *Nature* **439,** 55–59 (2006).
12. Eldridge, M. D., Madden, P. A. & Frenkel, D. Entropy-driven formation of a superlattice in a hard-sphere binary mixture. *Nature* **365,** 35–37 (1993).
13. Shevchenko, E. V., Talapin, D. V., Murray, C. B. & O'Brien, S. Structural characterization of self-assembled multifunctional binary nanoparticle superlattices. *J. Am. Chem. Soc.* **128,** 3620–3637 (2006).
14. Leunissen, M. E. *et al.* Ionic colloidal crystals of oppositely charged particles. *Nature* **437,** 235–240 (2005).
15. Kalsin, A. M. *et al.* Electrostatic self-assembly of binary nanoparticle crystals with a diamond-like lattice. *Science* **312,** 420–424 (2006).
16. Grünbaum, B. & Shephard, G. C. *Tilings and Patterns* (Freeman, 1986).
17. Ueda, K., Dotera, T. & Gemma, T. Photonic band structure calculations of two-dimensional Archimedean tiling patterns. *Phys. Rev. B* **75,** 195122 (2007).
18. Frank, F. C. & Kasper, J. S. Complex alloy structures regarded as sphere packing. II. Analysis and classification of representative structures. *Acta Crystallogr.* **12,** 483–499 (1959).
19. Sopousek, J. & Kruml, K. Sigma-phase equilibrium and nucleation in Fe–Cr–Ni alloys at high temperature. *Scripta Mater.* **35,** 689–693 (1996).
20. Widom, M. Bethe ansatz solution of the square-triangle random tiling model. *Phys. Rev. Lett.* **70,** 2094–2097 (1993).
21. Oxborrow, M. & Henley, C. L. Random square-triangle tilings: a model for twelve fold-symmetric quasicrystals. *Phys. Rev. B* **48,** 6966–6998 (1993).
22. Leung, P. W., Henley, C. L. & Chester, G. V. Dodecagonal order in a two-dimensional Lennard-Jones system. *Phys. Rev. B* **39,** 446–458 (1989).
23. Ishimasa, T., Nissen, H.-U. & Fukano, Y. New ordered state between crystalline and amorphous in Ni-Cr particles. *Phys. Rev. Lett.* **55,** 511–513 (1985).
24. Glotzer, S. C. & Keys, A. S. A tale of two tilings. *Nature* **454,** 420–421 (2008).
25. Chen, Z. & O'Brien, S. Structure direction of II−VI semiconductor quantum dot binary nanoparticle superlattices by tuning radius ratio. *ACS Nano* **2,** 1219–1229 (2008).
26. Joseph, D. & Elser, V. A model of quasicrystal growth. *Phys. Rev. Lett.* **79,** 1066–1069 (1997).
27. Zoorob, M. E., Charlton, M. D. B., Parker, G. J., Baumberg, J. J. & Netti, M. C. Complete photonic bandgaps in 12-fold symmetric quasicrystals. *Nature* **404,** 740–743 (2000).
28. Hyeon, T., Lee, S. S., Park, J., Chung, Y. & Na, H. B. Synthesis of highly crystalline and monodisperse maghemite nanocrystallites without a size-selection process. *J. Am. Chem. Soc.* **123,** 12798–12801 (2001).
29. Hines, M. A. & Scholes, G. D. Colloidal PbS nanocrystals with size-tunable near-infrared emission: observation of post-synthesis self-narrowing of the particle size distribution. *Adv. Mater.* **15,** 1844–1849 (2003).
30. Park, J. *et al.* Ultra-large-scale syntheses of monodisperse nanocrystals. *Nature Mater.* **3,** 891–895 (2004).

Supplementary Information is linked to the online version of the paper at www.nature.com/nature.

Acknowledgements We thank S. O'Brien, W. Heiss, A. P. Alivisatos, T. Witten, W. Green and J. Urban for discussions and V. Altoe for help with analytical TEM studies. D.V.T. acknowledges support from the US National Science Foundation (NSF) CAREER Program under award number DMR-0847535 and the NSF MRSEC Program under award number DMR-0213745. M.I.B. acknowledges financial support from the Austrian Nanoinitiative. The work at the Center for Nanoscale Materials, Argonne National Laboratory, was supported by the US Department of Energy under contract number DE-AC02-06CH11357.

Author Contributions E.V.S. carried out experimental studies of the Fe_2O_3–Au nanoparticle system, M.I.B. studied the PbS–Pd system and X.Y. and J.C. studied the Fe_3O_4–Au system. D.V.T. analysed the experimental data. D.V.T. and C.B.M initiated and supervised the work. D.V.T and E.V.S. wrote the paper. All authors discussed the results and commented on the manuscript.

Author Information Reprints and permissions information is available at www.nature.com/reprints. Correspondence and requests for materials should be addressed to D.V.T. (dvtalapin@uchicago.edu) or E.V.S. (eshevchenko@anl.gov).

nature Vol 461|15 October 2009|doi:10.1038/nature08484

LETTERS

Scaleable catalytic asymmetric Strecker syntheses of unnatural α-amino acids

Stephan J. Zuend[1], Matthew P. Coughlin[1], Mathieu P. Lalonde[1] & Eric N. Jacobsen[1]

α-Amino acids are the building blocks of proteins and are widely used as components of medicinally active molecules and chiral catalysts[1–5]. Efficient chemo-enzymatic methods for the synthesis of enantioenriched α-amino acids have been developed, but it is still a challenge to obtain non-natural amino acids[6,7]. Alkene hydrogenation is broadly useful for the enantioselective catalytic synthesis of many classes of amino acids[8,9], but it is not possible to obtain α-amino acids bearing aryl or quaternary alkyl α-substituents using this method. The Strecker synthesis—the reaction of an imine or imine equivalent with hydrogen cyanide, followed by nitrile hydrolysis—is an especially versatile chemical method for the synthesis of racemic α-amino acids[10,11]. Asymmetric Strecker syntheses using stoichiometric amounts of a chiral reagent have been applied successfully on gram-to-kilogram scales, yielding enantiomerically enriched α-amino acids[12–14]. In principle, Strecker syntheses employing sub-stoichiometric quantities of a chiral reagent could provide a practical alternative to these approaches, but the reported catalytic asymmetric methods have seen limited use on preparative scales (more than a gram)[15,16]. The limited utility of existing catalytic methods may be due to several important factors, including the relatively complex and precious nature of the catalysts and the requisite use of hazardous cyanide sources. Here we report a new catalytic asymmetric method for the syntheses of highly enantiomerically enriched non-natural amino acids using a simple chiral amido-thiourea catalyst to control the key hydrocyanation step. This catalyst is robust, without sensitive functional groups, so it is compatible with aqueous cyanide salts, which are safer and easier to handle than other cyanide sources; this makes the method adaptable to large-scale synthesis. We have used this new method to obtain enantiopure amino acids that are not readily prepared by enzymatic methods or by chemical hydrogenation.

The urea- and thiourea-catalysed Strecker synthesis of (*R*)-*tert*-leucine developed several years ago by our group[17,18] illustrates many of the factors that have limited the application of catalytic asymmetric imine hydrocyanation methods towards routine preparative-scale syntheses (Figs 1 and 2). Although this synthesis provides (*R*)-*tert*-leucine in high yield and enantiomeric excess, the hydrocyanation reaction is run at cryogenic temperatures and uses a hazardous cyanide source: either trimethylsilyl cyanide (TMSCN)/methanol (MeOH) or HCN. In addition, the syntheses of either polystyrene-bound catalyst **1a** or homogeneous analogue **1b** require eight chemical steps, and the conversion of the α-aminonitrile to the α-amino acid requires four chemical steps.

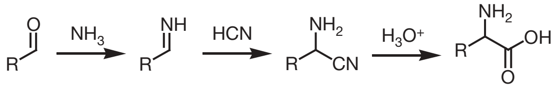

Figure 1 | Strecker synthesis of α-amino acids. (R = aliphatic or aromatic organic substituent).

In mechanistically and synthetically guided efforts to identify simpler small-molecule H-bond donors for enantioselective imine hydrocyanation, we discovered that amido-thiourea derivatives lacking the diaminocyclohexane moiety in **1** (refs 19, 20) are efficient catalysts for the hydrocyanation of *N*-benzhydryl-protected imines using HCN generated *in situ* from TMSCN and MeOH (Table 1)[21]. Whereas simple amido-thiourea **4a** induced low levels of enantioselectivity in hydrocyanation of both aliphatic and aromatic imines (entry 1 in Table 1), the corresponding phenyl-substituted amido-thioureas proved more effective (entries 2–4). The highest enantioselectivities were observed in reactions catalysed by *N*-benzhydryl-substituted catalyst **4e** (entry 5). This catalyst contains a single stereogenic centre and is prepared in three steps from commercially available reagents (74% overall yield on the 5-g scale), and is thus readily accessible compared with chiral Strecker catalysts identified previously[15,16].

Amido-thiourea derivative **4e** proved effective and highly enantioselective for the hydrocyanation of imines derived from alkyl (Table 2, entries 1–5), aryl (entries 7–16), heteroaryl (entries 17–19), and alkenyl aldehydes (entries 20–22). Lower enantioselectivities are obtained with less sterically demanding imines (entries 6 and 23). In general, (*R*)-α-aminonitriles are obtained from the catalyst derived from (*S*)-*tert*-leucine. This fortuitous outcome introduces an important practical feature of this method, because (*S*)-*tert*-leucine is readily available inexpensively by enzymatic methods[6], but practical catalytic methods

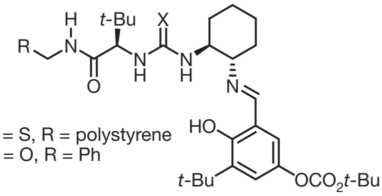

1a: X = S, R = polystyrene
1b: X = O, R = Ph

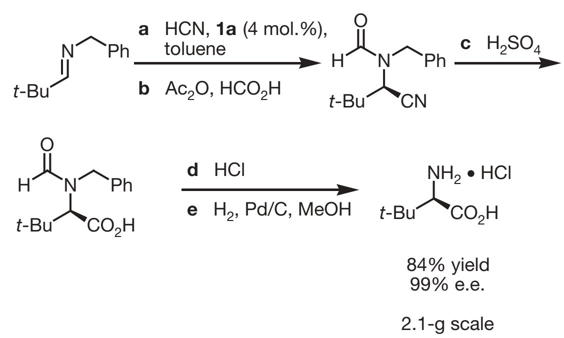

Figure 2 | First-generation thiourea-catalysed asymmetric Strecker synthesis of *tert*-leucine. **a**, HCN (1.3 equiv.), **1a** (4 mol.%), toluene, –75 °C, 15 h. **b**, Acetic anhydride (Ac_2O), HCO_2H, 5 min. **c**, 65% aqueous H_2SO_4, 45 °C, 20 h. **d**, Concentrated HCl, 13 h. **e**, H_2, Pd/C (0.1 equiv.), methanol (MeOH), 8 h. Ph, phenyl; *t*-Bu, *tert*-butyl; e.e., enantiomeric excess.

[1]Harvard University, Department of Chemistry and Chemical Biology, Cambridge, Massachusetts 02138, USA.

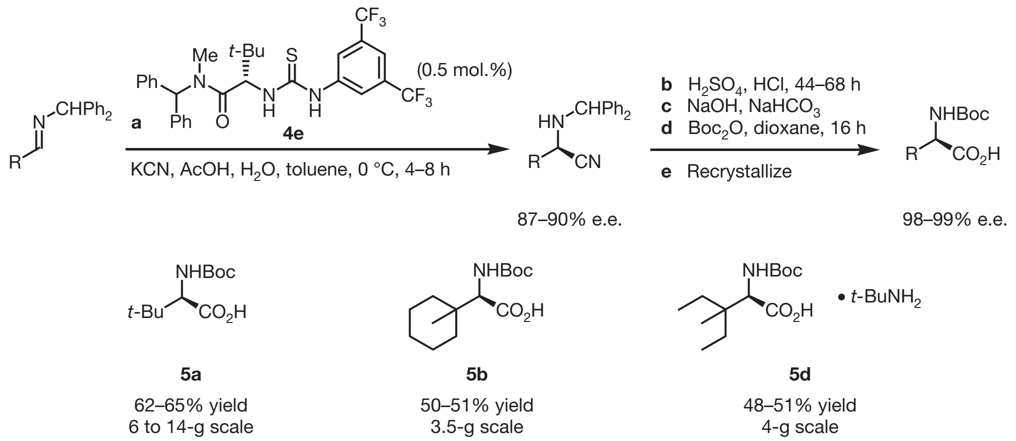

Figure 3 | Potassium cyanide-mediated Strecker synthesis. **a**, Catalyst **4e** (0.5 mol.%), KCN (2 equiv.), acetic acid (AcOH, 1.2 equiv.), H_2O (4 equiv.), toluene, 0 °C, 4–8 h. **b**, Aqueous H_2SO_4 and HCl, 120 °C, 44–68 h. **c**, NaOH, $NaHCO_3$. **d**, Di-*tert*-butyl dicarbonate (Boc_2O, 2.5–3 equiv.), dioxane, 16 h. **e**, Recrystallize directly from hexanes/diethyl ether or as the *tert*-butylamine (*t*-$BuNH_2$) salt from tetrahydrofuran/ethanol. Me, methyl; Boc = *tert*-butoxycarbonyl.

do not exist for the synthesis of (*R*)-*tert*-leucine and related (*R*)-amino acids[22].

High yields and enantioselectivities are obtained in these imine hydrocyanations catalysed by **4e**; however, TMSCN is expensive, and the stoichiometric HCN generated upon combination with methanol introduces serious practical and safety liabilities that limit application on preparative scale. Potassium cyanide (KCN) and sodium cyanide (NaCN) represent inexpensive, alternative cyanide sources for Strecker syntheses[13,14,23], but these reagents have found limited application in catalytic asymmetric imine hydrocyanations developed to date. This may be attributed to the poor solubility of cyanide salts in organic solvents, and the incompatibility of known catalysts to aqueous media. In contrast, catalyst **4e** lacks any sensitive functional groups, and therefore might be adaptable to use under aqueous or biphasic conditions. Indeed, treatment of toluene solutions of imine **2a** with KCN, acetic acid, water and catalyst **4e** led to the formation of α-aminonitriles with enantioselectivity similar to that observed in the homogeneous, TMSCN/MeOH-mediated reaction (Fig. 3). Only small decreases in enantioselectivity were observed at higher temperatures and concentrations, and reactions carried out under these more practical conditions proceeded at substantially higher rates.

The efficiency of this reaction is relatively insensitive to small changes in reagent and catalyst concentration: using an optimized protocol, hydrocyanation experiments using 0.5 mol.% catalyst were executed reproducibly and safely at the 25–100 mmol scale for the preparation of protected amino acid derivatives **5a**, **5b** and **5d** (Fig. 3). The requisite imines **2a**, **2b** and **2d** (Table 2) were prepared on multi-gram scales in one or two steps from commercially available aldehydes[24]. The hydrocyanation reaction mixtures were treated with aqueous K_2CO_3 before workup to quench any unreacted HCN generated under the reaction conditions. The enantiomerically enriched α-aminonitriles were isolated in crude form by routine extraction and solvent removal procedures, and converted to the corresponding *tert*-butoxycarbonyl-protected (*R*)-α-amino acids by a two-step sequence involving

Table 1 | Dependence of imine hydrocyanation enantioselectivity on catalyst structure

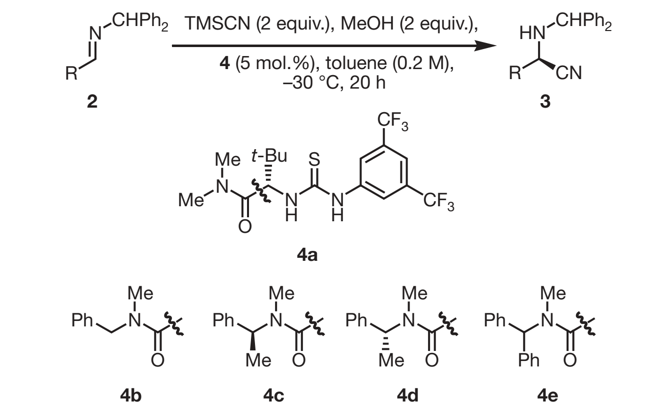

Entry	Catalyst	Enantiomeric excess (%), *R* = *tert*-Bu	Enantiomeric excess (%), *R* = C_6H_5
1	**4a**	–14	41
2	**4b**	30	86
3	**4c**	58	90
4	**4d**	77	97
5	**4e**	93	98

Enantiomeric excess determined by chiral HPLC analysis using commercially available columns. Me, methyl.

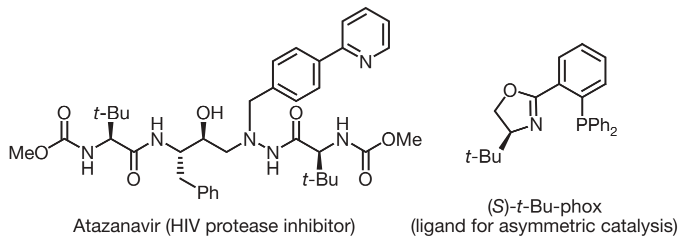

Figure 4 | Examples of a pharmaceutical product and a chiral ligand derived from *tert*-leucine.

Table 2 | Scope of asymmetric imine hydrocyanation

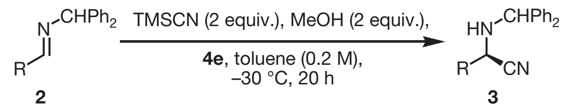

Entry	Imine **2** (R =)	**4e** (mol.%)	Yield (%)	Enantiomeric excess (%)
1	*tert*-butyl (**a**)	2	99	93
2	Et_2MeC (**b**)	2	99	96
3	$PhMe_2C$ (**c**)	2	97	85
4	(1-methyl)cyclohexyl (**d**)	2	99	95
5	1-adamantyl (**e**)	2	99	93
6	cyclohexyl (**f**)	2	99	74
7	*p*-$OMeC_6H_4$ (**g**)	2	99	99
8	*p*-MeC_6H_4 (**h**)	2	98	98
9	C_6H_5 (**i**)	2	98	98
10	*p*-ClC_6H_4 (**j**)	2	97	98
11	*p*-$CF_3C_6H_4$ (**k**)	2	98*	96
12	*p*-CNC_6H_4 (**l**)	10	96*	93
13	*p*-BrC_6H_4 (**m**)	2	98	99
14	*o*-$OMeC_6H_4$ (**n**)	2	97	88
15	*o*-BrC_6H_4 (**o**)	2	96*	97
16	*m*-BrC_6H_4 (**p**)	2	97*	92
17	2-furyl (**q**)	2	99	93
18	3-furyl (**r**)	2	98	97
19	2-thiophenyl (**s**)	2	97*	95
20	1-cyclohexenyl (**t**)	2	99	95
21	(*E*)-1-methyl-pent-1-enyl (**u**)	2	98	91
22	(*E*)-cinnamyl (**v**)	2	99	95
23	(*E*)-hexenyl (**w**)	2	97	73

Isolated yields of **3** after silica gel chromatography of reactions run on 1.0 mmol scale. Enantiomeric excess determined by chiral HPLC analysis using commercially available columns.
*Reactions run at 0 °C. Et, ethyl.

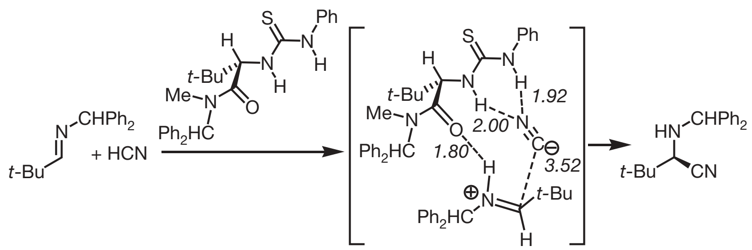

Figure 5 | Proposed catalytic mechanism. The structure in brackets is the iminium/cyanide ion pair intermediate that directly precedes C–C bond formation, as calculated using the B3LYP/6-31G(d) level of density functional theory within Gaussian 03. Bond distances are shown in angstroms (italic numbers). Three-dimensional coordinates are included in the Supplementary Information.

H_2SO_4/HCl-mediated hydrolysis followed by treatment of the resulting aqueous amino acid solutions with di-*tert*-butyl dicarbonate (Boc_2O)[25,26]. The highly enantiomerically enriched, sterically demanding protected α-amino acids were then isolated on multi-gram scales by recrystallization. In each case, the synthetic sequence required no chromatographic purification or specialized equipment.

α-Amino acids bearing quaternary alkyl substituents, especially *tert*-leucine, are common components of pharmaceuticals[3] or medicinal chemistry targets[27], and their derivatives have been found to be highly effective as components of chiral ligands[5] and organocatalysts[28] used in small-molecule asymmetric catalysis (Fig. 4). Use of these α-amino acids has largely been limited to (*S*)-*tert*-leucine, which may be prepared efficiently by enzymatic methods[6]. The method described in this paper allows for efficient access both to the (*R*)-enantiomer of *tert*-leucine and to more sterically demanding analogues, thereby expanding the pool of α-amino acids that can be used in medicinal and other applications.

A detailed experimental and computational[29] analysis of the hydrocyanation reaction catalysed by **4e** points to a mechanism involving initial amido-thiourea-induced imine protonation by HCN to generate a catalyst-bound iminium/cyanide ion pair (Fig. 5). Collapse of this ion pair and C–C bond formation to form the α-aminonitrile then occurs in a post–rate-limiting step. Complete details of this novel mechanistic hypothesis and the basis for enantioselectivity will be reported separately[30].

METHODS SUMMARY

Reactions were carried out in round-bottomed flasks under nitrogen, unless otherwise noted. Commercially available reagents were purchased and used as received unless otherwise noted. Catalysts, imines and α-amino acids were characterized by nuclear magnetic resonance (NMR) and infrared spectroscopy, and by mass spectrometry. The enantiomeric excess of chiral, non-racemic α-amino acids was determined by chiral high-performance liquid chromatography (HPLC) analysis of the benzyl ester derivatives. α-Aminonitriles were characterized by NMR and infrared spectroscopy, and the enantiomeric excesses were determined by chiral HPLC analysis. For experimental details and spectroscopic characterization data, chiral HPLC traces of racemic and non-racemic α-aminonitriles and benzyl esters of α-amino acids, ^{1}H and ^{13}C NMR spectra of catalyst **4e** and α-amino acids, and the geometry of the calculated intermediate, see the Supplementary Information.

Full Methods and any associated references are available in the online version of the paper at www.nature.com/nature.

Received 18 May; accepted 28 August 2009.

1. Bhat, S. V., Nagasampagi, B. A. & Sivakumar, M. *Chemistry of Natural Products* 317–393 (Springer, 2005).
2. Wang, L. & Shultz, P. G. Expanding the genetic code. *Angew. Chem. Int. Edn Engl.* **44,** 34–66 (2005).
3. Tsantrizos, Y. S. Peptidomimetic therapeutic agents targeting the protease enzyme of the human immunodeficiency virus and hepatitis C virus. *Acc. Chem. Res.* **41,** 1252–1263 (2008).
4. Davie, E. A. C., Mennen, S. M., Xu, Y. J. & Miller, S. J. Asymmetric catalysis mediated by synthetic peptides. *Chem. Rev.* **107,** 5759–5812 (2007).
5. Helmchen, G. & Pfaltz, A. Phosphinooxazolines—a new class of versatile, modular P,N-ligands for asymmetric catalysis. *Acc. Chem. Res.* **33,** 336–345 (2000).
6. Bommarius, A. S., Schwarm, M. & Drauz, K. Comparison of different chemoenzymatic process routes to enantiomerically pure amino acids. *Chimia* **55,** 50–59 (2001).
7. Breuer, M. *et al.* Industrial methods for the production of optically active intermediates. *Angew. Chem. Int. Edn Engl.* **43,** 788–824 (2004).
8. Knowles, W. S. Asymmetric hydrogenation. *Acc. Chem. Res.* **16,** 106–112 (1983).
9. Nájera, C. & Sansano, J. M. Catalytic asymmetric synthesis of α-amino acids. *Chem. Rev.* **107,** 4584–4671 (2007).
10. Block, R. J. The isolation and synthesis of the naturally occurring α-amino acids. *Chem. Rev.* **38,** 501–571 (1946).
11. Miller, S. L. Production of some organic compounds under possible primitive earth conditions. *J. Am. Chem. Soc.* **77,** 2351–2361 (1955).
12. Harada, K. Asymmetric synthesis of α-amino acids by the Strecker synthesis. *Nature* **200,** 1201 (1963).
13. Kuethe, J. T., Gauthier, D. R. Jr, Beutner, G. L. & Yasuda, N. A concise synthesis of (*S*)-*N*-ethoxycarbonyl-α-methylvaline. *J. Org. Chem.* **72,** 7469–7472 (2007).
14. Shu, L. & Wang, P. Synthesis of enantiopure Fmoc-α-methylvaline. *Org. Process Res. Dev.* **12,** 298–300 (2008).
15. Gröger, H. Catalytic enantioselective Strecker reactions and analogous syntheses, *Chem. Rev.* **103,** 2795–2827 (2003).
16. Merino, P., Marqués-López, E., Tejero, T. & Herrara, R. P. Organocatalyzed Strecker reactions. *Tetrahedron* **65,** 1219–1234 (2009).
17. Sigman, M. S., Vachal, P. & Jacobsen, E. N. A general catalyst for the asymmetric Strecker reaction. *Angew. Chem. Int. Edn Engl.* **39,** 1279–1281 (2000).
18. Doyle, A. G. & Jacobsen, E. N. Small-molecule H-bond donors in asymmetric catalysis. *Chem. Rev.* **107,** 5713–5743 (2007).
19. Wenzel, A. G., Lalonde, M. P. & Jacobsen, E. N. Divergent stereoinduction mechanisms in urea-catalyzed additions to imines. *Synlett* 1919–1922 (2003).
20. Reisman, S. E., Doyle, A. G. & Jacobsen, E. N. Enantioselective thiourea-catalyzed additions to oxocarbenium ions. *J. Am. Chem. Soc.* **130,** 7198–7199 (2008).
21. Mai, K. & Patil, G. Alkylsilyl cyanides as silylating agents. *J. Org. Chem.* **51,** 3545–3548 (1986).
22. Bélanger, E., Pouliot, M.-F. & Paquin, J.-F. Use of 5,5-(dimethyl)-*i*-Pr-PHOX as a practical equivalent to *t*-Bu-PHOX in asymmetric catalysis. *Org. Lett.* **11,** 2201–2204 (2009).
23. Ooi, T., Uematsu, Y. & Maruoka, K. Asymmetric Strecker reaction of aldimines using aqueous potassium cyanide by phase-transfer catalysis of chiral quaternary ammonium salts with a tetranaphthyl backbone. *J. Am. Chem. Soc.* **128,** 2548–2549 (2006).
24. Anderson, J. C., Denton, R. M., Hickin, H. G. & Wilson, C. Synthesis of dibenzofuran-1,4-diones using the Dotz benzannulation. *Tetrahedron* **60,** 2327–2335 (2004).
25. Corey, E. J. & Grogan, M. J. Enantioselective synthesis of alpha-amino nitriles from *N*-benzhydryl imines and HCN with a chiral bicyclic guanidine as catalyst. *Org. Lett.* **1,** 157–160 (1999).
26. Krueger, C. A. *et al.* Ti-catalyzed enantioselective addition of cyanide to imines. a practical synthesis of optically pure alpha-amino acids. *J. Am. Chem. Soc.* **121,** 4284–4285 (1999).
27. Arasappan, A. *et al.* Practical and efficient method for amino acid derivatives containing beta quaternary center: application toward synthesis of hepatitis C virus NS3 serine protease inhibitors. *Tetrahedr. Lett.* **48,** 6343–6347 (2007).
28. Mita, T. & Jacobsen, E. N. Bifunctional asymmetric catalysis with hydrogen chloride: enantioselective ring-opening of aziridines catalyzed by a phosphinothiourea. *Synlett* 1680–1684 (2009).
29. Frisch, M. J. *et al. Gaussian 03* Revision E.01 (Gaussian, Inc., 2004).
30. Zuend, S. J. & Jacobsen, E. N. Mechanism of amido-thiourea catalyzed enantioselective imine hydrocyanation: transition state stabilization via multiple non-covalent interactions. *J. Am. Chem. Soc.* doi:10.1021/ja9058958 (in the press).

Supplementary Information is linked to the online version of the paper at www.nature.com/nature.

Acknowledgements This work was supported by the NIH, and through fellowships from the American Chemical Society and Roche (to S.J.Z.) and the Natural Sciences and Engineering Research Council of Canada (to M.P.L.).

Author Contributions S.J.Z. and M.P.L. synthesized and evaluated the catalysts; M.P.C. evaluated the scope of the TMSCN-mediated reaction; S.J.Z. developed the KCN-mediated syntheses and the large-scale procedures; S.J.Z. and E.N.J. wrote the manuscript; E.N.J. guided the research.

Author Information Reprints and permissions information is available at www.nature.com/reprints. Correspondence and requests for materials should be addressed to E.N.J. (jacobsen@chemistry.harvard.edu).

METHODS

Preparation of α-aminonitrile 3a by KCN-mediated hydrocyanation. Caution! HCN is produced. The experiment should be executed in a well-ventilated fume hood.

A 250-ml round-bottomed flask containing a 4-cm-long stir bar was charged with KCN (5.21 g, 80 mmol, 2.0 equiv.) and toluene (76 ml), capped with a virgin rubber septum, and cooled at 0 °C for 10 min under N_2. Acetic acid (2.75 ml, 48 mmol, 1.2 equiv.) and water (2.88 ml, 160 mmol, 4.0 equiv.) were added sequentially via syringe, and the N_2 inlet was removed. The resulting white, heterogeneous mixture was stirred vigorously at 0 °C. After 5 min the upper organic layer had become a clear, colourless solution, and the lower aqueous layer contained a chunky, white precipitate. After stirring for 20 min, the N_2 inlet was restored, and a freshly prepared stock solution of **2a** (9.79–9.93 g, prepared from 40 mmol of aminodiphenylmethane as described in the Supplementary Information) and **4e** (116 mg, 0.20 mmol, 0.0050 equiv.) in toluene (24 ml) was added via syringe in 10-ml portions over 1 min. The flask containing the stock solution was rinsed with additional toluene (2 × 3 ml), and the rinses were added to the reaction. The N_2 inlet was removed, and the mixture was stirred at 0 °C. The reaction was monitored as follows: a 100 μl aliquot was removed via syringe, filtered through a 1-cm-high plug of Na_2SO_4, rinsed with hexanes (2 × 3 ml), and concentrated under reduced pressure. The sample was dissolved in 600 μl $CDCl_3$ and analysed by ^{1}H-NMR spectroscopy. After 2.5 h, conversion was estimated to be 95% by integration of the benzhydryl resonances of the starting material (5.4 p.p.m.) and product (5.2 p.p.m.). After 4 h, the reaction mixture was allowed to warm to room temperature over 5 min. The septum was removed, and the reaction mixture was treated with 50 ml of a 0.2 g ml^{-1} aqueous K_2CO_3 solution. The mixture was transferred to a 250-ml separatory funnel in a fume hood, the reaction flask was rinsed with diethyl ether (3 × 5 ml), and the rinses were added to the separatory funnel. The organic and aqueous layers were thoroughly mixed, and the aqueous layer removed. The organic layer was washed with another 50 ml of K_2CO_3 solution and then with brine (50 ml). The aqueous layers were disposed in a waste container that was maintained at basic pH and stored in a fume hood. The clear, colourless organic layer was dried over Na_2SO_4, decanted into a 500-ml round-bottomed flask, rinsing with diethyl ether (3 × 5 ml), and concentrated to a volume of approximately 100 ml using a rotary evaporator. The flask was then charged with a 2-cm-long stir bar, placed in a 25 °C water bath, and concentrated to a volume of approximately 15 ml by vacuum transfer into a dry ice/acetone bath. A sample of the clear, colourless liquid residue was analysed by chiral HPLC analysis (Chiralpak AS-H column, Chiral Technologies), 1 ml min^{-1}, 5% *iso*-propanol/hexanes, 220 nm): retention time t_R(minor) = 6.18 min, t_R(major) = 9.09 min, 87–88% enantiomeric excess (range of three experiments). The liquid was transferred to a 100-ml round-bottomed flask, rinsing with CH_2Cl_2 (3 × 4 ml). The solution was concentrated to a mass of 12 g under reduced pressure (30 torr down to 1 torr). ^{1}H-NMR analysis of the clear, colourless oil revealed approximately 30 mol.% remaining toluene. Crude **3a** was used in the next step without further purification. Experimental procedures for the hydrolysis of **3a** and for the isolation of (*R*)-Boc-*tert*-leucine are provided in the Supplementary Information.

LETTERS

Extensive dynamic thinning on the margins of the Greenland and Antarctic ice sheets

Hamish D. Pritchard[1], Robert J. Arthern[1], David G. Vaughan[1] & Laura A. Edwards[2]

Many glaciers along the margins of the Greenland and Antarctic ice sheets are accelerating and, for this reason, contribute increasingly to global sea-level rise[1–7]. Globally, ice losses contribute ~1.8 mm yr^{-1} (ref. 8), but this could increase if the retreat of ice shelves and tidewater glaciers further enhances the loss of grounded ice[9] or initiates the large-scale collapse of vulnerable parts of the ice sheets[10]. Ice loss as a result of accelerated flow, known as dynamic thinning, is so poorly understood that its potential contribution to sea level over the twenty-first century remains unpredictable[11]. Thinning on the ice-sheet scale has been monitored by using repeat satellite altimetry observations to track small changes in surface elevation, but previous sensors could not resolve most fast-flowing coastal glaciers[12]. Here we report the use of high-resolution ICESat (Ice, Cloud and land Elevation Satellite) laser altimetry to map change along the entire grounded margins of the Greenland and Antarctic ice sheets. To isolate the dynamic signal, we compare rates of elevation change from both fast-flowing and slow-flowing ice with those expected from surface mass-balance fluctuations. We find that dynamic thinning of glaciers now reaches all latitudes in Greenland, has intensified on key Antarctic grounding lines, has endured for decades after ice-shelf collapse, penetrates far into the interior of each ice sheet and is spreading as ice shelves thin by ocean-driven melt. In Greenland, glaciers flowing faster than 100 m yr^{-1} thinned at an average rate of 0.84 m yr^{-1}, and in the Amundsen Sea embayment of Antarctica, thinning exceeded 9.0 m yr^{-1} for some glaciers. Our results show that the most profound changes in the ice sheets currently result from glacier dynamics at ocean margins.

To quantify ice loss from ice sheets, three different methods have so far been used: calculation of flux imbalance from separate measurements of snow accumulation and ice flow velocity, detection of changing gravitational anomalies and measurement of changing ice-sheet surface elevation. Each approach has limitations: flux-imbalance estimates suffer from inaccuracies in snow accumulation rate[13], and satellite gravity measurements have poor spatial resolution and are prone to problems in modelling crustal rebound[14]. Direct measurement of volume change by satellite radar altimeters is limited to latitudes between 81.5° S and 81.5° N and to surface slopes below ~1°. Resolution is limited to a footprint width of 2–3 km, measurement density is low (being restricted to ground-track crossover points) and radar surface penetration is imperfectly known. Current radar systems perform poorly where change is most rapid, namely along the relatively steep and narrow glaciers fringing the ice sheets[12]. Furthermore, conversion from volume to mass change requires knowledge of the density of snow or ice added or lost. Additional information is needed to distinguish between these in low-resolution radar altimeter measurements[12].

An entirely different experiment, the Geoscience Laser Altimeter System, launched in 2002 on board NASA's ICESat, was designed to overcome several of these issues. Here we report a method of comparing data from near-repeat ICESat tracks. This produces a much greater measurement density than was previously available, revealing the pattern of change from local to continental scales, including the steep ice-sheet margins.

Figure 1 shows two examples demonstrating that our technique provides coherent measurements of change, significant on length scales on the order of 100 m along the satellite ground track. This high resolution allows us, in many areas, to distinguish between changes in elevation that result from dynamical changes associated with fast-flowing ice and those that result from other causes (snowfall, melt and so on), by comparing the rate of change in adjacent slow- and fast-flowing areas in the same climatic setting (Fig. 1b, Supplementary Figs 5, 6, 7, 8, 9 and 10 and Supplementary Tables 2, 4 and 5).

Comparison of Fig. 2 with those produced using the >10-yr records obtained by radar altimetry[12,15,16] shows that our technique successfully reproduces the large-scale patterns of ice-sheet change and, in both Antarctica and Greenland, shows features not previously seen.

Prominent in Greenland is the strong thinning of the southeast and northwest ice-sheet margins (Supplementary Fig. 3); higher areas in the south thickened. These margins have a positive surface mass balance (SMB) and, hence, a high proportion of discharge through tidewater glaciers. Southeastern glaciers accelerated between 1996 and 2005, but those in the northwest showed little change in flow[2]. The widespread dynamic thinning we identify in the northwest therefore implies a sustained period of dynamic imbalance. For the ice sheet as a whole, areas of fast flow[1] (>100 m yr^{-1} (ref. 2)) thinned significantly more rapidly than slow-flowing areas (0.84 m yr^{-1} versus 0.12 m yr^{-1}), a discrepancy that cannot be explained by variability in SMB (Supplementary Table 2). We find that of 111 glaciers surveyed, 81 thinned dynamically at rates greater than twice the thinning rate on nearby slow-flowing ice at the same altitude (Supplementary Tables 5 and 6). Dynamic thickening is scarce but notable on quiescent surge-type glaciers Storstrømmen[17] (Fig. 2, inset; S) and neighbouring L. Bistrup Bræ (Supplementary Fig. 3). For the first time, low-altitude changes are discernible across the slower-flowing, land-terminating ice sheet and on many small, fringing ice caps. North of 80° N, thinning of the slow-flowing margin peaked at 0.15 ± 0.002 m yr^{-1} at an altitude of 900 m but was close to zero at 450 and 1,450 m (Supplementary Fig. 4), with changes most likely driven by SMB anomalies. In contrast, the southwestern margin thickened at all altitudes, at up to 0.44 ± 0.005 m yr^{-1}. Dynamic thinning has penetrated deep into the ice sheet: on Jakobshavn Isbræ, Helheim and Kangerdlugssuaq glaciers (Fig. 2, inset; respectively J, H and K), it is detectable from the snout to 120, 95 and 100 km inland, respectively, at altitudes of 1,600 m to 2,000 m above sea level. If these changes are driven by the reported recent glacier retreat and acceleration[18], this would imply remarkable rates

[1]British Antarctic Survey, Natural Environment Research Council, Madingley Road, Cambridge CB3 0ET, UK. [2]School of Geographical Sciences, University of Bristol, Bristol BS8 1SS, UK.

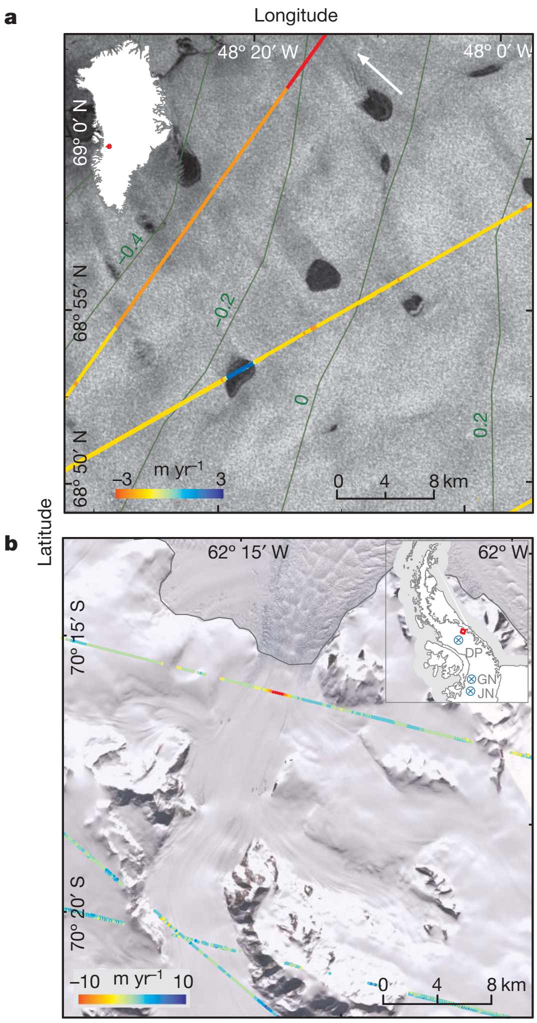

Figure 1 | High-resolution change measurements from along-track interpolation of ICESat data. a, The filling of a melt pond (blue; see colour scale) is resolved against a trend of dynamic thinning (yellow to red) on Jakobshavn Isbræ, Greenland. Thinning increases strongly towards the glacier centre, to the northeast. White arrow, main ice flow direction; green contours, mean SMB (metres water equivalent per year) (after ref. 2); background, synthetic-aperture-radar image. See also Supplementary Fig. 2. **b**, Rapid dynamic thinning (up to 13 m yr^{-1}) of Clifford Glacier, feeding the southern part of the Larsen Ice Shelf, Antarctic Peninsula. Background, Landsat Image Mosaic of Antarctica (grounding line in grey). Data are unfiltered. Inset, global-positioning-system ground-control points from Supplementary Table 1 (JN, Jurassic Nunatak; GN, Gomez Nunatak; DP, Dyer Plateau).

of propagation (Supplementary Fig. 5). Furthermore, deeply penetrating dynamic thinning has spread to high northern latitudes, for example on Tracy Glacier at 77.6° N (Supplementary Table 3 and Supplementary Fig. 6).

In Antarctica, we find significant dynamic thinning of fast-flowing ice at rates greater than plausible through interannual accumulation variability for drainage sectors[19] F′G and GH (Fig. 2), with significant dynamic thickening of sector A′B (Supplementary Table 4). On the glacier scale, thinning is strongest in the Amundsen Sea embayment (ASE), where it is confirmed as being localized on the fast-flowing glaciers and their tributaries (Fig. 3 and Supplementary Fig. 7). The area close to the Pine Island Glacier grounding line thinned in the period 2003–2007 at up to 6 m yr^{-1}, neighbouring Smith Glacier thinned at a rate in excess of 9 m yr^{-1} and Thwaites Glacier thinned at a rate of around 4 m yr^{-1}. These rates are higher than those reported for the 2002–2004 period[20]. Numerous small, independent glaciers feeding the same, rapidly thinning ice shelves, namely the Crosson and Dotson ice shelves[21], are also thinning dynamically, which is strong evidence of a common, ocean-driven cause (Supplementary Fig. 7). Surface lowering is apparent across almost the whole area of the drainage basins of the Kohler, Smith, Pope and Haynes glaciers of the Amundsen Sea embayment, and up to the northern drainage divide of Pine Island Glacier. We calculate the mean elevation rate for sector GH to be -0.139 ± 0.07 m yr^{-1} (whereas a rate of -0.092 ± 0.007 m yr^{-1} was reported for 1995–2003[22]), giving a volume change of -57 ± 29 km^3 yr^{-1}.

Several new features in the pattern of Antarctic elevation change are now visible. The 'polar hole' resulting from the orbital limit of satellites is reduced from the area south of 81.5° S for current radar altimetry to that south of 86° S for ICESat; hence, we now see the full Antarctic grounding line, including the Siple Coast (Fig. 2; SC). This allows us to confirm expectations of previous studies of the shutdown of the Kamb Ice Stream around 130 yr ago[12,23–25]. We see thickening of the ice stream reaching 0.65 ± 0.07 m yr^{-1} close to the transition between its fast-flowing tributaries and stagnant trunk (Fig. 4). The fast-flowing (>200 m yr^{-1}) sections of the neighbouring Whillans Ice Stream are thickening, but this is clearly bounded by the ice-stream shear margins, with the interstream ridges and slower-flowing upper drainage basins conversely thinning at up to 0.25 ± 0.07 m yr^{-1}.

Assuming that these volume changes are of ice with a density of 917 kg m^{-3}, our observations allow an independent assessment of the flux imbalance. For drainage sector E′E′′ as a whole (Fig. 4), the net change was $+36 \pm 16$ Gt yr^{-1} ($+39$ km^3 yr^{-1}), which is substantially greater than estimates based on the partial radar altimetry coverage[12,16], but agrees with estimates from flux imbalance[13,26].

On the Amundsen Sea coast of West Antarctica, our laser altimetry method resolves rapid dynamic thinning along the full length of the grounded ice-sheet margin feeding the Getz Ice Shelf (Fig. 3; GIS) on finer spatial scales than are possible using radar altimetry[12]. This reveals thinning at the grounding line at rates of up to several metres per year over areas of fast flow; this thinning attenuates inland but more than outweighs gains on the interior of the drainage basin. The net volume change for sector F′G is -14 ± 9 km^3, in agreement with flux-imbalance calculations[13,24] (assuming losses are of ice). Here also, the more dynamic glaciers on offshore islands bounded by the Getz Ice Shelf are thinning rapidly on their lower reaches, suggesting that the common cause is the ocean-driven thinning of this shelf at 2–3 m yr^{-1} (ref. 27).

Conversely, for the 400 km of coast feeding the Abbott Ice Shelf (AIS), whose thickness is unchanging[27], the drainage basin thickened strongly down to the grounding line, presumably driven by recent anomalously high snowfall rates (Fig. 3). This is partly offset by dynamic thinning of adjacent Eltanin Bay (EB) glaciers, giving a net volume gain of $+8 \pm 24$ km^3 yr^{-1} (loss of 8 km^3 yr^{-1} plus gain of 16 km^3 yr^{-1}) for sector HH′; hence, we do not find evidence for the large negative flux imbalance (-49 Gt yr^{-1}) reported previously[13].

In East Antarctica, we observe dynamic thinning on some outlets, particularly between 90° and 165° E (Supplementary Figs 8 and 9). Thinning of Totten Glacier, the highest-flux East Antarctic outlet, is three times greater than previously reported[28]. The similar behaviour of its smaller, independent neighbours indicates a common, regional and perhaps ocean-driven cause.

With ICESat, we can view elevation change over the full Antarctic Peninsula for the first time (Fig. 2), and find that slow-flowing ice caps and divides along the Bellingshausen Sea (BS) coast are thickening at up to 1 m yr^{-1} (comparable to radar altimetry measurements of the neighbouring inland ice sheet for the preceding 13 yr (ref. 12)). This signal extends at high altitude to the peninsula's northern tip, contrasting strongly with profound dynamic thinning of collapsed-ice-shelf tributary glaciers flowing from the plateau to both the east and west coasts (see, for example, Supplementary Fig. 10). These glaciers are thinning at some of the highest rates recorded either in Antarctica or Greenland (up to tens of metres per year), and ongoing thinning is detectable right up to the headwalls, or well into the inland ice sheet,

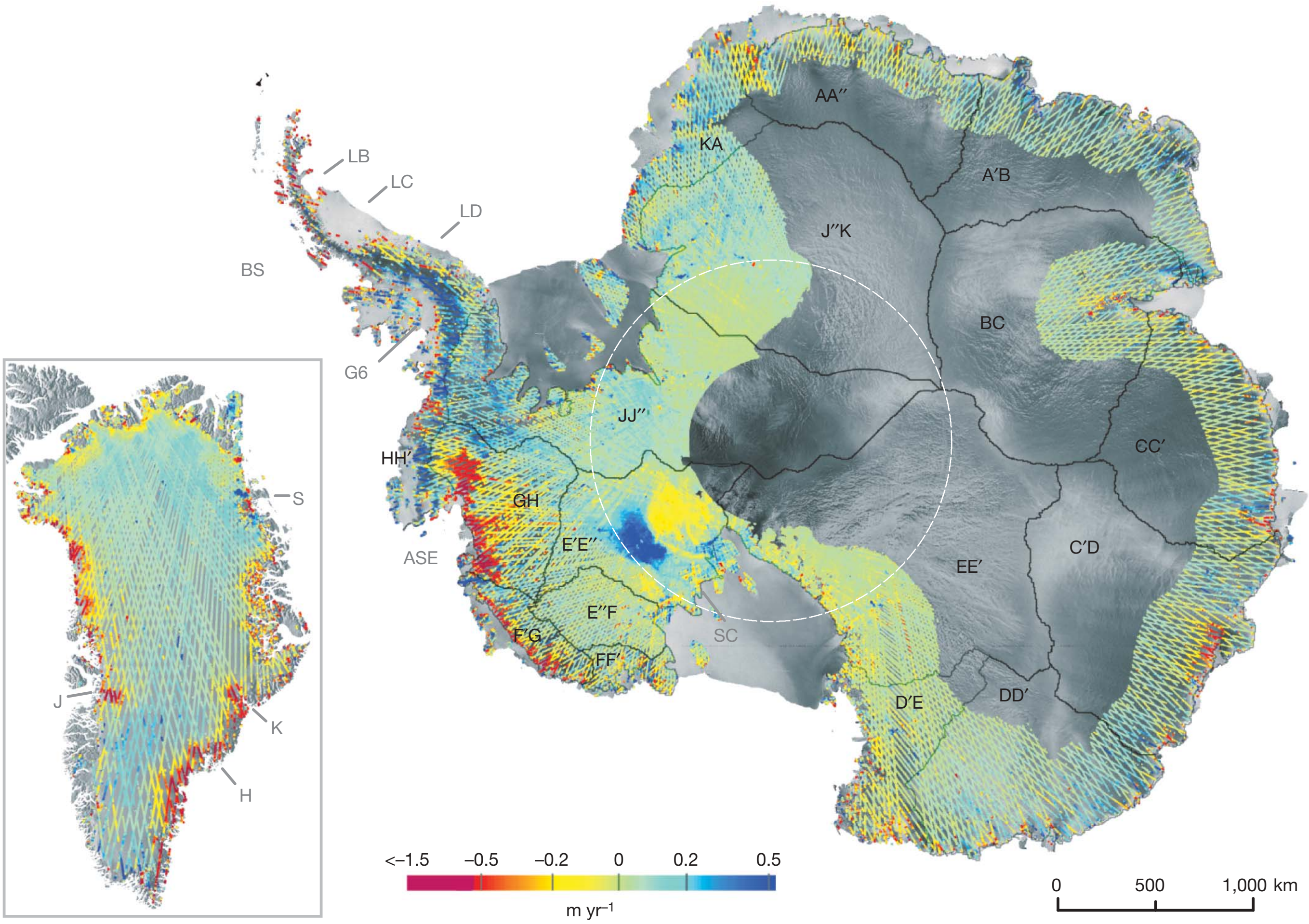

Figure 2 | Rate of change of surface elevation for Antarctica and Greenland. Change measurements are median filtered (10-km radius), spatially averaged (5-km radius) and gridded to 3 km, from intervals (Δt) of at least 365 d, over the period 2003–2007 (mean Δt is 728 d for Antarctica and 746 d for Greenland). East Antarctic data cropped to 2,500-m altitude. White dashed line (at 81.5° S) shows southern limit of radar altimetry measurements. Labels are for sites and drainage sectors (see text).

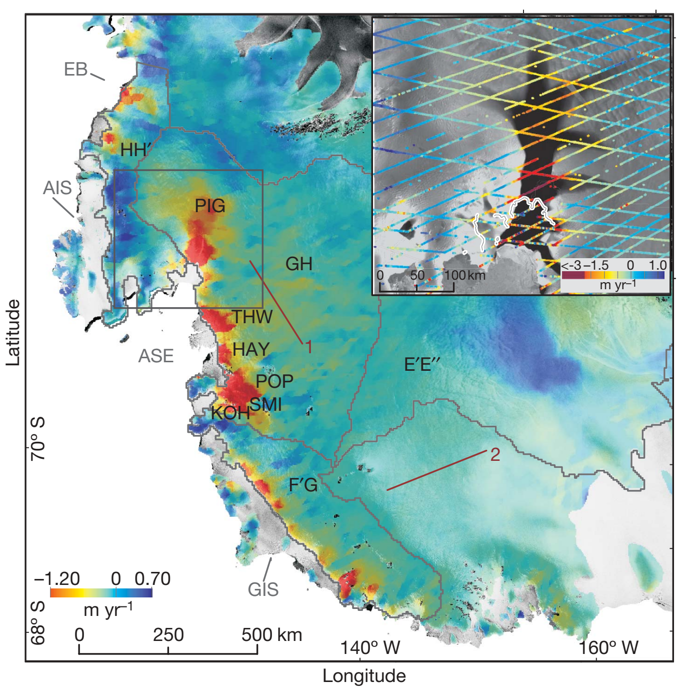

Figure 3 | Rate of elevation change of coastal West Antarctica. Filtered, spatially averaged (10-km radius) $\Delta h/\Delta t$ data (background, Radarsat Antarctic Mapping Project (RAMP) mosaic). We note fast thinning on the Amundsen Sea embayment (ASE) glaciers Pine Island (PIG), Thwaites (THW), Haynes (HAY), Pope (POP), Smith (SMI) and Kohler (KOH) and on tributaries of the thinning Getz Ice Shelf (GIS). Tributaries of the unchanging Abbott Ice Shelf (AIS) thickened. Profiles 1 and 2 are discussed in Supplementary Methods. Inset, high-resolution data over Pine Island Glacier. Dynamic thinning is strongly concentrated on the fast-flowing trunk (dark grey in background[28]). Change becomes highly variable on the floating, fissured ice-shelf downstream of the year-2000 grounding line (outlined in white).

even up to 30 yr after shelf collapse. Glacier tributaries feeding the surviving but thinning parts of the Larsen Ice Shelf (Fig. 2; LC and LB)[29], plus the George VI Ice Shelf (G6) and the little-studied, southern part of the Larsen Ice Shelf (Fig. 2; LD), also thinned at rates of up to several metres per year. This behaviour, similar to that seen on Getz, Crosson and Dotson ice-shelf tributaries, demonstrates an unexpectedly marked dynamic response of glaciers flowing into intact but thinning ice shelves.

To conclude, our simple technique for using ICESat along-track data to measure ice-sheet change is an effective tool for mapping continental and local-scale changes and can deliver two orders of magnitude more measurements than crossover analysis, increasing spatial coverage and resolution. The ICESat data constitute complete, consistent and directly comparable maps of elevation change for the entire grounded margins of the Antarctic and Greenland ice sheets, where rapid change is concentrated. They broadly agree with those from radar altimetry but show changes farther south in Antarctica, closer to the ice-sheet margins, on coastal ice caps and ice rises, and on the mountainous Antarctic Peninsula and Greenland margins. The high spatial resolution allows us in many places to make the distinction between dynamic thinning of faster-flowing ice and other elevation-change signals. Our independent measurements act as arbiter in areas where existing methods fail to agree on the magnitude of ice-sheet volume change: we find support for the results of flux-balance studies on the Siple Coast and Getz Ice Shelf areas of West Antarctica.

The pattern of change now apparent across Antarctica and Greenland is complex, exhibiting the influence of changing precipitation, atmospheric temperature and oceanographic conditions, but the most profound changes clearly result from glacier dynamic effects. Much of the Greenland ice-sheet margin is thinning slowly as SMB becomes more negative, but many coastal glaciers at all latitudes show evidence specifically of rapid dynamic thinning as a result of acceleration of flow. Where strong dynamic thinning has begun, it has spread rapidly, deep into the ice-sheet interior and up to high altitudes. In Antarctica, dynamic thinning has accelerated at the grounding lines of the major glaciers of the Amundsen Sea embayment, and in places has penetrated to within 100 km of the ice divides. Ice-shelf-collapse glaciers show particularly strong thinning that has persisted for years to decades after collapse and in places has penetrated to their headwalls. Although losses are partly offset by strong gains on the spine and western flank of the Antarctic Peninsula, numerous glaciers feeding intact Antarctic Peninsula, West Antarctic and East Antarctic ice shelves are also thinning dynamically. We infer that grounded glaciers and ice streams are responding sensitively not only to ice-shelf collapse but to shelf thinning owing to ocean-driven melting. This is an apparently widespread phenomenon that does not require climate warming sufficient to initiate ice-shelf surface melt. Dynamic thinning of Greenland and Antarctic ice-sheet ocean margins is more sensitive, pervasive, enduring and important than previously realized.

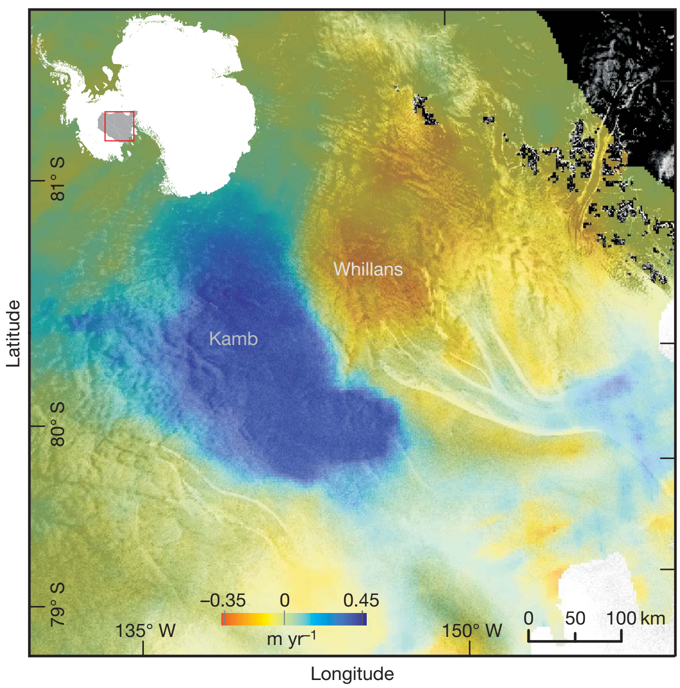

Figure 4 | Rate of elevation change on the Siple Coast, Antarctica. Filtered, spatially averaged (10-km radius) $\Delta h/\Delta t$ data (background, RAMP synthetic-aperture-radar mosaic). The Kamb Ice Stream is thickening, as are the fast-flowing sections of the Whillans Ice Stream. Much of the Whillans catchment and many of the interstream ridges are thinning. Inset, location (red) and drainage sector E′E′′ (grey).

METHODS SUMMARY

ICESat samples surface elevation over 65-m footprints every 172 m along the satellite orbit, and closely repeats ground tracks on the Greenland and Antarctic ice sheets. However, technical issues limit the number of repeated tracks[30], and they are rarely repeated precisely—most are offset by up to a few hundred metres. This has made height-change measurement difficult without knowledge of the cross-track slope[3]. Attention has therefore focused on measuring change at relatively sparse ground-track crossovers, discarding the bulk of along-track data.

Our approach maximizes coverage by using the along-track data, allowing us to resolve ice-sheet change in greater detail. We applied our method to the entire grounded Greenland ice sheet and its fringing ice caps (6,700,000 measurements of height change rate, $\Delta h/\Delta t$), and to the grounded Antarctic ice sheet below 2,500 m, including islands and ice caps (43,500,000 $\Delta h/\Delta t$ measurements).

We used ICESat Release 28 GLA12 data[31] from between February 2003 and November 2007. We fitted planar surfaces to parallel tracks of point height and date measurements that are close in space ($<$ 300 m) and time ($<$ 2 yr). We then subtracted the height and date of later point measurements that overlap these interpolated surfaces, giving us $\Delta h/\Delta t$ (Supplementary Figs 1 and 2). We repeated this process for all possible combinations of interpolated and overlapping tracks that fit our criteria. This approach sacrifices temporal resolution to gain spatial coverage. We estimate the uncertainty in our spatially averaged $\Delta h/\Delta t$ values to be $\pm 0.07\ \mathrm{m\,yr^{-1}}$ at the 1σ level.

Received 23 October 2008; accepted 28 August 2009.
Published online 23 September 2009.

1. Joughin, I. *et al.* Continued evolution of Jakobshavn Isbrae following its rapid speedup. *J. Geophys. Res.* **113**, doi:10.1029/2008JF001023 (2008).
2. Rignot, E. & Kanagaratnam, P. Changes in the velocity structure of the Greenland ice sheet. *Science* **311**, 986–990 (2006).
3. Scambos, T. A., Bohlander, J. A., Shuman, C. A. & Skvarca, P. Glacier acceleration and thinning after ice shelf collapse in the Larsen B embayment, Antarctica. *Geophys. Res. Lett.* **31**, doi:10.1029/2004GL020670 (2004).
4. Krabill, W. *et al.* Greenland ice sheet: increased coastal thinning. *Geophys. Res. Lett.* **31**, doi:10.1029/2004GL021533 (2004).
5. Pritchard, H. D. & Vaughan, D. G. Widespread acceleration of tidewater glaciers on the Antarctic Peninsula. *J. Geophys. Res.* **112**, doi:10.1029/2006JF000597 (2007).
6. Sole, A., Payne, T., Bamber, J., Nienow, P. & Krabill, W. Testing hypotheses of the cause of peripheral thinning of the Greenland Ice Sheet: is land-terminating ice thinning at anomalously high rates? *Cryosphere* **2**, 205–218 (2008).
7. Scott, J. B. T. *et al.* Increased rate of acceleration on Pine Island Glacier strongly coupled to changes in gravitational driving stress. *Cryosphere* **3**, 125–131 (2009).
8. Meier, M. F. *et al.* Glaciers dominate eustatic sea-level rise in the 21st century. *Science* **317**, 1064–1067 10.1126/science.1143906 (2007).
9. Vieli, A., Funk, M. & Blatter, H. Flow dynamics of tidewater glaciers: a numerical modelling approach. *J. Glaciol.* **47**, 595–606 (2001).
10. Schoof, C. Ice sheet grounding line dynamics: steady states, stability and hysteresis. *J. Geophys. Res.* **112**, doi:10.1029/2006JF000664 (2007).
11. Bindoff, N. L. *et al.* in *Climate Change 2007: The Physical Science Basis* (eds Solomon, S. *et al.*) 385–432 (Cambridge Univ. Press, 2007).
12. Wingham, D., Shepherd, A., Muir, A. & Marshall, G. J. Mass balance of the Antarctic ice sheet. *Phil. Trans. R. Soc. A* **364**, 1627–1636 (2006).
13. Rignot, E. *et al.* Recent Antarctic ice mass loss from radar interferometry and regional climate modelling. *Nature Geosci.* **1**, 106–110 (2008).

14. Velicogna, I. & Wahr, J. Acceleration of Greenland ice mass loss in spring 2004. *Nature* **443,** 329–331 (2006).
15. Zwally, H. J. *et al.* Mass changes of the Greenland and Antarctic ice sheets and shelves and contributions to sea-level rise: 1992–2002. *J. Glaciol.* **51,** 509–527 (2005).
16. Davis, C. H., Yonghong, L., McConnell, J. R., Frey, M. M. & Hanna, E. Snowfall-driven growth in East Antarctic ice sheet mitigates recent sea-level rise. *Science* **308,** 1898–1901 (2005).
17. Reeh, N., Mohr, J. J., Madsen, S. N., Oerter, H. & Gundestrup, N. S. Three-dimensional surface velocities of Storstrømmen glacier, Greenland, derived from radar interferometry and ice-sounding radar measurements. *J. Glaciol.* **49,** 210–219 (2003).
18. Howat, I. M., Joughin, I. R. & Scambos, T. A. Rapid changes in ice discharge from Greenland outlet glaciers. *Science* **315,** 1559–1561 (2007).
19. Liu, H. X., Jezek, K. C. & Li, B. Development of Antarctic DEM by integrating cartographic and remotely sensed data: a GIS-based approach. *J. Geophys. Res.* **104,** 23199–23213 (1999).
20. Thomas, R. *et al.* Accelerated sea-level rise from West Antarctica. *Science* **306,** 255–258 (2004).
21. Rignot, E. & Jacobs, S. S. Rapid bottom melting widespread near Antarctic ice sheet grounding lines. *Science* **296,** 2020–2023 (2002).
22. Helsen, M. M. *et al.* Elevation changes in Antarctica mainly determined by accumulation variability. *Science* **320,** 1626–1629 (2008).
23. Smith, B. E., Bentley, C. R. & Raymond, C. F. Recent elevation changes on the ice streams and ridges of the Ross Embayment from ICESat crossovers. *Geophys. Res. Lett.* **32,** doi:10.1029/2005GL024365 (2005).
24. Rignot, E. & Thomas, R. H. Mass balance of polar ice sheets. *Science* **297,** 1502–1506 (2002).
25. Joughin, I. & Tulaczyk, S. Positive mass balance of the Ross Ice Streams, West Antarctica. *Science* **295,** 476–480 (2002).
26. Joughin, I., Tulaczyk, S., Bindschadler, R. & Price, S. F. Changes in west Antarctic ice stream velocities: observation and analysis. *J. Geophys. Res.* **107,** doi:10.1029/2001JB001029 (2002).
27. Shepherd, A., Wingham, D. & Rignot, E. Warm ocean is eroding West Antarctic ice sheet. *Geophys. Res. Lett.* **31,** doi:10.1029/2004GL021106 (2004).
28. Rignot, E. Changes in ice dynamics and mass balance of the Antarctic ice sheet. *Phil. Trans. R. Soc. Lond. A* **364,** 1637–1655 (2006).
29. Shepherd, A., Wingham, D., Payne, T. & Skvarca, P. Larsen ice shelf has progressively thinned. *Science* **302,** 856–859 (2003).
30. Abshire, J. B. *et al.* Geoscience Laser Altimeter System (GLAS) on the ICESat Mission: on-orbit measurement performance. *Geophys. Res. Lett.* **32,** doi:10.1029/2005GL024028 (2005).
31. Zwally, H. J. *et al.* GLAS/ICESat L2 Antarctic and Greenland Ice Sheet Altimetry Data V028. *Boulder, CO: National Snow and Ice Data Center* ⟨http://nsidc.org/data/gla12.html⟩ (2007).

Supplementary Information is linked to the online version of the paper at www.nature.com/nature.

Acknowledgements We are extremely grateful to the ICESat science team and all those at NASA involved in producing the ICESat data products distributed through the US National Snow and Ice Data Center. This work was funded by the UK Natural Environment Research Council.

Author Contributions H.D.P. designed the research; H.D.P. and R.J.A. performed the research; L.A.E. compiled velocity data; H.D.P., R.J.A. and D.G.V. analysed the data; H.D.P. wrote the paper.

Author Information Reprints and permissions information is available at www.nature.com/reprints. Correspondence and requests for materials should be addressed to H.D.P. (hprit@bas.ac.uk).

Vol 461|15 October 2009|doi:10.1038/nature08465

LETTERS

Ammonia oxidation kinetics determine niche separation of nitrifying Archaea and Bacteria

Willm Martens-Habbena[1], Paul M. Berube[1]†, Hidetoshi Urakawa[1], José R. de la Torre[1]† & David A. Stahl[1]

The discovery of ammonia oxidation by mesophilic and thermophilic Crenarchaeota and the widespread distribution of these organisms in marine and terrestrial environments indicated an important role for them in the global nitrogen cycle[1–7]. However, very little is known about their physiology or their contribution to nitrification[8]. Here we report oligotrophic ammonia oxidation kinetics and cellular characteristics of the mesophilic crenarchaeon '*Candidatus* Nitrosopumilus maritimus' strain SCM1. Unlike characterized ammonia-oxidizing bacteria, SCM1 is adapted to life under extreme nutrient limitation, sustaining high specific oxidation rates at ammonium concentrations found in open oceans. Its half-saturation constant (K_m = 133 nM total ammonium) and substrate threshold (≤10 nM) closely resemble kinetics of *in situ* nitrification in marine systems[9,10] and directly link ammonia-oxidizing Archaea to oligotrophic nitrification. The remarkably high specific affinity for reduced nitrogen (68,700 l per g cells per h) of SCM1 suggests that *Nitrosopumilus*-like ammonia-oxidizing Archaea could successfully compete with heterotrophic bacterioplankton and phytoplankton. Together these findings support the hypothesis that nitrification is more prevalent in the marine nitrogen cycle than accounted for in current biogeochemical models[11].

Aerobic ammonia oxidation is the first, rate-limiting step of nitrification, a two-step process catalysed by ammonia-oxidizing and nitrite-oxidizing microorganisms. It is the only oxidative biological process linking reduced and oxidized pools of inorganic nitrogen in nature[12,13]. This key process in the global nitrogen cycle was thought to be restricted to ammonia-oxidizing bacteria (AOB), two narrow clades of Beta- and Gammaproteobacteria[8,13]. These slow-growing, autotrophic bacteria use ammonia oxidation as their sole source of energy. The growth rates of AOB are thus directly linked to the availability of ammonium and the kinetics of its oxidation[13,14]. *In situ* rate measurements in natural marine and terrestrial environments, however, indicate that nitrification occurs almost ubiquitously, even in the most oligotrophic environments with ammonium levels significantly below the growth threshold of AOB[9–11,13–15], raising the question whether these bacteria could represent the dominant ammonia-oxidizer assemblage in oligotrophic environments[9,10,13,14].

The demonstration of autotrophic ammonia oxidation by mesophilic and thermophilic Crenarchaeota[3–6] and the widespread distribution of putative archaeal ammonia monooxygenase (*amo*) genes in marine and terrestrial environments[1–4,6,8] changed the perspective on nitrification. The isolation of ammonia-oxidizing Archaea (AOA) strains affiliated with Crenarchaeota clades constituting up to 39% of microbial plankton in meso- and bathypelagic oceans suggested that AOA could potentially play an important part in nitrification[8,16–18]. However, AOA would need to compete with AOB, organotrophic bacterioplankton and perhaps even phytoplankton for ammonium[11,12,19]. To test this hypothesis, we determined the ammonia oxidation stoichiometry and kinetics in the only isolated AOA strain, '*Candidatus* Nitrosopumilus maritimus' strain SCM1. The results demonstrate that ammonia oxidation by AOA could indeed sustain significant growth rates and standing stocks of these Crenarchaeota, even in nutrient-depleted natural marine and terrestrial environments.

In ammonium-limited batch cultures, SCM1 grew exponentially with high rates and depleted ammonium below the detection limit of 10 nM (n = 4; Fig. 1). This ammonium concentration approaches values measured in oligotrophic open ocean water[11,16] and is more than 100-fold lower than the minimum concentration required for growth (>1 μM near neutral pH) of cultivated AOB[13,15]. SCM1 attained maximum growth rates (0.027 h^{-1}; doubling time = 26 h) and activities (51.9 μmol ammonium per mg protein per h) comparable to AOB strains (range 30–80 μmol ammonium per mg protein per h)[13] (Fig. 1, Supplementary Note 1). Thus, SCM1 seems particularly well adapted to growth at ammonium levels prevailing in nutrient-limited open oceans.

We observed that growth of SCM1 was significantly impaired by agitation, compared to static batch cultures, which precluded continuous culture experiments (Supplementary Note 1). To gain insight into the ammonia oxidation kinetics of SCM1, we therefore independently determined ammonium and oxygen uptake with ammonium-depleted (<10 nM) cells from batch cultures (Fig. 2). Ammonium-depleted, early-stationary phase cells consumed very low amounts of oxygen (0.51 μM O_2 h^{-1} = 0.67 μmol O_2 per mg protein per h, s.d. 0.29, n = 10). Oxygen uptake increased more than 50-fold to maximum rates of 27.51 μM O_2 h^{-1} (36.29 μmol O_2 per mg protein per h, s.d. 3.35, n = 10; ≈ 24.2 μmol ammonium per mg

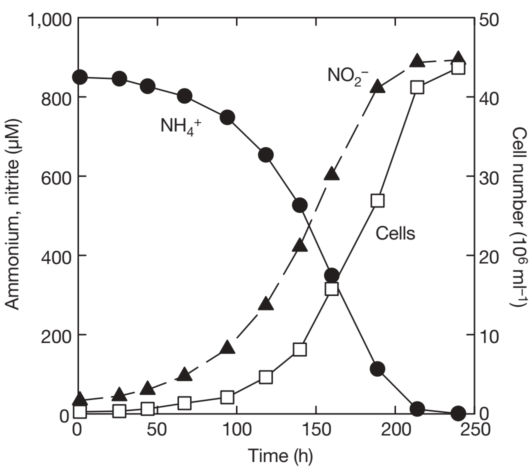

Figure 1 | Growth of SCM1 in ammonium-limited artificial sea water batch culture. Cultures entered stationary phase after ammonium was depleted below the detection limit of 10 nM.

[1]Department of Civil & Environmental Engineering, University of Washington, Seattle, Washington 98105, USA. †Present addresses: Department of Civil and Environmental Engineering, Massachusetts Institute of Technology, Cambridge, Massachusetts 02139, USA (P.M.B.); Department of Biology, San Francisco State University, San Francisco, California 94132, USA (J.R.T.).

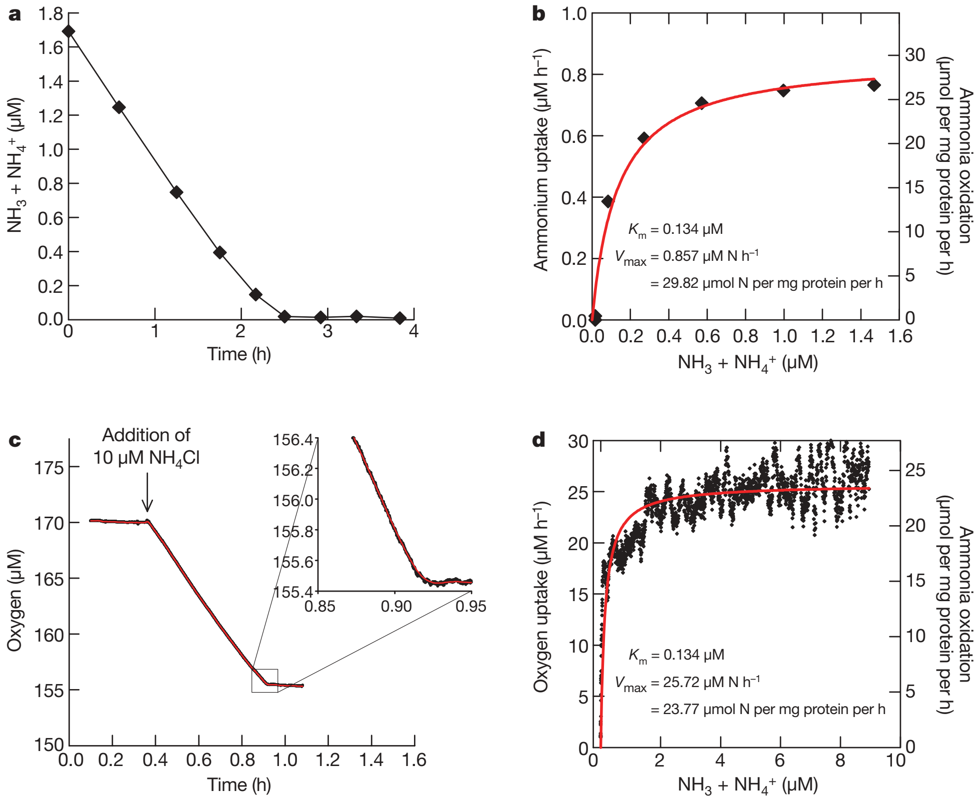

Figure 2 | Ammonia oxidation kinetics of SCM1. a, Ammonium uptake of early-stationary SCM1 cells on transfer to fresh medium containing 1.7 μM ammonium. **b**, Michaelis–Menten plot of ammonium uptake. **c**, Ammonium-dependent oxygen uptake of early-stationary phase SCM1 cells. Suspensions of cells were equilibrated for ~20 min before the experiment was started by the addition of 10 μM ammonium chloride. **d**, Michaelis–Menten plot of ammonium-dependent oxygen uptake. Uptake rates were calculated from smoothed data (red line in **c**). For calculation of kinetic parameters, a Michaelis–Menten equation was fitted to the data. See Methods for experimental details and calculations.

protein per h) within a few minutes of ammonium addition. Ammonium and oxygen were consumed with an AOB-like stoichiometry of 1:1.52 (s.d. 0.06, $n = 10$). Notably, late-exponential and early-stationary phase SCM1 cells both exhibited maximum rates of ammonium and oxygen uptake at as low as 2 μM ammonium (Fig. 2b, d and Supplementary Fig. 1b).

Ammonia oxidation by SCM1 followed Michaelis–Menten-type kinetics (Fig. 2b, d and Supplementary Fig. 1b). The mean apparent half-saturation constants (K_m) for ammonium uptake (0.132 μM $NH_3+NH_4^+$, range 0.005, $n = 2$, equivalent to ~3 nM NH_3) and oxygen uptake (0.133 μM $NH_3+NH_4^+$, s.d. 0.038, $n = 13$) were indistinguishable. Supplementation with as little as 0.2 μM ammonium chloride triggered more than 50% of maximum oxygen uptake. In contrast, identical experiments with *Nitrosomonas europaea* and *Nitrosococcus oceani* cells showed no stimulation of activity by 0.2 μM ammonium. Their K_m values, determined by the same methods used to characterize SCM1, were in a typical range previously reported (Supplementary Note 2). Identical K_m values and activities of SCM1 were observed in up to 5 cycles of substrate addition and depletion, up to 2 mM ammonium, and even with cells from late-exponential cultures which had not experienced ammonium concentrations below 250 μM for more than 50 generations of exponential growth (Supplementary Fig. 1b). More frequent ammonium additions, as well as high ammonium concentrations (≥2 mM), caused a decline of activity (data not shown, Supplementary Note 3). Together these data suggest that SCM1 has a constitutively low apparent half-saturation constant for ammonium.

Previous studies have indicated that *amo* gene copy numbers of AOA significantly outnumber those of AOB in oligotrophic ocean gyres and unfertilized natural soils, suggesting that substrate availability may account for the abundance patterns of AOA and AOB[7,8,16,20]. A comparison of the apparent K_m value for SCM1 to *in situ* measurements strongly supports this hypothesis (Fig. 3a). The K_m of SCM1 is by far the lowest half-saturation constant determined of any ammonia-oxidizing microorganism to date; it is very similar to *in situ* nitrification measurements made in oligotrophic, ammonium-depleted oceanic provinces[9,10] and is even lower than in natural unfertilized soils[21] (Fig. 3a). Assuming Michaelis–Menten-type saturation kinetics, an apparent K_m of ammonia oxidation of ~0.15 μM ammonium was estimated in the upper oxic Cariaco basin[9] (Fig. 3a), and it was found that in the primary nitrite maximum off the coast of California, ammonia oxidation was saturated at 0.1 μM ammonium[10]. Similarly, the K_m values for nitrification in uncultivated soil areas were significantly lower than the K_m of known AOB[21]. To account for these *in situ* nitrification measurements, organisms with *Nitrosopumilus*-like kinetics must vastly outnumber organisms typified by AOB. In contrast, a kinetic response consistent with the activity of known AOB becomes prevalent only in coastal environments and soils with higher nutrient levels[21,22] (Fig. 3a). Nonetheless, even in nutrient-poor marine environments, organic-matter-rich particles provide niches for nitrifiers with probably significantly different kinetic properties[23,24]—for example, members of the *Nitrosomonas eutropha* lineage[24]. However, significant ammonium is lost to the surrounding water during particle-associated mineralization[23], and these AOB lineages occur in very low numbers in oligotrophic open ocean gyres[7,23]. Although it remains unknown if as-yet uncultured AOB lineages (for example, members of the marine *Nitrosospira* cluster 1 (ref. 25) or novel, unidentified organisms) participate in oligotrophic nitrification, these data suggest that *Nitrosopumilus*-related AOA indeed are predominantly responsible for the observed nitrification in oligotrophic environments.

Using the specific affinity[26,27] (a^0) for ammonium as a basis for comparison, the kinetic characteristics of SCM1 further suggest that *Nitrosopumilus*-related AOA might successfully compete with other

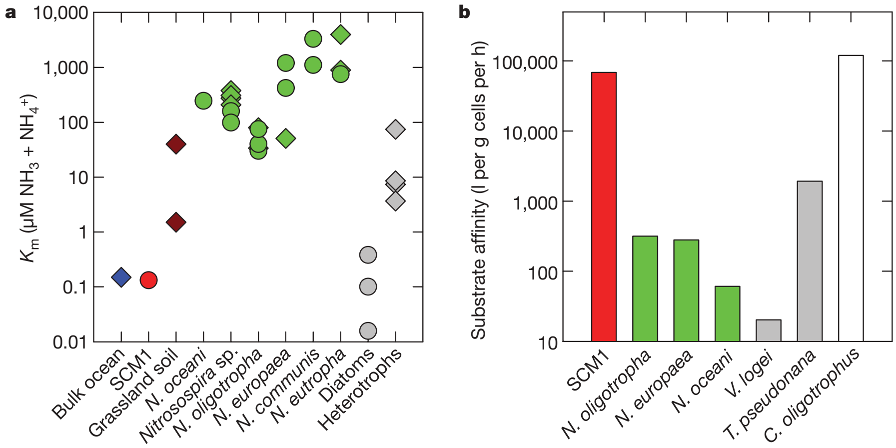

Figure 3 | High-affinity ammonia oxidation by AOA dominates in oligotrophic environments. **a**, Apparent K_m of SCM1 (red), the AOB strains *Nitrosococcus oceani*, *Nitrosospira* spp. cluster 0, 2 and 3, *Nitrosomonas oligotropha*, *Nitrosomonas europaea*, *Nitrosomonas communis*, *Nitrosomonas eutropha* (green), *in situ* nitrification in ocean water (blue) and soils (brown), as well as the lowest K_m for ammonium assimilation of diatoms and heterotrophic bacteria (grey). K_m values are given for activity measurements (circles) and growth (diamonds). **b**, Specific affinitiy (a^0) of SCM1 (red), bacterial ammonia oxidizers (green), as well as the highest values for ammonium-assimilating diatoms, and heterotrophic bacteria (grey). The highest reported specific affinity of an organotrophic organism (*Cycloclasticus oligotrophus*, open bar) for its carbon substrate is shown for comparison. See Methods for calculations and references.

marine phototrophs and chemotrophs for ammonium, the preferred inorganic nitrogen source for assimilation[28] (Fig. 3b) . The specific affinity of SCM1 (68,700 l per g wet weight per h) is among the highest affinities reported for microbial substrates (Fig. 3b). It exceeds that of AOB by more than 200-fold and is still 30-fold higher than of the oligotrophic diatom, *Thalassiosira pseudonana*[29]. Although limited data are available for the specific ammonium affinity of marine heterotrophs, it is unlikely that ammonium-assimilating organisms possess higher specific ammonium affinities than *Nitrosopumilus*. The highest specific affinity reported for an oligotrophic heterotroph for its carbon and energy source (120,000 l per g wet weight per h, *Cycloclasticus oligotrophus*)[26,27] is only twofold higher than the ammonium affinity of SCM1 (Fig. 3b). If ammonium served as the sole source of nitrogen (C:N ratio of 5:1, 50% of carbon substrate assimilated into biomass)[27] and the K_m for ammonium was comparable to the carbon source, the specific ammonium affinity of *C. oligotrophus*-like heterotrophs would still be >5 times lower (~12,000 l per g wet weight per h) than that of SCM1. The highest reported ammonium affinities of marine heterotrophs (for example, marine *Vibrio* strains) are in fact significantly lower (Fig. 3b). Hence, we predict that, in direct nutrient-limited competition, the ammonium turnover per unit biomass of *Nitrosopumilus*-like AOA would be at least 5 times higher than of oligotrophic heterotrophs, and more than 30 times higher than of the most oligotrophic diatoms known so far. These data suggest that *Nitrosopumilus*-like AOA not only out-compete AOB under limiting ammonium concentrations, but may well compete effectively with heterotrophs and phytoplankton, especially in deeper water layers.

A previously unrecognized competition for ammonium by AOA is entirely consistent with a recent synopsis of global oceanic nitrification rates which suggested that up to 50% of the nitrite and nitrate assimilated by phytoplankton is generated from ammonium by nitrification near the water surface, rather than transported from deeper water layers[11]. Our results strongly indicate that *Nitrosopumilus*-like AOA supply the oxidized nitrogen, offering an ecophysiological explanation for the conspicuously high nitrification rates in nutrient-poor oceanic regions[9,10,14,22] as well as the high nitrite/nitrate assimilation rates of heterotrophs and phototrophs[28]. Although the true maintenance energy demand of SCM1 cells remains to be determined, the low endogenous respiration rates of SCM1 (1.8% of maximum metabolic activity) may be suggestive of a small maintenance requirement. The growth threshold concentration of SCM1 could thus be as low as 10–20 nM ammonium, suggesting a strong competition by *Nitrosopumilus*-like AOA even in nutrient-poor meso- and bathypelagic waters.

Despite the isolation of strain SCM1 from the gravel of a marine aquarium and not directly from natural sea water, the kinetic and cellular characteristics of strain SCM1 presented here are unequivocal evidence for the existence of oligotrophic ammonia oxidizers among the Crenarchaeota and their ability to compete for ammonium as energy source in nutrient-deprived oligotrophic oceans. Notably, similar growth rates, cell yields or low residual ammonium concentrations have also been reported in the thermophilic enrichment cultures '*Candidatus* Nitrosocaldus yellowstonii' and '*Candidatus* Nitrososphaera gargensis'[4,6]. Moreover, it has been reported[6] that even CO_2 fixation in '*Candidatus* Nitrososphaera gargensis' was inhibited by ammonium concentrations similar to those that inhibited SCM1, supporting a widespread distribution of oligotrophic ammonia oxidation within the Crenarchaeota.

Substrate availability is unlikely to be the only factor determining the abundance and distribution of AOA and AOB and the ecological niches of these organisms[7,8,16,20]. For example, if AOA may indeed compete with phototrophs and thus be responsible for the detected nitrification rates in euphotic surface water[10,11], specialized ecotypes or AOA in general should be considerably more light tolerant than previously investigated AOB strains[13]. As recognized AOA now span considerable diversity within the Crenarchaeota[1,2,8], we also anticipate that significant physiological diversity will ultimately be revealed among its members. For example, analysis of the SCM1 genome sequence revealed several putative ABC-type transporter systems for organic carbon acquisition (C. B. Walker *et al*., unpublished results), consistent with previous findings of organic matter assimilation by marine Crenarchaeota *in situ*[18,30]. If the marine Crenarchaeota also harbour lineages of obligate organotrophs as suggested[16,18,30], these organisms seem to be competitive only in permanently nutrient-deprived deep ocean provinces with ammonium concentrations significantly below 10 nM. Although the genome sequence has revealed two Amt-type ammonium transporters (C. B. Walker *et al*., unpublished results) that could have unusually high affinity for ammonia, the mechanistic basis for the unprecedented capacity for ammonium acquisition and the biochemical pathway for its oxidation remain unknown. Nonetheless, this novel metabolism probably rendered mesophilic ammonia-oxidizing Crenarchaeota one of the dominant microbial clades in the ocean, with fundamental impact on the global biogeochemical cycles of nitrogen and carbon[1,4,8].

METHODS SUMMARY

All experiments with '*Candidatus* Nitrosopumilus maritimus' strain SCM1 were carried out in HEPES-buffered synthetic Crenarchaeota medium (SCM, 32‰ salinity, pH 7.5, 1 mM NH_4Cl). *Nitrosomonas europaea* strain ATCC 19718 was grown in basal mineral medium (pH 7.8, 0.0003% phenol red, 10 mM NH_4Cl). *Nitrosococcus oceani* strain ATCC 19707 was cultured in HEPES-buffered SCM medium (10 mM NH_4Cl). All strains were maintained at 30 °C in the dark. Nitrite and ammonium were determined spectrophotometrically and fluorometrically, respectively. Cells were counted by epi-fluorescence microscopy after SybrGreen I staining. Protein was quantified using the Nano Orange kit (Invitrogen). Oxygen uptake was monitored using Clark-type oxygen microsensors in 2-ml respiration chambers in a modified micro-respirometry system (Unisense AS) at 30 °C in a thermostatted water bath. Ammonium uptake activity was examined in static 5-l batches inoculated with early-stationary phase cells. Kinetic constants were obtained by fitting a Michaelis–Menten equation to oxygen and ammonium uptake rates using the equation:

$$V = (V_{\max} \times [S]) \times (K_m + [S])^{-1}$$

Here V is velocity, $V_{\max}$ is maximum velocity (μM h^{-1}), K_m is half-saturation constant for ammonium oxidation (μM), and $[S]$ is concentration of ammonium (μM). Specific affinities were calculated from kinetic constants of SCM1 and literature data of AOB, diatoms and heterotrophic bacteria using the equation:

$$a^0 = V_{\max} \times K_m{}^{-1}$$

Here a^0 is specific affinity (l per g wet cells per h), $V_{\max}$ is maximum velocity (g substrate per g wet cells per h) and K_m is half-saturation constant (in g substrate)[27].

Full Methods and any associated references are available in the online version of the paper at www.nature.com/nature.

Received 26 June; accepted 28 August 2009.
Published online 30 September 2009.

1. Schleper, C., Jurgens, G. & Jonuscheit, M. Genomic studies of uncultivated archaea. *Nature Rev. Microbiol.* **3**, 479–488 (2005).
2. Francis, C. A., Roberts, K. J., Beman, J. M., Santoro, A. E. & Oakley, B. B. Ubiquity and diversity of ammonia-oxidizing archaea in water columns and sediments of the ocean. *Proc. Natl Acad. Sci. USA* **102**, 14683–14688 (2005).
3. Könneke, M. *et al.* Isolation of an autotrophic ammonia-oxidizing marine archaeon. *Nature* **437**, 543–546 (2005).
4. de la Torre, J. R., Walker, C. B., Ingalls, A. E., Könneke, M. & Stahl, D. A. Cultivation of a thermophilic ammonia oxidizing archaeon synthesizing crenarchaeol. *Environ. Microbiol.* **10**, 810–818 (2008).
5. Wuchter, C. *et al.* Archaeal nitrification in the ocean. *Proc. Natl Acad. Sci. USA* **103**, 12317–12322 (2006).
6. Hatzenpichler, R. *et al.* A moderately thermophilic ammonia-oxidizing crenarchaeote from a hot spring. *Proc. Natl Acad. Sci. USA* **105**, 2134–2139 (2008).
7. Mincer, T. J. *et al.* Quantitative distribution of presumptive archaeal and bacterial nitrifiers in Monterey Bay and the North Pacific Subtropical Gyre. *Environ. Microbiol.* **9**, 1162–1175 (2007).
8. Prosser, J. I. & Nicol, G. W. Relative contributions of archaea and bacteria to aerobic ammonia oxidation in the environment. *Environ. Microbiol.* **10**, 2931–2941 (2008).
9. Hashimoto, L. K., Kaplan, W. A., Wofsy, S. C. & McElroy, M. B. Transformations of fixed nitrogen and N_2O in the Cariaco Trench. *Deep-Sea Res.* **30**, 575–590 (1983).
10. Olson, R. J. ^{15}N tracer studies of the primary nitrite maximum. *J. Mar. Res.* **39**, 203–226 (1981).
11. Yool, A., Martin, A. P., Fernandez, C. & Clark, D. R. The significance of nitrification for oceanic new production. *Nature* **447**, 999–1002 (2007).
12. Gruber, N. & Galloway, J. N. An Earth-system perspective of the global nitrogen cycle. *Nature* **451**, 293–296 (2008).
13. Prosser, J. I. in *Advances in Microbial Physiology* (eds Rose, A. H. & Tempest, D. W.) 125–181 (Academic, 1989).
14. Ward, B. B. in *Nitrification* (ed. Prosser, J. I.) 157–184 (IRL Press, 1986).
15. Bollmann, A., Bär-Gilissen, M.-J. & Laanbroek, H. J. Growth at low ammonium concentrations and starvation response as potential factors involved in niche differentiation among ammonia-oxidizing bacteria. *Appl. Environ. Microbiol.* **68**, 4751–4757 (2002).
16. Agogué, H., Brink, M., Dinasquet, J. & Herndl, G. J. Major gradients in putatively nitrifying and non-nitrifying Archaea in the deep North Atlantic. *Nature* **456**, 788–791 (2008).
17. Karner, M. B., DeLong, E. F. & Karl, D. M. Archaeal dominance in the mesopelagic zone of the Pacific Ocean. *Nature* **409**, 507–510 (2001).
18. Kirchman, D. L., Elifantz, H., Dittel, A. I., Malmstrom, R. R. & Cottrell, M. T. Standing stocks and activity of Archaea and Bacteria in the western Arctic Ocean. *Limnol. Oceanogr.* **52**, 495–507 (2007).
19. Laanbroek, H. J. & Woldendorp, J. W. in *Advances in Microbial Ecology* (ed. Jones, J. G.) 275–304 (Plenum, 1995).
20. Leininger, S. *et al.* Archaea predominate among ammonia-oxidizing prokaryotes in soils. *Nature* **442**, 806–809 (2006).
21. Stark, J. M. & Firestone, M. K. Kinetic characteristics of ammonium-oxidizer communities in a California oak woodland-annual grassland. *Soil Biol. Biochem.* **28**, 1307–1317 (1996).
22. Ward, B. B., Talbot, M. C. & Perry, M. J. Contributions of phytoplankton and nitrifying bacteria to ammonium and nitrite dynamics in coastal waters. *Cont. Shelf Res.* **3**, 383–398 (1984).
23. Karl, D. M., Knauer, G. A., Martin, J. H. & Ward, B. B. Bacterial chemolithotrophy in the ocean is associated with sinking particles. *Nature* **309**, 54–56 (1984).
24. Phillips, C. J., Smith, Z., Embley, T. M. & Prosser, J. I. Phylogenetic differences between particle-associated and planktonic ammonia-oxidizing bacteria of the β subdivision of the class Proteobacteria in the northwestern Mediterranean Sea. *Appl. Environ. Microbiol.* **65**, 779–786 (1999).
25. Freitag, T. E., Chang, L. & Prosser, J. I. Changes in the community structure and activity of betaproteobacterial ammonia-oxidizing sediment bacteria along a freshwater-marine gradient. *Environ. Microbiol.* **8**, 684–696 (2006).
26. Button, D. K., Robertson, B. R., Lepp, P. W. & Schmidt, T. M. A small, dilute-cytoplasm, high-affinity, novel bacterium isolated by extinction culture and having kinetic constants compatible with growth at ambient concentrations of dissolved nutrients in seawater. *Appl. Environ. Microbiol.* **64**, 4467–4476 (1998).
27. Button, D. K. Nutrient uptake by microorganisms according to kinetic parameters from theory as related to cytoarchitecture. *Microbiol. Mol. Biol. Rev.* **62**, 636–645 (1998).
28. Kirchman, D. L. The uptake of inorganic nutrients by heterotrophic bacteria. *Microb. Ecol.* **28**, 255–271 (1994).
29. Eppley, R. W., Rogers, J. N. & McCarthy, J. J. Half-saturation constants for uptake of nitrate and ammonium by marine phytoplankton. *Limnol. Oceanogr.* **14**, 912–920 (1969).
30. Ouverney, C. C. & Fuhrman, J. A. Marine planktonic archaea take up amino acids. *Appl. Environ. Microbiol.* **66**, 4829–4833 (2000).

Supplementary Information is linked to the online version of the paper at www.nature.com/nature.

Acknowledgements We thank A. M. Gee for technical assistance and C. B. Walker, K. C. Costa, S. Flagan, D. K. Button, M. G. Klotz, L. Bakken, S. Sandfest, M. Könneke, K. L. Hillesland and L. H. Larsen for discussions. This work was supported by NSF award MCB-0604448 to D.A.S. and J.R.T. and by NSF award OCE-0623174 to A. E. Ingalls, D.A.S. and A. H. Devol.

Author Contributions W.M.-H., J.R.T. and D.A.S. designed research; W.M.-H., P.M.B. and H.U. performed research; W.M.-H., J.R.T. and D.A.S. analysed the data; and W.M.-H. and D.A.S. wrote the paper.

Author Information Reprints and permissions information is available at www.nature.com/reprints. Correspondence and requests for materials should be addressed to W.M.-H. (willmmh@u.washington.edu) or D.A.S. (dastahl@u.washington.edu).

METHODS

Strain cultivation and maintenance. Cultures of '*Candidatus* Nitrosopumilus maritimus' strain SCM1 were maintained and all physiological experiments were carried out in synthetic Crenarchaeota medium (SCM) as described earlier[3] with the following modifications: all necessary glassware used for media preparation or cultivation was solely used for this purpose and carefully acid washed (1% HCl) and rinsed with MilliQ water (>18.2 MΩ resistance) before use. The basal artificial sea water was autoclaved, cooled to room temperature, and supplemented with the following sterile stock solutions (per litre): 10 ml HEPES (1 M HEPES, 0.6 M NaOH, pH 7.8), 2 ml sodium bicarbonate (1 M), 5 ml KH_2PO_4 (0.4 g l^{-1}), 1 ml FeNaEDTA (7.5 mM), 1 ml modified non-chelated trace element solution. The trace element solution contained (per litre) 8 ml conc. HCl (~12.5 M), 30 mg H_3BO_3, 100 mg $MnCl_2\cdot4H_2O$, 190 mg $CoCl_2\cdot6H_2O$, 24 mg $NiCl_2\cdot6H_2O$, 2 mg $CuCl_2\cdot2H_2O$, 144 mg $ZnSO_4\cdot7H_2O$, 36 mg $Na_2MoO_4\cdot2H_2O$. The medium was finally supplemented with 0.5 to 1 ml of NH_4Cl (1 M). The final pH of this medium at 30 °C was ~7.5. Strain SCM1 did not grow if directly transferred from solely bicarbonate-buffered medium[3] to HEPES-buffered medium. However, no difference in growth rates between both media was observed if the HEPES concentration was incrementally increased to 10 mM during exponential growth over three consecutive transfers. Cultures were subsequently maintained in HEPES-buffered SCM medium at 25 °C or 30 °C in the dark and transferred (0.1 to 1% inoculum size) to fresh medium when ~2/3 of the ammonium was oxidized. Shaking and stirring were avoided. Purity of the culture was monitored by phase contrast microscopy and by quantitative real-time PCR (qPCR) of bacterial 16S rRNA genes and *amoA* genes (see below). Contaminations were neither detected by quantitative PCR, nor by phase contrast microscopy of 10 µl samples of 200-fold concentrated suspensions of late exponential SCM1 cultures.

Nitrosomonas europaea strain ATCC 19718 was grown in liquid medium supplemented with phenol red as pH indicator (0.0003% final concentration) as described elsewhere[31]. *Nitrosococcus oceani* strain ATCC 19707 was grown in HEPES-buffered SCM medium as described above containing 10 mM NH_4Cl. Both strains were cultured at 30 °C on a rotary shaker (150 r.p.m.).

qPCR assays were carried out on a LightCycler System (Roche Applied Science) using the LightCycler FastStart DNA Master SYBR Green I kit (Roche) with the following reaction chemistry: 1 µl of LightCycler FastStart DNA master mix, 3.5 mM $MgCl_2$, 0.5 µM each primer and 0.01–1 ng of DNA template in a final volume of 10 µl. Bacterial 16S rRNA gene abundance was quantified using the GM3 and EUB338 primer set[3] with the following real-time PCR amplification protocol: initial denaturation at 95 °C for 5 min; followed by 55 cycles of 95 °C for 10 s, 55 °C for 10 s, and 72 °C for 20 s, and a melting curve analysis (60 °C to 95 °C) with a heating rate of 0.1 °C s^{-1}. Bacterial *amoA* genes were quantified using the same reaction chemistry with the bacterial *amoA* primer set[32] and the following PCR conditions: initial denaturation 95 °C for 5 min; 55 cycles of 95 °C for 7 s, 55 °C for 20 s and 72 °C for 20 s and a detection step at 78 °C for 7 s, followed by a melting curve analysis (65 °C to 95 °C) with a heating rate of 0.1 °C s^{-1}. The standard curves for both bacterial 16S rRNA genes and *amoA* genes were generated using *N. europaea* genomic DNA in a dilution series of 10^1–10^6 copies per reaction. Data were analysed with the second derivative maximum method using the Light Cycler Software (ver. 3.5.3).

Nutrient measurements, cell counts, and protein quantification. Nitrite was determined spectrophotometrically[33]. Ammonium was determined by fluorescence measurement after *o*-phthaldialdehyde derivatization in a Triology Laboratory fluorometer (Turner Designs) or a fluorescence microplate reader (Tecan Inc.)[34]. Detection limits were 5–10 nM, and 100 nM, respectively. Cell counts were performed on the day of sampling by epi-fluorescence microscopy after SybrGreen I staining as described elsewhere[35]. Protein content of mid- and late-exponential cultures was quantified using the Nano Orange kit (Invitrogen) according to manufacturer's instructions after cells were collected by centrifugation in Centricon YM-100 units (Amicon Inc.) and rinsed with MilliQ water to remove salt.

Activity measurements. Oxygen uptake was measured in a micro-respiration system (Unisense AS) equipped with 2-ml glass micro-respiration chambers, glass-coated stir bars, Clark-type OX-MR oxygen microsensors, PA 2000 picoammeter, and MicOx 2.6 data acquisition software. Oxygen microsensors were polarized continuously for >7 days before use. Oxygen uptake of the employed sensors was insignificant (below 1 nM d^{-1})[36] and 90% response time was <10 s (Supplementary Fig. 3a). To reduce electronic noise and interference from other laboratory and computer equipment, all electrical components were powered by a stabilized power source and the data transmission from AD-converter to PC computer was shielded using an USB port optical isolator (Black Box). All measurements were done in a re-circulated water bath at 30 °C ($\Delta T <$ 0.1 °C) and 100 r.p.m. stirring. Initial kinetic measurements with cells from late-exponential cultures of *N. europaea* and *N. oceani* collected by centrifugation or filtration as described previously[37,38] were performed to test the set-up (Supplementary Note 2, Supplementary Fig. 2). Cells of SCM1 lost more than 90% of activity through a similar centrifugation or filtration treatment. Activity measurements with late-exponential or early-stationary phase cells were therefore carried out as follows: ammonia oxidation and nitrite production of SCM1 cultures was monitored daily. Depletion of substrate was predictable within two to four hours. Aliquots of 20–30 ml were removed from cultures either within a few hours before (late-exponential) or up to 12 h after ammonium depletion (early-stationary phase) and immediately transferred to pre-warmed 40-ml glass vials in a 30 °C water bath. Sub-samples were then filled into 2-ml micro-respiration vessels with several volumes of overflow, carefully sealed with glass lids, and immediately immersed in the water bath. Oxygen uptake was monitored continuously after an initial equilibration of at least 10 min. Ammonium or nitrite was added as necessary from concentrated stock solutions in basal SCM salts by means of a Hamilton syringe.

Ammonium uptake activity was determined in static 5-l batches of fresh, pre-warmed SCM medium with given ammonium concentrations at 30 °C inoculated with early-stationary phase cells. Sub-samples (80 ml) were withdrawn and immediately assayed for residual ammonium concentration as described above.

Calculation of kinetic constants and specific affinities. Kinetic characteristics of SCM1 were estimated from multiple individual oxygen traces. High-frequency noise was removed using the 'Smooth 2D data' function implemented in Sigma Plot 8.0 (SPSS Inc.). Ammonium concentrations were calculated from oxygen uptake according to the ratio of ammonia oxidation to oxygen uptake of 1:1.5. Michaelis–Menten plots of oxygen uptake and ammonium uptake rates by SCM1 versus total ammonium concentration were then obtained by fitting a Michaelis–Menten kinetic to the data. Kinetic data of AOB, diatoms, organotrophic microorganisms, soil and ocean water were compiled from refs 9, 13, 21, 26, 27, 29 and 37–50. If only NH_4^+ or NH_3 concentrations were given by the authors, the corresponding values were calculated based on given salinity, temperature and pH and the respective stoichiometric dissociation constants of NH_3 and NH_4^+ given in ref. 51. For the estimation of specific affinities (a^0; ref. 27), we calculated growth rates, μ (h^{-1}), metabolic coefficients, q (g substrate per g wet cells per h), and cell yields, Y (g wet cells per g substrate), as described[26,27,40]. If necessary, the following conversion factors were used: 3 g wet weight per g dry weight, 5.7 g wet weight per g protein (ref. 27), and 0.55 g carbon per g dry weight (refs 52, 53).

31. Berube, P. M., Samudrala, R. & Stahl, D. A. Transcription of all *amoC* copies is associated with recovery of *Nitrosomonas europaea* from ammonia starvation. *J. Bacteriol.* **189**, 3935–3944 (2007).
32. Rotthauwe, J.-H., Witzel, K. P. & Liesack, W. The ammonia monooxygenase structural gene *amoA* as a functional marker: molecular fine-scale analysis of natural ammonia-oxidizing populations. *Appl. Environ. Microbiol.* **63**, 4704–4712 (1997).
33. Stickland, J. D. H. & Parsons, T. R. *A Practical Handbook of Seawater Analysis* (Fisheries Research Board of Canada, 1972).
34. Holmes, R. M., Aminot, A., Kérouel, R., Hooker, B. A. & Peterson, B. J. A simple and precise method for measuring ammonium in marine and freshwater ecosystems. *Can. J. Fish. Aquat. Sci.* **56**, 1801–1809 (1999).
35. Lunau, M., Lemke, A., Walther, K., Martens-Habbena, W. & Simon, M. An improved method for counting bacteria from sediments and turbid environments by epifluorescence microscopy. *Environ. Microbiol.* **7**, 961–968 (2005).
36. Gundersen, J. K., Ramsing, N. B. & Glud, R. N. Predicting the signal of O_2 microsensors from physical dimensions, temperature, salinity, and O_2 concentration. *Limnol. Oceanogr.* **43**, 1932–1937 (1998).
37. Suzuki, I., Dular, U. & Kwok, S. C. Ammonia or ammonium ion as substrate for oxidation by *Nitrosomonas europaea* cells and extracts. *J. Bacteriol.* **120**, 556–558 (1974).
38. Ward, B. B. Kinetic studies on ammonia and methane oxidation by *Nitrosococcus oceanus*. *Arch. Microbiol.* **147**, 126–133 (1987).
39. Bollmann, A., Schmidt, I., Saunders, A. M. & Nicolaisen, M. H. Influence of starvation on potential ammonia-oxidizing activity and *amoA* mRNA levels of *Nitrosospira briensis*. *Appl. Environ. Microbiol.* **71**, 1276–1282 (2005).
40. Button, D. K. Kinetics of nutrient-limited transport and microbial growth. *Microbiol. Rev.* **49**, 270–297 (1985).
41. Eppley, R. W. & Renger, E. H. Nitrogen assimilation of an oceanic diatom in nitrogen-limited continuous culture. *J. Phycol.* **10**, 15–23 (1974).
42. Glover, H. E. The relationship between inorganic nitrogen oxidation and organic-carbon production in batch and chemostat cultures of marine nitrifying bacteria. *Arch. Microbiol.* **142**, 45–50 (1985).
43. Jiang, Q. Q. & Bakken, L. R. Comparison of *Nitrosospira* strains isolated from terrestrial environments. *FEMS Microbiol. Ecol.* **30**, 171–186 (1999).
44. Keen, G. A. & Prosser, J. I. Steady state and transient growth of autotrophic nitrifying bacteria. *Arch. Microbiol.* **147**, 73–79 (1987).
45. Loureiro, S. *et al.* The significance of organic nutrients in the nutrition of *Pseudo-nitzschia delicatissima* (Bacillariophyceae). *J. Plankt. Res.* **31**, 399–410 (2009).

46. Reay, D. S., Nedwell, D. B., Priddle, J. & Ellis-Evans, J. C. Temperature dependence of inorganic nitrogen uptake: reduced affinity for nitrate at suboptimal temperatures in both algae and bacteria. *Appl. Environ. Microbiol.* 65, 2577–2584 (1999).
47. Stehr, G., Böttcher, B., Dittberner, P., Rath, G. & Koops, H. P. The ammonia-oxidizing nitrifying population of the River Elbe estuary. *FEMS Microbiol. Ecol.* 17, 177–186 (1995).
48. Suwa, Y., Imamura, Y., Suzuki, T., Tashiro, T. & Urushigawa, Y. Ammonia-oxidizing bacteria with different sensitivities to $(NH_4)_2SO_4$ in activated sludges. *Wat. Res.* 28, 1523–1532 (1994).
49. Ward, B. B. Kinetics of ammonia oxidation by a marine nitrifying bacterium: methane as a substrate analogue. *Microb. Ecol.* 19, 211–225 (1990).
50. Watson, S. W. Characteristics of a marine nitrifying bacterium, *Nitrosocystis oceanus* sp. N. *Limnol. Oceanogr.* 10, R274–R289 (1965).
51. Clegg, S. L. & Whitfield, M. A chemical model of seawater including dissolved ammonia and the stoichiometric dissociation constant of ammonia in estuarine water and seawater from −2 to 40°C. *Geochim. Cosmochim. Acta* 59, 2403–2421 (1995).
52. Lee, S. & Fuhrman, J. A. Relationships between biovolume and biomass of naturally derived marine bacterioplankton. *Appl. Environ. Microbiol.* 53, 1298–1303 (1987).
53. Simon, M. & Azam, F. Protein content and protein synthesis rates of planktonic marine bacteria. *Mar. Ecol. Prog. Ser.* 51, 201–213 (1989).

LETTERS

Cheater-resistance is not futile

Anupama Khare[1], Lorenzo A. Santorelli[1,2], Joan E. Strassmann[2], David C. Queller[2], Adam Kuspa[1,2,3] & Gad Shaulsky[1,2]

Cooperative social systems are susceptible to cheating by individuals that reap the benefits of cooperation without incurring the costs[1]. There are various theoretical mechanisms for the repression of cheating[2] and many have been tested experimentally. One possibility that has not been tested rigorously is the evolution of mutations that confer resistance to cheating. Here we show that the presence of a cheater in a population of randomly mutated social amoebae can select for cheater-resistance. Furthermore, we show that this cheater-resistance can be a noble strategy because the resister strain does not necessarily exploit other strains. Thus, the evolution of resisters may be instrumental in preserving cooperative behaviour in the face of cheating.

Dictyostelium cells propagate as unicellular amoebae in the soil. Upon starvation, they aggregate into multicellular structures and differentiate into viable spores and dead stalk cells[3]. Stalk-cell differentiation supports spore maturation and dispersal, but this altruistic behaviour can be exploited by cheaters that make more than their fair share of spores in chimaeric fruiting bodies[4]. The genetic potential for cheating is high[5] and cheaters abound in nature[4], but cheating behaviour can be restrained by various mechanisms, such as intrinsic lower fitness of the cheater[6], pleiotropy of the cheater gene[7], high genetic relatedness in natural populations[8], and kin discrimination[9,10].

Evolution of cheating-resistance is another mechanism that could restrict the spread of a specific cheater allele in the population and it could be manifested in several ways. One way is the evolution of other cheaters, but such a mechanism could lead to an arms-race of cheating strategies that would contribute to the rapid demise of cooperation. We therefore tested whether selection for cheating-resistance in *Dictyostelium* could yield mutants that resist cheating while remaining cooperative. Our strategy was to mix a population of mutated cells derived from the wild-type AX4 with a cheater strain, allow them to grow and develop into chimaeric fruiting bodies, and select spores. Under these conditions, the cheater would exploit most of the cells in the mutant population, thus increasing the proportion of any cheater-resistant mutants. We chose a strong cheater mutant, LAS5 (ref. 5) (which we renamed cheater C, *chtC*) as the selector. This mutant strain has a plasmid insertion in the *DDB_G0290959* gene, which is predicted to encode a protein with a signal peptide anchor and a transmembrane domain at the amino terminus. We generated a population of 1,000 strains in the wild-type background, each containing one insertional mutation that also conferred resistance to the antibiotic blasticidin S (BSR). We mixed *chtC* (which is sensitive to blasticidin S) with the mutant population at a ratio of 4:1 and allowed the cells to develop into chimaeric fruiting bodies. We germinated the spores and allowed the amoebae to grow in the presence of blasticidin S, thus eliminating the *chtC* cells. We then mixed the enriched mutant population with fresh *chtC* cells and developed them again, to maintain similar levels of selection in six such cycles of selection (Fig. 1a). We predicted that most of the mutant strains in the population would be cheated upon by *chtC*, eventually leading to their disappearance, and to the enrichment of any cheater-resistant strains that were present in the pool. We carried out this selection on several independent pools of mutants.

To test the population dynamics during the screen, we assessed population complexity of the mutant pool by Southern blot analysis of total genomic DNA, with a probe against the BSR marker. The initial population contained numerous strains, each giving a different banding pattern, which resulted in a smeared signal on the Southern blot (Fig. 1b). As the selection proceeded, the levels of various mutants fluctuated, as shown by the appearance and disappearance of bands on the blot. However, by the fourth cycle of selection, the population became enriched predominantly with a single mutant, suggesting that the presence of the cheater selected for a specific strain, which we predicted to be cheater-resistant. We isolated the enriched mutant and found an insertion in *DDB_G0271758*, a gene that has not been annotated in *Dictyostelium discoideum* and has no annotated homologues in other organisms. We then interrogated the above Southern blot with a probe against *DDB_G0271758* and found that the wild-type allele disappeared from the population, whereas the mutant allele became abundant as the selection progressed (Fig. 1c). We also used quantitative PCR (qPCR) to quantify the progressive enrichment of the mutant allele during the selective process and observed a 100-fold increase in the allele abundance by the sixth selection cycle (Fig. 1d).

To verify that the insertion in *DDB_G0271758* caused the observed phenotype, we regenerated the insertion in fresh wild-type cells, and named the resulting mutant and the mutated gene *rccA* (resister of *chtC* A). Both growth and development of the *rccA* mutant were indistinguishable from the wild-type AX4, suggesting that the *rccA* mutation did not confer obvious fitness costs. We then carried out direct cheating assays. We mixed either wild-type or *rccA* mutant cells at a 1:1 ratio with *chtC* and determined the proportion of spores formed by each strain. When mixed with *chtC* cells, the *rccA* mutant formed almost 50% of the spores. This proportion was significantly higher than the number of spores formed by AX4 in a mix with *chtC* cells (Fig. 2a), but not significantly lower than the hypothesized value of 50% (one-sample one-tailed *t*-test, $P = 0.28$). This observation supports the hypothesis that the *rccA* mutant can resist cheating by *chtC*. We also tested whether *rccA* was a specific resister of *chtC* or a resister of other cheaters as well, by performing similar mixes with LAS1, another facultative cheater that was isolated from the screen that yielded *chtC*[5]. We found that *rccA* did not resist cheating by LAS1 (Fig. 2a), indicating that *rccA* is unable to resist all cheaters. Therefore, it is likely that the ability to resist cheating will depend on the cheating mechanism of the specific cheater.

Cheating-resistance might be due to counter-cheating, such that the presence of a specific cheater would select for equivalent or even stronger cheaters. An alternative would be that cheater-resisters would be neutral, or noble, so they would not cheat on strains victimized by the original cheater. To distinguish between these

[1]Department of Molecular and Human Genetics, Baylor College of Medicine, One Baylor Plaza, Houston, Texas 77030, USA. [2]Department of Ecology and Evolutionary Biology, Rice University, Houston, Texas 77005, USA. [3]Department of Biochemistry and Molecular Biology, Baylor College of Medicine, One Baylor Plaza, Houston, Texas 77030, USA.

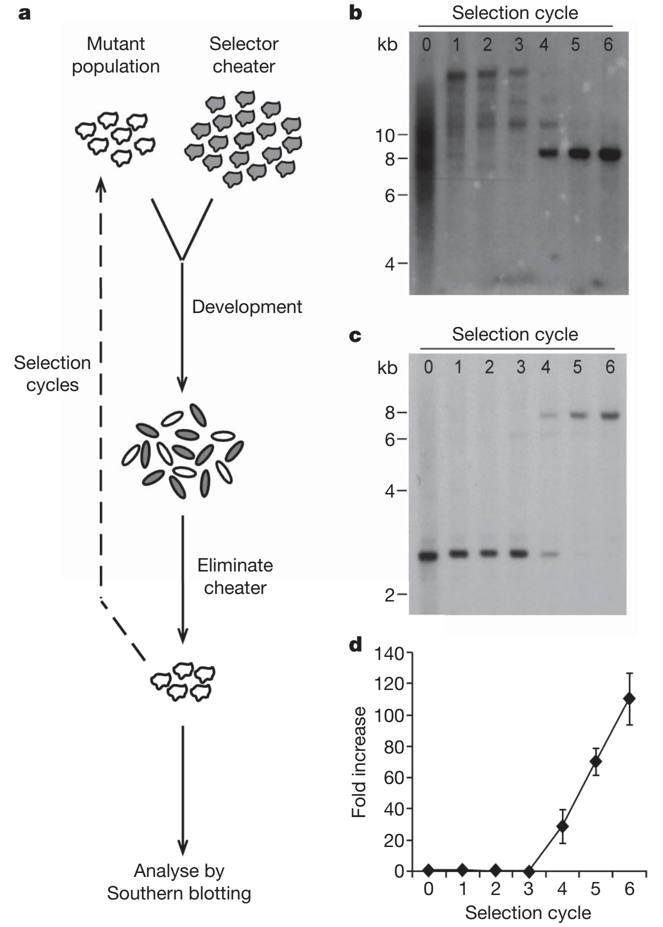

Figure 1 | The presence of a cheater selects for cheater-resistance. **a**, Selection: we mixed *chtC* with mutant populations, grew and developed the mixtures, collected spores and then eliminated *chtC*, for six selection cycles. **b**, Southern blot analysis of DNA from the population at each cycle, probed against the insertional plasmid. Decreased population complexity is reflected by progressively simpler banding patterns. kb, kilobases. **c**, The same Southern blot as in **b** interrogated with a probe against *rccA*. The lower band (wild-type allele) disappeared during the selection, whereas the higher band (insertion allele) became enriched. **d**, qPCR on DNA from each selection cycle to determine the levels of the *rccA* insertion allele. Results (means ± s.d. of three technical measurements) are depicted as the fold change relative to cycle 0.

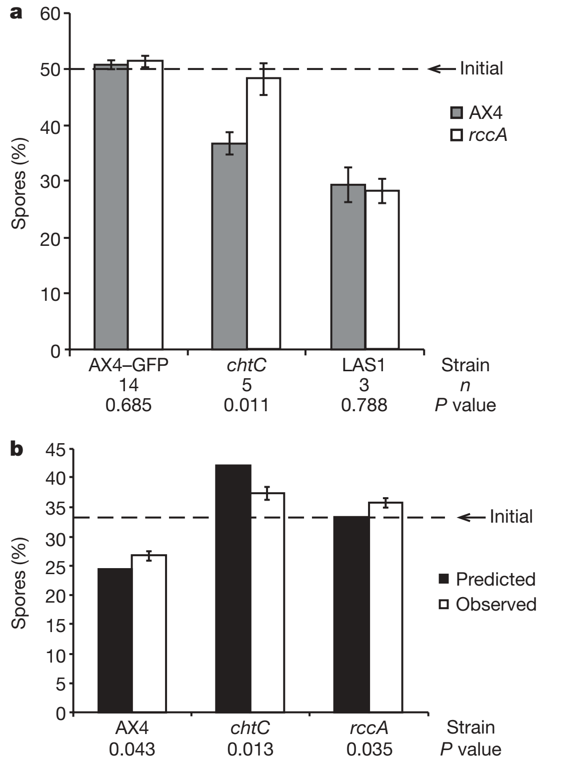

Figure 2 | *rccA* is a noble, specific cheater-resister. **a**, We determined the proportion of AX4 or *rccA* spores, when mixed individually with AX4–GFP, *chtC* or LAS1, as indicated. The results are means ± s.e.m. The number of independent replications (*n*) and the *P* values for a Student's *t*-test on arcsine square-root transformed data are shown. *rccA* was significantly different from AX4 only when mixed with *chtC*. **b**, We mixed AX4–GFP, *chtC* and *rccA* and determined the proportion of spores formed by each strain. The predictions are on the basis of the respective pairwise mixes. The observations are means ± s.e.m. of five independent experiments. All strains formed significantly different numbers of spores compared to the predictions. The *P* values for a one-sample two-sided *t*-test on arcsine square-root transformed data are shown.

possibilities, we developed either AX4 or *rccA* cells in 1:1 chimaerae with green fluorescent protein (GFP)-labelled AX4 (AX4–GFP) cells and tested the proportion of the green-fluorescent spores in the population. The results support the latter alternative—the *rccA* mutant formed a similar number of spores as the AX4 control in 1:1 chimaerae with AX4–GFP (Fig. 2a), indicating that *rccA* is not a cheater.

Although *rccA* resists cheating by *chtC* in a 1:1 mix, it is more likely to exist in mixtures that include both cheaters and victims. To test the behaviour of *rccA* under such conditions, we carried out a three-way mix between AX4–GFP, *chtC* and *rccA* at a 1:1:1 ratio, and determined the proportion of spores formed by each strain. The simplest prediction, on the basis of the respective pairwise mixes, was that *rccA* would remain unchanged in the population, whereas *chtC* would increase its proportion at the expense of the wild type. Surprisingly, we observed that both the wild type and *rccA* formed more spores than predicted (marginally significant) and *chtC* formed significantly fewer spores than predicted (Fig. 2b). This finding suggests that the presence of *rccA* may help to reduce the cheating of *chtC* on the wild type and might further contribute to restricting the spread of *chtC*.

Altogether, we carried out the selection for cheater-resistant strains (as described earlier and shown in Fig. 1a) separately on a total of seven different pools of mutants that were generated by independent mutagenesis experiments. In each of these pools, one or two mutants became enriched at different cycles during the selection (data not shown). From these pools, we obtained six mutants (other than *rccA*), which we named *rcc1–6*. All the mutants were resistant to *chtC* when mixed at a 1:1 ratio (Fig. 3), suggesting that selection for cheater-resistance is a common occurrence when a cheater is present in a population. Unlike *rccA*, one of the mutants (*rcc2*) significantly cheated on *chtC*, and two others (*rcc1* and *rcc4*) were close to significance. Notably, when we re-created these insertions in fresh wild-type cells, the new strains did not resist cheating by *chtC*. This finding indicates that the cheater-resistance of the original mutants was dependent on a genetic event other than the insertion, suggesting that spontaneous mutations that arose in the population contributed to cheating-resistance. These mutants retained their cheater-resistance phenotype in several experimental replications, suggesting that the underlying mutations were stable. We also tested the six original mutant strains against the wild-type AX4 and found that one was a cheater and five were noble (data not shown).

Cheater mutants can be either obligate, such that they cannot cooperate among themselves, or facultative, such that they cooperate among themselves, but cheat other strains. Experiments in the bacterium *Myxococcus xanthus* have shown that mutations that restore cooperation in an obligate cheater genotype can be selected for, and these mutations might also confer cheater-resistance against the

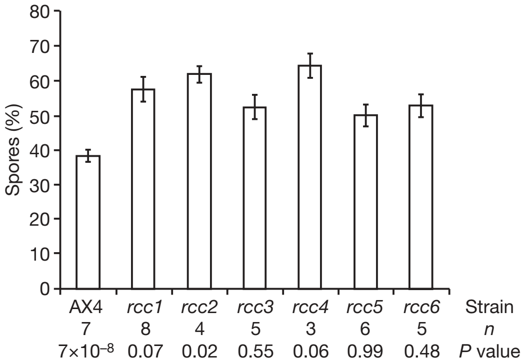

Figure 3 | Cheater-resistance is a general phenomenon. All of the independently derived mutants (*rcc1–rcc6*) formed more spores than AX4 when mixed at a 1:1 ratio with *chtC* (Student's *t*-test on arcsine square-root transformed data, $P < 0.005$). Results (percentage mutant spores recovered) are shown as means ± s.e.m. The *rcc2* strain made more spores than *chtC*, and the other strains were not significantly different from the hypothesized value of 50%. The number of independent replications (n) and the P values for a one-sample two-sided t-test on arcsine square-root transformed data are shown.

parental cheater strain[11]. Our experiments demonstrate that the introduction of a facultative cheater into a population can directly select for cheater-resistance behaviour in other strains. Thus, cheater-resistance may be an important mechanism of cheater control and might provoke molecular arms-races, similar to those seen in host–pathogen interactions[12]. More importantly, the resistant strains can be noble strains that do not cheat, suggesting that such selection could yield strategies that allow cheater-resistance while preserving cooperation.

Cheater resistance in animals takes forms such as policing[13], punishment[14] and partner choice[15], which are hard to study at the level of individual genes, but it has been largely neglected in microbial systems, where cheating is easily studied at the genetic level[16–18]. This could be because cheating in many microbial social systems takes a passive form of declining to produce and secrete public goods, and it is difficult to resist such cheating without converting the cheaters back to being producers. The active cheating in social amoebae is more similar to animal sociality, and is therefore a good model system for exploring the complex evolutionary dynamics of genes affecting cooperation, cheating, and cheater-resistance.

METHODS SUMMARY

Strains, cell growth and transformation. We generated all of the mutations in the laboratory wild-type AX4 strain[19]. AX4–GFP[7] was used for mixes. The *chtC* mutant has the same insertion site as LAS5 (ref. 5), with the pLPBLP plasmid[20] replacing pBSR1, and the BSR cassette removed by transformation with the pDEX-NLS-Cre plasmid[20]. We grew cells and carried out plasmid transformation essentially as described[10].

Mutagenesis, selection and identification of the mutated gene. We performed restriction enzyme-mediated integration (REMI) mutagenesis, and pooled 1,000 mutants[21]. We mixed spores from the pool and from *chtC* at a ratio of 1:4, grew and developed the mixture, collected genomic DNA and selected spores[5]. We then germinated the spores, and eliminated *chtC*. The selection cycle was repeated with the mutant pool and a fresh culture of *chtC*. This was done individually on seven independent pools of mutants. We carried out plasmid rescue as described[22].

Nucleic acid analysis. We prepared genomic DNA as described[23] and performed Southern blot analysis by standard methods[24]. We used linearized pBSR1 (ref. 21) as a probe for the BSR cassette, and a PCR fragment for the *rccA* gene[25]. We performed quantitative PCR as described[26] using primers for the *rccA* mutant allele and the unrelated *DDB_G0276785* gene for normalization.

Mixing experiments. We grew cells separately and developed mixtures, essentially as described[10]. We collected spores and counted them as described for the GFP-labelled strains[10]. For the mix between LAS1 and *rccA*, we plated out the spores, transferred cells from individual plaques into HL5 liquid medium in 96-well plates, prepared genomic DNA, and tested for the mutant LAS1 and *rccA* alleles by PCR. For the other mixes, we grew cells in HL5 containing blasticidin S in 96-well plates as described earlier, and scored for drug-resistance. In the three-way mix experiment, we scored AX4–GFP on the basis of fluorescence, and *rccA* on the basis of drug-resistance.

Full Methods and any associated references are available in the online version of the paper at www.nature.com/nature.

Received 7 August; accepted 3 September 2009.
Published online 30 September 2009.

1. Maynard Smith, J. & Szathmáry, E. *The Major Transitions in Evolution* (Oxford Univ. Press, 1997).
2. Travisano, M. & Velicer, G. J. Strategies of microbial cheater control. *Trends Microbiol.* **12**, 72–78 (2004).
3. Kessin, R. H. *Dictyostelium: Evolution, Cell Biology, and the Development of Multicellularity* (Cambridge Univ. Press, 2001).
4. Strassmann, J. E., Zhu, Y. & Queller, D. C. Altruism and social cheating in the social amoeba *Dictyostelium discoideum*. *Nature* **408**, 965–967 (2000).
5. Santorelli, L. A. *et al.* Facultative cheater mutants reveal the genetic complexity of cooperation in social amoebae. *Nature* **451**, 1107–1110 (2008).
6. Ennis, H. L., Dao, D. N., Pukatzki, S. U. & Kessin, R. H. *Dictyostelium* amoebae lacking an F-box protein form spores rather than stalk in chimeras with wild type. *Proc. Natl Acad. Sci. USA* **97**, 3292–3297 (2000).
7. Foster, K. R., Shaulsky, G., Strassmann, J. E., Queller, D. C. & Thompson, C. R. L. Pleiotropy as a mechanism to stabilize cooperation. *Nature* **431**, 693–696 (2004).
8. Gilbert, O. M., Foster, K. R., Mehdiabadi, N. J., Strassmann, J. E. & Queller, D. C. High relatedness maintains multicellular cooperation in a social amoeba by controlling cheater mutants. *Proc. Natl Acad. Sci. USA* **104**, 8913–8917 (2007).
9. Mehdiabadi, N. J. *et al.* Social evolution: kin preference in a social microbe. *Nature* **442**, 881–882 (2006).
10. Ostrowski, E. A., Katoh, M., Shaulsky, G., Queller, D. C. & Strassmann, J. E. Kin discrimination increases with genetic distance in a social amoeba. *PLoS Biol.* **6**, e287 (2008).
11. Fiegna, F., Yu, Y. T. N., Kadam, S. V. & Velicer, G. J. Evolution of an obligate social cheater to a superior cooperator. *Nature* **441**, 310–314 (2006).
12. Marques, J. T. & Carthew, R. W. A call to arms: coevolution of animal viruses and host innate immune responses. *Trends Genet.* **23**, 359–364 (2007).
13. Ratnieks, F. L. W., Foster, K. R. & Wenseleers, T. Conflict resolution in insect societies. *Annu. Rev. Entomol.* **51**, 581–608 (2006).
14. Clutton-Brock, T. H. & Parker, G. A. Punishment in animal societies. *Nature* **373**, 209–216 (1995).
15. Sachs, J. L., Mueller, U. G., Wilcox, T. P. & Bull, J. J. The evolution of cooperation. *Q. Rev. Biol.* **79**, 135–160 (2004).
16. Vulic, M. & Kolter, R. Evolutionary cheating in *Escherichia coli* stationary phase cultures. *Genetics* **158**, 519–526 (2001).
17. Greig, D. & Travisano, M. The Prisoner's Dilemma and polymorphism in yeast *SUC* genes. *Proc. R. Soc. Lond. B* **271**, 25–26 (2004).
18. Griffin, A. S., West, S. A. & Buckling, A. Cooperation and competition in pathogenic bacteria. *Nature* **430**, 1024–1027 (2004).
19. Knecht, D. A., Cohen, S. M., Loomis, W. F. & Lodish, H. F. Developmental regulation of *Dictyostelium discoideum* actin gene fusions carried on low-copy and high-copy transformation vectors. *Mol. Cell. Biol.* **6**, 3973–3983 (1986).
20. Faix, J., Kreppel, L., Shaulsky, G., Schleicher, M. & Kimmel, A. R. A rapid and efficient method to generate multiple gene disruptions in *Dictyostelium discoideum* using a single selectable marker and the Cre-*loxP* system. *Nucleic Acids Res.* **32**, e143 (2004).
21. Shaulsky, G., Escalante, R. & Loomis, W. F. Developmental signal transduction pathways uncovered by genetic suppressors. *Proc. Natl Acad. Sci. USA* **93**, 15260–15265 (1996).
22. Kuspa, A. & Loomis, W. F. Tagging developmental genes in *Dictyostelium* by restriction enzyme-mediated integration of plasmid DNA. *Proc. Natl Acad. Sci. USA* **89**, 8803–8807 (1992).
23. Katoh, M. *et al.* Developmentally regulated DNA methylation in *Dictyostelium discoideum*. *Eukaryot. Cell* **5**, 18–25 (2006).
24. Vollrath, D., Davis, R. W., Connelly, C. & Hieter, P. Physical mapping of large DNA by chromosome fragmentation. *Proc. Natl Acad. Sci. USA* **85**, 6027–6031 (1988).
25. Feinberg, A. P. & Vogelstein, B. A technique for radiolabeling DNA restriction endonuclease fragments to high specific activity. *Anal. Biochem.* **132**, 6–13 (1983).
26. Huang, E. *et al.* bZIP transcription factor interactions regulate DIF responses in *Dictyostelium*. *Development* **133**, 449–458 (2006).

Acknowledgements This work was supported by a grant from the National Science Foundation. A. Khare was supported by a pre-doctoral fellowship from the Cullen Foundation.

Author Contributions A. Khare conducted the experimental work and wrote the paper, L.A.S. isolated the original LAS5 and LAS1 cheater strains. All of the authors conceived the study, discussed the results and commented on the manuscript.

Author Information Reprints and permissions information is available at www.nature.com/reprints. Correspondence and requests for materials should be addressed to G.S. (gadi@bcm.edu).

METHODS

Strains. We generated all of the mutations in the laboratory wild-type AX4 strain[19]. The AX4–GFP strain[7] was used for mixing experiments. The *chtC* mutant has the same insertion site as LAS5 (ref. 5). We cloned the region of homology from the original rescue plasmid pLAS5, and inserted it into the ClaI restriction endonuclease site of pLPBLP[20]. We used the resulting vector to re-create the insertion in AX4 by homologous recombination. We then generated the *chtC* mutant by transforming the cells with the pDEX-NLS-Cre plasmid[20] to remove the BSR cassette.

Cell growth and transformation. We grew cells in shaking suspension in HL5 liquid broth with the necessary supplements, or on SM-agar plates in association with *Klebsiella aerogenes*[10]. Plasmid transformation was carried out as described[10], with the following modifications: cells were resuspended at a final density of 3×10^7 cells ml^{-1} before transformation, electroporated twice, and the transformants were recovered in HL5 with 10% FBS for 24 h before the addition of either blasticidin S (10 μg ml^{-1}) or G418 (5 μg ml^{-1}).

Mutagenesis, selection and identification of the mutated gene. We performed REMI mutagenesis, pooled 1,000 mutants, and plated the pool on SM-agar plates as described[21]. We grew the *chtC* mutant on SM-agar plates in association with bacteria. We collected spores from the pool and from *chtC* as described[21], mixed them at a ratio of 1:4, and plated a total of 2×10^6 spores on each of two SM-agar plates in association with bacteria. We collected cells to prepare genomic DNA from one of the plates after 44–48 h. We selected spores from the second plate after 4 days, germinated them, and grew the amoebae in submerged cultures in HL5 with 10 μg ml^{-1} blasticidin S to eliminate *chtC*. The mutant pool, and a fresh culture of *chtC* were then grown separately in suspension culture, mixed and plated on SM plates as above to repeat the selection cycle. This was done individually on seven pools of mutants generated by independent REMI mutagenesis experiments. We carried out plasmid rescue using ClaI to obtain the plasmid pRccA and identified the insertion site by sequencing the flanking regions[22]. The gene names in the manuscript (*DDB_G0290959* and *DDB_G0271758*) refer to the accession numbers in dictyBase (http://dictybase.org).

Nucleic acid analysis. We prepared genomic DNA as described[23] and performed Southern blot analysis by standard methods[24]. The blots were hybridized with radioactive DNA probes made by random-primer labelling[25]. We used linearized pBSR1 (ref. 21) as a probe for the BSR cassette, and a PCR fragment as a probe for the *rccA* gene (primers: 5′-TCGTTGTCATCTTGGTTTG-3′ and 5′-GATTT CAGTTTACCCACCG-3′). We performed qPCR as described[26] using primers for the *rccA* mutant allele: 5′-TGCTGAAAATGTATTACCACC-3′ and 5′-ATTTAGGTGACACTATAG-3′ and primers for the unrelated *DDB_G0276785* gene to normalize for the amount of genomic DNA: 5′-TGATTGCCAA TGGATCATC-3′ and 5′-ATAGTTTACTTCTACCAACATTAGG-3′.

Mixing experiments. For mixing experiments, we grew the cells separately and mixed them before development on nitrocellulose filters. We developed cells as described[10] with the following modifications: cells were washed with KK2 buffer (16.3 mM KH_2PO_4, 3.7 mM K_2HPO_4, pH 6.2), resuspended at a density of 1×10^8 cells ml^{-1}, and 5×10^7 cells were deposited per filter. We collected all the spores (after 36–48 h), and in the case of GFP-labelled strains, we counted them as described[10]. For all of the other mixes (except that between LAS1 and *rccA*), we plated out the spores clonally on SM-agar plates in association with *K. aerogenes*, transferred cells from individual plaques into HL5 containing 10 μg ml^{-1} blasticidin S in 96-well plates, and scored for drug-resistance. For each mix, we counted spores from either one or two 96-well plates (96–192 spores). In the three-way mix experiment, we scored AX4–GFP spores based on fluorescence, and *rccA* spores based on blasticidin S resistance. For the mix between LAS1 and *rccA*, we grew cells in 96-well plates as above. We prepared genomic DNA from the cells in these wells by washing the cells once with water, lysing them by incubation in lysis buffer (67.7 mM Tris-HCl, pH 8.9, 16.6 mM $(NH_4)_2SO_4$, 2 mM $MgCl_2$, 10 mM dithiothreitol (DTT), 0.5% glycerol, 0.5% Tween 20, 0.5% NP40, 50 μg ml^{-1} proteinase K) at 56 °C for 45 min, and then inactivating the proteinase K by incubating at 95 °C for 10 min. We tested for the presence of both the mutant LAS1 allele and the mutant *rccA* allele by PCR (LAS1 primers: 5′-TAATACGACTCACTATAGGG-3′ and 5′-GTAGAAATTG TAACATTACAGG-3′, and *rccA* primers: 5′-ATTTAGGTGACACTATAG-3′ and 5′-CACTAATAACTGAAAATCAACTACC-3′).

Vol 461 | 15 October 2009 | doi:10.1038/nature08461

An anatomical signature for literacy

Manuel Carreiras[1,2,3,4], Mohamed L. Seghier[5], Silvia Baquero[6], Adelina Estévez[4], Alfonso Lozano[6], Joseph T. Devlin[7] & Cathy J. Price[5]

Language is a uniquely human ability that evolved at some point in the roughly 6,000,000 years since human and chimpanzee lines diverged[1,2]. Even in the most linguistically impoverished environments, children naturally develop sophisticated language systems[3]. In contrast, reading is a learnt skill that does not develop without intensive tuition and practice. Learning to read is likely to involve ontogenic structural brain changes[4–6], but these are nearly impossible to isolate in children owing to concurrent biological, environmental and social maturational changes. In Colombia, guerrillas are re-integrating into mainstream society and learning to read for the first time as adults. This presents a unique opportunity to investigate how literacy changes the brain, without the maturational complications present in children. Here we compare structural brain scans from those who learnt to read as adults (late-literates) with those from a carefully matched set of illiterates. Late-literates had more white matter in the splenium of the corpus callosum and more grey matter in bilateral angular, dorsal occipital, middle temporal, left supramarginal and superior temporal gyri. The importance of these brain regions for skilled reading was investigated in early literates, who learnt to read as children. We found anatomical connections linking the left and right angular and dorsal occipital gyri through the area of the corpus callosum where white matter was higher in late-literates than in illiterates; that reading, relative to object naming, increased the interhemispheric functional connectivity between the left and right angular gyri; and that activation in the left angular gyrus exerts top-down modulation on information flow from the left dorsal occipital gyrus to the left supramarginal gyrus. These findings demonstrate how the regions identified in late-literates interact during reading, relative to object naming, in early literates.

After decades spent fighting, members of the guerrilla forces have begun re-integrating into mainstream Colombian society, introducing a sizeable population of illiterate adults who have no formal education. Upon putting down their weapons and returning to society, some had the opportunity to learn to read for the first time in their early twenties, providing the perfect natural situation for experiments investigating structural brain differences associated with the acquisition of literacy in the absence of other types of schooling or maturational development. To this end, we obtained high-resolution T_1-weighted magnetic resonance imaging (MRI) scans from 42 right-handed healthy adults: 20 late-literates who had completed a literacy program in adulthood in their native tongue (Spanish) and 22 age- and culturally matched illiterates who had not yet started that literacy program. Thus, unlike in studies of developmental dyslexia, there were no known between-group differences in reading potential. Moreover, our analyses factored out variability in more general cognitive skills.

The results of a voxel-based morphometry (VBM) comparison (experiment one; Fig. 1) showed that late-literates had more grey matter than illiterates in five posterior brain regions that form a subset of those activated in functional imaging studies of reading[7,8]. Specifically, grey-matter density increases were identified in bilateral dorsal occipital areas associated with higher-level visual processing, in left supramarginal and superior temporal areas associated with phonological processing and in the angular gyri and posterior middle temporal regions associated with semantic processing. In addition, and as observed previously[5,6], the ability to read was associated with a greater amount of white matter in the splenium of the corpus callosum (SCC), which is frequently damaged in pure alexic patients who are unable to read despite good language function[9]. These structural differences in known reading areas were observed even in subgroups of participants who were closely matched on a range of different cognitive abilities (Fig. 1). They are therefore likely to be consequences of learning to read, consistent with longitudinal studies that have shown regional changes in brain structure with the acquisition of new skills in adults[4] as well as in children[10].

Although the identified areas are all within the known reading network[7,8], neither the voxel-based structural analysis nor previous results indicate how the areas are anatomically or functionally connected to one another. The aim of our second experiment was to integrate the grey- and white-matter results from experiment one using tractography analyses with diffusion tensor imaging (DTI). Specifically, we looked for an interhemispheric white-matter track that linked left- and right-hemisphere homologues (that is, angular gyri and/or dorsal occipital areas) through the region of the SCC area where white-matter amount differed according to literacy. In ten adults who learnt to read English in childhood, we found strong interhemispheric paths linking the left angular and dorsal occipital gyri with the right angular and dorsal occipital gyri through the precise region of the SCC identified in the first experiment (Fig. 2). Long range connections through the SCC are laid down *in utero* and will therefore be present irrespective of literacy experience. On the basis of experiment two, we suggest that learning to read in adulthood alters the properties of the interhemispheric links between the left and right angular and dorsal occipital gyri. This perspective integrates the grey- and white-matter findings from experiment one into the same anatomical system; however, we can not rule out the possibility that the white-matter differences in late-literates relative to illiterates pertain to other tracts through the same area of the corpus callosum (for example, those connecting the temporal lobes).

To investigate the functional connectivity within the identified anatomical system, our third experiment used functional magnetic resonance imaging (fMRI) and dynamic causal modelling (DCM) in 20 adults who learnt to read English in childhood. Reading activity was compared with object-naming activity in the regions showing structural differences between late-literates and illiterates in experiment one. We chose object naming as the baseline to control for

[1]Basque Center on Cognition Brain and Language, Donostia-San Sebastián 20009, Spain. [2]IKERBASQUE, Basque Foundation for Science, Bilbao 48011, Spain. [3]Departamento de Filología Vasca, Universidad del País Vasco, Bilbao 48940, Spain. [4]Universidad de La Laguna, Tenerife 38055, Spain. [5]Wellcome Trust Centre for Neuroimaging, Institute of Neurology, University College London, London WC1N 3BG, UK. [6]Universidad Nacional de Colombia, Bogotá 3165000, Colombia. [7]Cognitive, Perceptual and Brain Sciences, University College London, London WC1E 6BT, UK.

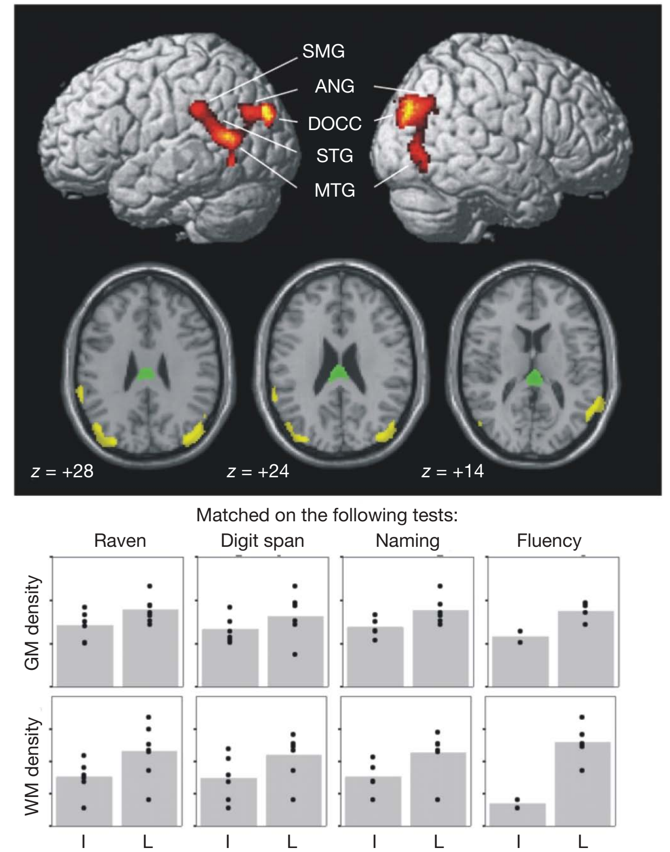

Figure 1 | The effect of literacy on brain structure. Upper images show the locations of grey-matter increases in 20 literates relative to 22 illiterates, with a height threshold of $P < 0.001$ and an extent threshold of $P < 0.05$, corrected for multiple comparisons across the whole brain. Data were processed using VBM procedures in the brain-imaging software SPM5 with covariates of no interest that factored out the effects of age, gender, global intensity and neuropsychological performance. The images below these are axial slices (left side of image corresponds to left hemisphere) showing grey-matter (yellow) and white-matter (green) differences with literacy. Peak *x*, *y* and *z* coordinates in MNI (Montreal Neurological Institute) space were (−47, −74, +28) and (+50, −72, +32) in the left and right angular gyri (ANG), respectively; (−34, −86, +26) and (+34, −86, +26) in the left and right dorsal occipital gyri (DOCC), respectively; (−54, −62, +10) and (+60, −72, −4) in the left and right middle temporal gyri (MTG), respectively; (−64, −38, +30) and (−62, −46, +22) in the left supramarginal gyrus (SMG) and the posterior superior temporal gyri (STG), respectively; and (0, −26, +16) and (−6, −36, +6) in the left- and right-hemispherical corpus callosum, respectively. No differences in left ventral occipito-temporal grey matter were identified even when the statistical threshold was reduced to $P < 0.05$ uncorrected. Bottom rows: Grey-matter (GM) and white-matter (WM) (density in arbitrary units) extracted from and summed over all the identified voxels in the VBM analysis for subgroups of illiterates (I) and literates (L) who were matched for scores on four tests of intellectual ability. Each dot represents the value for an individual subject, and the height of the bar indicates the average of these values. See Supplementary Table 1 for full details.

processes involved in the recognition of complex visual stimuli, name retrieval and speech production[11]. Although our DCM analyses only included the areas that in experiment one were associated with learning to read in adulthood, the influence of all other reading areas is implicitly assumed (Supplementary Information).

Our first functional connectivity analysis showed that reading, relative to object naming, increased interhemispheric functional connectivity between the left and right angular gyri but not between the left and right dorsal occipital regions (Fig. 3a). Therefore, the results of all three experiments associate interhemispheric connections with the left and right angular gyri. Moreover, the results of experiments one and three highlight the importance of these connections for

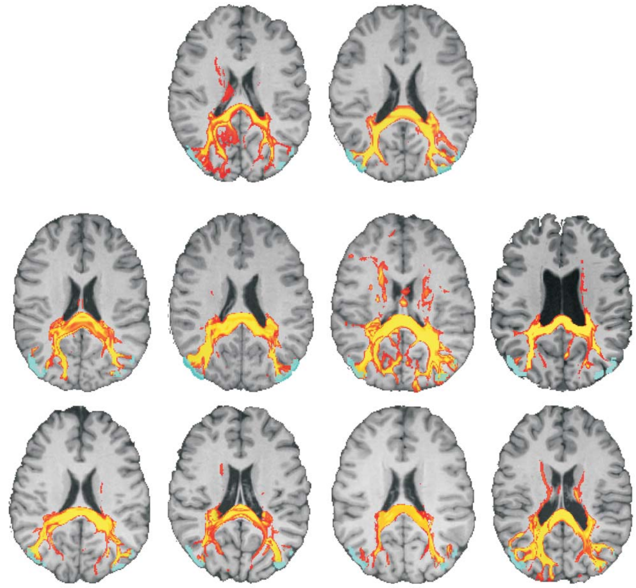

Figure 2 | Anatomical connectivity results. Diffusion-weighted magnetic resonance images from ten early-literates were acquired with a *b* value of 1,000 s mm^{-2} uniformly distributed across 60 gradient directions. Paths through the corpus callosum region of interest were identified using a Markov-chain Monte Carlo technique with 25,000 samples in each voxel in the left and right angular and dorsal occipital gyri that was structurally different (at $P < 0.001$) in the late-literates and illiterates (shown in blue). The resulting images (yellow/red) represent empirically determined probability distributions linking the left and right hemisphere regions of interest in each subject.

reading. This correspondence across experiments was observed despite the use of different methods (VBM, DTI and DCM) in different populations varying in age of reading acquisition, language spoken and reading ability.

Experiment three also allowed us to investigate how activity for reading, relative to object naming, is propagated through the left-hemisphere anatomical system identified in experiment one. The results (Fig. 3b) suggest that reading increased the functional coupling from visual (DOCC) to phonological (SMG) processing areas either directly or by means of semantics (in MTG). This is consistent with reading increasing the demands on the retrieval and assembly of speech sounds[11–16]. In addition, the angular gyrus had a top-down modulatory effect on dorsal occipital activity. This may reflect top-down constraints on the discrimination of visually similar words with different meanings (for example, chain and chair).

Our findings can now be used to revisit structural and functional imaging studies of acquired and developmental dyslexia. In particular, an understanding of the anatomical mechanisms that support the process of learning to read can be used to determine whether neuronal abnormalities are a cause or a consequence of the inability to read. For example, many studies have shown that developmental dyslexics have reduced left temporoparietal grey matter[17–20] and reduced SCC white matter[21–23]. The effect of literacy in the present study suggests that this might be the consequence of reading experience rather than the cause of reading difficulties.

Finally, we consider why experiment one did not reveal structural brain differences for literates relative to illiterates in the left ventral occipito-temporal region, where damage can result in pure alexia[10]. Previous functional imaging studies of children have shown that in the early stages of learning to read English, dorsal parietal activation predominates, after which skilled reading utilizes more ventral occipito-temporal areas[24,25] that also support object naming[11]. We therefore predict that the dorsal system may be more important than the ventral system in early stages of reading—when reading is less proficient and not yet automatic—and in transparent orthographies (like Spanish)

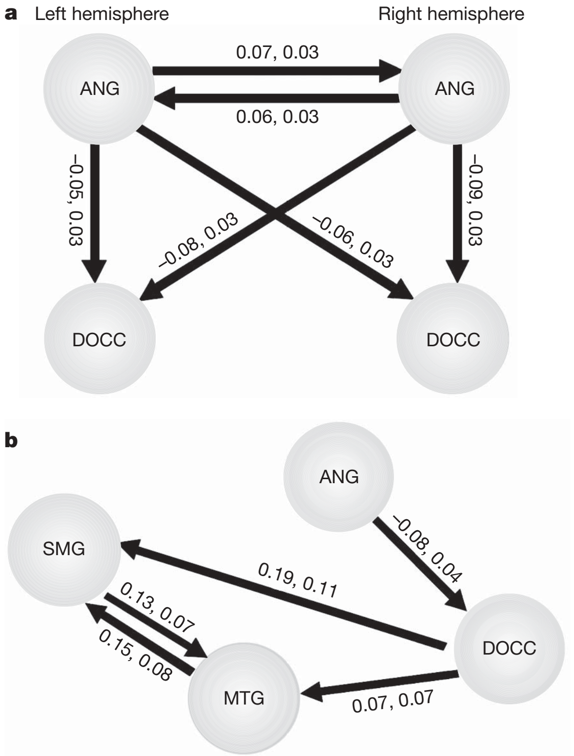

Figure 3 | Functional connectivity results. Two dynamic causal models were defined and estimated in each of 20 literate subjects using standard procedures in SPM5. All forward and backward connections were specified (fully connected dynamic causal models) but only illustrated where the modulatory effect of reading was significantly stronger ($P < 0.05$) than that for object naming. The values on each connection refer to the strengths of intrinsic connections and modulatory effects, respectively (in hertz). **a**, Assessment of the interhemispheric effective connectivity between left and right dorsal occipital gyri and left and right angular gyri. Driving inputs (words and objects) were connected to left and right occipital gyri. Only the interhemispheric connections that involved the angular gyrus were significant. **b**, Assessment of the interactions of the four left-hemisphere regions that belong to the anatomical system identified in experiment one. Driving inputs (word and objects) were connected to the left occipital gyrus. Note that the only significant top-down (backward) modulation to this input region is exerted by the angular gyrus.

in which there is a consistent relationship between spelling and sound. In contrast, the ventral system may be more important in later stages—when skilled reading is fast and automatic—and in deeper orthographies (like English[26]) that necessitate parallel letter processing because of the inconsistent spelling–sound relationships. Future longitudinal studies are required to test these predictions.

In conclusion, we have identified structural brain differences in late-literates relative to illiterates and used these results to guide anatomical and functional connectivity analyses in early-literates. Our findings shed light on neurological models of reading. First, they suggest that learning to read strengthens the coupling between left and right angular gyri and that this coupling is mediated by anatomical white-matter pathways through the SCC. Second, they show that when words are read aloud, the angular gyrus provides top-down constraints on the functional interactions between visual processing in the dorsal occipital gyrus and speech processing in the supramarginal gyrus. This contradicts the classic version of the neurological model, which posits that information flows from visual areas through the angular gyrus to the superior temporal gyrus[27–30]. We suggest that reading increases the functional connectivity between the left and right angular gyri and on information flow from the left dorsal occipital gyrus to the left supramarginal gyrus, with the left angular gyrus playing a top-down modulatory role.

Future studies are required to investigate anatomical and functional connectivity in late-literates and to tease apart which components of their literacy training were effective in generating the structural brain differences. Nevertheless, this study demonstrates that learning to read in adulthood can have a significant effect on the structure of brain regions that are important for skilled reading in early-literates.

METHODS SUMMARY

Experiment one compared structural MRI scans from 22 late-literates and 20 culturally matched illiterates. Grey- and white-matter density was estimated on the basis of T_1-weighted anatomical whole-brain images acquired using a GE 1.5T MRI system. VBM statistical analyses were conducted using SPM5 separately for grey- and white-matter images. Linear contrasts produced two *t*-statistic maps, one for activation that was greater in literates than in illiterates and one for activation that was greater in illiterates than in literates.

Experiment two used DTI and tractography analyses in 10 adults who learnt to read in childhood (early-literates). Diffusion-weighted magnetic resonance images were collected using a 1.5T Siemens Sonata MRI system. The aim of the tractography analyses was to investigate the link between the grey- and white-matter regions identified in experiment one.

Experiment three used fMRI to compare reading and object naming in 20 early-literates. There were three conditions: naming pictures of objects, reading the written names of the objects and articulating "1, 2, 3" in response to unfamiliar symbols and pictures. The fMRI analysis using SPM5 investigated regional activation differences for reading relative to picture naming in the significant regions of interest identified in the VBM analysis. Peak activations were identified using the peak coordinates from experiment one with a 6-mm-radius search volume. In addition, a DCM analysis was performed to investigate how the brain regions interacted during reading relative to object naming. For each region, eigenvectors were extracted in each participant at the closest maxima within a distance of 4 mm from the group peaks. The first dynamic causal model tested the effective connectivity between left and right hemispheres in DOCC and ANG regions. The second dynamic causal model tested the effective connectivity between the left-hemisphere regions of interest from the anatomical reading system identified in experiment one.

Full Methods and any associated references are available in the online version of the paper at www.nature.com/nature.

Received 10 June; accepted 26 August 2009.

1. Hauser, M. D., Chomsky, N. & Fitch, W. T. The faculty of language: what is it, who has it, and how did it evolve? *Science* **298**, 1569–1579 (2002).
2. Fisher, S. E. & Marcus, G. F. The eloquent ape: genes, brains and the evolution of language. *Nature Rev. Genet.* **7**, 9–20 (2006).
3. Senghas, A., Kita, S. & Ozyurek, A. Children creating core properties of language: evidence from an emerging sign language in Nicaragua. *Science* **305**, 1779–1782 (2004).
4. Draganski, B. *et al.* Neuroplasticity: changes in grey matter induced by training. *Nature* **427**, 311–312 (2004).
5. Castro-Caldas, A. *et al.* Influence of learning to read and write on the morphology of the corpus callosum. *Eur. J. Neurol.* **6**, 23–28 (1999).
6. Petersson, K. M., Silva, C., Castro-Caldas, A., Ingvar, M. & Reis, A. Literacy: a cultural influence on functional left–right differences in the inferior parietal cortex. *Eur. J. Neurosci.* **26**, 791–799 (2007).
7. Turkeltaub, P. E., Gareau, L., Flowers, D. L., Zeffiro, T. A. & Eden, G. F. Development of neural mechanisms for reading. *Nature Neurosci.* **6**, 767–773 (2003).
8. Price, C. J. & Mechelli, A. Reading and reading disturbance. *Curr. Opin. Neurobiol.* **15**, 231–238 (2005).
9. Damasio, A. R. & Damasio, H. The anatomic basis of pure alexia. *Neurology* **33**, 1573–1583 (1983).
10. Sowell, E. R. *et al.* Longitudinal mapping of cortical thickness and brain growth in normal children. *J. Neurosci.* **24**, 8223–8231 (2004).
11. Price, C. J. *et al.* How reading differs from object naming at the neuronal level. *Neuroimage* **29**, 643–648 (2006).
12. Lundberg, I., Olofsson, Å. & Wall, S. Reading and spelling skills in the first school years predicted from phonemic awareness skills in kindergarten. *Scand. J. Psychol.* **21**, 159–173 (1980).
13. Morais, J., Cary, L., Alegria, J. & Bertelson, P. Does awareness of speech as a sequence of phones arise spontaneously? *Cognition* **7**, 323–331 (1979).
14. Carreiras, M. & Grainger, J. Sublexical representations and the 'front end' of visual word recognition. *Lang. Cogn. Process.* **19**, 321–331 (2004).
15. Booth, J. R. *et al.* Development of brain mechanisms for processing orthographic and phonologic representations. *J. Cogn. Neurosci.* **16**, 1234–1249 (2004).
16. Wagner, R. K. & Torgesen, J. K. The nature of phonological processing and its causal role in the acquisition of reading skills. *Psychol. Bull.* **101**, 192–212 (1987).

17. Brambati, S. M. *et al.* Neuropsychological deficits and neural dysfunction in familial dyslexia. *Brain Res.* **1113,** 174–185 (2006).
18. Hoeft, F. *et al.* Neural basis of dyslexia: a comparison between dyslexic and nondyslexic children equated for reading ability. *J. Neurosci.* **26,** 10700–10708 (2006).
19. Silani, G. *et al.* Brain abnormalities underlying altered activation in dyslexia: a voxel based morphometry study. *Brain* **128,** 2453–2461 (2005).
20. Steinbrink, C. *et al.* The contribution of white and gray matter differences to developmental dyslexia: insights from DTI and VBM at 3.0 T. *Neuropsychologia* **46,** 3170–3178 (2008).
21. Dougherty, R. F. *et al.* Temporal-callosal pathway diffusivity predicts phonological skills in children. *Proc. Natl Acad. Sci. USA* **104,** 8556–8561 (2007).
22. Robichon, F. & Habib, M. Abnormal callosal morphology in male adult dyslexics: Relationships to handedness and phonological abilities. *Brain Lang.* **62,** 127–146 (1998).
23. Rumsey, J. M. *et al.* Corpus callosum morphology, as measured with MRI, in dyslexic men. *Biol. Psychiatry* **39,** 769–795 (1996).
24. Pugh, K. R. *et al.* Neurobiological studies of reading and reading disability. *J. Commun. Disord.* **34,** 479–492 (2001).
25. Shaywitz, B. A. *et al.* Disruption of posterior brain systems for reading in children with developmental dyslexia. *Biol. Psychiatry* **52,** 101–110 (2002).
26. Paulesu, E. *et al.* A cultural effect on brain function. *Nature Neurosci.* **3,** 91–96 (2000).
27. Binder, J. R. & Mohr, J. P. The topography of callosal reading pathways. A case-control analysis. *Brain* **115,** 1807–1826 (1992).
28. Dejerine, J. Contribution a l'étude anatomo-pathologique et clinique des differentes varietés de cecité verbale. *Mem. Soc. Biol. Fr.* **4,** 61–90 (1892).
29. Geschwind, N. Disconnexion syndromes in animals and man. *Brain* **88,** 237–294 (1965).
30. Price, C. J. The anatomy of language: contributions from functional neuroimaging. *J. Anat.* **197,** 335–359 (2000).

Supplementary Information is linked to the online version of the paper at www.nature.com/nature.

Acknowledgements We thank K. Friston for advice on data analyses and A. Leff, T. Münte and T. Shallice for their help with the presentation of the manuscript. This work was funded by a CONSOLIDER-INGENIO grant from the Spanish Ministry of Education and Science and by the Wellcome Trust.

Author Contributions M.C., M.L.S., J.T.D. and C.J.P. designed the experiments, performed the data analyses and wrote the paper. S.B., A.E. and A.L. performed experiment one.

Author Information Reprints and permissions information is available at www.nature.com/reprints. Correspondence and requests for materials should be addressed to M.C. (m.carreiras@bcbl.eu) or C.J.P. (c.price@fil.ion.ucl.ac.uk).

METHODS

We conducted three different experiments (see Supplementary Information for full discussion).

Experiment one: structural imaging of late-literates and illiterates. This study was approved by the ethics committee of the University of La Laguna.

Forty-two right-handed[31] native Spanish-speakers from Colombia provided written consent to participate. Most were members of the Colombian guerrilla forces that had put down their weapons. The rest were housewives from a similar socio-economic background. The 22 illiterates (11 males and 11 females, with a mean age of 32.8 years) were about to start a literacy program. The 20 literates (10 males and 10 females, with a mean age of 31.5 years) had already completed the literacy program in adulthood. This was primarily based on learning to recognize words on the basis of spelling–sound relationships in Spanish. All 20 literates had been actively reading and writing in Spanish for at least five years. They had a normal neuropsychological profile[32–37] (see Supplementary Table 1 for details) and performed at ceiling on standardized tests of Spanish reading designed for 7–12-year-old children[38]. When tested for comprehension of sentences and small texts, they responded 98% correctly to the comprehension questions asked afterwards, showing a good reading level. Finally, on the most difficult task (text comprehension[38]) they scored an average of 85% (range, 64–100%). Overall, these results confirm a good level of reading proficiency, consistent with the increased grey matter that they expressed in known reading areas.

The criteria for inclusion in the illiterate sample were as follows: (1) lack of formal schooling, owing to there being no opportunity to gain any; (2) inability to read more than five simple words following tests including the reading and writing of words, the reading of sentences and the comprehension of a text[38], as administered to the literate participants; (3) normal performance in daily-life activities according to their socio-cultural environment; (4) right-handedness according to the Edinburgh inventory[31]; and (5) a normal neuropsychological profile[32–37] (see Supplementary Table 1 for details) on the Raven test (Raven), digit span (Digit), picture naming (Naming) and verbal fluency (Fluency).

Focal grey- and white-matter densities were estimated on the basis of T_1-weighted anatomical whole-brain images acquired in a GE 1.5T MRI system. We used a whole-brain three-dimensional (3D) sequence to acquire two structural images in the axial and coronal planes that were subsequently averaged to ensure the best signal contrast. The 3D spoiled-gradient-recalled acquisition sequence was obtained with the following acquisition parameters: TR = 15.8 ms; TE = 4.2 ms; TI = 450 ms; flip angle, 20°; slice thickness, 1.5 mm; field of view, 24 cm; matrix size, 256 × 192 pixels.

Data were processed using the SPM5 software package (Wellcome Trust Centre for Neuroimaging; http://www.fil.ion.ucl.ac.uk/spm/) after checking all images for artefacts. The unified segmentation algorithm in SPM5 involves alternating between tissue classification, bias correction and spatial normalization in the inversion of a single generative model[39] and outputs grey- and white-matter probability images that were smoothed using an isotropic Gaussian kernel with a full-width at half-maximum (FWHM) of 12 mm. Statistical analyses were conducted separately for grey- and white-matter images with proportional scaling to remove global signal-intensity differences. Each analysis used the general linear model with two groups (literates and illiterates) and seven covariates of no interest that factored out the effect of age, gender and performance on the five neuropsychological tests[32–37] (digit span, Raven, picture naming, phonological fluency and mini-mental state examination). Neither gender nor age differed between groups (for example, the mean age was 31.5 years for the literates and 32.8 years for the illiterates, and the age range was 21–52 years for the literates and 20–52 years for the illiterates; see Supplementary Table 1). By modelling age and gender as covariates of no interest in the multiple regression, we aimed to reduce within-group error variance. As expected, performance in the five neuropsychological tests was higher on average in the literate and illiterate groups. This is likely to be a consequence of learning to read[40,41]. Nevertheless, we wanted to factor out this variance to ensure that our findings focused on structural changes related to reading ability rather than other cognitive skills.

Linear contrasts produced two *t*-statistic maps, one for activation that was greater in literates than in illiterates and one for activation that was greater in illiterates than in literates (after factoring out the effect of the seven additional regressors). Regional differences were reported as significant at $P < 0.05$ after family-wise error correction for multiple comparisons either at the height or the volume level. In addition, we checked specifically for differences between literates and illiterates in the left occipito-temporal region that is sometimes referred to as the visual word form area[42] by defining a 10-mm-radius spherical region of interest around the coordinates (−42, −56, −14). No significant effects were observed in this region even when the statistical threshold was reduced to $P < 0.05$ uncorrected (*Z* score, >1.64).

Experiment two: diffusion tensor imaging. Data for experiment two were collected at the Oxford Centre for Magnetic Resonance imaging in the UK because the protocols and facilities were not available in Bogotá. However, as indicated above and in the main text, the basic pattern of long-range connections that this study identified are laid down *in utero* and are therefore expected to be present irrespective of literacy experience. In other words, learning to read will not generate *de novo* anatomical connections; instead, it modifies existing pathways. Moreover, there were advantages to collecting corresponding data in a different sample of individuals. In particular, experiment two allows us to confirm predictions from experiment one.

Diffusion-weighted magnetic resonance images were collected from ten healthy, literate volunteers (six male, four female) aged 18–37 years (mean, 24 years), all of whom provided informed consent after explanation of the protocol. Scanning was performed at the Oxford Centre for Magnetic Resonance Imaging on a 1.5T Siemens Sonata with a maximum gradient strength of $40\,\mathrm{mT\,m^{-1}}$. Two sets of echo-planar images of the whole head were acquired (60 2.5-mm thick axial slices; in-plane resolution, 2.5 mm × 2.5 mm). Each set comprised three non-diffusion-weighted and 60 diffusion-weighted images acquired with a *b* value of $1{,}000\,\mathrm{s\,mm^{-2}}$ uniformly distributed across 60 gradient directions[43]. These were pre-processed to correct for eddy currents and remove minor head motions[44], averaged to improve the signal-to-noise ratio and converted into voxel-wise 3D probability density functions assuming a single fibre direction except where the evidence merited increasing the model complexity by including crossing fibres[45]. Finally, we also acquired a high-resolution T_1-weighted image (3D FLASH sequence; TR = 12 ms; TE = 5.60 ms; flip angle, 19°; voxel size, 1 mm × 1 mm × 1 mm) for anatomical localization.

The aim of the tractography analyses was to investigate the link between the grey- and white-matter VBM results. Specifically, we tested the hypothesis that the white-matter differences in the SCC reflected an interhemispheric anatomical connection between left- and right-hemisphere homologue regions where there were significant grey-matter differences in the structural comparison of grey matter in literates and illiterates in both hemispheres. The only two areas with significant effects (corrected for multiple comparisons) in both left and right hemispheres in experiment one were the angular gyrus and the dorsal occipital cortex. We did not include the temporal regions, because the location of the effects in the left and right middle temporal areas were more than 14 mm apart ((−54, −62, 10), (+60, −72, −4)), and the effects in the supramarginal/superior temporal areas only reached significance in the left hemisphere.

Corticocortical connections linking the left and right angular gyri were traced using a probabilistic tractography algorithm[46] in each of the ten subjects. Because the VBM findings were group results localized in MNI space but the tractography was carried out in individuals (in native space), the first step was to map the VBM results from experiment one onto each participant's anatomy. This involved the following procedure. First, structural images for each of the ten subjects were converted to MNI space using a linear transformation. The voxels showing significant effects in experiment one ($P < 0.001$ uncorrected) were then transposed onto the structural image in MNI space. To ensure that registration was accurate, we only excluded voxels if they had a 20% or less chance of being grey matter. In other words, the only voxels used to seed each DTI analysis were those from the VBM results that were present in that individual's angular gyrus and dorsal occipital gyrus grey matter. These were manually checked to verify the accuracy of this process. For all tractography analyses, each of the seed voxels was converted back into native space by reversing the linear transformation.

Paths were determined three times using a Markov-chain Monte Carlo technique with 1,000, 5,000 or 250,000 samples per seed voxel. All paths that did not intersect the SCC identified by the VBM white-matter analyses (and mapped on the individual's own corpus callosum) were excluded. The resulting images represent empirically determined probability distributions linking left- and right-hemisphere voxels through the region of the SCC identified in the VBM white-matter analysis. The results revealed a clear pathway linking the left- and right-hemisphere seed regions through the SCC irrespective of whether 1,000, 5,000 or 250000 samples were used. This suggests that the pathway is robust and easily traced. It was also present across a range of different seed voxels (Fig. 3).

Experiment three: functional imaging of reading versus picture naming. Data for experiment three were collected at the Wellcome Trust Centre for Neuroimaging. The study was approved by the joint ethics committee of the Institute of Neurology and University College London Hospital.

Twenty healthy, right-handed skilled readers (8 males and 12 females; age range, 13–71 years; mean, 35 years) gave written informed consent to participate in this study. All were literate, native English-speakers, had normal or corrected-to-normal vision, with no history of neurological or psychiatric disorders. They were all highly educated and are therefore likely to have been much more proficient readers than the adult literates included in experiment one. Critically, however, we looked for consistencies between studies rather than differences.

There were three tests: naming pictures of objects that have familiar names of three to six letters, reading the written names of the objects used for picture naming and articulating "1, 2, 3" in response to unfamiliar symbols and pictures of three unfamiliar 3D shapes. Responses were spoken aloud and recorded with an in-house MRI-compatible auditory recording system. To facilitate task switching, the conditions were blocked with 12 stimuli per block that alternated with 14.4 s of fixation. Within a block, the 12 stimuli were presented in four sequential trials (one each 4.3 s) with three stimuli per trial, one above fixation and two below fixation. The participants were asked to name the objects or read the word in the same order (top, bottom left, bottom right) and to say "1, 2, 3" in response to the unfamiliar stimuli while looking sequentially at the top, bottom-left and bottom-right pictures. Over the experiment, each participant responded to 32 trials (96 stimuli) of each condition. Within subject, a different set of objects was used for picture naming and reading, but across subjects, articulation was matched for picture naming and reading. Thus, we had a total of 192 objects, divided into sets A and B. Half the subjects saw set A as pictures and set B as written names; the other half saw set B as pictures and set A as written names. Name agreement across subjects was ensured by a pilot study. The total scanning time for all conditions was 12 minutes in two separate six-minute runs.

To ensure that the task was understood correctly, all subjects were provided with detailed instructions and underwent a short training session before entering the scanner. To minimize artefacts from head motion, participants were instructed to whisper their response with minimal mouth movement. Their movement within the scanner was assessed. The 20 participants included in the analyses reported below were selected from a larger sample after excluding those who moved more than 1.5 mm in any direction in the scanner.

Data were acquired on a 1.5T Siemens Sonata MRI system. Functional imaging comprised an echo-planar-imaging gradient-echo sequence (TR = 3,600 ms; TE = 50 ms; flip angle, 90°; FOV = 192 mm; 40 axial slices with 3 mm × 3 mm × 3 mm voxel size). The echo-planar-imaging gradient-echo sequence used here was optimized to minimise signal dropout by adjusting the slice tilt, the direction of the phase encoding and the *z*-shim moment[47]. Functional, scanning was always preceded by 14.4 s of dummy scans to ensure tissue steady-state magnetization.

Data processing and statistical analyses were performed using SPM5. All functional volumes were spatially realigned, unwarped, normalized to the MNI space using the unified normalization-segmentation procedure of SPM5 (ref. 40) and smoothed with an isotropic Gaussian kernel with 6-mm FWHM, with resulting voxels size of 2 mm × 2 mm × 2 mm. Time series from each voxel were high-pass filtered (1/128-Hz cut-off) to remove low-frequency noise and signal drift. The pre-processed functional volumes for each subject were then submitted to a fixed-effects analysis, using the general linear model at each voxel. The onset of each stimulus was modelled as an event encoded in condition-specific 'stick-functions'. Correct and incorrect responses were modelled separately. The resulting stimulus functions were convolved with a canonical haemodynamic response function to form regressors for the general linear model. Parameter estimates (that is, beta images) were assessed using least-squares regression analysis. The appropriate contrast image (that is, a contrast of maximum-likelihood-parameter estimates) was then entered into a second-level random-effects analysis to allow inferences at the group level in the regions showing structural differences between literates and illiterates (Supplementary Table 1 and Supplementary Fig. 1). This analysis was used to identify regional activation differences for reading and picture naming and to extract the time series for each region from the F map for all conditions.

First we created a mask of the significant voxels in the structural comparison (experiment one). Then we applied this mask to the second-level analysis of the functional data. Peak activations were identified using the peak coordinates from experiment one using a 6-mm-radius search volume. The coordinates of the six local F-map peaks closest to our regions of interest from experiment one were as follows: left DOCC at (−30, −88, +20), right DOCC at (+30, −88, +20), left ANG at (−48, −74, +28), right ANG at (+50, −70, +32), left MTG at (−54, −54, +10) and left SMG at (−52, −42, +26). See Supplementary Table 2 for comparison of structural imaging results (experiment one) and functional imaging results (experiment three).

For the rationale behind DCM and our choice of analysis, please see Supplementary Information. The procedures were as follows. For each region, eigenvectors (that is, time series) were extracted in each participant at the closest maxima within a distance of 4 mm from the group peaks (individual map threshold, $P < 0.05$) from experiment one. Critically, this 4-mm limit ensured that DCM models were comparable across participants[48]. Regions of interest were extracted for each session separately within a 4-mm-radius sphere and the principal eigenvariates were adjusted to the F contrast of each participant. For each subject, we extracted region-of-interest time series that were concatenated over the two runs and incorporated in two DCM models. The first DCM model (Supplementary Fig. 2a) tested the effective connectivity between left and right hemispheres in left DOCC and ANG regions. It was a fully connected model between left and right DOCC and left and right ANG regions; the driving inputs (that is, objects, words, symbols and non-objects) were connected to both the left and the right DOCC regions; and object naming and word reading were used as modulatory inputs on all connections.

The second DCM model (Supplementary Fig. 2b) tested the effective connectivity between the different regions of the anatomical reading system identified in experiment one (that is, four left-hemisphere regions). It was a fully connected model (all forward and backward connections specified) between the left DOCC and ANG regions, the MTG and the SMG; the driving inputs (that is, objects, words, symbols and non-objects) were connected to the left DOCC region; and word reading and object naming were used as modulatory inputs on all connections to estimate the change in connection strengths as a function of the context (for example reading versus naming). Both DCM analyses identified the interactions that increased selectively during reading aloud when visual processing and articulation were controlled.

All parameters of both DCM models (intrinsic and modulatory values) and their posterior probabilities were assessed using Bayesian inversion by means of expectation and maximization[49,50]. The intrinsic and modulatory effects of each subject were submitted to *t*-tests at the group level to infer consistent findings across our 20 subjects[50]. Critically, only connections that showed stronger modulatory effects for word reading than for object naming ($P < 0.05$) are considered relevant in our context. For the first DCM model, we also carried out a factorial analysis (that is, analysis of variance) on the strength of the modulatory effects, to test the effects of task (reading or naming), region (left DOCC or ANG) and interhemispheric coupling (left to right versus right to left). Significant effects for these factors and their interactions were reported at $P < 0.05$.

31. Oldfield, R. C. The assessment and analysis of handedness: the Edinburgh inventory. *Neuropsychologia* **9**, 97–113 (1971).
32. Peña-Casanova, J. *Programa Integrado de Exploración Neuropsicológica: Test Barcelona* (Masson, 1995).
33. Folstein, M. F., Folstein, S. & McHugh, P. R. 'Mini-mental state': a practical method for grading the cognitive state of patients for the clinician. *J. Psych. Res* **12**, 189–198 (1975).
34. Wechsler, D. *Wechsler Memory Scale Revised* (Psychological Corporation, 1987).
35. Raven, J. C. *Progressive Matrices: A Perceptual Test of Intelligence* (Lewis, 1938).
36. Snodgrass, J. G. & Vanderwart, M. A standardized set of 260 pictures: Norms for name agreement, image agreement, familiarity, and visual complexity. *J. Exp. Psychol. Hum. Learn. Mem.* **6**, 174–215 (1980).
37. Spreen, O. & Strauss, E. *A Compendium of Neuropsychological Tests* (Oxford Univ. Press, 1991).
38. Cuetos Vega, F., Rodríguez, B. & Ruano Hernández, E. (1996). *Batería de Evaluación de los Procesos Lectores de los Niños de Educación Primaria (PROLEC)* (T.E.A. Ediciones, 1996).
39. Ashburner, J. & Friston, K. J. Unified segmentation. *Neuroimage* **26**, 839–851 (2005).
40. Reis, A. & Castro-Caldas, A. Illiteracy. A bias for cognitive development. *J. Int. Neuropsychol. Soc.* **3**, 444–450 (1997).
41. Reis, A., Guerreiro, M. & Petersson, K. M. A sociodemographic and neuropsychological characterization of an illiterate population. *Appl. Neuropsychol.* **10**, 191–204 (2003).
42. Cohen, L. *et al.* The visual word form area: spatial and temporal characterization of an initial stage of reading in normal subjects and posterior split-brain patients. *Brain* **123**, 291–307 (2000).
43. Jones, D. K., Horsfield, M. A. & Simmons, A. Optimal strategies for measuring diffusion in anisotropic systems by magnetic resonance imaging. *Magn. Reson. Med.* **42**, 515–525 (1999).
44. Jenkinson, M. Bannister, P. Brady, M. & Smith, S. Improved optimization for the robust and accurate linear registration and motion correction of brain images. *Neuroimage* **17**, 825–841 (2002).
45. Behrens, T. E., Berg, H. J., Jbabdi, S., Rushworth, M. F. & Woolrich, M. W. Probabilistic diffusion tractography with multiple fibre orientations: What can we gain? *Neuroimage* **34**, 144–155 (2007).
46. Behrens, T. E. J. *et al.* Characterization and propagation of uncertainty in diffusion-weighted MR imaging. *Magn. Reson. Med.* **50**, 1077–1088 (2003).
47. Weiskopf, N., Hutton, C., Josephs, O. & Deichmann, R. Optimal EPI parameters for reduction of susceptibility-induced BOLD sensitivity losses: A whole-brain analysis at 3 T and 1.5 T. *Neuroimage* **33**, 493–504 (2006).
48. Stephan, K. E., Marshall, J. C., Penny, W. D., Friston, K. J. & Fink, G. R. Interhemispheric integration of visual processing during task-driven lateralization. *J. Neurosci.* **27**, 3512–3522 (2007).
49. Friston, K. J., Harrison, L. & Penny, W. Dynamic causal modelling. *Neuroimage* **19**, 1273–1302 (2003).
50. Penny, W. D., Stephan, K. E., Mechelli, A. & Friston, K. J. Modelling functional integration: a comparison of structural equation and dynamic causal models. *Neuroimage* **23**, S264–S274 (2004).

Vol 461 | 15 October 2009 | doi:10.1038/nature08495

LETTERS

Specialized cells tag sexual and species identity in *Drosophila melanogaster*

Jean-Christophe Billeter[1], Jade Atallah[1], Joshua J. Krupp[1], Jocelyn G. Millar[2] & Joel D. Levine[1]

Social interactions depend on individuals recognizing each other, and in this context many organisms use chemical signals to indicate species and sex[1]. Cuticular hydrocarbon signals are used by insects, including *Drosophila melanogaster*, to distinguish conspecific individuals from others[1–3]. These chemicals also contribute to intraspecific courtship and mating interactions[1–3]. However, the possibility that sex and species identification are linked by common chemical signalling mechanisms has not been formally tested. Here we provide direct evidence that a single compound is used to communicate female identity among *D. melanogaster*, and to define a reproductive isolation barrier between *D. melanogaster* and sibling species. A transgenic manipulation eliminated cuticular hydrocarbons by ablating the oenocytes, specialized cells required for the expression of these chemical signals. The resulting oenocyte-less (oe$^-$) females elicited the normal repertoire of courtship behaviours from males, but were actually preferred over wild-type females by courting males. In addition, wild-type males attempted to copulate with oe$^-$ males. Thus, flies lacking hydrocarbons are a sexual hyperstimulus. Treatment of virgin females with the aversive male pheromone *cis*-vaccenyl acetate (cVA) significantly delayed mating of oe$^-$ females compared to wild-type females. This difference was eliminated when oe$^-$ females were treated with a blend of cVA and the female aphrodisiac (7*Z*,11*Z*)-heptacosadiene (7,11-HD), showing that female aphrodisiac compounds can attenuate the effects of male aversive pheromones. 7,11-HD also was shown to have a crucial role in heterospecific encounters. Specifically, the species barrier was lost because males of other *Drosophila* species courted oe$^-$ *D. melanogaster* females, and *D. simulans* males consistently mated with them. Treatment of oe$^-$ females with 7,11-HD restored the species barrier, showing that a single compound can confer species identity. These results identify a common mechanism for sexual and species recognition regulated by cuticular hydrocarbons.

D. melanogaster produces hydrocarbons of various chain lengths, including unbranched alkanes, methyl-branched alkanes, alkenes and derivatives thereof. The alkenes are expressed sex-specifically, and have been associated with both sex and species discrimination[2–5]. Compared to females, males express high levels of the monoalkene (*Z*)-7-tricosene (7-T), which has been reported to increase females' receptivity to mating attempts[6]. Moreover, 7-T is repulsive to other males and may prevent male–male interactions[7]. In contrast, females produce sex-specific dienes such as (7*Z*,11*Z*)-heptacosadiene (7,11-HD) and (7*Z*,11*Z*)-nonacosadiene (7,11-ND), which act as aphrodisiac pheromones for *D. melanogaster* males[2,8]. Hydrocarbons are strongly associated with sexual recognition, because wild-type males court males that have been genetically modified to express female hydrocarbons, indicating that the mutants are perceived as females[9].

There are still large gaps in our knowledge of the functions of individual hydrocarbons and the tissues where these compounds are synthesized. As in other insects[10], specialized cells called oenocytes, located on the inner surface of the abdominal cuticle, are thought to be the site of hydrocarbon biosynthesis in *D. melanogaster*[3]. Consistent with this hypothesis, *desaturase 1* (*desat1*), which encodes an enzyme involved in hydrocarbon synthesis[11], is expressed in *Drosophila* oenocytes[12] (Fig. 1a). Previous studies have demonstrated that genetic feminization of these cells results in production of female hydrocarbons by male flies[9]; however, these and other manipulations have been confounded by the concurrent feminization of cells in many other sexually dimorphic tissues, including the central nervous system[5,9]. To test the hypothesis that these cells are required for production of chemical signals used in sexual and species recognition, we used the Gal4-UAS system[13] to target transgene expression specifically to the adult oenocytes. We generated an oenocyte Gal4 driver (Fig. 1b) derived from the regulatory sequence of one of the *desat1* promoters[11] that is expressed specifically in oenocytes of adult females (Fig. 1a–c). The driver is also expressed in the larval oenocytes and in the reproductive organs of adult males (Fig. 1a, c and Supplementary Fig. 1). We used this driver to ablate adult oenocytes by inducing expression of the pro-apoptotic gene *head involution defective* (*hid*; also called *Wrinkled*)[14]. This approach initially caused lethality in larvae, probably due to the destruction of the larval oenocytes[15]. To circumvent this problem we blocked the driver's action during development using the *Tubulin-Gal80^{ts}* transgene[16]. Using this method, we generated adult flies without oenocytes (oe$^-$) (Fig. 1d, e). Analysis of whole-body hydrocarbon extracts confirmed that both oe$^-$ males and females were essentially devoid of these compounds (Fig. 1f, g and Supplementary Tables 1 and 2 for quantification), showing that the oenocytes are necessary for hydrocarbon display in *D. melanogaster*. The male pheromone *cis*-vaccenyl acetate (cVA) was unaffected in oe$^-$ males (Fig. 1f, g) because this compound is synthesized in the ejaculatory bulb[17]. The oe$^-$ transgenic strain therefore provided a 'blank slate' for evaluating the role of hydrocarbons in intra- and interspecific communication.

We assayed sexual behaviour of oe$^-$ flies to test hydrocarbon function during reproduction. Despite the association of hydrocarbon signals and *Drosophila* courtship, absence of these signals did not alter courtship behaviours *per se*. The oe$^-$ males displayed normal courtship behaviour towards wild-type females, but slightly less intense than control males (Fig. 2a and Supplementary Table 3). However, wild-type females were less receptive to oe$^-$ males than control males, with oe$^-$ males taking almost four times as long to achieve mating (Fig. 2a). Thus, hydrocarbons of males do not seem to affect their own courtship behaviour, but rather, influence the receptivity of females to their mating attempts. However, we cannot exclude the influence of non-oenocyte cells within the male reproductive organs that may have been affected by the ablation. Notably, oe$^-$ males elicited courtship and copulation attempts from both

[1]Department of Biology, University of Toronto at Mississauga, 3359 Mississauga Road, Mississauga, Ontario L5L 1C6, Canada. [2]Department of Entomology, University of California, 3401 Watkins Drive, Riverside, California 92521, USA.

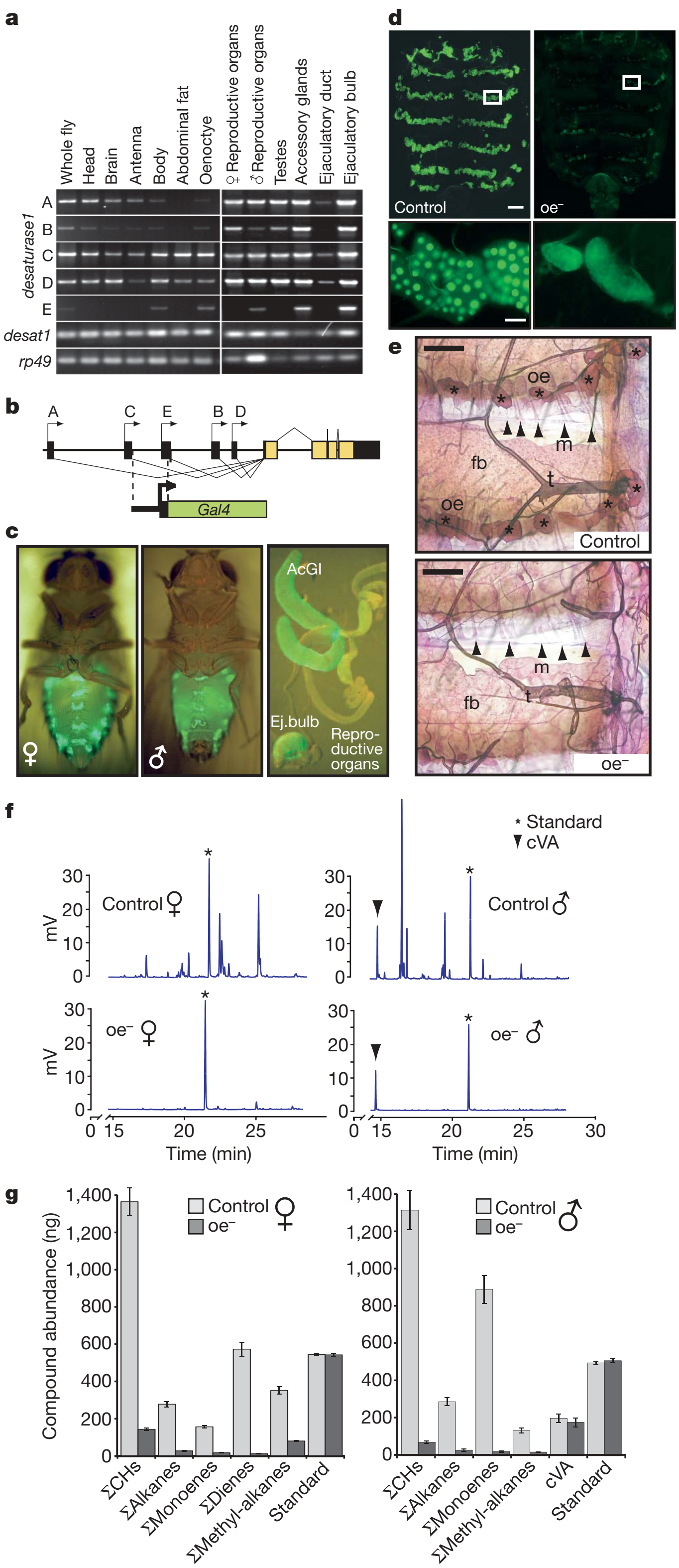

Figure 1 | Oenocytes produce cuticular hydrocarbons. **a**, Tissue-specific expression of *desat1* type E isoform in the adult oenocytes. RT–PCR on *desat1* transcripts from different adult tissues. Transcript-specific primer combinations were used to detect *desat1* isoforms A–E. Gene-specific primers for *desat1* and *rp49* were used as controls. **b**, Organization of the *desat1* locus. Black boxes, non-coding exons; orange; coding. A–E are alternative promoters. **c**, *PromE(800)-gal4* driver recapitulates *desat1*-E isoform expression. *PromE(800)-gal4* driving *UAS-nuclear GFP* expression in adults is shown. AcGL, accessory glands; Ej. bulb, ejaculatory bulb. **d**, Dorsal abdominal fillet preparations of control (*PromE(800)-gal4, TubP-GAL80^{ts}/UAS-nuclearGFP*) and oenocyte-ablated (oe$^-$) females (*PromE(800)-gal4, TubP-GAL80^{ts}/UAS-hid, UAS-nuclear GFP*) demonstrating the loss of GFP expression after cell-death induction. Scale bar, 200 μm. Weak fluorescence in oe$^-$ animals comes from necrotic tissues devoid of nuclear structures (inserts magnified in lower panels: scale bar, 20 μm). **e**, Haematoxylin and eosin staining of abdominal fillet as in **d**, demonstrating disruption of the oenocytes in oe$^-$ flies. Other abdominal tissues appear normal. fb, fat bodies; m, muscles (arrowhead); oe, oenocytes (indicated by asterisks, form a strip strapped under the dorsal abdominal muscles); t, trachea. Scale bars, 100 μm. **f**, Cuticular hydrocarbons of single flies were analysed using gas chromatography. Chromatograms plot the peak area associated with the amount of a specific hydrocarbon, scale is in millivolts (mV). **g**, Mean sum of cuticular hydrocarbons (∑CHs). Genotypes as in **d**. Hydrocarbon quantification broken down by chemical classes. Error bars indicate s.e.m. $n = 20,21$. Supplementary Tables 1 and 2 show values for individual compounds and for additional control genotypes.

wild-type males and other oe$^-$ males, indicating that oe$^-$ males were perceived as females, even though all other male characteristics were present (Fig. 2b and Supplementary Table 4). The vigorous courtship of oe$^-$ males by each other resulted in unnatural behaviours such as engaging one another by rotating in a head-to-head orientation, and males attempting copulation with each other's heads (Fig. 2b, Supplementary Table 4 and Supplementary Movies 1 and 2). These behaviours were suppressed by treatment of oe$^-$ males with synthetic 7-T (Fig. 2b and Supplementary Table 4), confirming the function of 7-T in inhibiting male–male interactions[7].

Wild-type males exhibited normal courtship behaviour towards oe$^-$ females, apparently undeterred by the lack of female hydrocarbons (Fig. 2c). However, mating latency was significantly shorter (Fig. 2c), and when given a choice between an oe$^-$ and a control female, wild-type males preferred oe$^-$ females (Fig. 2d). Together, these data indicate that females lacking hydrocarbons are more attractive than those with a normal hydrocarbon profile. This suggests that female hydrocarbons normally act to slow down male mating attempts, facilitating assessment of a potential partner's species and fitness. Thus, any oe$^-$ fly, irrespective of its development as female or male, seems to sexually hyperstimulate males. We hypothesize that hydrocarbons normally act to superimpose sexual identity on an otherwise attractive fly substrate.

The results described above suggested that female attractiveness depends on a balance between attraction/stimulation and repulsion/deterrence. We investigated this by treating females with the aphrodisiac compound 7,11-HD, and with cVA, which males transfer to females via the ejaculate[2,18] to deter further mating attempts by other males[18,19]. Whereas cVA decreases the probability that females will remate, wild-caught females produce offspring from multiple sires, indicating that polyandry is common[20] and that the effect of cVA is not absolute. We treated oe$^-$ flies with doses of these compounds approximating wild-type levels (see Methods). The mating latency of wild-type males with oe$^-$ females treated with 7,11-HD was not different from that with untreated oe$^-$ females ($P > 0.7$), indicating that 7,11-HD alone does not affect attractiveness of oe$^-$ females (Fig. 2e). As expected, treating wild-type females with increasing doses of cVA delayed mating accordingly (Fig. 2f), and the effect was even more pronounced with oe$^-$ females treated with the same doses of cVA (Fig. 2f). This effect was not due to differences in the rates of release of cVA from the control and oe$^-$ flies, as shown by the profiles of cumulative loss of cVA over time for the two genotypes (Supplementary Fig. 2). Instead, the exaggerated effect of cVA on oe$^-$ females is consistent with our hypothesis that the aversive effects of this compound are normally moderated by the presence of other hydrocarbons. Indeed, when cVA and 7,11-HD were applied together, the mating latencies of oe$^-$ and wild-type females were indistinguishable (Fig. 2g). Apparently, 7,11-HD mitigated the deterrent effects of cVA. The data suggest that a male's perception of a female's availability is normally regulated by a mixture of attractive and aversive signals (Fig. 2f, g). From an evolutionary perspective, the combined effect of a female attractant with a male deterrent may

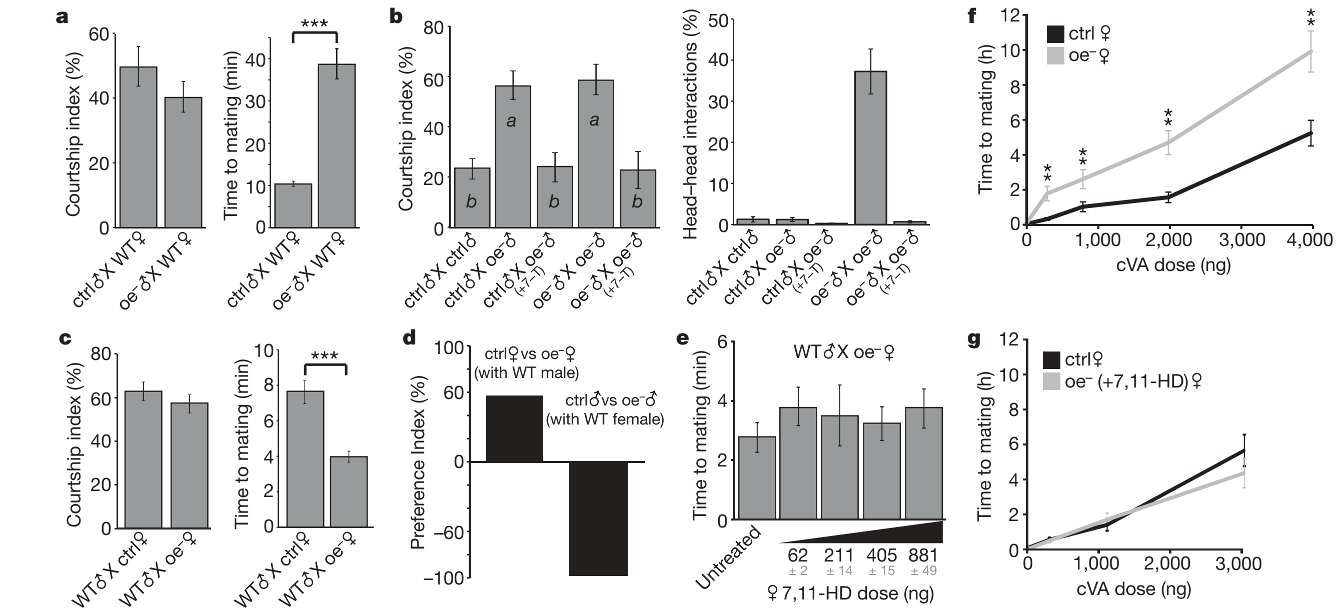

Figure 2 | Hydrocarbons regulate sexual attractiveness. a, Sexual behaviour of oe⁻ and control (ctrl) males with wild-type (WT) virgin females. Courtship indices are not significantly different ($P = 0.30$). $n = 27,38$ for courtship index and 158,148 for mating latency. **b**, Male–male interaction of oe⁻ males paired with wild-type or oe⁻ males. oe⁻ males labelled (+7-T) were treated with approximately 1 μg of synthetic 7-T. Bars labelled by the same letter (*a* or *b*) in the histograms are not statistically different (ANOVA, $P < 0.01$; $n = 10$–19). **c**, Behaviour of wild-type males towards oe⁻ females. $n = 38,39$ for courtship index and 139,146 for mating latency. **d**, Competitive mating assays in which oe⁻ females or males were pitted against a control animal of the same sex for copulation with a wild-type male or female. The preference index is the relative advantage of oe⁻ animal over the control. $n = 70,15$. **e**, oe⁻ virgin females treated with increasing amounts of synthetic 7,11-HD. Females were paired with wild-type males and the time between introduction to mating initiation was recorded. $n = 11$–12. **f**, Control and oe⁻ virgin females treated with increasing amounts of synthetic cVA. Treated females were paired with wild-type males and assayed as in **e**. Asterisks indicate significant differences between genotypes as determined by a two-tailed Student's *t*-test (** $P < 0.01$). There was a significant dose effect (ANCOVA, $F_{1,191} = 125.27$, $P = <0.001$) and dose by genotype interaction (ANCOVA, $F_{1,191} = 9.0$, $P = 0.003$). $n = 22$–29. **g**, Control and oe⁻ virgin females treated with cVA and assayed as in **f**. All oe⁻ females were treated with approximately 400ng of 7,11-HD. No significant differences were observed between genotypes and there was no significant dose by genotype interaction (ANCOVA, $F_{1,176} = 2.2$, $P = 0.14$), but the dose effect remains (ANCOVA, $F_{1,176} = 90.1$, $P < 0.001$). $n = 11$–37. Error bars indicate s.e.m.

illustrate an instance of post-copulatory sexual conflict[21] in which the attractant solicits additional mates despite the first male's effort to render a female unattractive by marking her with cVA.

In addition to mediating conspecific reproductive interactions, the hydrocarbons of female *D. melanogaster* have an important role in reproductive isolation between species[3–5]. For example, within the nine species of the *melanogaster* subgroup, only *D. melanogaster*, *D. sechellia* and *D. erecta* produce female-specific dienes[3,22]. Females in the rest of the subgroup express the same hydrocarbons as males[3,22]. Males of species with non-sexually dimorphic hydrocarbons generally do not court females from dimorphic species, indicating that the dienes might act as reproductive isolation barriers between these species groups[4,23]. Furthermore, males from dimorphic species do not vigorously court females from non-dimorphic species[2,4,23]. In contrast, males of all species in the *melanogaster* subgroup have similar hydrocarbons, including abundant 7-T[22]. Finally, *D. melanogaster* females lacking hydrocarbons are courted by at least two sibling species, *D. simulans* and *D. mauritiana*[5]. We tested the behaviour of males from other species in the *melanogaster* subgroup towards oe⁻ females, to assess the contribution of oenocytes and hydrocarbons to reproductive isolating mechanisms. We chose *D. simulans* and *D. yakuba* as test species because they represent species in which the females lack dienes. We included *D. erecta* because it differs from *D. melanogaster* in the pattern of dienes expressed[22] (Fig. 3a).

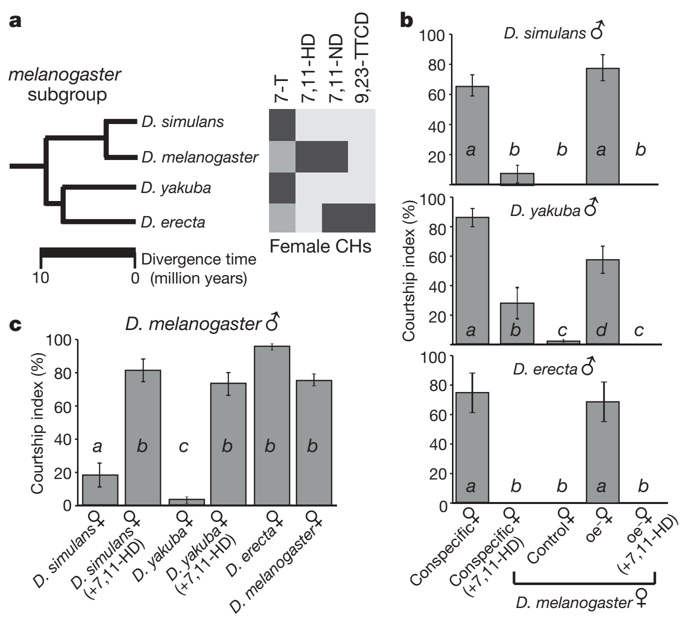

Figure 3 | 7,11-HD regulates courtship between *Drosophila* species.
a, Phylogenetic relationships of the four *Drosophila* species used in this study, along with a timescale for evolution in this group[29]. Partitioning of the four major female hydrocarbon compounds (7,11-HD; 7,11-ND; 9,23-TTCD, (9*Z*, 23*Z*)-tritriacontadiene) in these different species[22]: light grey indicates absence, grey indicates minor amounts, and black indicates a major fraction of the total hydrocarbon. **b**, Wild-type males courtship behaviour in intra- and interspecific pairings with females of the indicated species and genotype. $n = 10$–19. **c**, Wild-type *D. melanogaster* male courtship towards females from the indicated species. $n = 10$–12. Females labelled (+7,11-HD) were treated with approximately 500 ng of synthesized 7,11-HD. Error bars indicate s.e.m. Bars labelled by the same letter (*a*, *b*, *c* or *d*) in the histograms are not statistically different (ANOVA, $P < 0.01$).

Males of all three species courted oe⁻ *D. melanogaster* females, but exhibited limited or no courtship towards control *D. melanogaster* females (Fig. 3b and Supplementary Table 5). This indicates that oenocytes and their hydrocarbon products are major components of the reproductive isolation barrier, ensuring that courtship and mating attempts are only initiated between conspecifics. It has been proposed that 7,11-HD functions to create this barrier in *D. melanogaster*[4,5]. To test this directly, oe⁻ *D. melanogaster* females and wild-type females from the different species were treated with synthetic 7,11-HD. Treatment suppressed courtship by males of all three species (Fig. 3b and Supplementary Table 5), demonstrating that 7,11-HD alone is sufficient to create a species barrier. Interestingly, *D. erecta* males were blocked by 7,11-HD (Fig. 3b and Supplementary Table 5), despite the fact that hydrocarbons of *D. erecta* females include other dienes in common with those of *D. melanogaster* (Fig. 3a). Furthermore, *D. melanogaster* males actively courted *D. erecta* females (Fig. 3c), possibly because the diene 7,11-ND is also expressed by *D. melanogaster* females[22,23] (Fig. 3a). *D. simulans* and *D. yakuba* females treated with 7,11-HD elicited strong courtship from *D. melanogaster* males (Fig. 3c and Supplementary Table 5). These results demonstrate the multifunctional role of 7,11-HD as an attractant and/or stimulant for some species and as a deterrent for others.

Despite attempting copulation (Supplementary Table 5), *D. erecta* males never mated with oe⁻ females, suggesting that signals other than hydrocarbons are required to induce receptivity in these females[24]. However, within a 24-h period, nearly all oe⁻ *D. melanogaster* females mated with *D. simulans* males, whereas no control *D. melanogaster* females mated with these males (Fig. 4a). Treatment of oe⁻ females with 7,11-HD completely blocked interspecific mating with *D. simulans* males, even at a dose five times lower than the amount found in females of our wild-type *D. melanogaster* strain (Fig. 4b). Similar treatment of *D. simulans* females with 7,11-HD only delayed mating by *D. simulans* males (Fig. 4b). We hypothesized that 7-T counters the

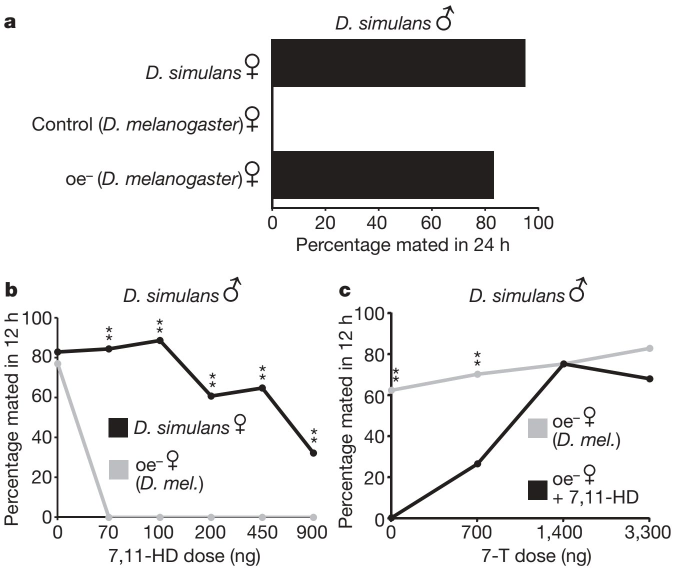

Figure 4 | Mating between *D. melanogaster* females and *D. simulans* males is prevented by 7,11-HD. a, Percentage of females of the indicated species and genotype that mated with *D. simulans* males in a 24-h period. $n = 18$–48. **b**, Percentage of *D. simulans* or oe⁻ *D. melanogaster* females that mated with *D. simulans* males in a 12-h period. Females were treated with increasing amounts of synthetic 7,11-HD. Single virgin females were paired with single *D. simulans* males. The fraction of pairs that mated within 12 h is reported. Asterisks indicate significant differences between genotypes as determined by a chi-squared test (**$P < 0.01$). $n = 10$–25. **c**, oe⁻ females treated with increasing amounts of synthetic 7-T and paired with *D. simulans* males as in **b**. One group of oe⁻ females was treated with approximately 200 ng of 7,11-HD in addition to 7-T. $n = 19$–37.

effect of 7,11-HD in *D. simulans* females. This is because 7-T functions as an aphrodisiac for *D. simulans* males and is expressed in higher quantities in *D. simulans* females than in *D. melanogaster* females[2]. We assayed *D. simulans* males with oe⁻ females treated with either 7-T alone, or in combination with 7,11-HD. Synthetic 7-T alone induced a slight decrease in mating latency, indicating that 7-T is an attractant for *D. simulans* males (Fig. 4c). However, the striking effect of 7-T was to reduce the effect of 7,11-HD in a dose-dependent manner (Fig. 4c). These data parallel the balancing effect of 7,11-HD on cVA for *D. melanogaster* males. Thus, we have demonstrated that female hydrocarbons orchestrate mating both within and between the species. Whereas a single compound such as 7,11-HD may be enough to establish a species barrier, the effect of this compound is moderated by the relative quantity of other signals. Indeed, the effects of 7,11-HD are particularly noteworthy because it functions as an attractant in an intraspecific context, whereas in an interspecific context, it aids in species recognition, thereby placing social communication and speciation on the same continuum.

The logic of pheromonal communication in *Drosophila* seems to be based on a foundation that imparts general attractiveness to a fly (Supplementary Fig. 3). In our study female oenocytes are the primary organ for communicating species and sex identity to males. Others have shown that males use species-specific acoustic tags within their love song for females during courtship[24–26]. Thus, both acoustic and pheromonal tags establish a context for social interactions by regulating sex and species recognition. Given that individual flies regulate their own hydrocarbon display in accord with their social surroundings[27], it is plausible that these compounds also function in individual recognition.

METHODS SUMMARY

Constructs and RT–PCR. cDNAs were synthesized from whole animals or dissected tissues using RNeasy Micro kit (Qiagen) and StrataScript cDNA synthesis kit (Stratagene). Oenocytes were dissected from 5–7-day-old adult flies as previously described[12]. *Desaturase 1* and *rp49* transcript- and/or gene-specific primers were described previously[11,12]. The *desat1* promoter E region (nucleotides 83507–84375 in GenBank accession AC007594) was amplified from bacterial artificial chromosome clone BACR28I14 (GenBank accession AC007594) overlapping *desaturase 1* and cloned upstream of the Gal4 coding sequence in a modified version of the insulated transformation vector pStingerII[28].

Fly strains. The *Canton-S* strain was used as the wild-type *D. melanogaster* strain. The *D. simulans* strain came from the Bloomington stock centre. The *D. erecta* and *D. yakuba* strains were gifts from N. Gompel. The *UAS-nuclear GFP* reporter was *UAS-StingerII*[28]. *UAS-hid* (ref. 14) and *tubP-Gal80^{ts}* (ref. 16) were obtained from the Bloomington stock centre. All transgenes, originally in a *white*-minus background, were placed in a *white*-plus background for behavioural studies. Adults lacking oenocytes were obtained from the progeny of the cross of '+: *PromE(800)-Gal4, tubP-Gal80^{ts}*;+' to '+: *UAS-StingerII, UAS-hid/CyO*;+'. Control adults were obtained from the progeny of the cross of '+: *PromE(800)-Gal4, tubP-Gal80^{ts}*;+' to '+: *UAS-StingerII*;+'.

Anatomical observations. Abdominal fillets and staining were performed as previously described[12].

Statistical analysis. Statistical analyses were performed with the SPSS software (version 16.0, SPSS inc.). Mating latency data were log-transformed, and courtship data arcsine-transformed, unless the raw values defined a normal distribution. All ANOVA tests were followed by the post-hoc Tukey–Kramer test.

Hydrocarbon treatment and analysis as well as behavioural assays and fly rearing are described in the Methods.

Full Methods and any associated references are available in the online version of the paper at www.nature.com/nature.

Received 23 May; accepted 9 September 2009.

1. Wyatt, T. D. *Pheromones and Animal Behaviour: Communication by Smell and Taste* (Cambridge Univ. Press, 2003).
2. Jallon, J. M. A few chemical words exchanged by *Drosophila* during courtship and mating. *Behav. Genet.* **14,** 441–478 (1984).
3. Ferveur, J. F. Cuticular hydrocarbons: their evolution and roles in *Drosophila* pheromonal communication. *Behav. Genet.* **35,** 279–295 (2005).
4. Coyne, J. A., Crittenden, A. P. & Mah, K. Genetics of a pheromonal difference contributing to reproductive isolation in *Drosophila*. *Science* **265,** 1461–1464 (1994).

5. Savarit, F., Sureau, G., Cobb, M. & Ferveur, J. F. Genetic elimination of known pheromones reveals the fundamental chemical bases of mating and isolation in *Drosophila. Proc. Natl Acad. Sci. USA* **96,** 9015–9020 (1999).
6. Grillet, M., Dartevelle, L. & Ferveur, J. F. A *Drosophila* male pheromone affects female sexual receptivity. *Proc. Biol. Sci.* **273,** 315–323 (2006).
7. Lacaille, F. *et al.* An inhibitory sex pheromone tastes bitter for *Drosophila* males. *PLoS One* **2,** e661 (2007).
8. Antony, C., Davis, T. L., Carlson, D. A., Pechine, J. M. & Jallon, J. M. Compared behavioral responses of male *Drosophila melanogaster* (*Canton S*) to natural and synthetic aphrodisiacs. *J. Chem. Ecol.* **11,** 1617–1629 (1985).
9. Ferveur, J. F. *et al.* Genetic feminization of pheromones and its behavioral consequences in *Drosophila* males. *Science* **276,** 1555–1558 (1997).
10. Fan, Y., Zurek, L., Dykstra, M. J. & Schal, C. Hydrocarbon synthesis by enzymatically dissociated oenocytes of the abdominal integument of the German Cockroach, *Blattella germanica. Naturwissenschaften* **90,** 121–126 (2003).
11. Marcillac, F., Bousquet, F., Alabouvette, J., Savarit, F. & Ferveur, J. F. A mutation with major effects on *Drosophila melanogaster* sex pheromones. *Genetics* **171,** 1617–1628 (2005).
12. Krupp, J. J. *et al.* Social experience modifies pheromone expression and mating behavior in male *Drosophila melanogaster. Curr. Biol.* **18,** 1373–1383 (2008).
13. Venken, K. J. & Bellen, H. Emerging technologies for gene manipulation in *Drosophila melanogaster. Nature Rev. Genet.* **6,** 167–178 (2005).
14. Zhou, L. *et al.* Cooperative functions of the *reaper* and *head involution defective* genes in the programmed cell death of *Drosophila* central nervous system midline cells. *Proc. Natl Acad. Sci. USA* **94,** 5131–5136 (1997).
15. Gutierrez, E., Wiggins, D., Fielding, B. & Gould, A. P. Specialized hepatocyte-like cells regulate *Drosophila* lipid metabolism. *Nature* **445,** 275–280 (2007).
16. McGuire, S. E., Le, P. T., Osborn, A. J., Matsumoto, K. & Davis, R. L. Spatiotemporal rescue of memory dysfunction in *Drosophila. Science* **302,** 1765–1768 (2003).
17. Butterworth, F. M. Lipids of *Drosophila*: a newly detected lipid in the male. *Science* **163,** 1356–1357 (1969).
18. Mane, S. D., Tompkins, L. & Richmond, R. C. Male Esterase 6 catalyzes the synthesis of a sex pheromone in *Drosophila melanogaster* females. *Science* **222,** 419–421 (1983).
19. Kurtovic, A., Widmer, A. & Dickson, B. J. A single class of olfactory neurons mediates behavioural responses to a *Drosophila* sex pheromone. *Nature* **446,** 542–546 (2007).
20. Imhof, M., Harr, B., Brem, G. & Schlötterer, C. Multiple mating in wild *Drosophila melanogaster* revisited by microsatellite analysis. *Mol. Ecol.* **7,** 915–917 (1998).
21. Hosken, D. J., Stockley, P., Tregenza, T. & Wedell, N. Monogamy and the battle of the sexes. *Annu. Rev. Entomol.* **54,** 361–378 (2009).
22. Jallon, J. M. & David, J. R. Variations in cuticular hydrocarbons among the eight species of the *Drosophila melanogaster* subgroup. *Evolution* **41,** 294–302 (1987).
23. Cobb, M. & Jallon, J. Pheromones, mate recognition and courtship stimulation in the *Drosophila melanogaster* species subgroup. *Anim. Behav.* **39,** 1058–1067 (1990).
24. Cowling, D. E. & Burnet, B. Courtship songs and genetic control of their acoustic characteristics in sibling species of the *Drosophila melanogaster* subgroup. *Anim. Behav.* **29,** 924–935 (1981).
25. Kyriacou, C. P. & Hall, J. C. Interspecific genetic control of courtship song production and reception in *Drosophila. Science* **232,** 494–497 (1986).
26. Wheeler, D. A. *et al.* Molecular transfer of a species-specific behavior from *Drosophila simulans* to *Drosophila melanogaster. Science* **251,** 1082–1085 (1991).
27. Kent, C., Azanchi, R., Smith, B., Formosa, A. & Levine, J. D. Social context influences chemical communication in *D. melanogaster* males. *Curr. Biol.* **18,** 1384–1389 (2008).
28. Barolo, S., Carver, L. A. & Posakony, J. W. GFP and β-galactosidase transformation vectors for promoter/enhancer analysis in *Drosophila. Biotechniques* **29,** 726–732 (2000).
29. Russo, C. A., Takezaki, N. & Nei, M. Molecular phylogeny and divergence times of drosophilid species. *Mol. Biol. Evol.* **12,** 391–404 (1995).

Supplementary Information is linked to the online version of the paper at www.nature.com/nature.

Acknowledgements We thank H. Pavlou for help with RNA collection; N. Gompel for sharing fly strains; and A. Dornan, S. Douglas, J. C. Hall, I. Dover, C. Kent, C. Kyriacou, K. Luoto, S. Goodwin, M. Ritchie, J. Schneider and M. Sokolowski for critical comments on the manuscript. J.-C.B. was supported by a fellowship for advanced researcher from the Swiss National Science Foundation. This work was supported by the Canadian Institutes of Health Research and Canada Research Chair grants awarded to J.D.L.

Author Contributions J.-C.B. and J.D.L designed and interpreted the study. J.-C.B., J.G.M. and J.D.L. wrote the paper. J.-C. B. generated the Gal4 transgenic line. J.-C.B. and J.A. performed the behavioural experiments and GC-FID analyses, and analysed the behavioural and analytical chemical data. J.J.K. performed the anatomical analyses of the oenocyte-less flies. J.G.M. synthesized and characterized 7-T and 7,11-HD. All authors read and commented on the paper.

Author Information Reprints and permissions information is available at www.nature.com/reprints. Correspondence and requests for materials should be addressed to J.D.L. (joel.levine@utoronto.ca).

METHODS

Fly rearing. All fly strains were reared on medium containing agar, glucose, sucrose, yeast, cornmeal, wheat germ, soya flour, molasses, propionic acid and Tegosept in a 12:12 h light/dark cycle at 25 °C, unless stated otherwise. Virgin adults were collected shortly after eclosion using CO_2 anaesthesia and were kept in same-sex groups of 20 in food vials, unless stated otherwise, and aged for 6–7 days.

Adults lacking oenocytes were obtained from the progeny of the cross of '+: *PromE(800)-Gal4, tubP-Gal80*^{ts};+' to '+: *UAS-StingerII, UAS-hid/CyO*;+'. Control adults were obtained from the progeny of the cross of '+: *PromE(800)-Gal4, tubP-Gal80*^{ts};+' to '+: *UAS-StingerII*;+'. Progeny were kept at 18 °C until eclosion. Adult progeny were collected at room temperature and kept at 25 °C for at least 24 h. Adults were subjected to three overnight heat treatments at 30 °C (on days 2, 3 and 4) and returned to 25 °C between treatments. Adults were briefly checked for GFP fluorescence on day 5 and left to recover for at least 24 h before experiments. Females appeared to tolerate these treatments better than males, which exhibited a high rate of mortality if not frequently transferred to fresh food vials. This is linked with the oenocyte ablation because control males tolerated the heat treatment better. We evaluated the oe^{-} flies for hypoactivity. Flies were monitored using the DAM system (Trikinetics). When monitored over a period of 5 days beginning with 6-day-old flies in the dark, the locomotor activity level of oe^{-} males was approximately 20% higher than control males ($P = 0.009$). The mean activity for oe^{-} males was 58.8 ± 3.5 counts h^{-1} ($n = 25$). Mean activity for control males was 46.7 ± 2.5 counts h^{-1} ($n = 24$). Thus the poor performance of oe^{-} males in mating and preference assays was not related to low levels of activity relative to controls.

Cuticular hydrocarbon analysis and treatment of flies with synthetic hydrocarbons. For hydrocarbon analysis, flies were anaesthetized with ether and placed into individual glass microvials containing 50 µl of hexane spiked with 10 ng ml^{-1} each of octadecane (C18) and 10 ng ml^{-1} of hexacosane (C26) as internal standards. Hydrocarbons were analysed using a Varian CP3800 gas chromatograph with a flame ionization detector as described previously[12]. Varian Star Integrator software (Varian Inc.) was used to quantify compounds based on peak areas.

For application of synthetic compounds, the compound of interest was dissolved in 1 ml of hexane (Sigma) and pipetted into a 2-ml glass vial (Varian Inc.). The hexane was evaporated under a nitrogen gas flow, leaving the compound as a residue coating the bottom of the vial. Groups of seven flies were transferred to coated vials and subjected to three medium vortex pulses lasting 20 s, with 20-s pauses between each pulse. This process did not seem to harm the flies. The treated flies were transferred to a fresh vial with food medium and allowed to recover and groom for 1 h. Four flies from each group were used for behavioural tests and the remaining three flies were subjected to hydrocarbon analysis to monitor effective transfer of the test compound to the flies. Hydrocarbon analysis for the three flies was taken as a proxy for the four flies used in the behavioural test. These measurements were performed for each experiment. The amount of compound used to coat the vial was determined empirically. For 7-T, 7,11-HD and cVA approximately 18%, 28% and 26% respectively of the compound in the vial was transferred onto the seven flies (or 2.6%, 4.0% and 3.7% per fly respectively). High purity cVA (~99%) was obtained from Pherobank. 7-T and 7,11-HD were synthesized as indicated in the Supplementary Information.

Behavioural assays. Flies were transferred to assay chambers using a mouth pipette, with the tip changed between flies to avoid hydrocarbon contamination. Courtship assays of male–female *D. melanogaster* were performed in a cylindrical Plexiglas chamber (10 mm diameter × 5 mm depth). The courtship index is the fraction of a 10-min observation period spent by the male exhibiting courtship steps such as following, tapping, wing extension, licking and attempting copulation. The wing extension index represents the fraction of a 10-min observation period during which the male performed the discrete courtship step of extending one of its wings. Attempted copulations represent the number of occurrences over a 10-min observation period of a male bending its abdomen at an angle greater than 90° according to his anterior–posterior body axis towards a subject being courted and failing to initiate copulation. Male–male behavioural observations were performed as for male–female interactions, except that males were collected shortly after eclosion and aged individually for 6–7 days in small vials with food medium. The courtship index of male–male interactions was also determined over a 10-min period, but starting from the onset of courtship and not from introduction as in male–female pairs. Courtship assays were scored blind to the genotype or treatment by two independent observers.

For heterospecific courtship assays, observations of single male–female pairs were made in 35 mm × 10 mm single use plastic Petri dish with a layer of food medium coating the bottom. Pairs were video recorded for 1 h. The courtship index was determined over a 10-min period starting from the time of courtship initiation. Given the similarity of courtship within the *melanogaster* subgroup[30], behavioural indices were determined using the same criteria as for *D. melanogaster* pairs. In the specific case of *D. yakuba*, males did not always court oe^{-} females. We excluded pairs in which males courted for less than 30 s. This represented 30% of the assays.

For mating latency assays, single male–female pairs were placed in 35 mm × 10 mm single use plastic Petri dishes as described above. Females were allowed to acclimate for at least 5 min before introduction of a male. Experiments were started around circadian time 8 and run for 24 h at 25 °C in a 12:12 h light/dark cycle with constant red light (680 nm) illumination. Pairs were observed live with a video camera for the first 30 min, and then via time-lapse images with 2-min intervals for 24 h. Images were scored for the time at which copulation events occurred. The time between male introduction and the onset of copulation was defined as the mating latency.

For the competitive mating assays, two males or two females were placed in a plastic Petri dish as described above and exposed to a single *Canton-S* adult of the opposite sex. Upon mating, the genotype of the flies was determined by observation under a dissecting microscope equipped with fluorescent illumination to determine the genotype of the mating pair. The control animals are GFP-positive and oe^{-} are GFP-negative. The *Canton-S* mating preference index was measured as the number of matings with oe^{-} flies minus the number of matings with control flies divided by the number of assays.

30. Cobb, M., Connolly, K. & Burnet, B. Courtship behaviour in the *melanogaster* species sub-group of *Drosophila*. *Behaviour* 95, 203–230 (1985).

Vol 461|15 October 2009|doi:10.1038/nature08430

LETTERS

A secreted complement-control-related protein ensures acetylcholine receptor clustering

Marie Gendrel[1,2], Georgia Rapti[1,2], Janet E. Richmond[3] & Jean-Louis Bessereau[1,2]

Efficient neurotransmission at chemical synapses relies on spatial congruence between the presynaptic active zone, where synaptic vesicles fuse, and the postsynaptic differentiation, where neurotransmitter receptors concentrate. Diverse molecular systems have evolved to localize receptors at synapses, but in most cases, they rely on scaffolding proteins localized below the plasma membrane[1–3]. A few systems have been suggested to control the synaptic localization of neurotransmitter receptors through extracellular interactions, such as the pentraxins that bind AMPA receptors and trigger their aggregation[4]. However, it is not yet clear whether these systems have a central role in the organization of postsynaptic domains *in vivo* or rather provide modulatory functions[5]. Here we describe an extracellular scaffold that is necessary to cluster acetylcholine receptors at neuromuscular junctions in the nematode *Caenorhabditis elegans*. It involves the ectodomain of the previously identified transmembrane protein LEV-10 (ref. 6) and a novel extracellular protein, LEV-9. LEV-9 is secreted by the muscle cells and localizes at cholinergic neuromuscular junctions. Acetylcholine receptors, LEV-9 and LEV-10 are interdependent for proper synaptic localization and physically interact based on biochemical evidence. Notably, the function of LEV-9 relies on eight complement control protein (CCP) domains. These domains, also called 'sushi domains', are usually found in proteins regulating complement activity in the vertebrate immune system[7]. Because the complement system does not exist in protostomes, our results suggest that some of the numerous uncharacterized CCP proteins expressed in the mammalian brain might be directly involved in the organization of the synapse, independently from immune functions.

Ionotropic acetylcholine receptors (AChRs) are pentameric ligand-gated ion channels. In *C. elegans*, both heteromeric and homomeric ionotropic AChRs are present at neuromuscular junctions. Heteropentameric AChRs are activated by the drug levamisole—a nematode-specific cholinergic agonist which causes muscle hypercontraction and death of wild-type animals at high concentrations[8,9]—and are inhibited by nicotine[10]. A second type of receptor, activated by nicotine and partially blocked by levamisole, is most likely composed of homomers of the ACR-16 subunit[10–12]. Notably, distinct machineries have evolved to localize levamisole-sensitive heteromeric AChRs (L-AChRs) and nicotine-sensitive homomeric AChRs (N-AChRs) at the synapse. LEV-10, a type 1 transmembrane protein with a large extracellular region comprising five CUB (complement, urchin EGF, BMP) domains and one LDLa (low-density lipoprotein receptor class A) domain, is required for the clustering of L-AChRs but not N-AChRs at the neuromuscular junction[6]. LEV-10 is expressed in muscle cells and co-localizes with L-AChRs at cholinergic neuromuscular junctions. When LEV-10 is absent, L-AChRs are expressed at levels similar to the wild type, correctly transported to the plasma membrane, but remain diffusely distributed at the surface of muscle cells. Interestingly, the synaptic localization of LEV-10 itself requires the expression of L-AChRs. Because the sole ectodomain of LEV-10 was demonstrated to be necessary and sufficient for the clustering activity of this protein, these results suggested a novel mechanism for AChR clustering relying on extracellular protein–protein interactions.

To identify additional components of this clustering machinery, we searched for mutants with a phenotype similar to *lev-10(0)* animals. *lev-9* mutants were originally identified in a screen for resistance to levamisole after chemical mutagenesis of the wild-type N2 strain[8]. Additional *lev-9* alleles were generated by insertional mutagenesis using the *Drosophila* transposon *Mos1* (refs 13, 14). Similar to *lev-10(0)* animals, all strains containing a mutation of the *lev-9* locus became paralysed on 1 mM levamisole but were more resistant than the wild type on lower drug concentrations (Supplementary Fig. 1). *lev-9* was identified as *T07H6.5* based on genetic mapping, identification of seven independent mutations in this locus, and rescue experiments (Fig. 1a, b). The *lev-9* messenger RNA is *trans*-spliced to the splice leader SL1, 210 bp upstream of the start codon (Fig. 1a; see Methods). It encodes a predicted 622-amino-acid secreted protein containing a signal peptide followed by a WAP (whey acidic protein) domain and eight CCP modules (Fig. 1b and Supplementary Fig. 2). WAP domains are present in various known proteins implicated in cell migration and cell adhesion as well as in secreted proteins with antimicrobial activity[15]. They seem to act mainly as proteinase inhibitors. However, animals with a deletion destroying the WAP domain are wild type, indicating that the WAP domain is not required for LEV-9 function (data not shown). CCP domains (also referred to as the 'sushi domain' and the 'short consensus repeat' SCR) are modules frequently found in regulators of complement activation in mammals[7]. The three-dimensional structure of numerous CCPs has been solved, showing that about 60 residues form a hydrophobic core wrapped by β-sheets held together by two strictly conserved disulphide bonds[16]. As in LEV-9, CCPs are frequently arranged in a chain, joined by linking sequences of three to eight amino acids, and provide interacting surfaces for proteins or glycans. Proteins containing one amino-terminal WAP domain followed by CCP repeats could be identified in other nematodes, as well as insects and fishes (Supplementary Fig. 3), but none has a characterized function.

To characterize the *lev-9* expression pattern, a green fluorescent protein (GFP) coding sequence preceded by a SL2 splice leader acceptor site was fused to the *lev-9* genomic fragment. This construct behaves as an artificial operon and leads to the expression of *lev-9* and *gfp* mRNAs in identical cells using *lev-9* regulatory sequences. Transgenic *lev-9* mutants expressed GFP solely in body wall muscle cells (Fig. 1c) and were rescued for levamisole sensitivity (Fig. 1d). To confirm that *lev-9* expression in muscle was sufficient, we expressed a

[1]ENS, Biology Department, Paris, F-75005 France. [2]INSERM, U789, Biologie cellulaire de la synapse, Paris F-75005, France. [3]Department of Biology, University of Illinois, Chicago, Illinois 60607, USA.

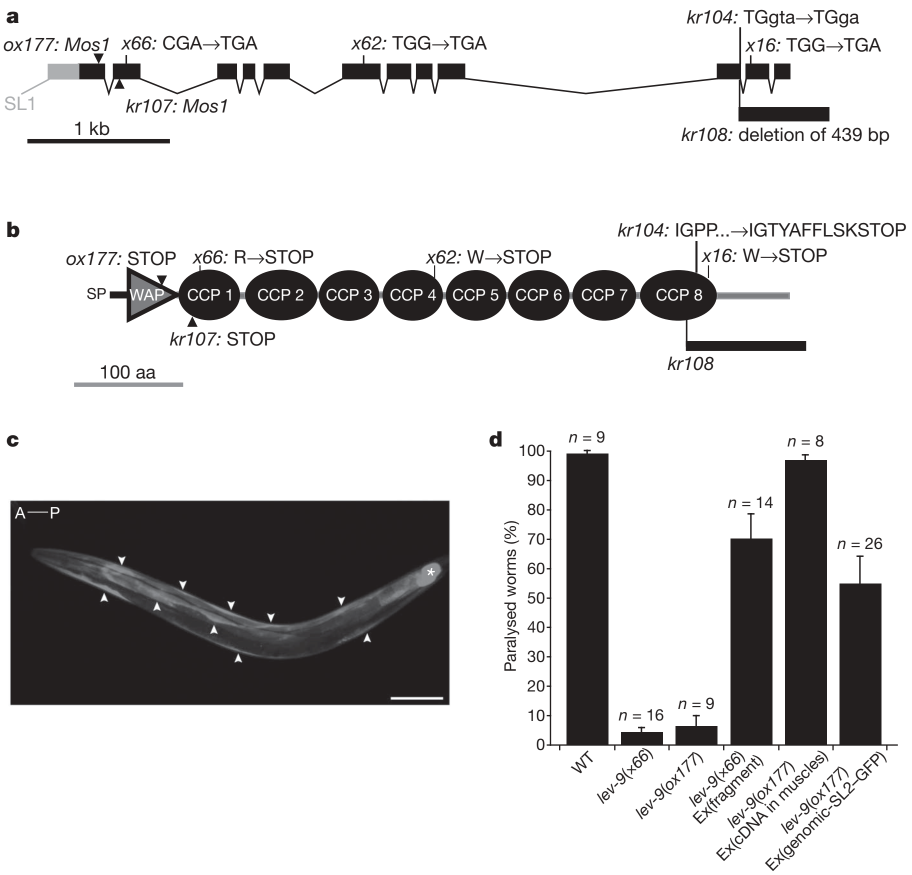

Figure 1 | *lev-9* encodes a muscle-expressed protein containing a WAP domain and eight CCP domains. **a**, Structure of the *lev-9* locus. Black boxes, coding regions; grey box, 5′ untranslated region; SL1, SL1 *trans*-spliced leader; black triangle, *Mos1* insertion; vertical black lines, point mutations. The starting codon is 141 bp upstream of the predicted ATG in Wormbase (WS200). **b**, LEV-9 is predicted to be a secreted protein. Horizontal black line, signal peptide; WAP, whey acidic protein domain; CCP, complement control protein domain; black triangle, *Mos1* insertion creating a premature STOP codon; vertical black line, point mutation resulting in the presence of a premature STOP codon; black box, deletion. **c**, *lev-9* is expressed in body wall muscle cells. An artificial operon containing a *lev-9* genomic fragment and a *gfp* drives GFP expression in body wall muscle cells (white arrows). Nonspecific fluorescence in posterior gut cells (white asterisk) is thought to be an indirect consequence of the *unc-54* 3′ untranslated region (UTR)[29]. A–P, anterior–posterior. Scale bar, 100 μm. **d**, A *lev-9* genomic fragment or a *lev-9* cDNA expressed in body wall muscle rescues the mutant phenotype. Bar graphs represent the percentage of dead animals after overnight exposure to 1 mM levamisole. (mean ± s.e.m., *n* = number of independent experiments, total number of tested animals is from 177 to 320). Transgenic *lev-9* animals have a wild-type (WT) phenotype when they contain the *lev-9* genomic fragment, the same *lev-9* genomic fragment in an artificial operon with *gfp*, or the *lev-9* cDNA under the control of the muscle promoter *Pmyo-3*.

lev-9 cDNA under the control of the muscle-specific promoter *Pmyo-3* and demonstrated the rescue of levamisole sensitivity of a *lev-9* mutant (Fig. 1d).

The primary sequence of LEV-9 predicts it to be a secreted protein. To test this prediction, we expressed a GFP–LEV-9 translational fusion in muscle. Fluorescence was detected in the pseudocoelomic cavity and in coelomocytes, six scavenger cells that filter the pseudocoelomic fluid[17] (Supplementary Fig. 5). Therefore, we concluded that LEV-9 is effectively secreted from body-wall muscle cells. To analyse the subcellular localization of LEV-9, we took advantage of the recently developed *Mos*TIC technique[18] to knock-in a T7 epitope tag sequence in the chromosomal *lev-9* locus, just after the signal peptide (Supplementary Fig. 6). *lev-9::T7* animals display a similar sensitivity to levamisole as wild-type animals. Immunofluorescence staining using anti-T7 antibodies specifically detected T7–LEV-9 as puncta distributed along the ventral and dorsal nerve cords and in the nerve ring where head muscles are innervated (Fig. 2a, b). These puncta were juxtaposed to cholinergic varicosities (Fig. 2c–e) and co-localized with L-AChR clusters (Fig. 2f–h and Supplementary Fig. 7). Together these results indicated that LEV-9 is a protein secreted by muscle cells, which localizes at cholinergic neuromuscular junctions, most probably in the synaptic cleft.

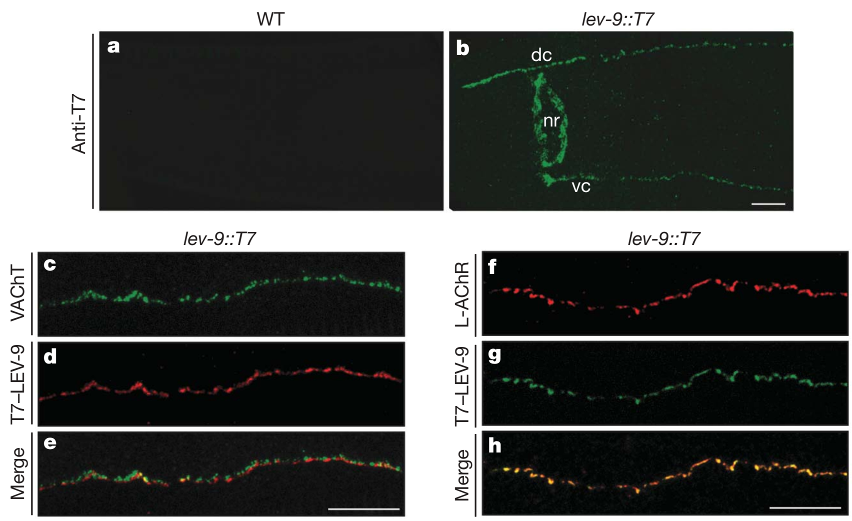

Figure 2 | LEV-9 localizes at cholinergic neuromuscular junctions. **a**, **b**, Immunofluorescence staining using anti-T7 antibodies specifically detects the T7–LEV-9 fusion protein in a *lev-9* knock-in animal at the nerve ring (nr), the dorsal (dc) and the ventral (vc) nerve cord. Scale bar, 10 μm. **c–e**, T7–LEV-9 clusters (**d**) are juxtaposed to cholinergic boutons visualized by immunostaining of the vesicular ACh transporter (VAChT) UNC-17 (**c**). Scale bar, 10 μm. **f–h**, T7–LEV-9 clusters (**g**) co-localize with L-AChR clusters visualized by immunostaining of the UNC-38 subunit (**h**). Scale bar, 10 μm.

The reduced sensitivity of the *lev-9* mutants to levamisole suggested that disrupting *lev-9* impairs L-AChR function. Consistently, immunofluorescence staining of L-AChRs in *lev-9* mutants was no longer detectable along the ventral and the dorsal nerve cords (Fig. 3a, b) and only weak staining was observed in the nerve ring (data not shown). To characterize the expression of N-AChRs, we raised antibodies against the ACR-16 subunit. L- and N-AChRs co-localized in the wild type (Supplementary Fig. 8c–h). In contrast to L-AChRs, the distribution of the N-AChRs was unaltered in *lev-9* mutants (Fig. 3c, d), suggesting that cholinergic synapses still differentiate. In agreement with this hypothesis, the staining pattern of cholinergic boutons in *lev-9* mutants was indistinguishable from wild-type animals (Fig. 3e, f). Because muscle cells also receive GABAergic innervation, we analysed the distribution of the muscle $GABA_A$ receptor UNC-49 by immunofluorescence. In *lev-9* mutants UNC-49 was properly clustered as in the wild type (Fig. 3g, h). Hence, the loss of *lev-9* function causes a specific loss of L-AChRs at the synapse. Western blot analysis of fractionated worm extracts indicated that L-AChRs were expressed at similar levels in the wild type and *lev-9* mutants (Fig. 3i). To test if L-AChRs were properly inserted in the plasma membrane and functional, we performed electrophysiological analysis. Pressure ejection of levamisole on to voltage-clamped muscle cells elicited similar currents in the wild type and *lev-9* mutants (Fig. 3j). These data indicated that the overall number of functional L-AChRs in the plasma membrane of *lev-9* mutants was the same as in the wild type. To probe the synaptic population of L-AChRs, we stimulated motor neurons in the ventral nerve cord and recorded evoked currents in individual muscle cells. This analysis was performed in an *unc-49;acr-16* double mutant background to eliminate currents due to GABA receptor and N-AChR activation. In *unc-49;acr-16;lev-9* triple mutants, the size of the evoked response was decreased by 84% compared with that of the double mutant *unc-49;acr-16* ($P = 0.0002$; Fig. 3k). In addition, the time to peak and decay time of the evoked currents were increased in *unc-49;acr-16;lev-9* as compared to *unc-49;acr-16* mutants, in agreement with a diffuse distribution of L-AChRs. In contrast, N-AChR-dependent evoked currents recorded in *unc-49;lev-9* and in *unc-49* mutants did not reveal any significant difference (2,654 ± 386 pA ($n = 5$) versus 2,140 ± 168 pA ($n = 9$), respectively; $P = 0.18$). In combination with immunostaining data, these results indicate that LEV-9 is specifically required for the clustering of L-AChRs at cholinergic synapses.

Disrupting either *lev-9* or *lev-10* genes causes extremely similar phenotypes. Because LEV-9 is a secreted protein and LEV-10 functions through its ectodomain, both proteins might be part of the same extracellular clustering machinery. To test this hypothesis, we analysed the respective distribution of the two proteins by immunofluorescence. Double labelling of the *lev-9::T7* knock-in strain using anti-T7 and anti-LEV-10 antibodies demonstrated that both proteins co-localized in discrete clusters (Fig. 4a–c). In *lev-9(ox177)* animals the LEV-10 synaptic clusters disappeared (Fig. 4d–g). However, western blot analysis of fractionated worm extracts indicated that LEV-10 was still expressed at a wild-type level in *lev-9* animals (Fig. 4h). These results were similar to those obtained in mutants lacking L-AChRs where LEV-10 was expressed but no longer detected at the synapse by immunofluorescence[6]. Hence, the clustering of LEV-10 requires LEV-9 and L-AChRs at the neuromuscular junctions.

We next analysed the distribution of LEV-9 in *lev-10(kr26)* and in *unc-29(x29)* null mutants. The T7–LEV-9 protein was no longer detectable in animals that did not express LEV-10 or L-AChRs (Fig. 4i–n). To quantify the overall amount of protein present in the different mutant backgrounds, we had to immunoprecipitate the T7–LEV-9 protein because it could not be detected simply by western blot experiments using worm extracts (data not shown). An approximately 68-kDa protein was specifically identified in *lev-9::T7* worm extracts using anti-T7 antibodies (Fig. 4o), in agreement with the size predicted from the LEV-9 primary sequence. By contrast, T7–LEV-9 was undetectable in *lev-10(kr26)* and *unc-29(x29)* worm

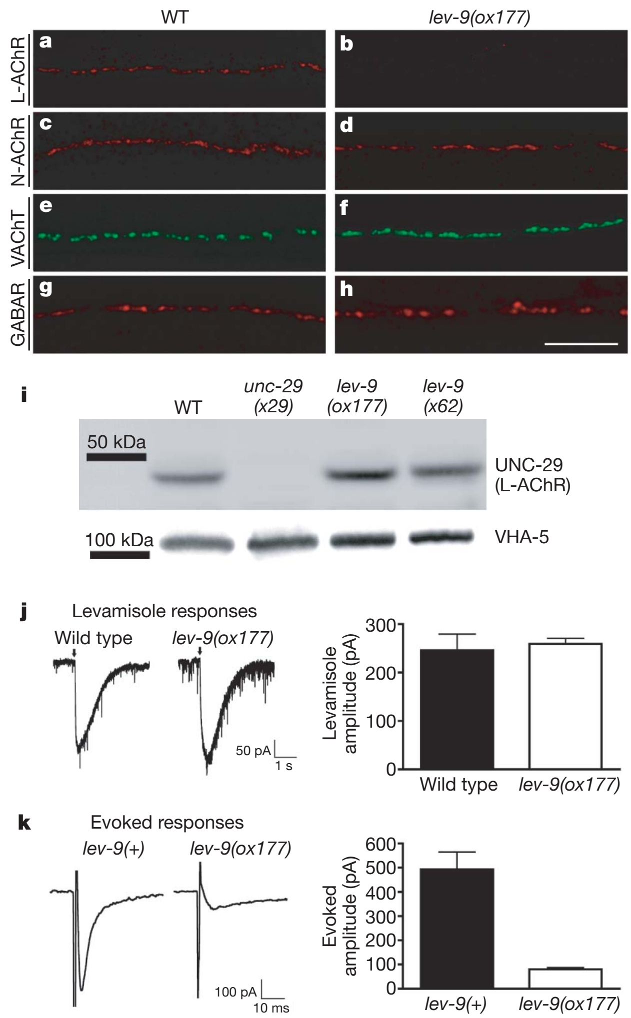

Figure 3 | LEV-9 is specifically required to localize L-AChRs at the neuromuscular junction. a–h, The L-AChR UNC-29 subunit cannot be detected at the dorsal cord by immunostaining in the *lev-9(ox177)* mutant (**b**) as compared to wild type (**a**). The N-AChR distribution is not affected in *lev-9(ox177)* mutants based on ACR-16 immunostaining (**c**, **d**). Presynaptic cholinergic varicosities have a similar distribution in wild-type (**e**) and *lev-9(ox177)* mutants (**f**). Immunostaining of the GABA receptor at neuromuscular junctions using anti-UNC-49 antibody reveals a similar distribution in wild-type animals (**g**) and in *lev-9(ox177)* mutants (**h**). Scale bar, 10 μm. **i**, L-AChRs are expressed at similar levels in wild-type and *lev-9* mutants based on western blot analysis. UNC-29 levels were normalized to VHA-5, the V0 'a' subunit of the vacuolar proton-translocating ATPase[30] (percentage of wild-type levels in *lev-9(ox177)* and *lev-9(x62)* was 124 ± 32% ($n = 2$) and 116 ± 45% ($n = 2$), respectively; mean ± absolute deviation). **j**. L-AChRs are functional in *lev-9* mutants. Currents recorded from voltage-clamped body-wall muscles in response to pressure ejection of levamisole are similar in wild type and *lev-9(ox177)* mutants. Black arrows mark the 100-ms application onset for 5×10^{-4} M levamisole. Error bars indicate mean of levamisole-elicited current amplitude plus s.e.m.; N2, $n = 11$; *lev-9(ox177)*, $n = 5$. **k**, L-AChRs are specifically reduced at cholinergic synapses. Evoked currents recorded in a body-wall muscle after eliciting neurotransmitter release by ventral nerve cord depolarization are strongly reduced in *lev-9(ox177)* mutants compared to wild-type animals. Experiments were performed in an *unc-49(e407);acr-16(ok789)* background to eliminate currents due to GABAR and N-AChR activation, respectively. Error bars indicate mean of evoked response amplitude plus s.e.m.; *lev-9(+)*, $n = 11$; *lev-9(ox177)*, $n = 6$. Time to peak and decay time were increased in *unc-49;acr-16;lev-9* as compared to *unc-49;acr-16* (6.45 ± 0.6 ms ($n = 6$) versus 4.2 ± 0.3 ms ($n = 7$), $P = 0.0035$, and 22.4 ± 2.6 ms ($n = 6$) versus 4.3 ± 0.6 ms ($n = 7$), $P = 0.0001$, respectively), in agreement with a diffuse distribution of L-AChRs.

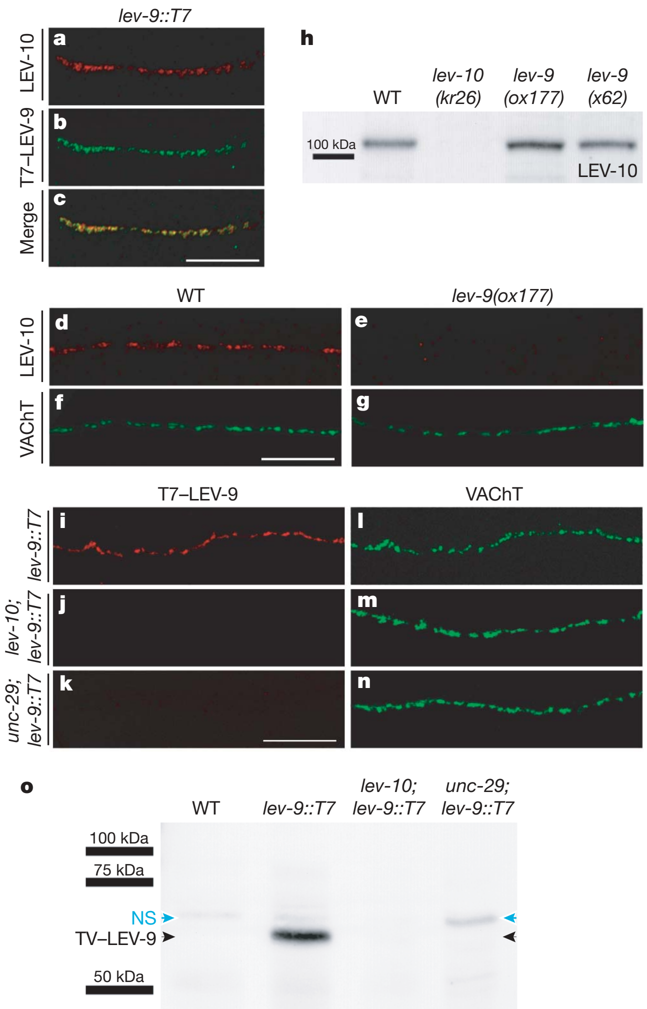

Figure 4 | LEV-9 and LEV-10 are interdependent for proper localization of L-AChRs. a–c, LEV-10 immunostaining in the dorsal cord (**a**) of a *lev-9::T7* knock-in animal shows that T7–LEV-9 clusters (**b**) co-localize with LEV-10 (**c**). Scale bar, 10 μm. **d–g**, LEV-10 clusters (**d**) are not detected in the *lev-9* mutant background (**e**). Immunostaining of the vesicular ACh transporter (VAChT) UNC-17 indicated that presynaptic differentiation is similar in wild type (**f**) and in *lev-9* mutants (**g**). Scale bar, 10 μm. **h**, LEV-10 is expressed at wild-type levels in *lev-9* mutants based on western blot analysis of total worm extracts. In *lev-9(ox177)* and in *lev-9(x62)*, levels of LEV-10 were similar to those in the wild type (107 ± 31% ($n = 3$) and 120 ± 46% ($n = 3$), respectively; mean ± s.e.m.). **i–n**, T7–LEV-9 is no longer clustered in *lev-10(kr26)* (**j**) or *unc-29(x29)* (**k**) mutant backgrounds. Immunostaining of the VAChT UNC-17 shows that presynaptic terminals are still correctly formed in all mutant backgrounds (**l–n**). Scale bar, 10 μm. **o**, T7–LEV-9 immunoprecipitation on total extracts of wild type or *lev-9::T7* knock-in animals in wild-type, *lev-10(kr26)* and *unc-29(x29)* backgrounds. The T7–LEV-9 protein has an apparent molecular mass of 68 kDa. Black arrows, $n = 2$ independent experiments; blue arrows, nonspecific (NS) bands.

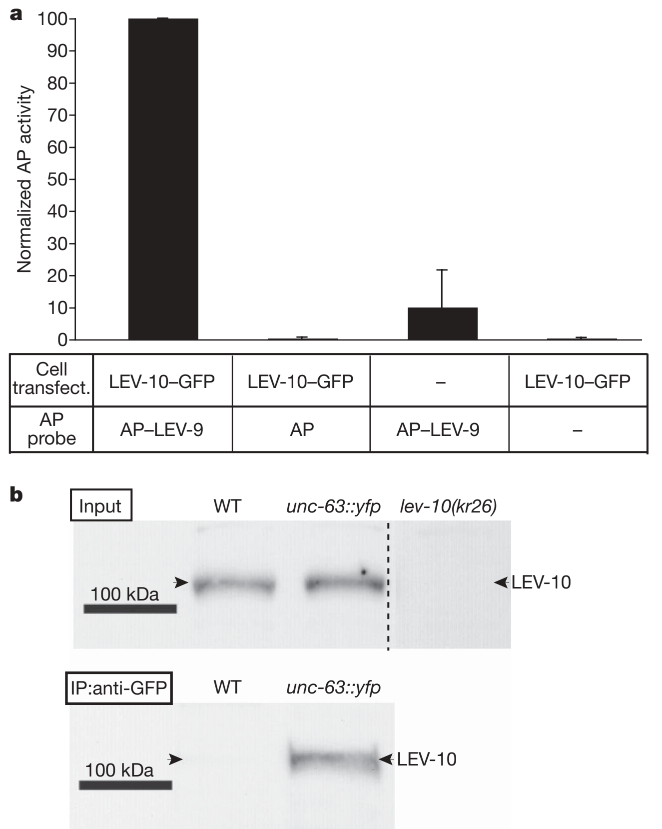

Figure 5 | LEV-9 physically interacts with LEV-10 and LEV-10 physically interacts with L-AChR. a, An alkaline phosphatase (AP)–LEV-9 fusion protein produced in HEK cells was used to probe S2 cells expressing the LEV-10–GFP fusion protein. Binding between LEV-9 and LEV-10 was monitored using the fluorogenic alkaline phosphatase substrate *p*-nitrophenyl phosphate. AP activities are normalized to the values obtained using AP–LEV-9 in combination with LEV-10–GFP (mean ± s.e.m., $n = 4$ independent experiments). AP alone and non-transfected S2 cells were used for controls. **b**, Immunoprecipitation of UNC-63–YFP using anti-GFP antibodies was followed by western blot to detect LEV-10. A specific LEV-10 signal is detected in the immunoprecipitation products of *unc-63::yfp* but not wild-type worm extracts ($n = 2$ independent experiments).

extracts, although *lev-9* mRNA levels were unchanged and GFP–LEV-9 was still secreted (not shown). These data, therefore, indicated that LEV-9, LEV-10 and L-AChRs are interdependent for synaptic localization. Unlike LEV-10 and L-AChRs, the levels of which remain unaltered when they fail to be concentrated at synapses, LEV-9 is probably degraded in the pseudocoelomic cavity when it cannot interact with LEV-10 and L-AChRs at the synapse.

To test if the three proteins LEV-9, LEV-10 and L-AChRs might assemble in one multi-molecular complex, we first used an alkaline phosphatase (AP)–LEV-9 fusion protein produced in HEK cells to probe *Drosophila* S2 cells expressing a LEV-10–GFP fusion protein. AP–LEV-9 specifically bound to cells expressing LEV-10 as reflected by quantitative measurement of AP activity (Fig. 5a), indicating that LEV-9 and LEV-10 can interact directly. Next, we performed immunoprecipitation experiments to test the interaction between LEV-10 and L-AChRs. To circumvent the lack of suitable antibodies for immunoprecipitation, we again used homologous recombination to introduce the *yfp* sequence in the chromosomal region coding for the TM3–TM4 intracellular loop of the L-AChR UNC-63 subunit. The UNC-63–YFP subunit localized properly at the synapse and was expressed at levels similar to the wild type based on electrophysiological analysis (Supplementary Fig. 9). Anti-GFP antibodies co-immunoprecipitated LEV-10 and L-AChRs from *unc-63::yfp* but not wild-type extracts (Fig. 5b), demonstrating that both proteins interact in a stable complex *in vivo*.

Altogether, our data suggest that LEV-9 and LEV-10 form an extracellular scaffold critical for localizing L-AChRs at the synapse, but they are dispensable for normal expression and insertion of the receptors in the plasma membrane. The presence of extrasynaptic L-AChRs in *lev-10* mutants was independently confirmed recently using the patch-clamp technique[19]. In this study, no L-AChRs could be detected in membrane patches from muscle cell bodies of wild-type animals, which are exclusively extrasynaptic, whereas active L-AChRs were detectable in similar membrane patches from *lev-10* mutants. On the basis of the multi-modular structure of LEV-9 and LEV-10, both proteins are likely to engage multiple interactions in this scaffold. LEV-10 interacts directly with LEV-9 and might also

interact with L-AChRs as LEV-10 and L-AChRs can be immunoprecipitated *in vivo*. Such a direct interaction could resemble the direct association of CUB-domain-containing proteins similar to LEV-10 with ionotropic receptors, such as the *C. elegans* SOL-1 with GLR-1 (ref. 20) and the mouse NETO1 and NETO2 with NMDA (*N*-methyl-D-aspartate) and kainate receptors, respectively[21,22].

The function of LEV-9 relies on a series of CCP domains, which have been mainly described in proteins of the complement system, either in regulators of complement activity or in components of the proteolytic cascade[7,23]. However, a growing number of CCP proteins do have a documented neuronal function. For example, Hikaru genki (Hig) is a secreted *Drosophila* protein containing four CCP domains which was detected in the synaptic cleft in the neuropile and proposed to modulate synapse physiology[24,25]. More recently, mutations in the human gene *SRPX2*, which encodes a secreted protein with three CCP domains and an immunoglobulin-related domain, were demonstrated to cause rolandic seizures associated with oral and speech dyspraxia and mental retardation[26]. Altogether, out of 52 genes encoding predicted CCP-domain-containing proteins in the mouse genome, 24 are expressed in the central nervous system based on the Brain Allen database. Because the complement system does not exist in protostomes[27], our results suggest that neuronal functions remain to be identified for these proteins in the mammalian brain apart from regulation of the immune system.

METHODS SUMMARY

***Mos*TIC experiments.** Generation of the KI strains was done as previously described[18,28]. Germline expression of the *Mos* transposase in animals containing the *Mos1* transposon triggers its excision and causes a DNA double-strand break at the excision site. The break can then be repaired by homologous recombination using a repair template containing sequence homologous to the broken locus provided on an extrachromosomal transgenic array. PCR screening identifies animals that inserted the sequence present in the repair template into the locus (Supplementary Fig. 6).

For generation of the *lev-9::T7* KI strain, *lev-9(ox177::Mos1)* animals were injected with a mixture of pJL44 (*hsp-16.48::MosTase*), pMG22 (repair template) and pPD118.33 (*Pmyo-2::gfp*). After transgenic lines were established, transgenic animals were heat-shocked and *Mos*TIC events were screened by PCR as described[18,28] using primers 5′-GCTAGCATGGCTTCTATGAC-3′ and 5′-TTTCTGGGTATTTTGAGTGG-3′ for the first PCR (1.5 mM $MgCl_2$; annealing time, 30 s; annealing temperature, 62 °C) and primers 5′-GAGGACAGCAGATGGGAGTC-3′ and 5′-TGTGGATATATTGCGGTTGC-3′ for the nested PCR (2.5 mM $MgCl_2$; annealing time, 1 min; annealing temperature, 62 °C).

For the *unc-63::yfp* KI strain, transgenic *unc-63(kr19::Mos1)* animals containing the *unc-63* repair template and pJL44 were generated as described above. After heat-shock, animals were allowed to recover overnight at 20 °C. Pools of 10 P0 worms were transferred to fresh plates every 12–24 h for 2 days to synchronize their progeny. *unc-63(kr19::Mos1)* animals show mild uncoordination. To isolate *Mos*TIC events, we screened for individuals with wild-type locomotion and wild-type sensitivity to levamisole. Individual candidates were cloned and wild-type phenotypes were confirmed.

Full Methods and any associated references are available in the online version of the paper at www.nature.com/nature.

Received 5 July; accepted 14 August 2009.
Published online 30 September 2009.

1. Elias, G. M. & Nicoll, R. A. Synaptic trafficking of glutamate receptors by MAGUK scaffolding proteins. *Trends Cell Biol.* **17,** 343–352 (2007).
2. Kneussel, M. & Loebrich, S. Trafficking and synaptic anchoring of ionotropic inhibitory neurotransmitter receptors. *Biol. Cell* **99,** 297–309 (2007).
3. Sanes, J. R. & Lichtman, J. W. Induction, assembly, maturation and maintenance of a postsynaptic apparatus. *Nature Rev. Neurosci.* **2,** 791–805 (2001).
4. O'Brien, R. J. *et al.* Synaptic clustering of AMPA receptors by the extracellular immediate-early gene product Narp. *Neuron* **23,** 309–323 (1999).
5. Bjartmar, L. *et al.* Neuronal pentraxins mediate synaptic refinement in the developing visual system. *J. Neurosci.* **26,** 6269–6281 (2006).
6. Gally, C., Eimer, S., Richmond, J. E. & Bessereau, J. L. A transmembrane protein required for acetylcholine receptor clustering in *Caenorhabditis elegans*. *Nature* **431,** 578–582 (2004).
7. Kirkitadze, M. D. & Barlow, P. N. Structure and flexibility of the multiple domain proteins that regulate complement activation. *Immunol. Rev.* **180,** 146–161 (2001).
8. Lewis, J. A., Wu, C. H., Berg, H. & Levine, J. H. The genetics of levamisole resistance in the nematode *Caenorhabditis elegans*. *Genetics* **95,** 905–928 (1980).
9. Fleming, J. T. *et al. Caenorhabditis elegans* levamisole resistance genes *lev-1*, *unc-29*, and *unc-38* encode functional nicotinic acetylcholine receptor subunits. *J. Neurosci.* **17,** 5843–5857 (1997).
10. Boulin, T. *et al.* Eight genes are required for functional reconstitution of the *Caenorhabditis elegans* levamisole-sensitive acetylcholine receptor. *Proc. Natl Acad. Sci. USA* **105,** 18590–18595 (2008).
11. Touroutine, D. *et al. acr-16* encodes an essential subunit of the levamisole-resistant nicotinic receptor at the *Caenorhabditis elegans* neuromuscular junction. *J. Biol. Chem.* **280,** 27013–27021 (2005).
12. Francis, M. M. *et al.* The Ror receptor tyrosine kinase CAM-1 is required for ACR-16-mediated synaptic transmission at the *C. elegans* neuromuscular junction. *Neuron* **46,** 581–594 (2005).
13. Bessereau, J. L. *et al.* Mobilization of a *Drosophila* transposon in the *Caenorhabditis elegans* germ line. *Nature* **413,** 70–74 (2001).
14. Williams, D. C., Boulin, T., Ruaud, A. F., Jorgensen, E. M. & Bessereau, J. L. Characterization of *Mos1*-mediated mutagenesis in *Caenorhabditis elegans*: a method for the rapid identification of mutated genes. *Genetics* **169,** 1779–1785 (2005).
15. Bingle, C. D. & Vyakarnam, A. Novel innate immune functions of the whey acidic protein family. *Trends Immunol.* **29,** 444–453 (2008).
16. Soares, D. C. *et al.* Large-scale modelling as a route to multiple surface comparisons of the CCP module family. *Protein Eng. Des. Sel.* **18,** 379–388 (2005).
17. Fares, H. & Greenwald, I. Genetic analysis of endocytosis in *Caenorhabditis elegans*: coelomocyte uptake defective mutants. *Genetics* **159,** 133–145 (2001).
18. Robert, V. & Bessereau, J. L. Targeted engineering of the *Caenorhabditis elegans* genome following *Mos1*-triggered chromosomal breaks. *EMBO J.* **26,** 170–183 (2007).
19. Qian, H., Robertson, A. P., Powell-Coffman, J. A. & Martin, R. J. Levamisole resistance resolved at the single-channel level in *Caenorhabditis elegans*. *FASEB J.* **22,** 3247–3254 (2008).
20. Zheng, Y., Mellem, J. E., Brockie, P. J., Madsen, D. M. & Maricq, A. V. SOL-1 is a CUB-domain protein required for GLR-1 glutamate receptor function in *C. elegans*. *Nature* **427,** 451–457 (2004).
21. Ng, D. *et al.* Neto1 is a novel CUB-domain NMDA receptor-interacting protein required for synaptic plasticity and learning. *PLoS Biol.* **7,** e41 (2009).
22. Zhang, W. *et al.* A transmembrane accessory subunit that modulates kainate-type glutamate receptors. *Neuron* **61,** 385–396 (2009).
23. Arlaud, G. J., Barlow, P. N., Gaboriaud, C., Gros, P. & Narayana, S. V. Deciphering complement mechanisms: the contributions of structural biology. *Mol. Immunol.* **44,** 3809–3822 (2007).
24. Hoshino, M., Suzuki, E., Nabeshima, Y. & Hama, C. Hikaru genki protein is secreted into synaptic clefts from an early stage of synapse formation in *Drosophila*. *Development* **122,** 589–597 (1996).
25. Hoshino, M. *et al.* Neural expression of hikaru genki protein during embryonic and larval development of *Drosophila melanogaster*. *Dev. Genes Evol.* **209,** 1–9 (1999).
26. Roll, P. *et al. SRPX2* mutations in disorders of language cortex and cognition. *Hum. Mol. Genet.* **15,** 1195–1207 (2006).
27. Nonaka, M. & Yoshizaki, F. Primitive complement system of invertebrates. *Immunol. Rev.* **198,** 203–215 (2004).
28. Robert, V. J., Katic, I. & Bessereau, J. L. *Mos1* transposition as a tool to engineer the *Caenorhabditis elegans* genome by homologous recombination. *Methods* doi:10.1016/j.ymeth.2009.02.013 (in the press).
29. Boulin, T., Etchberger, J. F. & Hobert, O. Reporter gene fusions. *WormBook* doi/10.1895/wormbook.1.106.1, 1–23 (2006).
30. Liegeois, S., Benedetto, A., Garnier, J. M., Schwab, Y. & Labouesse, M. The V0-ATPase mediates apical secretion of exosomes containing Hedgehog-related proteins in *Caenorhabditis elegans*. *J. Cell Biol.* **173,** 949–961 (2006).

Supplementary Information is linked to the online version of the paper at www.nature.com/nature.

Acknowledgements We thank E. M. Jorgensen and D. Williams for the *lev-9(ox171::Mos1)* strain, M. Labouesse for the anti-VHA-5 antibodies, J. Rand for the anti-UNC-17 antibodies, A. Fire for the GFP vectors, the Caenorhabditis Genetic Center and W. R. Schafer for strains, I. Katic, M. Zhen and S. Marty for critical reading of the manuscript, and H. Gendrot and B. Mathieu for technical help. M.G. was supported by a fellowship from the Ministère de la Recherche and by the Association Française contre les Myopathies. G.R. is a Ministère de la Recherche fellow. This work was funded by an INSERM Avenir grant, the Agence Nationale de la Recherche (ANR-07-NEURO-032-01) and the Association Française contre les Myopathies. J.E.R. was supported by NIH RO1 MH073156.

Author Contributions M.G. performed most of the experiments. J.E.R. performed all the electrophysiology experiments (Fig. 3j, k and Supplementary Fig. 9d). G.R. generated and characterized the *unc-63::YFP* knock-in strain. M.G. and J.-L.B. wrote the manuscript. J.-L.B. supervised the project.

Author Information The EMBL database accession number for *lev-9* cDNA is FN433774. Reprints and permissions information is available at www.nature.com/reprints. Correspondence and requests for materials should be addressed to J.-L.B. (jlbesse@biologie.ens.fr).

METHODS

General methods and strains. Strains were maintained at 20 °C on NG agar plates under standard conditions[31]. OP50 *Escherichia coli* was used for feeding, except for strains used for biochemistry, which were maintained on enriched peptone plates with HB101 *E. coli* for feeding. The wild-type reference strain was N2 Bristol. The following mutant alleles were used in this study: *lev-9(ox177::Mos1)*, *lev-9(x66)*, *lev-9(x62)*, *lev-9(x16)*, *lev-9(kr107::Mos1)*, *lev-9(kr104)*, *lev-9(kr108)*, *lev-9(kr184::T7)*, *lev-10(kr26::Mos1)*, *unc-29(x29)*, *unc-38(x20)*, *acr-16(ok789)*, *lin-15(n765ts)*, *unc-49(e407)*, *unc-49(e407);acr-16(ok789)*, *unc-49(e407);acr-16(ok789);lev-9(ox177)*, *unc-29(x29);lev-9(kr184::T7)*, *lev-10(kr26::Mos1);lev-9(kr184::T7)*, *lev-9(ox177::Mos1) lin-15(n765ts)*, *unc-63(kr19::Mos1 sd)*, *unc-63(kr98::yfp)*.

The following transgenic lines were generated for this study: (1) in *lev-9(x66)*: *krEx231* [*Plev-9(big)::lev-9;Pmyo-3::rfp;Prab-3::gfp*]; *krEx232* and *krEx233* [*Plev-9(small)::lev-9;Pmyo-3::gfp;Prab-3::gfp*]. (2) In *lev-9(ox177)*: *krEx245* and *krEx246* [*Pmyo-3::lev-9(cDNA)-gfp*;*Pmyo-2::gfp*]; *krEx371*, *krEx372* and *krEx373* [*lev-9 Mos*TIC fragment with T7 insertion;*Pmyo-2::gfp*;*Phsp::MosTransposase*]. (3) In *lev-9(ox177) lin-15(n765ts)*: *krEx247* and *krEx248* [*Pmyo-3::lev-9(cDNA)-gfp;lin-15(+)*]; *kr289* and *kr290* [*Pmyo-3::gfp-lev-9(cDNA)*;pEKL15 *lin-15(+)*]; *krEx402*, *krEx403* and *krEx404* [*Plev-9(small)::lev-9-SL2-gfp*, pEKL15 *lin-15(+)*]. (4) In *unc-63(kr19)*: *krEx227* [pGR06 (*Mos*TIC template *unc-63.rep.venus*);*Pmyo-2::gfp*;*Phsp::MosTransposase*].

Plasmid construction and PCR amplification. For *Plev-9(big)::lev-9*, a 6-kb genomic fragment corresponding to *C. elegans T07H6.5* was PCR-amplified from N2 genomic DNA using Taq polymerase (Invitrogen) (primers 5′- TCTG CAAATCACCTGAACACA-3′ and 5′-GGGGAAACAGTTCTGAAATAGC-3′).

For *Plev-9(small)::lev-9*, a 5.7-kb genomic fragment corresponding to *C. elegans T07H6.5* was PCR-amplified from N2 genomic DNA using Taq polymerase (Invitrogen) (primers 5′-TGAAAGTAAATGAAAAATCTTGCTG-3′ and 5′-GG GGAAACAGTTCTGAAATAGC-3′) .

For pMG11, *Pmyo-3::lev-9(cDNA)-gfp*, *lev-9* cDNA was cloned by RT–PCR using (1) primers 5′-CGCACGTGACCGGTATGCGATTTCTACTACTACTC G-3′ and 5′-TCTTCTCTGACTGGCACCAA-3′ and (2) primers 5′-CGCACGT GTCGGCCCTATCTTGTCCGGA-3′ and 5′-CGTCTAGAAAGGTACCGAGCT CACAGACCGAGACTCCATTGTC-3′. Phusion polymerase (Promega) was used. These PCR fragments were cloned in pPD115.62 using restriction sites AgeI, SpeI and KpnI.

For pMG12, *Pmyo-3::lev-9SP-NheI-SalI-lev-9*, the *lev-9 SP* (signal peptide) was PCR-amplified from pMG11 using 5′-CCACTAGATCCATCTAGAGG-3′ and 5′-CGGTCGACGCTAGCTAGTAGGGCCGACGCGTAGGTAATGG-3′ (fragment 1). *lev-9* cDNA without *SP* was PCR-amplified from pMG11 using 5′-CGGTCGACTCTTGTCCGGAAGTTACTCT-3′ and 5′-CGGAATTCGAGC TCTCAACAGACCGAGACTCCATTGTC-3′ (fragment 2). Fragment 1 was digested by XbaI and SalI, and fragment 2 was digested by SalI and EcoRI. These two digested fragments were ligated together into pPD115.62 digested by XbaI and EcoRI. PCRs were done using Phusion polymerase (Promega).

For pMG13, *Pmyo-3::lev-9SP-gfp-lev-9*, GFP was PCR-amplified from pPD115.62 using 5′-GCGCTAGCAAAGGAGAAGAACTTTTCACTG-3′ and 5′-GCGTCGACTTTGTATAGTTCATCCATGCCA-3′. The PCR fragment was cloned in pMG12 using restriction sites NheI and SalI. PCR was done using Phusion polymerase (Promega).

For pMG22, *lev-9::T7* (*Mos*TIC repair template for *lev-9* KI), the two primers 5′-CTAGCATGGCTTCTATGACCGGAGGACAGCAGATGGGAG-3′ and 5′-TC GACTCCCATCTGCTGTCCTCCGGTCATAGAAGCCATG-3′ were hybridized in a 50 mM NaCl 5 mM $MgCl_2$ buffer. The resulting fragment was subcloned in pMG12 using restriction sites NheI and SalI to generate pMG20. A 3.6-kb genomic fragment around the *Mos1* insertion site of *ox177* was PCR-amplified from N2 genomic DNA using Phusion polymerase (Promega) (primers 5′-GCGAAGCT TCACCAGCGAACGAAACTGACT-3′ and 5′-CGCGGTATACGCGTCTAACAA AAGGGGACA-3′). The PCR fragment was cloned in pATHScCRE using the restriction sites HindIII and Bst1107I to generate pMG21. pMG22 was obtained by subcloning a EagI–MluI fragment from pMG20 into pMG21. The sequence coding for the T7 tag (MASMTGGQQMG) was inserted at a position corresponding to residue 17 in LEV-9.

For pGR06, *unc-63::venus* (*Mos*TIC repair template for *unc-63* KI), the *unc-63* 3′ UTR was PCR-amplified from N2 genomic DNA using Phusion polymerase (Promega) (primers 5′-ATCGATCCCCAACAACACAT-3′ and 5′-AGCG GCCGCCGTAAGCTACCGGATTTCCA-3′) and inserted in pAF67[32] using the restriction sites PstI and NotI to generate pGR01. Two unique restriction sites, BglII and NheI, were inserted in the *unc-63* gene coding sequence to generate pGR02. The *venus* sequence optimized for expression in *C. elegans* was PCR-amplified from a *venus* vector (gift from D. Y. M. Coudreuse)[33] using Phusion polymerase (Promega) (primers 5′-ATAAGATCTAAAGGAGAAGAACTTTT CACTGG-3′ and 5′- AGCTAGCTTTGTATAGTTCATCCATGCCAAG-3′). The *venus* sequence was inserted in-frame with *unc-63* using the BglII–NheI restriction sites in pGR02, at a position corresponding to residue 383 in the TM3–TM4 loop (pGR04). The repair template pGR06 was generated by internal deletion of pGR04 by Acc651 and Bsp120I digestion and self-religation.

For pMG23, *Plev-9(small)::lev-9-SL2-gfp*, a 5.7-kb genomic fragment corresponding to *C. elegans T07H6.5* was PCR-amplified from N2 genomic DNA using Phusion polymerase (Promega) (primers 5′-CGGCATGCGGGGAAACA GTTCTGAAATAGC-3′ and 5′-CGGGTACCTCAACAGACCGAGACTCCAT TG-3′). This PCR fragment was cloned in pEXPR *gcy-32-egl-2(gf)* (gift from M. de Bono) at the restriction sites SphI and KpnI.

For pMG26, *PMT-lev-10-egfp*, *lev-10* cDNA was PCR-amplified using Phusion polymerase (Promega) using 5′-CGCGATATCATGCATTTGATC TACCTATTC-3′ and 5′-CGCGCTCGAGAGCATACATATCACGCGATG-3′ from pCG034[6] (fragment 1). eGFP was PCR-amplified using Phusion polymerase (Promega) from pIRES2-eGFP (5′-GCGCTCGAGATGGTGAGCAAGGGC GAGGAG-3′ and 5′-CGCGGGTACCTTACTTGTACAGCTCGTCC-3′) (fragment 2). Fragment 1 was digested by EcoRV and XhoI, and fragment 2 was digested by XhoI and KpnI. The digested fragments were then ligated together into pMT-GAL4 digested by EcoRV and KpnI (MT stands for metallothionein promoter).

For pMG27, *pCMV::T7-AP-lev-9(cDNA)-myc-his*, *lev-9* cDNA was PCR-amplified using Phusion polymerase from pMG11 (5′-GGCTCGAGCTATCTT GTCCGGAAGTTAC-3′ and 5′-GCTCTAGAGAACAGACCGAGACTCCAT TG-3′) (fragment 1). Hybridization of the two primers 5′-AGCTTTAATGG CTTCTATGACCGGAGGACAGCAGATGGGAA-3′ and 5′-GATCTTCCCA TCTGCTGTCCTCCGGTCATAGAAGCCATTAA-3′ was done in a 50 mM NaCl, 5 mM $MgCl_2$ buffer (fragment 2). Fragment 1 was digested by XhoI and XbaI and cloned into APtag-5 (ref. 34) to generate pMG25. Fragment 2 was digested by HindIII and BglII and subcloned into pMG25.

Germline transformation. Transformation was performed by microinjection of plasmid DNA into the gonad[35].

For *lev-9(x66)* rescue, animals were injected with a DNA mixture containing the large *lev-9* genomic fragment (5 ng μl^{-1}), pAF75 (*Pmyo-3::rfp*; 10 ng μl^{-1}), pHU4 (*Prab-3::gfp*; 20 ng μl^{-1}) and 1 kb$^+$ DNA ladder (Invitrogen; 65 ng μl^{-1}), or a small *lev-9* genomic fragment (1 ng μl^{-1}), pPD115.62 (*Pmyo-3::gfp*; 5 ng μl^{-1}), pHU4 (*Prab-3::gfp*; 20 ng μl^{-1}) and 1 kb$^+$ DNA ladder (Invitrogen; 74 ng μl^{-1}).

For the expression pattern, pMG23 (*Plev-9(small)::lev-9-SL2-gfp*) was injected either in *lev-9(ox177)* at 10 ng μl^{-1} with pAF75 (*Pmyo-3::rfp*; 10 ng μl^{-1}) as co-injection marker and 1 kb$^+$ DNA ladder (Invitrogen; 80 ng μl^{-1}) or in *lev-9(ox177) lin-15(n765ts)* at 1 ng μl^{-1} with pEKL15 (*lin-15(+)*; 99 ng μl^{-1}).

For tissue-specific rescue, pMG11 (*Pmyo-3::lev-9(cDNA)-gfp*) was injected either in *lev-9(ox177)* at 10 ng μl^{-1} with pPD118.33 (*Pmyo-2::gfp*; 10 ng μl^{-1}) as co-injection marker and 1 kb$^+$ DNA ladder (Invitrogen; 80 ng μl^{-1}) or in *lev-9(ox177) lin-15(n765ts)* at 1 ng μl^{-1} with pEKL15 (*lin-15(+)*; 80 ng μl^{-1}) as co-injection marker. pMG13 (*Pmyo-3::lev-9SP-gfp-lev-9(cDNA* without *SP)*) was injected in *lev-9(ox177) lin-15(n765ts)* at 10 ng μl^{-1} with pEKL15 (*lin-15(+)*; 90 ng μl^{-1}).

For *Mos*TIC experiments, pMG22 (*lev-9* repair template) was injected in *lev-9(ox177)* either at 50 ng μl^{-1} or at 25 ng μl^{-1} with pPD118.33 (*Pmyo-2::GFP*; 5 ng μl^{-1}) as co-injection marker and pJL44 (*hsp-16.48::transposase*; 50 ng μl^{-1}). pGR06 (*unc-63* repair template) was injected at 10 ng μl^{-1} with pPD118.33 (*Pmyo-2::gfp*; 5 ng μl^{-1}) as co-injection marker and pJL44 (*hsp-16.48::transposase*; 50 ng μl^{-1}).

Levamisole resistance assay. (−)-Tetramisole (Sigma) was dissolved in water and added to 55 °C-equilibrated NG agar at a concentration of 0.2 mM, 0.4 mM, 0.6 mM, 0.8 mM or 1 mM just before plates were poured. For the 1 mM levamisole overnight exposure assay, young adult worms were placed overnight at 20 °C on 1 mM levamisole plates seeded with OP50 *E. coli*. Surviving animals were then scored. For the levamisole dose response curve, young adult worms were scored blind for paralysis after a 2 h exposure to different levamisole concentrations. The plates were tapped ten times on the bench before scoring animals moving the distance of at least one body length.

***Mos*TIC experiments.** Generation of the KI strains was done as previously described[18,28].

For generation of the *lev-9::T7* KI strain, *lev-9(ox177::Mos1)* animals were injected with a mixture of pJL44 (*hsp-16.48::MosTase*), pMG22 (repair template) and pPD118.33 (*Pmyo-2::gfp*). After transgenic lines were established, transgenic animals were heat-shocked and *Mos*TIC events were screened by PCR as described[18,28] using primers 5′-GCTAGCATGGCTTCTATGAC-3′ and 5′-TTT CTGGGTATTTTGAGTGG-3′ for the first PCR (1.5 mM $MgCl_2$; annealing time, 30 s; annealing temperature, 62 °C) and primers 5′-GAGGACAGCAGATG

GGAGTC-3′ and 5′-TGTGGATATATTGCGGTTGC-3′ for the nested PCR (2.5 mM $MgCl_2$; annealing time, 1 min; annealing temperature, 62 °C).

For the *unc-63::yfp* KI strain, transgenic *unc-63(kr19::Mos1)* animals containing the *unc-63* repair template and pJL44 were generated as described above. After heat-shock, animals were allowed to recover overnight at 20 °C. Pools of 10 P0 worms were transferred to fresh plates every 12–24 h for 2 days to synchronize their progeny. *unc-63(kr19::Mos1)* animals show mild uncoordination. To isolate *Mos*TIC events, we screened for individuals with wild-type locomotion and wild-type sensitivity to levamisole. Individual candidates were cloned and wild-type phenotypes were confirmed.

Antibody production. For anti-UNC-38 antibodies, a DNA fragment encoding UNC-38 amino acids 375–418 was inserted into pGEX-3X. The glutathione *S*-transferase (GST)–UNC-38 fusion protein was expressed in *E. coli* and purified. Rabbits were injected with 100 μg of fusion protein and boosted three times with 100 μg each. Antibodies were then purified as previously described[36] using fusion protein GST–UNC-38 blotted on nitrocellulose.

For anti-ACR-16 antibodies, a DNA fragment encoding ACR-16 amino acids 348–459 was inserted into pATHSc. The histidine (His)–ACR-16 fusion protein was expressed using BL21(DE3)pLysS bacteria and purified. Guinea-pigs were injected with 50 μg of fusion protein and boosted three times with 50 μg each. Antibodies were then purified as previously described[36] using fusion protein His–ACR-16 blotted on nitrocellulose.

Antibodies against UNC-49, UNC-29 and LEV-10 were produced as previously described[6,37].

Immunocytochemical staining. Worms were prepared using the freeze-crack method described previously[38] using SuperFrost slides (Menzel-Glaser) and then fixed either in −20 °C methanol for 5 min and in −20 °C acetone for 5 min or in PFA 4% (paraformaldehyde) for 15 min when using anti-T7 antibodies. Worms were then collected in PBS 1× and immunofluorescence staining was performed on fixed nematodes in suspension. Samples were blocked for 30 min at room temperature with 0.2% gelatine from fish (Sigma). Anti-UNC-49 antibodies were used at a 1:800 dilution. Anti-UNC-38 antibodies were used at a 1:800 dilution. Anti-ACR-16 antibodies were used at a 1:100 dilution. Anti-GFP monoclonal antibodies (Roche) were used at a 1:500 dilution. Incubations were done overnight at 4 °C.

For double-labelling experiments, procedures were optimized for the combination of proteins to detect. Anti-UNC-17 monoclonal antibodies[39] were used at a 1:3,000 dilution and incubated for 1 h at room temperature, and after a 1 h wash, either anti-UNC-29 (1:800) or anti-LEV-10 antibodies were incubated overnight at 4 °C. Anti-UNC-38 antibodies or rabbit anti-GFP (Molecular Probes; 1:500) were incubated overnight at 4 °C, and after a 1 h wash, anti-UNC-17 antibodies were incubated 1 h at room temperature. Anti-UNC-38 or anti-UNC-29 were incubated overnight at 4 °C, then after 1 h of washing anti-GFP monoclonal antibodies were incubated for 1 h at room temperature. Anti-ACR-16 and anti-UNC-38 antibodies or anti-ACR-16 and anti-UNC-49 antibodies were incubated together overnight at 4 °C. Anti-T7 monoclonal antibodies (Novagen) were used at a 1:500 dilution and were incubated overnight at 4 °C. For double-labelling experiments, mouse anti-T7 and anti-UNC-38 antibodies, mouse anti-T7 and anti-LEV-10 antibodies, and rabbit anti-T7 (Genetex; 1:1,000) and anti-UNC-17 antibodies were incubated together overnight at 4 °C.

Secondary antibodies included Cy3-labelled goat anti-rabbit IgG (H+L) (Jackson ImmunoResearch Laboratories) used at a 1:1,000 dilution, Cy3-labelled goat anti-guinea-pig IgG (H+L) (Jackson ImmunoResearch Laboratories) 1:1,000, Alexa-488-labelled goat anti-mouse (Molecular Probes) 1:500, Alexa-488-labelled goat anti-rabbit IgG (H+L) (Molecular Probes) 1:2,000, and Cy3-labelled goat anti-mouse IgG (H+L) (Jackson ImmunoResearch Laboratories) 1:1,000.

Electrophysiological studies. Electrophysiological methods were as previously described[40,41]. Animals were immobilized with cyanoacrylic glue and a lateral cuticle incision was made exposing the ventral medial body wall muscles. Muscle whole-cell voltage-clamp recordings were obtained at a holding potential of –60 mV using an EPC-10 patch-clamp amplifier and digitized at 1 kHz. The extracellular solution consisted of (in mM): NaCl 150, KCl 5, $CaCl_2$ 5, $MgCl_2$ 4, glucose 10, sucrose 5, HEPES 15 (pH 7.3, ~340 mOsm). The patch pipette was filled with (in mM): KCl 120, KOH 20, $MgCl_2$ 4, *N*-tris[hydroxymethyl] methyl-2-aminoethane-sulphonic acid 5, $CaCl_2$ 0.25, Na^2ATP 4, sucrose 36, EGTA 5 (pH 7.2, ~315 mOsm). Data were acquired using Pulse software (HEKA) run on a Dell computer. Subsequent analysis and graphing were performed using Pulsefit (HEKA), Mini analysis (Synaptosoft Inc.) and Igor Pro (Wavemetrics).

Protein extraction and western blotting. A mixed stage population of worms (2 ml) was frozen at −80 °C until use. For extraction, worm pellets were ground under liquid nitrogen and thawed in an equal volume of ice-cold homogenization buffer (50 mM HEPES pH 7.7, 50 mM KCl, 2 mM $MgCl_2$, 250 mM sucrose, 1 mM EDTA pH 8, 2 mM PMSF and two tablets of complete Protease inhibitor cocktail (Roche) in 50 ml). The suspension was further homogenized by sonication and centrifuged at 5,800*g* for 12 min at 4 °C to remove worm debris. The low speed supernatant (LSS) was either kept to detect the presence of LEV-10 protein or centrifuged at 100,000*g* for 1 h at 4 °C to produce a high speed pellet (HSP). The HSP was then dissolved in 100–500 μL of resuspension buffer (10 mM Tris pH 8, 0.1% Triton X-100, 1 mM EDTA pH 8). UNC-29 protein was detected within the HSP fraction. Western blot experiments were performed as described[6].

Immunoprecipitation and western blotting. For GFP immunoprecipitation, the LSS, obtained as described above, was brought up to 15 ml with homogenization buffer supplemented with 100 mM NaCl and 1% Triton X-100, to which 50 μl of agarose-conjugated anti-GFP beads (MBL) was added. After overnight incubation at 4 °C, beads were sedimented and washed once in 50 mM HEPES pH 7.7, 100 mM NaCl, 50 mM KCl, 2 mM $MgCl_2$, 250 mM sucrose, 1 mM EDTA, 1% Triton X-100, and once in 50 mM HEPES pH 7.7, 50 mM NaCl. Proteins were eluted in Laemmli buffer and analysed by western blot as above. LEV-10 was detected using anti-LEV-10 antibodies (dilution 1:250).

For T7 immunoprecipitation, a mixed stage population of worms (2 ml) was cleaned using sucrose floatation and frozen at −80 °C before use. Worm lysate was generated as above except the homogenization buffer contained 50 mM Tris pH 8 (instead of HEPES), 150 mM NaCl and 5 mM EDTA. The lysate volume was brought up to 15 ml with homogenization buffer supplemented with 1% Triton X-100, 1% SDS and 1% deoxycholate and mixed for 6 h at 4 °C. Afterwards, the suspension was centrifuged at 5,800*g* for 12 min at 4 °C to remove worm debris. A total of 5 μl of rabbit anti-T7 antibodies (MBL) were incubated with the supernatant overnight at 4 °C. Protein G sepharose beads (Sigma) were then added and mixed for 1 h at 4 °C. Beads were sedimented and washed three times with the homogenization buffer containing the detergents and three times with 50 mM HEPES pH 7.7, 50 mM NaCl. Proteins were eluted in Laemmli buffer and analysed by western blot as above. T7–LEV-9 was detected using anti-T7 monoclonal antibodies (Novagen; dilution 1:10,000).

Binding assays. S2 cells were maintained in Schneider's *Drosophila* medium (Invitrogen) with 10% FBS. pMG26 (*PMT-lev-10-gfp*) was transfected into S2 cells with Lipofectamine (Invitrogen). Twenty-four hours after transfection, the metallothionein (MT) promoter was activated by adding $CuSO_4$ at a 700 μM final concentration.

For AP–LEV-9 production, pAPtag-5 (*pCMV::AP-myc-his*) and pMG27 (*pCMV::T7-AP-lev-9-myc-his*) were transfected into HEK293T cells with Lipofectamine (Invitrogen). Three days after transfection, supernatants of cultured cells were collected and concentrated using iCON concentrator 9K (Pierce) devices. The relative amount of AP fusion protein contained in the supernatant was evaluated using phosphatase substrate (*p*-nitrophenyl phosphate; Sigma) turning yellow in the presence of AP and that can be read spectrophotometrically at 405 nm.

Quantitative assays were performed as described[34]. In brief, concentrated HEK supernatants were applied to S2 cells for 90 min. The presence of AP on S2 cells was detected by scraping cells and measuring AP activity using *p*-nitrophenyl phosphate.

Microscopy. Animals were anaesthetized with M9 buffer containing 3.8 mM tricaine, 0.42 mM tetramisole and 20 mM sodium azide, mounted on 1× M9, 2% agarose pads, and examined using either a Leica SP2 confocal microscope or a Leica 5000B microscope and spinning disk CSU10 (Yokogawa). Immunofluorescence staining was examined under the Leica 5000B microscope. Image reconstruction and merges were obtained with Image J.

31. Brenner, S. The genetics of *Caenorhabditis elegans*. *Genetics* **77**, 71–94 (1974).
32. Ruaud, A. F. & Bessereau, J. L. Activation of nicotinic receptors uncouples a developmental timer from the molting timer in *C. elegans*. *Development* **133**, 2211–2222 (2006).
33. Coudreuse, D. Y., Roel, G., Betist, M. C., Destree, O. & Korswagen, H. C. Wnt gradient formation requires retromer function in Wnt-producing cells. *Science* **312**, 921–924 (2006).
34. Flanagan, J. G. *et al.* Alkaline phosphatase fusions of ligands or receptors as *in situ* probes for staining of cells, tissues, and embryos. *Methods Enzymol.* **327**, 19–35 (2000).
35. Mello, C. C., Kramer, J. M., Stinchcomb, D. & Ambros, V. Efficient gene transfer in *C. elegans*: extrachromosomal maintenance and integration of transforming sequences. *EMBO J.* **10**, 3959–3970 (1991).
36. Miller, K. G., Emerson, M. D., McManus, J. R. & Rand, J. B. RIC-8 (Synembryn): a novel conserved protein that is required for $G_q\alpha$ signaling in the *C. elegans* nervous system. *Neuron* **27**, 289–299 (2000).
37. Gally, C. & Bessereau, J. L. GABA is dispensable for the formation of junctional GABA receptor clusters in *Caenorhabditis elegans*. *J. Neurosci.* **23**, 2591–2599 (2003).
38. Duerr, J. S. *et al.* The *cat-1* gene of *Caenorhabditis elegans* encodes a vesicular monoamine transporter required for specific monoamine-dependent behaviors. *J. Neurosci.* **19**, 72–84 (1999).
39. Duerr, J. S., Gaskin, J. & Rand, J. B. Identified neurons in *C. elegans* coexpress vesicular transporters for acetylcholine and monoamines. *Am. J. Physiol. Cell Physiol.* **280**, C1616–C1622 (2001).

40. Richmond, J. E., Davis, W. S. & Jorgensen, E. M. UNC-13 is required for synaptic vesicle fusion in *C. elegans*. *Nature Neurosci.* **2**, 959–964 (1999).

41. Richmond, J. E. Electrophysiological recordings from the neuromuscular junction of *C. elegans*. *WormBook* doi/10.1895/wormbook.1.112.1, 1–8 (2006).

Vol 461 | 15 October 2009 | doi:10.1038/nature08446

LETTERS

Spatiotemporal control of cell signalling using a light-switchable protein interaction

Anselm Levskaya[1,2,3], Orion D. Weiner[1,4], Wendell A. Lim[1,5] & Christopher A. Voigt[1,3]

Genetically encodable optical reporters, such as green fluorescent protein, have revolutionized the observation and measurement of cellular states. However, the inverse challenge of using light to control precisely cellular behaviour has only recently begun to be addressed; semi-synthetic chromophore-tethered receptors[1] and naturally occurring channel rhodopsins have been used to perturb directly neuronal networks[2,3]. The difficulty of engineering light-sensitive proteins remains a significant impediment to the optical control of most cell-biological processes. Here we demonstrate the use of a new genetically encoded light-control system based on an optimized, reversible protein–protein interaction from the phytochrome signalling network of *Arabidopsis thaliana*. Because protein–protein interactions are one of the most general currencies of cellular information, this system can, in principle, be generically used to control diverse functions. Here we show that this system can be used to translocate target proteins precisely and reversibly to the membrane with micrometre spatial resolution and at the second timescale. We show that light-gated translocation of the upstream activators of Rho-family GTPases, which control the actin cytoskeleton, can be used to precisely reshape and direct the cell morphology of mammalian cells. The light-gated protein–protein interaction that has been optimized here should be useful for the design of diverse light-programmable reagents, potentially enabling a new generation of perturbative, quantitative experiments in cell biology.

A quantitative understanding of living cells will require methods to perturb and control the activities of their constituent proteins at fine spatial and temporal resolutions. By measuring responses to precise perturbations, predictive models of cellular networks can be tested and iteratively improved[4,5]. A promising approach is to couple the activity of targeted proteins to light signals, either by incorporating photoactive allosteric modulators semisynthetically[1,6,7], or by exploiting naturally occurring light-sensitive domains[2,3,8–10]. A particularly useful light-sensitive interaction for creating a general genetically encoded light-control system for cell biology comes from the phytochrome signalling network of plants.

Phytochromes are photoreceptive signalling proteins responsible for mediating many light-sensitive processes in plants, including seed germination, seedling de-etiolation and shade avoidance[11]. They detect red and near-infrared light through the photoisomerization of a covalently bound tetrapyrrole chromophore such as phycocyanobilin (PCB)[11]. This photoisomerization event is coupled to an allosteric transition in the phytochrome between two conformational states called Pr (red-absorbing) and Pfr (far-red-absorbing) (Fig. 1a). In one well studied signalling pathway, upon stimulation with red (650 nm) light, the *Arabidopsis thaliana* phytochrome B (PhyB) protein binds directly to a downstream transcription factor, phytochrome interaction factor 3 (PIF3), translocates to the nucleus as a heterodimer and directly modulates the transcription of response genes. PIF3 binds only the red-light-exposed form of phytochrome, Pfr, and shows no measurable binding affinity for the dark- or infrared-exposed Pr state[12]. Thus, this interaction can be reversed by infrared

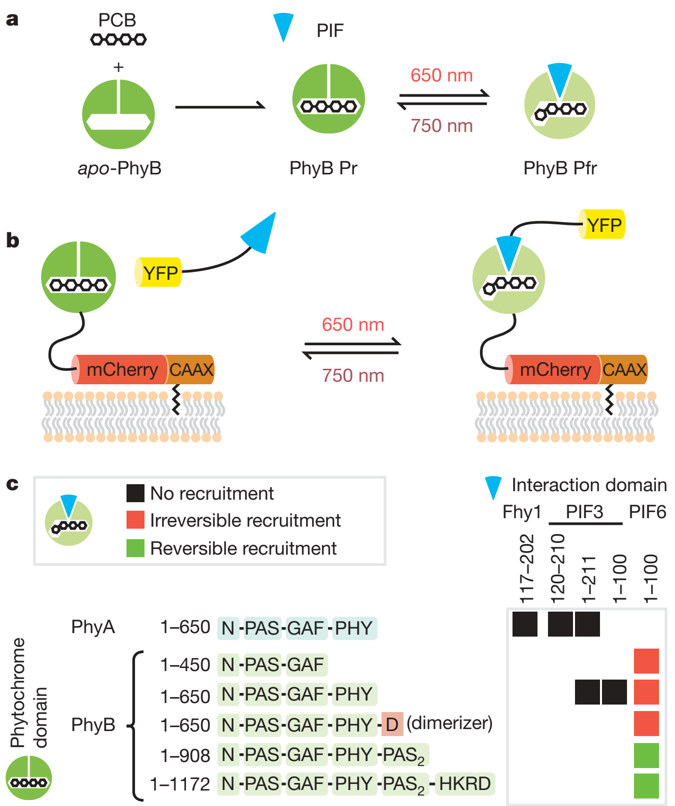

Figure 1 | The phytochrome–PIF interaction can be used to reversibly translocate proteins to the plasma membrane in a light-controlled fashion. **a**, *apo*-PhyB covalently binds to the chromophore phycocyanobilin (PCB) to form a light-sensitive holoprotein. PhyB undergoes conformational changes between the Pr and Pfr states catalysed by red and infrared light, reversibly associating with the PIF domain only in the Pfr state. **b**, This heterodimerization interaction can be used to translocate a YFP-tagged PIF domain to PhyB tagged by mCherry and localized to the plasma membrane by the C-terminal CAAX motif of Kras. **c**, Phytochrome and PIF domains functional in mammalian cells were tested for reversible light-dependent recruitment of YFP to the plasma membrane using confocal microscopy. Previously published PIF constructs either failed to show visible recruitment or showed irreversible recruitment. Only PhyB constructs harbouring tandem PAS repeats (unique to the plant phytochromes) showed detectable but reversible recruitment *in vivo*.

[1]The Cell Propulsion Lab, UCSF/UCB NIH Nanomedicine Development Center, [2]Graduate Program in Biophysics, [3]Department of Pharmaceutical Chemistry, [4]Cardiovascular Research Institute, [5]Howard Hughes Medical Institute and Department of Cellular and Molecular Pharmacology, University of California, San Francisco, California 94158-2517, USA.

light. This light-sensitive interaction has been mapped to the 650-residue amino-terminal photosensory core of PhyB and a conserved 100-residue N-terminal activated phytochrome binding (APB) domain of PIF3 (ref. 13).

In previous work, this light-sensitive interaction has been used in yeast to construct a photoreversible two-hybrid transcriptional activator to tune the expression level of a targeted reporter gene[10], to target split intein domains to titrate the conditional protein splicing of a reporter gene[14], and *in vitro* to target directly Cdc42 to its effector WASP to regulate actin nucleation[15]. Collectively this work suggests that the PhyB–PIF interaction can be functionally coupled to a wide variety of signalling processes through engineered fusion proteins.

So far, however, no reported system using the PhyB–PIF interaction has been demonstrated to enable fine spatiotemporal control of dimerization *in vivo*. Indeed, the relatively weak binding strength and slow reverse kinetics of the reported domains[15] have prevented us from successfully applying these earlier interaction pairs for *in vivo* control of signalling. We have optimized the phytochrome interaction to enable its spatiotemporal control in experiments with live mammalian cells.

We first confirmed that PhyB could covalently bind externally supplied PCB chromophore in mammalian cells by using a PhyB mutant (Y276H) that fluoresces at far-red frequencies in the PCB-coupled state only[16]. NIH3T3 cells transfected with this construct show fluorescence after only 30 min of exposure to 5 μM PCB, confirming rapid autoligation at physiological conditions (Supplementary Fig. 1). Multiple potential phytochrome–PIF pairs were screened by a fluorescence translocation assay in NIH3T3 cells with confocal microscopy. We measured the red-light-induced translocation of yellow fluorescent protein (YFP) fused to PIF domains to co-expressed phytochrome domains fused through a flexible linker to mCherry and localized to the plasma membrane by a carboxy-terminal polybasic, prenylation sequence from Kras[17] (Fig. 1b). Of all previously reported PIF domains[13,18,19], only the N terminus of PIF6 is strong enough to cause significant translocation of YFP to the membrane (Fig. 1c). However, its interaction with the PhyB photosensory core (residues 1–650) is irreversible in infrared light. Assaying it against different variants of PhyB revealed that the tandem C-terminal PAS domains of plant phytochromes are necessary to confer rapid photoreversibility under infrared light, underlining the importance of a previously reported autoinhibitory interaction for phytochrome signalling[20]. We refer to the optimized, reversible PhyB–PIF6 interaction simply as the 'Phy–PIF' interaction.

Using this optimized Phy–PIF pair we observe rapid translocation to the plasma membrane under dilute red light (650 nm, 20 μmol m^{-2} s^{-1}) and from the membrane under infrared light (>750 nm, 300 μmol m^{-2} s^{-1}) (Fig. 2a and Supplementary Movies 1 and 2). Kinetic measurements of the Phy-induced cytoplasmic depletion of PIF–YFP under maximum illumination yield translocation time constants of 1.3 ± 0.1 s (s.d. $n = 3$) for membrane recruitment and 4 ± 1 s (s.d. $n = 3$) for membrane release (Fig. 2a and Supplementary Fig. 2), demonstrating second-timescale control. These rates are an order of magnitude faster than previous chemically induced translocation systems[21] and are very near the physical limits for whole-cell diffusion (see calculation in Supplementary Information). The Phy–PIF translocation proved very robust—it could be cycled over a hundred times by alternating red and infrared illumination with no measurable decrease in recruitment ratios over time, despite many cycles of imaging at photon fluxes far higher than those phytochromes are exposed to in natural lighting conditions (Fig. 2b and Supplementary Movie 3).

The rapid forward and reverse kinetics of our Phy–PIF pair allow for fine spatial control of membrane recruitment by simultaneously exposing cells to patterned light at the two antagonizing wavelengths. In NIH3T3 cells co-expressing the above Phy–Kras(CAAX) and PIF–YFP recruitment pair, a nitrogen dye cell laser was used to deliver pulses of 'activating' red light (650 nm, 20 Hz) to a focused point on the sample plane, while the whole sample was bathed in continuous

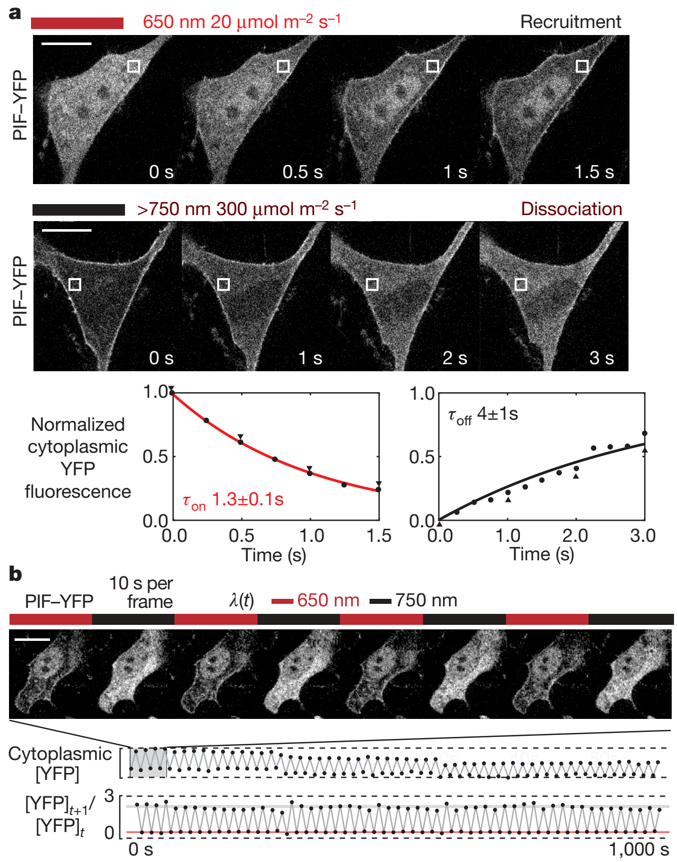

Figure 2 | Confocal microscopy demonstrating the second-scale kinetics and photostability of the Phy–PIF photoswitchable membrane recruitment system. **a**, Confocal microscopy of NIH3T3 cells reveals rapid translocation of YFP between cytosol and plasma membrane under red and infrared light. Fitting exponentials to the cytoplasmic depletion of YFP gives typical time constants of 1.3 ± 0.1 s for recruitment and 4 ± 1 s for dissociation ($n = 3$). White rectangles show regions sampled for plotted traces. Arrowheads in graphs mark the time points shown (Supplementary Movies 1 and 2). **b**, Rapid alternation between the 650 and 750 nm light can generate oscillations in the cytoplasmic concentrations of YFP. Absolute cytoplasmic concentration of YFP for this series is plotted along with the ratio change between time points to adjust for photobleaching and cell drift. The red and grey bars represent the standard deviations of the recruited and released cytosolic fluorescence, demonstrating near-fixed recruitment ratios over more than a hundred iterations (Supplementary Movie 3). Scale bars in **a** and **b**, 20 μm.

'inactivating' infrared light obtained by filtering the microscope bright-field source (>750 nm) (Fig. 3a). When the cell membrane is imaged by total internal reflectance (TIRF) microscopy we observe a sharp spot of membrane-localized YFP several micrometres in diameter around the irradiated point (Fig. 3c). The rapid 'off' kinetics of the Phy–PIF interaction traps the membrane-recruited YFP pool to this spot, as any YFP diffusing away is dissociated from the membrane by the surrounding infrared light. This spot of recruited YFP can be rapidly relocated across the cell by repositioning the point of incident light (Supplementary Movie 4).

We developed a second, fully automated method of controlling the distribution of both light frequencies on the cell membrane by using a digital micromirror array to project patterned light on to the sample plane of the microscope at micrometre resolutions[22]. By irradiating the sample with 650-nm and 750-nm light sources oriented to take advantage of both micromirror angle states, a complementary two-colour red/infrared pattern can be projected on to the sample plane, allowing one to 'paint' high-resolution inverse distributions of Pfr and Pr phytochrome on to the membrane of the cell (Fig. 3b). We were able to project faithfully a simple pixel-based movie into the

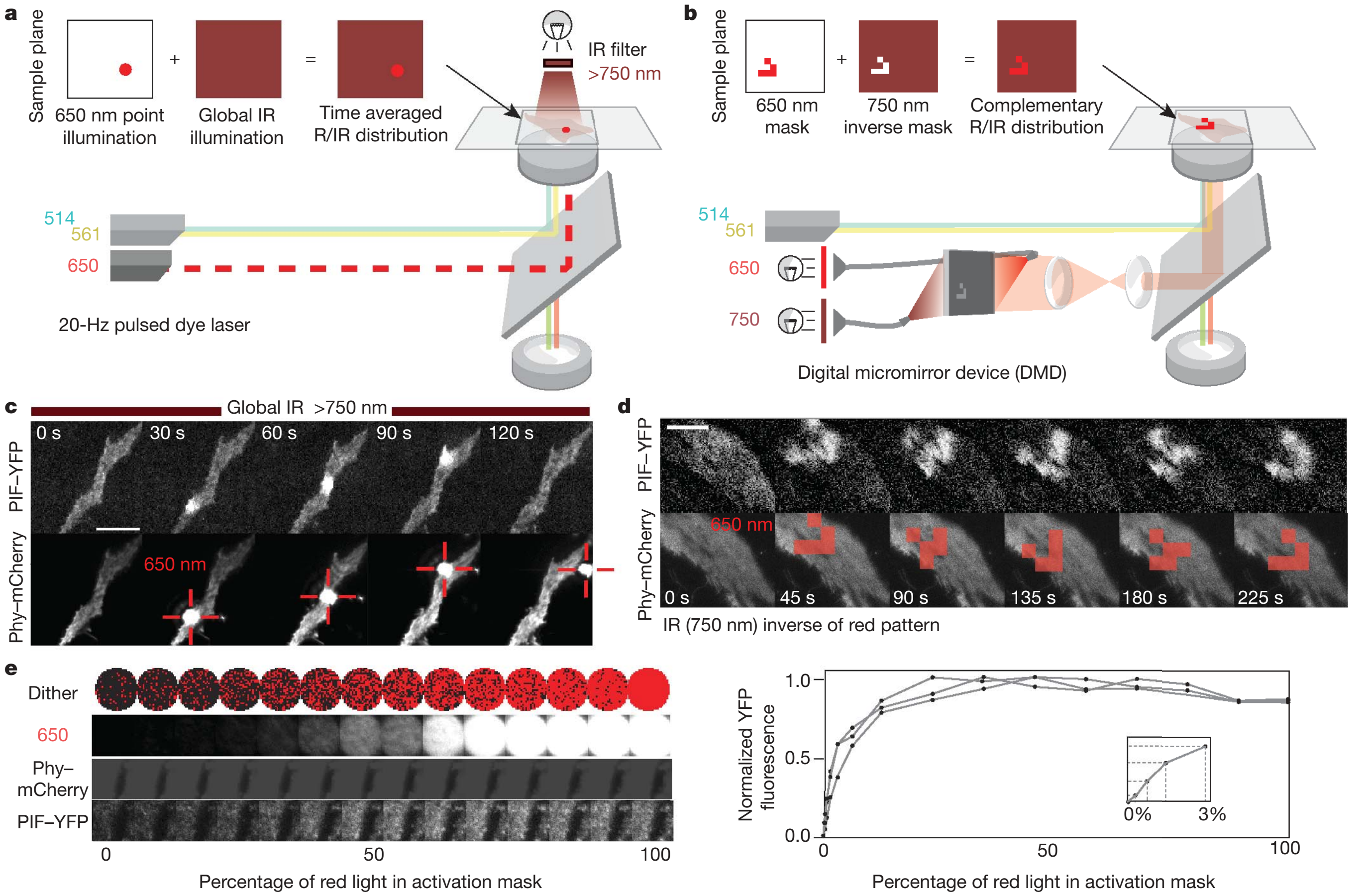

Figure 3 | Recruitment to the plasma membrane can be controlled spatially by simultaneously irradiating cells with patterned red and infrared light. **a**, A nitrogen dye cell laser exciting a 650-nm rhodamine dye was focused on to the sample plane of the microscope at 20 Hz while infrared (IR)-filtered white light continuously bathed the entire sample. **b**, A digital micromirror device focused on to the sample plane was used to send high-resolution patterns of 650 nm/750 nm light from a DG-4 source into the microscope under software control. This results in complementary red and infrared distributions on the sample plane. **c**, TIRF imaging of localized membrane recruitment by a point source as in **a** shows highly localized YFP recruitment (Supplementary Movie 4). The recruited YFP spot's diameter is roughly 3 μm and can be quickly moved by repositioning the laser. The final frame shows that the YFP spot is not merely bleed-through of the excitatory laser light, but genuine local fluorescent protein recruitment. **d**, TIRF movies of structured membrane recruitment by programmatically updating masks for red and infrared light using a digital micromirror device as in **b** were collected, revealing a faithful reproduction in the recruited YFP distribution of a movie of the cellular automaton 'game-of-life glider' that was projected (Supplementary Movie 5). **e**, Images show the raw traces of titrated input 650-nm light and recruited PIF–YFP. The plot (right panel) shows the recruitment level as a function of 650-nm ratio for three typical experiments. Inset shows the non-saturated regime. Scale bars, 20 μm.

membrane-recruited PIF–YFP distribution of a NIH3T3 cell. TIRF imaging reveals fine features at five micrometres, demonstrating an unprecedented degree of control over protein localization in living cells (Fig. 3d and Supplementary Movie 5). Additionally, by dithering the average amount of red light in the target mask through software, we could smoothly titrate the fraction of active Phy and recruited PIF–YFP, demonstrating effective 'greyscale' control of the chemical potential (Fig. 3e and Supplementary Movie 6). Using this data, we estimate the *in vivo* dissociation constant of the PhyB–PIF6 interaction to be approximately $K_d = 20$–100 nM (Supplementary Fig. 5).

We were motivated to engineer a membrane recruitment system because many signalling proteins are, at least in part, activated by interactions that relocalize them to the membrane. Moreover, plasma membrane recruitment systems have been successfully used as a platform for small-molecule-induced chemical biology control systems[21,23–25]. For example, chemically induced membrane translocation of the Rho- and Ras-family small G proteins[21,23] or the guanine nucleotide exchange factors (GEFs) that activate them[21] can generate global morphological changes. We reasoned that Phy–PIF-induced translocation might generate similar morphological changes, but with much higher spatial and temporal resolution. We chose to focus on spatiotemporal control of the Rho-family GTPases Rac1, Cdc42 and RhoA, given their central role in the dynamic spatial regulation of the actin cytoskeleton at the polarized edges of motile cells (Fig. 4a).

Gated-recruitment constructs were made from the isolated catalytic modules (the DH-PH domain) of the RacGEF Tiam, the Cdc42GEF intersectin and the RhoGEF Tim. The optimal construct topologies for DH-PH activation were found by screening for Tiam-DH-PH activity via the global morphological changes that occurred in transfected, serum-depleted NIH3T3 cells when the entire field was exposed to red light. Global recruitment of the optimal PIF–Tiam-DH-PH chimaera caused a pronounced lamellipodial phenotype within 20 min in most (>80%) co-transfected cells, compared to PIF–YFP-only recruitment or control cells lacking the PCB chromophore (Fig. 4b). This potent effect of recruiting the Tiam GEF activity to the membrane is similar to that observed using chemical dimerizers[21]. We further tested the generality of this construct topology by confirming that global RhoGEF recruitment induced cell body contraction in fibroblasts (Supplementary Movie 9).

Given the strong global morphological effects of Tiam DH-PH domain membrane translocation, we then tested the effects of spatially localized light-activated translocation. Red laser stimulation was used for localized recruitment of the Tiam DH-PH domain in serum-depleted NIH3T3 cells (within a background of global repression by infrared light), effecting within 5–10 min a localized lamellipodial

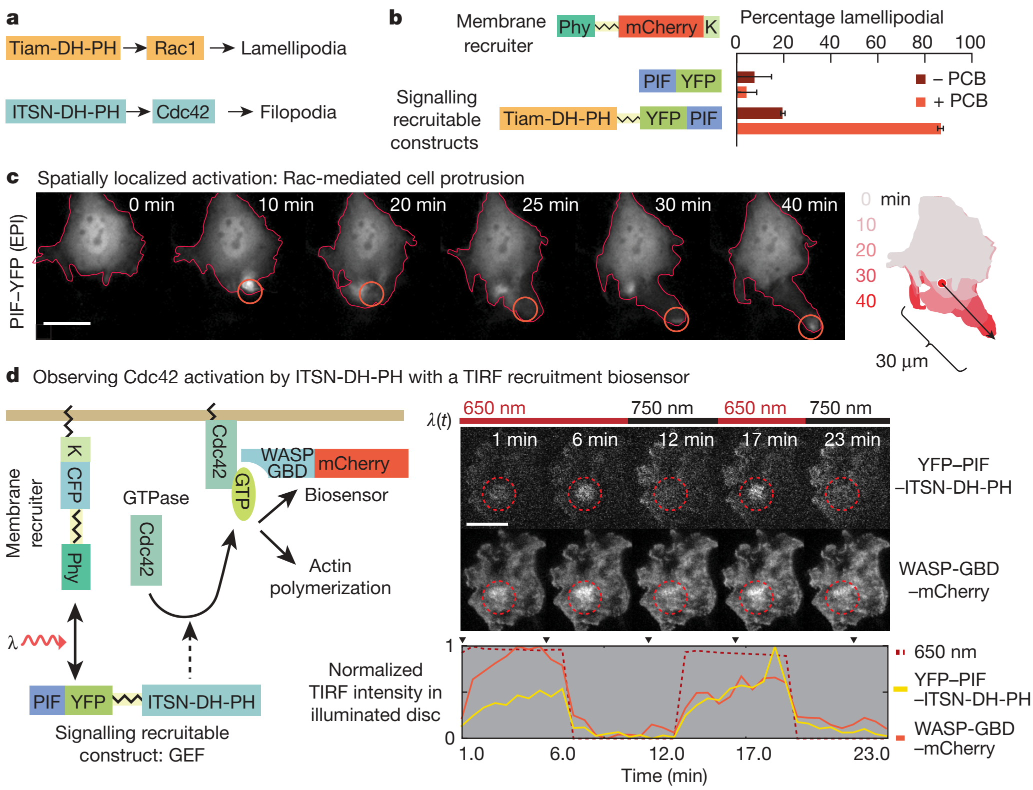

Figure 4 | Rho-family G-protein signalling can be controlled by the light-activated translocation system. a, The catalytic DH-PH domains of RhoGEFs Tiam and intersectin (ITSN) activate their respective G proteins Rac1 and Cdc42, which in turn act through effector proteins to modify the actin cytoskeleton. **b,** Recruitable constructs with Tiam DH-PH domains were assayed for their ability to induce lamellipodia in NIH3T3 cells by exposing serum-depleted cells transfected with the indicated constructs to red (650 nm) light and counting the percentage of cells that produced lamellipodia within 20 min under live microscopy. Error bars indicate s.e.m. ($n = 2$, average 30 cells; P-value $= 0.0004$ for Tiam). **c,** Local induction and 'extrusion' of lamellipodia in live NIH3T3 cells (epifluorescence imaging, EPI) was demonstrated by globally irradiating the whole sample with an infrared (750 nm) light source while focusing a red (650 nm) laser on to a small portion of the cell as in Fig. 2a and slowly extending this red-targeted region from the cell body. Superimposed outlines of the cell show directed extension 30 μm along the line of light movement (Supplementary Movie 7). **d,** Cdc42-GTP binding domain (WASP-GBD) linked to mCherry was used to measure the 'response function' of intersectin-DH-PH recruitment over several iterations in time and in space at equilibrium (Supplementary Movie 11). Scale bars in **c** and **d**, 20 μm.

'bloom' (Supplementary Movie 8). By slowly extending the point of activating light away from the cell, it is even possible to 'draw out' an extended process up to 30 μm from the main body of the cell that is stable after the light has been withdrawn. This indicates the future possibility of programmatically specifying cell geometries and intercellular connections with light (Fig. 4c and Supplementary Movies 7 and 8).

We further verified the signalling activity of our PIF-DH-PH reagents by verifying that point induction causes local, transient increases of the active form of GTPase as measured by the membrane enrichment of biosensors—either mCherry-tagged GBD-binding domains from WASP (Fig. 4d and Supplementary Movie 11) or PAK (Supplementary Fig. 4)—by TIRF microscopy. Using these biosensors we see that GTPase activation occurs rapidly, within seconds, indicating that a subsequent signalling step is responsible for the typical delay of 5–10 min for lamellipodial and filopodial protrusions.

We have developed a genetically encoded, light-switchable Phy–PIF interaction module which, because it has a properly titrated tight but reversible interaction, has the potential to be applied to control any live cell process that is dependent on a recruitment event. Unlike classical uncaging techniques, photoreversibility allows our system to defeat diffusive spreading by using patterned light. Furthermore, the direct relationship between the recruited fluorescent fraction and signalling activity also enables measurable 'dosage' of signalling flux for quantitative perturbations. We show here that the system works robustly in mammalian cells with external PCB, extending previous demonstrations in yeast[10] and its natural domain in plants, indicating that it is compatible with most eukaryotic cells. For genetically manipulable cells, it is, in principle, simple to include genes for enzymes that will generate PCB from haem or biliverdin[26].

The high spatial and temporal resolution of light control allows this module to function as a novel analytical tool, in which highly complex spatial or temporal patterns can be used to drive a process. We have also demonstrated here how this module can be used as a high-resolution control module to sculpt cell shape in an unprecedented manner. Because of the generic nature of this interaction module, it is likely that it can be used to control an extremely broad range of cell biological processes without the need for laborious case-by-case protein engineering.

METHODS SUMMARY

Phycocyanobilin (PCB) purification. PCB was extracted by methanolysis at 70 °C from protein precipitates of *Spirulina* cell lysate (Seltzer Chemical) that were pre-washed to remove other tetrapyrroles species. Free PCB was handled under a green safelight (λ_{max} of 550 nm).

Light control experiments. NIH3T3 cells transiently transfected with the phytochrome and PIF constructs were pre-incubated in the dark with 5 μM PCB for 30 min and then washed before experiments. Non-coherent control-light frequencies were obtained by filtering white-light sources with 650-nm and 750-nm 20-nm band-pass filters (Edmund Optics) or a near-infrared RG9 glass filter (Newport). For morphology experiments, cells were serum-depleted (1% Bovine Calf Serum) for at least 12 h before imaging.

Received 8 July; accepted 24 August 2009.
Published online 13 September 2009.

1. Szobota, S. *et al.* Remote control of neuronal activity with a light-gated glutamate receptor. *Neuron* **54,** 535–545 (2007).

2. Boyden, E. S., Zhang, F., Bamberg, E., Nagel, G. & Deisseroth, K. Millisecond-timescale, genetically targeted optical control of neural activity. *Nature Neurosci.* **8**, 1263–1268 (2005).
3. Han, X. & Boyden, E. S. Multiple-color optical activation, silencing, and desynchronization of neural activity, with single-spike temporal resolution. *PLoS One* **2**, e299 (2007).
4. Mettetal, J. T., Muzzey, D., Gómez-Uribe, C. & van Oudenaarden, A. The frequency dependence of osmo-adaptation in *Saccharomyces cerevisiae. Science* **319**, 482–484 (2008).
5. Bennett, M. R. *et al.* Metabolic gene regulation in a dynamically changing environment. *Nature* **454**, 1119–1122 (2008).
6. Ghosh, M. *et al.* Cofilin promotes actin polymerization and defines the direction of cell motility. *Science* **304**, 743–746 (2004).
7. Gorostiza, P. & Isacoff, E. Y. Optical switches for remote and noninvasive control of cell signaling. *Science* **322**, 395–399 (2008).
8. Levskaya, A. *et al.* Synthetic biology: engineering *Escherichia coli* to see light. *Nature* **438**, 441–442 (2005).
9. Lee, J. *et al.* Surface sites for engineering allosteric control in proteins. *Science* **322**, 438–442 (2008).
10. Shimizu-Sato, S., Huq, E., Tepperman, J. M. & Quail, P. H. A light-switchable gene promoter system. *Nature Biotechnol.* **20**, 1041–1044 (2002).
11. Quail, P. H. Phytochrome photosensory signalling networks. *Nature Rev. Mol. Cell Biol.* **3**, 85–93 (2002).
12. Ni, M., Tepperman, J. M. & Quail, P. H. Binding of phytochrome B to its nuclear signalling partner PIF3 is reversibly induced by light. *Nature* **400**, 781–784 (1999).
13. Khanna, R. *et al.* A novel molecular recognition motif necessary for targeting photoactivated phytochrome signaling to specific basic helix-loop-helix transcription factors. *Plant Cell* **16**, 3033–3044 (2004).
14. Tyszkiewicz, A. B. & Muir, T. W. Activation of protein splicing with light in yeast. *Nature Methods* **5**, 303–305 (2008).
15. Leung, D. W., Otomo, C., Chory, J. & Rosen, M. K. Genetically encoded photoswitching of actin assembly through the Cdc42-WASP-Arp2/3 complex pathway. *Proc. Natl Acad. Sci. USA* **105**, 12797–12802 (2008).
16. Su, Y. & Lagarias, J. C. Light-independent phytochrome signaling mediated by dominant GAF domain tyrosine mutants of *Arabidopsis* phytochromes in transgenic plants. *Plant Cell* **19**, 2124–2139 (2007).
17. Heo, W. D. *et al.* PI(3,4,5)P_3 and PI(4,5)P_2 lipids target proteins with polybasic clusters to the plasma membrane. *Science* **314**, 1458–1461 (2006).
18. Al-Sady, B., Ni, W., Kircher, S., Schäfer, E. & Quail, P. H. Photoactivated phytochrome induces rapid PIF3 phosphorylation prior to proteasome-mediated degradation. *Mol. Cell* **23**, 439–446 (2006).
19. Genoud, T. *et al.* FHY1 mediates nuclear import of the light-activated phytochrome A photoreceptor. *PLoS Genet.* **4**, e1000143 (2008).
20. Chen, M., Tao, Y., Lim, J., Shaw, A. & Chory, J. Regulation of phytochrome B nuclear localization through light-dependent unmasking of nuclear-localization signals. *Curr. Biol.* **15**, 637–642 (2005).
21. Inoue, T., Heo, W. D., Grimley, J. S., Wandless, T. J. & Meyer, T. An inducible translocation strategy to rapidly activate and inhibit small GTPase signaling pathways. *Nature Methods* **2**, 415–418 (2005).
22. Wang, S. *et al.* All optical interface for parallel, remote, and spatiotemporal control of neuronal activity. *Nano Lett.* **7**, 3859–3863 (2007).
23. Castellano, F. *et al.* Inducible recruitment of Cdc42 or WASP to a cell-surface receptor triggers actin polymerization and filopodium formation. *Curr. Biol.* **9**, 351–361 (1999).
24. Suh, B., Inoue, T., Meyer, T. & Hille, B. Rapid chemically induced changes of PtdIns(4,5)P_2 gate KCNQ ion channels. *Science* **314**, 1454–1457 (2006).
25. Inoue, T. & Meyer, T. Synthetic activation of endogenous PI3K and Rac identifies an AND-gate switch for cell polarization and migration. *PLoS One* **3**, e3068 (2008).
26. Gambetta, G. A. & Lagarias, J. C. Genetic engineering of phytochrome biosynthesis in bacteria. *Proc. Natl Acad. Sci. USA* **98**, 10566–10571 (2001).

Supplementary Information is linked to the online version of the paper at www.nature.com/nature.

Acknowledgements We thank B. El-Sady, J. Tepperman, K. Thorn, G. Kapp and members of the Voigt, Weiner and Lim laboratories for assistance and discussion. We thank Molecular Devices and Photonics Instruments for the loan and customization of a Mosaic spatial light modulator. Data for this study were acquired at the Nikon Imaging Center at UCSF. This work was supported by a NSFGR fellowship (A.L.); NIH R01 GM084040 and Searles Scholar Award.(O.D.W.); Packard Fellowship, the Howard Hughes Medical Institute, and NIH grants GM55040, GM62583 and EY016546 (NIH Roadmap Nanomedicine Development Centers) (W.A.L.); Pew Fellowship, the Office of Naval Research, Packard Fellowship, NIH EY016546, NIH AI067699, NSF BES-0547637, UC-Discovery and the SynBERC NSF ERC (C.A.V.).

Author Contributions Concept was conceived by A.L., W.A.L. and C.A.V.; experiments were executed by A.L.; spatiotemporal microscopy methods were developed by A.L. and O.D.W.; all authors were involved in interpretation of results and preparation of the manuscript.

Author Information Plasmids will be available from Addgene (http://www.addgene.org). Reprints and permissions information is available at www.nature.com/reprints. Correspondence and requests for materials should be addressed to W.A.L. (lim@cmp.ucsf.edu).

Vol 461|15 October 2009|doi:10.1038/nature08468

LETTERS

Integrin-linked kinase is an adaptor with essential functions during mouse development

Anika Lange[1], Sara A. Wickström[1], Madis Jakobson[2], Roy Zent[3], Kirsi Sainio[2] & Reinhard Fässler[1]

The development of multicellular organisms requires integrin-mediated interactions between cells and their extracellular environment. Integrin binding to extracellular matrix catalyses assembly of multiprotein complexes, which transduce mechanical and chemical signals that regulate many aspects of cell physiology[1,2]. Integrin-linked kinase (Ilk) is a multifunctional protein that binds β-integrin cytoplasmic domains and regulates actin dynamics by recruiting actin binding regulatory proteins such as α- and β-parvin[3]. Ilk has also been shown to possess serine/threonine kinase activity[4] and to phosphorylate signalling proteins such as Akt1 and glycogen synthase kinase 3β (Gsk3β) in mammalian cells[5]; however, these functions have been shown by genetic studies[6,7] not to occur in flies and worms. Here we show that mice carrying point mutations in the proposed autophosphorylation site of the putative kinase domain and in the pleckstrin homology domain are normal. In contrast, mice with point mutations in the conserved lysine residue of the potential ATP-binding site of the kinase domain, which mediates Ilk binding to α-parvin, die owing to renal agenesis. Similar renal defects occur in α-parvin-null mice. Thus, we provide genetic evidence that the kinase activity of Ilk is dispensable for mammalian development; however, an interaction between Ilk and α-parvin is critical for kidney development.

Genetic studies in *Drosophila melanogaster*, *Caenorhabditis elegans*, zebrafish, and mice show that Ilk regulates integrin-mediated adhesion strengthening and actin organization[6–9]. In addition to this scaffolding role, Ilk is proposed to function as a serine/threonine kinase[4] for substrates such as Akt and Gsk3β in mammalian cells[5]. However, mutations in residues critical for Ilk kinase activity in mammalian cells fully rescue Ilk-null mutants in *D. melanogaster*[6] and *C. elegans*[7].

To determine whether catalytic activity of the putative kinase domain of Ilk is specific to mammals, we established mouse strains with point mutations in residues shown to abolish Ilk kinase activity *in vitro*. We substituted: (1) serine 343 of the potential autophosphorylation site with either an alanine (S343A) or aspartate (S343D), leading to a kinase-dead or hyperactive Ilk[10], respectively; (2) arginine 211 with an alanine (R211A) in the pleckstrin homology domain leading to a kinase-dead Ilk[10]; (3) lysine 220 with an alanine (K220A) or methionine (K220M) in the ATP-binding site, leading to a kinase-dead Ilk associated with either diminished or unchanged binding to β-parvin[11,12], respectively (Supplementary Fig. 1a, b). All mutations were introduced into embryonic stem cells by homologous recombination and confirmed by Southern blot (Supplementary Fig. 1c) and sequencing (data not shown). Heterozygous knock-in embryonic stem cells were injected into blastocysts and the *loxP*-flanked neomycin (*neo*) gene was removed by intercrossing the knock-in strains with a deleter-Cre line resulting in mice carrying a *loxP* site in exon 13 and defined point mutations in the *Ilk* gene (Supplementary Fig. 1a, b). The presence of the knock-in allele was confirmed by PCR (Supplementary Fig. 1d) and genomic sequencing (data not shown). Importantly, control mice carrying *loxP* sites in exon 13 without mutations in the *Ilk* gene were normal (Supplementary Fig. 2a), had normal levels of *Ilk* messenger RNA and protein, normal expression of the *Taf10* gene nested within the Ilk locus (Supplementary Fig. 2b, c) and normal organ development (Supplementary Fig. 2d and data not shown), indicating that the *loxP* site does not affect Ilk function.

Mice homozygous for the S343A or S343D mutations were born in the expected Mendelian ratio ($n = 230$) and were normal (Fig. 1a and data not shown). Because conditional deletion of Ilk dramatically affects epidermis and heart development[13–15], and the kinase activity of Ilk was proposed to have a role in cardiac hypertrophy[16], our analysis focused on these tissues. Mutant Ilk localized normally to integrin adhesion sites in the epidermis (Supplementary Fig. 3a) and histology of skin and heart from S343A and S343D mice was normal (Fig. 1b, c).

If Ilk kinase activity regulates integrin signalling, the S343A or S343D cells should demonstrate abnormalities in their actin cytoskeleton. However, Ilk(S343A) and Ilk(S343D) localized normally to focal adhesions in primary keratinocytes (Fig. 1d, e), which also spread, connected their actin cytoskeleton to mature focal adhesions (Fig. 1d, e and Supplementary Fig. 3b–d), and adhered normally to extracellular matrix substrates (Fig. 1f). Moreover, phosphorylation of Akt1 and Gsk3β in heart and epidermal tissues was not altered (Fig. 1g, h and Supplementary Fig. 3e, f). These results show that the 'kinase dead' S343A mutation and the 'kinase hyperactive' S343D mutation do not alter mouse development, tissue function, key substrate phosphorylation or actin-dependent cell processes.

Mice carrying an R211A mutation in the pleckstrin homology domain, also reported to result in a kinase-dead Ilk[10], were born in the expected Mendelian ratio ($n = 79$) and appeared normal (Supplementary Fig. 4a and data not shown). In addition, histology of skin and heart from these mice showed no defects (Supplementary Fig. 4b, c). These data confirm that residues shown to be essential for Ilk kinase activity *in vitro* do not affect mouse development.

Mice carrying K220A or K220M mutations in the ATP-binding site of Ilk were present in expected Mendelian ratio and were of normal size and appearance at embryonic day (E) 18.5 (Supplementary Fig. 5a–c). At birth (postnatal day (P) 0), fewer K220A and K220M mutant mice were present (Supplementary Fig. 5b, c) and those surviving were pale, had a bent body posture and did not feed (Fig. 2a, b). All mutants died shortly after birth (Supplementary Fig. 5b, c). Skin, heart and several other tissues were normal (Supplementary Fig. 6a and data not shown). Despite normal protein levels of Ilk and its main binding partners Pinch-1 and α/β-parvin (Supplementary Fig. 6b), all mutant mice displayed renal agenesis or severe dysgenesis (Fig. 2c and Supplementary Fig. 7a); 70% lacked both kidneys, 27% had unilateral kidney aplasia and in 8% of these the other ureter was

[1]Department of Molecular Medicine, Max Planck Institute of Biochemistry, Martinsried 82152, Germany. [2]Institute of Biomedicine, Medical Biochemistry and Developmental Biology, University of Helsinki, Helsinki 00014, Finland. [3]Division of Nephrology, Department of Medicine, Vanderbilt Medical Center and Veterans Affairs Hospital, Nashville, Tennessee 37232, USA.

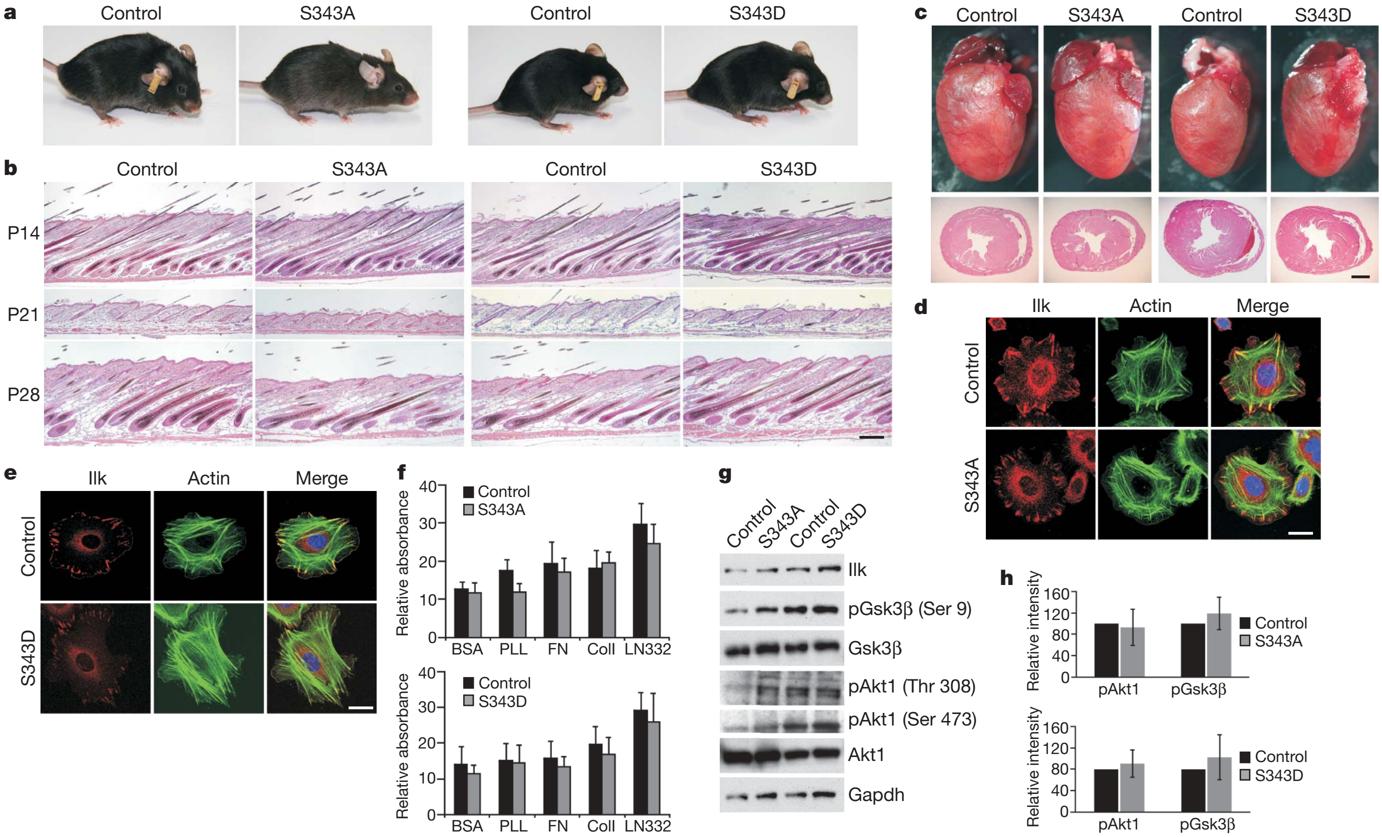

Figure 1 | Mutating serine 343 of Ilk does not alter mouse development. **a–c**, Nine-month-old S343A and S343D knock-in mice appear normal (**a**), have normal skin (**b**), and normal hearts (**c**). **d**, **e**, Primary S343A (**d**) or S343D (**e**) keratinocytes stained for Ilk and F-actin. Note normal localization of Ilk, normal cell spreading, and actin cytoskeleton organization. **f**, Mutant cells adhered normally to fibronectin (FN), collagen I (ColI), laminin $\alpha3\beta3\gamma2$ (LN332), bovine serum albumin (BSA) and poly-L-lysine (PLL) (mean + s.e.m.; $n = 3/3$). **g**, Control, S343D and S343A heart tissues show equal levels of Akt1 and Gsk3β phosphorylation. **h**, Quantification of Akt1 and Gsk3β phosphorylation (mean ± s.e.m.; $n = 3/3$). Scale bars: **b**, 100 μm; **c**, 1 mm; **d**, **e**, 15 μm.

missing. 3% had dysgenic or hypoplastic kidneys (Supplementary Fig. 7b).

The kidney develops from epithelial, mesenchymal and stromal compartments. At ~E11.0 the ureteric bud (UB) grows out of the Wolffian duct (WD) in response to inductive cues, such as glial cell derived neurotrophic factor (GDNF) or fibroblast growth factors (FGFs) secreted by the metanephric mesenchyme (MM). The growing UB interacts with the MM, which leads to nephron formation[17]. At E11.5 no UB could be detected in the MM of most K220M mutant embryos, and at E12.5/13.5 UB branching was impaired (Fig. 2d, e). By E13.5 the MM underwent apoptosis (Fig. 2f), and most mutants lacked both kidneys (Fig. 2d, e). In rare cases of successful UB invasion into the MM, the kidneys were hypoplastic with reduced numbers of collecting ducts and nephrons (Supplementary Fig. 8a, b). No urine was detected in the bladders of these mice (data not shown). However, proliferation as well as Akt1 phosphorylation was normal in these kidneys (Supplementary Fig. 8c–f).

Urogenital tracts were isolated from kidneys at the T-bud stage (E11.5) to define whether the principal abnormality was in the WD, UB or MM. Ilk was expressed in both the UB and MM (Supplementary Fig. 9). Mutant WDs and UBs were positive for *Wnt9b*, a factor essential for nephron induction[18] (Supplementary Fig. 10a). The WDs were normal, but the UBs were hypoplastic (Fig. 3a), suggesting the defect was in the UB and/or the MM. When isolated urogenital blocks were grown *in vitro*, the mutants were unable to form ectopic UBs in response to GDNF (Fig. 3b), a growth factor critical for initial UB induction and branching[19] and had an attenuated response to FGF7+Follistatin, other growth factors that control UB branching[20] (Fig. 3b). The defect was not due to abnormal expression of *Gdnf* in the MM or its receptor c-Ret in the UB (Supplementary Fig. 10b, c). Impaired UB invasion was due, at least in part, to intrinsic defects in the UB as isolated UBs from E11.5 mutant embryos failed to branch in GDNF-containing matrigel, whereas control UBs underwent extensive branching (Fig. 3c). The mutant mesonephros was also abnormal as numbers of mesonephric tubules were reduced in isolated urogenital blocks (Fig. 3d, e). When nephrogenesis was induced in isolated kidneys by lithium treatment[21], brush-border-positive proximal tubules were absent in the mutants (Supplementary Fig. 11a), despite normal expression of Pax2, the master regulator of renal differentiation[22] (Supplementary Fig. 11b). Furthermore, isolated wild-type MM did not undergo nephrogenesis when recombined with mutant UB (Supplementary Fig. 11c) and the wild-type UB branched less well when recombined with mutant MM (Fig. 3f). Thus, renal agensis/dysgenesis in the K220A or K220M mice results from intrinsic abnormalities of the UB and MM as well as defective inductive tissue interactions between them.

To analyse whether the K220A or K220M mutations affect the kinase activity of Ilk *in vitro*, we performed *in vitro* kinase assays using the myelin basic protein (MBP) as a substrate[23]. The phosphorylation levels of MBP induced by all point mutants were comparable to wild-type Ilk and did not differ from background levels of control lysates, whereas Erk induced a robust phosphorylation of MBP (Supplementary Fig. 12a). Moreover, phosphorylation levels of putative Ilk targets such as Akt1 and Gsk3β were normal *in vivo* (Supplementary Fig. 12b, c).

As no evidence for kinase activity was detected, we determined whether mutations in the putative ATP-binding site of Ilk affect its ability to act as a scaffold protein. To do this we used Ilk-null collecting duct (CD) cells derived from *Ilk* floxed mice[24] where Ilk was deleted *in vitro* by adenoviral expression of Cre recombinase that were reconstituted with Flag-tagged wild-type Ilk, Ilk(K220A), Ilk(K220M) or

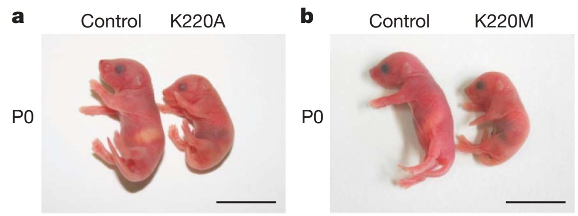

Developmental age	E11.5	E12.5
Control	*n* = 56	*n* = 26
Ureteric bud (UB) invasion	56	26
UB branching	-	26
K220A	*n* = 18	*n* = 4
UB not in mesenchyme	12	2
1 UB, in mesenchyme, no branching	6	0
2 UB, in mesenchyme, no branching	-	2
1 UB, in mesenchyme, branching	-	0
2 UB, in mesenchyme, branching	-	0
K220M	*n* = 40	*n* = 16
UB not in mesenchyme	34	6
1 UB, in mesenchyme, no branching	6	0
2 UB, in mesenchyme, no branching	-	2
1 UB, in mesenchyme, branching	-	4
2 UB, in mesenchyme, branching	-	4

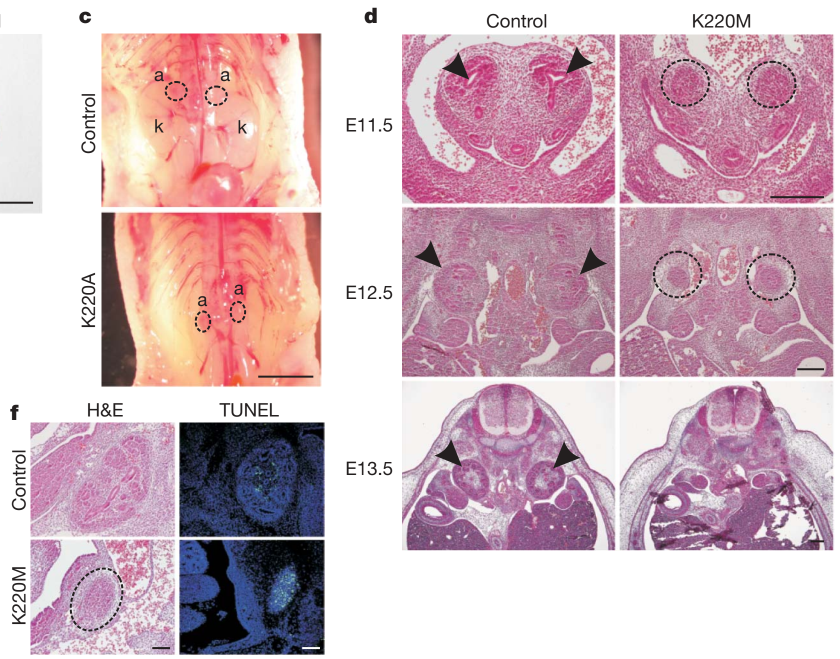

Figure 2 | Perinatal lethality and severe renal dysgenesis in Ilk(K220A) and Ilk(K220M) mice. **a**, **b**, P0 Ilk(K220A) (**a**) and Ilk(K220M) (**b**) mutant mice are smaller with a bent posture. **c**, Mutant mice have kidney (k) agenesis but normal adrenal glands (a). **d**, Frontal sections of E11.5, E12.5, and E13.5 control and K220M mutant embryos show failed UB growth into the MM (dotted circle) in mutant mice. Arrowheads mark UB invasion. **e**, Quantification of UB invasion (E11.5) into the MM and branching (E12.5). **f**, TUNEL staining of E12.5 embryos shows increased apoptosis in the mutant MM. H&E, haematoxylin and eosin. Scale bars: **a**–**c**, 1 cm; **d**, 250 μm; **f**, 50 μm.

Ilk(S343A). Although Ilk(K220A) and Ilk(K220M) still localized to focal adhesions (Fig. 4a), these cells displayed increased cortical actin bundles, impaired stress fibre formation and large peripheral focal adhesions (Fig. 4a and Supplementary Fig. 13a). The defect in actin organization was confirmed in primary UB cells isolated from K220M mice (Supplementary Fig. 13b). In addition, K220A mutant cells displayed loss of directional migration towards a chemotactic gradient and increased random migration velocity and distance, closely resembling the migration pattern of *Ilk*$^{-/-}$ CD cells (Fig. 4b, c). Pull down experiments revealed that Ilk(K220A) and Ilk(K220M) bound normal

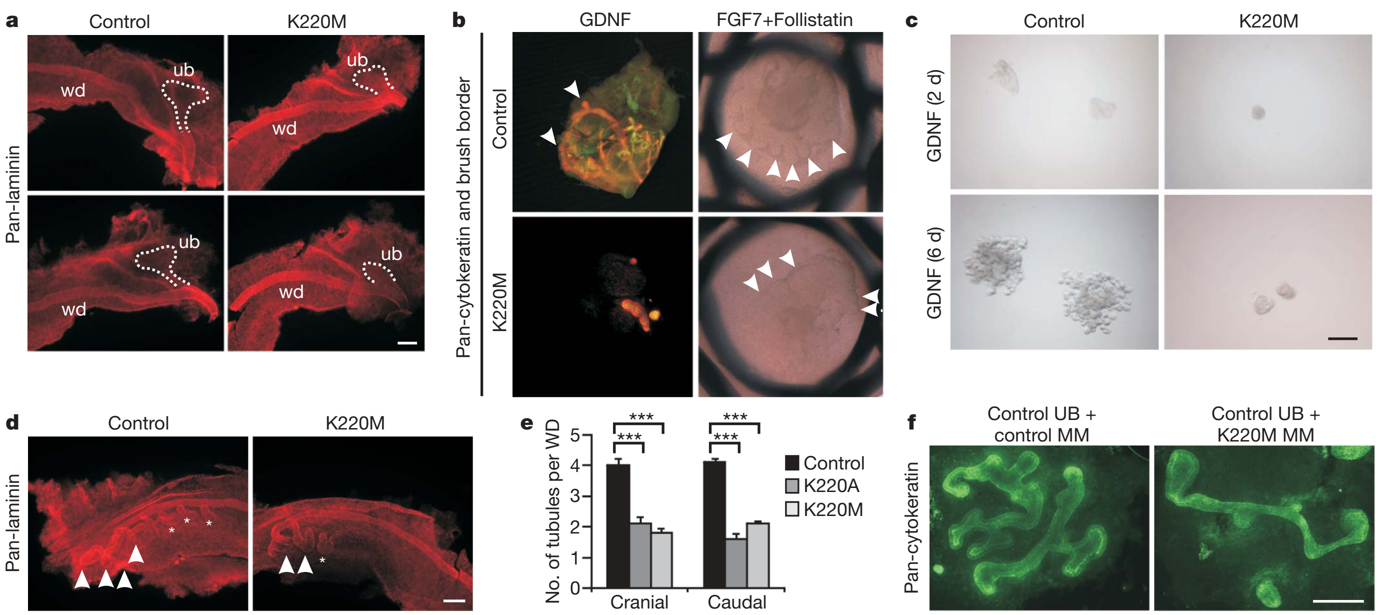

Figure 3 | Ilk(K220A) and Ilk(K220M) mutant mice show defects in the UB and nephrogenic mesenchyme. **a**, Pan-laminin stained E11.5 urogenital blocks. Controls show fully developed WDs and UBs (dotted line) but UBs fail to develop in mutants. **b**, Controls but not mutants develop UBs (arrowheads) in E11.5 urogenital blocks cultured in GDNF or FGF7+Follistatin. Stained for brush border epitopes (green) and pan-cytokeratin (red). **c**, Mutant UBs cannot branch in GDNF-containing matrigel. d, days. **d**, Less cranial (arrowheads) and caudal (asterisks) mesonephric tubules in mutant pan-laminin stained E11.5 urogenital tissues. **e**, Mesonephric tubule quantification (mean + s.e.m.; $n = 10/10/10$; $***P < 0.0003$). **f**, Control and K220M MM recombined with wild-type UB stained with pan-cytokeratin antibodies. Mutant MM induces attenuated wild-type UB branching. Scale bars: **a**, **b**, **d**, 300 μm; **c**, 250 μm; **f**, 30 μm.

amounts of Pinch-1, but significantly reduced amounts of α-parvin (Fig. 4d, e) while binding of β-parvin was only slightly decreased (Fig. 4d). The reduced binding of α-parvin to the K220A/M mutants was confirmed in a cell free system using recombinant α-parvin (Supplementary Fig. 13c). Although α-parvin was still found to localize to focal adhesions in K220A mutant cells (Supplementary Fig. 13d), actin and focal adhesion dynamics were abnormal, characterized by increased cell contractility and centripetal motility of large, actin-associated focal adhesions (Supplementary Movies 1 and 2). These results show that the K220 of Ilk kinase domain mediates α-parvin binding, and that mutations in this site impair Ilk-mediated actin dynamics and focal adhesion turnover leading to defective directional cell motility.

As the biochemical evidence suggested that defective α-parvin binding causes the defects in kidney development, we examined kidney development in α-parvin-deficient mice[25]. These mice had severe kidney agenesis/dysgenesis and absent UB growth into the MM (Fig. 4f, g).

Our study demonstrates that the scaffold protein function of Ilk is conserved throughout evolution and, as in flies and worms[6,7], the kinase activity of Ilk is not required for mammalian development or postnatal life. We further show that the K220 in the ATP-binding site of Ilk is required for α-parvin binding, and that this interaction is critical for directed cell migration and UB invasion into the MM and subsequent kidney morphogenesis. β-parvin binding was less severely affected, which might explain the tissue-restricted phenotype of the mutant mice. Interestingly, mutations in K220 did not impair *Drosophila* development[6], which could be explained by the fact that flies have nephron-like filtration units instead of kidneys, which detoxify haemolymph and are not essential for development[26]. Our findings thus highlight specific requirements for mammalian integrin adhesion complexes that have evolved to fulfil specialized functions in cell types such as the intermediate mesoderm derived renal components. They also open new avenues for understanding the functions of these complexes in mammalian tissue morphogenesis.

METHODS SUMMARY

Generation of knock-in mice. A *loxP*-flanked neomycin cassette was inserted into exon 13 of mouse Ilk genomic clones[9], after which point mutations were introduced in exons 8 and 11 using site-directed mutagenesis (QuickChangeII; Stratagene). The constructs were electroporated into R1 embryonic stem cells, and clones that underwent homologous recombination were identified by Southern blot using genomic DNA and internal and 3′ external probes, and injected into blastocysts to generate germline chimaeras. Upon germline transmission, mutant mice were intercrossed with deleter-Cre transgenic mice[27] to obtain heterozygous E13 *loxP*, S343A/D, R211A and K220A/M mutant mice, which were subsequently interbred to obtain homozygous mutant mice. Genotyping was performed by Southern blot or PCR analysis.

***In vitro* analysis of kidney morphogenesis.** For induction of extra-UBs, urogenital blocks were isolated from E11.0–E11.5 embryos and cultured in DMEM/F12 (Calbiochem) containing 10% fetal calf serum (FCS; Calbiochem) in the presence of 100 ng ml^{-1} GDNF (R&D Systems) or a mixture of 100 ng ml^{-1} FGF7 and 100 ng ml^{-1} Follistatin288 (R&D Systems). The preparations were fixed in methanol, washed, and incubated with primary antibodies against

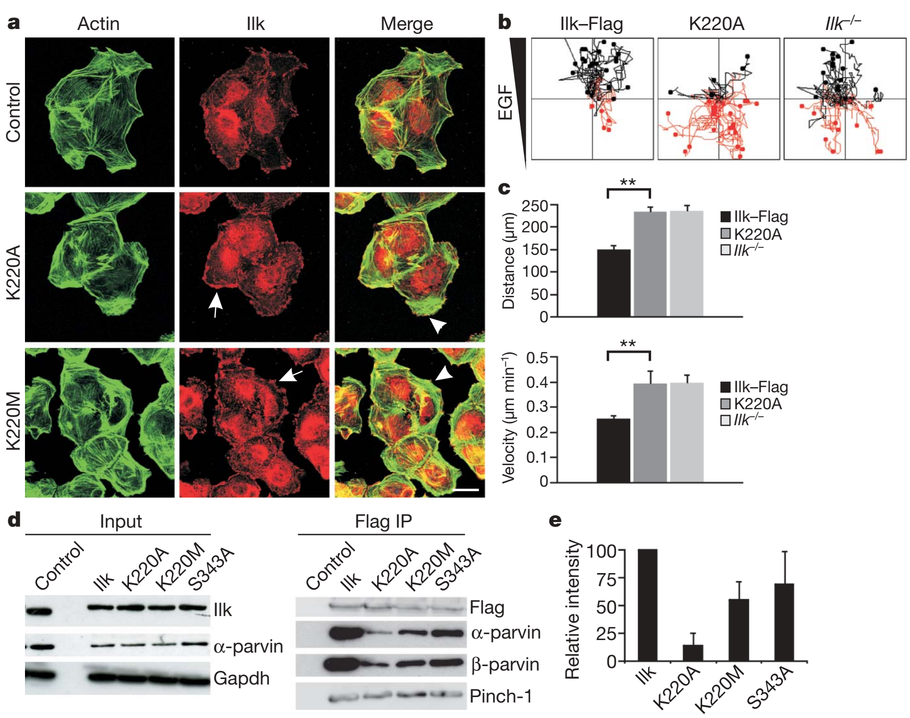

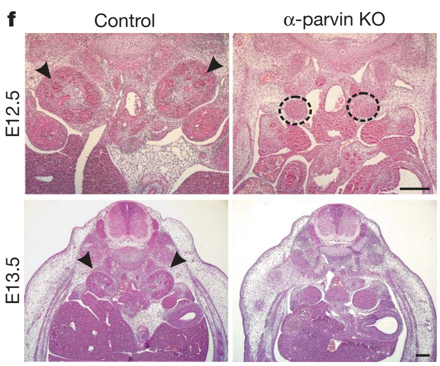

g

Developmental age	E11.5	E12.5	E13.5
Control	$n = 2$	$n = 12$	$n = 4$
Ureteric bud (UB) invasion	2	12	4
UB branching	-	12	4
α-parvin KO	$n = 2$	$n = 12$	$n = 4$
UB not in mesenchyme	2	12	4
1 UB, in mesenchyme, no branching	-	0	0
2 UB, in mesenchyme, no branching	-	0	0
1 UB, in mesenchyme, branching	-	0	0
2 UB, in mesenchyme, branching	-	0	0

Figure 4 | Mutations of lysine 220 of Ilk impair directional cell motility and binding to α-parvin. **a**, Ilk and F-actin staining. Mutant Ilk localizes to large focal adhesions (arrows) and actin bundles accumulate at the cell cortex (arrowheads). **b**, Mutant Ilk cells lose directed migration towards a chemotactic gradient. Black is migration towards and red away from the gradient. **c**, K220A and *Ilk*$^{-/-}$ cells show increased migration distance and velocity (mean + s.e.m.; $n = 4/4/4$; $^{**}P = 0.00286$). **d**, Ilk–Flag immunoprecipitation (IP) of K220A and K220M show a decrease in α-parvin binding and slightly reduced interaction with β-parvin but not Pinch-1. **e**, Quantification of α-parvin binding (mean + s.e.m.; $n = 3$). **f**, UBs branch (arrowheads) in MM of control but not α-parvin deficient (KO) embryos (dotted circles). **g**, Quantification of UB invasion (E11.5) and branching (E12.5 and E13.5). Scale bars: **a**, 15 μm; **f**, 250 μm.

pan-cytokeratin (Sigma) and brush border epitopes (a gift from A. Miettinen, University of Helsinki), and subsequently with fluorescent secondary antibodies, mounted on glass slides, and analysed by confocal microscopy (DMIRE2; Leica).

For the UB branching analysis, UBs were isolated from the surrounding mesenchyme of E11.5 embryos using pancreatin-trypsin treatment, cultured in a mixture of matrigel (BD Biosciences) and DMEM/F12 supplemented with 10% charcoal/dextran treated FCS, 200 nM *cis*- and *trans*-retinoic acid, and 100 ng ml^{-1} GDNF, and analysed using light microscopy.

For *in vitro* nephrogenesis assays, MM was separated from UBs, recombined, and cultured on Nuclepore (Costar) filters for 5 d. Alternatively, urogenital tissue blocks were cultured for 3 d in 10 mM lithium chloride containing DMEM/F12 with 10% FCS, followed by immunofluorescence analysis as described above.

Full Methods and any associated references are available in the online version of the paper at www.nature.com/nature.

Received 27 May; accepted 26 August 2009.

1. Hynes, R. O. Integrins: bidirectional, allosteric signaling machines. *Cell* **110,** 673–687 (2002).
2. Legate, K. R., Wickström, S. A. & Fässler, R. Genetic and cell biological analysis of integrin outside-in signaling. *Genes Dev.* **23,** 397–418 (2009).
3. Legate, K. R., Montanez, E., Kudlacek, O. & Fässler, R. ILK, PINCH and parvin: the tIPP of integrin signalling. *Nature Rev. Mol. Cell Biol.* **7,** 20–31 (2006).
4. Hannigan, G. E. *et al.* Regulation of cell adhesion and anchorage-dependent growth by a new β1-integrin-linked protein kinase. *Nature* **379,** 91–96 (1996).
5. Hannigan, G., Troussard, A. A. & Dedhar, S. Integrin-linked kinase: a cancer therapeutic target unique among its ILK. *Nature Rev. Cancer* **5,** 51–63 (2005).
6. Zervas, C. G., Gregory, S. L. & Brown, N. H. *Drosophila* integrin-linked kinase is required at sites of integrin adhesion to link the cytoskeleton to the plasma membrane. *J. Cell Biol.* **152,** 1007–1018 (2001).
7. Mackinnon, A. C., Qadota, H., Norman, K. R., Moerman, D. G. & Williams, B. D. C. *elegans* PAT-4/ILK functions as an adaptor protein within integrin adhesion complexes. *Curr. Biol.* **12,** 787–797 (2002).
8. Postel, R., Vakeel, P., Topczewski, J., Knoll, R. & Bakkers, J. Zebrafish integrin-linked kinase is required in skeletal muscles for strengthening the integrin-ECM adhesion complex. *Dev. Biol.* **318,** 92–101 (2008).
9. Sakai, T. *et al.* Integrin-linked kinase (ILK) is required for polarizing the epiblast, cell adhesion, and controlling actin accumulation. *Genes Dev.* **17,** 926–940 (2003).
10. Persad, S. *et al.* Regulation of protein kinase B/Akt-serine 473 phosphorylation by integrin-linked kinase: critical roles for kinase activity and amino acids arginine 211 and serine 343. *J. Biol. Chem.* **276,** 27462–27469 (2001).
11. Filipenko, N. R., Attwell, S., Roskelley, C. & Dedhar, S. Integrin-linked kinase activity regulates Rac- and Cdc42-mediated actin cytoskeleton reorganization via alpha-PIX. *Oncogene* **24,** 5837–5849 (2005).
12. Yamaji, S. *et al.* A novel integrin-linked kinase-binding protein, affixin, is involved in the early stage of cell-substrate interaction. *J. Cell Biol.* **153,** 1251–1264 (2001).
13. Lorenz, K. *et al.* Integrin-linked kinase is required for epidermal and hair follicle morphogenesis. *J. Cell Biol.* **177,** 501–513 (2007).
14. Nakrieko, K. A. *et al.* Impaired hair follicle morphogenesis and polarized keratinocyte movement upon conditional inactivation of integrin-linked kinase in the epidermis. *Mol. Biol. Cell* **19,** 1462–1473 (2008).
15. White, D. E. *et al.* Targeted ablation of ILK from the murine heart results in dilated cardiomyopathy and spontaneous heart failure. *Genes Dev.* **20,** 2355–2360 (2006).
16. Lu, H. *et al.* Integrin-linked kinase expression is elevated in human cardiac hypertrophy and induces hypertrophy in transgenic mice. *Circulation* **114,** 2271–2279 (2006).
17. Dressler, G. R. The cellular basis of kidney development. *Annu. Rev. Cell Dev. Biol.* **22,** 509–529 (2006).
18. Carroll, T. J., Park, J. S., Hayashi, S., Majumdar, A. & McMahon, A. P. Wnt9b plays a central role in the regulation of mesenchymal to epithelial transitions underlying organogenesis of the mammalian urogenital system. *Dev. Cell* **9,** 283–292 (2005).
19. Sainio, K. *et al.* Glial-cell-line-derived neurotrophic factor is required for bud initiation from ureteric epithelium. *Development* **124,** 4077–4087 (1997).
20. Maeshima, A. *et al.* Glial cell-derived neurotrophic factor independent ureteric bud outgrowth from the Wolffian duct. *J. Am. Soc. Nephrol.* **18,** 3147–3155 (2007).
21. Kuure, S., Popsueva, A., Jakobson, M., Sainio, K. & Sariola, H. Glycogen synthase kinase-3 inactivation and stabilization of β-catenin induce nephron differentiation in isolated mouse and rat kidney mesenchymes. *J. Am. Soc. Nephrol.* **18,** 1130–1139 (2007).
22. Brodbeck, S. & Englert, C. Genetic determination of nephrogenesis: the Pax/Eya/Six gene network. *Pediatr. Nephrol.* **19,** 249–255 (2004).
23. Delcommenne, M. *et al.* Phosphoinositide-3-OH kinase-dependent regulation of glycogen synthase kinase 3 and protein kinase B/AKT by the integrin-linked kinase. *Proc. Natl Acad. Sci. USA* **95,** 11211–11216 (1998).
24. Grashoff, C., Aszodi, A., Sakai, T., Hunziker, E. B. & Fässler, R. Integrin-linked kinase regulates chondrocyte shape and proliferation. *EMBO Rep.* **4,** 432–438 (2003).
25. Montanez, E., Wickström, S. A., Altstätter, J., Chu, H. & Fässler, R. α-parvin controls vascular mural cell recruitment to vessel wall by regulating RhoA/ROCK signalling. *EMBO. J.* (in the press).
26. Weavers, H. *et al.* The insect nephrocyte is a podocyte-like cell with a filtration slit diaphragm. *Nature* **457,** 322–326 (2009).
27. Betz, U. A., Vosshenrich, C. A., Rajewsky, K. & Muller, W. Bypass of lethality with mosaic mice generated by Cre–*loxP*-mediated recombination. *Curr. Biol.* **6,** 1307–1316 (1996).

Supplementary Information is linked to the online version of the paper at www.nature.com/nature.

Acknowledgements We thank M. Bösl and M. Moser for help with the generation of the mutant mice, E. Montanez for help with the analysis of the α-parvin-null mice, M. Grzejszczyk and S. Bach for technical assistance, O. Kudlacek for help with initial vector construction, M. Aumailley (Univ. Cologne) for laminin322, A. A. Noegel (Univ. Cologne) for α-parvin cDNA, A. Miettinen (Univ. Helsinki) for the brush border antibody, and R. Böttcher for careful reading of the manuscript. This work was supported by the Sigrid Juselius Foundation (to S.A.W. and M.J.), the Academy of Finland (to S.A.W., M.J. and K.S.), the Finnish Cultural Foundation (to S.A.W.), NIDDK DK065123, DK075594, DK65123, an AHA established investigator award and a Merit award from the Department of Veterans Affairs (to R.Z.), the Austrian Science Funds (grant SFB021) and the Max Planck Society (to R.F.).

Author Contributions R.F. initiated and supervised the project. A.L., S.A.W., M.J., R.Z., K.S. and R.F. conceived ideas, designed experiments and analysed data. A.L., S.A.W., M.J. and R.Z. performed experiments. A.L., S.A.W., R.Z. and R.F. wrote the manuscript. All authors edited and reviewed the manuscript.

Author Information Reprints and permissions information is available at www.nature.com/reprints. Correspondence and requests for materials should be addressed to R.F. (Faessler@biochem.mpg.de).

METHODS

Cell culture. Primary keratinocytes were isolated and cultured as described previously[13]. CD cells were isolated from kidneys of *Ilk*$^{f/f}$ mice and immortalized with SV40. Single cell clones were obtained after which the *Ilk* gene was deleted by adenoviral expression of Cre-recombinase. Ilk-null CD cell clones were retrovirally infected with Flag-tagged wild-type Ilk, K220A, K220M and S343A constructs to establish stable cell lines. CD cells were cultured in DMEM/F12 supplemented with 10% FCS.

RT–PCR. Total RNA was extracted from organs using Trizol (Invitrogen) according to the manufacturer's protocol. 1 μg RNA was used for first-strand synthesis using SuperScript III polymerase (Invitrogen) and random hexamer primers. Specific cDNA fragments were amplified using the following primers: *Ilk*-forward: 5′-CATGCACTCAATAGCCGCAG-3′, *Ilk*-reverse: 5′-CTCCACA TGTCTGCTGAGCG-3′, *Taf10*-forward: 5′-GCAATGTCTAACGGGGTTTAC G-3′, *Taf10*-reverse: 5′-CTTGCTCTTGCTCCGGGAGCTG-3′.

Histological analysis. Tissue pieces or embryos were fixed in 4% paraformaldehyde (PFA) overnight at 4 °C, dehydrated in a graded alcohol series, and embedded in paraffin (Paraplast X-tra, Sigma). Paraffin sections were stained with H&E according to standard protocols.

Immunohistochemistry and immunofluorescence. Tissues were frozen in OCT (Thermo Shandon) after which immunohistochemical staining was carried out on 8-μm-thick sections as described previously[28]. For cellular immunostaining, cells were grown on chamber slides (Nunc) coated with 30 μg ml^{-1} collagen I and 10 μg ml^{-1} fibronectin and allowed to adhere and spread for 48 h. Cells were fixed in 3% PFA, rinsed with PBS (170 mM NaCl, 10 mM sodium phosphate buffer, pH 7.4) and permeabilized with 0.2% Triton X-100 when necessary. Nonspecific protein binding sites were saturated with 3% bovine serum albumin (BSA) and 5% goat serum in PBS, followed by incubation with indicated primary antibodies and Alexa488-, Alexa647- (Invitrogen) or Cy3- (Jackson ImmunoResearch Laboratories) labelled secondary antibodies. Finally, the coverslips were washed and mounted on glass slides with elvanol. The fluorescent images were collected by laser scanning confocal microscopy (DMIRE2; Leica) using Leica Confocal Software version 2.5 Build 1227 with ×63 or ×100 oil objectives. All images were collected at room temperature. The following primary antibodies were used: rabbit anti-Ilk (Cell Signaling Technology); FITC-conjugated anti-integrin α6 (BD Biosciences); mouse anti-paxillin (BD Biosciences), phalloidin Alexa488 (Invitrogen), mouse anti-vinculin (Sigma), rabbit anti-α-parvin (Cell Signaling Technology), rabbit anti-Pax-2 (Covance), rat anti-Nidogen (Chemicon), rat anti-Ki67 (Dako Cytomation), and anti-c-Ret (R&D Systems). Quantification of cell area and focal adhesion size was performed using the Metamorph software (Molecular Devices). Quantifications represent at least 3 independent experiments with >50 cells per experiment.

Preparation of cell and tissue extracts, immunoprecipitation and western blotting. Organs dissected from staged mice or cells grown on polystyrene dishes were rinsed in PBS, suspended in lysis buffer (50 mM Tris-HCl buffer (pH 8.0), containing 150 mM NaCl, 1% Triton X-100, 0.05% sodium deoxycholate, 10 mM EDTA, protease and phosphatase inhibitors), homogenized using a Dounce homogenizer (Kinematica), and cleared by centrifugation. The lysates were then reduced in Laemmli sample buffer at 95 °C, separated by polyacrylamide gel electrophoresis in the presence of SDS, transferred onto PVDF membranes and subjected to western blot analyses. Quantification of band intensities was carried out using MultiGauge 3.0 software (Fujifilm). The Flag immunoprecipitation was carried out according to the manufacturers' protocol (Sigma).

The following antibodies were used for western blot analyses: mouse anti-Ilk (BD Biosciences); rabbit anti-Akt and phospho-Akt (Ser473, Thr308; Cell Signaling); rabbit anti-Gsk3β and phospho-Gsk3β (Ser9; Cell Signaling); rabbit anti-mTor and phospho-mTor (Ser2448; Cell Signaling); rabbit anti-p42/44 MAPK and phospho-p42/44 MAPK (Thr202/Tyr204; Cell Signaling); rabbit anti-α/β-parvin[29] rabbit anti-Pinch-1 (ref. 30); mouse anti-Gapdh (Calbiochem); and goat anti-mouse HRP, and goat anti-rabbit HRP (Bio-Rad Laboratories).

Adhesion assay. Cells (1×10^5 cells per well) were plated onto 96-well plates coated with BSA, poly-L-lysine (Sigma), fibronectin (Sigma), laminin332 (a gift from M. Aumailley, Univ. Cologne) or collagen I (Cohesin). After 45 min incubation, adherent cells were lysed in a substrate buffer (7.5 mM NPAG (Sigma), 0.1 M Na citrate, pH 5, 0.5% Triton X-100) overnight at 37 °C. The reaction was stopped by adding 50 mM glycine, pH 10.4, 5 mM EDTA after which absorbance at 405 nm was measured.

TUNEL assay. Apoptotic cells from 6-μm-thick paraffin-embedded embryo sections were detected using the *in situ* Cell Death Detection kit (Roche) according to the manufacturers' instructions.

***In situ* hybridization.** Whole mount *in situ* hybridization was performed with InSituPro Automate (Intavis) on PFA-fixed embryos as described previously[31]. For visualization of *Gdnf*, stained embryos were embedded into 4% low-melting agarose after which sections (10 μm) were cut using a VT-1000S vibratome (Leica). The DIG-labelled RNA probes were prepared from cDNAs of *Gdnf* (gift from J. G. Pichel, Univ. Salamanca) and *Wnt9b* (gift from A. McMahon, Harvard Univ.).

***In vitro* kinase assay.** Flag-tagged Ilk constructs were immunoprecipitated from CD cell extracts using a Flag affinity resin according to the manufacturers' protocol (Sigma). The immunoprecipitates were washed 3× with lysis buffer and 3× with kinase buffer (Cell Signaling; 25 mM Tris-HCl (pH 7.5), 5 mM β-glycerophosphate, 2 mM dithiothreitol, 0.1 mM Na_3VO_4, 10 mM $MgCl_2$, phosphatase and protease inhibitors). Resin-bound proteins were eluted using an excess of Flag peptide in 90 μl kinase buffer. Finally, 45 μl of the eluate, 10 μCi of [γ-^{32}P] ATP (Perkin Elmer), 80 μM cold ATP (Cell Signaling) and 15 μg myelin basic protein (MBP; Upstate) were incubated for 30 min at 30 °C, reduced in Laemmli sample buffer at 95 °C, separated by polyacrylamide gel electrophoresis in the presence of SDS and subjected to autoradiography. Recombinant Erk2 (1 ng; Upstate) was used as a positive control.

***In vitro* three-dimensional chemotaxis assay.** The assays were carried out essentially as described previously[32]. Briefly, cells were suspended in type I collagen (3.0 mg ml^{-1}; PureCol, Cohesion), and cast in custom built chambers. After polymerization the gels were overlaid with growth medium containing epidermal growth factor (1 μg ml^{-1}) and subsequently imaged using phase contrast microscopy (Zeiss) for 10 h. The data were analysed using ImageJ software (version 1.37v; NIH) using Manual tracking and Chemotaxis plug-in tools.

Live cell imaging. EGFP–α-parvin was generated by cloning the murine α-parvin cDNA (gift from A. Noegel, Univ. Cologne) into the pEGFP-C1 vector (Clontech). CD cells plated on 3-cm dishes with a glass bottom were transfected with EGFP–α-parvin and RFP–Lifeact[33] using Lipofectamine 2000 (Invitrogen) according to the manufacturers' instructions. Total internal reflection fluorescence (TIRF) images were captured using an Axiovert 200M inverted microscope (Zeiss) with a ×100 oil objective and a cooled CoolSnap HQ CCD camera (Photometrics). Acquisition was controlled by Metamorph software (Molecular Devices). All images were collected at room temperature. The collected images were processed by 3×3 Gaussian low pass or median filtering and linear contrast enhancement.

GST pull downs. α-parvin cDNA was cloned into the pGEX expression vector (GE Healthcare) and transformed into BL-21 *E. coli*. Recombinant protein was expressed and purified from *E. coli* under non-denaturing conditions. Five micrograms of recombinant protein was incubated with 500 μg cell lysate from cells expressing Flag-tagged wild-type, K220A, K220M, or S343A Ilk in lysis buffer (50 mM Tris, pH 7.4, 150 mM NaCl, 1 mM EDTA, 1% Triton X-100) overnight. Glutathione *S*-transferase (GST)-constructs were precipitated with glutathione beads (Novagen). Subsequent western blots were probed with antibodies against Ilk and GST.

Statistical analysis. Statistical evaluation was performed using the GraphPad Prism software (GraphPad, version 5.0). Statistical significance was determined by the Mann–Whitney U-test.

28. Brakebusch, C. *et al.* Skin and hair follicle integrity is crucially dependent on β1 integrin expression on keratinocytes. *EMBO J.* **19**, 3990–4003 (2000).
29. Chu, H. *et al.* γ-Parvin is dispensable for hematopoiesis, leukocyte trafficking, and T-cell-dependent antibody response. *Mol. Cell. Biol.* **26**, 1817–1825 (2006).
30. Li, S. *et al.* PINCH1 regulates cell-matrix and cell-cell adhesions, cell polarity and cell survival during the peri-implantation stage. *J. Cell Sci.* **118**, 2913–2921 (2005).
31. Kuure, S. *et al.* Crosstalk between Jagged1 and GDNF/Ret/GFRα1 signalling regulates ureteric budding and branching. *Mech. Dev.* **122**, 765–780 (2005).
32. Lämmermann, T. *et al.* Rapid leukocyte migration by integrin-independent flowing and squeezing. *Nature* **453**, 51–55 (2008).
33. Riedl, J. *et al.* Lifeact: a versatile marker to visualize F-actin. *Nature Methods* **5**, 605–607 (2008).

Vol 461 | 15 October 2009 | doi:10.1038/nature08456

LETTERS

DNA demethylation in hormone-induced transcriptional derepression

Mi-Sun Kim[1,2,3], Takeshi Kondo[2], Ichiro Takada[2], Min-Young Youn[2], Yoko Yamamoto[2], Sayuri Takahashi[2], Takahiro Matsumoto[1,2], Sally Fujiyama[1,2], Yuko Shirode[1,2], Ikuko Yamaoka[1,2], Hirochika Kitagawa[2], Ken-Ichi Takeyama[2], Hiroshi Shibuya[3], Fumiaki Ohtake[1,2] & Shigeaki Kato[1,2]

Epigenetic modifications at the histone level affect gene regulation in response to extracellular signals[1,2]. However, regulated epigenetic modifications at the DNA level, especially active DNA demethylation, in gene activation are not well understood[3–5]. Here we report that DNA methylation/demethylation is hormonally switched to control transcription of the cytochrome p450 27B1 (*CYP27B1*) gene. Reflecting vitamin-D-mediated transrepression of the *CYP27B1* gene by the negative vitamin D response element (nVDRE)[6,7], methylation of CpG sites (^{5m}CpG) is induced by vitamin D in this gene promoter. Conversely, treatment with parathyroid hormone, a hormone known to activate the *CYP27B1* gene[8], induces active demethylation of the ^{5m}CpG sites in this promoter. Biochemical purification of a complex associated with the nVDRE-binding protein (VDIR, also known as TCF3)[6,7] identified two DNA methyltransferases, DNMT1 and DNMT3B, for methylation of CpG sites[9], as well as a DNA glycosylase, MBD4 (ref. 10). Protein-kinase-C-phosphorylated MBD4 by parathyroid hormone stimulation promotes incision of methylated DNA through glycosylase activity[11], and a base-excision repair process seems to complete DNA demethylation in the MBD4-bound promoter. Such parathyroid-hormone-induced DNA demethylation and subsequent transcriptional derepression are impaired in *Mbd4*$^{-/-}$ mice[12]. Thus, the present findings suggest that methylation switching at the DNA level contributes to the hormonal control of transcription.

CYP27B1 is the final enzyme in vitamin D biosynthesis, and it is primarily expressed in the renal proximal tubule[6–8]. Two calcemic hormones strictly regulate *CYP27B1* gene transcription[6,7]. Parathyroid hormone (PTH) induces CYP27B1 expression by activating protein kinase A and C (PKA and PKC, respectively)[8,13]. 1α,25-dihydroxyvitamin D_3 (1α,25$(OH)_2D3$), a hormonally active form of vitamin D3, is a repressive signal that binds to and activates the nuclear vitamin D receptor (VDR)[14–16]. A basic helix–loop–helix transcriptional activator (VDR interacting repressor, VDIR) regulates the transcription of *CYP27B1* by the negative vitamin D response element (nVDRE)[6,7]. Heterodimers of vitamin-D-bound VDR and retinoid X receptor (RXR) repress the activation of VDIR that is bound upon the nVDRE by means of the histone deacetylase (HDAC) co-repressor complex[6].

We found that the HDAC inhibitor tricostatin A (TSA) did not fully abrogate vitamin-D-induced transrepression in either 293F cells or mouse cortical tubular (MCT) cells (Supplementary Fig. 2). Using newly established stable 293F and MCT transformants expressing Flag–VDIR, we tested for other factor(s)/complex(es) that co-repressed transcription[17,18] (Supplementary Fig. 3a). The VDIR and VDR interactants consisted of several complexes when fractionated on an ion-exchange column (Supplementary Fig. 3b) and a glycerol gradient (data not shown)[17,18]. We identified DNA methyltransferases 1 and 3B (DNMT1 and DNMT3B)[9] as VDIR and VDR interactants (Fig. 1a) with DNMT activity (Fig. 1g). Generally, DNMT family members methylate cytosines at specific DNA sequences to repress gene expression[19]. In a luciferase assay in 293F cells, both DNMT1 and DNMT3B acted as co-repressors for vitamin-D-induced transrepression of the *CYP27B1* promoter (Supplementary Fig. 5). Vitamin-D-induced DNA methylation of cytosines (^{5m}C) was found in the CpG regions of the promoter in 293F cells (see Fig. 1b) and MCT cells (data not shown), as assessed by bisulphite sequencing (Fig. 1c and Supplementary Fig. 6), methylation-specific PCR (Supplementary Fig. 7), and chromatin immunoprecipitation and quantitative PCR (ChiP-qPCR) with an anti-^{5m}C antibody (Fig. 1d). This methylation step required DNMT1 and DNMT3B (Fig. 1d and Supplementary Fig. 8) based on knockdown assays (Supplementary Fig. 4). The knockdown of DNMTs abrogated vitamin-D-induced transrepression of endogenous *CYP27B1* (Fig. 1e), and a DNMT inhibitor, 5-azacytidine, plus TSA, abolished vitamin-D-induced transrepression (Supplementary Fig. 2). Vitamin-D-induced recruitment of DNMT1 and DNMT3B was detected at the *CYP27B1* promoter by ChIP analysis (Fig. 1f and Supplementary Fig. 9), presumably as direct VDR interactants as observed in an *in vitro* glutathione *S*-transferase (GST)-pull-down assay (Supplementary Fig. 10). DNA methylation of the CpG sites in the promoter and coding regions (Fig. 1c, d), as well as histone deacetylation (Fig. 1d, f), were induced by vitamin D, but a heterochromatin marker, HP1α[18,20], was not detected (Supplementary Fig. 11). Upregulation of DNMT activity of the VDIR immunocomplex by vitamin D was reduced in the presence of PTH (Fig. 1g). Continued PTH treatment of cells that had been pre-incubated with vitamin D induced demethylation of the ^{5m}CpGs (Figs 1c, 2d and Supplementary Fig. 7).

Next, we assayed for a PTH effect in DNA replication. In proximal renal tubule cells expressing the *Cyp27b1* gene in mice, bromodeoxyuridine (BrdU) incorporation (Supplementary Fig. 12a)[20] was not affected by either 48 h PTH treatment or VDR deficiency ($Vdr^{-/-}$)[21] (Fig. 2a). Likewise, PTH-induced DNA demethylation of the *CYP27B1* promoter in 293F cells was detected despite 24 h arrest of the cell cycle after serum depletion or treatment with aphidicolin[22] (Fig. 2b and Supplementary Fig. 12b, c). It was thus unlikely that ^{5m}C replaces C in the newly synthesized DNA during DNA replication.

We characterized MBD4 (refs 10, 12) further because MBD4 recruitment to the promoter coincided with the state of DNA methylation (Fig. 2c, d and Supplementary Fig. 13). MBD4 belongs to the 5-methyl-CpG binding domain (MBD) family, which is implicated in

[1]ERATO, Japan Science and Technology Agency, 4-1-8 Honcho, Kawaguchisi, Saitama 332-0012, Japan. [2]Institute of Molecular and Cellular Biosciences, University of Tokyo, 1-1-1 Yayoi, Bunkyo-ku, Tokyo 113-0032, Japan. [3]Department of Molecular Cell Biology, Medical Research Institute and School of Biomedical Science, Tokyo Medical and Dental University, Yushima, Bunkyo-ku, Tokyo 113-8510, Japan.

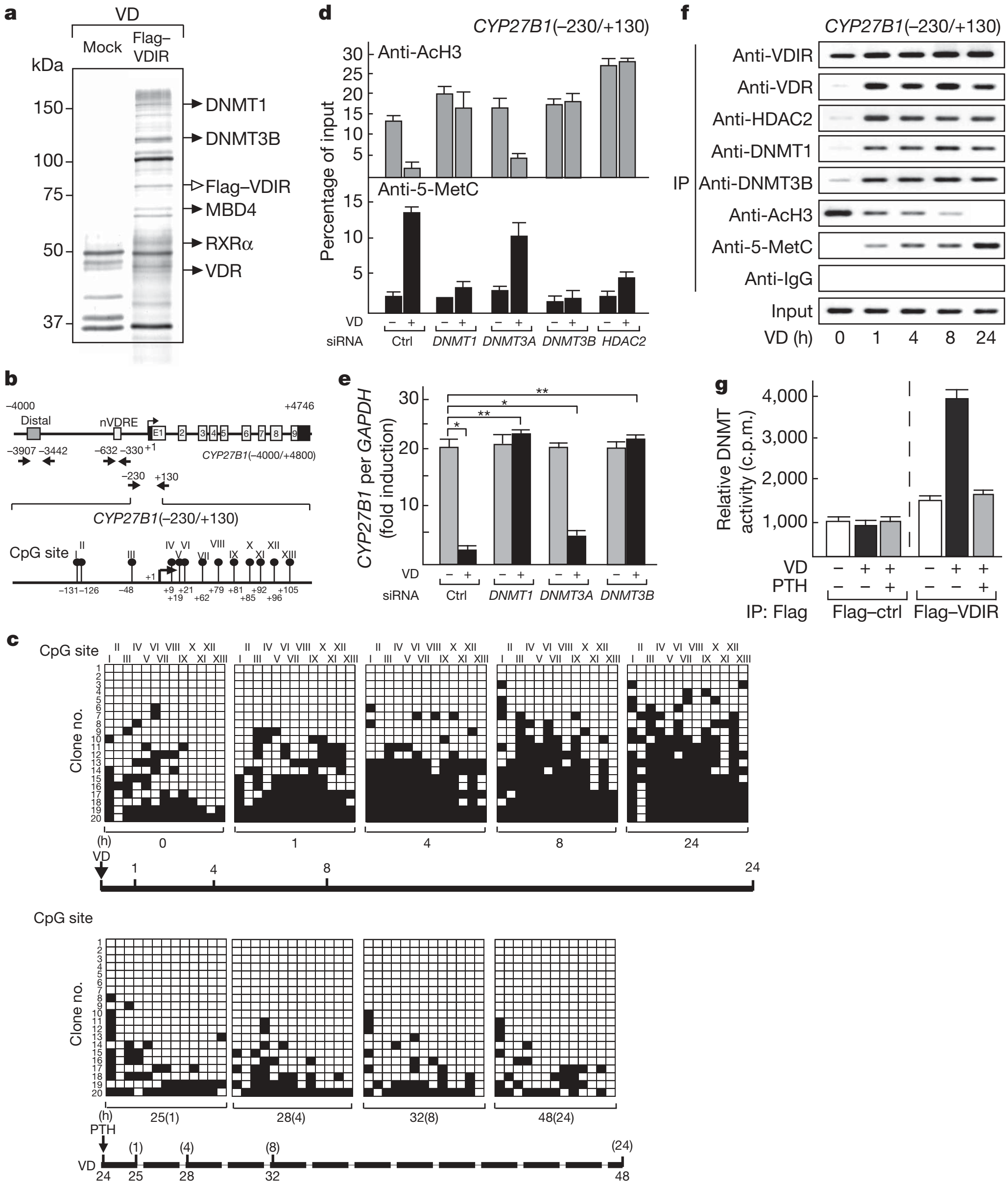

Figure 1 | Hormonal control of DNA methylation/demethylation of the *CYP27B1* gene promoter. a, Silver staining of anti-Flag-affinity purification, followed by anion-exchange column chromatography using vitamin D (VD; 100 nM)-treated MCT cells expressing Flag–VDIR. **b**, Schematic representation of the CpG sites in the *CYP27B1* promoter and coding region. Black filled circles indicate CpG sites. **c**, Time course of DNA methylation/demethylation in *CYP27B1*(−230/+130) region. Bisulphite sequencing was performed using vehicle-treated, vitamin D (100 nM)-treated and vitamin D/PTH (1 μM)-treated 293F cells for the indicated time. Numbers in parentheses denote time after PTH treatment. White and black squares indicate unmethylated and methylated CpGs, respectively. **d**, **e**, ChIP–qPCR analyses of 293F cells transfected with indicated short interfering RNAs (siRNAs), treated with vitamin D (100 nM) for 24 h (means ± s.d., $n = 3$) (**d**) and qPCR (means ± s.d., $n = 3$, $*P < 0.005$, $**P > 0.2$) (**e**). Ctrl, control. **f**, Time-dependent ChIP analyses using 293F cells with vitamin D (100 nM) treatments for the indicated times. **g**, DNMT activity using Flag–VDIR immunoprecipitants (IP) in vitamin D/PTH-treated 293F cells. Activity (means ± s.d., $n = 3$) is shown as c.p.m. of *S*-adenosyl-L-[methyl-^{3}H]-methionine incorporated into oligonucleotide substrate. Background activity was measured in the control experiments performed with Flag-alone immunoprecipitants.

transcriptional repression[23]. Unlike other MBD family members, MBD4 functions in DNA repair as a thymine glycosylase to remove T/G mismatches generated after the deamination of ^{5m}C (refs 10, 24). ChIP analyses showed that MBD4 was the only MBD protein identified at the *CYP27B1* promoter (Fig. 2c). MBD4 was co-immunoprecipitated with VDIR in the presence of vitamin D, and remained associated after co-treatment of vitamin D with PTH independent of the dissociation of DNMTs from VDIR (Fig. 2e). These hormonal effects were not seen in the reported MBD4-binding ^{5m}CpGs sites in the multidrug resistance (*MDR*, also known as *ABCB1*) gene promoter[25] (Supplementary Fig. 14). VDIR seemed to be indispensable for MBD4 recruitment to the promoter (Fig. 2f and Supplementary Fig. 15), presumably through physical interaction (Supplementary Fig. 16). It was recently reported that in transcriptionally active promoters, demethylation of ^{5m}CpGs requires DNMT3A/B for deamination of ^{5m}CpGs for further T/G mismatch repair[26]. However, in 293F cells pretreated with vitamin D for 24 h, DNMT1, DNMT3B or thymine-DNA glycosylase (TDG) was dispensable for PTH-induced demethylation of ^{5m}CpGs within the *CYP27B1* promoter (Fig. 2g). Knockdown of *MBD4*, but not *MBD2*, blocked PTH-induced demethylation of ^{5m}CpGs (Fig. 2h, i and Supplementary Fig. 17). Given the efficient binding of MBD4 to ^{5m}CpG (ref. 10), we proposed that the DNA glycosylase activity of MBD4 induced active DNA demethylation of the ^{5m}CpG sites. We tested this idea with an MBD4 mutant with a deletion in the putative

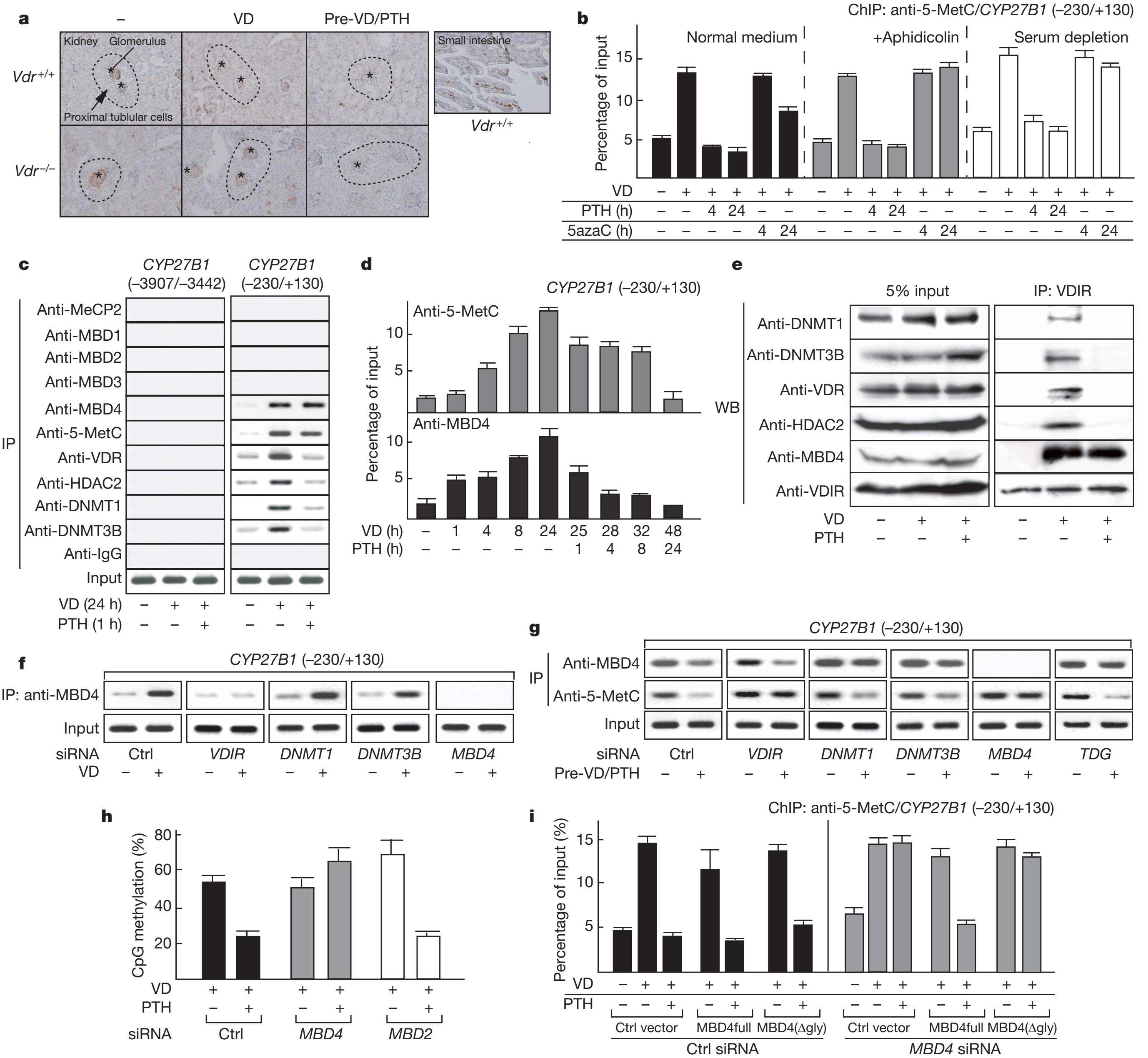

Figure 2 | MBD4 is indispensable for PTH-induced DNA demethylation in the *CYP27B1* promoter. **a**, *In vivo* BrdU incorporation in the kidney and small intestine (control) of mice with indicated genotypes. Proximal tubular cells surrounding the glomerulus (asterisk) are circled by a dashed line. Original magnification, ×200. Experimental details are presented in Supplementary Fig. 11a. **b**, ChIP–qPCR analyses using 293F cells treated with aphidicolin (5 μM) or cultured with serum-free DMEM (means ± s.d., $n = 3$). 5azaC, 5-azacytidine. **c**, **d**, ChIP analyses (**c**) and ChIP–qPCR analyses (means ± s.d., $n = 3$) (**d**) using vitamin D/PTH-treated 293F cells. **e**, Western blotting (WB) using immunoprecipitants with anti-VDIR antibody in vitamin D/PTH-treated MCT cells. **f**, ChIP analyses using 293F cells transfected with indicated siRNAs for 24 h, and then treated with vitamin D (24 h). **g**, ChIP analyses using vitamin-D-treated 293F cells transfected with indicated siRNAs for 24 h, then further treated with PTH (24 h). **h**, Bisulphite sequencing using 293F cells transfected with indicated siRNAs for 24 h, then further treated with vitamin D and PTH (24 h) (means ± s.d., three independent experiments, $n = 15$). **i**, ChIP–qPCR analyses of vitamin D/PTH-treated 293F cells transfected with siRNAs and rescue vectors containing wild-type MBD4 (MBD4full) or a MBD4(Δgly) for 48 h in the presence or absence of vitamin D (48 h) and/or PTH (24 h) (means ± s.d., $n = 3$).

glycosylase catalytic domain (Δgly) (Supplementary Figs 19a and 21a). This mutant was defective in PTH-induced DNA demethylation in cells deficient of endogenous MBD4 (Fig. 2i and Supplementary Fig. 18).

To test the idea that downstream signalling of PTH activates MBD4-mediated DNA demethylation, phosphorylation of putative sites on MBD4 by PKA and PKC (downstream signalling factors of PTH)[13] was measured with recombinant proteins (Supplementary Fig. 19). MBD4 was phosphorylated by PKC *in vitro* (Fig. 3a) and in 293F cells (Fig. 3b and Supplementary Fig. 20). With MBD4 recombinant mutants, serine residues (165 and 262) were mapped as PKC-phosphorylation sites (Fig. 3c). We addressed whether MBD4 has DNA glycosylase activity with mismatched and methylated CpG oligonucleotides, using TDG as a control, in *in vitro* assays[23,26]. Strand incisions by unphosphorylated MBD4 were clearly seen in T/G mismatched oligonucleotides, confirming the reported glycosylase activity of MBD4 for T/G mismatch (Fig. 3d, e and Supplementary Fig. 21)[10,26]. Although the direct DNA binding of MBD4 to both oligonucleotides was detected on electrophoretic mobility shift assays (EMSA) (Supplementary Fig. 22), strand incision of the methylated CpG oligonucleotides was less pronounced. However, strand incision of methylated CpG oligonucleotides was

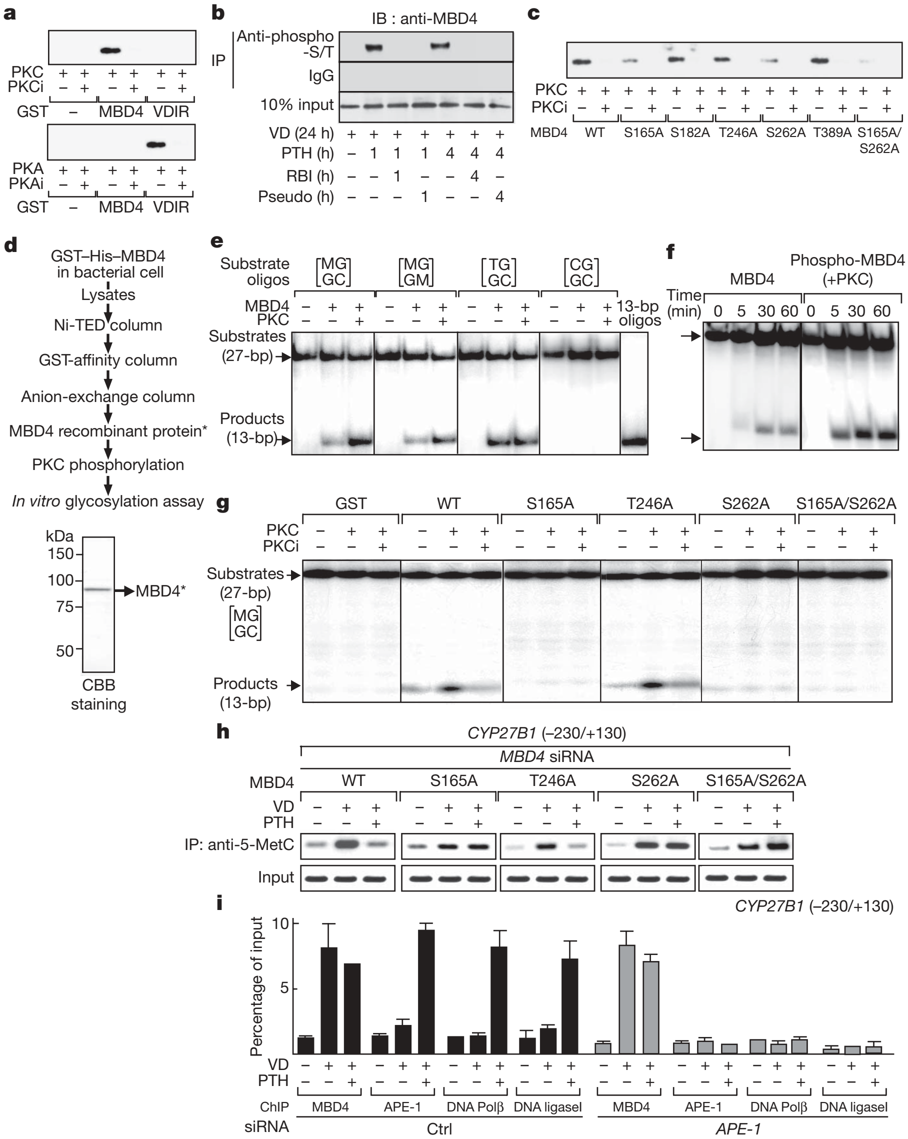

Figure 3 | The DNA glycosylase activity of MBD4 is potentiated by PKC-phosphorylation. a, *In vitro* kinase assay using GST–MBD4 and GST–VDIR with recombinant PKC or PKA. PKC inhibitors (PKCi; RBI and PKC pseudosubstrate) or a PKA inhibitor (H89) were added to the reactions as indicated. **b**, Western blotting with anti-MBD4 using immunoprecipitants with anti-phospho-S/T antibody on the treatments as indicated. **c**, *In vitro* kinase assay using recombinant MBD4 mutants, in which alanine replacements were introduced into the serine or threonine residues. **d**, *In vitro* glycosylation assay protocol (top) and CBB staining of human recombinant MBD4 (bottom). Experimental details of recombinant MBD4 preparations are presented in Supplementary Fig. 21. **e**, *In vitro* glycosylation assay with 0.5 μg of recombinant MBD4 and 5 nM of indicated oligonucleotides: hemi-methylated CpG [MG/GC], symmetrical methylated CpG [MG/GM], mismatched [TG/GC] and unmethylated CpG [CG/GC]. The top arrow indicates substrates (27-base pair (bp) oligonucleotides) and the bottom arrow indicates breakage products (13-bp oligonucleotides). **f**, The kinetics of the PKC-mediated ^{5m}CpG glycosylation activity of MBD4 with MG/GC. **g**, *In vitro* glycosylation assay using phosphorylation-defective MBD4 mutants. **h**, ChIP analyses of 293F cells transfected with *MBD4* siRNA and rescue vectors containing indicated MBD4 derivatives. **i**, ChIP–qPCR analyses of vitamin D/PTH-treated 293F cells transfected with *APE-1* siRNAs (means ± s.d., $n = 3$).

significant when MBD4 was phosphorylated by PKC[22] (Fig. 3e, f and Supplementary Fig. 23). A PKC inhibitor attenuated the enzymatic activity of MBD4 (Fig. 3g). Consistent with this, phosphorylation mutants attenuated PTH-induced DNA demethylation in 293F cells deficient in endogenous MBD4 (Fig. 3h), although their DNA-binding activities were retained (Supplementary Fig. 24). We then evaluated whether major factors responsible for DNA repair were involved in this mechanism[11,26,27]. ChIP analyses showed that apurinic/apyrimidinic (AP) endonuclease-1 (APE-1, also known as APEX1), DNA ligase I and polymerase (Pol) β—components of the base-excision repair process—were recruited simultaneously to the promoter together with MBD4 (Fig. 3i and Supplementary Fig. 25). APE-1 was pivotal in the recruitment of these DNA repair factors (Fig. 3i). These data indicate that DNA demethylation is completed through a base-excision repair process after glycosylation by MBD4. Consistent with the role of MBD4 in PTH-induced DNA demethylation, MBD4 knockdown reversed the effects of PTH on the *CYP27B1* promoter (Fig. 4a) and endogenous gene expression (Supplementary Fig. 26). Neither the MBD4 phosphorylation mutants nor the catalytic domain deletion mutant (Δgly) conferred a response to PTH (Fig. 4b and Supplementary Fig. 27). In ChIP analyses of the *CYP27B1* promoter, PTH-induced DNA demethylation was coupled to histone acetylation, H3K4 methylation and Ser-5-phosphorylated RNA Pol II recruitment[3] (Fig. 4c and Supplementary Fig. 28). Such PTH-induced alterations were abolished by depletion of MBD4 (Fig. 4c).

Finally, the physiological role of MBD4 in PTH-induced derepression was tested in *Mbd4*$^{-/-}$ mice. Vitamin D treatment for 3 days effectively suppressed endogenous *Cyp27b1* gene expression (Fig. 4d,

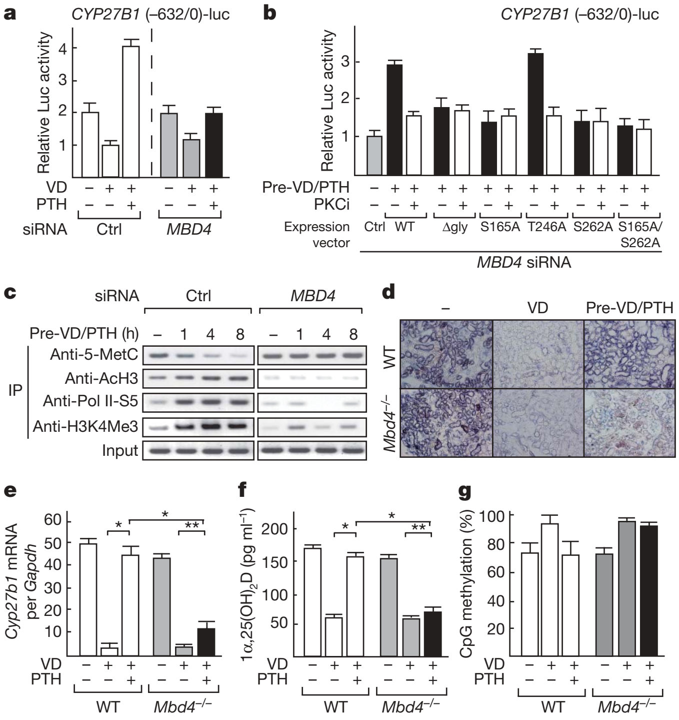

Figure 4 | MBD4-mediated DNA demethylation derepresses transcription of the vitamin D-transrepressed *CYP27B1* gene. **a**, Luciferase assay using 293F cells. The cells were transfected with *MBD4* siRNA for 24 h, and luciferase reporter containing the *CYP27B1*(−632/0) promoter, in the presence or absence of vitamin D (48 h) and/or PTH (last 24 h) (means ± s.d., $n = 3$). **b**, Luciferase assay using MBD4-knockdown 293F cells, transfected with phosphorylation-defective MBD4 mutants. **c**, ChIP analyses of vitamin D/PTH-treated 293F cells transfected with indicated siRNAs. **d**, *In situ* hybridization analysis of murine kidneys using antisense riboprobe for *Cyp27b1*. The *Cyp27b1* mRNAs (dark blue) are broadly localized in the uriniferous tubule cells. Original magnification, ×200. **e**, **f**, qPCR from total RNAs isolated from murine kidneys (**e**) and serum levels of $1\alpha,25(OH)_2D$ (**f**) with the indicated genotypes (wild type, $Mbd4^{-/-}$ medium-chain triglyceride vehicle-treated group, $n = 4$; wild type, $Mbd4^{-/-}$ vitamin-D-treated group, $n = 3$; wild type, $Mbd4^{-/-}$ pre-vitamin-D-PTH-treated group, $n = 7$) (means ± s.d., $*P < 0.001$, $**P > 0.2$). **g**, Bisulphite sequencing using whole murine kidneys (means ± s.d., three independent experiments, $n = 30$).

e) and induced DNA methylation in the kidneys of wild-type and $Mbd4^{-/-}$ mice (Fig. 4g and Supplementary Fig. 29). Administration of PTH to vitamin-D-pretreated, wild-type mice derepressed *Cyp27b1*, as determined by qPCR with reverse transcription (qRT–PCR; Fig. 4e) and *in situ* hybridization (Fig. 4d). The recovery of serum $1\alpha,25(OH)_2D$ levels (Fig. 4f) as well as DNA demethylation (Fig. 4g) were consistently seen. In $Mbd4^{-/-}$ mice, PTH effects were significantly impaired (Fig. 4d–g), confirming the *in vitro* observations.

Active DNA demethylation has been implicated in the derepression of silenced gene promoters during early development[3–5]. The involvement of active DNA demethylation of gene promoters for regulated transcription is, however, largely unknown. Here we found that DNA methylation/demethylation that determined the function of the *CYP27B1* gene promoter was regulated by hormonal switching (see Supplementary Fig. 1). Transcriptional derepression of the *CYP27B1* gene by active DNA demethylation was hormonally inducible. Thus, epigenetic switching at the DNA level reflects, at least in part, well-established hormonal actions on gene regulation.

Hormonally regulated DNA demethylation of the *CYP27B1* gene promoter is mediated by glycosylase activity of MBD4 by PKC-mediated phosphorylation. Although MBD4 is involved in repairing mismatched T/G, structural alteration of MBD4 caused by phosphorylation may shift its substrate specificity. Considering the association of base-excision repair factors with MBD4 on ^{5m}CpG sites in the *CYP27B1* gene promoter, it is likely that this form of active DNA demethylation involves a base-excision repair process. The dissociation of DNMTs from VDIR and MBD4 in the presence of PTH seems to preclude re-methylation of the repaired cytosine. Thus, DNA repair-mediated DNA demethylation in metazoans is probably accomplished by diverse processes that are dependent on the epigenetic context[25,28–30].

METHODS SUMMARY

Biochemical purification of VDIR-associated proteins. Preparation of the nuclear extracts, anti-Flag affinity purification, and mass spectrometry were performed as previously described[17]. Details are provided in Supplementary Methods.

***In vitro* glycosylation assay.** *In vitro* glycosylation assays were performed essentially as previously described[10,23,26]. Recombinant GST–MBD4 and its derivatives were purified from *Escherichia coli*, and subjected to a phosphorylation reaction by PKC. 5′-end [γ-^{32}P]-ATP-labelled DNA substrates were incubated with phosphorylated or non-phosphorylated GST–MBD4 as detailed in the Supplementary Methods.

Bisulphite sequencing and methyl-specific PCR. Genomic DNA was isolated from cell lines and wild-type or *Mbd4*-deficient mice, treated with vehicle, vitamin D or PTH as indicated. Bisulphite treatment and sequencing were performed as described. Results are representative of at least three independent experiments. Details are provided in Supplementary Methods.

DNMT assay. The VDIR complex was purified by immunoprecipitation. 293F cells were transfected as indicated with Flag-tagged VDIR, and cultured in the presence or absence of vitamin D for 24 h, and then PTH for 24 h. After 48 h, the cells were collected, and the Flag-tagged VDIR complex was purified by Flag M2 agarose (Sigma). DNA methyltransferase activity was found in the VDIR immunoprecipitates from the 293F cells only after treatment with vitamin D. Activity is displayed as counts per minute (c.p.m.) of *S*-adenosyl-L-[methyl-^{3}H]-methionine incorporated into an oligonucleotide substrate.

Received 18 August 2008; accepted 24 August 2009.

1. Goldberg, A. D., Allis, C. D. & Bernstein, E. Epigenetics: a landscape takes shape. *Cell* **128**, 635–638 (2007).
2. Trojer, P. & Reinberg, D. Histone lysine demethylases and their impact on epigenetics. *Cell* **125**, 213–217 (2006).
3. Reik, W. Stability and flexibility of epigenetic gene regulation in mammalian development. *Nature* **447**, 425–432 (2007).
4. Bird, A. Perceptions of epigenetics. *Nature* **447**, 396–398 (2007).
5. Egger, G., Liang, G., Aparicio, A. & Jones, P. A. Epigenetics in human disease and prospects for epigenetic therapy. *Nature* **429**, 457–463 (2004).
6. Murayama, A. *et al.* The promoter of the human 25-hydroxyvitamin $D_3 1\alpha$-hydroxylase gene confers positive and negative responsiveness to PTH, calcitonin, and $1\alpha,25(OH)_2D_3$. *Biochem. Biophys. Res. Commun.* **249**, 11–16 (1998).
7. Murayama, A. *et al.* Transrepression by a liganded nuclear receptor via a bHLH activator through co-regulator switching. *EMBO J.* **23**, 1598–1608 (2004).
8. Brenza, H. L. *et al.* Parathyroid hormone activation of the 25-hydroxyvitamin D_3-1α-hydroxylase gene promoter. *Proc. Natl Acad. Sci. USA* **95**, 1387–1391 (1998).
9. Rhee, I. *et al.* DNMT1 and DNMT3b cooperate to silence genes in human cancer cells. *Nature* **416**, 552–556 (2002).
10. Hendrich, B. *et al.* The thymine glycosylase MBD4 can bind to the product of deamination at methylated CpG sites. *Nature* **401**, 301–304 (1999).
11. Jiricny, J. & Menigatti, M. DNA cytosine demethylation: are we getting close? *Cell* **135**, 1167–1169 (2008).
12. Millar, C. B. *et al.* Enhanced CpG mutability and tumorigenesis in MBD4-deficient mice. *Science* **297**, 403–405 (2002).
13. Potts, J. T. & Gardella, T. J. Progress, paradox, and potential: parathyroid hormone research over five decades. *Ann. NY Acad. Sci.* **1117**, 196–208 (2007).
14. Chambon, P. A decade of molecular biology of retinoic acid receptors. *FASEB J.* **10**, 940–954 (1996).
15. Haussler, M. R. *et al.* The nuclear vitamin D receptor: biological and molecular regulatory properties revealed. *J. Bone Miner. Res.* **13**, 325–349 (1998).
16. McKenna, N. J. & O'Malley, B. W. Combinatorial control of gene expression by nuclear receptors and coregulators. *Cell* **108**, 465–474 (2002).
17. Ohtake, F. *et al.* Dioxin receptor is a ligand-dependent E3 ubiquitin ligase. *Nature* **446**, 562–566 (2007).
18. Fuks, F. *et al.* DNA methyltransferase Dnmt1 associates with histone deacetylase activity. *Nature Genet.* **24**, 88–91 (2000).
19. Maison, C. & Almouzni, G. HP1 and the dynamics of heterochromatin maintenance. *Nature Rev. Mol. Cell Biol.* **5**, 296–305 (2004).
20. Yoshizawa, T. *et al.* Mice lacking the vitamin D receptor exhibit impaired bone formation, uterine hypoplasia and growth retardation after weaning. *Nature Genet.* **16**, 391–396 (1997).

21. Takezawa, S. *et al.* A cell cycle-dependent co-repressor mediates photoreceptor cell-specific nuclear receptor function. *EMBO J.* **26,** 764–774 (2007).
22. Ballestar, E. & Wolffe, A. P. Methyl-CpG-binding proteins. Targeting specific gene repression. *Eur. J. Biochem.* **268,** 1–6 (2001).
23. Zhu, B. *et al.* 5-Methylcytosine DNA glycosylase activity is also present in the human MBD4 (G/T mismatch glycosylase) and in a related avian sequence. *Nucleic Acids Res.* **28,** 4157–4165 (2000).
24. El-Osta, A., Kantharidis, P., Zalcberg, J. R. & Wolffe, A. P. Precipitous release of methyl-CpG binding protein 2 and histone deacetylase 1 from the methylated human multidrug resistance gene (*MDR1*) on activation. *Mol. Cell. Biol.* **22,** 1844–1857 (2002).
25. Métivier, R. *et al.* Cyclical DNA methylation of a transcriptionally active promoter. *Nature* **452,** 45–50 (2008).
26. Waters, T. R., Gallinari, P., Jiricny, J. & Swann, P. F. Human thymine DNA glycosylase binds to apurinic sites in DNA but is displaced by human apurinic endonuclease 1. *J. Biol. Chem.* **274,** 67–74 (1999).
27. Tini, M. *et al.* Association of CBP/p300 acetylase and thymine DNA glycosylase links DNA repair and transcription. *Mol. Cell* **9,** 265–277 (2002).
28. Gehring, M. *et al.* DEMETER DNA glycosylase establishes *MEDEA* polycomb gene self-imprinting by allele-specific demethylation. *Cell* **124,** 495–506 (2006).
29. Barreto, G. *et al. Gadd45a* promotes epigenetic gene activation by repair-mediated DNA demethylation. *Nature* **445,** 671–675 (2007).
30. Kangaspeska, S. *et al.* Transient cyclical methylation of promoter DNA. *Nature* **452,** 112–115 (2008).

Supplementary Information is linked to the online version of the paper at www.nature.com/nature.

Acknowledgements We thank A. Murayama, K. Saito and A. Matsukage for discussions, Y. Imai and R. Fujiki for technical assistance, K. Sugasawa for plasmids, and M. Yamaki and H. Yamazaki for preparing the manuscript. This work was supported in part by priority areas from the Ministry of Education, Culture, Sports, Science and Technology (to F.O. and S.K.).

Author Contributions M.-S.K., F.O. and S.K. designed the experiments. M.-S.K., S.F. and F.O. performed biochemical assays. M.-S.K., M.-Y.Y., Y.Y., Y.S. and I.Y. conducted the promoter analysis. T.K., S.T. and T.M. carried out the animal study. M.-S.K. and K.-I.T. were responsible for the data interpretation. M.-S.K. and S.K. wrote the manuscript. All authors discussed the results and commented on the manuscript.

Author Information Reprints and permissions information is available at www.nature.com/reprints. Correspondence and requests for materials should be addressed to S.K. (uskato@mail.ecc.u-tokyo.ac.jp).

Q&A

Chemist **Krzysztof Matyjaszewski** of Carnegie Mellon University in Pittsburgh, Pennsylvania, is the winner of this year's Presidential Green Chemistry Challenge academic award.

How did you get into this field?

My basic area of research is polymer chemistry, which intersects in many important ways with green chemistry. The challenge is to find clean substitutions for more toxic chemical processes that cost the same or less. The ideal situation is replacing something toxic with something environmentally friendly — such as replacing a toxic metal in a catalytic compound with a vitamin that biodegrades.

What research problems do you work on?

We focus on three areas: working towards cleaner, more effective catalysts; creating degradable materials by controlling macromolecular structures; and working at the interface of biochemistry and materials science to create smart polymers that safely deliver agents to specific sites.

Do green projects have enough funding?

Funding support is important, but more important is the balance between how much something costs and how important it is. Sometimes, if you want to make something more environmentally friendly, it is more expensive.

How important has a mentor been to you?

Always, you rely on mentors. Years ago in Poland I started working with a professor who impressed on me the need to approach a problem in a systematic manner, but never to close your mind to possibly important avenues that could be hidden in the details.

How did you get from Poland to Pittsburgh?

I was a postdoc in 1978–79 at the University of Florida. I returned to Poland expecting change when [the trade union movement] Solidarity happened. But that hope was not realized. I spent a year in Paris. A professor leaving Carnegie Mellon told me I should apply for his position, as it had good funding and support in a nice city. Pittsburgh is a very good example of the green spirit. It was one of the most polluted US cities; now it is one of the cleanest.

What's your approach to advising students?

Even though I generally have 10–15 graduate students and 5 postdocs, I try to interact with each on a one-to-one basis. We also have group meetings weekly and meet twice a year with our industry consortium members. Sometimes even a first-year graduate student can teach someone from industry how to do something better.

What's the importance of exposing graduate students to industry?

Maybe half will go to industry. So I hold regular group meetings, like in industry, to discuss progress on longer-term objectives. I also teach them to consider more than one part of the problem: not just synthesis but also characterization and the search for potential applications. ■

Interview by Paul Smaglik

POSTDOC JOURNAL

Heart matters

My new role as a freelance writer has brought some interesting assignments, including interviewing students and writing their profiles for a university postgraduate handbook. Although their responses proved fascinating, it also made me question my recent decision to leave academia.

As I delved into their childhood dreams and aspirations, I saw many parallels to my own life and career that made me nostalgic for my previous life. I miss research and the social interactions of a busy lab — discussions with my three-year-old son only go so far! I was even compelled to undertake late-night searches for tenure-track positions.

But real life soon made me realize the advantages of my chosen path. My stepmother is still recovering from a heart attack that occurred five days into her holiday when she came to visit us in Colorado. During the past week at the hospital, I have been thankful for the extra time and flexibility that freelancing gives me to spend with my family. Such time is precious and transitory — my parents are getting older and my son is growing up fast.

For me right now, academia just doesn't seem flexible enough to accommodate the family life I strive for. But I am in awe of the countless women who do juggle career and family with prowess. And I wish every success to my interviewees as they embark on their research careers. ■

Joanne Isaac was a postdoc in climate-change effects on biodiversity at James Cook University, Townsville, Australia. She is now in the United States so that her husband can complete a postdoc.

IN BRIEF

Call for cluster funding

A report by the Center for American Progress, a think tank in Washington DC, calls for Congress to fund the development of regional innovation clusters similar to California's Silicon Valley. This will create jobs and maintain US competitiveness despite limited state resources, it says.

Issued last month, 'The Geography of Innovation' proposes a competitive matching-grants programme to fund training, research centres or business incubators that focus on priorities such as energy technologies. Representative Jared Polis (Democrat, Colorado) touted the report on 6 October, advocating federal support for regional partnerships to enhance economic efficiency and growth.

Psychology overhaul

US psychologists need an accreditation system that verifies their science acumen, according to the US Association for Psychological Science (APS).

A report by the association says that clinical psychologists too often are unaware of validated treatment methods. It assails the American Psychological Association's current accreditation system as a "one size fits all" approach that lumps together disparate subfields. The APS advocates an accreditation system that, for instance, gauges whether incoming students have science and maths skills, whether faculty members have published science-based research and whether students apply clinical knowledge in presentations and publications.

Genomics gets a boost

The US National Institutes of Health recently announced $45 million in grants to fund new genome-science centres in Wisconsin and North Carolina, as well as existing centres in California and Maryland. The grants will be used to develop genomics tools.

The Wisconsin centre will receive $8 million over three years, and will team up with the Medical College of Wisconsin and Marquette University, both in Milwaukee, and the University of Wisconsin-Madison. Over the next five years, the three centres at the University of North Carolina in Chapel Hill, the University of Southern California, Los Angeles, and the Johns Hopkins University in Baltimore will receive $8.6 million, $12 million and $16.8 million, respectively.

Escapism

Where there's a will ...

Nick Mamatas

Piotr was in prison for life for a crime he could not help but commit. He was a scientist, and his theories were borne out by the evidence. The Universe is holographic, two dimensions inscribed across the cosmological horizon.

The Politburo thugs, and they were all thugs to a man, could not tolerate the idea of presiding over a Universe where things were not what they seemed — where they could not stand at least a tiny bit taller than the rest. This wasn't what Piotr meant, but that is what the government heard. Piotr could not recant. He would not. A boot on the back of one's neck *was* not data, threats were not evidence, torture not proof.

They put Piotr deep underground, in a hole in a honeycomb prison from which no one had ever escaped. His papers were burned, an axe taken to his computers, and his assistant taken away in the night. *Like Galileo*, Piotr thought, but there was no Inquisition for Piotr, no nobles who had taken his side, no eventual reprieve and exile to a far-off villa. For Piotr there was just a black hole and the rest of the world in all directions on the other side of the dark.

Piotr licked the condensation off the walls to live. He ate worms and rats and fought the other rats for those tiny bits of flesh he pulled from their comrades' papery bones. Strong enough to stand for longer than any guard or warden would have imagined, Piotr tried to escape.

He pressed himself up against the hewn stone walls of his cell, which had been built around him, and pushed hard. There was a chance, a small chance. A quantum chance. One in ten quadrillion, but it was there — Piotr could just flow through the wall. His mostly nothing and its mostly nothing, meshing perfectly. *Well no*, Piotr told himself, even as he pushed hard against the dark. *I am just insane. My cosmological horizon stops at my now-blind eyes.* It was those New-Agers with their breathless speeches and ridiculous websites, they're the ones who believe that rot. The Politburo let them run free, those "harmless kooks" (Piotr snorted as he thought those words), because the silly husbands and foolish wives of the powerful were taken with the pleasing notion of a reality that reorders itself to one's wishes. That attribute of the Universe was even an objective and observable phenomenon as far as the sufficiently wealthy (and sufficiently limited in imagination) were concerned.

The black hole he was in, Piotr reminded himself, was not a black hole. He was not a particle contained in the fluctuations of an event horizon. This wasn't a cage of maximum entropy, or a divot in the field of space-time. And there wasn't some other particle somewhere else on the other side of the wall to which Piotr was bound by ghostly chains of instantaneous information transmission. Piotr's home was just a hole dug by men so that other men could die in private for the public peace.

JACEY

However, Piotr had nothing else to do. And he could run his lips and tongue against the wall, sucking up what little water there was. And he could push, alone in the dark, waiting for the cosmos to fall apart around him.

Piotr pushed for days, months. He stopped only to eat and to eliminate. At times he felt a groove in the wall, a groove shaped like his body. It was a trick of the dark — and his desperate mind, he thought at other times. Sometimes he scraped against the cool rock with his fingernails, seeking a seam or even imagining scratching his way to freedom. Perhaps there was only a five in one quadrillion chance of that. *Double my odds*, he thought. But he was tired, his limbs and digits weak from the diet of brackish water and rats that could squeeze through the cracks he never seemed to find in the wall.

One day — or was it night? — Piotr pushed hard against the wall, limbs spread, chest and groin pressed against rock, his own hot breath hanging like a cloud. There was a shift. He was no longer explicate — a thing to be moved about by the deeper reality of political expediency, of dark forces and unseen hands and subtle strings like those bound to the joints of a marionette. Piotr was the implicate, the thing at the dark centre reaching and expanding outwards across the plane of the world. He was the Unmoved Mover of non-locality and all that which could be called locality both, the logarithmic shadow on the horizon of his black hole and that which cast the shadow as well. *Sistemi del mondo!* Piotr didn't think. He was. In and out. Information everywhere, written across the whole of the cosmos.

With a whoosh of cold air, something gave way, and there was a yowl and an impact that shook the cell, warping its walls like a soap bubble. Light! Grey and coruscating like a far of explosion seen from under ocean waves, but light. "I did it!" shouted Piotr's assistant, a man of rags and bones and wide red eyes. "I'm free! I fell right through the floor of my cell and ..." he trailed off and squinted up at Piotr. "Oh."

Piotr offered his congratulations, colleague to colleague. ■

Nick Mamatas is the author of two novels and the short story collection *You Might Sleep...* His website is cleverly located at www.nick-mamatas.com, as if by design.

Join the discussion of Futures in *Nature* at go.nature.com/QMAm2a

FUTURES

NIH Intramural Research Program is Recruiting
"Earl Stadtman Investigators"

The National Institutes of Health, the nation's premier agency for biomedical and behavioral research, is pleased to announce the launch of its search for top-tier tenure-track candidates to become "NIH Earl Stadtman Investigators."

Earl Stadtman was an outstanding NIH scientist who mentored many current leaders in the biomedical community. In his honor, the NIH is recruiting basic, clinical and population-based investigators who seek the flexibility of scientific exploration in an intellectual and supportive environment. NIH investigators have the ability to focus on research that is high risk; they can quickly redeploy resources to explore new directions, collaborate freely on multidisciplinary teams, and contribute to the NIH mission of improving human health. The receipt of prestigious awards and honors—Nobel prizes, Lasker awards, elections to the NAS and IOM, among others—demonstrates the scientific rigor of our NIH intramural investigators.

We offer competitive startup packages and a collaborative, academic environment with more than 1,100 principal investigators engaged in cutting-edge basic, translational, clinical and population-based research. Our scientists focus entirely on their research with ample opportunities to mentor and train outstanding fellows at all levels. One special feature of our research program is the NIH Clinical Center, the world's largest hospital entirely devoted to biomedical research.

Qualifications/Eligibility: Candidates must have an M.D., Ph.D., D.D.S./D.M.D., D.V.M, D.O. or equivalent doctoral degree and have an outstanding record of research accomplishments as evidenced by publications in major peer-reviewed journals. Preference will be given to applicants who are in the early stages of their research careers. Candidates in any area of biomedical, clinical and behavioral research are invited to apply. Appointees may be U.S. citizens, resident aliens or non-resident aliens with, or eligible to obtain, a valid employment-authorized visa.

Salary: Successful candidates are offered competitive salaries commensurate with experience and qualifications, and they are assigned ample research space, supported positions and an operating budget.

To Apply: Complete applications should be received by November 1, 2009; however, applications will be accepted until available positions are filled. Interested applicants should submit a curriculum vitae, a three-page description of proposed research, and three letters of recommendation through our online application system, at http://tenuretrack.nih.gov. No paper applications will be accepted.

For information on the NIH Intramural Research Program, refer to http://intramural.nih.gov/search and http://www1.od.nih.gov/oir/sourcebook/sci-prgms/sci-prgms-toc.htm. Specific questions regarding this recruitment effort may be directed to Dr. Roland Owens, Assistant Director, NIH Office of Intramural Research at owensrol@mail.nih.gov.

We seek original and interactive thinkers to be part of the next generation of research leaders. Become part of a team that continues to make history.

NW186235R

The NIH is dedicated to building a diverse community in its training and employment programs

Opportunities @ NIH The National Institutes of Health

Department of Health and Human Services
National Institutes of Health
Intramural Research Programs
NCI, NEI, NHLBI, NIAID, NIDDK, NIMH, NINDS and CIT
Bethesda, MD

Tenure Track/Tenured Positions In Systems Biology

The NIH Intramural Research Program (IRP) is recruiting outstanding systems biologists at the tenure-track or tenured levels. These individuals will direct independent research programs on the NIH campus in Bethesda, MD and participate in a Trans-NIH Initiative in Systems Biology promoting interaction between experimentalists, theoreticians and computational investigators. Candidates will have demonstrated an ability to conduct outstanding independent biomedical research on key topics in systems biology such as computational modeling of biological processes at various scales, analysis of global datasets, construction and analysis of biological networks, and 'omic' scale interrogation of biological systems. The internationally recognized NIH faculty covers a wide range of basic and clinical research topics with a growing strength, support and emphasis on systems biology and informatic approaches to biomedicine.

The NIH IRP promotes creative and innovative science unconstrained by the conventional support mechanisms demanded at academic or private research institutes. Investigators have ready access to and support from state-of-the art experimental and computational cores and facilities, and a variety of programs to recruit graduate students and post-doctoral fellows.

Candidates must have an M.D. and/or Ph.D., or equivalent doctoral degree, and an outstanding record of research accomplishment and peer-reviewed publications. Recruits will be provided a competitive salary commensurate with experience and qualifications, and will be assigned ample research space, supported positions, operating budget, and start-up funds. Appointees may be US citizens, resident aliens, or eligible foreign nationals. Review of applications will commence on Nov.1, 2009 and continue until the positions are filled. Please submit a curriculum vitae, brief (not to exceed 3 pages) statement of research interests that includes how you see your research group helping to create a world-class, integrated systems biology effort at NIH, and three letters of reference in .pdf or MS word format only (no paper applications will be accepted) to: **http://tenuretrack.nih.gov/apply/**

National Institutes of Health
National Institute of Arthritis and Musculoskeletal and Skin Diseases, Intramural Research Program

Tenured/Tenure-Track Investigator(s)

The Intramural Research Program of the National Institute of Arthritis and Musculoskeletal and Skin Diseases (NIAMS) of the National Institutes of Health (NIH) in the Department of Health and Human Services (DHHS) is recruiting outstanding tenure-track and/or senior (tenured) scientists (M.D., Ph.D, or M.D./Ph.D) active in any of the following areas relevant to musculoskeletal biology or diseases:

- Basic, Translational and Clinical Research in Orthopaedics, Bone, Cartilage, or Muscle
- Nanotechnology related to Bone, Cartilage, Tendon/Ligaments, or Muscle
- Biology of inducible pluripotent stem (iPS) and mesenchymal stem cells for the study of human disorders
- Biological/Tissue Engineering
- Regenerative Medicine

Emphasis will be placed on the applicants' demonstrated track record of high-quality research and the originality and promise of their future plans. Successful applicants will be expected to develop energetic, creative, independent research programs within an existing highly interactive scientific environment. The ideal candidate would benefit from pre-existing expertise within NIAMS.

This position(s) is located on the NIH campus in Bethesda, Maryland, a suburb of Washington, D.C. NIAMS and the NIH offer tremendous depth and breadth of intellectual and technological resources, as well as opportunities for collaboration with investigators both within and outside of the NIH. NIAMS is also a major user of the NIH Clinical Research Center, a state-of-the-art research hospital on the campus of the NIH in Bethesda, Maryland. The research environment is highly conducive to advancing basic and translational research and highly collaborative, encouraging multidisciplinary and interdisciplinary team science.

The mission of NIAMS is to support research into the causes, treatment, and prevention of arthritis and musculoskeletal and skin diseases, the training of basic and clinical scientists to carry out this research, and the dissemination of information on research progress in these diseases.

Applicants should submit a cover letter that includes a short research interest statement (two page maximum), a curriculum vitae and complete bibliography, along with complete contact information of three referees. Applications should be submitted by **February 1, 2010**.

Applications should be submitted to: **Mrs. Wanda White – RE: Musculoskeletal Initiative, Building 31 Room 4C-12, 9000 Rockville Pike, Bethesda MD 20892, Email: whitewan@mail.nih.gov**

NW185964R

Tenure-Track/Tenured Investigator Laboratory of Immunology

The Laboratory of Immunology (LI), Division of Intramural Research, National Institute of Allergy and Infectious Diseases, National Institutes of Health (NIH) invites applications for a tenure-track/tenured investigator position in immunology. Applicants should have a Ph.D., M.D., or equivalent degree; an outstanding record of postdoctoral accomplishment; and an interest in any area of biomedical research related to immunology.

Specifically, we seek a highly creative individual who will establish an independent, world-class research program that takes full advantage of the special opportunities afforded by the stable, long-term funding of the intramural research program at NIH. She or he should be interested in developing and applying novel approaches to the study of problems of major biological and/or medical importance, which could include a significant clinical or translational effort in addition to bench research. In the former case, the successful candidate would have access to the NIH Clinical Center, a state-of-the-art research hospital on the NIH campus in Bethesda, MD, and ample opportunity to participate in the activities of the Trans-NIH Center for Human Immunology.

Generous ongoing support for salary, technical personnel, postdoctoral fellows, equipment, and research supplies will be provided. Available core or collaborative facilities include flow cytometry, advanced optical imaging, microarray generation and analysis, high throughput sequencing, computational biology, production of transgenic and gene-manipulated mice, biosafety level (BSL)-3 facilities, chemical genomics, and support for projects involving RNAi screening. The successful applicant will also have access to Trans-NIH initiatives involving technology development, translational investigation, and multidisciplinary science. In addition to an outstanding international postdoctoral community, a superior pool of graduate and undergraduate students is available to the successful applicant.

LI has a distinguished history of accomplishment in immunology. We strongly encourage application by outstanding investigators who can continue and enhance this record of achievement. Current LI investigators are Ronald Germain, Michael Lenardo, David Margulies, Stefan Muljo, William Paul, Ethan Shevach, and Tsan Xiao.

To apply, e-mail curriculum vitae, bibliography, and outline of a proposed research program (no more than two pages) to Ms. Yushekia Hill at NIAID.DIR.Search@niaid.nih.gov. In addition, three letters of reference must be sent directly from the referee to Drs. Giorgio Trinchieri and Dan Kastner, Co-Chairs, NIAID Search Committee, c/o Ms. Yushekia Hill, at NIAID.DIR.Search@niaid.nih.gov or 10 Center Drive, MSC 1356, Building 10, Room 4A22, Bethesda, MD 20892-1356. E-mail is preferred. Applications will be reviewed starting **11/16/09** and will be accepted until the position is filled. Please refer to ad #028 on all communications. For further information about this position, contact Dr. William Paul at 301-496-5046 or wpaul@niaid.nih.gov.

A full package of benefits (including retirement and health, life, and long-term care insurance) is available. Women and minorities are especially encouraged to apply. U.S. citizenship is not required.

NIAID

National Institute of Allergy and Infectious Diseases

To learn more about NIAID and how you can work in this exciting research organization, please visit us on the web at **www.niaid.nih.gov/careers/nti**.

U.S. DEPARTMENT OF HEALTH AND HUMAN SERVICES
National Institutes of Health

National Institute of Allergy and Infectious Diseases

Proud to be Equal Opportunity Employers

NW185964R

OPPORTUNITIES @ NIH THE NATIONAL INSTITUTES OF HEALTH

THE NIH IS DEDICATED TO BUILDING A DIVERSE COMMUNITY IN ITS TRAINING AND EMPLOYMENT PROGRAMS

Ateliers de formation Inserm
101 rue de Tolbiac
75654 Paris Cedex 13 France
Tel: 33 (0) 144.23.62.04
Fax: 33 (0) 144.23.62.93
ateliers@inserm.fr
www.rh.inserm.fr

Instituts thématiques

Inserm

French Institute of Health and Medical Research

Inserm Workshops 2010

201 Lentiviral vectors: tools for fondamental and clinical research

Phase I Critical assessment: March 3-5, 2010 - Saint-Raphaël
Organizers: Tuan Huy Nguyen (Inserm U948, Nantes), Emmanuel Payen (Inserm U962, Fontenay aux Roses), Els Verhoeyen (Inserm U758, Lyon).
Tentative list of speakers: Muriel Audit (Evry, France), Natalie Cartier (Paris, France), Mary Collins (London, UK), Anne Galy (Evry, France), Tuan Huy Nguyen (Nantes, France), Luigi Naldini (Torino, Italy), Didier Nègre (Lyon, France), Jean-Christophe Pagès (Tours, France), Ali Saïb (Paris, France), Axel Schambach (Hannover, Germany), Didier Trono (Lausanne, Switzerland), Els Verhoeyen (Lyon, France), Rafael Yanez-Munoz (London, UK).

Phase II Technical workshop: March 8-12, 2010 - Lyon
Registration deadline: January 8, 2010

202 *In silico* discovery of molecular probes and drug-like compounds: success and challenges

Phase I Critical assessment: March 23-25, 2010 - Saint-Raphaël
Organizers: Maria Miteva (Inserm U973, Paris), Véronique Stoven (Inserm U900, Paris), Bruno Villoutreix (Inserm U973, Paris).
Tentative list of speakers: Ruben Abagyan (La Jolla, USA), Andreas Bender (Leiden, The Netherlands), John Hickmann (Paris, France), Denise Hirsch (Paris, France), Richard Jackson (Leeds, UK), Gerard Kleywegt (Uppsala, Sweden), Bernard Maigret (Nancy, France), Maria Miteva (Paris, France), Xavier Morelli (Marseille, France), Stefano Moro (Padova, Italy), Brian Shoichet (San Francisco, USA), Jean-Philippe Vert (Paris, France), Michel Vidal (Paris, France), Michael Wiese (Bonn, Germany).

Phase II Technical Workshop: November 2010 - Paris
Registration deadline: January 25, 2010

203 Interactomics: at the crossroads of biology and bioinformatics

Phase I Critical assessment: March 30 - April 1st, 2010 - Saint-Raphaël
Organizers: Christine Brun (TAGC U628, Marseille), Jérôme Reboul (Inserm U891, Marseille), Nicolas Thierry-Mieg (TIMC-IMAG, La Tronche).
Tentative list of speakers: Javier De Las Rivas (Salamanca, Spain), Etienne Formstecher (Paris, France), Anne-Claude Gavin (Heidelberg, Germany), Kristin Gunsalus (New York, USA), Henning Hermjakob (Hinxton, UK), Carl Herrmann (Marseille, France), Vincent Lotteau (Lyon, France), Fabio Piano (New York, USA), Fanny Pilot-Storck (Maisons-Alfort, France), Jolanta Polanowska (Marseille, France), Sylvie Ricard-Blum (Lyon, France), Benno Schwikowski (Paris, France), Jacques Van Helden (Brussels, Belgium), Marc Vidal (Boston, USA).

Phase II Technical workshop: May 2010
Registration deadline: January 29, 2010

204 Human induced pluripotent stem cells, reprogramming and differentiation

Phase I Critical assessment: April 21-23, 2010 - Saint-Raphaël
Organizers: Annelise Bennaceur-Griscelli (Inserm U935, Paris), Ludovic Vallier (University of Cambridge, UK).
Tentative list of speakers: Simone Bateman (Paris, France), Christopher Baum (Hannover, Germany), Annelise Bennaceur-Griscelli (Paris, France), Laure Coulombel (Paris, France), Laurence Daheon (Boston, USA), Chris Denning (Birmingham, UK), Sheng Ding (San Diego, USA), John Gurdon (Cambridge, UK), Konrad Hochedlinger (Boston, USA), Keisuke Kaji (Edinburgh, UK), Marc Peschanski (Evry, France), Katherine Plath (Los Angeles, USA), Jean-Paul Renard (Paris, France), Pierre Savatier (Lyon, France), Hans Scholer (Bohn, Germany), Alexandre Simon (Paris, France), Jose Silva (Cambridge, UK), Ludovic Vallier (Cambridge, UK).

Phase II Technical workshop: October 11-13, 2010
Registration deadline: February 19, 2010

205 Mixture modelling for longitudinal data

Phase I Critical assessment: June 2-4, 2010 - Saint-Raphaël
Organizers: Bruno Falissard (Inserm U669, Paris), Christophe Genolini (Université Paris X, Paris), Helene Jacqmin-Gadda (Inserm U897, Bordeaux), Cécile Proust-Lima (Inserm U897, Bordeaux).
Tentative list of speakers: Tihomir Asparouhov (Los Angeles, USA), Jose Cortinas (Diepenbeek, Belgium), Sylvana Cote (Montreal, Canada), Maria De Loro (London, UK), Bruno Falissard (Paris, France), Christophe Genolini (Paris, France), Helene Jacqmin-Gadda (Bordeaux, France), Jacques Juhel (Rennes, France), Bengt Muthen (Los Angeles, USA), Daniel Nagin (Pittsburgh, USA), Cécile Proust-Lima (Bordeaux, France).

Phase II Technical workshop: June 7-8, 2010
Registration deadline: : April 2, 2010

206 Microtubule dynamics in cell migration: molecular interactions, functional consequences and therapeutic perspectives in cancerology

Phase I Critical assessment: September 15-17, 2010 - Saint-Raphaël
Organizers: Stéphane Honoré (Inserm U911, Marseille), Diane Braguer (Inserm U911, Marseille).
Tentative list of speakers: Anna Akhmanova (Rotterdam, The Netherlands), Annie Andrieux (Grenoble, France), Ali Badache (Marseille, France), Denis Chrétien (Rennes, France), Sandrine Etienne-Manneville (Paris, France), Elaine Fuchs (New-York, USA), Niels Galjart (Rotterdam, The Netherlands), Greg Gundersen (New-York, USA), Stéphane Honoré (Marseille, France), Irina Kaverina (Nashville, USA), Laurence Lafanachère (Grenoble, France), Xavier Morelli (Marseille, France), Véronique Proux (Paris, France), Michel Steinmetz (Villigen, Switzerland).

Phase II Technical workshop: October 27-29, 2010 - Marseille
Registration deadline: : July 15, 2010

207 Targeted genome modification using custom-made endonucleases

Phase I Critical assessment: September 30- October 2nd, 2009 Saint-Raphael
Organizers: Jean-Paul Concordet (Inserm U567, Paris), Carine Giovannangeli (Inserm U565, Paris).
Tentative list of speakers: I. Anegon (Nantes, France), S-J. Boulton (South Mimms, UK), D. Carroll (Salt Lake City, USA), T. Cathomen (Berlin, Germany), J-P. Concordet (Paris, France), C. Giovannangeli (Paris, France), M. Holmes (Richmond, USA), B. Lopez (Fontenay-aux-Roses, France), G. Montoya (Madrid, Spain), L. Naldini (Milan, Italy), F. Pâques (Romainville, France), S. Wolfe (Worcester, USA).
Registration deadline: August 6, 2010

W185917E

DIRECTOR: Transgenesis and Archiving of Animal Models Unit

The French National Centre for Scientific Research, CNRS, is seeking a new director for its service unit Transgenesis and Archiving of Animal Models, UPS44, (http://transgenose.cnrs-orleans.fr/eng/taam/presentation.php) located in Orleans (130km South of Paris). This research infrastructure is playing a major role providing an access to the mouse models of human disease and for fundamental research both at the French level (www.ibisa.net) and as a part of a distributed pan European infrastructure, Infrafrontier (www.infrafrontier.eu). The unit encompasses 3 departments devoted to Transgenesis, zootechnics and imaging with more than 73 highly qualified engineers and technicians. It participates actively in the European Mouse Mutant Archive (www.emmanet.org) and to the federation of International Mouse Resource (www.FIMRe.org)

The position of head is a higher-ranking appointment for a searcher, an engineer or an experienced project manager, reporting directly to the Institute of Biological Sciences (INSB) of the CNRS and backed by a strong commitment to excellence and investment in managing resource. This is a stimulating opportunity to join the unit and to be involved in the development of its activities both at the national, European and international levels. The director is responsible for leading a skilled and enthusiastic team and for developing state-of-the-art services for the scientific community. She/he will have an opportunity to develop her/his own research group in a dynamic environment with a privileged access to state-of-the-art mouse facility and services.

To meet these challenging tasks, the ideal candidate will have a vision of mouse genetics, strong leadership and be able to demonstrate commercial understanding. She or he should have a Ph.D. or Veterinarian degree, good experience, skills in management and the understanding of quality insurance. A strong background in mouse genetics would be an advantage. The ideal candidate will have innovative and creative ideas for the future development of the service units. A key aspect of this position is interacting with the scientific community. The successful candidates must therefore, be dynamic, outgoing, prepared to travel and have excellent management and personal skills.

If you need further information's please contact Dr. Yann Herault at herault@cnrs-orleans.fr.

To apply please send your CV, a summary of previous experience, details of your ongoing position, letter of motivation and name of 2-3 referees to Dr. Yann Herault by November 15th, 2009.

W186374R

ÉCOLE POLYTECHNIQUE FÉDÉRALE DE LAUSANNE

EPFL Center for Neuroprosthetics

Faculty Positions at the interface of Neuroscience and Bioengineering at Ecole polytechnique fédérale de Lausanne (EPFL)

The Institute of Bioengineering and the Brain-Mind Institute at EPFL invite applications for faculty positions at all ranks, from **tenure track assistant professor to full professor,** for the newly-launched **Center for Neuroprosthetics.** The Center, situated between the School of Engineering and the School of Life Sciences, seeks outstanding individuals working in (1) hearing, and (2) other areas of neuroprosthetics, such as invasive and non-invasive sensing and stimulation in restoration of motor control or sensory perception such as vision. The open faculty positions are offered in an environment of both theoretical and experimental research, rich for the development of novel enabling technologies as well as for seeking deeper understanding of fundamental mechanisms underlying the field of neuroprosthetics.

The School of Engineering and the Institute of Bioengineering offer strength in areas that include bio-MEMS/NEMS, bioelectronics, robotics and learning, integrated systems, biomaterials, biophotonics, molecular and computational systems biology, and stem cell biotechnology. The Brain-Mind Institute offers a broader context of neuroscience, with strengths in cognition, behavior, cellular and molecular neuroscience, computational neuroscience, and neurodegeneration, among others.

Excellent experimental infrastructure are available including core facilities in animal physiological and behavioral phenomics, animal and human imaging, quantitative light microscopy, genomics and proteomics, micro- and nano-fabrication, and electron microscopy and surface analysis.

Successful candidates are expected to initiate independent, creative research programs and participate in undergraduate and graduate teaching. Internationally competitive salaries, start-up resources and benefits are offered.

Applications should include a curriculum vitae with a list of publications, a concise statement of research and teaching interests, and the names and addresses (including e-mail) of at least five referees. Applications should be uploaded to:

http://neuroprosthetics-rec.epfl.ch

The deadline for applications is **1 February 2010.**

Enquiries may be addressed to:
Prof. Jeffrey A. Hubbell,
E-mail: neuroprosthetics-rec@epfl.ch

For additional information on EPFL, the Schools of Engineering and Life Sciences, the Institute of Bioengineering, and the Brain-Mind Institute, and Institute of Bioengineering, please consult the web sites: **http://www.epfl.ch, http://sti.epfl.ch, http://sv.epfl.ch, http://bmi.epfl.ch, and http://ibi.epfl.ch**

EPFL aims to increase the presence of women amongst its faculty, and qualified female candidates are strongly encouraged to apply.

W186250R

Have a look at our vacancies at

www.esrf.eu/jobs

- Scientists
- Post doctoral fellows
- PhDstudents
- Engineers
- Technicians
- Administrative staff

The European Synchrotron Radiation Facility (ESRF) is Europe's most powerful light source. The ESRF offers you an exciting opportunity to work with international teams using synchrotron light in Grenoble, in the heart of the French Alps.

Contact us at **recruitment@esrf.eu**

European Synchrotron Radiation Facility
BP 220, F-38043 Grenoble Cedex 9, FRANCE
Tel. +33 476 88 20 00
www. esrf.eu

A light for science ESRF

W186058R

L'Université d'Orléans

Ancrée dans le territoire, ouverte à l'international
Rooted in the region, open to the international world

FACULTY POSITION

The Biology Department of the University of Orleans, France, invites application for a faculty position at the full Professor level. The new faculty member will teach genetics at the university (in French) and join a research unit of CNRS, National Centre for Scientific Research (Molecular Immunology and Embryology, UMR6218) associated to a platform for Transgenesis and Animal Models (UPS44). The fully equipped research laboratories comprise experts in infectious diseases, lung inflammation, allergy and genetics.

The qualified candidate will have an established record of excellence in research and is expected to develop an independent research program in genetics or immunology.

Please be aware that you first need to register for Qualification before October 29, 2009, at: **https://galaxie.enseignement sup-recherche.gouv.fr/antares/can/index.jsp**

Candidates wishing more details should contact Valerie Quesniaux, Director **(quesniaux@cnrs-orleans.fr)** or Bernhard Ryffel (tel: +33 6 82 82 80 79).

Web: **http://transgenose.cnrs-orleans.fr/iem/**

DIRECTOR

Further, a Director position for the CNRS Service Unit UPS44 is open, who may develop his/her research project in UMR6218. Visit:

http://transgenose.cnrs-orleans.fr/eng/taam/presentation.php

W186262R

IN 2010
CNRS IS RECRUITING FOR

400 TENURED RESEARCHER POSITIONS IN ALL FIELDS OF SCIENCE

- MATHEMATICS • PHYSICS
- NUCLEAR AND HIGH-ENERGY PHYSICS
- CHEMISTRY
- SCIENCE AND TECHNOLOGY OF INFORMATION AND ENGINEERING
- UNIVERSE AND EARTH SCIENCE
- ENVIRONMENT AND SUSTAINABLE DEVELOPMENT
- LIFE SCIENCES • HUMANITIES AND SOCIAL SCIENCES

CNRS encourages junior and senior scientists from around the world to apply for its tenured researcher positions.

CNRS provides an enriching scientific environment:
- numerous large-scale facilities
- highly skilled technical support
- multiple international and interdisciplinary networks
- access to university research and teaching
- lab-to-lab and international mobility

Application from December 2, 2009 to January 5, 2010
www.cnrs.fr

W185858R

Institut Pasteur

A post doctoral position

founded by E.U. is open in the Pasteur Institute in Paris to carry out structural work on bacterial homologues of cys-loop receptors. The position will be equally shared between the "Channel-Receptors" group for protein production and the "Structural Dynamics of Macromolecules" unit for crystallization, synchrotron data collection and structure refinement. Expertise in crystallography is required, as well as the ability to work in collaboration. Knowledge in membrane protein biochemistry and/or in structural bioinformatics would be a plus.

Contact

Either Marc Delarue (delarue@pasteur.fr) or Pierre-Jean Corringer (pjcorrin@pasteur.fr)

W186127R

UNIVERSITÉ DE BORDEAUX Inserm

BERGONIE CANCER INSTITUTE POST-DOCTORAL FELLOWSHIPS

The INSERM unit at the Bergonié Cancer Institute in Bordeaux has open positions for two post-doctoral fellows to develop tumour models and to study the role of tumour-host interactions in the response to anticancer drugs (Farmer et al Nature Medicine 2009; Duss et al Breast Cancer Res 2007).

Applications with a CV and the names of two referees should be sent to iggo@bergonie.org. For more details see www.bergonie.org/en/basic-research/richard-iggo.html.

W186229R